

# AJNR

## AMERICAN JOURNAL OF NEURORADIOLOGY

DECEMBER 2013  
VOLUME 34  
NUMBER 12  
WWW.AJNR.ORG

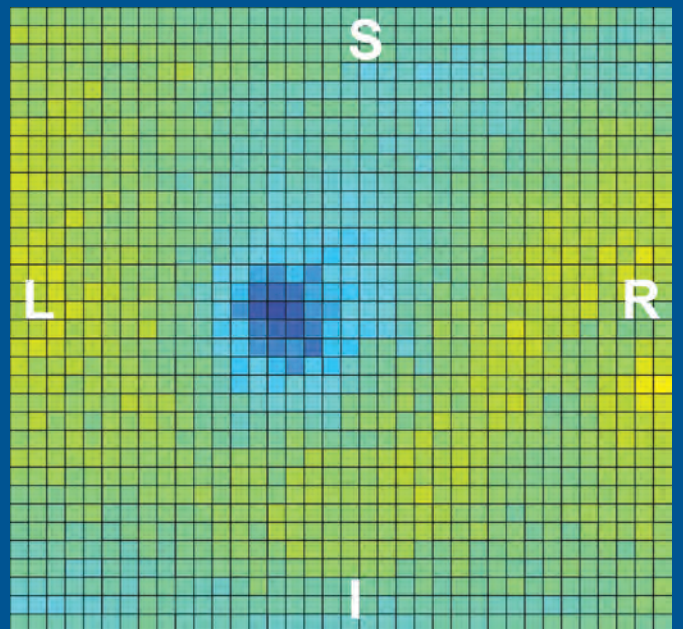
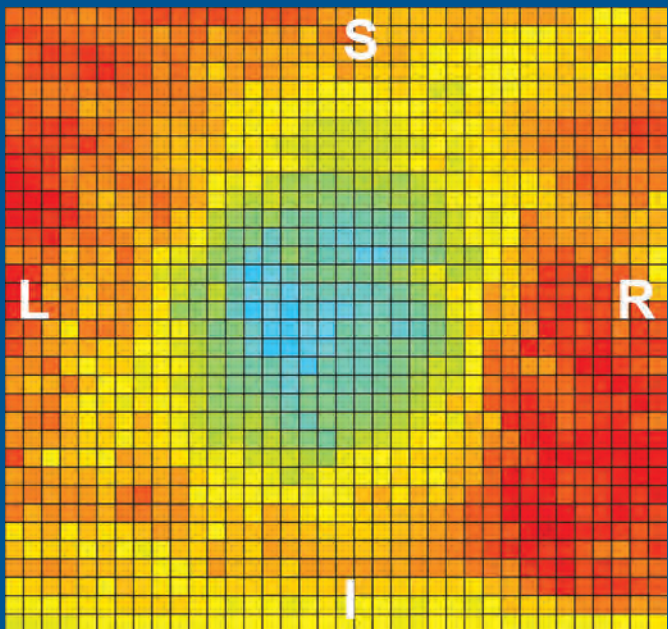
THE JOURNAL OF DIAGNOSTIC AND  
INTERVENTIONAL NEURORADIOLOGY

Imaging of symptomatic intracranial  
atherosclerotic plaques

Women and *apolipoprotein* carriers have  
higher rates of clinical decline

Imaging of surfer's myelopathy

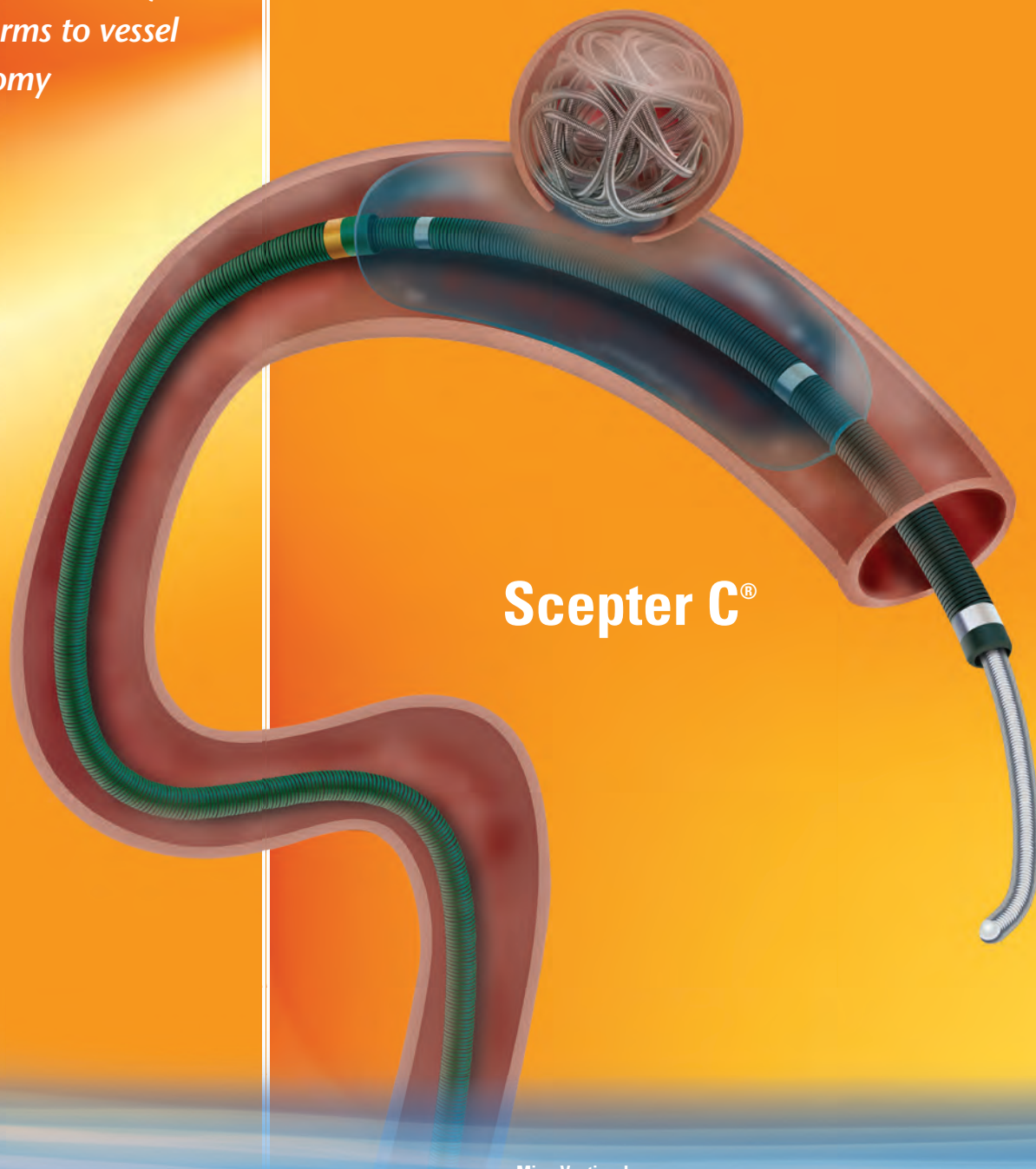
Official Journal ASNR • ASFNR • ASHNR • ASPNR • ASSR



**Scepter C<sup>®</sup>**  
Occlusion Balloon  
Catheter

**The New Standard of Excellence, Redefining**

*Compliant balloon  
designed for reliable  
vessel occlusion yet  
conforms to vessel  
anatomy*



**Scepter C<sup>®</sup>**

For more information or a product demonstration,  
contact your local MicroVention representative:

**MicroVention, Inc.**  
**Worldwide Headquarters**  
1311 Valencia Avenue  
Tustin, CA 92780 USA  
MicroVention United Kingdom  
MicroVention Europe, S.A.R.L.  
MicroVention Deutschland GmbH  
**Web**

PH +1.714.247.8000

PH +44 (0) 191 258 6777  
PH +33 (1) 39 21 77 46  
PH +49 211 210 798-0  
**microvention.com**

**Deliverability**

**Versatility** and **Control**

**Scepter XC**<sup>®</sup>  
Occlusion Balloon  
Catheter

### Occlusion Balloon with .014" Guidewire Compatibility

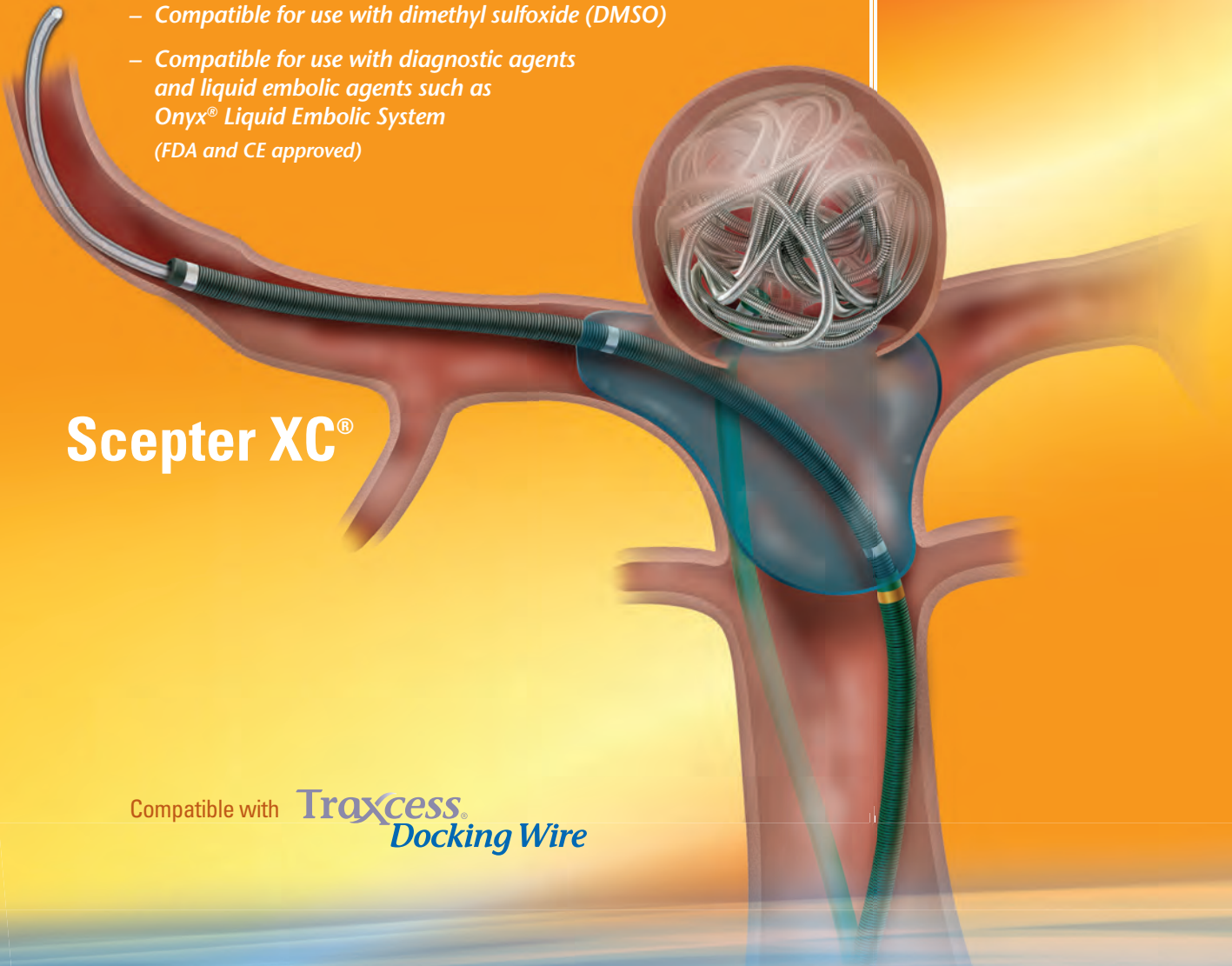
- Maximizing the utility of a unique coaxial shaft, Scepter Occlusion Balloon Catheter incorporates many new product features
- Balloon diameters range from 2mm to 6mm

### Key Compatible Agents

- Compatible for use with dimethyl sulfoxide (DMSO)
- Compatible for use with diagnostic agents and liquid embolic agents such as Onyx<sup>®</sup> Liquid Embolic System (FDA and CE approved)

*Xtra Compliant  
balloon conforms to  
extremely complex  
anatomies where  
neck coverage is  
more challenging*

**Scepter XC**<sup>®</sup>



Compatible with **Traxcess**<sup>®</sup>  
Docking Wire

CE  
0297

MICROVENTION, Scepter C, Scepter XC and Traxcess are registered trademarks of MicroVention, Inc. Onyx Liquid Embolic System is a registered trademark of Covidien. • Scientific and clinical data related to this document are on file at MicroVention, Inc. Refer to Instructions for Use for additional information. Federal (USA) law restricts this device for sale by or on the order of a physician. © 2013 MicroVention, Inc. 10/13

 **MicroVention**<sup>®</sup>  
**TERUMO**



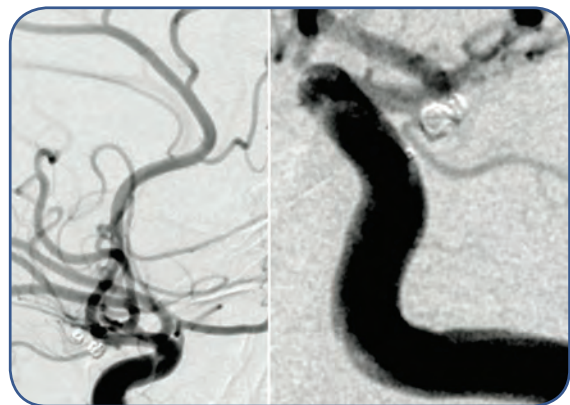
# BARRICADE™ COIL SYSTEM

## PERFORMANCE DELIVERED

SATOSHI TATESHIMA, M.D. | LONG BEACH MEMORIAL HOSPITAL | LONG BEACH, CALIFORNIA



PRE-TREATMENT



POST-TREATMENT

- ◆ Male patient in early 30's presented with Hunt and Hess Grade 1 subarachnoid hemorrhage
- ◆ Posteriorly projecting ruptured ICA Terminus-ACA A1 Aneurysm (2.7x2mm with a 1.8mm neck) and unruptured ICA Anterior Choroidal Artery Aneurysm (4.5x5mm with a 4mm neck)
- ◆ Each aneurysm successfully treated with 2 Barricade Coils

“The Barricade Coil provided me with great control and I was very impressed with the softness of the finishing coils.”

SATOSHI TATESHIMA, M.D.



**BLOCKADE**  
M E D I C A L

18 TECHNOLOGY DRIVE #169, IRVINE CA 92618  
P 949.788.1443 | 888.712.3502 | F 949.788.1444  
[WWW.BLOCKADEMEDICAL.COM](http://WWW.BLOCKADEMEDICAL.COM)



CE  
0297  
MKTG-029 REV. A



# AJNR

## AMERICAN JOURNAL OF NEURORADIOLOGY

DECEMBER 2013  
VOLUME 34  
NUMBER 12  
WWW.AJNR.ORG

Publication Preview at [www.ajnr.org](http://www.ajnr.org) features articles released in advance of print. Visit [www.ajnrblog.org](http://www.ajnrblog.org) to comment on AJNR content and chat with colleagues and AJNR's News Digest at <http://ajnrdigest.org> to read the stories behind the latest research in neuroimaging.

### EDITORIAL

#### PERSPECTIVES

- 2223 **iConsent** *M. Castillo*

#### REVIEW ARTICLES

- 2225 **Clinical Semiology and Neuroradiologic Correlates of Acute Hyponatremic Osmotic Challenge in Adults: A Literature Review** *F.Y. Ismail, A. Szóllics, M. Szólics, N. Nagelkerke, and M. Ljubisavljevic*
- 2233 **Illustrated Review of the Embryology and Development of the Facial Region, Part 1: Early Face and Lateral Nasal Cavities** *P.M. Som and T.P. Naidich*

#### RESEARCH PERSPECTIVES

- 2241 **Hot Topics in Functional Neuroradiology** *S.H. Faro, F.B. Mohamed, J.A. Helpert, J.H. Jensen, K.R. Thulborn, I.C. Atkinson, H.I. Sair, and D.J. Mikulis*

#### GENETICS VIGNETTE

- 2250 **Neurofibromatosis: Types 1 and 2** *S. Borofsky and L.M. Levy*

#### BRAIN

- 2252 **T1 Gadolinium Enhancement of Intracranial Atherosclerotic Plaques Associated with Symptomatic Ischemic Presentations** *P. Vakil, J. Vranic, M.C. Hurley, R.A. Bernstein, A.W. Korutz, A. Habib, A. Shaibani, F.H. Dehkordi, T.J. Carroll, and S.A. Ansari*
- 2259 **Intracranial-Derived Atherosclerosis Assessment: An In Vitro Comparison between Virtual Histology by Intravascular Ultrasonography, 7T MRI, and Histopathologic Findings** *S. Majidi, J. Sein, M. Watanabe, A.E. Hassan, P.-F. Van de Moortele, M.F.K. Suri, H.B. Clark, and A.I. Qureshi*
- 2265 **Automated White Matter Total Lesion Volume Segmentation in Diabetes** *J.A. Maldjian, C.T. Whitlow, B.N. Saha, G. Kota, C. Vandergriff, E.M. Davenport, J. Divers, B.I. Freedman, and D.W. Bowden*
- 2271 **Potential Role of Preoperative Conventional MRI Including Diffusion Measurements in Assessing Epidermal Growth Factor Receptor Gene Amplification Status in Patients with Glioblastoma** *R.J. Young, A. Gupta, A.D. Shah, J.J. Graber, A.D. Schweitzer, A. Prager, W. Shi, Z. Zhang, J. Huse, and A.M.P. Omuro*
- 2278 **Prediction of Pseudoprogression in Patients with Glioblastomas Using the Initial and Final Area Under the Curves Ratio Derived from Dynamic Contrast-Enhanced T1-Weighted Perfusion MR Imaging** *C.H. Suh, H.S. Kim, Y.J. Choi, N. Kim, and S.J. Kim*

★ Indicates Editor's Choices selection

📖 Indicates Fellows' Journal Club selection

🔑 Indicates open access to non-subscribers at [www.ajnr.org](http://www.ajnr.org)

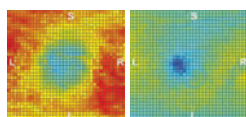
📄 Indicates article with supplemental on-line table

📷 Indicates article with supplemental on-line photo

📺 Indicates article with supplemental on-line video

EBM 1 Indicates Evidence-Based Medicine Level 1

EBM 2 Indicates Evidence-Based Medicine Level 2



Automatic quantitative maps of mild and severe optic nerve protrusion are useful in predicting papilledema and treatment response in intracranial hypertension.

# ASNR 52<sup>ND</sup> ANNUAL MEETING & THE FOUNDATION OF THE ASNR SYMPOSIUM 2014

MAY 17-22 | Montreal ■ Palais des congrés de Montreal

ASNR 2014 PROGRAM CHAIR/PRESIDENT-ELECT - Gordon K. Sze, MD, FACR

THE FOUNDATION OF THE ASNR



## The Foundation of the ASNR Symposium 2014: Inflammatory and Infectious Diseases of the CNS

### SYMPOSIUM 2014:

- The Role of Inflammation and Infections in Stroke, Seizures, White Matter Diseases, etc.
- Advanced Imaging Techniques in the Evaluation of Inflammatory CNS Diseases
- Infectious Agents for Human Good: Oncolytic Viruses, Viral Vector Gene Therapy and Advanced Imaging

### ADDITIONAL NEW EDUCATIONAL COURSE PROGRAM IN 2014 (concurrent program with the Symposium 2014): Inflammatory and Infectious Diseases

#### EDUCATIONAL COURSE 2014: with world class speakers including

- Anne G. Osborn, MD, Thomas P. Naidich, MD, Donald Resnick, MD, James G. Smirniotopoulos, MD, Jeffrey S. Ross, MD, Kelly K. Koeller, MD, FACR, David M. Yousem, MD, MBA, Laurie A. Loevner, MD, Peter M. Som, MD, Patricia A. Hudgins, MD, Robert D. Zimmerman MD, FACR, Hugh D. Curtin, MD, M. Judith Donovan Post, MD, FACR, and More...

### ANNUAL MEETING:

- One-day **MINI SYMPOSIUM on STROKE** - Organized by Pina C. Sanelli, MD, MPH and Max Wintermark, MD
- One-day **MINI SYMPOSIUM on TUMORS** - Organized by Girish M. Fatterpekar, MD, MBBS, DNB, Whitney B. Pope, MD, PhD and Gordon K. Sze, MD, FACR
- Nobel Prize Laureate, Stanley Prusiner, MD, Keynote Speaker, on Prions and Alzheimer's Disease, Parkinson's Disease, and Other Neurodegenerative Disorders
- More "Hands-On" Experience Applicable to Your Practices
- Young Professionals Programming
- Expanded Self-Assessment Module (SAM) Session Programming Throughout the Week

### PROGRAMMING DEVELOPED IN COOPERATION WITH THE...

- American Society of Functional Neuroradiology (ASFNR) David J. Mikulis, MD
- American Society of Head and Neck Radiology (ASHNR) Yoshimi Anzai, MD, MPH
- American Society of Pediatric Neuroradiology (ASPNR) Richard L. Robertson, MD
- American Society of Spine Radiology (ASSR) Meng Law, MD, MBBS, FRACR
- Society of NeuroInterventional Surgery (SNIS) Peter A. Rasmussen, MD



ASFNR ASHNR ASPNR ASSR SNIS

TO REQUEST PROGRAMMING AND REGISTRATION MATERIALS FOR THE ASNR 52<sup>ND</sup> ANNUAL MEETING, CONTACT:

#### ASNR 52<sup>ND</sup> ANNUAL MEETING

c/o American Society of Neuroradiology  
800 Enterprise Drive, Suite 205  
Oak Brook, Illinois 60523-4216

Phone: 630-574-0220  
Fax: 630-574-0661  
Email: [meetings@asnr.org](mailto:meetings@asnr.org)  
Website: [www.asnr.org/2014](http://www.asnr.org/2014)



Scan Now  
to visit our website

-    **2287 Higher Rates of Decline for Women and *Apolipoprotein E* ε4 Carriers**  
*D. Holland, R.S. Desikan, A.M. Dale, and L.K. McEvoy, for the Alzheimer's Disease Neuroimaging Initiative*
-  **2294 Changes of Pituitary Gland Volume in Kennedy Disease** *C.C. Pieper, I.K. Teismann, C. Konrad, W.L. Heindel, and H. Schiffbauer*
-  **2298 Stroke-Like Migraine Attacks after Radiation Therapy (SMART) Syndrome Is Not Always Completely Reversible: A Case Series** *D.F. Black, J.M. Morris, E.P. Lindell, K.N. Krecke, G.A. Worrell, J.D. Bartleson, and D.H. Lachance*

### FUNCTIONAL

-  **2304 Sex Differences in Resting-State Functional Connectivity in Multiple Sclerosis** *K.A. Koenig, M.J. Lowe, J. Lin, K.E. Sakaie, L. Stone, R.A. Bermel, E.B. Beall, S.M. Rao, B.D. Trapp, and M.D. Phillips*

**INTERVENTIONAL** *Published in collaboration with  
Interventional Neuroradiology*

-   **2312 Reduced Mortality and Severe Disability Rates in the SENTIS Trial**  
*P.D. Schellinger, A. Shuaib, M. Köhrmann, D.S. Liebeskind, T. Jovin, M.D. Hammer, S. Sen, D.Y. Huang, S. Solander, R. Gupta, R.R. Leker, and J.L. Saver, for the SENTIS Trial Investigators*
-   **2317 Endovascular Treatment of Distal Anterior Cerebral Artery Aneurysms: Single-Center Experience and a Systematic Review** *C.L. Sturiale, W. Brinjikji, M.H. Murad, H.J. Cloft, D.F. Kallmes, and G. Lanzino*
-  **2321 Incidence of Microemboli and Correlation with Platelet Inhibition in Aneurysmal Flow Diversion** *M.R. Levitt, B.V. Ghodke, D.K. Hallam, L.N. Sekhar, and L.J. Kim*
- 2326 Spontaneous Delayed Migration/Shortening of the Pipeline Embolization Device: Report of 5 Cases** *N. Chalouhi, S.I. Tjoumakaris, L.F. Gonzalez, D. Hasan, P.J. Pema, G. Gould, R.H. Rosenwasser, and P.M. Jabbour*

### EXTRACRANIAL VASCULAR

-   **2331 CTA for Screening of Complicated Atherosclerotic Carotid Plaque—American Heart Association Type VI Lesions as Defined by MRI**  
*M. Trelles, K.M. Eberhardt, M. Buchholz, A. Schindler, A. Bayer-Karpinska, M. Dichgans, M.F. Reiser, K. Nikolaou, and T. Saam*

### HEAD & NECK

-   **2338 CT Perfusion Can Predict Overexpression of CXCL8 (Interleukin-8) in Head and Neck Squamous Cell Carcinoma** *S.Y. Jo, P.I. Wang, J.E. Nör, E.L. Bellile, Z. Zhang, F.P. Worden, A. Srinivasan, and S.K. Mukherji*
-  **2343 Differentiation of Recurrent Tumor and Posttreatment Changes in Head and Neck Squamous Cell Carcinoma: Application of High b-Value Diffusion-Weighted Imaging** *I. Hwang, S.H. Choi, Y.-J. Kim, K.G. Kim, A.L. Lee, T.J. Yun, J.-h. Kim, and C.-H. Sohn*
- 2349 Optimized Cutoff Value and Indication for Washout Thyroglobulin Level According to Ultrasound Findings in Patients with Well-Differentiated Thyroid Cancer** *J.Y. Jung, J.H. Shin, B.-K. Han, and E.Y. Ko*
-  **2354 Automated Quantitation of the Posterior Scleral Flattening and Optic Nerve Protrusion by MRI in Idiopathic Intracranial Hypertension**  
*N. Alperin, A.M. Bagci, B.L. Lam, and E. Sklar*

### PEDIATRICS

-   **2360 Diffusion MRI Improves the Accuracy of Preoperative Diagnosis of Common Pediatric Cerebellar Tumors among Reviewers with Different Experience Levels** *K. Koral, S. Zhang, L. Gargan, W. Moore, B. Garvey, M. Fiesta, M. Seymour, L. Yang, D. Scott, and N. Choudhury*

## Call for *AJNR* Editorial Fellowship Candidates

ASNR and *AJNR* are pleased once again in 2014 to join efforts with other imaging-related journals that have training programs on editorial aspects of publishing for trainees or junior staff (3–5 years after training) such as *Radiology* (Olmsted fellowship), *AJR* (Figley and Rogers fellowships [USA and international respectively]), and *Radiologia* (from Spain).

### Goals:

1. Increase interest in “editorial” and publication-related activities in younger individuals.
2. Increase understanding and participation in the *AJNR* review process.
3. Incorporate into *AJNR*’s Editorial Board younger individuals who have previous experience in the review and publication process.
4. Fill a specific need in neuroradiology not offered by other similar fellowships.
5. Increase the relationship between “newer” generations of neuroradiologists and more established individuals.
6. Increase visibility of *AJNR* among younger neuroradiologists.

### Activities of the Fellowship:

1. Serve as “Editorial Fellow” for one year. This individual will be listed on the masthead as such and will receive a certificate stating his/her activities at the end of the service period.
2. Review at least one manuscript per month for 12 months. Evaluate all review articles submitted to *AJNR*. Access to our electronic manuscript review system will be granted so that the candidate can learn how these systems work.
3. Be involved in the final decision of selected manuscripts together with the EIC.
4. Participate in all monthly telephone Senior Editor conference calls.
5. Participate in all meetings of the Editors and Publications Committee during the annual meetings of ASNR and RSNA as per candidate’s availability. *AJNR*/ASNR will not provide funding for this activity but may offer a discounted fee for its annual meeting.
6. Evaluate progress and adjust program to specific needs in biannual meeting or telephone conference with the EIC.
7. Write at least one editorial for *AJNR*.
8. Embark on an editorial scientific or bibliometric project that will lead to the submission of an article to *AJNR* or another appropriate journal as determined by *AJNR*’s EIC. This project can be done in conjunction with the EIC or one of the Senior Editors.
9. Serve as liaison between *AJNR* and ASNR’s Young Professionals Network and the 3 YPs appointed to *AJNR* as special consultants. Participate in meetings and telephone calls with this group. Design one electronic survey/year polling the group regarding readership attitudes and wishes.
10. Recruit trainees as reviewers as determined by the EIC.
11. Participate in Web improvement projects.
12. Potentially become a member of *AJNR*’s Editorial Board at the end of the fellowship.
13. Invite Guest Editors for *AJNR*’s News Digest to cover a variety of timely topics.

### Qualifications:

1. Be a fellow in neuroradiology from North America, including Canada (this may be extended to include other countries).
2. Be a junior faculty neuroradiology member (<3 years) in either an academic and private environment.
3. Provide an “end” of fellowship report to *AJNR*’s EIC and ASNR’s Publications Committee.
4. Be an “in-training” or member of ASNR in any other category.

### Application:

1. Include a short letter of intent with statement of goals and desired research project. CV must be included.
2. Include a letter of recommendation from the Division Chief or fellowship program director. A statement of protected time to perform the functions outlined is desirable.
3. Applications will be evaluated by *AJNR*’s Senior Editors and the Chair of the Publications Committee prior to the ASNR meeting. The name of the selected individual will be announced at the meeting.
4. Applications should be received by March 3, 2014 and sent to Ms. Karen Halm, *AJNR* Managing Editor, electronically at [khalm@asnr.org](mailto:khalm@asnr.org).

- ★ ☰ 2366 **No Evidence for Impairment of Venous Hemodynamics in Children or Young Adults with Pediatric-Onset Multiple Sclerosis** *S. Laughlin, C.K. Macgowan, J. Traubici, K. Chan, S. Khan, D.L. Arnold, R.A. Marrie, and B. Banwell*
- ☰ 2373 **Prevalence of Subdural Collections in Children with Macrocrania** *M.V. Greiner, T.J. Richards, M.M. Care, and J.L. Leach*
- 🔑 2379 **White Matter Microstructural Abnormality in Children with Hydrocephalus Detected by Probabilistic Diffusion Tractography** *A. Rajagopal, J.S. Shimony, R.C. McKinstry, M. Altay, T. Maloney, F.T. Mangano, D.D. Limbrick, S.K. Holland, B.V. Jones, S. Simpson, D. Mercer, and W. Yuan*
- ☰ 2386 **Abnormal Functional Network Connectivity among Resting-State Networks in Children with Frontal Lobe Epilepsy** *E. Widjaja, M. Zamyadi, C. Raybaud, O.C. Snead, and M.L. Smith*

#### SPINE

- ☰ 2393 **Surfer's Myelopathy: A Radiologic Study of 23 Cases** *B.K. Nakamoto, A.M. Siu, K.A. Hashiba, B.T. Sinclair, B.J. Baker, M.S. Gerber, A.M. McMurtray, A.M. Pearce, and J.W. Pearce*
- 2399 **Evaluation of the Intervertebral Disk Angle for the Assessment of Anterior Cervical Diskoligamentous Injury** *L.M. Alhilali and S. Fakhran*

#### ONLINE FEATURES ([www.ajnr.org](http://www.ajnr.org))

#### LETTERS

- E128 **Can We Perform <sup>1</sup>H-MR Spectroscopy in Daily Clinical Practice?**  
*L.C. Hygino da Cruz Jr*
- E130 **Reply** *A. Hock, A. Henning, and S.S. Kollias*

#### BOOK REVIEWS *R.M. Quencer, Section Editor*

Please visit [www.ajnrblog.org](http://www.ajnrblog.org) to read and comment on Book Reviews.

Publication Preview at [www.ajnr.org](http://www.ajnr.org) features articles released in advance of print. Visit [www.ajnrblog.org](http://www.ajnrblog.org) to comment on AJNR content and chat with colleagues and AJNR's News Digest at <http://ajnrdigest.org> to read the stories behind the latest research in neuroimaging.

DECEMBER 2013 • VOLUME 34 • NUMBER 12 • WWW.AJNR.ORG

### Official Journal:

American Society of Neuroradiology  
American Society of Functional Neuroradiology  
American Society of Head and Neck Radiology  
American Society of Pediatric Neuroradiology  
American Society of Spine Radiology

### EDITOR-IN-CHIEF

#### Mauricio Castillo, MD

Professor of Radiology and Chief, Division of Neuroradiology, University of North Carolina, School of Medicine, Chapel Hill, North Carolina

### SENIOR EDITORS

#### Harry J. Cloft, MD, PhD

Professor of Radiology and Neurosurgery, Department of Radiology, Mayo Clinic College of Medicine, Rochester, Minnesota

#### Nancy J. Fischbein, MD

Professor of Radiology, Otolaryngology-Head and Neck Surgery, Neurology, and Neurosurgery and Chief, Head and Neck Radiology, Department of Radiology, Stanford University Medical Center, Stanford, California

#### Lucien M. Levy, MD, PhD

Professor of Radiology, Chief and Program Director of Neuroradiology, George Washington University Medical Center, Washington, DC

#### Jeffrey S. Ross, MD

Staff Neuroradiologist, Barrow Neurological Institute, St. Joseph's Hospital, Phoenix, Arizona

#### Pamela W. Schaefer, MD

Clinical Director of MRI and Associate Director of Neuroradiology, Massachusetts General Hospital, Boston, Massachusetts, and Associate Professor, Radiology, Harvard Medical School, Cambridge, Massachusetts

#### Charles M. Strother, MD

Professor of Radiology, Emeritus, University of Wisconsin, Madison, Wisconsin

### EDITORIAL BOARD

Ashley H. Aiken, Atlanta, Georgia  
A. James Barkovich, San Francisco, California  
Walter S. Bartynski, Charleston, South Carolina  
Barton F. Branstetter IV, Pittsburgh, Pennsylvania  
Jonathan L. Brisman, Lake Success, New York  
Julie Bykowski, San Diego, California  
Donald W. Chakeres, Columbus, Ohio  
Alessandro Cianfoni, Lugano, Switzerland  
Colin Derdeyn, St. Louis, Missouri  
Rahul S. Desikan, San Diego, California  
Richard du Mesnil de Rochemont, Frankfurt, Germany  
Clifford J. Eskey, Hanover, New Hampshire  
Massimo Filippi, Milan, Italy  
David Fiorella, Cleveland, Ohio  
Allan J. Fox, Toronto, Ontario, Canada  
Christine M. Glastonbury, San Francisco, California  
John L. Go, Los Angeles, California  
Wan-Yuo Guo, Taipei, Taiwan  
Rakesh K. Gupta, Lucknow, India  
Lotfi Hacein-Bey, Sacramento, California  
David B. Hackney, Boston, Massachusetts  
Christopher P. Hess, San Francisco, California  
Andrei Holodny, New York, New York  
Benjamin Huang, Chapel Hill, North Carolina  
Thierry A.G.M. Huisman, Baltimore, Maryland  
George J. Hunter, Boston, Massachusetts  
Mahesh V. Jayaraman, Providence, Rhode Island  
Valerie Jewells, Chapel Hill, North Carolina  
Timothy J. Kaufmann, Rochester, Minnesota  
Kenneth F. Layton, Dallas, Texas  
Ting-Yim Lee, London, Ontario, Canada  
Michael M. Lell, Erlangen, Germany  
Michael Lev, Boston, Massachusetts  
Karl-Olof Lovblad, Geneva, Switzerland  
Lisa H. Lowe, Kansas City, Missouri  
Franklin A. Marden, Chicago, Illinois  
M. Gisele Matheus, Charleston, South Carolina  
Joseph C. McGowan, Merion Station, Pennsylvania  
Kevin R. Moore, Salt Lake City, Utah  
Christopher J. Moran, St. Louis, Missouri  
Takahisa Mori, Kamakura City, Japan

Suresh Mukherji, Ann Arbor, Michigan  
Amanda Murphy, Toronto, Ontario, Canada  
Alexander J. Nemeth, Chicago, Illinois  
Laurent Pierot, Reims, France  
Jay J. Pillai, Baltimore, Maryland  
Whitney B. Pope, Los Angeles, California  
M. Judith Donovan Post, Miami, Florida  
Tina Young Poussaint, Boston, Massachusetts  
Joana Ramalho, Lisbon, Portugal  
Otto Rapalino, Boston, Massachusetts  
Álex Rovira-Cañellas, Barcelona, Spain  
Paul M. Ruggieri, Cleveland, Ohio  
Zoran Rumboldt, Charleston, South Carolina  
Amit M. Saindane, Atlanta, Georgia  
Erin Simon Schwartz, Philadelphia, Pennsylvania  
Aseem Sharma, St. Louis, Missouri  
J. Keith Smith, Chapel Hill, North Carolina  
Maria Vittoria Spampinato, Charleston, South Carolina  
Gordon K. Sze, New Haven, Connecticut  
Krishnamoorthy Thamburaj, Hershey, Pennsylvania  
Kent R. Thielen, Rochester, Minnesota  
Cheng Hong Toh, Taipei, Taiwan  
Thomas A. Tomsick, Cincinnati, Ohio  
Aquila S. Turk, Charleston, South Carolina  
Willem Jan van Rooij, Tilburg, Netherlands  
Arastoo Vossough, Philadelphia, Pennsylvania  
Elysa Widjaja, Toronto, Ontario, Canada  
Max Wintermark, Charlottesville, Virginia  
Ronald L. Wolf, Philadelphia, Pennsylvania  
Kei Yamada, Kyoto, Japan

### EDITORIAL FELLOW

Falgun H. Chokshi, Atlanta, Georgia

### YOUNG PROFESSIONALS ADVISORY COMMITTEE

Asim K. Bag, Birmingham, Alabama  
Anna E. Nidecker, Sacramento, California  
Peter Yi Shen, Sacramento, California

### HEALTH CARE AND SOCIOECONOMICS EDITOR

Pina C. Sanelli, New York, New York

Founding Editor

Juan M. Taveras

Editors Emeriti

Robert I. Grossman, Michael S. Huckman,  
Robert M. Quencer

Special Consultants to the Editor

Sandy Cheng-Yu Chen, Girish Fatterpekar,  
Ryan Fitzgerald, Yvonne Lui,  
Louise M. Henderson, Greg Zaharchuk

INR Liaisons

Timo Krings, Karel terBrugge

Managing Editor

Karen Halm

Electronic Publications Manager

Jason Gantenberg

Editorial Assistant

Mary Harder

Executive Director, ASNR

James B. Gantenberg

Director of Communications, ASNR

Angelo Artemakis

AJNR (Am J Neuroradiol ISSN 0195-6108) is a journal published monthly, owned and published by the American Society of Neuroradiology (ASNR), 800 Enterprise Drive, Suite 205, Oak Brook, IL 60523. Annual dues for the ASNR include \$170.00 for journal subscription. The journal is printed by Cadmus Journal Services, 5457 Twin Knolls Road, Suite 200, Columbia, MD 21045; Periodicals postage paid at Oak Brook, IL and additional mailing offices. Printed in the U.S.A. POSTMASTER: Please send address changes to American Journal of Neuroradiology, P.O. Box 3000, Denville, NJ 07834, U.S.A. Subscription rates: nonmember \$370 (\$440 foreign) print and online, \$300 online only; institutions \$430 (\$495 foreign) print and basic online, \$850 (\$915 foreign) print and extended online, \$355 online only (basic), extended online \$770; single copies are \$35 each (\$40 foreign). Indexed by PubMed/Medline, BIOSIS Previews, Current Contents (Clinical Medicine and Life Sciences), EMBASE, Google Scholar, HighWire Press, Q-Sensei, RefSeek, Science Citation Index, and SCI Expanded. Copyright © American Society of Neuroradiology.



## iConsent

M. Castillo, *Editor-in-Chief*

In medicine, a “consent form” is the legal instrument through which we must give our patients sufficient information (positive, such as benefits, and negative, such as risks and complications) regarding any treatment or procedure they will receive. The idea behind it is that an informed patient can accept or more importantly decline a treatment (for personal and/or religious reasons) even if the physician disagrees with this decision. The key word here is “physician.” A consent form, under most circumstances, must be administered only by a full-fledged physician, never a medical student, nurse, or technologist. The attending physician can (and does in many academic centers) delegate obtaining consent to a resident or fellow (who already is an MD). In the United States, minors cannot give consent and their parents or legal guardians must give it.\* Patients in extreme emergency situations and those with limited cognition are exceptions; and when no family member or legal guardian is available, 1 or more physicians may sign the patient’s consent form. As we get older and move into specialized care institutions far away from our families, the caregiver may consent to emergency treatments. The Caregiver Consent Form must be prepared in advance; a lawyer is not needed in the decision making process. For parentless children, a similar form can be used. Consent forms from parents, grandparents, and others are available in most large institutions.

The most common consent form used is, however, the generic one. Regardless of their specifics, all consent forms must meet certain minimum legal standards. Any impairment of reasoning faculties and/or judgment (including previous sedation) makes it impossible (and illegal) to administer the consent form, regardless of its type. Waivers of consent may also be obtained and are not uncommonly used by large institutions such as the Army when a treatment involves minimal risk, benefits the patient, advances medicine, and is carried out under laws established by the US Food and Drug Administration.<sup>1</sup> The need for consent is so ever-present that there are commercial companies that specialize in designing and administering these forms.

Access to the Internet and medical knowledge has considerably changed many aspects of consent. Until a few decades ago, medical treatment was administered following the concept that “doctors know better.” This idea originated in Greece and follows the precepts of the Hippocratic Oath.<sup>2</sup> Many of us become irritated when patients try to steer their treatments (coil embolization versus clipping of intracranial aneurysms is a typical example) on the basis of information found on the Internet because we have been brought up to believe in the Hippocratic Oath (ie, we know better). This concept did not really change until the 18th century, when doctors began to believe that sharing as much in-

formation as possible with patients was beneficial, but in the end, physicians always made the most important and final decisions. The idea the “doctor knows better” has been called “benevolent deception,” and it has been fought against since the mid-1800s. In the United States, the most important aspect of consent is “what is being said” rather than “who is saying it” and “where it is being said” (this may not be the case in other cultures and countries).

As we now know it, the consent form is a recent invention and stems from the consequences of various unethical (to say the least) situations during and around World War II. After the war trials against illegal human experiments by Nazi physicians, the Council for War Crimes published the “Nuremberg Code.”<sup>3</sup> This set of rules defines legitimate medical research and is accepted by the Declaration of Helsinki and the US Department of Health and Human Services and is incorporated into the law in many states and countries. One of the most important aspects of the “Nuremberg Code” is informed consent without coercion. Violations of the Code continued after the War even in the United States. Perhaps the best known is the “Tuskegee Syphilis Experiment.”<sup>4</sup> This experiment (if one can call it that) extended for 40 years (up to 1972) and was “administered” by the US Public Health Service in Tuskegee, Alabama. In it, the natural progression of syphilis was assessed while infected patients thought they were getting the appropriate medical treatment. Six hundred poor African American agricultural workers were recruited, and 400 who had syphilis went untreated (they were given free burial insurance by the government). Remember that 15 years after the beginning of the “experiment,” there was irrefutable scientific evidence that penicillin (widely available by then) was the standard treatment for syphilis. Although this is not the only occasion of human rights violations, it is certainly the most infamous one, and in 1978, it led to the “Belmont Report,” which sets the guidelines for the protection of subjects in clinical and research trials in health care.<sup>5</sup> The report led to the creation of the Office for Human Research Protections and Institutional Review Boards (IRBs) in medical schools, academic centers, and hospitals.

IRBs are decentralized committees that review and monitor biomedical research in humans. IRBs themselves are overseen by the Office for Human Research Protections. Before becoming an IRB member at any institution, any conflict of interest (such as working for the industry as a consultant) must be disclosed. IRBs must comprise at least 5 experienced individuals (both male and female), have representatives of different professions (scientists versus nonscientists), and include community members.<sup>6</sup> All research projects and, in many institutions, all publications must be granted permission by an IRB. These IRBs approve research projects only when bona fide consent will be obtained from all participants. When the project is closed, most IRBs require notification and summary of the results.

Most of us who have been (or are) involved in research know how difficult and lengthy the process of IRB approval is. Many blame the relative decline of US research on this while other coun-

<http://dx.doi.org/10.3174/ajnr.A3426>

tries with less complex approval processes are making headway in research. To ease the process, many IRBs offer exemptions. In medicine, the most common exemption is for research that involves the analysis of already-existing data as long as the identities of the subjects are protected. For this, some IRBs have special shorter forms while others demand that their long forms be completed. For most exemptions, consent from individual subjects is not required. The problem with IRBs is that data obtained from patients are so closely guarded that access is not available to other researchers who would benefit from them. Just try getting your own data after participating in a research project that has been completed. Even worse, try getting your own medical record released. The owner of the medical record is not the patient but the health service provider who created it, and similarly, the owner of data collected during research is the institution or company funding the project and not the subjects.

Research data are kept in “information silos” understandably guarded from prying eyes but also fragmented. Similar to grain silos that house one type of product, data collected are mined only for proving or disproving a specific hypothesis, and all other information contained in the silo is not used. In this era of fast computing, data transfer, and crowdsourcing and sharing, this process may not be the best way to advance science. “Open source” medicine and research are coming our way, and we need to adapt more than our consent forms to take advantage of them. Apple (Cupertino, California) and Google (Mountain View, California) already keep track of an enormous amount of personal data; Microsoft (Bothell, Washington) keeps track of all data transmitted by using their products such as Outlook for e-mail and calendars. Very soon, science will not survive without data-sharing, integration, and networking. It could be that the consent form that was created to protect us is now, in its current form, detrimental to science.

John Wilbanks has created the WeConsent.us Web site and data base (<http://weconsent.us/>).<sup>7</sup> Mr Wilbanks said, “All too many observations lie isolated and forgotten on personal hard drives and CDs, trapped by technical, legal and cultural barriers.” A critical and innovative aspect of this idea is the use of a special consent form that states that if kept anonymously, your (and my) medical data (particularly health and genomics) can be used by third parties as long as our identity remains protected. This consent is called a “Portable Legal Consent” because you carry it with you, and you attach it (thus its portability) to any data you want to donate. Think about it as having a consent form in your iPhone (Apple) and electronically transmitting it when you need. Personally, I would not mind sharing my medical data if my identity is protected, but I cannot do this because I do not own it! Mr Wilbanks stated that we need to move from information silos to “information commons.”

Vanderbilt University (in collaboration with Northwestern University) has started a DNA biorepository and combining it with electronic medical records, an information commons expected to shed light on diabetes, Alzheimer disease, and heart disease is being built.<sup>8</sup> When asked, nearly 95% of patients state that they would be willing to share their medical data.<sup>9</sup> Applications for the iPhone (ie, MyMedical) that allow you to keep your own medical record and share all or parts of it are available. The Eatery application allows you to photograph what you eat and share it (anonymously) with other users to try to improve your eating habits. The goal of the WeConsent.us Web site is to get 100,000 individuals in its first year (and 1 million in 5 years) to donate their medical data, which will then be available for analysis by mathematicians and other scientists.

The future of medical research lies in its power, and its power lies in numbers. However, this power can only be realized if we own our data and we consent to share it. Data accumulated with time do not have to wait to be uploaded and shared but should be dynamically shared in real time. Imagine carrying your own consent form in your mobile device and attaching it to newly available data that you can share when you want to. This consent form could be malleable and would adapt to different needs and situations, taking advantage of the incredible interaction possible on the Web. I think that the time for the iConsent is here.

\*In other countries (especially England), the Gillick standard states that a child younger than 16 years of age may, under certain circumstances, be judged mature enough to consent.<sup>10</sup>

## REFERENCES

1. McManus J, Mehta SG, McClinton AR, et al. **Informed consent and ethical issues in military medical research.** *Acad Emerg Med* 2005;12:1120–26
2. Informed consent. Wikipedia. [http://en.wikipedia.org/wiki/Informed\\_consent](http://en.wikipedia.org/wiki/Informed_consent). Accessed October 24, 2012
3. Nuremberg Code. National Institutes of Health. <http://history.nih.gov/research/downloads/nuremberg.pdf>. Accessed June 20, 2012
4. Tuskegee syphilis experiment. Wikipedia. [http://en.wikipedia.org/wiki/Tuskegee\\_syphilis\\_experiment](http://en.wikipedia.org/wiki/Tuskegee_syphilis_experiment). Accessed October 24, 2012
5. Sims JM. **A brief review of the Belmont Report.** *Dimens Crit Care Nurs* 2010;29:173–74
6. Institutional Review Board. Wikipedia. [http://en.wikipedia.org/wiki/Institutional\\_Review\\_Board](http://en.wikipedia.org/wiki/Institutional_Review_Board). Accessed October 24, 2012
7. John Wilbanks: let's pool our medical data. [http://www.ted.com/talks/john\\_wilbanks\\_let\\_s\\_pool\\_our\\_medical\\_data.html](http://www.ted.com/talks/john_wilbanks_let_s_pool_our_medical_data.html). Accessed October 24, 2012
8. The eMerge Network. <http://emerge.mc.vanderbilt.edu>. Accessed October 24, 2012
9. Most consumers willing to share personal data. NorthPoint Domain. <http://www.northpointdomain.com/default/index.cfm/expertise-and-insight/iq360-insight/industry-spotlight/most-consumers-willing-to-share-personal-data>. Accessed October 24, 2012
10. Gillick competence. [http://en.wikipedia.org/wiki/Gillick\\_competence](http://en.wikipedia.org/wiki/Gillick_competence). Accessed October 24, 2012

# Clinical Semiology and Neuroradiologic Correlates of Acute Hyponatremic Osmotic Challenge in Adults: A Literature Review

F.Y. Ismail, A. Szóllics, M. Szólics, N. Nagelkerke, and M. Ljubisavljevic



## ABSTRACT

**SUMMARY:** The complex interplay between hyponatremic osmotic disturbances and cerebral lesions is yet to be clarified. In this review, we discuss, on the basis of the reported data of hyponatremic CNS challenge in the adult population, the clinical and radiologic features of the condition. Our search captured 20 case studies and 1 case series with 30 patients in total who acquired acute hyponatremia due to different etiologies and developed CNS lesions. We explored the associations between premorbid conditions, clinical presentation, hyponatremic state, correction rate, and radiologic appearance, including the localization of brain lesions and the outcomes. The results revealed that altered mental status was the most commonly reported symptom and osmotic demyelination syndrome in the form of extrapontine myelinolysis was the prevailing radiologic pattern. Finally, we contrasted, when appropriate, clinical and experimental data related to hyponatremic and hyponatremic osmotic insults to aid the understanding of the pathophysiology of CNS osmotic brain injury.

**ABBREVIATIONS:** BG = basal ganglia; CPM = central pontine myelinolysis; EPM = extrapontine myelinolysis; GCS = Glasgow Coma Scale; ODS = osmotic demyelination syndrome

The associations between hyponatremic osmotic disturbances and cerebral lesions are well-established and studied. Classically, the lesions were recognized to involve demyelination in the pons.<sup>1</sup> The term “central pontine myelinolysis” was devised to delineate the character of pathologic insult. Subsequently, the concept was extended with the recognition that lesions may occur beyond the pons. Thus, the term “extrapontine myelinolysis” was coined. Although initially recognized to appear in the malnourished and alcoholics,<sup>1</sup> CPM/EPM has also been reported in adults with a variety of serious illnesses, and a link between these disorders and the rapid correction of sodium in patients with hyponatremia was eventually established. Finally, an umbrella “osmotic demyelination syndrome” term, which included both CPM and EPM, was coined. CPM and EPM are believed to be the same disease, sharing the same pathology, associations, and time course but differing in clinical manifestations. However, it has been in-

creasingly recognized that ODS can occur in the setting of other osmotic challenges such as hyperglycemia<sup>2-5</sup> and hypoglycemia,<sup>6,7</sup> as well as normonatremia<sup>8</sup> and hyponatremia.<sup>9</sup>

Furthermore, experimental data suggest that different anatomic locations in the brain may have different susceptibility to osmotic stress, depending on their ionic, organic, and inorganic makeup. These subtle variations of the CNS osmotic “ecosystem” may influence the response and effectiveness of processes of adaptation (during insult) and de-adaptation (during recovery) of the brain.<sup>10</sup>

While hyponatremic insult has been widely examined and reported, the hyponatremic osmotic insult, primarily due to its comparative scarcity in adults, is relatively poorly described and understood. Therefore, it is still unclear whether the vulnerability of different brain regions to osmotic stress is similar in states of hyponatremia and hyponatremia and whether they share similar clinical and radiologic presentations.

## OBJECTIVES

In this review, we discuss the clinical and neuroradiologic presentations of acute hyponatremic CNS injury in the adult population on the basis of the reported literature data. We also explore the associations between premorbid conditions, clinical presentation, hyponatremic state, correction, location of brain lesions, and clinical outcomes. Finally we compare, when appropriate, clinical and experimental data in the setting of hypo- and hyper-

From the Departments of Pediatrics (F.Y.I.) and Physiology (M.L.) and Institute of Public Health (N.N.), College of Medicine and Health Sciences, United Arab Emirates (UAE) University, Al Ain, UAE; Department of Radiology (A.S.), Kálmán Pándy Békes County Hospital, Gyula, Hungary; and Division of Neurology (M.S.), Department of Medicine, Tawam Hospital, Al Ain, Abu-Dhabi, UAE.

Please address correspondence to M. Ljubisavljevic, MD, PhD, Department of Physiology, Faculty of Medicine and Health Sciences, UAE University, PO Box 17666, Al Ain, United Arab Emirates; e-mail: milos@uaeu.ac.ae

Indicates open access to non-subscribers at [www.ajnr.org](http://www.ajnr.org)

Indicates article with supplemental on-line table.

<http://dx.doi.org/10.3174/ajnr.A3392>

natremia with the aim of better understanding the pathophysiology of CNS osmotic brain injury.

## METHODOLOGY

We conducted PubMed and ScienceDirect database searches (until June 3, 2012) by using the following keywords: hypernatremia AND demyelination, hypernatremia AND myelinolysis, hypernatremia AND CNS, hypernatremia AND cortical laminar necrosis, hypernatremia AND edema, hypernatremia AND MR imaging, hypernatremia AND imaging, hypernatremia AND CT, and hypernatremia AND brain. This initial strategy yielded 697 articles in PubMed and 242 articles in ScienceDirect, with significant overlap. English and non-English articles were initially populated, and reference lists in retrieved reports were examined. Five non-English articles were not included (Japanese, Danish, French, and 2 in Spanish) because the original manuscripts were not available.

We included and further analyzed studies reporting clinical and radiologic cases that fulfilled the following criteria: patients older than 18 years of age, acute hypernatremia (sodium  $>145$  mEq/L) developing within 48 hours, presence of abnormal neurologic signs and symptoms, and documented neuroradiologic investigation. Exclusion criteria included the following: presence of a hyponatremic state (sodium  $<135$  mEq/L) before the onset of symptoms and presence of CNS pathology that might account for or mask abnormal radiologic findings. When available, initial and highest sodium ion ( $\text{Na}^+$ ) levels and the rate and duration of the correction were also examined.

Descriptive analysis, linear regression, 2-sided Student *t* test, Mann-Whitney and Fisher exact tests, linear-by-linear association, and binary logistics were used to analyze categoric and continuous data. Statistical significance was defined as  $P < .05$ . To further explore the associations among radiologic features, we developed a demyelination score (0–6) that represents the sum of the number of areas affected by demyelination: pons, white matter, corpus callosum, basal ganglia, cerebellum, and cortex.

## RESULTS

A total of 20 case studies and 1 case series in English, Spanish, and Japanese languages reporting 30 adult patients who developed acute hypernatremia due to different etiologies with abnormal clinical and neuroradiologic findings (Table) were eventually included.

### Clinical Characteristics

The age of patients ranged between 18 and 73 years (mean age,  $36.93 \pm 16.9$  years) (On-line Table). Twenty-four (80%) were women.

The patients were clustered on the basis of morbid history into 4 groups: previously healthy individuals, patients with direct CNS comorbidity, patients with indirect CNS comorbidity, and patients with non-CNS comorbidities. “Direct nervous system comorbidity” denotes the presence of CNS pathology (eg, tumor or hydrocephalus), while “indirect CNS comorbidity” represents conditions that have secondary pathologic effects on the CNS (eg, liver failure and/or hepatic encephalopathy). The rationale behind such clustering was to highlight conditions that might mask

the development of abnormal neuroradiologic findings and/or render the brain more vulnerable to osmotic challenges.

Thirteen patients (43.3%) were previously healthy with no pre- or comorbid conditions. Ten patients (33.3%) had non-CNS comorbidities that were not etiologically related to acute hypernatremia per se, including hydatid cyst of the liver ( $n = 5$ ), heart disease ( $n = 1$ ), gestational diabetes mellitus ( $n = 1$ ), acute respiratory distress syndrome ( $n = 1$ ), chronic lithium therapy ( $n = 1$ ), and chronic alcoholism ( $n = 1$ ). Three patients had direct CNS comorbidities (10%) in the form of suprasellar tumor ( $n = 1$ ), lymphocytic neuroinfundibulohypophysitis ( $n = 1$ ), and pituitary craniopharyngioma and hydrocephalus ( $n = 1$ ), while 4 patients (13.3%) had indirect CNS comorbidity, including end-stage liver disease and renal failure.

The etiologies of acute hypernatremia in the reported cases were categorized from a pathophysiologic point of view into 2 main categories: exogenous sodium overload in 36.7% ( $n = 11$ ), and hypotonic volume depletion in 63.3% ( $n = 19$ ) of patients. In cases of exogenous sodium overload, we identified the following factors: post-liver transplantation ( $n = 1$ ), post-heart surgery ( $n = 1$ ), hydatid cyst lavage with hypertonic saline ( $n = 5$ ), excessive lactulose ( $n = 1$ ), dialysis error ( $n = 1$ ), sodium bicarbonate therapy for end-stage liver disease ( $n = 1$ ), and nonaccidental sodium chloride ingestion ( $n = 1$ ). The following predisposing factors were reported in cases of volume depletion: central diabetes insipidus ( $n = 5$ ), nephrogenic diabetes insipidus ( $n = 1$ ), postpartum dehydration ( $n = 11$ ), hunger strike ( $n = 1$ ), and anorexia ( $n = 1$ ).

The presenting symptoms, reported in decreasing frequency, were the following: altered mental status ranging from apathy, inattention, and confusion to deep coma in 76.7% ( $n = 23$ ); motor deficit mainly in the form of quadriparesis/plegia in 66.7% ( $n = 20$ ); myoclonic or secondary generalized tonic clonic seizures in 43.3% ( $n = 13$ ); and cranial nerve dysfunction, including bulbar symptoms such as dysphagia and dysarthria, in 43.3% ( $n = 13$ ) of patients. Glasgow Coma Scale scores on presentation ranged from 3 to 14 (mean,  $8.6 \pm 3.2$ ). While the exact GCS score was reported in 4 studies, in other studies the reported clinical presentation was used to estimate the GCS score (13 studies). In 3 studies, the provided clinical description did not allow estimating GCS.

The information about the presence and extent of concomitant electrolyte abnormalities was incomplete. Therefore, we limited our comparison to changes in initial  $\text{Na}^+$  and osmolality, which were reported in all studies. The initial  $\text{Na}^+$  level at the time of presentation was 142–200 mEq/L (mean,  $175.1 \pm 16.8$  mEq/L). Serum osmolality ranged between 314 and 459 mOsm/kg<sup>-1</sup> (mean,  $387.6 \pm 39.9$  mOsm/kg<sup>-1</sup>).

Data for 18 subjects were not reported in detail, while in those reported, the correction rate was variable. The duration of correction was as rapid as 13 hours and as slow as 5 days. More specifically,  $\text{Na}^+$  was corrected within 24 hours in 4 patients (33.3%), within 48 hours in 3 patients (25%), and in  $>48$  hours in 5 patients (41.7%).

### Neuroradiologic Findings

All patients underwent neuroimaging (CT and/or MR imaging) at certain points in the course of their illnesses. Neuroradiologic

findings were grouped into 4 patterns that are not mutually exclusive: central pontine myelinolysis, extrapontine myelinolysis, vascular changes, and cerebral and CSF volume changes. In 2 patients, the neuroimaging findings were normal (6.7%).<sup>11,12</sup>

### **Osmotic Demyelination Syndrome**

ODS was found in 80% of patients ( $n = 24$ ). CPM was evident as an isolated pathology in 16.7% of patients ( $n = 5$ ). Pontine demyelination was located either centrally or dorsolaterally with hyperintense T2 signal.

On the other hand, “stand-alone” EPM was demonstrated in 33.3% of patients ( $n = 10$ ). Nine patients (30%) developed CPM and EPM simultaneously. Topographic distribution of extrapontine lesions whether alone or in combination with CPM were as follows: white matter (centrum semiovale), 41.4% ( $n = 12$ ); corpus callosum, 41.4% ( $n = 12$ ); basal ganglia, 34.5% ( $n = 10$ ); hippocampus, 34.5% ( $n = 10$ ); cerebellum, 34.5% ( $n = 10$ ); and cortex, 10.3% ( $n = 3$ ). When we examined the topographic distribution of ODS lesions, 37.9% ( $n = 11$ ) had both supra- and infratentorial structure involvement, while 20.7% ( $n = 6$ ) had supratentorial involvement only and 20.7% ( $n = 6$ ) had infratentorial involvement alone.

### **Vascular Changes**

Seven patients (23.3%) had vascular events, including infarction 20% ( $n = 6$ ) and subdural hematoma and sinus venous thrombosis ( $n = 1$ ).

### **Brain and CSF Volume Changes**

Seven patients (23.3%) had changes in cerebral volume that manifested as cerebral edema in 16.7% ( $n = 5$ ) and shrinkage in 6.7% ( $n = 2$ ). Two patients had changes in CSF volume (6.7%) in the form of hydrocephalus ( $n = 1$ ) and subdural effusion ( $n = 1$ ). After correction of Na<sup>+</sup>, 1 patient had reversibility of brain-volume shrinkage.<sup>13</sup>

### **Clinical Outcome and Follow-Up**

The clinical outcome after acute hypernatremic challenge was variable. Among reported cases, 8 patients achieved satisfactory recovery (26.7%) with minimal neurologic deficits. On the other hand, 17 patients sustained persistent neurologic deficits with significant morbidities (56.7%), while 5 (16.7%) died between 12 hours and 3 weeks after presentation. Eight patients had follow-up MR imaging between 2 weeks and 10 months after the onset of osmotic insult. Radiologic findings were variable. Complete neuroradiologic recovery was documented in 3 patients.<sup>12-14</sup> Residual findings in the form of brain atrophy,<sup>23</sup> decrease in ODS-related T2 signal intensities,<sup>26,27,30</sup> and patchy contrast enhancement<sup>23</sup> were reported.

### **Correlations among Variables**

Younger age was associated with white matter ( $P = .05$ ,  $t$  test), corpus callosum ( $P = .010$ ,  $t$  test), and basal ganglia ( $P = .007$ ,  $t$  test) lesions but not with CPM, other EPM sites, or vascular lesions. However, older age was associated with brain volume changes, in the form of edema and shrinkage, compared with younger age ( $P = .035$ ,  $t$  test).

Clinical symptoms on presentation (altered mental status, GCS score, seizures, cranial nerve dysfunction, and motor deficit) had no association with radiologic patterns. The presence of seizures was not associated with development of edema, and development of edema was not related to initial Na<sup>+</sup> level, serum osmolality, or correction rate. GCS and initial Na<sup>+</sup> level were not associated with the severity of outcome ( $P > .05$ , linear regression).

The mean demyelination score was  $2.6 \pm 2$ , indicating that a number of pontine and extrapontine areas were affected by demyelination. The spatial distribution of demyelinating lesions was not the same across categories of comorbidities ( $P = .01$ , Mann-Whitney). The presence of comorbidities was significantly associated with EPM lesions, namely corpus callosum ( $P = .003$ , linear regression), WM ( $P = .039$ , linear regression), BG ( $P = .024$ , linear regression), and hippocampus ( $P = .024$ , linear regression). Among patients with ODS, those with comorbidities had lower Na<sup>+</sup> levels, while the presence of indirect CNS pathology (hepatic or renal failure) predisposed to development of ODS at lower levels of Na<sup>+</sup>. The clinical profile, symptoms, and Na<sup>+</sup> levels did not predict the development of demyelinating lesions on MR imaging ( $P > .05$ , linear regression). The presence of vascular complications was not predicted by Na<sup>+</sup> level, osmolality, and correction rate, and it was not related to age, comorbid history, etiology, or outcome ( $P > .05$ , linear regression).

Initial Na<sup>+</sup> level correlated with hippocampus involvement ( $P = .003$ , linear regression) but not with other extrapontine lesions (WM, corpus callosum, BG, cerebellum, and cortex). Na<sup>+</sup> correction rate was not associated with a pattern of radiologic changes or severity of outcome ( $P > .05$ , linear-by-linear association).

In general, older age was significantly associated with better recovery ( $P = .036$ , linear regression). The presence of ODS lesions was associated with persistent neurologic dysfunction ( $P = .027$ , Pearson  $\chi^2$ ), while the presence of EPM lesions reduced the probability of full recovery (odds ratio = 0.118; 95% confidence interval, 0.017–0.802;  $P = .029$ , binary logistics).

Poor outcome, defined by the presence of long-term neurologic deficits or death, was found to be significantly associated with higher lesion load ( $P = .021$ , linear-by-linear association). Most interesting, among patients with WM ( $P = .009$ , Fisher exact test), BG ( $P = .027$ , Fisher exact test), and hippocampal lesions ( $P = .027$ , Fisher exact test), none had achieved satisfactory recovery. These results suggest that the absence of these lesions on MR imaging was in favor of better recovery. Conversely, vascular complications and parenchymal volume changes were not associated with the severity of outcome ( $P > .05$ , linear regression).

## **DISCUSSION**

In this review, to better delineate the impact of hypernatremic challenge on the CNS, we analyzed the clinical and neuroradiologic profiles of 30 previously reported cases. The results show that altered mental status was the most commonly reported symptom and ODS was the prevailing radiologic pattern. In the following sections, we discuss the spectrum of clinical and radiologic manifestations and their association with other factors in-

cluding age, presence of pre- and comorbid conditions, the absolute level of  $\text{Na}^+$ , the magnitude of  $\text{Na}^+$  change from baseline, the duration of hypernatremic insult, and the potential effects of  $\text{Na}^+$  correction rate.

### **Clinical Characteristics of Patients with Hypernatremic Challenge**

The clinical symptoms of CNS injury ranged from subtle changes of cognitive functions to life-threatening autonomic and brain stem dysfunction and death. This spectrum of clinical manifestations is similar to that found in hyponatremia.<sup>31,32</sup>

In our review, clinical symptoms did not correlate with age, presence of comorbid conditions, initial  $\text{Na}^+$ , serum osmolality, or  $\text{Na}^+$  correction rate. This finding would suggest that neither type of clinical symptom nor its severity is influenced by the severity of osmotic challenge. However, in hyponatremia, some studies reported no association between the degree of osmotic derangement and the clinical situation,<sup>33,34</sup> while some reported that lower  $\text{Na}^+$  level and more rapid  $\text{Na}^+$  correction rates<sup>35</sup> were associated with a more severe clinical presentation. It appears that the absolute level of  $\text{Na}^+$ , whether abnormally high or low, does not result in a specific set of symptoms and that the emerging clinical presentation is shaped by different sets of factors and mechanisms impacting various components of the neuronal apparatus, including neurons, glia, blood-brain barrier, and CSF. The presence of additional metabolic derangements like hypokalemia<sup>36</sup> and hyperglycemia<sup>2</sup> is considered an independent risk factor for ODS development, which is not covered in this review.

All patients included in this review endured acute hypernatremia. While cases of chronic hypernatremia were not included, the distinction between acute and chronic challenge is important because different mechanisms of brain-volume regulation exhibit differential dynamics in acute-versus-chronic osmotic challenge. Data emerging from experimental animal studies indicate that under extreme osmotic challenge, the engagement of organic brain osmoles occurs later in the course of osmotic insult and develops more slowly than the instant changes in inorganic ions, potentially setting a course of different changes in brain tissue. In acute hypernatremia, osmotic differences are actually subtle due to rapid ionic and water shifts across the cell membrane with little effect on cell volume but with significant effect on extracellular space volume, which decreases significantly. In chronic hypernatremia, organic osmoles seem to play a much more important role in helping to maintain the osmotic gradient.<sup>37-40</sup> The temporal dissociation between these 2 adaptive osmoregulating mechanisms, whether at the acute or chronic stage, could account, at least in part, for the nature and severity of neurologic symptoms. General clinical observations suggest that patients with acute hypernatremia or hyponatremia develop a more clinically severe condition and have worse outcomes than those with chronic challenges.<sup>41</sup>

### **Neuroradiologic Features of Patients with Hypernatremic Challenge**

Examination in our study of neuroradiologic features of hypernatremic challenge showed the prevailing appearance of ODS (CPM or EPM or both) followed by cerebral volume changes (edema

and shrinkage) and vascular complications (hemorrhage and infarction).

### **Osmotic Demyelination Syndrome**

CPM and EPM (ODS) are classically described as clinical and radiologic manifestations of osmotic myelinolysis, affecting different brain regions, confined to the pons in cases of CPM and extrapontine sites in cases of EPM. The radiologic description of CPM entails the presence of “trident-shaped” symmetric hypointense lesions on T1 and corresponding hyperintense lesions on T2-weighted images located in the brain stem, and sparing of other brain regions.<sup>42</sup> In cases of EPM, the same features are noted typically in sites such as the internal capsule, basal ganglia, cerebellum, and cerebrum.<sup>43</sup>

The neuroradiologic features of ODS lesions in the context of hyponatremia are frequently reported not to match the severity of clinical symptoms because the features might be absent despite clinical abnormalities or at times may persist well beyond clinical resolution.<sup>44,45</sup> We observed similar clinical-radiologic dissociation in cases of hypernatremia. This may potentially be explained by the variability of time intervals between the onset of symptoms and radiologic imaging, the sensitivity of the radiologic technique used, or the presence of gliosis-related abnormal signals that persists well beyond clinical recovery.<sup>46</sup>

In reviewed data, other variables seemed to be more correlated. The presence of an indirect CNS comorbid condition (hepatic or renal failure) before hypernatremic challenge rendered the brain more vulnerable to ODS even with mildly elevated  $\text{Na}^+$  levels in comparison with patients with no comorbid conditions. More specifically, those patients presented with more corpus callosum, WM, BG, and hippocampus lesions. Patients with liver disease or those who had transplantation are more at risk for developing CNS complications, including ODS, probably secondary to metabolic and cerebral hemodynamic derangements<sup>47,48</sup> that might render osmotic regulatory mechanisms insufficient.

Hippocampal lesions were reported in more than one-third of patients and were associated with higher initial  $\text{Na}^+$  levels. The high hippocampal involvement may be related to its high vulnerability to the neurotoxic effects of osmotic derangements<sup>49</sup> and systemic stresses in general.<sup>50,51</sup>

In reviewed cases, contrast enhancement associated with ODS lesions was reported in 1 patient,<sup>23</sup> which has also been reported in some cases of hyponatremia.<sup>52</sup> Although inconsistently found, contrast enhancement is in agreement with the pathophysiologic changes observed in experimental models of ODS, in which BBB disruption occurs secondary to osmotic stress and is thought to be one of the leading factors in pathogenesis of ODS. A disruption of the BBB during the first 24 hours of hyponatremia was found to be associated with a 70% risk of developing demyelination.<sup>53</sup> By contrast, the risk of developing subsequent demyelination was only 8% when the BBB was intact.<sup>53</sup> Furthermore, the use of dexamethasone, known to protect the BBB, was reported to decrease the risk of ODS both in animal studies<sup>54</sup> and case reports.<sup>55</sup>

Cortical laminar necrosis has been described occasionally in patients with severe ODS that follows rapid correction of hyponatremia.<sup>56-59</sup> In the present study, we identified 2 patients pre-

senting with cortical laminar necrosis.<sup>23,24</sup> These lesions may be associated with hypoxia-ischemia, which may coexist with ODS, or severe demyelination that subsequently triggers cortical neuronal loss. It has been suggested that cortical lesions in the context of ODS present more often with ischemia than with demyelination.<sup>60</sup>

### **Topographic Distribution of ODS in Hyponatremia: Relation to Region-Specific Vulnerability**

In ODS, regardless of the etiology, CPM is consistently reported to be more common than EPM or CPM/EPM combined.<sup>45,61</sup> However, in a large case series of patients with hyponatremia and ODS, the combined form was more common than EPM and CPM alone.<sup>33</sup> As we have already stated, the reviewed data of hypernatremic osmotic challenge have revealed that EPM was more common than CPM or CPM/EPM combined. Whether this hints at a possible predilection of a hypernatremic challenge for extrapontine sites warrants further investigations.

Age appears to be an important factor in the topographic vulnerability to hyperosmotic conditions. Younger adults had different topographic distributions than older adults, with the white matter, corpus callosum, and basal ganglia particularly affected.

Unlike in the adult population, hypernatremic osmotic brain injury is far more common in the pediatric population. Most interesting, the neurologic manifestations of hypernatremia in the pediatric population are strikingly similar to observations made in adults, with some variation in severity and reversibility. Both CPM<sup>62,63</sup> and EPM presentations are frequently encountered in pediatric patients, with extrapontine lesions reported to be thalamic,<sup>64,65</sup> in the basal ganglia,<sup>66</sup> and hippocampal.<sup>67</sup> Despite similar distributions of lesions, pediatric patients have better recovery and the associated MR imaging lesions are more reversible,<sup>41,68</sup> results that may be related to age-associated changes in osmotic regulatory mechanisms. It has been shown that water, electrolytes, and organic osmole (mainly taurine) content in the brain of normonatremic rats decreases with age, implying that young brains might have a greater capacity to counteract osmotic perturbations.<sup>69</sup>

Furthermore, experimental data support the notion that different brain regions exhibit different “buffering capacities” to osmolar stress, a feature depending largely on the individual composition of electrolytes and osmolytes. Sodium and chloride ions were found to be highest in the medulla oblongata, while the lowest values were found in the cerebellum and vice versa for potassium.<sup>70</sup> Organic osmoles were also found to significantly differ among different gray and white matter regions. More specifically, the cortex and cerebellum had the highest concentration of glutamate, glutamine, taurine, and betaine, whereas glycine was predominantly present in the pons and medulla. However, other organic osmoles, such as myo-inositol, creatine, glycerylphosphorylcholine, and glycerylphosphorylethanolamine, were found to be distributed evenly across all brain regions.<sup>71</sup>

Furthermore, different dynamics of changes in ionic and organic osmoles may also contribute to different susceptibility of different brain regions to osmotic challenge. Animal studies show upregulation of Na/myo-inositol co-transporters in the early stages of acute hypernatremia<sup>72</sup> and an absence of changes

in the concentration of brain organic osmoles. Most interesting, during the de-adaptation (recovery) phase, all osmoles except myo-inositol seem to return to a normal range. This may suggest that myo-inositol may play a role either in the development of cerebral edema accompanying correction of hypernatremia,<sup>71</sup> or alternatively, it may play a protective role as suggested by some experimental studies, which demonstrated that it reduces cell loss resulting from hypernatremia.<sup>73</sup> Furthermore, myo-inositol is involved in the maintenance of brain cell volume during severe hypernatremia but not in hyponatremia.<sup>74</sup> Thus, re-establishment of organic osmoles in hyponatremia may differ among brain regions, with the pons and midbrain exhibiting the least recovery capacity and the cortex and cerebellum having greater potential to regain lost organic osmoles.<sup>75</sup> Therefore, it is conceivable that brain response to osmotic challenges is influenced by the inherent region-specific differences in inorganic and organic metabolic makeup, preferential temporal and concentration-dependent involvement of osmolytes, and morphologic and functional characteristics of the adjacent BBB apparatus.

Another interesting difference emerging from these data is the topographic distribution of EPM lesions. In reviewed data, white matter and corpus callosum lesions were the most frequently reported (41.4%), while cortex involvement was the least reported (10.3%). In hyponatremic challenge, the cerebellum was the most frequently reported site, while the caudate was the least reported one.<sup>61</sup> It would be relevant to explore whether the difference in susceptibility to different osmotic challenges may be related to the differential dynamics of response of various brain regions to osmotic challenge as indicated earlier.

### **Cerebral Volume Changes**

In reviewed cases, cerebral edema associated with hypernatremic challenge correlated with older age but not with clinical symptoms, rise in the Na<sup>+</sup> level, correction rate, or severity of outcome. In most studies, conventional CT or MR imaging was used to delineate edema-related pathologies. Only 2 studies also used DWI and ADC mapping.<sup>30,76</sup> The potential advantage of using DWI and ADC stems from the role of cytotoxic and vasogenic edema in the development of lesions, especially in white matter regions, given its highly compartmentalized structure. Using serial ADC mapping at different time points after the onset of symptoms showed lower ADC values early after the onset of symptoms and a gradual increase to normal or above-normal values thereafter.<sup>77</sup> This finding corresponded to the emergence of cytotoxic edema (lower ADC) and subsequent vasogenic edema (higher ADC) at different time intervals. It appears that coupling of DWI and ADC yields higher specificity for ODS lesions, in which lower ADC values correlate better with ODS.<sup>76</sup>

### **Vascular Complications**

Although less frequently reported in this cohort of patients, vascular events (infarction and hemorrhage) were not uncommon. Five patients had cerebral infarction, and 1 patient had cerebral hemorrhage. Vascular complications were not significantly associated with age, comorbid history, Na<sup>+</sup> level, osmolality, and correction rate, nor were they linked to outcome.

It is not clear whether these vascular complications in hyper-

natremia are osmotically driven. Experimental data suggest that cerebral blood flow may be affected by disruption of the BBB and a concomitant widespread vascular endothelium reaction. Most interesting, changes in CBF may be regionally distributed, varying between cortical and subcortical regions depending on the dynamics of development and correction of hypernatremia,<sup>53</sup> suggesting a differential endothelium response and sensitivity to osmotic stress. Whether CBF changes might account for cerebral events (infarctions or hemorrhages) seen in patients with hypernatremic osmotic challenge would require further study.

### Outcomes of Hypernatremic Osmotic Challenge

In reviewed cases, a slower Na<sup>+</sup> correction rate (>48 hours) was not associated with the presence of radiologic changes or outcome. However, the exact correction rate was not provided in most of studies; this omission prevented statistical analysis.

In our review, satisfactory recovery was reported in 26.7% of patients, persistent neurologic dysfunction, in 56.7%; and death, in 16.7%. In reviews of ODS in the context of hyponatremia, favorable recovery was seen in one-third<sup>33</sup> and two-thirds,<sup>45</sup> while mortality was reported in one-fifth of patients.<sup>33,45</sup>

In our review, the outcome was not correlated with the severity of clinical presentation, Na<sup>+</sup> level, or correction rate, findings compatible with previous observations in cases of hyponatremia<sup>34</sup> and ODS of different etiologies.<sup>45,78</sup> However, we found that younger adults had worse outcomes compared with older adults. Moreover, the GCS score was not associated with the outcome, probably due to under-reporting of actual GCS scores in most studies. In a case series of 25 patients with hyponatremia and ODS, older age, premorbid conditions, and pattern of ODS were not found to be predictive of better outcome. However, higher GCS scores, better scores in functional scales, less severe hyponatremia, and absence of hypokalemia predicted favorable outcome after correction of a hyponatremic state.<sup>33</sup>

Finally, clinical outcome was better predicted by the presence, load, and pattern of ODS lesions among reviewed cases. More specifically, the presence of EPM lesions, mainly WM, BG, and hippocampal lesions (but not CPM) reduced the probability of full recovery. Similar associations between radiologic features and outcome were not observed in ODS in the setting of hyponatremia.<sup>33,45,79</sup>

### CONCLUSIONS

The analysis of reviewed cases shows striking similarities between the impact of hyper- and hyponatremic osmotic challenge on the CNS. However, several differences have also emerged. The primary one seems to be related to the appearance and distribution of CNS lesions. EPM lesions were prominent in hypernatremic osmotic challenge; among them, corpus callosum lesions were the most common. However, although most reviewed patients presented with neuroradiologic abnormalities, negative initial imaging did not exclude ODS, suggesting that serial imaging with different modalities may be warranted for detecting subtle changes associated with early cellular destruction and water-diffusion anomalies. Although the lack of comprehensive clinical data related to the correction rate precludes specific conclusions, the data suggest that adhering to clinical guidelines when correcting

hypernatremia may decrease the risk but does not necessarily prevent ODS development. Finally, the data suggest that the absence of EPM lesions, namely in the WM, BG, and hippocampus might hold better prognostic value for outcome. The reviewed results could have been potentially influenced by selection bias of patients introduced in the original studies, as well as other immediately nonapparent factors, necessitating further clinical observations to better understand the pathophysiology, impact, and outcome of hypernatremic osmotic challenge.

Disclosures: Milos Ljubisavljevic—UNRELATED: Stock/Stock Options: Various stocks not related to current submission or pharmaceutical or other relevant industries.

### REFERENCES

1. Adams RD, Victor M, Mancall EL. **Central pontine myelinolysis: a hitherto undescribed disease occurring in alcoholic and malnourished patients.** *AMA Arch Neurol Psychiatry* 1959;81:154–72
2. McComb RD, Pfeiffer RF, Casey JH, et al. **Lateral pontine and extrapontine myelinolysis associated with hypernatremia and hyperglycemia.** *Clin Neuropathol* 1989;8:284–88
3. Kuwahara H. **Central pontine myelinolysis associated with pancreatic diabetes.** *J Neurol* 2012;259:353–54
4. Lou F. **A good prognosis of central pontine myelinolysis in a type 2 diabetic patient.** *Ann Acad Med Singapore* 2011;40:384–86
5. Akyol A. **Association of central pontine myelinolysis and extrapontine myelinolysis in diabetic patient.** *Neuro Endocrinol Lett* 2007;28:252–54
6. Morales-Buenrostro LE, Tellez-Zenteno JF, Posadas-Calleja JG, et al. **Pontine myelinolysis after a hypoglycemic episode [in Spanish].** *Rev Invest Clin* 2002;54:181–84
7. Rajbhandari SM, Powell T, Davies-Jones GA. **Central pontine myelinolysis and ataxia: an unusual manifestation of hypoglycaemia.** *Diabet Med* 1998;15:259–61
8. Kiliç M, Benli US, Can U. **Osmotic myelinolysis in a normonatremic patient.** *Acta Neurol Belg* 2002;102:87–89
9. Clark WR. **Diffuse demyelinating lesions of the brain after the rapid development of hypernatremia.** *West J Med* 1992;157:571–73
10. Verbali JG. **Brain volume regulation in response to changes in osmolality.** *Neuroscience* 2010;168:862–70
11. Gage TP, Vivian G. **Hypernatremia after hypertonic saline irrigation of an hepatic hydatid cyst.** *Ann Intern Med* 1984;101:405
12. Albi A, Baudin F, Matmar M, et al. **Severe hypernatremia after hypertonic saline irrigation of hydatid cysts.** *Anesth Analg* 2002;95:1806–08, table of contents
13. Machino T, Machino T, Yoshizawa T. **Brain shrinkage due to acute hypernatremia.** *Neurology* 2006;67:880
14. Go M, Amino A, Shindo K, et al. **A case of central pontine myelinolysis and extrapontine myelinolysis during rapid correction of hypernatremia [in Japanese].** *Rinsho Shinkeigaku* 1994;34:1130–35
15. Wacks I, Oster JR, Roth D, et al. **Severe cerebral edema in a patient with anasarca and hypernatremia.** *Clin Nephrol* 1992;37:19–22
16. Konno S, Nakagawa T, Yoshida T, et al. **A case report of central pontine myelinolysis associated with serum hyperosmolality after open heart surgery [in Japanese].** *Kyobu Geka* 1993;46:150–54
17. Dobato JL, Barriga FJ, Pareja JA, et al. **Extrapontine myelinolyses caused by iatrogenic hypernatremia following rupture of a hydatid cyst of the liver with an amnesic syndrome as sequela [in Spanish].** *Rev Neurol* 2000;31:1033–35
18. Chua GC, Chua GC, Sitoh YY, et al. **MRI findings in osmotic myelinolysis.** *Clin Radiol* 2002;57:800–06
19. Kamijo Y, Soma K, Hamanaka S, et al. **Dural sinus thrombosis with severe hypernatremia developing in a patient on long-term lithium therapy.** *Clinical Toxicology* 2003;41:359–62
20. van der Helm-van Mil AH, van Vugt JP, Lammers GJ, et al. **Hypernatremia from a hunger strike as a cause of osmotic myelinolysis.** *Neurology* 2005;64:574–75

21. Al-Sarraf AJ, Haque M, Pudek M, et al. **Central pontine myelinolysis after orthotopic liver transplant: a rare complication.** *Exp Clin Transplant* 2010;8:321–24
22. Lee IW, Su MT, Kuo PL, et al. **Gestational diabetes and central pontine myelinolysis with quadriplegia: a case report.** *J Matern Fetal Neonatal Med* 2010;23:728–31
23. Szolics M, Ljubicavljivic M, Samir HA, et al. **Extrapontine myelinolysis and cortical laminar necrosis caused by severe hypernatremia following peritoneal lavage for ruptured hydatid cyst of the liver: a case report and review of the literature.** *The Neuroradiology Journal* 2010;1:325–31
24. Cagnin A, Manara R, Piron L, et al. **Hypernatremia-induced limbic system damage.** *Anesthesiology* 2011;114:175
25. Odier C, Nguyen DK, Panisset M, et al. **Central pontine and extrapontine myelinolysis: from epileptic and other manifestations to cognitive prognosis.** *J Neurol* 2010;257:1176–80
26. Chang L, Harrington DW, Milkotic A, et al. **Unusual occurrence of extrapontine myelinolysis associated with acute severe hypernatremia caused by central diabetes insipidus.** *Clin Endocrinol (Oxf)* 2005;63:233–35
27. Kawahara I, Tokunaga Y, Ishizaka S, et al. **Reversible clinical and magnetic resonance imaging of central pontine myelinolysis following surgery for craniopharyngioma: serial magnetic resonance imaging studies.** *Neurol Med Chir (Tokyo)* 2009;49:120–23
28. Vin-Christian K, Arieff AI. **Diabetes insipidus, massive polyuria, and hypernatremia leading to permanent brain damage.** *Am J Med* 1993;94:341–42
29. Kendall R, Lafuente J, Hosie KB. **Central pontine myelinolysis after an operation.** *J R Soc Med* 1997;90:445–46
30. Naik KR, Saroja AO. **Seasonal postpartum hypernatremic encephalopathy with osmotic extrapontine myelinolysis and rhabdomyolysis.** *J Neurol Sci* 2010;291:5–11
31. Riggs JE. **Neurologic manifestations of electrolyte disturbances.** *Neurol Clin* 2002;20:227–39, vii
32. Adrogué HJ, Madias NE. **Hypernatremia.** *N Engl J Med* 2000;342:1493–99
33. Kallakatta RN, Radhakrishnan A, Fayaz RK, et al. **Clinical and functional outcome and factors predicting prognosis in osmotic demyelination syndrome (central pontine and/or extrapontine myelinolysis) in 25 patients.** *J Neurol Neurosurg Psychiatry* 2011;82:326–31
34. Menger H. **Outcome of central pontine and extrapontine myelinolysis (n = 44).** *J Neurol* 1999;246:700–05
35. Brunner JE, Redmond JM, Haggar AM, et al. **Central pontine myelinolysis and pontine lesions after rapid correction of hyponatremia: a prospective magnetic resonance imaging study.** *Ann Neurol* 1990;27:61–66
36. Davenport C, Liew A, Vic Lau P. **Central pontine myelinolysis secondary to hypokalaemic nephrogenic diabetes insipidus.** *Ann Clin Biochem* 2010;47:86–89
37. Strange K. **Regulation of solute and water balance and cell volume in the central nervous system.** *J Am Soc Nephrol* 1992;3:12–27
38. De Petris L, Luchetti A, Emma F. **Cell volume regulation and transport mechanisms across the blood-brain barrier: implications for the management of hypernatraemic states.** *Eur J Pediatr* 2001;160:71–77
39. Holliday MA, Kalayci MN, Harrah J, et al. **Factors that limit brain volume changes in response to acute and sustained hyper- and hyponatremia.** *J Clin Invest* 1968;47:1916–28
40. Cserr HF, DePasquale M, Nicholson C, et al. **Extracellular volume decreases while cell volume is maintained by ion uptake in rat brain during acute hypernatremia.** *J Physiol* 1991;442:277–95
41. Arieff AI. **Central nervous system manifestations of disordered sodium metabolism.** *Clin Endocrinol Metab* 1984;13:269–94
42. Rippe DJ, Edwards MK, D'Amour PG, et al. **MR imaging of central pontine myelinolysis.** *J Comput Assist Tomogr* 1987;11:724–26
43. Bekiesińska-Figatowska M, Bulski T, Rózczycka I, et al. **MR imaging of seven presumed cases of central pontine and extrapontine myelinolysis.** *Acta Neurobiol Exp (Wars)* 2001;61:141–44
44. Clifford DB, Gado MH, Levy BK. **Osmotic demyelination syndrome: lack of pathologic and radiologic imaging correlation.** *Arch Neurol* 1989;46:343–47
45. Graff-Radford J, Fugate JE, Kaufmann TJ, et al. **Clinical and radiologic correlations of central pontine myelinolysis syndrome.** *Mayo Clin Proc* 2011;86:1063–67
46. Thompson PD, Miller D, Gledhill RF, et al. **Magnetic resonance imaging in central pontine myelinolysis.** *J Neurol Neurosurg Psychiatry* 1989;52:675–77
47. Ardizzone G, Arrigo A, Schellino MM, et al. **Neurological complications of liver cirrhosis and orthotopic liver transplant.** *Transplant Proc* 2006;38:789–92
48. Ardizzone G, Arrigo A, Panaro F, et al. **Cerebral hemodynamic and metabolic changes in patients with fulminant hepatic failure during liver transplantation.** *Transplant Proc* 2004;36:3060–64
49. Goldman MB, Torres IJ, Keedy S, et al. **Reduced anterior hippocampal formation volume in hyponatremic schizophrenic patients.** *Hippocampus* 2007;17:554–62
50. Fotuhi M, Do D, Jack C. **Modifiable factors that alter the size of the hippocampus with ageing.** *Nat Rev Neurol* 2012;8:189–202
51. Vexler ZS, Ayus JC, Roberts TP, et al. **Hypoxic and ischemic hypoxia exacerbate brain injury associated with metabolic encephalopathy in laboratory animals.** *J Clin Invest* 1994;93:256–64
52. Dervisoglu E, Yegenaga I, Anik Y, et al. **Diffusion magnetic resonance imaging may provide prognostic information in osmotic demyelination syndrome: report of a case.** *Acta Radiol* 2006;47:208–12
53. Adler S, Verbalis JG, Meyers S, et al. **Changes in cerebral blood flow and distribution associated with acute increases in plasma sodium and osmolality of chronic hyponatremic rats.** *Exp Neurol* 2000;163:63–71
54. Ke QH, Chen JH, Zheng SS, et al. **Prevention of central pontine myelinolysis in rats by early treatment with dexamethasone [in Chinese].** *Zhejiang Da Xue Xue Bao Yi Xue Ban* 2006;35:424–29
55. Sakamoto E, Hagiwara D, Morishita Y, et al. **Complete recovery of central pontine myelinolysis by high dose pulse therapy with methylprednisolone [in Japanese].** *Nihon Naika Gakkai Zasshi* 2007;96:2291–93
56. Cho AH, Choi CG, Lee SA. **Cortical laminar necrosis associated with osmotic demyelination syndrome.** *J Clin Neurol* 2005;1:174–76
57. Niwa K, Matsushima K, Yamamoto M, et al. **Morel's laminar necrosis like findings on MRI in a case of extra-pontine myelinolysis [in Japanese].** *Rinsho Shinkeigaku* 1991;31:327–30
58. Shoji M, Kimura T, Ota K, et al. **Cortical laminar necrosis and central pontine myelinolysis in a patient with Sheehan syndrome and severe hyponatremia.** *Intern Med* 1996;35:427–31
59. Susa SD. **Acute intermittent porphyria with central pontine myelinolysis and cortical laminar necrosis.** *Neuroradiology* 1999;41:835–39
60. Cho AH, Choi CG, Lee SA. **Cortical laminar necrosis associated with osmotic demyelination syndrome.** *J Clin Neurol* 2005;1:174–76
61. Martin RJ. **Central pontine and extrapontine myelinolysis: the osmotic demyelination syndromes.** *J Neurol Neurosurg Psychiatry* 2004;75(suppl 3):iii22–28
62. Shah B, Tobias JD. **Osmotic demyelination and hypertonic dehydration in a 9-year-old girl: changes in cerebrospinal fluid myelin basic protein.** *J Intensive Care Med* 2006;21:372–76
63. Mastrangelo S, Arlotta A, Cefalo MG, et al. **Central pontine and extrapontine myelinolysis in a pediatric patient following rapid correction of hypernatremia.** *Neuropediatrics* 2009;40:144–47
64. Ozdemir H, Kabakus N, Kurt AN, et al. **Bilateral symmetrical hypodensities in the thalamus in a child with severe hypernatraemia.** *Pediatr Radiol* 2005;35:449–50
65. Achiwa S, Ando K, Ishikura R, et al. **A case of extrapontine myelinolysis precipitated by correction of a hyper-osmolar state [in Japanese].** *Nihon Igaku Hoshasen Gakkai Zasshi* 2004;64:310–12
66. AlOrainy IA, O'Gorman AM, Decell MK. **Cerebral bleeding, in-**

- farcts, and presumed extrapontine myelinolysis in hypernatraemic dehydration. *Neuroradiology* 1999;41:144–46
67. Brown WD, Caruso JM. Extrapontine myelinolysis with involvement of the hippocampus in three children with severe hypernatremia. *J Child Neurol* 1999;14:428–33
  68. Fahrbach J, Rozzelle CJ. Transient ventriculomegaly in a child presenting with hypernatremia: case report. *J Neurosurg* 2006;104 (3 suppl):192–94
  69. Trachtman H, Yancey PH, Gullans SR. Cerebral cell volume regulation during hypernatremia in developing rats. *Brain Res* 1995;693:155–62
  70. Reulen HJ, Hase U, Fenske A, et al. Extracellular space and electrolyte distribution in grey and white matter of the dog brain [in German]. *Acta Neurochir (Wien)* 1970;22:305–25
  71. Lien YH, Shapiro JJ, Chan L, et al. Effects of hypernatremia on organic brain osmoles. *J Clin Invest* 1990;85:1427–35
  72. Minami Y, Inoue K, Shimada S, et al. Rapid and transient up-regulation of Na<sup>+</sup>/myo-inositol cotransporter transcription in the brain of acute hypernatremic rats. *Brain Res Mol Brain Res* 1996;40:64–70
  73. Hijab S, Havalad S, Snyder AK. The role of organic osmolytes in the response of cultured astrocytes to hyperosmolarity. *Am J Ther* 2011;18:366–70
  74. Trachtman H. Cell volume regulation: a review of cerebral adaptive mechanisms and implications for clinical treatment of osmolal disturbances. I. *Pediatr Nephrol* 1991;5:743–50
  75. Lien YH. Role of organic osmolytes in myelinolysis: a topographic study in rats after rapid correction of hyponatremia. *J Clin Invest* 1995;95:1579–86
  76. Chu K, Kang DW, Ko SB, et al. Diffusion-weighted MR findings of central pontine and extrapontine myelinolysis. *Acta Neurol Scand* 2001;104:385–88
  77. Hurley RA, Filley CM, Taber KH. Central pontine myelinolysis: a metabolic disorder of myelin. *J Neuropsychiatry Clin Neurosci* 2011;23:369–74
  78. Louis G, Megarbane B, Lavoué S, et al. Long-term outcome of patients hospitalized in intensive care units with central or extrapontine myelinolysis. *Crit Care Med* 2012;40:970–72
  79. Menger H, Mackowski J, Jörg J, et al. Pontine and extra-pontine myelinolysis: early diagnostic and prognostic value of cerebral CT and MRI [in German]. *Nervenarzt* 1998;69:1083–90

# Hot Topics in Functional Neuroradiology

S.H. Faro, F.B. Mohamed, J.A. Helpen, J.H. Jensen, K.R. Thulborn, I.C. Atkinson, H.I. Sair, and D.J. Mikulis

## ABSTRACT

**SUMMARY:** Functional neuroradiology represents a relatively new and ever-growing subspecialty in the field of neuroradiology. Neuroradiology has evolved beyond anatomy and basic tissue signal characteristics and strives to understand the underlying physiologic processes of central nervous system disease. The American Society of Functional Neuroradiology sponsors a yearly educational and scientific meeting, and the educational committee was asked to suggest a few cutting-edge functional neuroradiology techniques (hot topics). The following is a review of several of these topics and includes “Diffusion Tensor Imaging of the Pediatric Spinal Cord”; “Diffusional Kurtosis Imaging”; “From Standardization to Quantification: Beyond Biomarkers toward Bioscales as Neuro MR Imaging Surrogates of Clinical End Points”; Resting-State Functional MR Imaging”; and “Current Use of Cerebrovascular Reserve Imaging.”

**ABBREVIATIONS:** CVR = cerebrovascular reserve; DKI = diffusional kurtosis imaging; FA = fractional anisotropy; ISNCSI = Standards for Neurologic Classification of Spinal Cord Injury; MD = mean diffusivity; rs-fMRI = resting-state fMRI; SCI = spinal cord injury

## DIFFUSION TENSOR IMAGING OF THE PEDIATRIC SPINAL CORD

**Scott Faro, MD, and Feroze Mohamed, PhD; Department of Radiology, Temple University School of Medicine, Philadelphia, Pennsylvania**

Diffusion tensor imaging is a relatively new noninvasive MR imaging technique that quantifies the multidirectional diffusion of water molecules. There are many applications of DTI in the brain, and there is rising interest in exploring DTI applications in the spine. The unique characteristic architecture of the spinal cord is that its highly anisotropic nature may allow DTI to localize white matter, separate white from gray matter, and assess structural pathologic changes of the cord. Recent work has shown the clinical utility of DTI in spinal cord compression and cervical myelopathy in adults.<sup>1,2</sup> Pediatric DTI has also been explored recently, and several advances have been made in the field of DTI of pediatric spinal cord injury (SCI).<sup>3,4</sup> A variety of DTI indices has been explored, including fractional anisotropy (FA), mean diffusivity (MD), radial diffusivity, and axial diffusivity. Spinal cord injury occurs in both adults and children, with an estimated 11,000 cases occurring yearly in the United States. In this review, we will specifically look at the importance of DTI in pediatric SCI.

Currently, the evaluation and classification of neurologic im-

pairment in adults and children with SCI are assessed by using the International Standards for Neurologic Classification of Spinal Cord Injury (ISNCSI). These standards involve testing of motor and sensory functions of the limbs, trunk, rectum, and anorectal area and are used to predict recovery of neurologic function, plan treatment, and determine treatment effectiveness. The ISNCSI have relatively low utility in the pediatric population and can lead to unreliable assessment of neurologic abnormalities. An objective assessment of SCI may provide important information complementary to conventional clinical and imaging evaluation and may lead to a more accurate prognosis of recovery from SCI.

DTI of the spinal cord is technically limited by various factors. Specifically in pediatric populations, the small cord volume (approximately 1 cm in diameter) leads to a low SNR. Cerebral spinal fluid pulsation and blood flow can produce prominent ghosting artifacts and degrade image quality. The spinal cord is also subject to respiratory and cardiac movements, which cause image blurring and increased or decreased signal intensity. Different tissue interfaces (bone, soft tissue, or fluid) can create susceptibility artifacts. Swallowing or related motion artifacts are mostly seen when imaging the cervical spinal cord. Finally, in pediatric imaging especially, the possibility of increased subject motion makes obtaining accurate and reproducible DTI parameter values difficult. Artifact-reducing techniques can be used to overcome some of these issues. However, particularly in pediatric imaging, these techniques are not without challenges. Cardiac gating and respiratory compensation may increase acquisition time, and sedation

Please address correspondence to Scott H. Faro, MD, Department of Radiology, Temple University School of Medicine, 3401 N. Broad St, Philadelphia, PA 19140; e-mail: faros@tuhs.temple.edu

<http://dx.doi.org/10.3174/ajnr.A3721>

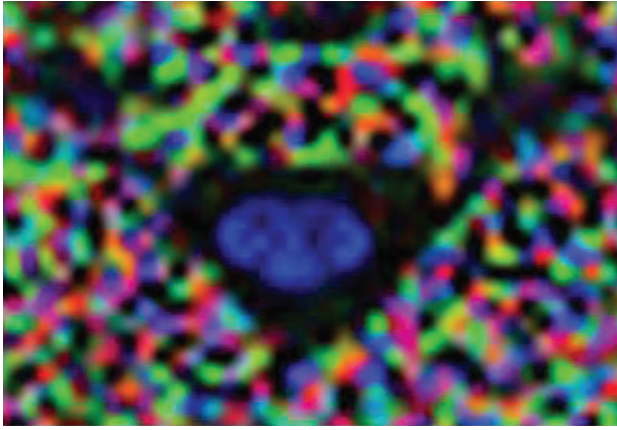


**FIG 1.** Axial color FA map of a normal midcervical spine in a healthy pediatric subject.

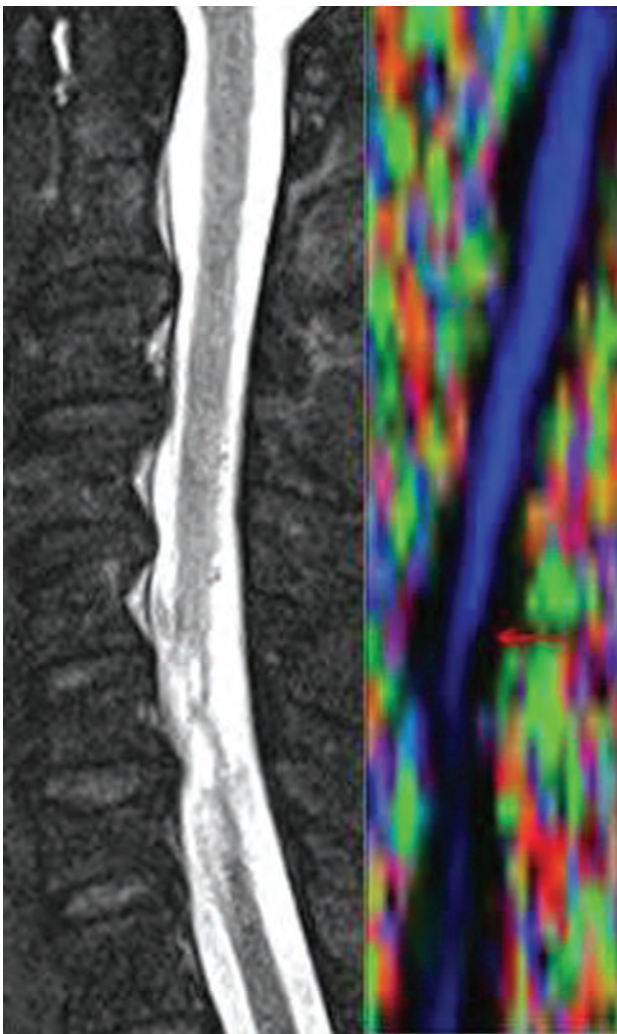


**FIG 2.** Color FA map of a patient with SCI (right) and a corresponding T2-weighted sagittal image (left) demonstrating SCI at the C5 level (arrow).

is typically not desirable in children. Thus, fast, reliable, and high-resolution imaging is needed to image pediatric subjects.

In Figs 1 and 2, we show the use of an inner FOV DTI imaging based on 2D radiofrequency excitations of the pediatric cervical

spinal cord. Figure 1 shows an axial color FA map of a healthy pediatric patient, which demonstrates very good gray/white matter differentiation and cord/CSF conspicuity. Figure 2 shows a sagittal color FA map and a TSE T2 image of a pediatric patient with a spinal cord injury, demonstrating a change in FA signal that corresponds to a lower cervical injury. Figure 3 shows a graphic representation of the DTI indices (FA, MD, radial diffusivity, and axial diffusivity) through the cervical spine in a pediatric patient with a focal C6 SCI. This graph shows, in addition to focal changes in DTI indices in the lower cervical spine (decreased FA, increased MD, radial diffusivity, and axial diffusivity), diffusion changes throughout the cord above the level of injury compared with a healthy control. The cervical cord above the injury did not demonstrate any abnormal signal on the T2-weighted images. This technique has been shown to be very useful in generating reliable and repeatable DTI data from the pediatric spinal cord and is a promising technique for quantification of SCI.

DTI will help our understanding of the pathophysiology of SCI and may give added information related to the clinical care of patients with SCI. Preliminary work has shown good correlation of ISNSCI scoring with DTI indices in these patients.<sup>5</sup> Research related to pediatric patients can be translatable to adult patients with SCI. Continued research by using DTI is needed to assess neurologic damage after traumatic SCI and to improve care, treatment, and rehabilitation methods.

#### **DIFFUSIONAL KURTOSIS IMAGING**

**Joseph A. Helpert, PhD, and Jens H. Jensen, PhD;**  
**Department of Radiology and Radiological Science,**  
**Medical University of South Carolina, Charleston,**  
**South Carolina**

The nominal resolution of human brain MR imaging is typically no more than a millimeter at best. This level of resolution provides excellent anatomic images, but the cellular microstructure, with characteristic lengths of tens of microns, is essentially invisible. This is a substantial limitation because disease processes often manifest themselves most clearly in terms of microstructural changes; this shortcoming is precisely the reason histopathology plays such a prominent role in the diagnosis of numerous maladies.

A powerful and elegant MR imaging method for investigating cellular microstructure is diffusion MR imaging. Diffusion MR imaging yields information about cellular microstructure due, in part, to a fortuitous matching of typical cellular sizes with the water diffusion lengths in biologic tissues during the time when the diffusion gradients are applied. Thus diffusing water is a natural reporter molecule for probing cellular microstructure.

To date, the leading MR imaging technique used to assess brain tissue microarchitecture is diffusion tensor imaging. Although DTI is powerful, it yields only a fraction of the potential information possible because it assumes that all water diffusion is Gaussian, even though we know it is not. In fact, by neglecting diffusional non-Gaussianity, DTI discards much of the microstructural information that diffusion MR imaging is, in principle, capable of detecting.

To have a diffusion MR imaging method that maintains the practical advantages of DTI (ease of implementation, time efficient) but also allows diffusional non-Gaussianity to be quantified, our group has developed an extension of DTI called diffu-

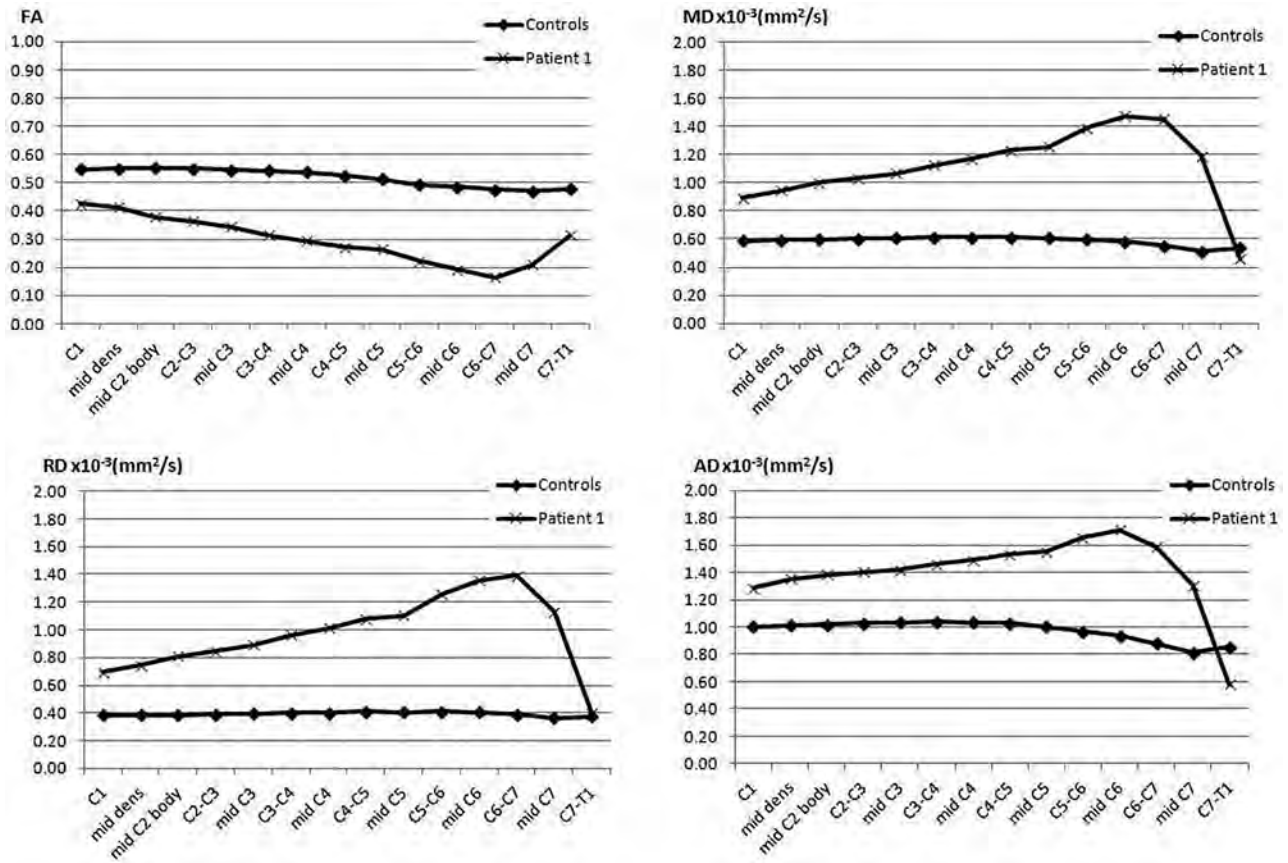


**FIG 3.** Healthy control and a patient with SCI at the mid-C6 level displaying changes in various DTI indices (FA, MD, radial diffusivity, and axial diffusivity) from C1 to C7.

sional kurtosis imaging (DKI).<sup>6-8</sup> Kurtosis is a well-established and widely used dimensionless statistical measure for quantifying the non-Gaussianity of arbitrary probability distributions, like that of diffusion. The significance of this approach is that diffusional non-Gaussianity effects are natural indicators of tissue microarchitectural complexity (ie, integrity) and may be used to improve tissue characterization, including changes associated with disease processes.

Since its introduction in 2005, DKI has been used to investigate several neuropathologies including brain cancer,<sup>9,10</sup> prostate cancer,<sup>11</sup> ischemic stroke,<sup>12,13</sup> attention deficit/hyperactivity disorder,<sup>14</sup> epilepsy,<sup>15</sup> Huntington disease,<sup>16</sup> brain trauma,<sup>17</sup> and spondylotic myelopathy.<sup>18</sup> For brain cancer, 2 prior studies<sup>9,10</sup> indicate that the additional information provided by DKI may improve the sensitivity and specificity for grading gliomas. For ischemic stroke,<sup>12,13</sup> large changes of 50%–100% in diffusional kurtosis may occur within ischemic lesions, suggesting profound changes in microstructural complexity. In addition, mismatches in the regions with decreased diffusivity and those with increased kurtosis are sometimes observed, suggesting that the 2 metrics are quantifying distinct microstructural changes. For brain trauma,<sup>17</sup> diffusional kurtosis has demonstrated sensitivity to microstructural damage exceeding that of conventional diffusion metrics obtainable with DTI. Figure 4 shows the mean diffusivity and mean kurtosis maps of a patient with subacute ischemic stroke. Notice the distinct ischemic lesion signal heterogeneity on mean kurtosis, which is not apparent on MD maps (red arrows).

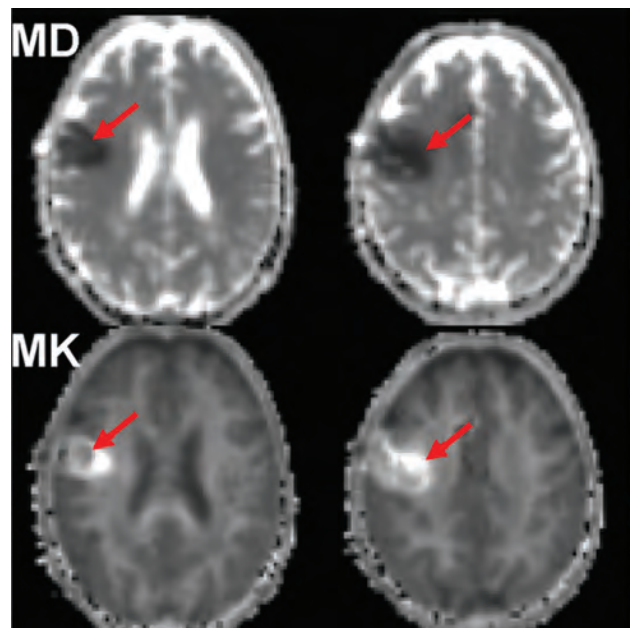


**FIG 4.** Mean diffusivity and mean kurtosis maps of a patient with subacute ischemic stroke. Notice the distinct ischemic lesion signal heterogeneity on mean kurtosis that is not apparent on MD maps (red arrows).

With standard clinical scanners and pulse sequences, high-quality, whole-brain DKI datasets may now be acquired within 7 minutes, making feasible its incorporation into many clinical and

## Features for a bioscale that enable its role as a surrogate for a clinical end point beyond the NIH definition of a biomarker

No.	Properties of a Bioscale	Implications
1	Image-derived map of the disease site	More sensitivity to earlier disease than diluted remote biomarkers
2	Spatially resolved quantitative parameter	Precise and accurate measurement
3	Small biologic variance in the healthy population	Sensitivity to early disease
4	Continuously and monotonically varying with disease progression	Sensitivity to disease progression or response to treatment
5	Intrinsically related to the disease mechanism	Highly conserved metabolic parameter, essential for use as a surrogate of a clinical end point

**Note:**—NIH indicates National Institutes of Health.

research protocols. Moreover, the application of DKI obviates DTI, because DKI provides all the metrics obtainable from DTI and with improved accuracy. Thus, upgrading from DTI to DKI only adds a few minutes of additional scanning time. In the near future, the imaging times for diffusion MR imaging in general, and DKI in particular, are likely to be substantially improved with the advent of multiband echo-planar sequences. Thus, the acquisition time will not be a significant obstacle for the widespread adoption of DKI. The DKI sequence is now a work in progress of Siemens Health Care (Erlangen, Germany) and is currently being tested at several medical centers worldwide. To learn more about DKI and to download free software for analysis, please go to <http://academicdepartments.musc.edu/cbi/dki/>.

### FROM STANDARDIZATION TO QUANTIFICATION: BEYOND BIOMARKERS TOWARD BIOSCALES AS NEURO MR IMAGING SURROGATES OF CLINICAL END POINTS

**Keith R. Thulborn and Ian C. Atkinson; Center for Magnetic Resonance Research, University of Illinois at Chicago, Chicago, Illinois**

The term “biomarker” has been defined by the National Institutes of Health as “a characteristic that is objectively measured and evaluated as an indicator of normal biologic processes, pathogenic processes, or pharmacologic responses to a therapeutic intervention.” Biomarkers have conventionally been genes, gene products, or metabolites that are obtained from bodily fluids, often remote from the site of disease and measured as concentrations by using standard analytic techniques that have established accuracies. The use of such nonimaging biomarkers as surrogates for clinical end points (eg, high blood pressure is an early indicator for cardiac disease) has a long history that is encapsulated statistically in the controversies of the Prentice criterion.<sup>19</sup> The validation of a biomarker as equivalent to a true outcome is non-trivial because that validity requires a full trial that makes the need for the subsequent use of a biomarker questionable in some circumstances.<sup>20</sup> In fact, the reality is that even the most highly cited biomarkers introduced into medicine from single studies fail to prove useful in subsequent meta-analyses.<sup>21</sup> Despite these concerns, the incentive for pursuing surrogate measures of a true clinical end point is the possibility of shortening durations and decreasing population sizes required for clinical trials.

Despite these controversial issues of biomarker validity, imaging characteristics have been proposed as potential biomarkers. Imaging parameters are typically arbitrary signal-intensity scales that require the acquisition procedures to be quantified if the scale is to be compared during a certain time or between patients.

“Quantification” is a term that contains the concept of accuracy relative to a known standard and has dimensional units.

For imaging to provide a useful surrogate end point for clinical trials, the imaging characteristic must be calibrated to establish its distribution (mean, variance) in the normal population. Ideally, the biologic variance should be small. Because the progression from healthy to illness is usually continuous, any parameter measuring this progression should also be continuous. A parameter that continuously reflects normal to progressively worsening disease is unlikely to discriminate early disease unless it undergoes changes that are large compared with the normal variance. This possible outcome is an expression of the Prentice criterion,<sup>19</sup> in that the surrogate parameter must be related mechanistically to the progression of the disease. This simple rationale suggests some features that are needed for an imaging parameter to be useful as a surrogate of a clinical end point (Table). Imaging potentially offers sensitivity to early disease by having direct access to the site of disease rather than being dependent on the release of biomarker molecules into bodily fluids that are only sampled remotely after dilution.

The signal intensity of clinical MR imaging is not only a reflection of the concentration and nuclear properties of the hydrogen nuclei in the patient but is highly dependent on acquisition parameters and equipment performance. The nuclear properties of protons, expressing the nuclear and electronic dipolar interactions of the hydrogen atoms in water and fat, as summarized by the longitudinal and transverse relaxation parameters, only distantly reflect the biology of the tissue. The MR signal from water reflects the tissue milieu rather than metabolic reactions. However, high concentrations are required to generate sufficient MR signal for spatial encoding into an image at a relevant resolution in an acceptable acquisition time for patients. This requirement limits metabolic observations. Although MR imaging is remarkably good at displaying anatomy, especially of the brain, anatomy is not a useful surrogate of early disease because of its wide biologic variance. For example, brain volume decreases with age in cognitively healthy subjects and in patients with dementia. Although, on average, patients with dementia have smaller brain volumes than healthy subjects, brain volumes vary greatly and have considerable overlap between these groups so that brain volume does not allow an individual patient to be classified confidently into either category. This example illustrates that useful surrogates must not only be measured accurately but also have small biologic variance to provide sensitivity for the detection of early disease and its progression. In contrast to the desirable diversity (ie, variance) of anatomy that drives evolution, a small biologic variance suggests the need for a parameter that is highly conserved and vital for biologic health.

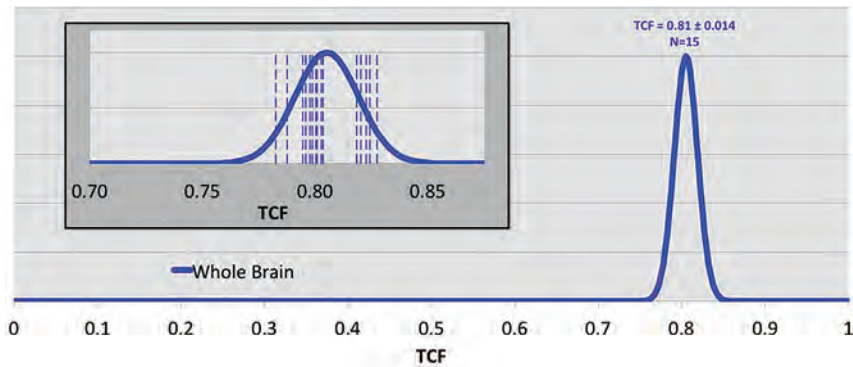


**FIG 5.** Distribution of tissue cell fraction measured in brain parenchyma for the whole brain, including gray and white matter (blue,  $0.81 \pm 0.014$ ) for cognitively healthy individuals ( $n = 15$ ). The inset shows the individual measurements (*vertical dashed lines*) of each individual. The SD of the distribution of cell attenuation in healthy subjects is  $<2\%$  of the total range of possible cell densities.

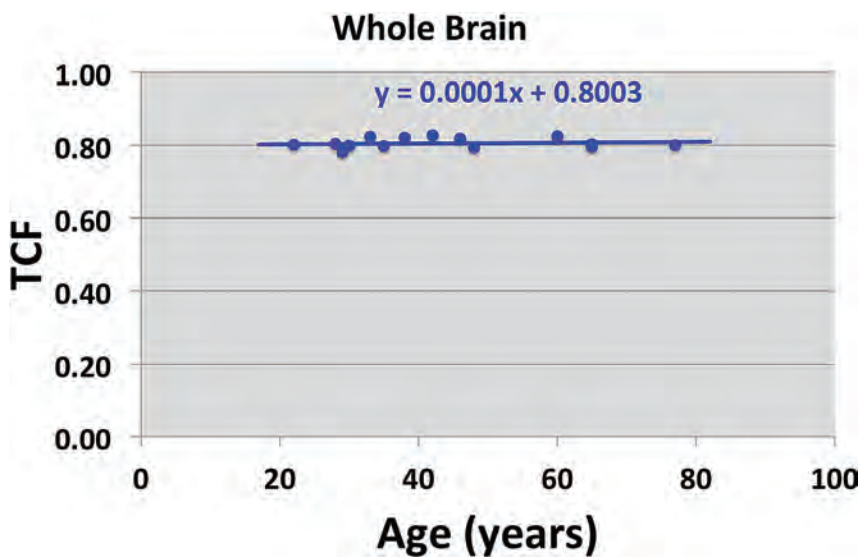


**FIG 6.** Tissue cell fraction as a function of age (years) in the cognitively healthy subjects in Fig 1. The fitted line has a near-zero gradient, indicating that there is no age dependence for mean kurtosis in the whole brain of cognitively healthy individuals.

A pertinent example of a highly conserved metabolic process is sodium ion homeostasis in the brain.<sup>22</sup> This tightly regulated process is controlled by systemic, tissue, and cellular events to ensure a stable resting membrane potential across the neuron cell membrane that fuels the action potentials of brain function. Sodium MR imaging can quantify this homeostatic process by measuring the tissue sodium concentration, TSC, and its derived equivalent of tissue cell fraction, TCF.<sup>23</sup> These parameters can be measured precisely with an experimental error of approximately 5% after B0 and B1 corrections and calibration in  $<30$  minutes of patient time at 3T at a nominal isotropic spatial resolution of 5 mm. The mean kurtosis parameter has a narrow variance, as shown in Fig 5, and may be very sensitive to hippocampal cell loss in mild cognitive impairment and probably Alzheimer disease. Its independence of subject age in cognitively healthy individuals, as shown in Fig 6, indicates the importance of cell density for normal cognitive function. An operational definition of cell viability is its ability to maintain the integrity of its cell membrane. Examples of the sensitivity of tissue sodium concentration and

mean kurtosis measurements in the settings of acute stroke and treatment response of brain tumors have been published.<sup>24,25</sup>

Rather than use the term “imaging biomarker,” which refers to a descriptive risk factor for predicting clinical outcomes, the term “bioscale” has been coined to reflect the features of an imaging-based parameter needed to be a useful surrogate marker in clinical states. A bioscale is a continuous variable that is quantified against a standard with a defined accuracy. The bioscale has a small range (small variance) of normal values indicating its fundamental importance for health. A bioscale should directly reflect the cellular processes that are disrupted by the disease, as required by the validity criteria.<sup>20</sup> Bioscale encompasses the concept of noninvasive spatial quantification that is available in an image of the site of the disease. As the imaging parameter is mechanistically linked to the disease process, the validity criteria that underlie the concept of surrogate markers are addressed. The statistical requirements of surrogate markers of clinical outcomes suggest that metabolic imaging by using nuclei (sodium 23) other than protons may have added value, especially now that there are solutions to the lower intrinsic sensitivity of these nuclei at higher field strengths.<sup>26</sup>

## RESTING-STATE FUNCTIONAL MR IMAGING

**Haris Sair, MD; Department of Radiology, Johns Hopkins School of Medicine, Baltimore, Maryland**

Resting-state functional MR imaging (rs-fMRI) has emerged as a novel tool to supplement task-based fMRI in the evaluation of brain function. Spontaneous low-frequency fluctuations in regional cerebral blood flow have been demonstrated with blood oxygen level–dependent imaging, occurring at a frequency of approximately 0.01–0.1 Hz<sup>27</sup>; these spatially distinct, however temporally synchronous, fluctuations constitute “functionally related” brain areas, whose regions form intrinsic brain networks.<sup>28,29</sup> A relatively consistent set of reproducible brain networks has been demonstrated by various groups.<sup>30,31</sup> Although a universal set of intrinsic networks has not been agreed on, several major networks have been investigated in detail, including the motor network, language network (Fig 7), and the default mode network, the most studied of these networks.

There are several advantages of using rs-fMRI in contrast to traditional task-based fMRI. First, these intrinsic low-frequency fluctuations account for a large percentage of blood oxygen level–dependent modulation, even in task-based fMRI experiments, thereby allowing higher sensitivity in signal detection.<sup>32</sup> Second, a limitation of task-based fMRI is the necessity of designing a spe-

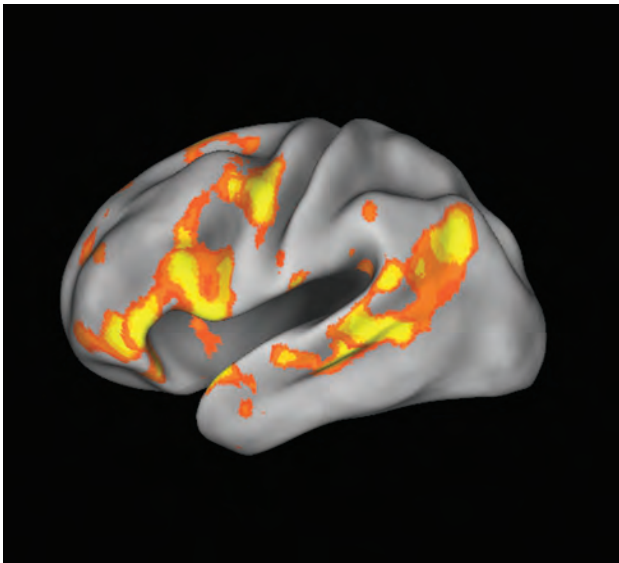


**FIG 7.** Language network extracted from resting-state fMRI by using independent component analysis in a single healthy control demonstrates Broca and Wernicke areas.

sific task paradigm to interrogate changes associated with a specific neurobehavioral response. No specific task is designated in rs-fMRI (other than instructions on keeping the eyes either closed or open, the latter either fixated on a cross-hair or allowing random eye motion). Third, related to the second advantage is the fact that in many situations, a subject may not be able to perform the task adequately to elicit a reliable blood oxygen level–dependent modulation response. This scenario can occur in various circumstances, for example, in imaging children, debilitated patients, and those whose native language is different from the that in the paradigm used. Last, rs-fMRI has the potential benefit of allowing shorter imaging time to generate more information compared with task fMRI. For example, in clinical presurgical mapping in which motor and language tasks are used, there may be a variety of paradigms used in task fMRI, with several of them repeated to ensure reliability. Although the optimum scanning time for reliable network mapping in individual subjects using rs-fMRI is still being investigated, at the group level, approximately 6–7 minutes of scanning time has been shown to be adequate for reliable network detection.<sup>31</sup> Furthermore, instead of being able to generate only one specific domain such as language-related brain areas, the benefit of rs-fMRI is that multiple brain networks may be generated using a single run.

In analyzing functional connectivity at rest, several approaches are used, the most common being region of interest–based correlations, as well as model-free analysis using independent component analysis or clustering.<sup>33</sup> In addition to connectivity within the respective intrinsic brain networks, information regarding between-network correlations also yields important clues in normal brain function and disruption of those relationships in disease.<sup>34</sup>

Disruptions of brain networks have been demonstrated in various diseases, including Alzheimer disease, major depression, and epilepsy, to name a few. Although the list of findings in rs-fMRI pertaining to disease is extensive and beyond the scope of this article,

several categories of clinical rs-fMRI applications can be demonstrated. First, rs-fMRI may serve as an adjunct tool for clinical or preclinical diagnosis. As an example of patients with cognitive disorders, a difference in default mode network connectivity was demonstrated in patients with mild cognitive impairment who eventually converted to Alzheimer disease compared with mild cognitive impairment nonconverters.<sup>35</sup> Rs-fMRI may also allow better subsegmentation of heterogeneous diseases such as schizophrenia or the various dementias<sup>36</sup> or identification of patients in whom pharmacologic intervention may or may not be successful on the basis of intrinsic connectivity before treatment.<sup>37</sup> Furthermore, rs-fMRI may be used as a potential biomarker for outcome, for example, in the setting of traumatic brain injury. An especially important use of rs-fMRI, presurgical mapping, is emerging, in particular in epileptogenic localization<sup>38</sup> or in brain tumors.<sup>39</sup>

Although the majority of rs-fMRI literature has focused on group-level analyses, the challenge of rs-fMRI is to demonstrate utility at the subject level. Preliminary studies of motor mapping in presurgical mapping have yielded promising results,<sup>39</sup> with motor-network extraction possible, even with the patient under anesthesia.<sup>40</sup>

Specific challenges are encountered when attempting to analyze rs-fMRI at the subject level. Mueller et al<sup>41</sup> demonstrated that there is high intersubject variability in intrinsic brain networks generated from rs-fMRI, with differences in variability across cortical regions. For networks that are inherently variable across subjects, it will, therefore, be difficult to determine whether deviations from “known normal” connectivity of a particular network in an individual are related to that individual’s specific connectivity profile or whether they are due to disease. In addition, functional connectivity may be altered depending on a subject’s state, rather than trait. The optimum scanning length and parameters for reliable subject-level brain mapping using rs-fMRI are yet to be established.

These differences in acquisition parameters and processing/analysis pipelines may also yield vastly different results in rs-fMRI data. Head motion can introduce significant spurious functional correlations.<sup>42</sup> Nuisance removal, which also is not standardized, may introduce errors.<sup>43</sup> There is ongoing debate on the issue of instructing the subject to keep his or her eyes open or closed. Further work is necessary to determine a possible standardization, which would be important for using rs-fMRI as a clinically viable tool.

## CURRENT USE OF CVR IMAGING IN CLINICAL NEURORADIOLOGY

**David Mikulis, MD; Department of Medical Imaging, University of Toronto, University Health Network, Toronto Western Hospital, Toronto, Ontario, Canada**

The high metabolic rate of the brain places significant demand on energy resources, even at resting levels of activity.<sup>44</sup> The demand dramatically increases up to 3-fold during functional activation.<sup>45</sup> If the delivery of energy substrates, primarily oxygen and glucose, is not matched to metabolic demand, even for brief periods of time, functional impairment and even permanent injury can occur. A highly regulated mechanism has therefore evolved to control blood flow to match supply with demand. The flow-control mechanism achieves this by modulating the diameter of all arteries ranging from large arteries to arterioles. Most interesting, the capacity to dynamically modulate resistance increases with decreasing arterial size.<sup>46</sup> Blood

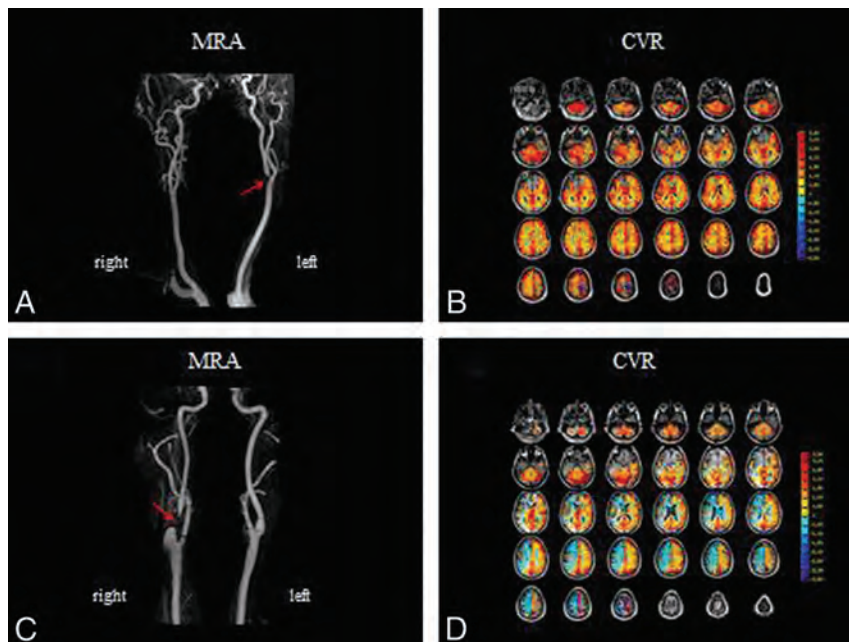


**FIG 8.** The results of CVR mapping by using a controlled elevation of arterial carbon dioxide during blood oxygen level–dependent MR imaging in 2 different patients presenting with transient ischemic attacks. Both patients (A and C) have >90% carotid stenosis on MR angiography (red arrows). Corresponding CVR maps are shown with red/orange/yellow indicating increased oxyhemoglobin and therefore increased blood flow with CO<sub>2</sub>-induced vasodilation and blue indicating increased deoxyhemoglobin and therefore decreased blood flow with CO<sub>2</sub>-induced vasodilation. In the first patient, CVR is normal (B), indicating excellent collaterals, implying an embolic origin of symptoms. In the second patient (D), the CVR map shows blue in the anterior circulation, indicating exhausted vascular reserve and steal physiology, implying that the symptoms are secondary to hemodynamic compromise. As opposed to the first patient, the second patient would not benefit from medical management alone requiring a flow-restoration procedure (endarterectomy or stent placement) to alleviate symptoms and stroke risk. Note that in both cases, findings of conventional perfusion imaging with MR imaging or CT by using dynamic bolus techniques would be abnormal, showing delays in transit time in the affected hemispheres.

flow to the microcirculation is, therefore, determined by 2 parameters: blood pressure and the overall resistance to flow in the upstream vasculature proximal to the capillary beds. The only caveats are the ability of capillary pericytes to contract<sup>47</sup> and the resistance present in the venous vasculature.

Primary defects in the flow-control mechanism itself have not been clearly established, though dysregulation of flow has been implicated in diseases such as migraine, posterior reversible encephalopathy syndrome, reversible cerebral vasospasm syndrome, and pseudotumor cerebri, to name a few. The most common clinical condition in which the flow-control mechanism plays a key role is in cerebrovascular steno-occlusive disease most commonly caused by transient cerebral arteriopathy of childhood in the pediatric age group and by atherosclerosis in adults. The presence of a stenosis or occlusion leads to compensatory vasodilation in the arterial vasculature distal to the stenosis, preserving resting cerebral blood flow at normal levels. Because the ability to vasodilate is not infinite, the vasodilatory response to stenosis or occlusion may exhaust itself in the attempt to maintain normal resting CBF. Under these circumstances, increased neuronal activity may not be met with increased blood flow. A mismatch between blood supply and demand ensues, which, by definition, represents ischemia unless it is matched by increased oxygen (and possibly glucose) extraction. Note that this does not represent failure of the flow-control mechanism per se. It simply indicates

exhaustion of an appropriate response by a normal flow-control mechanism. Resting cerebral blood flow may be normal even when autoregulation is exhausted, indicating that detection of this condition may not be achievable by using resting blood flow measurement techniques such as arterial spin-labeling. However, flow-measurement techniques that use bolus perfusion methods (perfusion CT and perfusion MRI) can yield, in addition to CBF, transit time and cerebral blood volume measures. Transit time and CBV will be abnormal when vascular reserve is exhausted, but they can also be abnormal with little or no exhaustion of vascular reserve if excellent collateral circulation has developed.

Exhaustion of vascular reserve can be detected by using any of several different modalities, including Doppler sonography, SPECT, xenon CT, perfusion CT, perfusion MRI, and blood oxygen level–dependent MR imaging. Each requires comparison of changes in blood flow before and after a vasodilatory stimulus. Is it important, however, to take this measurement if resting blood flow is normal? Is it if one considers that ischemia in patients with exhausted reserve is a dynamic condition occurring at a time when the brain needs flow the most—during neuronal activation. This concept of dynamic ischemia under conditions with normal CBF is not usually a clinical consideration, though the potential consequences of this abnormal flow physiology were first described by Fisher.<sup>48</sup> He observed progressive dementia in patients with bilateral carotid occlusions in the absence of acute ischemic events. More recently, we observed the effects of this condition on cortical thickness. Thinning of the cerebral cortex was found in areas where the control mechanism was exhausted.<sup>49</sup> Most surprisingly, rethickening was observed following revascularization.<sup>50</sup> The implications are that the chronic ischemic events occurring during neuronal activation (ie, neurovascular uncoupling) lead to nonlethal injury to the neuropil (possibly decreased dendritic arborization and decreased synaptic density), which recovers following revascularization.

Although no pathologic studies have been performed to prove this hypothesis, the concept has been further supported by evidence of decreased *N*-acetylaspartate acid levels (a marker of healthy neurons) in the cerebral cortex with exhausted vascular reserve (D.M., unpublished data). It is also supported by the Randomized Evaluation of Carotid Occlusion and Neurocognition (RECON) I study.<sup>51</sup> In this study, patients with carotid occlusion, who were recruited for the Carotid Occlusion Surgery Study (COSS),<sup>52</sup> were randomized into 2 groups: those with and those without an increased oxygen extraction fraction. A significant reduction in cognition was observed in the group with the increased

oxygen extraction fraction. A follow-up study in these patients has not yet been reported, to our knowledge, but it is anticipated that cognitive improvement would be observed in those with an increased oxygen extraction fraction following extracranial-intracranial bypass compared with those treated medically. This finding could influence the direction of future research to more thoroughly examine the relationship between cognitive decline and cervicocerebral steno-occlusive disease. Measurement of vascular reserve would obviously play a key role in this regard.

Exhaustion of cerebrovascular reserve (CVR) can also be associated with steal phenomenon. It is now well-established that paradoxical reductions in blood flow can occur in tissues supplied by vessels with stenoses or occlusions during a vasodilatory stimulus. Studies have shown that steno-occlusive disease, when accompanied by steal physiology, carries up to 5 times the risk of ischemic injury.<sup>53</sup> Despite this evidence, routine clinical application of CVR measurement is lacking. The reason for this is that current standards of practice have been based on trials (Asymptomatic Carotid Atherosclerosis Study and Asymptomatic Carotid Surgery Trial)<sup>54,55</sup> that advocate surgical management for asymptomatic carotid stenosis in excess of 70%. Under these conditions, further testing is unnecessary because the added information would not alter management. Recent studies such as the Stenting and Aggressive Medical Management for Preventing Recurrent Stroke in Intracranial Stenosis (SAMMPRIS) trial,<sup>56</sup> however, are beginning to show that aggressive or maximal medical management alone may match surgical outcomes. If under these circumstances, invasive treatment is only applied following failure in conservative management, then measurement of blood flow physiology remains moot.

So what is the clinical utility of CVR measurement? No prospective clinical trials have shown positive outcomes with measurement of vascular reserve embedded in management algorithms. Neither have there been positive clinical trials measuring resting blood flow parameters. However, in the future, 3 factors are likely to play an important role in proving the value of assessing flow physiology. The first is that proper selection of surgical candidates is critical for optimizing outcome. A criticism of the COSS study was that the oxygen extraction fraction thresholds used for selecting surgical candidates were too liberal so that the surgical group included a proportion of patients with less than severe flow deficits.<sup>57</sup> Future clinical trials are needed to more fully elucidate this issue. The second factor is cost. Conservative management is 3 to 8 times more cost-effective than surgical management,<sup>58</sup> again emphasizing the need for optimal selection strategies for costly invasive procedures. The final factor is the association of hemodynamic impairment with cognitive decline, especially if the decline can be shown to reverse after revascularization. The motivation to preserve or potentially improve cognition would clearly have profound effects on the standard of practice as it relates to caring for patients with steno-occlusive disease. Examples of the clinical use of CVR mapping are shown in Fig 8. These figures show the results of CVR by using a controlled elevation of arterial carbon dioxide during blood oxygen level-dependent MR imaging in 2 different patients presenting with transient ischemic attacks.

In summary, the importance of impaired blood flow control and blood flow hemodynamics has not yet entered mainstream management for patients with steno-occlusive diseases of the cervicocerebral vasculature. However, economics may eventually

pressure the health care system into making more cost-effective choices, especially when the high annual costs of endarterectomies are considered. With 140,000 carotid endarterectomies performed in the United States in 2009<sup>59</sup> and assuming \$8000 cost per operation,<sup>60</sup> the cost to the health care system for endarterectomies alone is on the order of is \$1.1 billion annually. Considerable work toward finding optimal patient selection criteria is needed without compromising health care. Measurement of blood flow hemodynamics is a promising tool that could provide the important information for achieving this goal.

## REFERENCES

1. Wang W, Qin W, Hao N, et al. **Diffusion tensor imaging in spinal cord compression.** *Acta Radiol* 2012;53:921–28
2. Sato T, Horikoshi T, Watanabe A, et al. **Evaluation of cervical myelopathy using apparent diffusion coefficient measured by diffusion-weighted imaging.** *AJNR Am J Neuroradiol* 2012;33:388–92
3. Mohamed F, Hunter L, Barakat N, et al. **Diffusion tensor imaging of the pediatric spinal cord at 1.5 T: preliminary results.** *AJNR Am J Neuroradiol* 2011;32:339–45
4. Barakat N, Mohamed F, Hunter L, et al. **Diffusion tensor imaging of the normal pediatric spinal cord using an inner-field of view echo-planar imaging sequence.** *AJNR Am J Neuroradiol* 2012;33:1127–33
5. Mulcahey MJ, Samdani A, Gaughan J, et al. **Diffusion tensor imaging in pediatric spinal cord injury: preliminary examination of reliability and clinical correlation.** *Spine (Phila Pa 1976)* 2012;37:E797–803
6. Jensen JH, Helpert JA, Ramani A, et al. **Diffusional kurtosis imaging: the quantification of non-gaussian water diffusion by means of magnetic resonance imaging.** *Magn Reson Med* 2005;53:1432–40
7. Lu H, Jensen JH, Ramani A, et al. **Three-dimensional characterization of non-gaussian water diffusion in humans using diffusion kurtosis imaging.** *NMR Biomed* 2006;19:236–47
8. Jensen JH, Helpert JA. **Progress in diffusion-weighted imaging: concepts, techniques and applications to the central nervous system.** *NMR Biomed* 2010;23:659–60
9. Raab P, Hattingen E, Franz K, et al. **Cerebral gliomas: diffusional kurtosis imaging analysis of microstructural differences.** *Radiology* 2010;254:876–81
10. Van Cauter S, Veraart J, Sijbers J, et al. **Gliomas: diffusion kurtosis MR imaging in grading.** *Radiology* 2012;263:492–501
11. Rosenkrantz AB, Sigmund EE, Johnson G, et al. **Prostate cancer: feasibility and preliminary experience of a diffusional kurtosis model for detection and assessment of aggressiveness of peripheral zone cancer.** *Radiology* 2012;264:126–35
12. Jensen JH, Falangola MF, Hu C, et al. **Preliminary observations of increased diffusional kurtosis in human brain following recent cerebral infarction.** *NMR Biomed* 2011;24:452–57
13. Hui ES, Fieremans E, Jensen JH, et al. **Stroke assessment with diffusional kurtosis imaging.** *Stroke* 2012;43:2968–73
14. Helpert JA, Adisetiyo V, Falangola MF, et al. **Preliminary evidence of altered gray and white matter microstructural development in the frontal lobe of adolescents with attention-deficit hyperactivity disorder: a diffusional kurtosis imaging study.** *J Magn Reson Imaging* 2011;33:17–23
15. Gao Y, Zhang Y, Wong CS, et al. **Diffusion abnormalities in temporal lobes of children with temporal lobe epilepsy: a preliminary diffusional kurtosis imaging study and comparison with diffusion tensor imaging.** *NMR Biomed* 2012;25:1369–77
16. Blockx I, Verhoye M, Van Audekerke J, et al. **Identification and characterization of Huntington related pathology: an in vivo DKI imaging study.** *Neuroimage* 2012;63:653–62
17. Grossman EJ, Ge Y, Jensen JH, et al. **Thalamus and cognitive impairment in mild traumatic brain injury: a diffusional kurtosis imaging study.** *J Neurotrauma* 2012;29:2318–27
18. Hori M, Fukunaga I, Masutani Y, et al. **New diffusion metrics for**

- spondylotic myelopathy at an early clinical stage. *Eur Radiol* 2012;22:1797–802
19. Prentice RI. **Surrogate endpoints in clinical trials: definition and operational criteria.** *Stat Med* 1989;8:431–40
  20. Berger VW. **Does the Prentice criterion validate surrogate endpoints?** *Stat Med* 2004;23:1571–78
  21. Ioannidis JP, Panagiotou OA. **Comparison of effect sizes associated with biomarkers reported in highly cited individual articles and in subsequent meta-analyses.** *JAMA* 2011;305:2200–10
  22. Lu A, Atkinson IC, Claiborne T, et al. **Quantitative sodium imaging with a flexible twisted projection pulse sequence.** *Magn Reson Med* 2010;63:1583–93
  23. Lu A, Atkinson IC, Thulborn KR. **Sodium magnetic resonance imaging and its bioscale of tissue sodium concentration.** In: Harris RK, Wasylshen RE, eds. *Encyclopedia of Magnetic Resonance*. Hoboken, New Jersey: John Wiley; September 15, 2010.
  24. Thulborn KR, Davis D, Snyder J, et al. **Sodium MR imaging of acute and subacute stroke for assessment of tissue viability.** *Neuroimaging Clin N Am* 2005 15:639–53
  25. Thulborn KR, Lu A, Atkinson IC, et al. **Quantitative sodium MR imaging and sodium bioscales for the management of brain tumors.** *Neuroimaging Clin N Am* 2009;19:615–24
  26. Thulborn KR. **The challenges of integrating a 9.4T MR scanner for human brain imaging.** In: Robitaille P-M, Berliner LJ, eds. *Ultra High Field Magnetic Resonance Imaging*. New York: Springer-Verlag Science and Business Media; 2006:105–26
  27. Biswal B, Yetkin FZ, Haughton VM, et al. **Functional connectivity in the motor cortex of resting human brain using echo-planar MRI.** *Magn Reson Med* 1995;34:537–41
  28. Beckmann CF, DeLuca M, Devlin JT, et al. **Investigations into resting-state connectivity using independent component analysis.** *Philos Trans R Soc Lond B Biol Sci* 2005;360:1001–13
  29. van den Heuvel MP, Mandl RC, Kahn RS, et al. **Functionally linked resting-state networks reflect the underlying structural connectivity architecture of the human brain.** *Hum Brain Mapp* 2009;30:3127–41
  30. Damoiseaux JS, Rombouts SA, Barkhof F, et al. **Consistent resting-state networks across healthy subjects.** *Proc Natl Acad Sci U S A* 2006;103:13848–53
  31. Van Dijk KR, Hedden T, Venkataraman A, et al. **Intrinsic functional connectivity as a tool for human connectomics: theory, properties, and optimization.** *J Neurophysiol* 2010;103:297–321
  32. Fox MD, Snyder AZ, Zacks JM, et al. **Coherent spontaneous activity accounts for trial-to-trial variability in human evoked brain responses.** *Nat Neurosci*. 2006;9:23–5
  33. Fox MD, Greicius M. **Clinical applications of resting state functional connectivity.** *Front Syst Neurosci* 2010;4:19
  34. Spreng RN, Sepulcre J, Turner GR, et al. **Intrinsic architecture underlying the relations among the default, dorsal attention, and fronto-parietal control networks of the human brain.** *J Cogn Neurosci* 2013;25:74–86
  35. Petrella JR, Sheldon FC, Prince SE, et al. **Default mode network connectivity in stable vs progressive mild cognitive impairment.** *Neurology* 2011;76:511–17
  36. Pievani M, de Haan W, Wu T, et al. **Functional network disruption in the degenerative dementias.** *Lancet Neurol* 2011;10:829–43
  37. Guo WB, Liu F, Chen JD, et al. **Abnormal neural activity of brain regions in treatment-resistant and treatment-sensitive major depressive disorder: a resting-state fMRI study.** *J Psychiatr Res* 2012;46:1366–73
  38. Stufflebeam SM, Liu H, Sepulcre J, et al. **Localization of focal epileptic discharges using functional connectivity magnetic resonance imaging.** *J Neurosurg* 2011;114:1693–97
  39. Zhang D, Johnston JM, Fox MD, et al. **Preoperative sensorimotor mapping in brain tumor patients using spontaneous fluctuations in neuronal activity imaged with functional magnetic resonance imaging: initial experience.** *Neurosurgery* 2009;65(6 suppl):226–36
  40. Breshears JD, Gaona CM, Roland JL, et al. **Mapping sensorimotor cortex with slow cortical potential resting-state networks while awake and under anesthesia.** *Neurosurgery* 2012;71:305–16
  41. Mueller S, Wang D, Fox MD, et al. **Individual variability in functional connectivity architecture of the human brain.** *Neuron* 2013;77:586–95
  42. Power JD, Barnes KA, Snyder AZ, et al. **Spurious but systematic correlations in functional connectivity MRI networks arise from subject motion.** *Neuroimage* 2012;59:2142–54
  43. Hallquist MN, Hwang K, Luna B. **The nuisance of nuisance regression: Spectral misspecification in a common approach to resting-state fMRI preprocessing reintroduces noise and obscures functional connectivity.** *Neuroimage* 2013;82:208–25
  44. Raichle ME, MacLeod AM, Snyder AZ, et al. **A default mode of brain function.** *Proc Natl Acad Sci U S A* 2001;98:676–82
  45. Attwell D, Laughlin SB. **An energy budget for signaling in the grey matter of the brain.** *Cereb Blood Flow Metab* 2001;21:1133–45
  46. Tuor UI, Farrar JK. **Pial vessel caliber and cerebral blood flow during hemorrhage and hypercapnia in the rabbit.** *Am J Physiol* 1984; 247(1 pt 2):H40–51
  47. Hamilton NB, Attwell D, Hall CN. **Pericyte-mediated regulation of capillary diameter: a component of neurovascular coupling in health and disease.** *Front Neuroenergetics* 2010;2. pii
  48. Fisher CM. **Occlusion of the carotid arteries: further experiences.** *AMA Arch Neurol Psychiatry* 1954;72:187–204
  49. Fierstra J, Poulblanc J, Han JS, et al. **Steal physiology is spatially associated with cortical thinning.** *J Neurol Neurosurg Psychiatry* 2010;81:290–93
  50. Fierstra J, Maclean DB, Fisher JA, et al. **Surgical revascularization reverses cerebral cortical thinning in patients with severe cerebrovascular steno-occlusive disease.** *Stroke* 2011;42:1631–37
  51. Marshall RS, Festa JR, Cheung YK, et al. **Cerebral hemodynamics and cognitive impairment: baseline data from the RECON trial.** *Neurology* 2012;78:250–55
  52. **Failure of extracranial-intracranial arterial bypass to reduce the risk of ischemic stroke: results of an international randomized trial—the EC/IC Bypass Study Group.** *N Engl J Med* 1985;313:1191–200
  53. Blaser T, Hofmann K, Buerger T, et al. **Risk of stroke, transient ischemic attack, and vessel occlusion before endarterectomy in patients with symptomatic severe carotid stenosis.** *Stroke* 2002;33:1057–62
  54. **Endarterectomy for asymptomatic carotid artery stenosis: Executive Committee for the Asymptomatic Carotid Atherosclerosis Study.** *J Am Med Assoc* 1995;273: 1421–28
  55. Halliday A, Mansfield A, Marro J, et al, for the MRC Asymptomatic Carotid Surgery Trial (ACST) Collaborative Group. **Prevention of disabling and fatal strokes by successful carotid endarterectomy in patients without recent neurological symptoms: randomised controlled trial.** *Lancet* 2004;363:1491–502. Erratum in *Lancet* 2004;364:416
  56. Chimowitz MI, Lynn MJ, Derdeyn CP, et al, for the SAMMPRIS Trial Investigators. **Stenting versus aggressive medical therapy for intracranial arterial stenosis.** *N Engl J Med* 2011;365:993–1003
  57. Yonas H, Carlson A, Nemoto EM. **Carotid Occlusion Surgery Study (COSS): Failure of concept or methodology?** In: *Proceedings of the XXVth Symposium of International Society of Cerebral Blood Flow and Metabolism and the Xth International Conference on the Quantification of Brain Function with PET*, Barcelona, Spain. May 25–28, 2011
  58. Abbott AL. **Medical (nonsurgical) intervention alone is now best for prevention of stroke associated with asymptomatic severe carotid stenosis: results of a systematic review and analysis.** *Stroke* 2009;40:e573–83
  59. National Hospital Discharge Survey 2009. Centers for Disease Control and Prevention. <http://www.cdc.gov/nchs/nhds.htm>. Accessed December 2010
  60. Kilaru S, Korn P, Kasirajan K, et al. **Is carotid angioplasty and stenting more cost effective than carotid endarterectomy?** *J Vasc Surg* 2003;37:331–39

# Neurofibromatosis: Types 1 and 2

S. Borofsky and L.M. Levy

## ABSTRACT

**SUMMARY:** Neurofibromatosis types 1 and 2 are a group of neurocutaneous syndromes resulting from disorders in cell regulation. Despite sharing a common name, neurofibromatosis types 1 and 2 are quite distinct phakomatoses, both clinically and genetically.

**ABBREVIATIONS:** NF-1 = neurofibromatosis type 1; NF-2 = neurofibromatosis type 2; MAPK = ras/mitogen-activated protein kinase pathway

Neurofibromatosis type 1 is seen in 1 of 3000–5000 people across the world.<sup>1</sup> This disease was first described in 1882 by von Recklinghausen, leading to the initial name of the condition, von Recklinghausen disease. The condition is manifested by a constellation of neurocutaneous tumors and vasculitis. Neurofibromatosis type 2 is a less common condition, seen in approximately 1 in 50,000 individuals and is characterized more often by central nervous system tumors.<sup>2</sup> The purpose of this vignette is to compare and contrast the manifestations and genetic backgrounds of these 2 entities.

## WHAT ARE THE CLINICAL MANIFESTATIONS OF NEUROFIBROMATOSIS TYPE 1?

Cutaneous neurofibromas are the most common manifestation of NF-1 and are seen in nearly every adult with this condition. Other common findings include plexiform tumors, optic gliomas, Lisch nodules (hamartomatous nodules in the iris), and café au lait macules. Additional manifestations can include learning disabilities, attention deficit/hyperactivity disorder, and vasculopathies. While cutaneous tumors related to this condition are most often benign, malignant degeneration and vasculopathy can occur, leading to early death. Plexiform tumors have a higher risk of degeneration, with malignancy occurring in approximately 10% of tumors.<sup>3,4</sup> Benign gliomas occur in 15% of patients with NF-1; and though most follow an indolent course, larger lesions can cause significant morbidity.<sup>5,6</sup>

## WHAT ARE THE CLINICAL MANIFESTATIONS OF NEUROFIBROMATOSIS TYPE 2?

The classic feature of neurofibromatosis type 2 is bilateral vestibular schwannomas, which occur in up to 95% of patients with the disorder. Schwannomas can involve other cranial nerves, most frequently III and V.<sup>2</sup> As such, the most common presenting clinical symptoms include hearing loss, dizziness, headaches, diplopia, and facial weakness. CNS tumors, including meningiomas and gliomas, are frequent occurrences in patients with NF-2. Multiple meningiomas are noted to occur in 50%–60% of these patients.<sup>7</sup> Spinal tumors, most frequently ependymomas, are other common manifestations involving approximately 90% of patients with NF-2. One-third of patients with spinal ependymomas are at risk for spinal cord compression.<sup>8</sup> Patients with NF-2 can also have cutaneous neurofibromas, though to a much lesser extent than in NF-1.

## WHAT IS THE NORMAL FUNCTION OF THE *NF1* GENE?

*NF1* is a tumor-suppressor gene encoded by chromosome 17q11.2, extending 283 kilobases.<sup>9</sup> Normally, the *NF1* gene encodes the protein neurofibromin, which is an inhibitor of the ras/mitogen-activated protein kinase pathway. This pathway is an important regulator of cellular growth and differentiation. The specific role of neurofibromin involves aiding the dephosphorylation of ras guanosine triphosphate.<sup>10</sup>

## WHAT IS THE FUNCTION OF THE *NF2* GENE?

*NF2* also encodes a tumor-suppressor gene on chromosome 22q12.2, extending 110 kilobases. Normally, this gene codes for the protein merlin, a regulator of cell growth, especially in Schwann cells. Merlin is quite atypical for a tumor-suppressor gene because it localizes to the cell membrane for regulation. Merlin acts as a cytoskeletal linker, interacting with multiple membrane proteins to regulate cell growth, motility, and remodeling.

Received January 13, 2013; accepted after revision January 22.

From the Department of Radiology, George Washington University Medical Center, Washington, DC.

Please address correspondence to Lucien M. Levy, MD, PhD, Professor of Radiology and Director of Neuroradiology, George Washington University Medical Center, 901 23rd St NW, Washington, DC 20037; e-mail: llevy@mfa.gwu.edu

<http://dx.doi.org/10.3174/ajnr.A3534>

Normally, merlin inhibits multiple intracellular pathways, including the MAPK signaling pathway (which is also involved in *NF1*).<sup>4</sup> A key method by which merlin inhibits cell growth is via contact-dependent inhibition.<sup>7</sup>

#### HOW DOES AN *NF1* MUTATION CAUSE DISEASE?

*NF1* is thought to cause disease by following characteristics of the “two-hit hypothesis,” first described by Alfred Knudson in 1971. All patients with *NF1* are heterozygous for the *NF1* mutation, and it is thought that somatic mutations lead to the development of tumors by causing a loss of heterozygosity.<sup>11</sup> The mutation most often results in truncation of neurofibromin, though >500 types of mutations have been described.<sup>5</sup> While the precise mechanisms are still being discovered, current hypotheses support the notion that a somatic mutation results in a “second hit,” leading to a loss in regulation of the cell cycle and resultant tumors. For instance, melanocytes cultured from café au lait macules were found to exhibit a somatic mutation in the *NF1* cell, implying that a loss of heterozygosity resulted in these lesions. However, the occurrence of tumors in Schwann cells, fibroblasts, neurons, epithelial cells, and perineural cells suggests that the condition may also originate from *NF1* mutations in multipotent precursor cells that give rise to these elements.<sup>10</sup>

#### HOW DOES AN *NF2* MUTATION CAUSE DISEASE?

Similar to those of *NF1*, *NF2* mutations follow the “two-hit hypothesis,” in which tumor formation begins when both alleles of the gene are inactivated. The first hit is from a de novo or germline mutation, and the second hit results in a loss of heterozygosity and in truncation of merlin, leading to abnormal function. In patients with abnormal merlin, Schwann cells cannot form stable adherens junctions; this deficit leads to a loss of contact-dependent inhibition. The loss of inhibition results in abnormal cell growth via multiple unregulated intracellular pathways.

#### WHAT ARE THE GENETICS OF NF-1?

Neurofibromatosis type 1 exhibits autosomal dominant transmission. Half of the patients with NF-1 inherit the mutation from their parents, while the other half develop the mutation de novo. The disease exhibits 100% penetrance, though the extent of symptoms varies widely among individuals.<sup>10</sup>

#### WHAT ARE THE GENETICS OF NF-2?

Neurofibromatosis type 2 also exhibits autosomal dominant transmission. Patients either inherit the gene via autosomal dominant transmission from their parents or develop the mutation de novo. Like neurofibromatosis type 1, de novo mutations are common because many patients with the disease have no family his-

tory.<sup>12</sup> Twenty to thirty percent of patients may exhibit mosaicism, resulting in mild disease or localized or unilateral tumors.<sup>8</sup>

#### WHAT IS THE ROLE OF RADIOLOGY IN THESE CONDITIONS?

MR imaging findings of neurofibromatosis type 1 include identification of focal areas of T2 hyperintensity, often in the brain stem, cerebellum, and basal ganglia. Pilocytic astrocytomas, brain stem gliomas, plexiform neurofibromas, and orbital gliomas are easily diagnosed and localized with the use of MR imaging. However, routine MR imaging screening for patients with clinically diagnosed NF-1 remains controversial.<sup>5</sup> Those in favor claim that MR imaging can diagnose potentially debilitating tumors before they become clinically evident. Those opposed argue that clinical treatment is rarely affected and note the necessity of sedation for some children and the high cost of MR imaging.

Conversely, routine MR imaging screening is always indicated for patients with NF-2, given the high prevalence of CNS tumors.<sup>7</sup> Contrast-enhanced MR imaging for NF-2 with gadolinium with thin sections through the brain stem is optimal for the identification of vestibular schwannomas. Cervical spine MR imaging is also suggested for the evaluation of spinal tumors, most commonly ependymomas.

#### REFERENCES

1. Solomon K, Warren E, Dombi N, et al. **Automated detection and volume measurement of plexiform neurofibromas in neurofibromatosis 1 using magnetic resonance imaging.** *Comput Med Imaging Graph* 2004;28:257–65
2. Chan JW. **Neuro-ophthalmic features of the neurocutaneous syndromes.** *Int Ophthalmol Clin* 2012;52:73–85
3. Van Meerbeeck SF, Verstraete KL, Janssens S, et al. **Whole body MR imaging in neurofibromatosis type 1.** *Eur J Radiol* 2009;69:236–42
4. Asthagiri AR, Parry DM, Butman JA, et al. **Neurofibromatosis type 2.** *Lancet* 2009;373:1974–86
5. Jett K, Friedman JM. **Clinical and genetic aspects of neurofibromatosis 1.** *Genet Med* 2010;12:1–11
6. Ullrich NJ, Raja AI, Irons MB, et al. **Brainstem lesions in neurofibromatosis type 1.** *Neurosurgery* 2007;61:762–66
7. Hanemann CO. **Magic but treatable? Tumours due to loss of merlin.** *Brain* 2008;131(pt 3):606–15
8. Ferner RE. **The neurofibromatosis.** *Pract Neurol* 2010;10:82–93
9. Laycock-van Spyk S, Thomas N, Cooper DN, et al. **Neurofibromatosis type 1-associated tumours: their somatic mutational spectrum and pathogenesis.** *Hum Genomics* 2011;5:623–90
10. Jouhilahti EM, Peltonen S, Heape AM, et al. **The pathoetiology of neurofibromatosis 1.** *Am J Pathol* 2011;178:1932–39
11. Legius E, Marchuk D, Collins F, et al. **Somatic deletion of the neurofibromatosis type 1 gene in a neurofibrosarcoma supports a tumor suppressor gene hypothesis.** *Nat Genet* 1993;3:122–26
12. Curto M, McClatchey AI. **Nf2/Merlin: a coordinator of receptor signalling and intercellular contact.** *Br J Cancer* 2008;98:256–62

# T1 Gadolinium Enhancement of Intracranial Atherosclerotic Plaques Associated with Symptomatic Ischemic Presentations

P. Vakil, J. Vranic, M.C. Hurley, R.A. Bernstein, A.W. Korutz, A. Habib, A. Shaibani, F.H. Dehkordi, T.J. Carroll, and S.A. Ansari



## ABSTRACT

**BACKGROUND AND PURPOSE:** Contrast enhancement of intracranial atherosclerotic plaques has recently been investigated using high field and high resolution MR imaging as a risk factor in the development of ischemic stroke. We studied the reliability of conventional MR imaging at 1.5T in evaluating intraplaque enhancement and its relationship with acute cerebrovascular ischemic presentations in patients with severe intracranial atherosclerotic disease.

**MATERIALS AND METHODS:** We retrospectively identified and analyzed 19 patients with 22 high-grade intracranial atherosclerotic disease plaques (>70% stenosis) in vessels cross-sectionally visualized by neuroanatomic MR imaging. Atherosclerotic plaques were classified as asymptomatic or symptomatic. Two blinded neuroradiologists independently ranked each lesion for the presence of intraplaque enhancement by use of a 5-point scale (1–5). Furthermore, plaque enhancement was quantified as the relative change in T1WI spin-echo signal intensity (postcontrast/precontrast) in the vessel wall at the site of each intracranial atherosclerotic disease lesion.

**RESULTS:** Intraplaque enhancement was observed in 7 of 10 (70%) symptomatic plaques, in contrast to 1 of 12 (8%) asymptomatic plaques. Interobserver reliability correlated well for intraplaque enhancement ( $\kappa = 0.82$ ). The degree of relative plaque enhancement in symptomatic versus asymptomatic lesions (63% versus 23%) was statistically significant ( $P = .001$ ,  $t$  test).

**CONCLUSIONS:** In this pilot study, we determined that intraplaque enhancement could be reliably evaluated with the use of cross-sectional imaging and analysis of vessels/plaques by use of conventional neuroanatomic MR imaging protocols. In addition, we observed a strong association between intraplaque enhancement in severe intracranial atherosclerotic disease lesions and ischemic events with the use of conventional MR imaging. Our preliminary study suggests that T1 gadolinium-enhancing plaques may be an indicator of progressing or symptomatic intracranial atherosclerotic disease.

**ABBREVIATIONS:** ICAD = intracranial atherosclerotic disease; IPE = intraplaque enhancement; T1w-SE = T1-weighted spin-echo; IPH = intraplaque hemorrhage; ACA = anterior cerebral artery

Intracranial atherosclerotic disease (ICAD) is a significant cause of stroke worldwide, accounting for 7–10% of acute ischemic stroke cases.<sup>1</sup> In symptomatic ICAD with high-grade stenoses

(>70%), the risk of stroke or death at 1 year is 12–22% with medical therapy based on the WASID<sup>1</sup> (Warfarin-Aspirin Symptomatic Intracranial Disease) and SAMMPRIS<sup>2</sup> (Stent placement versus Aggressive Medical Management for Preventing Recurrent Stroke in Intracranial Stenosis) trial.

The SAMMPRIS trial was designed to determine whether intracranial angioplasty/stent placement as a primary treatment option could benefit patients with severe ICAD in reducing the risk of stroke/death over aggressive medical management alone. However, patient recruitment in the SAMMPRIS trial was prematurely terminated as mandated by the National Institutes of Health/National Institute of Neurological Disorders and Stroke because of unexpectedly high stroke/death rates with endovascular intervention (14.7% at 30 days and 20% at 1 year) and better-than-expected outcomes with modern medical management (5.8% at 30 days and 12.2% at 1 year).<sup>2</sup> Hence, the role of intracranial angioplasty/stent placement was again relegated to a subpopulation of

Received October 1, 2012; accepted after revision March 7, 2013.

From the Departments of Radiology (P.V., J.V., M.C.H., A.W.K., A.H., A.S., T.J.C., S.A.A.), Neurology (R.A.B., S.A.A.), Neurosurgery (M.C.H., A.S., S.A.A.), and Biomedical Engineering (P.V., T.J.C.), Northwestern University, Feinberg School of Medicine, Chicago, Illinois; and Department of Economics and Decision Sciences (F.H.D.), Western Illinois University, Macomb, Illinois.

Please address correspondence to Sameer A. Ansari, MD, PhD, Department of Radiology, Neurology, and Neurosurgery, Northwestern University, Feinberg School of Medicine, 676 N St Clair St, Suite 800, Chicago, IL 60611-2927; e-mail: s-ansari@northwestern.edu

This study was supported by NIH/NHLBI grants R01 HL088437 and NIH/NIBIB T32 EB005170.

Indicates open access to non-subscribers at [www.ajnr.org](http://www.ajnr.org)

Indicates article with supplemental on-line table.

<http://dx.doi.org/10.3174/ajnr.A3606>

patients with severe ICAD who would fail optimum medical therapy. Although these patients remain at risk for recurrent TIAs or strokes, we have yet to develop a stratification scheme to identify this refractory subpopulation and perhaps alter their management (medical and/or surgical) before an ischemic presentation.

Increasing evidence indicates the role of neovascularization and intraplaque hemorrhage (IPH) in the progression and rupture of carotid atherosclerotic plaques analogous to the coronary literature.<sup>3,4</sup> Inflammation, which is associated with neovascularization and IPH, locally alters vascular endothelium permeability, potentially allowing gadolinium contrast uptake and visualization on T1WI. In fact, evidence of neovascularization and/or focal inflammation in the arterial wall of the cervical carotid arteries through atherosclerotic plaque enhancement has been correlated with a higher incidence of ipsilateral stroke secondary to extracranial atherosclerotic lesions.<sup>3,5,6</sup> Spagnoli et al<sup>7</sup> recently reported on the high-resolution MR imaging findings of both IPH and adventitial enhancement (neovascularization and/or inflammation) as being independently associated with symptomatic carotid stenoses and recent cerebrovascular ischemic events.

Inflammation may be an attractive imaging marker in the setting of ICAD for risk stratification, though the diminutive nature of intracranial vessels makes plaque evaluation challenging because of spatial resolution and signal-to-noise ratio concerns. Several groups have attempted high-field, high-spatial resolution, contrast-enhanced MR imaging of the intracranial vessel wall and atherosclerotic plaques with the use of dark-blood sequences.<sup>8-13</sup> Swartz et al<sup>9</sup> identified the existence of intracranial atherosclerotic plaque enhancement through the use of 3T high-resolution MR imaging. More recently, this type of high-resolution MR imaging assessment found strong enhancement in ICAD plaques in patients with acute ischemic stroke.<sup>14</sup> In this pilot study, it was our goal to determine whether postgadolinium T1 intracranial plaque enhancement (IPE) could be reliably delineated through the use of low-resolution, conventional neuroanatomic MR techniques in patients with severe ICAD (>70% stenosis) and whether IPE was associated with the occurrence of recent ischemic cerebrovascular events.

## MATERIALS AND METHODS

### Patients

Institutional review board approval was obtained for a retrospective study to identify patients with severe ICAD causing  $\geq 70\%$  stenosis, diagnosed with our institution's MR imaging/MRA stroke protocol between January 2008 and January 2011. A PACS-based report search was performed on this cohort to identify subjects with severe ICAD. The following key word search terms were used: "severe OR high-grade OR attenuation" AND "plaque OR stenosis." Patients with plaques that could be visualized on 3D time-of-flight (TOF) MRA and axial pregadolinium and postgadolinium contrast T1-weighted spin-echo (T1w-SE) sequences were selected for the study.

Patient exclusion criteria included imaging artifacts secondary to patient motion, metallic susceptibility from medical implants, or complete vessel occlusion. Additionally, intracranial aneurysms, multiple/tandem intracranial stenoses, or presence of moderate to severe atherosclerotic disease in cervical vessels sup-

plying the same vascular distribution were also excluded to allow clear association of symptoms with the corresponding intracranial lesion. The retrospective nature of this study prevented patient-specific optimization of imaging parameters such as orientation, section thickness, and coverage. At our institution, the T1w-SE sequences in the MR imaging/MRA brain stroke protocol are performed with the use of axial-oriented imaging and parameters optimized for maximum coverage of the neuroanatomy, limiting vessel coverage to approximately 24 thick (5-mm) axial sections with 1.5-mm gaps.

Although partial volume effects are a concern with 5-mm section imaging, our preliminary studies indicated that cross-sectionally visualized vessels could be successfully evaluated. Because most neuroanatomic MR imaging protocols use axially oriented imaging, vessels parallel to the imaging plane (ie, middle and posterior cerebral arteries), which were more severely affected by partial volume effects, were excluded. Hence, ICAD lesions evaluated in this study were found within the intracranial V4 segment of the vertebral arteries, the basilar artery, supraclinoid ICAs, or the A2 segment of the anterior cerebral artery (ACA). A total of 19 patients age  $68.7 \pm 9.6$  years (13 men, 6 women) fulfilled the stated criteria and were thus evaluated.

### Imaging Evaluation

Two experienced neuroradiologists (M.C.H. and S.A.A.) performed independent qualitative grading of each ICAD lesion while blinded to the study population: identity, symptoms, DWI abnormalities, and outcomes. Both reviewers confirmed >70% stenosis on 3D TOF and its cross-sectional visualization on precontrast and postcontrast T1w-SE imaging. On the basis of the T1w-SE precontrast and postcontrast imaging, the degree of IPE caused by gadolinium uptake was determined qualitatively and quantitatively by assessment of the degree of enhancement of the plaque/vessel wall. For qualitative assessment, values of 1, 2, 3, 4, or 5 were assigned to each lesion corresponding to "definite non-enhancement," "suspected nonenhancement," "uncertain," "suspected enhancement," and "definite enhancement," respectively. Scores rendered by each independent observer were averaged to determine the final degree of plaque enhancement. A plaque with an average score >3 was considered "enhancing" (eg, scores of 5/5, 5/4, 4/4, or 4/3), and a score <3 was considered nonenhancing (eg, scores of 3/2, 2/2, 2/1, or 1/1). In the event of interobserver disagreement, (eg, a score of 4/2), a third independent observer would be used to break the tie.

In a separate and independent evaluation conducted by both observers 1 month after qualitative evaluation, the degree of plaque enhancement was quantified as the relative increase in lesion T1-signal postcontrast. Circular ROIs were specifically localized to the lumen of the stenosed vessel and the outer boundary of the vessel wall at the site of the ICAD plaque. The outer wall area was defined and calculated as the difference between the area within the boundary of the vessel wall at the interface with the CSF and the area of the vessel lumen as in Xu et al<sup>15</sup> and Yuan et al<sup>16</sup> and demonstrated in Fig 1. The percent wall area was defined as the ratio of the outer wall area to the total wall area multiplied by 100%. Percent wall area was used for more meaningful comparison of plaque/vessel wall areas between subgroups containing vessels of different origin and sizes. Quantita-

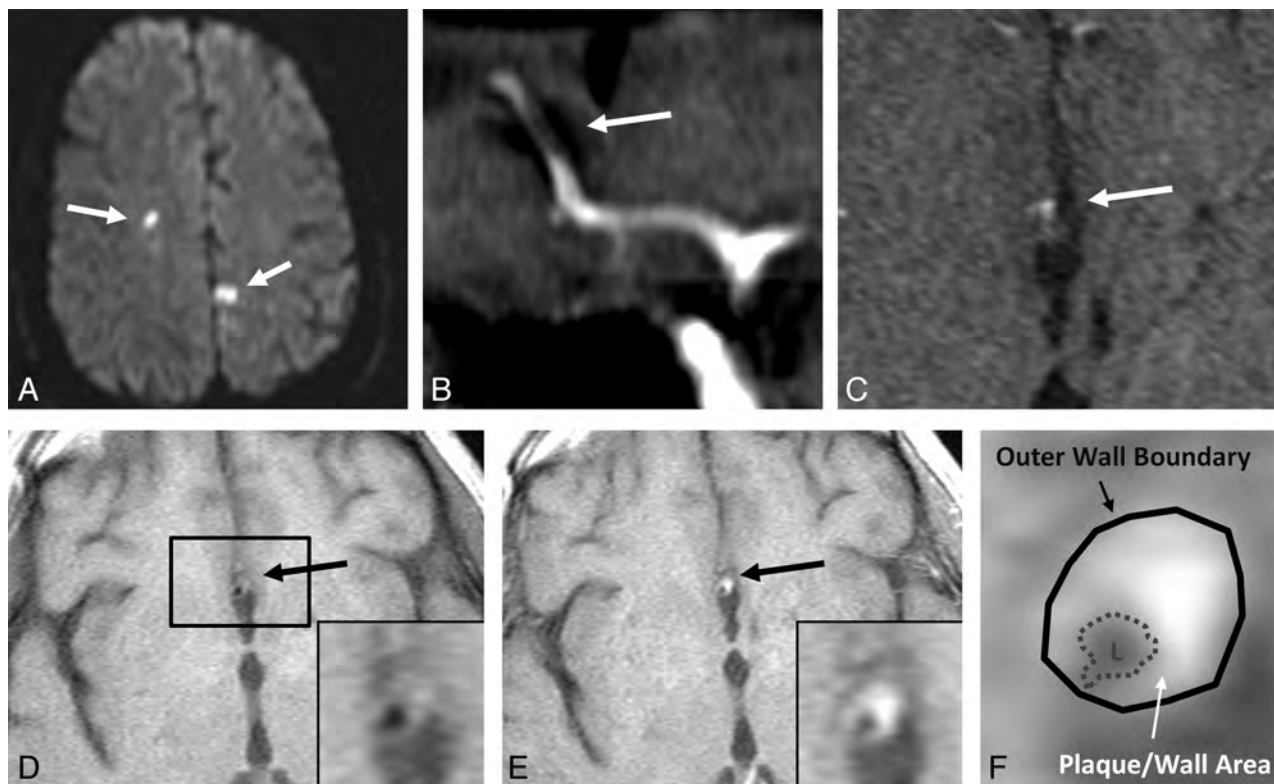


**FIG 1.** Symptomatic patient with MR DWI (A) demonstrating focal infarcts in the bilateral distributions (white arrows). TOF MR angiography MIP (B) and source images (C) confirm severe stenosis in an A2 azygous ACA segment. Axial T1-weighted-pre (D) and T1-weighted-post contrast (E) images identify enhancing ICAD plaque (inset) involving the azygous A2 ACA segment. Methodology of plaque/wall area measurements are demonstrated (F), with solid black line delineating outer wall boundary and dotted line segmenting the vessel lumen denoted as “L.”

tive plaque enhancement was defined as the mean T1 signal intensity in the outer wall area on postcontrast T1w-SE images divided by its precontrast T1 signal. All T1 signal intensity values in precontrast and postcontrast images were normalized with the signal in the ventricle to control for signal intensity differences between the 2 separate sequences. ROI analysis was conducted with the use of in-house software developed in Matlab (MathWorks, Natick, Massachusetts).

### Clinical Evaluation

All patient neurologic histories, physical examinations, and DWI findings, at the time of diagnostic MR imaging/MRA imaging, were recorded by means of medical record and PACS imaging review. Of the 19 patients, 16 received MR imaging within 24 hours of symptomatic presentations with suspected TIAs or strokes. Routine follow-up stroke protocol MR imaging was performed for an additional 3 patients with history of stroke; all 3 patients harbored severe intracranial stenoses but were asymptomatic at the time of imaging. Presentations with acute ischemic symptoms were classified into anterior or posterior circulation pathology.<sup>12</sup> A symptomatic ICAD plaque was defined as presenting with acute neurologic (ischemic) symptoms and/or restricted DWI abnormalities (acute watershed, thromboembolic, or perforator infarcts) corresponding to the vascular distribution of the intracranial stenosis. Asymptomatic patients either presented for follow-up imaging because of history of stroke or received first-time imaging in response to symptoms (typically TIAs) that were not associated with the plaque of interest, that is, symptoms that did not correlate to the vascular distribution of the intracranial stenosis.<sup>12</sup>

### MR Imaging

Patients referred to our institution who demonstrated symptoms of TIA or stroke, as determined from neurologic examination, received an MR imaging/MRA stroke imaging protocol. This included the following relevant sequences evaluated in this study: precontrast 3D TOF, DWI, axial T1w-SE before and after a single-dose (0.1 mmol/kg) injection of a gadolinium-based T1 shortening contrast agent (Magnevist; Bayer HealthCare Pharmaceuticals, Wayne, New Jersey). All patients received postcontrast T1 imaging within 20 minutes of contrast injection. MR imaging studies were performed on a 1.5T scanner (Avanto/Espre; Siemens, Erlangen, Germany) with the use of a receive-only head coil for signal reception. Typical imaging parameters were as follows:

**3D TOF.** TR/TE 23 ms/5.1 ms, 25° flip angle, 320 × 284 matrix, 220–240 mm FOV, voxel size 0.69 × 0.77 × 0.63 mm.

**T1w-SE.** TR/TE 663 ms/15 ms, 90° flip angle, 256 × 256 matrix with 220–240 mm FOV, section thickness = 5 mm, section gap = 1.5 mm, voxel size 0.9 × 0.9 × 5 mm.

**DWI.** TR/TE 4500/185 ms, 90° flip angle, 192 × 192 matrix, 220–240 mm FOV, section gap 1.5 mm, voxel size 1.3 × 1.3 × 5 mm.

### Statistical Analysis

The interobserver strength of agreement on qualitative grading of ICAD plaque enhancement was determined by means of quadrat-

**Table 1: Patient demographics, clinical history, and imaging assessment**

Patient Characteristics	Symptomatic	Asymptomatic
<i>n</i>	10	9
Age, y	66.7 (SD, 11.7; range, 46–83)	70.9 (SD, 6.7; range 60–81)
Sex	7 M; 3 F	6 M; 3 F
Active smoker	1 (10%)	1 (11%)
History of ischemic stroke	6 (60%)	0 (0%)
TIA	10 (100%)	1 (11%) <sup>a</sup>
Diabetes mellitus	5 (50%)	4 (44%)
Hypertension	10 (100%)	7 (78%)
Hyperlipidemia	9 (90%)	7 (78%)
Statin therapy	8 (80%)	5 (56%)
Antiplatelet therapy	6 (60%)	4 (44%)
Hypertension therapy	8 (80%)	5 (56%)
Atrial fibrillation	0 (0%)	0 (0%)
Anticoagulant therapy	2 (20%)	1 (11%)
IPE	7 (70%)	1 (11%)

<sup>a</sup>History of TIA.

ically weighted Cohen  $\kappa$  statistic for categoric variables. Reliabilities  $<0.4$  were defined as poor;  $0.4$ – $0.75$  as fair to good; and  $>0.75$  as excellent.<sup>13</sup> Interobserver agreement on measurements of plaque/vessel wall areas and quantitative T1 wall enhancement was assessed by means of the Wilcoxon rank sum test for continuous variables. With the use of a paired Student *t* test, the quantitative measure of T1 signal enhancement and percentage wall area were compared between symptomatic and asymptomatic lesion cohorts. Logistic regression was used to evaluate IPE as a predictor of ischemic symptoms. A value of  $P < .05$  was defined as statistically significant. All calculations were performed with the use of in-house software written in Matlab.

## RESULTS

Initially, 40 patients with severe ( $>70\%$ ) intracranial stenoses (confirmed on TOF MRA by both reviewers) were identified for this study. ICAD plaques in 21 patients were excluded for the following reasons: MR imaging studies in 4 patients were nondiagnostic because of severe motion or susceptibility (metallic implants) artifacts, 3 patients had total vessel occlusion, 1 patient had a partially thrombosed fusiform aneurysm distal to the stenosis, and 5 patients had various confounding stenoses in the same vascular distribution. In addition, 8 patients presented with intracranial stenoses involving the MCA or posterior cerebral artery preventing lesion evaluation with the standard 5-mm-thick axial imaging as stated in the Materials and Methods section. All remaining lesions were in the intracranial ICA, A2 ACA, basilar artery, or V4 vertebral arteries, with the stenosis cross-sectionally visualized in the axial plane.

A total of 22 severe ICAD plaques were evaluated independently in 19 patients by 2 neuroradiologists blinded to each subject's clinical data. Table 1 and the On-line Table provide pertinent patient demographics, clinical history, ICAD risk factors, and qualitative and quantitative results for each recruited subject and lesion. In our cohort of 22 ICAD plaques, 10 patients presented with 10 symptomatic plaques and 9 patients harbored 12 asymptomatic plaques. Asymptomatic plaques remained stable, with no attributed ischemic symptoms or acute infarcts on DWI for at least 3 months.

Within our symptomatic cohort, precontrast and postcontrast T1w-SE imaging revealed qualitative contrast enhancement in 7

of 10 (70%) atherosclerotic plaques, correlating with symptomatic presentations and/or acute infarcts on DWI. Conversely, within our asymptomatic cohort, 11 of 12 (92%) atherosclerotic plaques were determined to be nonenhancing according to precontrast and postcontrast T1w-SE imaging.

Vessels of symptomatic lesions did not have a higher percentage plaque/vessel wall area compared with asymptomatic lesions at the site of the ICAD plaque ( $89.7 \pm 4.0\%$  versus  $86.9 \pm 6.1\%$ , respectively,  $P = .2$  in Student *t* test). Furthermore, the cross-sectional areas of plaques in the symptomatic and asymptomatic cohort were not significantly different ( $12.8 \pm 5.9 \text{ mm}^2$  versus

$10.8 \pm 4.0 \text{ mm}^2$ , respectively,  $P = .4$ , Student *t* test). The mean increase in quantitative enhancement in the outer wall of symptomatic stenosed vessels at the site of the ICAD plaque was 63% (precontrast to postcontrast relative signal change of  $1.63 \pm 0.28$ ) compared with 23% in the outer wall of asymptomatic lesions ( $1.23 \pm 0.18$  relative signal change). A Student *t* test found this difference to be significant ( $P = .001$ ). In addition, a logistic regression model found IPE to be significantly associated with ischemic symptoms or positive DWI findings, that is, IPE-demonstrating plaques were 25 times more likely to be symptomatic ( $P = .0095$ ).

Interobserver agreement was excellent for determining qualitative plaque enhancement on T1w-SE imaging. A quadratic weighted Cohen  $\kappa$  value of 0.82 was found. Quantitative enhancement scores and outer plaque/wall area measurements were also found to be in agreement between both observers because the Wilcoxon signed rank sum test showed insignificant differences between independent measurements ( $P = .4$  between separate quantitative enhancement scores and  $P = .3$  between separate outer plaque/wall area measurements).

## Illustrative Cases

Patient 2 is a 60-year-old man with history of stroke/TIAs, hyperlipidemia, and hypertension, presenting at the time of imaging with acute lower-extremity weakness and acute infarcts on DWI in the bilateral ACA distributions (Fig 1A). Hence, the ICAD plaque was determined to be symptomatic. A severe intracranial stenosis involving the azygous A2 branch of the ACA was confirmed on TOF MRA sagittal MIP (Fig 1B) and source images (Fig 1C). Postcontrast enhanced T1w-SE images (Fig 1E) visualizing the ICAD plaque were graded to be “definitely enhancing” (scored 5), relative to precontrast T1 imaging (Fig 1D), by both observers. ROIs drawn (Fig 1F) around the vessel outer wall boundary, segmenting out the lumen, demonstrated quantitative enhancement of 78% between precontrast and postcontrast images.

Patient 14 is a 75-year-old man with a history of hypertension, hyperlipidemia, and prior vertebrobasilar TIAs/strokes in the posterior circulation but with no active symptoms or acute infarcts on DWI, presenting for follow-up imaging evaluation of



**FIG 2.** Asymptomatic patient with history of stroke receiving follow-up imaging. TOF MRA reveals severe basilar stenosis in MIP (A) and source images (B). Axial T1WI precontrast (C) and postcontrast (D) demonstrates nonenhancing ICAD plaque.

severe intracranial stenosis of the basilar artery. The patient's ICAD plaque, visualized on TOF MRA MIP (Fig 2A) and source images (Fig 2B), was subsequently determined to be asymptomatic. Precontrast (Fig 2C) and postcontrast (Fig 2D) T1w-SE imaging demonstrated a nonenhancing atherosclerotic plaque, receiving scores of 2 from both reviewers, with quantitative enhancement of 16%.

## DISCUSSION

In this study of severe ICAD, we found that IPE was strongly associated with symptomatic ischemic presentations. Furthermore, postgadolinium T1w-SE images with the use of conventional, low-resolution MR imaging were capable of reliably detecting IPE (high interobserver agreement;  $\kappa = 0.82$ ) when the acquisition sections allowed cross-sectional visualization of the vessels of interest. This may indicate that a more robust implementation of this protocol would require sagittal or oblique acquisitions for assessing atherosclerotic disease in the middle cerebral arteries. Given the association between IPE in carotid atherosclerotic disease, plaque destabilization, and thromboembolic events, our study suggests that an analogous process may occur in the intracranial vasculature in the setting of ICAD.

Prior MR imaging and histopathologic studies have shown that vulnerable carotid artery atherosclerotic plaques are characterized by a ruptured fibrous cap, a lipid-rich necrotic core, and IPH.<sup>7,17</sup> Furthermore, postgadolinium T1 enhancement of symptomatic carotid plaques suggests plaque neovascularization and/or inflammation may predispose plaques to IPH or ischemic/thromboembolic complications.<sup>13,18</sup> In fact, Kerwin et al<sup>19</sup> introduced several quantitative MR imaging parameters including higher  $K^{trans}$  measurements or adventitial contrast uptake with the use of dynamic contrast-enhanced MR imaging that correlated with macrophage infiltration (inflammation) and neovascularization on subsequent histopathologic analyses.<sup>20,21</sup>

Our study suggests that similar arterial wall pathology in ICAD may be the inciting factor for plaque progression and destabilization. Although neovascularization may be responsible for IPH as the result of rupture of fragile adventitial neovessels resulting in a thrombogenic lipid core, both neovascularization and IPH are associated with the recruitment of inflammatory cells. Conversely, because intracranial vessels usually lack the presence of vasa vasorum, atherosclerotic inflammation may promote a hypoxic environment and stimulate pathologic angiogenic factors such as vascular endothelial growth factor to promote neovascularization, contributing to plaque instability by means of edema, hemorrhage, and rupture.<sup>22</sup>

However, we recommend caution in interpreting our findings in the absence of IPE as stable atherosclerotic lesions. Ischemic complications related to ICAD may also be precipitated through independent mechanisms including thin or ruptured fibrous caps, a large lipid-rich necrotic core, and/or IPH.

Previous studies have reported differences in plaque/wall thickening between asymptomatic and symptomatic lesions.<sup>15,16</sup> This could bias enhancement scores because larger lesions could show greater enhancement. However, we observed no statistically significant differences in total plaque area or percentage wall area within the capacity of low-resolution 1.5T MR imaging techniques. We therefore do not believe that greater enhancement in the symptomatic group is attributable to differences in plaque/wall area size or percentage alone.

A paucity of previous literature has studied ICAD IPE through the use of high-resolution MR imaging techniques but with variable correlations to symptomatic ischemic presentations.<sup>9</sup> Klein et al<sup>10</sup> studied 6 patients with MCA stenoses, but both asymptomatic and symptomatic patients displayed plaque enhancement. Xu et al<sup>11</sup> recently characterized a large series of severe MCA stenoses (>70%

occlusion) with high-resolution MR imaging and detected a significantly increased rate of T1 hyperintensity indicative of IPH in symptomatic versus asymptomatic plaques (19.6% versus 3.2%).

The progression and instability of ICAD plaques secondary to neovascularization, IPH, and/or inflammation can present with either symptomatic ischemic or thromboembolic complications. In extracranial carotid atherosclerosis, end-stage hypoperfusion with watershed infarcts to the distal intracranial circulation requires an extensive plaque burden to achieve luminal stenosis. Conversely, acute inflammation/edema or IPH of even moderate ICAD stenoses could achieve significant percentage narrowing in small (diameter <3 mm), fragile intracranial vessels that lack an external elastic lamina and adventitial support, predisposing to watershed ischemia. Alternatively, local IPH and thrombogenic plaque rupture may result in adjacent small perforator occlusions or thromboembolic complications to the distal intracranial vasculature. These mechanisms may be an explanation for the propensity of symptomatic intracranial stenoses to present equivalently with ischemic watershed and thromboembolic infarcts.

Because inflammation is an integral component of atherosclerosis, it may be a transient or undulating process. Identification of active inflammation and/or neovascularization (IPE) could serve as future diagnostic imaging markers to characterize the susceptibility of an ICAD plaque for symptomatic presentations. Furthermore, there may be ramifications for treatment planning in ICAD whereby angioplasty/stent placement could be advocated, delayed, or contraindicated in favor of antiplatelet, anticholesterolemic (statins), novel anti-inflammatory, or anti-angiogenic medical therapies. In fact, statins have been shown to reduce at intervals the quantitative  $K^{\text{trans}}$  measurements of adventitial contrast enhancement after 1 year of therapy in cervical carotid atherosclerotic plaques.<sup>23</sup>

Our data suggest that identification of ICAD plaque neovascularization and/or inflammation with postcontrast T1WI may be used to assess lesion vulnerability for symptomatic ischemic or thromboembolic presentations. Interestingly, the failure of the SAMMPRIS trial has been attributed to high periprocedural risk (14.7% mean adverse events in <30 days).<sup>2</sup> The trial was designed to initiate intracranial angioplasty/stent placement early after enrollment of patients presenting with TIAs/strokes (<30 days) to maximize the potential clinical benefit of intervention, but this strategy may be flawed. Early imprudent enrollment with angioplasty/stent placement in the acute setting could disrupt potentially active, inflammatory, and/or thrombogenic atherosclerotic plaques, possibly accounting for the high periprocedural complications (thromboembolism/stroke dissection and vessel wall rupture/intracranial hemorrhage) in the trial.

We propose that future high-resolution and functional MR imaging will assist in better interpreting the vulnerability of ICAD plaques and hence risk stratification of severe intracranial stenoses for improved treatment planning. Future diagnostic imaging studies in ICAD may include high-resolution intracranial plaque visualization with symptomatic correlation, quantitative plaque T1/T2 intensity and contrast enhancement, contrast permeability ( $K^{\text{trans}}$ ) measurements, quantitative perfusion MR imaging, and oxygen extraction fraction (PET/MR imaging) parameters to document stage 2 hemodynamic failure and impaired cerebrovascular reserve.

Wall enhancement can be related to vasculitis or inflammation associated with atherosclerotic disease, and we cannot definitively exclude a vasculitic process in our patient cohort. However, because of the advanced age and findings of multiple atherosclerotic risk factors in the studied group as well as no demonstration of clinical or imaging evidence of cerebral vasculitis, the likelihood of a superimposed vasculitic etiology is small.

Our study posed several inherent limitations and challenges. The small sample size limits the power of the statistical results, and, as such, they should be interpreted with caution. Although T1w-SE imaging is an inherently dark-blood technique, slow-flow regions within small intracranial vessels adjacent to an atherosclerotic lesion may produce hyperintense signal that could be mistaken for wall enhancement, resulting in false-positive values and reducing the technique's specificity. Delineating boundaries of the vessel lumen by use of an appropriate diffusion-prepared dark-blood imaging technique<sup>24,25</sup> may mitigate this issue. Ultimately, high-resolution dark-blood imaging sequences, at high-field strengths with improved SNR, should be used to direct imaging to specific vessel morphology and pathology.<sup>8,10,24</sup>

Because of the retrospective nature of this study, we were limited to standard neurovascular anatomic protocols on a 1.5T scanner. The use of thick sections (5 mm) in the T1w-SE acquisitions improved the SNR limitations of the lower field magnet but could cause errors in plaque enhancement evaluation as a result of partial volume averaging. In addition, this protocol did not allow successful evaluation of vessels that projected parallel to the imaging plane, such as the MCAs, producing a selection bias of intracranial plaques. Therefore, we do not advocate conventional MR imaging protocols as sufficient or robust diagnostic tools for intracranial vessel and plaque interrogation.

## CONCLUSIONS

Standard low-resolution neuroanatomic MR imaging may provide useful information for the evaluation of ICAD by demonstrating IPE on precontrast and postcontrast T1w-SE imaging in severely stenotic vessels visualized cross-sectionally in the imaging plane. In these vessels, we found an association between IPE and ischemic/thromboembolic events through the use of conventional MR imaging. However, assessment of the true sensitivity, specificity, and predictive values of IPE in the setting of severe ICAD will require a large, prospective, longitudinal study with the use of high-resolution plaque MR imaging techniques and pathology correlation.

Disclosures: Parmede Vakil—RELATED: Grant: NIH\*; UNRELATED: Grants/Grants Pending: NIH.\* Richard Bernstein—UNRELATED: Consultancy: Boehringer Ingelheim, Janssen, Medtronic, Medscape, Comments: None relevant to this work; Payment for Lectures (including service on Speakers Bureaus): Boehringer Ingelheim, Janssen, Medtronic, Comments: None relevant; Payment for Development of Educational Presentations: Janssen Pharmaceuticals, Medscape, Boehringer Ingelheim. Timothy Carroll—RELATED: Grant: NIH. Comments: Two separate NIH grants supported this work; UNRELATED: Grants/Grants Pending: NIH (\*money paid to institutions).

## REFERENCES

1. Chimowitz MI, Lynn MJ, Howlett-Smith H, et al. **Comparison of warfarin and aspirin for symptomatic intracranial arterial stenosis.** *N Engl J Med* 2005;352:1305–16
2. Chimowitz MI, Lynn MJ, Derdeyn CP, et al. **Stenting versus aggressive medical therapy for intracranial arterial stenosis.** *N Engl J Med* 2011;365:993–1003

3. Yuan C, Mitsumori LM, Beach KW, et al. **Carotid atherosclerotic plaque: noninvasive MR characterization and identification of vulnerable lesions.** *Radiology* 2001;221:285–99
4. Wasserman BA, Wityk RJ, Trout HH 3rd, et al. **Low-grade carotid stenosis: looking beyond the lumen with MRI.** *Stroke* 2005;36:2504–13
5. Kerwin WS, O'Brien KD, Ferguson MS, et al. **Inflammation in carotid atherosclerotic plaque: a dynamic contrast-enhanced MR imaging study.** *Radiology* 2006;241:459–68
6. Saam T, Hatsukami TS, Takaya N, et al. **The vulnerable, or high-risk, atherosclerotic plaque: noninvasive MR imaging for characterization and assessment.** *Radiology* 2007;244:64–77
7. Spagnoli LG, Mauriello A, Sangiorgi G, et al. **Extracranial thrombotically active carotid plaque as a risk factor for ischemic stroke.** *JAMA* 2004;292:1845–52
8. Vergouwen MD, Silver FL, Mandell DM, et al. **Eccentric narrowing and enhancement of symptomatic middle cerebral artery stenoses in patients with recent ischemic stroke.** *Arch Neurol* 2011;68:338–42
9. Swartz RH, Bhuta SS, Farb RI, et al. **Intracranial arterial wall imaging using high-resolution 3-Tesla contrast-enhanced MRI.** *Neurology* 2009;72:627–34
10. Klein IF, Lavalley PC, Touboul PJ, et al. **In vivo middle cerebral artery plaque imaging by high-resolution MRI.** *Neurology* 2006;67:327–29
11. Xu WH, Li ML, Gao S, et al. **Middle cerebral artery intraplaque hemorrhage: prevalence and clinical relevance.** *Ann Neurol* 2012;71:195–98
12. Greenberg MS. *Handbook of Neurosurgery.* New York: Thieme Medical Publishers; 2010
13. Qiao Y, Steinman DA, Qin Q, et al. **Intracranial arterial wall imaging using three-dimensional high isotropic resolution black blood MRI at 3.0 Tesla.** *J Magn Reson Imaging* 2011;34:22–30
14. Skarpathiotakis M, Mandell DM, Swartz RH, et al. **Intracranial atherosclerotic plaque enhancement in patients with ischemic stroke.** *AJNR Am J Neuroradiol* 2013;34:299–304
15. Xu WH, Li ML, Gao S, et al. **In vivo high-resolution MR imaging of symptomatic and asymptomatic middle cerebral artery atherosclerotic stenosis.** *Atherosclerosis* 2010;212:507–11
16. Yuan C, Beach KW, Smith LH Jr, et al. **Measurement of atherosclerotic carotid plaque size in vivo using high resolution magnetic resonance imaging.** *Circulation* 1998;98:2666–71
17. Redgrave JN, Lovett JK, Gallagher PJ, et al. **Histological assessment of 526 symptomatic carotid plaques in relation to the nature and timing of ischemic symptoms: the Oxford plaque study.** *Circulation* 2006;113:2320–28
18. McCarthy MJ, Loftus IM, Thompson MM, et al. **Angiogenesis and the atherosclerotic carotid plaque: an association between symptomatology and plaque morphology.** *J Vasc Surg* 1999;30:261–68
19. Kerwin WS, Oikawa M, Yuan C, et al. **MR imaging of adventitial vasa vasorum in carotid atherosclerosis.** *Magn Reson Med* 2008;59:507–14
20. Kerwin W, Hooker A, Spilker M, et al. **Quantitative magnetic resonance imaging analysis of neovasculature volume in carotid atherosclerotic plaque.** *Circulation* 2003;107:851–56
21. Cai J, Hatsukami TS, Ferguson MS, et al. **In vivo quantitative measurement of intact fibrous cap and lipid-rich necrotic core size in atherosclerotic carotid plaque: comparison of high-resolution, contrast-enhanced magnetic resonance imaging and histology.** *Circulation* 2005;112:3437–44
22. Moreno PR, Purushothaman KR, Sirol M, et al. **Neovascularization in human atherosclerosis.** *Circulation* 2006;113:2245–52
23. Dong L, Kerwin WS, Chen H, et al. **Carotid artery atherosclerosis: effect of intensive lipid therapy on the vasa vasorum—evaluation by using dynamic contrast-enhanced MR imaging.** *Radiology* 2011;260:224–31
24. Ryu CW, Jahng GH, Kim EJ, et al. **High resolution wall and lumen MRI of the middle cerebral arteries at 3 Tesla.** *Cerebrovasc Dis* 2009;27:433–42
25. Koktzoglou I, Kirpalani A, Carroll TJ, et al. **Dark-blood MRI of the thoracic aorta with 3D diffusion-prepared steady-state free precession: initial clinical evaluation.** *AJR Am J Roentgenol* 2007;189:966–72

# Intracranial-Derived Atherosclerosis Assessment: An In Vitro Comparison between Virtual Histology by Intravascular Ultrasonography, 7T MRI, and Histopathologic Findings

S. Majidi, J. Sein, M. Watanabe, A.E. Hassan, P.-F. Van de Moortele, M.F.K. Suri, H.B. Clark, and A.I. Qureshi

## ABSTRACT

**BACKGROUND AND PURPOSE:** Atherosclerotic plaque composition and structure contribute to the risk of plaque rupture and embolization. Virtual histology by intravascular ultrasonography and high-resolution MR imaging are new imaging modalities that have been used to characterize plaque morphology and composition in peripheral arteries.

**MATERIALS AND METHODS:** The objectives of this study were 1) to determine the correlation between virtual histology–intravascular ultrasonography and histopathologic analysis (reference standard) and 2) to explore the comparative results of 7T MR imaging (versus histopathologic analysis), both to be performed in vitro by use of intracranial arterial segments with atherosclerotic plaques. Thirty sets of postmortem samples of intracranial circulation were prepared for the study. These samples included the middle cerebral artery ( $n = 20$ ), basilar artery ( $n = 8$ ), and anterior cerebral artery ( $n = 2$ ). Virtual histology–intravascular ultrasonography and 7T MR imaging were performed in 34 and 10 points of interest, respectively. The formalin-fixed arteries underwent tissue processing and hematoxylin-eosin staining. The plaques were independently categorized according to revised Stary classification after review of plaque morphology and characteristics obtained from 3 modalities. The proportion of fibrous, fibrofatty, attenuated calcium, and necrotic components in the plaques were determined in histology slides and compared with virtual histology–intravascular ultrasonography and MR imaging.

**RESULTS:** Of 34 points of interest in the vessels, 32 had atherosclerotic plaques under direct visualization. Plaques were visualized in gray-scale intravascular ultrasonography as increased wall thickness, outer wall irregularity, and protrusion. The positive predictive value of virtual histology–intravascular ultrasonography for identifying fibroatheroma was 80%. Overall, virtual histology–intravascular ultrasonography accurately diagnosed the type of the plaque in 25 of 34 samples, and  $\kappa$  agreement was 0.58 (moderate agreement). The sensitivity and specificity of virtual histology–intravascular ultrasonography readings for fibroatheroma were 78.9% and 73.3%, respectively. The overall sensitivity and specificity for virtual histology–intravascular ultrasonography were 73.5% and 96.6%, respectively. Plaques were identified in 7T MR imaging as increased wall thickness, luminal stenosis, or outer wall protrusion. The positive predictive value of 7T MR imaging for detecting fibrous and attenuated calcium deposits was 88% and 93%, respectively.

**CONCLUSIONS:** This in vitro study demonstrated that virtual histology–intravascular ultrasonography and high-resolution MR imaging are reliable imaging tools to detect atherosclerotic plaques within the intracranial arterial wall, though both imaging modalities have some limitations in accurate characterization of the plaque components. Further clinical studies are needed to determine the clinical utility of plaque morphology and composition assessment by noninvasive tests.

**ABBREVIATIONS:** IVUS = intravascular ultrasonography; SPACE = sampling perfection with application-optimized contrasts by use of different flip angle evolutions; VH = virtual histology

Intracranial atherosclerotic disease accounts for up to 10% of ischemic strokes.<sup>1</sup> Recent studies suggest that imaging of plaque burden, composition, and morphology provides additional in-

sight regarding the risk of thrombo-embolism and response to endovascular treatment in coronary and carotid artery plaques.<sup>2</sup> The consensus conference on intracranial atherosclerotic disease in 2009 identified plaque characterization as an important method of identification for patients with intracranial atherosclerotic disease who are at risk for ischemic events.<sup>3</sup> Intravascular ultrasonography (IVUS) and high-resolution MR imaging are gaining prominence in the imaging of characteristics of atherosclerotic plaques.<sup>4–6</sup> Despite numerous studies regarding the use of these modalities in coronary and carotid arteries, such data are lacking in intracranial arteries and atherosclerotic plaques. Intra-

Received February 13, 2013; accepted after revision March 26, 2013.

From the Zeenat Qureshi Stroke Research Center (S.M., M.W., A.E.H., M.F.K.S., A.I.Q.), Center for Magnetic Resonance Research (J.S., P.-F.V.d.M.), and Department of Laboratory Medicine and Pathology (H.B.C.), University of Minnesota, Minneapolis, Minnesota.

Please address correspondence to Shahram Majidi, MD, Zeenat Qureshi Stroke Research Center, University of Minnesota, 420 Delaware St SE, MMC 295, Minneapolis, MN 55455; e-mail: drsmajidi@gmail.com

<http://dx.doi.org/10.3174/ajnr.A3631>

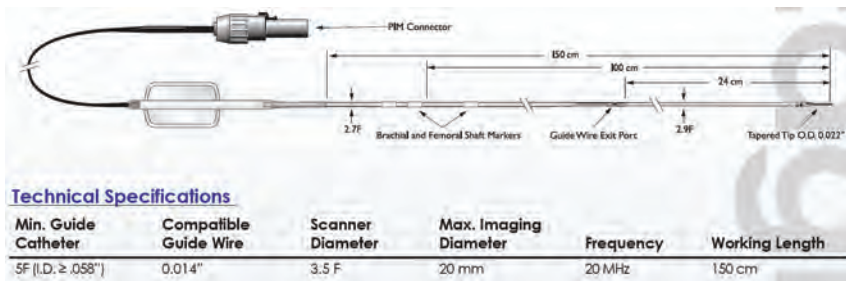


**FIG 1.** Characteristics of Eagle Eye Gold IVUS imaging catheter.

cranial arteries have unique features including a smaller wall-to-lumen ratio, thinner wall thickness, and thinner intima compared with coronary and carotid arteries.<sup>7,8</sup>

In this study, we evaluated the ability of virtual histology (VH) by IVUS to identify intracranial plaque characteristics compared with histopathologic analysis. Additional imaging data were collected on a 7T scanner in a subset of the samples to evaluate lesion detection capability on the basis of very high spatial resolution MR images.

## MATERIALS AND METHODS

The study protocol was reviewed and approved by the Anatomy Bequest Program at the University of Minnesota, Minneapolis. Ten human cadaver brains were inspected for selection of intracranial vessels with atherosclerotic plaques. A total of 30 different vessels including 8 basilar and 20 middle and 2 anterior cerebral arteries were selected for the study. The vessels were preserved in formalin for 8 weeks before the study. Decalcification was not performed before sectioning.

### Virtual Histology by IVUS

The vessel specimens were pinned on a gel by use of metal needles in a dissecting tray filled with normal saline at room temperature. The proximal and distal ends of each vessel were connected to a 6F catheter to allow flushing of the artery during the IVUS imaging. The 20-MHz IVUS catheter (Eagle Eye Gold, 20 MHz Digital, 64 Bement, s5 Imaging System; Volcano Corporation, Rancho Cordova, California) was then inserted into the vessel lumen and advanced beyond the atherosclerotic portion of the vessel. The IVUS signal derated intensity, spatial peak temporal average ( $I_{SPTA,3}$ ), was 2.68 (mW/cm<sup>2</sup>), with a maximum scanning diameter of the catheter of 20 mm (set at 10 mm during the experiment) (Fig 1). An electrocardiogram simulator (60 beats per minute) was connected to the system to enable the VH data acquisition. The IVUS catheter was then slowly pulled back by use of the catheter pullback device (Trak Back II; Volcano Corporation) at a speed of 0.5 mm/s. VH-IVUS data analysis was performed by an independent expert blinded to the baseline lesion characteristics. Percentages of the 4 different components of plaques were identified within the color-coded map on VH-IVUS as described below<sup>9</sup>:

- 1) Fibrous tissue: area of densely packed collagen (dark green component).
- 2) Fibrofatty tissue: area of collagen fibers with high lipid accumulation (light green component).
- 3) Necrotic tissue: area with high content of lipid, foam cells, and necrotic cells (red component).

- 4) Dense calcium: areas with compact calcium deposit without presence of necrosis (white component).

The plaques were also classified to 1 of the 6 categories of atherosclerotic plaque on the basis of a previously published classification<sup>10</sup>:

- 1) Pathologic intimal thickening: intima media thickness >300 μm, fibrofatty component >10%, necrotic core and calcium amount <10% of plaque area;
- 2) fibroatheroma: necrotic core >10% of plaque area;
- 3) calcified fibroatheroma: fibroatheroma with areas of calcium deposition;
- 4) thin-cap fibroatheroma: necrotic core confluent against the lumen with >10% of plaque area;
- 5) calcified thin-cap fibroatheroma: areas of calcium deposition in thin-cap fibroatheroma plaque; or
- 6) fibrocalcific: calcium deposition >10% of plaque area; fibrofatty and necrotic core comprise <10% of plaque.

### High-Resolution 7T MR Imaging

First, vessel specimens were placed between 2 plastic plates with a spacer between the plates immersed in a rectangular box (125 × 98 × 3 mm<sup>3</sup>) filled with Fomblin (perfluoropolyether; Ausimont, Morristown, New Jersey). Fomblin does not have water protons; thus, only signal from the specimen was measured in MR imaging.<sup>11</sup> The MR images were acquired on a 7T magnet (MagneX Scientific, Oxford, United Kingdom) driven with a Magnetom 7T console (Siemens Erlangen, Germany). A volume coverage head coil (16 transceiver channels) was used for excitation and reception, as previously described.<sup>12</sup> To improve signal-to-noise ratio, signal was also received on a home-built preamplifier-decoupled (Microwave Technology, Fremont, California) 2-loop receiver coil (5 cm each) made of 12-gauge silver-plated copper wire on which the sample box was directly positioned. In preliminary experiments with multi-echo and multi-inversion-recovery time sequences, average relaxation time T<sub>2</sub> and T<sub>1</sub> values of the vessel walls at 7T were estimated to be ~35 ms and ~1400 ms, respectively. Ex vivo 3D images were obtained by means of the 3D sampling perfection with application-optimized contrasts by use of different flip angle evolutions (SPACE) sequence,<sup>13</sup> with the following parameters: TR/TE = 3000/60 ms, FOV = 95 × 119 × 10.4 mm, echo-train length = 14, generalized autocalibrating partially parallel acquisition acceleration factor = 2. Scan duration was 7 hours, 33 minutes; voxel size = 0.13 mm<sup>3</sup>. 3D SPACE contrast is a combination of T<sub>1</sub> and T<sub>2</sub> contrast. The sequence parameters were chosen to provide a mixed contrast of T<sub>1</sub> and T<sub>2</sub> weight, dominated by T<sub>1</sub> weight.

### Histopathology

Formalin-fixed arterial specimens were cut into 4-mm sections and embedded in paraffin. Small sutures were placed in the arterial wall by use of 4–0 Prolene polypropylene suture (Ethicon, Somerville, New Jersey) and used as markers to enable matching the points of interest in IVUS and MR imaging with corresponding sections on histology. Subsequently, 6-μm sections were taken from the tissue blocks and stained with hematoxylin-eosin.

**Table 1: Comparison of different types of atherosclerotic plaques between VH-IVUS and histologic sections (as reference standard)**

Category of Plaque	Plaque Classification by Histological Analysis	Plaque Classification by VH-IVUS Analysis							
		True-Positive	True-Negative	False-Positive	False-Negative	Sensitivity	Specificity	PPV	NPV
No plaque	2	2	32	0	0	100	100	100	100
Pathologic intima thickening	6	3	28	0	3	50	100	100	90.3
Fibroatheroma	19	15	11	4	4	78.9	73.3	78.9	73.3
Calcified fibroatheroma <sup>a</sup>	0	0	33	1	0	0	97	0	100
Thin-cap fibroatheroma	3	2	30	1	1	66.6	96.7	66.6	96.7
Calcified thin-cap fibroatheroma	2	1	31	1	1	50	96.8	50	96.8
Fibrocalcific atheroma	2	2	32	0	0	100	100	100	100
Total	34	25	197	7	9	73.5	96.6	78.1	95.6

PPV indicates positive predictive value; NPV, negative predictive value.

<sup>a</sup>Number is small and requires cautious interpretation of false-positive or false-negative values.

**Table 2: Area of 4 different components of plaque types in histologic sections and VH-IVUS analyses**

	Histopathology, % (SD)	VH-IVUS, % (SD)	Pearson Correlation
Fibrous	45.6 (18.7)	50.8 (17.1)	0.66
Fibrofatty	35.6 (14.1)	12.5 (12.1)	0.34
Dense calcium	7.1 (7.6)	9.1 (5.2)	0.64
Necrosis	5.1 (4.6)	20.9 (10.9)	0.23

Histology slides were then reviewed by a neuropathologist who was blinded to the VH-IVUS and MR imaging data. The plaques were classified to one of the categories of atherosclerotic plaques types, based on the classification mentioned above.

Finally, histology slides were photographed under the microscope, and the area (mm<sup>2</sup>) of different components of the plaques including fibrous, fibrofatty, attenuated calcium, and necrosis were quantitatively measured with the use of the manual segmentation tools of Analyze software (AnalyzeDirect, Overland Park, Kansas) as described previously.<sup>14,15</sup> For calculating the area by use of Analyze software, the ROI was manually selected for each component. The total amount of each component was then calculated by summing all the ROIs for that component by use of the “sample option” function.

### Statistical Analysis

Statistical analyses were performed with the use of SAS software version 9.1 (SAS Institute, Cary, North Carolina). Kappa agreement, sensitivity and specificity, and positive and negative predictive values for VH-IVUS to identify different types of plaques<sup>10</sup> were calculated by use of classification on the basis of histologic findings as the reference standard (plaque categorization analysis). The positive and negative predictive values for VH-IVUS and MR images in identifying different plaque categories and fibrous and attenuated calcium components in the plaque were calculated using quantification on the basis of histologic findings as the reference standard (individual plaque component analysis). The correlation between areas (mm<sup>2</sup>) of various components measured by histology and by VH-IVUS images was also calculated. Finally, the overall sensitivity and specificity for VH-IVUS reading in accurately characterizing plaque type with the actual histologic findings were calculated using the total numbers of true and false identification with VH-IVUS. Spatially matched cross-sectional MR images of the arteries with their corresponding histologic sections and VH-IVUS images were studied to determine positive and negative predictive values.

## RESULTS

A total of 30 intracranial arterial segments (34 histologic sections) were examined by both VH-IVUS and microscopy of histologic sections. In exploratory analysis, 10 of the 30 intracranial arterial segments were also examined by 7T MR imaging.

### Correlation Between VH-IVUS and Histopathologic Analysis

In the plaque categorization analysis, VH-IVUS was able to detect the presence of atherosclerotic plaque in all specimens with morphologically visible abnormalities and absence of plaque in 2 specimens without atherosclerotic plaque by histology. VH-IVUS identification of plaque type correlated with histology sections analysis in 25 of 34 specimens ( $\kappa$  agreement was 0.58). The most frequent type of the plaques by histology was fibroatheroma, and VH-IVUS identification correlated with histology analysis in 15 of 19 corresponding points of interest within arteries (positive and negative predictive values of VH-IVUS were 78.9% and 73.3%, respectively). The sensitivity and specificity of VH-IVUS readings for fibroatheroma were 78.9% and 73.3%, respectively. As shown in Table 1, the overall sensitivity and specificity for VH-IVUS were 73.5% and 96.6%, respectively. Fig 2 demonstrates 2 samples of histology slides with their corresponding VH-IVUS images.

In the individual plaque component analysis, positive and negative predictive values of VH-IVUS to identify the presence of calcium in atherosclerotic plaque were 50% and 100%, respectively. Regarding the presence of necrosis, VH-IVUS had the positive and negative predictive values of 97% and 67%, respectively, for identifying necrosis. The quantitative proportions of different plaque components (fibrous, fibrofatty, necrosis, and attenuated calcium) were also measured in histology sections and compared with VH-IVUS images. Overall, fibrous component was the most frequent component of the plaques both in histologic sections and VH-IVUS imaging study. As shown in Table 2, the area of fibrous component and attenuated calcium deposits had the highest rates of correlation between histology and VH-IVUS images (Pearson correlations of 0.66 and 0.64, respectively).

### Correlation Between 7T MR Imaging and Histopathologic Analysis

MR imaging was successfully performed in 10 different points of interest including 3 basilar and 7 middle cerebral arterial segments. An increased wall thickness was detected by MR imaging in all sites in which plaques were identified in histologic sections.

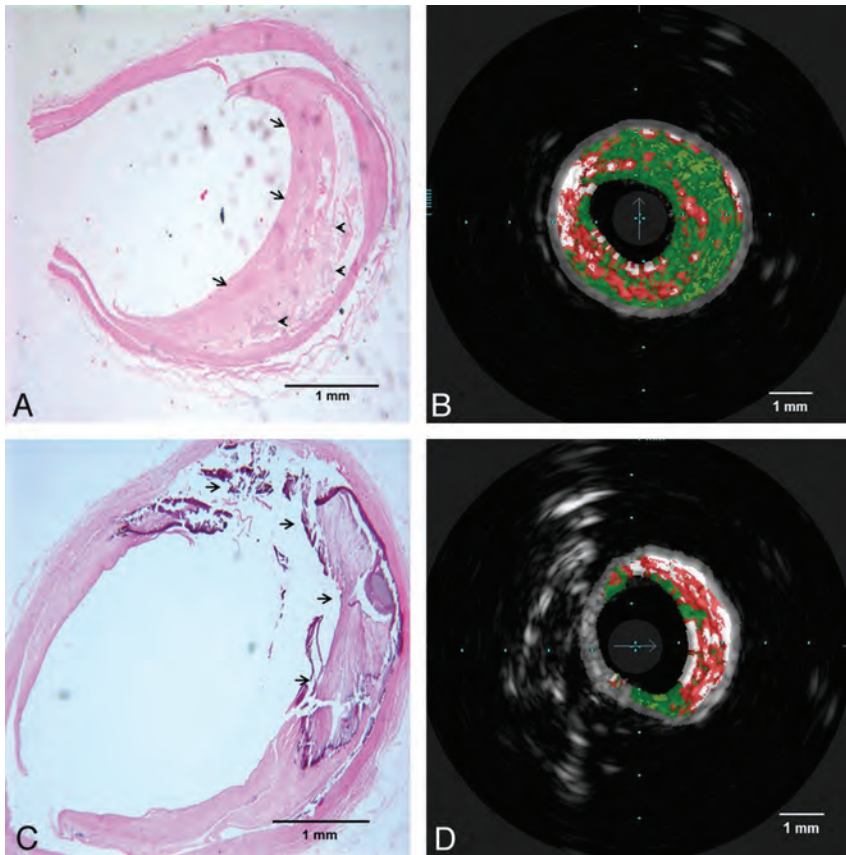


**FIG 2.** Histopathologic sections with corresponding VH-IVUS images. A and B, Fibrous (arrows in A) and fibrofatty (arrowheads in A) tissues in the histologic section are correlated with dark green and light green areas in VH-IVUS, respectively. C and D, attenuated calcium and necrotic area (arrows in C) and its corresponding area in VH-IVUS red (necrosis) and white (attenuated calcium) areas.

In a more detailed analysis of individual plaque components within each lesion, the fibrotic components were identified as areas of hyperintense signal in 3D SPACE MR images, whereas areas of attenuated calcium deposition were identified as areas of hypointense signal in the same image. Note that the SPACE MR imaging sequence provided a mixed contrast, combining T1 and T2 weights (Fig 3).

## DISCUSSION

As a result of compensatory dilation (remodeling), vessel wall thickening related to intracranial atherosclerosis may not cause proportional luminal narrowing.<sup>16,17</sup> Therefore, imaging modalities such as conventional angiography and CT angiography, which are based on detecting severity of luminal narrowing, may underestimate the severity and subsequent risk of ischemic events of intracranial atherosclerotic disease.

In this study focusing on intracranial arteries, VH-IVUS and 7T MR imaging were able to detect all of the atherosclerotic plaques as increased wall thickness. Normal vessels were visualized as vessels with no irregularity and/or thickness change in the wall, in both VH-IVUS and MR imaging. There was a moderate agreement ( $\kappa$  agreement of 0.58) between VH-IVUS and actual histologic evaluation in plaque categorization analysis. Considering all types of plaque, the overall sensitivity and specificity for VH-IVUS were 73.5% and 96.6%, respectively. We also vali-

dated the accuracy of high-resolution MR imaging and VH-IVUS for detecting fibrous content and attenuated calcium deposits. VH-IVUS had high yield for detection and quantitation of fibrous area and attenuated calcium deposits.

However, VH-IVUS underestimated the quantitative estimates of necrotic core and fibrofatty areas, which are limitations previously noted in analyses of coronary arteries.<sup>18-20</sup> The relative lack of identification of necrotic core can be partly explained by the different definitions used in histologic analysis and VH-IVUS.<sup>21</sup> In histologic analysis, the necrotic core is defined by areas with lipid-rich cellular debris and lack of extracellular matrix<sup>22,23</sup>; VH-IVUS relies on the presence of calcification to detect the necrotic core.<sup>9,24</sup> Moreover, the current resolution of VH-IVUS (100–200  $\mu$ m) is not high enough to detect thin-cap fibroatheroma and necrotic core.<sup>25</sup> To obtain greater accuracy, the use of contrast-enhanced ultrasonography, high-resolution MR imaging, multidetector CT, and concurrent VH-IVUS may be required.<sup>2,26,27</sup>

VIVA (VH-IVUS in Vulnerable Atherosclerosis)<sup>28</sup> and PROSPECT (Providing Regional Observations to Study Predictors of Events in the Coronary

Tree)<sup>29</sup> are 2 prospective studies that demonstrated that VH-IVUS can reliably identify the atherosclerotic plaques that are at increased risk of major adverse cardiac events. The unique features of intracranial vessels prevent extrapolation of current data regarding plaque characterization by use of different imaging modalities in extracranial vessels. Intracranial arteries have a smaller wall-to-lumen ratio, thinner wall thickness, and thinner intima compared with coronary and carotid arteries. In comparison to extracranial vessels, the intracranial vessels have a more prominent internal elastic layer and less advanced adventitia and media.<sup>30</sup> Only preliminary data regarding the clinical application of plaque characterization are available. Preliminary data suggest the existence of a nonatherosclerotic variant involving the anterior circulation that may be prone to high rates of restenosis after stent treatment.<sup>31,32</sup> However, angiography is unable to differentiate nonatherosclerotic from atherosclerotic disease and assess the burden of fibrosis within plaque. Therefore, plaque differentiation may be valuable in assessing the risk-benefit ratio of medical and endovascular treatment options.

The use of VH-IVUS is limited as an adjunct to an invasive procedure such as cerebral angiogram, intracranial angioplasty, or stent placement and is possible in selected proximal arteries without excessive tortuosity. The new generations of VH-IVUS

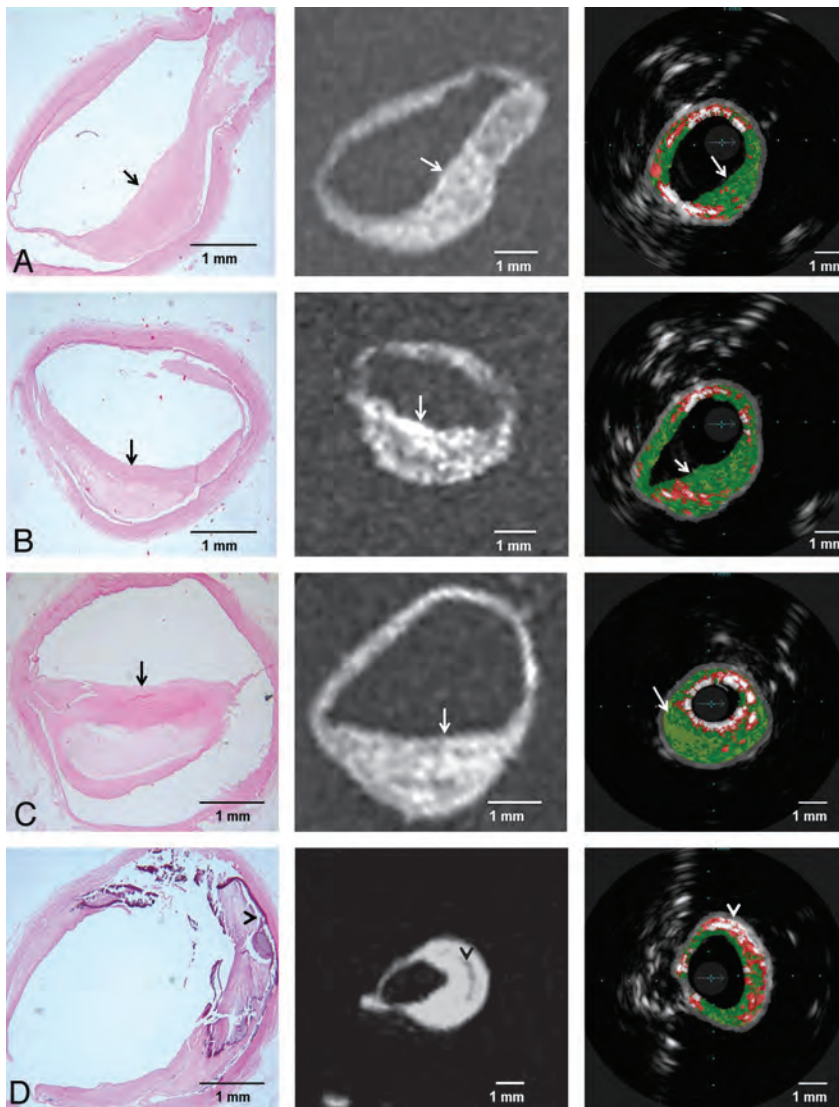


**FIG 3.** Four different histopathologic sections of intracranial vessels with atherosclerotic plaque and their corresponding 3D SPACE MR imaging (in the middle) and VH-IVUS (on the right) images. Fibrous areas (*arrows*) and attenuated calcium (*arrowheads*) consistently visualized as areas with hyperintense and hypointense signals in MR imaging, respectively.

catheters are expected to be more flexible, with a smaller profile, which would allow passage of these catheters through the tortuous intracranial arteries; henceforth, such imaging is expected to gain greater use in neuro-endovascular procedures.<sup>33</sup>

Regarding the MR imaging component of our experiment, we aimed to study the value of high-resolution MR imaging as a secondary or exploratory aim. Although the acquisition time of these initial MR imaging results was far beyond any affordable in vivo scan duration, we deliberately chose to benefit from the in vitro nature of the study to first determine whether plaque lesions could—at all—be imaged with the SPACE sequence at 7T MR imaging by use of a very high spatial resolution (voxel size approximately 500 times smaller than 1 mm<sup>3</sup>). The positive results reported here provide a strong rationale to further optimize MR acquisition protocols by use of lower spatial resolution, toward a trade-off, providing acceptable acquisition time while preserving plaque detectability. Further in vivo studies will also be necessary

to determine the sensitivity of such acquisitions to physiologic motion.

The experimental MR imaging setup (spatial extent of sensitivity of the coils smaller than in vitro specimens) and the length and alignment of arterial segments available for imaging prevented us from acquiring adequate 7T MR imaging in all plaques. We acknowledge that the relatively small sample size may not allow an adequate quantitative analysis of the value of high-resolution MR imaging in characterizing plaque categories.

Our study has several limitations. First, VH-IVUS and MR imaging were performed in in vitro settings with specimens fixed in formalin. The tissue handling and processing may induce some artifact in the size and morphology of the plaques. These changes may affect the generalization of the results to practical clinical settings. In vitro settings are appropriate for validation studies of VH-IVUS before clinical application.<sup>9,18</sup> Our sample size for some types of the plaques and negative sites (none atherosclerotic vessel) was very small, which requires cautious interpretation of the estimates for each of the plaque types separately.

## CONCLUSIONS

This study demonstrated that VH-IVUS and 7T MR imaging are reliable imaging modalities to detect atherosclerotic plaques and to quantify plaque burden within the intracranial arterial wall. Both imaging modalities have some limitations in accurate classification of plaque type and characterization of the plaque components. The application of these imaging techniques may provide additional risk stratification in regard to ischemic events and lesion progression in patients with intracranial atherosclerotic disease.

Disclosures: Ameer Hassan—UNRELATED: Payment for lectures (including service on speakers bureaus); MicroVention, Comments: Honorarium. Pierre-Francois Van de Moortele—RELATED: Grant: NIH.\* Muhammad Suri—RELATED: Grant: NIH, Comments: NIH K12 award; Support for travel to meetings for the study or other purposes: NIH, Comments: NIH K12 award. Adnan Qureshi—UNRELATED: Consultancy: Cornerstone Therapeutics Adnan I. Qureshi is supported by the National Institute of Neurological Diseases and Stroke. Principal Investigator, Antihypertensive Treatment in Acute Cerebral Hemorrhage (ATACH)-II. 1U01NS062091 (medication provided by EKR therapeutics) and the American Heart Association Established Investigator Award 0840053 N, Innovative Strategies for Treating Cerebral Hemorrhage. (\*money paid to institution).

## REFERENCES

1. Kasner SE, Chimowitz MI, Lynn MJ, et al. Predictors of ischemic stroke in the territory of a symptomatic intracranial arterial stenosis. *Circulation* 2006;113:555–63

2. Yuan C, Mitsumori LM, Beach KW, et al. **Carotid atherosclerotic plaque: noninvasive MR characterization and identification of vulnerable lesions.** *Radiology* 2001;221:285–99
3. Qureshi AI, Feldmann E, Gomez CR, et al. **Consensus conference on intracranial atherosclerotic disease: rationale, methodology, and results.** *J Neuroimaging* 2009;19(Suppl 1):1S–10S.
4. Nair A, Calvetti D, Vince DG. **Regularized autoregressive analysis of intravascular ultrasound backscatter: improvement in spatial accuracy of tissue maps.** *IEEE Trans Ultrason Ferroelectr Freq Control* 2004;51:420–31
5. van der Kolk AG, Zwanenburg JJ, Brundel M, et al. **Intracranial vessel wall imaging at 7.0-T MRI.** *Stroke* 2011;42:2478–84
6. Zacharatos H, Hassan AE, Qureshi AI. **Intravascular ultrasound: principles and cerebrovascular applications.** *AJNR Am J Neuroradiol* 2010;31:586–97
7. Walmsley JG, Canham PB. **Orientation of nuclei as indicators of smooth muscle cell alignment in the cerebral artery.** *Blood Vessels* 1979;16:43–51
8. Walmsley JG. **Vascular smooth muscle orientation in straight portions of human cerebral arteries.** *J Microsc* 1983;131:361–75
9. Nair A, Kuban BD, Tuzcu EM, et al. **Coronary plaque classification with intravascular ultrasound radiofrequency data analysis.** *Circulation* 2002;106:2200–06
10. Diethrich EB, Pauliina Margolis M, Reid DB, et al. **Virtual histology intravascular ultrasound assessment of carotid artery disease: the Carotid Artery Plaque Virtual Histology Evaluation (CAPITAL) study.** *J Endovasc Ther* 2007;14:676–86
11. Benveniste H, Kim K, Zhang L, et al. **Magnetic resonance microscopy of the C57BL mouse brain.** *NeuroImage* 2000;11:601–11
12. Adriany G, Van de Moortele PF, Ritter J, et al. **A geometrically adjustable 16-channel transmit/receive transmission line array for improved RF efficiency and parallel imaging performance at 7 Tesla.** *Magn Reson Med* 2008;59:590–97
13. Mugler JP III, Brookeman JR. **Efficient spatially-selective single-slab 3D turbo-spin-echo imaging.** *The International Society for Magnetic Resonance in Medicine (ISMRM) Twelve Scientific Meeting and Exhibition*, May, 15–21, 2004. Kyoto, Japan. [Abstract: 695]
14. Zimmerman RD, Maldjian JA, Brun NC, et al. **Radiologic estimation of hematoma volume in intracerebral hemorrhage trial by CT scan.** *AJNR Am J Neuroradiol* 2006;27:666–70
15. Divani AA, Majidi S, Luo X, et al. **The ABCs of accurate volumetric measurement of cerebral hematoma.** *Stroke* 2011;42:1569–74
16. Glagov S, Weisenberg E, Zarins CK, et al. **Compensatory enlargement of human atherosclerotic coronary arteries.** *N Engl J Med* 1987;316:1371–75
17. Ma N, Jiang WJ, Lou X, et al. **Arterial remodeling of advanced basilar atherosclerosis: a 3-Tesla MRI study.** *Neurology* 2010;75:253–58
18. Hishikawa T, Iihara K, Ishibashi-Ueda H, et al. **Virtual histology-intravascular ultrasound in assessment of carotid plaques: ex vivo study.** *Neurosurgery* 2009;65:146–52
19. Obaid DR, Calvert PA, McNab D, et al. **Identification of coronary plaque sub-types using virtual histology intravascular ultrasound is affected by inter-observer variability and differences in plaque definitions.** *Circ Cardiovasc Imaging* 2012;5:86–93
20. Timaran CH, Rosero EB, Martinez AE, et al. **Atherosclerotic plaque composition assessed by virtual histology intravascular ultrasound and cerebral embolization after carotid stenting.** *J Vasc Surg* 2010;52:1188–94
21. Thim T, Hagensen MK, Wallace-Bradley D, et al. **Unreliable assessment of necrotic core by virtual histology intravascular ultrasound in porcine coronary artery disease.** *Circ Cardiovasc Imaging* 2010;3:384–91
22. Mann J, Davies MJ. **Mechanisms of progression in native coronary artery disease: role of healed plaque disruption.** *Heart* 1999;82:265–68
23. Burke AP, Joner M, Virmani R. **IVUS-VH: a predictor of plaque morphology?** *Eur Heart J* 2006;27:1889–90
24. Nair A, Kuban BD, Obuchowski N, et al. **Assessing spectral algorithms to predict atherosclerotic plaque composition with normalized and raw intravascular ultrasound data.** *Ultrasound Med Biol* 2001;27:1319–31
25. Nakazawa G, Finn AV, Virmani R. **Virtual histology: does it add anything?** *Heart* 2007;93:897–98
26. Vancraeynest D, Pasquet A, Roelants V, et al. **Imaging the vulnerable plaque.** *J Am Coll Cardiol* 2011;57:1961–79
27. Yuan C, Mitsumori LM, Ferguson MS, et al. **In vivo accuracy of multispectral magnetic resonance imaging for identifying lipid-rich necrotic cores and intraplaque hemorrhage in advanced human carotid plaques.** *Circulation* 2001;104:2051–56
28. Calvert PA, Obaid DR, O'Sullivan M, et al. **Association between IVUS findings and adverse outcomes in patients with coronary artery disease: the VIVA (VH-IVUS in Vulnerable Atherosclerosis) Study.** *JACC Cardiovasc Imaging* 2011;4:894–901
29. Stone GW, Maehara A, Lansky AJ, et al. **A prospective natural-history study of coronary atherosclerosis.** *N Engl J Med* 2011;364:226–35
30. Merei FT, Gallyas F, Horvath Z. **Elastic elements in the media and adventitia of human intracranial extracerebral arteries.** *Stroke* 1980;11:329–36
31. Siddiq F, Chaudhry SA, Vazquez G, et al. **Intracranial stenosis in young patients: unique characteristics and risk factors.** *Neuroepidemiology* 2012;38:148–53
32. Qureshi AI, Feldmann E, Gomez CR, et al. **Intracranial atherosclerotic disease: an update.** *Ann Neurol* 2009;66:730–38
33. Takayama K, Taoka T, Nakagawa H, et al. **Successful percutaneous transluminal angioplasty and stenting for symptomatic intracranial vertebral artery stenosis using intravascular ultrasound virtual histology.** *Radiat Med* 2007;25:243–46

# Illustrated Review of the Embryology and Development of the Facial Region, Part 1: Early Face and Lateral Nasal Cavities

P.M. Som and T.P. Naidich



## ABSTRACT

**SUMMARY:** The early embryological development of the face has been reviewed. One repeating theme to note is the serial closing and then the re-opening of a space. This is seen in the separation of the nasal and oral cavities, the nostrils, and in part 2 the developing eyelids fusing and then re-opening. Part 2 will discuss the further facial development as well as the changes in facial bone appearance after birth.

Knowledge of the embryology of the facial region not only allows one insight into how normal variations in facial structure arise but also provides an understanding of how congenital deformities occur when normal facial development goes awry. This embryology can be considered as an anatomic series of complex, well-orchestrated changes in morphology or as a series of complex biochemical events that actually orchestrate the anatomic changes. The scope of this review (Part 1) is to present the current understanding of the early morphologic formation of the normal face. It will be presented in a highly illustrated format so that the reader can better understand how the normal facial region comes into being. Because many different areas develop virtually at the same time, we will present the embryology with a focus on regional development, making every attempt to clarify the sequential overlapping changes that occur. In addition, how the facial morphology changes during the transition from late fetal development to childhood and then to adulthood will be discussed in Part 2. Because the subject is complex, the literature reflects uncertainty about the timing of specific events and even the true nature of the events themselves. In this review, we present the prevalent interpretations in the literature.<sup>1,2</sup> Part 3 will address the molecular changes that coordinate and control the morphologic development.

### Overall Perspective: Where the Cells Come From

The major development of the facial region occurs between the fourth and eighth embryonic weeks via a series of highly coordinated and preprogrammed events. This process includes contribu-

tions from the head ectoderm, which will help form the face and oral cavity, and the neural crest mesenchyme, which contributes to the first branchial arch and its derivatives. This mesenchyme is derived from the neural crest and prechordal plate. It appears that the future frontonasal region has mesenchyme from 2 origins of neural crest cells. The midbrain neural crest cells migrate between the area of the future lens placode and the optic cup to reach the frontonasal region, just beneath the nasal placode region where they form the lateral nasal process. The forebrain neural crest cells appear destined to form the medial nasal processes (Figs 1 and 2).<sup>3</sup>

### Beginning

Shortly after the anterior neuropore closes in the late third to early fourth week, the forebrain enlarges and pushes the overlying ectoderm forward and laterally, creating the frontonasal process (Fig 3). The enlarging brain and frontonasal process contribute to an ectodermally covered invagination, the stomodeum, which develops below them in the early fourth week. The ectoderm over the stomodeum comes to abut the endoderm of the developing foregut to form the oropharyngeal membrane. In the fifth week, the oropharyngeal membrane disintegrates, creating communication between the foregut and the outside (Fig 2). At the same time, mesenchymal growth in the first branchial arch produces first the maxillary process and then the faster growing mandibular process on each side of the future face. The mandibular processes rapidly extend to the facial midline and merge. The stomodeum is now surrounded by the frontonasal process above, the paired maxillary processes on either side, and the paired mandibular processes below (future lower jaw) (Fig 3).<sup>1,2</sup>

### Nasal (Olfactory) Placodes

The sensory placodes arise from a common “preplacodal field” at the anterior neural crest border.<sup>4</sup> They then differentiate to eventually have individual developmental fates (this topic is more extensively

From the Department of Radiology, Mount Sinai School of Medicine, New York University, New York, New York.

Please address correspondence to Peter M. Som, MD, Department of Radiology, The Mount Sinai Hospital, One Gustave Levy Place, New York, NY 10029; e-mail: Peter.Som@MSSM.edu

Indicates open access to non-subscribers at [www.ajnr.org](http://www.ajnr.org)

<http://dx.doi.org/10.3174/ajnr.A3415>

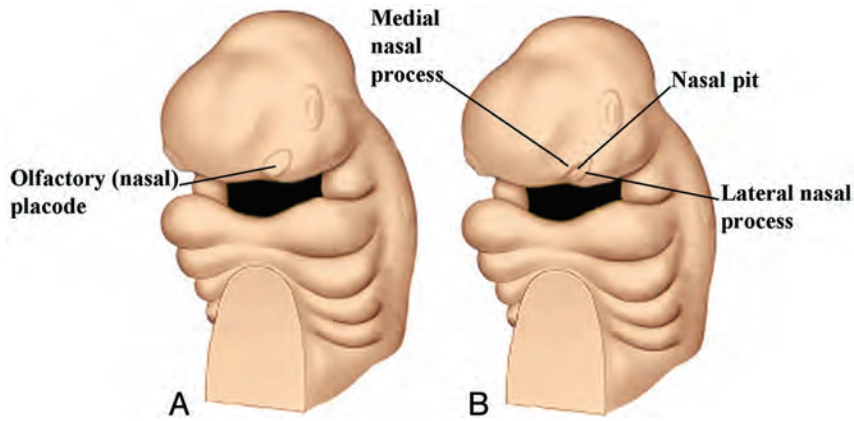


**FIG 1.** Anterior oblique drawing (A) of a 5-week embryo showing the appearance of the nasal (olfactory) placode. B, Drawing shows the development of the medial and lateral nasal processes forming a downward-facing “horseshoe” around the sinking nasal placode, which forms the nasal pit.

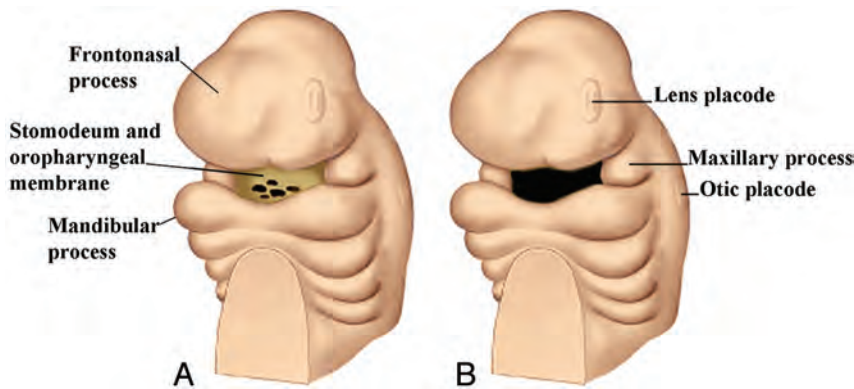


**FIG 2.** Anterior oblique drawing of an embryo in the late fourth week (A) shows the stomodeum with the oropharyngeal membrane surrounded by the further development of the frontonasal process and the maxillary and mandibular processes. B, Drawing shows the breakdown of the oropharyngeal membrane by the fifth week. The early appearance of the lens and otic placodes is also seen.

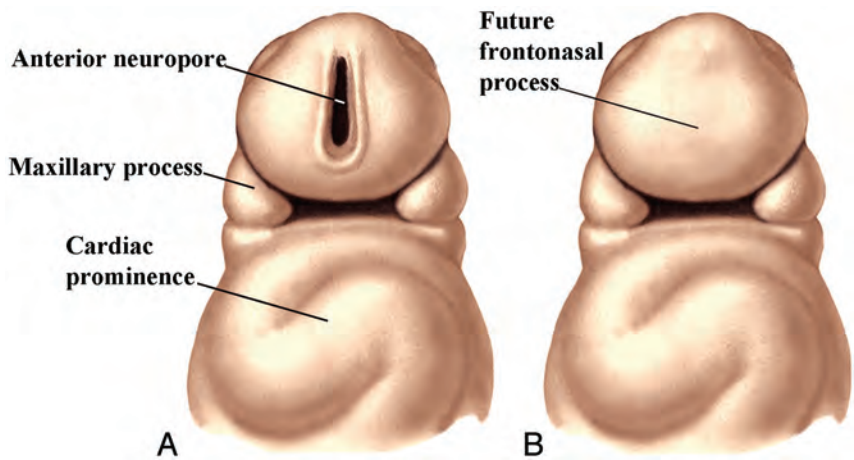


**FIG 3.** Drawing (A) of a ventral view of a 3- to 4-week embryo shows the anterior neuropore and the early formation of the maxillary processes. Drawing (B) in the late fourth week shows closure of the anterior neuropore and the location of the future frontonasal process. (Modified with permission from Netter’s Atlas of Human Embryology. Edited by Cochard, L.R., PhD. 2002. Icon Learning Systems, Teterboro, New Jersey, Figures 9.5. Netter Illustrations from www.netterimages.com, © Elsevier Inc, All rights reserved).

discussed in Part 3). These placodes are ectodermal thickenings that arise through cell division during neural tube formation (Fig 2A). By the end of the fourth week, the nasal placodes (or olfactory placodes) develop as well-defined epiblastic thickenings of 2–3 cell layers on either side of the frontonasal process (Fig 1A). Each nasal placode

begins to deepen as a result of a combination of active growth of the placodal epithelium and a proliferation of the mesenchyme deep to the edges of the placode. As each nasal placode starts to sink below the surface as a nasal groove, first the lateral nasal process develops in the early fifth week; then the medial nasal process develops shortly there-

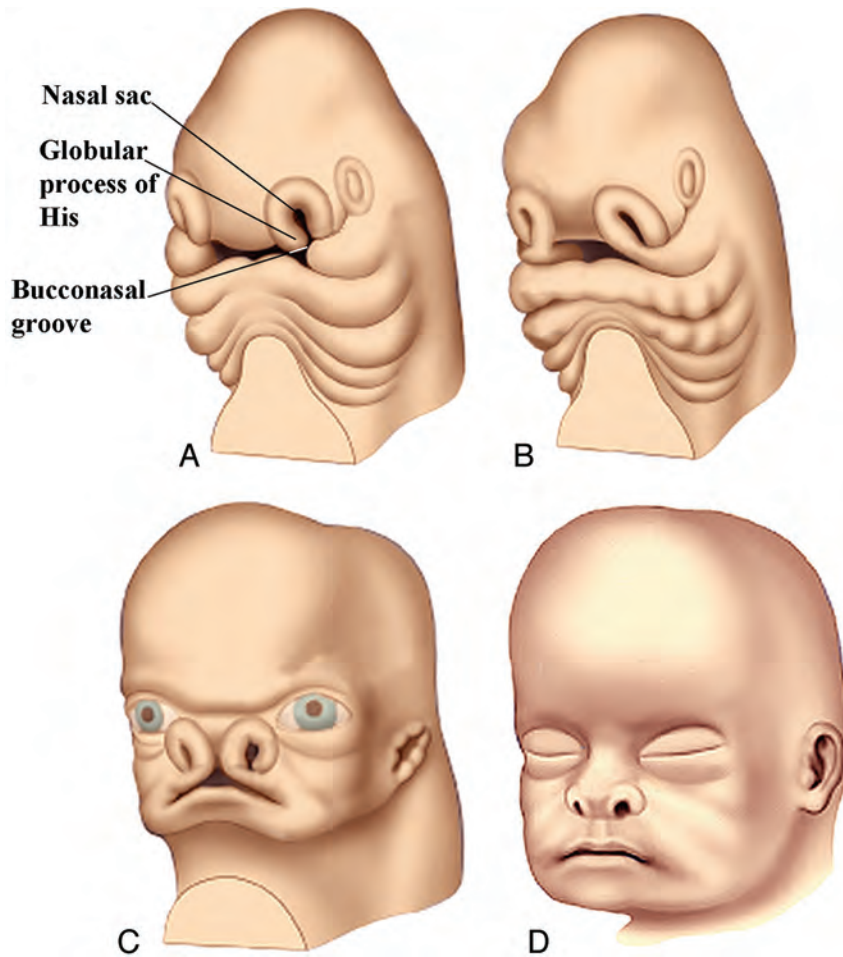


**FIG 4.** Anterior oblique drawing of a 5-week embryo (A) shows the further growth of the medial and lateral nasal processes and the development of the nasal sac. The bucconasal groove is shown. B, Anterior oblique drawing of a 6-week embryo shows closure of bucconasal groove completing the floor of the nasal cavity and progressive flattening of the nasal sac openings, mainly as a result of ventrolateral growth of the medial nasal processes. The nasal sacs are also pushed toward the midline as the maxillary processes grow. Anterior oblique drawing of a 7-week embryo (C) and a 10-week (D) embryo shows the progressive medial movement of the nasal sacs and the resulting progressive pushing upwards of the frontonasal process.

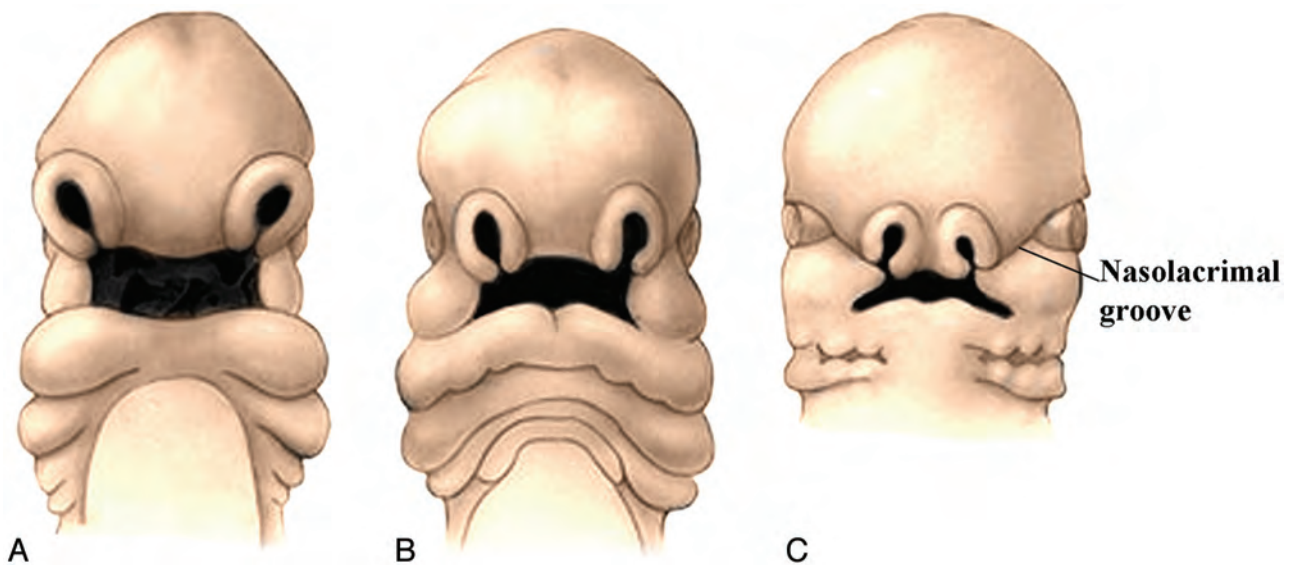


**FIG 5.** Frontal drawings of 4- to 5-week (A) and 5- to 6-week (B) embryos illustrate the progressive displacement of the nasal sacs toward the midline as a result of medial growth of the maxillary processes. Frontal view of a 6- to 7-week embryo (C) shows the nasolacrimal groove. Closure of this groove establishes continuity between the side of the nose formed by the lateral nasal process and the cheek formed by the maxillary process. (Modified with permission from Levine HL, Clemente MP, eds. Chapter 1, Surgical Anatomy of the Paranasal Sinus. China: 2005. Sinus Surgery Endoscopic and Microscopic Approaches. Figures 1-2. Thieme Medical Publishers Inc., Georg Thieme Verlag Stuttgart).

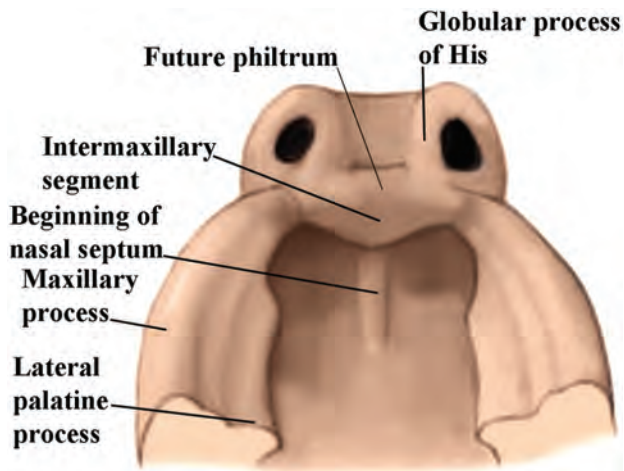


**FIG 6.** Drawing from below of a 6-week fetus showing the emergence of the intermaxillary segment below the medial nasal processes. This segment may actually arise from the globular processes of His. Also shown is the maxillary process and, arising from its medial surface, the lateral palatine process, which will form the secondary palate. (Modified with permission from Levine HL, Clemente MP, eds. Chapter 1, Surgical Anatomy of the Paranasal Sinus. China: 2005. Sinus Surgery Endoscopic and Microscopic Approaches. Figures 1-3. Thieme Medical Publishers Inc., Georg Thieme Verlag Stuttgart).

after. Together they form a downward-facing “horseshoe” with the open end facing the stomodeum (Fig 3). As the medial and lateral nasal processes develop and become more prominent, the nasal grooves deepen and become the nasal pits. By the late fifth week, these pits continue to actively deepen and are thrust back into the stomodeum, forming the nasal sacs (Fig 4). The medial nasal process is more prominent than the lateral nasal process, extending farther ventrally and caudally. Each medial nasal process has an enlarged caudal end that is called the “globular process of His” (Fig 4A).<sup>1,5</sup>

### Olfactory Epithelium and Nerves

During the early fifth week, the ectoderm in the upper one-third of each enlarging nasal sac becomes thickened and develops into the olfactory epithelium. Some cells will become spindle-shaped olfactory cells, while others will become supporting cells and basal cells. The neural epithelium facing the olfactory epithelium becomes thickened with strands of cells oriented toward the olfactory epithelium. By 5 weeks, the olfactory epithelium develops cellular buds and an associated vascular network as well as cells penetrating the basement membrane. These sensory epithelia send out nerve processes that form arborescences around the neural cells of the outgrowing olfactory lobe on each side. These will form the olfactory nerves. By late in the fifth week, a continuous cellular/vascular strand appears between each nasal sac and the olfactory field of the telencephalon.<sup>5</sup> By the late seventh week, the olfactory epithelium is confined to its “adult” location on the upper lateral nasal wall and the nasal septum.<sup>1</sup>

### Midfacial Development

During the fifth week, while the olfactory portions of the nasal sacs are developing, the maxillary processes grow medially. This medial growth results in medial displacement of the nasal sacs (Figs 4 and 5). At the same time, there is also some ventrolateral expansion of each medial nasal process, which causes compres-

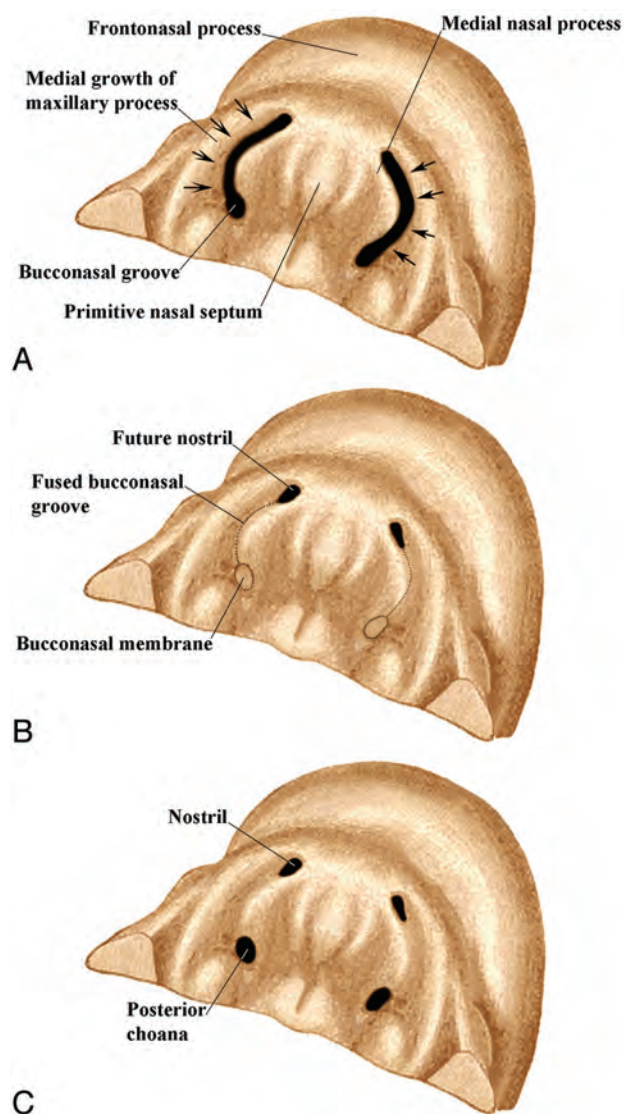


**FIG 7.** Drawings of the inferior view of an embryo from the sixth (A) to seventh weeks (C) show the bucconasal groove starting to close because of medial growth of the maxillary processes (A). B, There is fusion along most of the course of the bucconasal groove and membranous closure posteriorly by the bucconasal membrane. C, The oronasal membrane (thinned bucconasal membrane) has ruptured, creating an opening for communication between the primitive nasal and oral cavities (posterior choana).

sion of each nasal sac aperture into a slit-shaped opening (Fig 4B). In the sixth week, the medial aspects of the 2 medial nasal processes form a thickened mesodermal region anteriorly beneath and between the early nasal sacs. This constitutes the intermaxillary segment, and it may actually be formed by the joining of the globular processes of His (Fig 6). This will be discussed further when the development of the palate is discussed in Part 2.<sup>1,2</sup>

### Closing Off the Nasal Cavity

On each side of the developing face, the bucconasal groove is the groove between the maxillary process and the medial nasal process (Fig 4A). Fusion across this groove occurs in the fifth week as a result of medial growth of the maxillary process (Fig 7). Anteriorly, the fusion of the medial nasal and maxillary processes forms

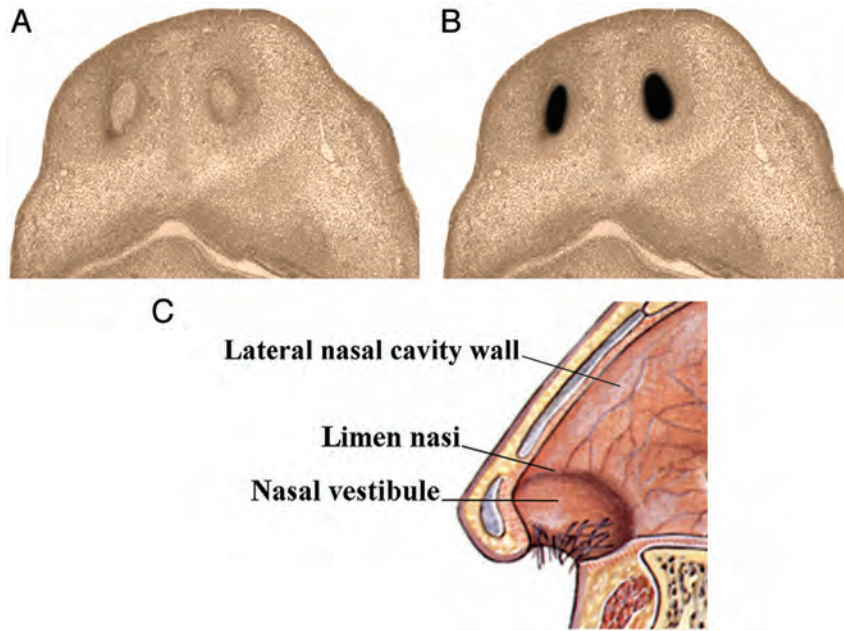


**FIG 8.** Drawings from below of a 7-week embryo (A) and a 13- to 15-week fetus (B) show epithelial plugs closing the nostrils (A) and then dissolving (B). If a plug does not dissolve, there will be atresia of the nostril. Lateral drawing of the anterior nose (C) shows the nasal vestibule and limen nasi. These areas mark the location of the nasal epithelial plugs.

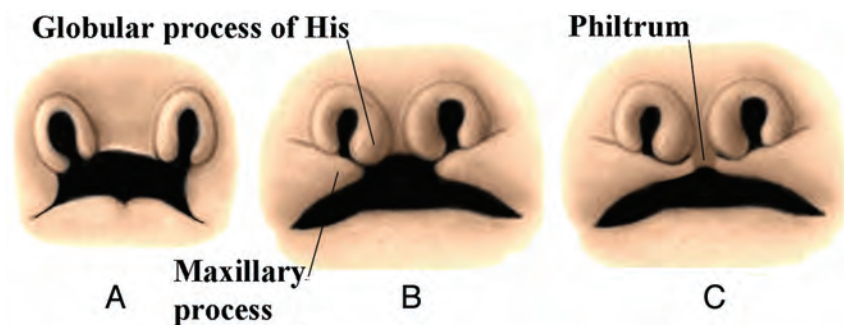


**FIG 9.** Frontal drawings of the upper lip region in embryos at 5 (A), 6 (B) and 7 (C) weeks show the progressive medial growth of the maxillary processes toward the midline. However, the actual midline of the upper lip (the philtrum) is formed by the medial nasal processes. (Modified with permission from Levine HL, Clemente MP, eds. Chapter 1, Surgical Anatomy of the Paranasal Sinus. China: 2005. Sinus Surgery Endoscopic and Microscopic Approaches. Figures 1-3. Thieme Medical Publishers Inc., Georg Thieme Verlag Stuttgart).

the lower nostril region (Fig 4B, -C). More posteriorly adjacent to the intermaxillary segment, the fusion across this bucconasal groove closes the floor of the nasal sac. At the most posterior margin of the groove, the closure across the bucconasal groove is not by fusion but by the growth of an epithelial membrane, the bucconasal membrane. The overall fusion across the bucconasal groove is often referred to as the nasal fin, and it separates the primitive nasal cavity from the primitive oral cavity. Before the closure of the bucconasal groove, the primitive nasal cavity and oral cavity were a common cavity. The dorsal epithelial membrane quickly begins to thin, and by the sixth week, it is just a 2-layered epithelium called the oronasal membrane. By the mid-sixth week, the oronasal membrane ruptures to form the primitive posterior choana. With the dissolution of the oronasal membrane, the primitive nasal cavity and posterior primitive oral cavity once more freely communicate (Fig 7). They will eventually again be separated by the development of the palate. Anteriorly

the future nostril is complete and separated from the developing oral cavity. Thus, by the seventh week, each nasal cavity opens to the outside through a nostril and communicates posteriorly with the pharynx via the primitive choana. If the oronasal membrane is not ruptured, the posterior choana is obstructed and congenital choanal atresia develops.<sup>1,2</sup>

#### Nasal Plugs

Paralleling these changes, a broadening of the head occurs behind the nasal pits, resulting in a shifting of the nasal pits from a lateral to a more ventromedial location, approaching the midline (Fig 5). By the mid-seventh week, the anterior lumen of each primitive nasal cavity becomes tightly filled by a proliferation of epithelial cells that form an epithelial plug (Fig 8A). By the 13th to 15th week, this plug dissolves, and by the mid-16th week, the nasal passages are complete and open (Fig 8B). The region occupied by the plug will become the nasal vestibule and the future limen

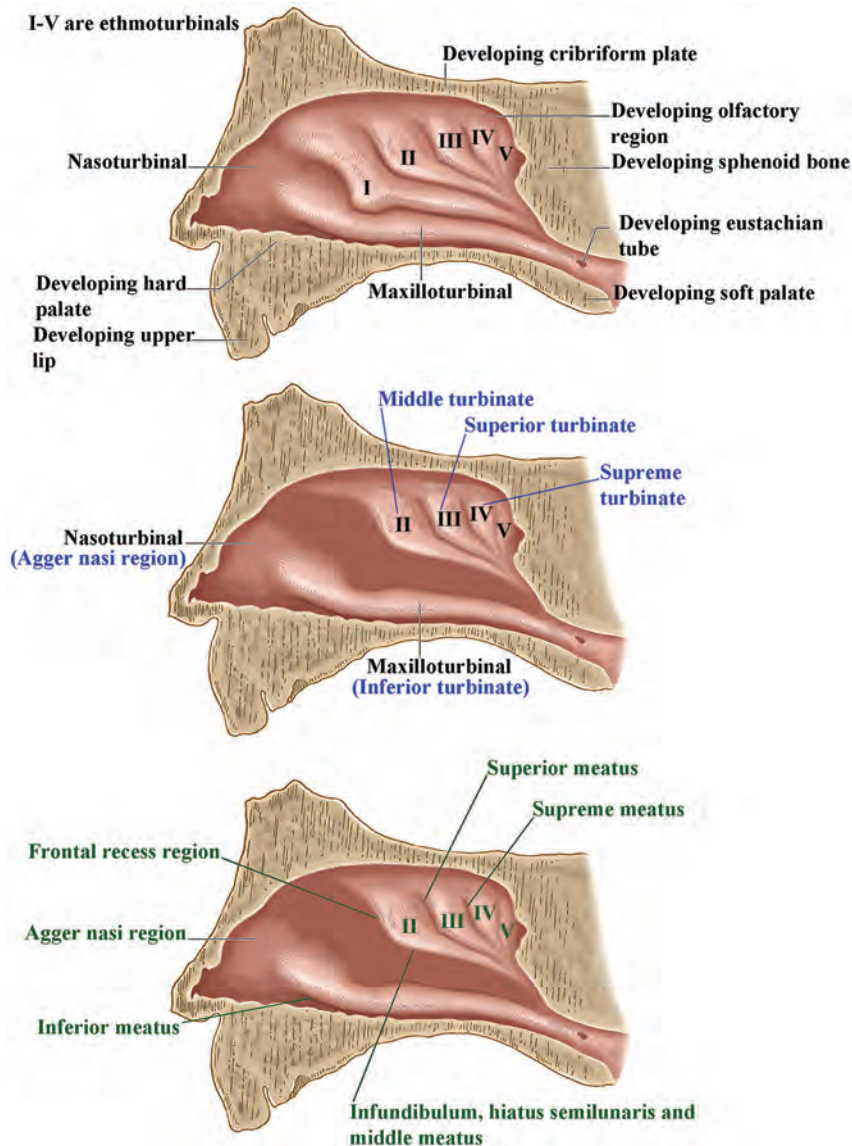


**FIG 10.** Lateral drawings of the developing lateral nasal wall showing the appearance of the nasal turbinals and their eventual development into the nasal turbinates and meati.

nasi, which is a ridge separating the nasal cavity proper from the vestibule of the nose (Fig 8C). As a consequence, the nasal vestibule consists of skin and adnexa derived from ectoderm. If this epithelial plug does not disintegrate, atresia of the nostril will occur.<sup>6</sup>

### **Forming the Upper Lip**

Ventrally, the fusion of the medial nasal processes with the maxillary processes will form most of the upper lip and upper jaw on both sides. The 2 merged medial nasal processes then form the philtrum and columella and complete the upper lip (Fig 9). The fusion of the 2 medial nasal processes displaces the frontonasal process superiorly and posteriorly (Figs 4C and 5C). As a result, although the frontonasal process formed the upper border of the stomodeum, it does not contribute to the definitive upper lip, jaw, or nasal tip. The medial migration of the maxillary processes forms not only the lateral upper lip but the upper cheek regions, resulting in continuity of the upper jaw and lip (Fig 4D).<sup>1,2</sup>

### **Lateral Nose and Nasolacrimal Duct**

By the end of the sixth week, the lateral nasal processes begin to merge with the maxillary processes to form the ala nasi or lateral nose and the lateral border of the nostril on both sides (Fig 4D). On each side of the face, along the junction between the maxillary and lateral nasal processes is the nasolacrimal groove (naso-optic furrow) (Fig 5C). The nasolacrimal groove extends between the developing lower lateral nose and the medial orbit. The ectoderm along the floor of each groove thickens to form a solid epithelial cord, which then detaches from the groove and canalizes to form the nasolacrimal duct and lacrimal sac. By the late fetal period, the nasolacrimal duct on each side extends from the medial corner of the orbit to the inferior meatus in the lateral wall of the nasal cavity. These ducts usually become completely patent only after birth. Closure of the nasolacrimal groove establishes continuity between the side of the nose formed by the lateral nasal process and the cheek formed by the maxillary process.<sup>1,2</sup>

## Summary of facial development<sup>a</sup>

Week	Description
Late 3rd to early 4th	Anterior neuropore closes; oropharyngeal membrane appears
Early 4th	Frontonasal process appears; early development of maxillary and mandibular processes creates stomodeum
Late 4th	Oropharyngeal membrane disintegrates; nasal (olfactory) placodes appear
Early 5th	Lateral nasal processes and then the medial nasal processes appear, forming nasal pit; mandibular processes meet in midline; olfactory epithelium starts to form in upper nasal cavities
Late 5th	Nasal sacs form; medial nasal processes fuse with maxillary processes and form nasal fins, separating primitive nasal and oral cavities; nasal sacs migrate more medially and become more slit-like; olfactory nerves form; Meckel cartilage forms
Early 6th	Oronasal membrane forms and disintegrates opening posterior nasal choana; medial nasal processes start to form primitive nasal septum and primary palate
Late 6th	Lateral palatine processes develop; they are initially directed caudally alongside and above the tongue; naso-optic furrow develops and nasolacrimal duct forms (will become patent at birth); external ear develops; labiogingival laminae appear; lips and gums separate; dental lamina appears; maxilloturbinal (future inferior turbinate) starts to form; remaining nasal turbinates form; eyelids start to form
Early 7th	Philtrum and upper lip complete; nasal septum further develops; external olfactory epithelium confined to upper nasal cavities and further develops
Late 7th	External ear fully developed; nasal plugs close nostrils (will open again in 16th week); cartilaginous nasal capsule develops; palatal shelves elevate and fuse, forming secondary palate; future nostril now complete; eyes move more to midline; fusion of maxillary and mandibular processes narrows the width of the mouth and completes lower cheeks
8th	Lateral nasal wall well-developed; facial muscle primordia appear (muscles develop by 9th week)
9th–10th	Nasal septum starts to fuse with palate (will be complete by 12th week); ossification of maxillas occurs
10th–11th	Uncinate process arises; infundibulum then develops; tooth buds become cup-shaped (teeth will be near complete in 6th month); eyelids fuse (will open in 26th–28th weeks)
12th	Ossification centers of all facial bones are present

<sup>a</sup> The timeline of development differs slightly in the references quoted in Parts 1 and 2 of these articles. The timeline in this Table represents a compilation of the various dates in these references, and because some normal variation is to be expected, this Table represents the best averaging of any differences in developmental dates that we could make.

### Nasal Septum and Turbinates

The last part of the chondrocranium to become cartilaginous is the nasal capsule. Condensation of the mesenchyme within the frontonasal process forms the precartilaginous nasal septum in the upper midline of the primitive nasal cavity (Fig 6). Cartilage from the body of the developing sphenoid bone then extends forward into the nasal septum, forming the primary cartilage of the nasal septum by the mid-sixth week. The roof of the capsule is formed by the coalescence of cartilage from the nasal septum and from extensions of cartilage from the ventral surface of the sphenoid and secondary centers in the lateral wall of the capsule. The cartilage is at first open on either side of the nasal septum to allow passage of the olfactory fasciculi. During the third month, cartilage fills in the capsule around these nerves, forming the cribriform plates. Lateral strips of cartilage then extend back to unite with the face of the sphenoid.

The cartilaginous nasal capsule develops as 2 separate masses around the forming nasal cavities and the developing nasal septum. While the median mass will become the progenitor of the nasal septum, the lateral masses will become the lateral nasal wall structures. By the third month, the nasal capsule is well-defined cartilage.

All of the turbinates and the paranasal sinuses arise from the cartilaginous nasal capsule. Several soft-tissue folds appear on the lateral wall of each nasal cavity, the preturbinates, which are first supported by cartilage and then by bone. The maxilloturbinal develops first and then is followed by 5 ethmoturbinates (in men, the first ethmoturbinal disappears). An additional rudimentary nasoturbinal arises anteriorly, appearing later as a slight elevation, the agger nasi (Fig 10). By the eighth week, the inferior and middle turbinate anlagen forms, followed by the superior turbinate anlagen. They develop by proliferation of mesenchymal cells and hypertrophy of the overlying epithelium. During the seventh

month, the maxilloturbinal separates from the lateral wall and becomes an independent bone in the adult.

By the eighth week, the lateral nasal wall is well-developed. The length of the lower 3 turbinates increases progressively and proportionally in uterine life, while the supreme turbinate remains at an average length of 5 mm from the 14th to 36th week and is present in only 65% of fetuses. The outpouchings of the nasal mucous membranes that will become the paranasal sinuses are thought to be a secondary phenomenon rather than a primary force in sinonasal development.<sup>7,8</sup>

The uncinate process arises from the cartilaginous capsule at 10 weeks. An air channel then progressively develops lateral to the uncinate process. This will be the primitive infundibulum by 10–11 weeks. The embryonic woven bone of the maxilla can be seen between 9 and 10 weeks, and it then enlarges relative to the nasal cavity. By 13–14 weeks, the expanding maxilla now forms the lateral wall of the inferior meatus as the cartilaginous capsule regresses.<sup>9</sup> By the 16th week, the primitive maxillary sinus starts to develop from the inferior margin of the infundibulum.<sup>10</sup>

In order to be concise and for future reference for Part 2, the Table summarizes the morphologic changes described in both Parts 1 and 2 of these reviews. One repeating theme is the serial closing and then the reopening of a space. This is seen in the separation of the nasal and oral cavities, the nostrils, and the developing eyelids fusing and then reopening in Part 2.

### REFERENCES

1. Kim CH, Park HW, Kim K, et al. Early development of the nose in human embryos: a stereomicroscopic and histologic analysis. *Laryngoscope* 2004;114:1791–800
2. Warbrick JG. The early development of the nasal cavity and upper lip in the human embryo. *J Anat* 1960;94:351–62

3. Osumi-Yamashita N. **Retinoic acid and mammalian craniofacial morphogenesis.** *J Biosci* 1996;21:313–27
4. Streit A. **The preplacodal region: an ectodermal domain with multipotential progenitors that contribute to sense organs and cranial sensory ganglia.** *Int J Dev Biol* 2007;51:447–61
5. Bossy J. **Development of olfactory and related structures in staged human embryos.** *Anat Embryol (Berl)* 1980;161:225–36
6. Nishimura Y. **Embryological study of nasal cavity development in human embryos with reference to congenital nostril atresia.** *Acta Anat (Basel)* 1993;147:140–44
7. Levine HL, Clemente MP. **Surgical anatomy of the paranasal sinus.** In: Levine HL, Clemente MP, eds. *Sinus Surgery: Endoscopic and Microscopic Approaches.* New York: Thieme; 2005
8. Bolger WE. **Anatomy of the paranasal sinuses.** In: Kennedy DW, Bolger WE, Zinreich SJ, eds. *Diseases of the Sinuses: Diagnosis and Management.* Hamilton, Ontario, Canada: B.C. Dekker; 2001:1–11
9. Bingham B, Wang RG, Hawke M, et al. **The embryonic development of the lateral nasal wall from 8 to 24 weeks.** *Laryngoscope* 1991;101:992–97
10. Lee KJ. *Essentials of Otolaryngology and Head and Neck Surgery.* 8th ed. New York: McGraw Hill; 2003: Chapter 19
11. Cochard LR, ed. *Netter's Atlas of Human Embryology.* Teterboro, New Jersey; Icon Learning Systems; 2002
12. Netter FL, Craig J, Machado C. netterimages.com. Netter Illustrations. Elsevier. www.netterimages.com. Accessed 2011

# Automated White Matter Total Lesion Volume Segmentation in Diabetes

J.A. Maldjian, C.T. Whitlow, B.N. Saha, G. Kota, C. Vandergriff, E.M. Davenport, J. Divers, B.I. Freedman, and D.W. Bowden



## ABSTRACT

**BACKGROUND AND PURPOSE:** WM lesion segmentation is often performed with the use of subjective rating scales because manual methods are laborious and tedious; however, automated methods are now available. We compared the performance of total lesion volume grading computed by use of an automated WM lesion segmentation algorithm with that of subjective rating scales and expert manual segmentation in a cohort of subjects with type 2 diabetes.

**MATERIALS AND METHODS:** Structural T1 and FLAIR MR imaging data from 50 subjects with diabetes (age,  $67.7 \pm 7.2$  years) and 50 nondiabetic sibling pairs (age,  $67.5 \pm 9.4$  years) were evaluated in an institutional review board–approved study. WM lesion segmentation maps and total lesion volume were generated for each subject by means of the Statistical Parametric Mapping (SPM8) Lesion Segmentation Toolbox. Subjective WM lesion grade was determined by means of a 0–9 rating scale by 2 readers. Ground-truth total lesion volume was determined by means of manual segmentation by experienced readers. Correlation analyses compared manual segmentation total lesion volume with automated and subjective evaluation methods.

**RESULTS:** Correlation between average lesion segmentation and ground-truth total lesion volume was 0.84. Maximum correlation between the Lesion Segmentation Toolbox and ground-truth total lesion volume ( $\rho = 0.87$ ) occurred at the segmentation threshold of  $k = 0.25$ , whereas maximum correlation between subjective lesion segmentation and the Lesion Segmentation Toolbox ( $\rho = 0.73$ ) occurred at  $k = 0.15$ . The difference between the 2 correlation estimates with ground-truth was not statistically significant. The lower segmentation threshold (0.15 versus 0.25) suggests that subjective raters overestimate WM lesion burden.

**CONCLUSIONS:** We validate the Lesion Segmentation Toolbox for determining total lesion volume in diabetes-enriched populations and compare it with a common subjective WM lesion rating scale. The Lesion Segmentation Toolbox is a readily available substitute for subjective WM lesion scoring in studies of diabetes and other populations with changes of leukoariaiosis.

**ABBREVIATIONS:** DM = type 2 diabetes mellitus; LST = Lesion Segmentation Toolbox; SPM8 = Statistical Parametric Mapping; TLV = total lesion volume; GT = ground-truth

Leukoariaiosis is a common WM pathologic lesion in older adults, characterized histologically by demyelination, loss of oligodendrocytes, and vacuolization resulting from small-vessel

ischemia of the WM.<sup>1</sup> On brain MR imaging, these lesions are commonly termed WM hyperintensities and appear as regions of increased signal on T2-weighted and FLAIR sequences. Increases in WM disease burden have been associated with risk factors, such as hypertension, type 2 diabetes mellitus (DM), and tobacco use.<sup>2</sup> Quantifying WM disease burden in the brain is important because it is an accurate and sensitive predictor of future stroke, dementia, and cognitive decline.<sup>3–6</sup>

Clinical evaluation of WM disease has been limited to subjective interpretation of disease burden, with typical modifiers including “few scattered lesions” and “mild,” “moderate,” or “severe” applied in radiologic reporting. This is because of the onerous and time-consuming task of manual delineation of WM lesion burden and the lack of robust automated tools for quantitative WM lesion grading. A semi-quantitative visual rating scheme was developed for use with large epidemiologic studies

Received December 22, 2012; accepted after revision February 24, 2013.

From Advanced Neuroscience Imaging Research (ANSIR) Laboratory (J.A.M., C.T.W., B.N.S., G.K., C.V., E.M.D.), Department of Radiology (J.A.M., C.T.W., B.N.S., G.K., C.V.), Translational Science Institute (C.T.W., B.N.S.), Department of Biomedical Engineering (E.M.D.), Public Health Sciences (J.D.), Department of Internal Medicine, Section on Nephrology (B.I.F.), and Center for Diabetes Research and Human Genomics (D.W.B.), Wake Forest School of Medicine, Winston-Salem, North Carolina.

This study was supported by NIH grants NS058700 (D.W.B.) and NS0075107 (J.A.M., B.I.F., J.D.).

Please address correspondence to Christopher T. Whitlow, MD, PhD, Department of Radiology, Neuroradiology, Translational Science Institute, Wake Forest School of Medicine, Medical Center Boulevard, Winston-Salem, NC 27157-8011; e-mail: cwhitlow@wakehealth.edu

Indicates open access to non-subscribers at [www.ajnr.org](http://www.ajnr.org)

Indicates article with supplemental on-line figures.

<http://dx.doi.org/10.3174/ajnr.A3590>

involving brain MR imaging. This WM hyperintensity grading scale is commonly used for research studies and is based on visual assessment by an experienced reader with the use of a semi-quantitative 10-point (0–9) scale with predefined methodology.<sup>7,8</sup>

A variety of automated methods for WM lesion quantification, involving combinations of thresholding, segmentation, prior information, lesion growing algorithms, and, most recently, machine learning algorithms, have been used in research studies of multiple sclerosis. It is beyond the scope of this work to describe all the developments in WM lesion segmentation. Rather, we focus on a recently described software tool for automated WM lesion segmentation, the Lesion Segmentation Toolbox (LST); it was developed for use in the Statistical Parametric Mapping (SPM8) environment, which is familiar to most neuroimaging researchers, is freely distributed open source code written in Matlab (MathWorks, Natick, Massachusetts), and is easily implemented/fully automated. Additionally, the LST uses widely available structural T1-weighted and FLAIR images for performing WM lesion segmentation. The LST was developed for use in multiple sclerosis and originally evaluated in a group of 52 subjects with multiple sclerosis and 18 control subjects, achieving excellent agreement with manual tracing ( $R^2$  values of 0.93).<sup>9</sup> A critical user-determined parameter in the LST procedure is the  $k$ -threshold, which was determined to be 0.3 in a multiple sclerosis population.

The purpose of our study is to compare the performance of total lesion volume (TLV) grading computed by means of the LST automated WM lesion segmentation algorithm to expert manual segmentation in a cohort of subjects with DM and to determine the optimum  $k$ -threshold in this population. A secondary objective is to compare the LST TLV with semi-quantitative subjective rating scales. Our hypothesis is that TLV computed with the LST will perform at least as well as subjective rating scales when compared with ground-truth (GT) TLV in DM. This report answers the important question of whether an automated toolbox developed for use in multiple sclerosis can be used reliably for grading WM lesion burden in populations with a different pathophysiologic mechanism for development of WM disease.

## MATERIALS AND METHODS

### Subjects

The Diabetes Heart Study is a genetic and epidemiologic study of 1443 European American and African American participants from 564 families with multiple cases of DM.<sup>10,11</sup> The Diabetes Heart Study–Mind is an extension of the Diabetes Heart Study family of studies and examines the genetic and brain imaging contributors to cognitive changes associated with DM. The study includes diabetes- and nondiabetes-affected siblings. All subjects provided written informed consent, and study protocols were approved by the blinded institutional review board. MR imaging studies from 100 subjects were randomly selected from the Diabetes Heart Study–Mind. These included 50 subjects with DM (27 women, 23 men), 52% smokers, mean  $\pm$  standard deviation (SD) age of  $67.7 \pm 7.2$  (age range, 52–84 years), body mass index of  $32.3 \pm 7.1$ , and hemoglobin A1C of  $7.6 \pm 1.48$ ; and 50 siblings without DM (35 women, 15 men), 46% smokers, mean  $\pm$  SD age of  $67.5 \pm 9.4$  (age range, 43–89 years), body mass index of  $28.5 \pm 6.5$ , and hemoglobin A1C of  $5.9 \pm 0.31$ .

### MR Imaging

Participants from the Diabetes Heart Study–Mind were scanned on a 1.5T scanner with twin-speed gradients, with the use of an 8-channel neurovascular head coil Twin Speed EXCITE; GE Healthcare, Milwaukee, Wisconsin. High-resolution T1 anatomic images were obtained by means of a 3D spoiled gradient-echo sequence (matrix,  $256 \times 256$ ; field of view, 20 cm; section thickness, 1.5 mm with no gap; number of sections, 124; in-plane resolution,  $0.781 \times 0.781$  mm) aligned parallel to the anterior/posterior commissures (anterior/posterior commissure line). FLAIR images were acquired in the axial plane for the purpose of evaluating WM hyperintensities (TR = 8002, TE = 108.5, TI = 2000, flip angle = 90, 24 cm FOV, matrix size =  $256 \times 256$  [ $0.94 \times 0.94$  mm], 3-mm section thickness).

### Semi-Quantitative WM Rating Scale

WM hyperintensity signal changes of each individual were assessed independently by 2 board-certified neuroradiologists by means of a semi-quantitative 10-point (0–9) scale with predefined methodology.<sup>7,8</sup> WM hyperintensity burden was estimated as the total extent of periventricular and subcortical white matter FLAIR signal hyperintensity that successively increases from no or barely detectable changes (grades 0 and 1, respectively) to almost all WM involved (grade 9). This scale has an inter-reader reliability agreement within 1 grade of 85.7%, with relaxed  $\kappa$  of 0.8, and intrareader reliability for agreement within 1 grade of 96.9%, with relaxed  $\kappa$  of 0.96.<sup>8</sup>

### Image Preprocessing

The structural T1-weighted images were segmented into gray matter, WM, and CSF, normalized to Montreal Neurological Institute imaging space, and modulated with the Jacobian determinants of the normalization procedure to obtain tissue volume maps by use of the Dartel high-dimensional warping and the SPM8 (Wellcome Department of Imaging Neuroscience, London, UK)<sup>12</sup> new segment procedure, as implemented in the VBM8 toolbox (<http://dbm.neuro.uni-jena.de/vbm.html>). In addition to normalized images in Montreal Neurological Institute imaging space, the procedure outputs native space segmentations and a native space partial volume estimate label image of the most likely tissue class for each voxel. The quality of the segmentation and normalization for all subjects was confirmed by visual inspection.

### WM Lesion Segmentation

WM lesion segmentation and TLV maps were generated by use of the LST<sup>9</sup> for SPM8 at 20 thresholds ( $k$ ), ranging from 0–1 at 0.05 increments. The algorithm operates in native space and initially coregisters the FLAIR images to the space of the native T1. Each voxel in the T1 image is assigned to 1 of 3 classes (gray matter, WM, CSF) by use of the VBM8 toolbox as described above (partial volume estimate label map in native space). The FLAIR intensity distribution is calculated for each of the 3 classes to determine outliers, weighted according to the spatial probability of being WM, resulting in 3 classes of belief maps, and summed to generate a single belief map. A binarized version of the gray matter lesion map is used to seed a region growing algorithm

with the summed belief map as the target. The user-selected  $k$ -threshold is used as the cutoff to generate the initial gray matter seed binarized belief map. The algorithm outputs WM lesion segmentations for each  $k$  threshold, as well as a table of total lesion volume (20 TLV values corresponding to each of the 20  $k$ -thresholds).

### **GT Segmentation**

A multi-tiered approach was used to generate the reference GT lesion volume segmentation. All stages involved expert manual segmentation by board-certified neuroradiologists. Two raters (each with 1–2 years of neuroradiology experience) initially manually segmented all the white matter lesions independently by use of in-house software. This generated 2 independent lesion volume datasets. The 2 datasets were merged by use of a binary union procedure to generate a single dataset representing the combination of all lesions identified by both raters. Two highly experienced neuroradiologists (with >15 years and >3 years of experience, respectively) then together performed a consensus reading, reviewing all lesions in the combination dataset. The consensus reading session was performed by use of MRICron (<http://www.sph.sc.edu/comd/rorden/mricron.html>)<sup>13</sup> with direct overlay onto the original FLAIR images and included the ability to manually add, remove, and edit the borders of all lesions. This final consensus lesion volume dataset served as the GT for the study.

### **Statistical Analysis**

Correlation and regression analyses were performed for 3 main comparisons: subjective WM lesion scores versus GT, LST versus GT for each  $k$ -threshold, and subjective WM lesion scores versus LST for each  $k$  threshold. These analyses were repeated by use of log (TLV) to account for nonlinearity in the relationship between TLV and subjective scores. The optimum  $k$ -threshold was determined as that providing the maximum correlation value compared with manual segmentation. Between-group and inter-rater comparisons were also performed for the subjective WM scores and correlations with GT. Fisher  $r$ -to- $z$  transformation<sup>14</sup> was used to test whether observed correlations were statistically different from zero. Steiger  $Z$ -test of correlated correlations<sup>15</sup> was used to determine if there was a significant difference in correlation values between subjective rating with GT and LST with GT. Bland-Altman plots were also computed between LST versus GT and LST versus subjective WM lesion scores to determine the mean difference between methods.

## **RESULTS**

### **Subjective WM Lesion Scores**

Mean WM score for the group was 2.0, with an SD of 1.5. The distribution of WM scores ranged from 0–7, with most values falling in the lower range of 0–3 (On-line Fig 1). Between-reader agreement was 88% within 1 grade, similar to that reported in the literature for this method.<sup>8</sup> There was no statistically significant difference in subjective WM scores between groups, with mean  $\pm$  SD of  $2.0 \pm 1.3$  for DM-affected and  $2.0 \pm 1.6$  for non-DM groups.

### **Subjective WM Lesion Scores Versus GT**

The Pearson correlation between average WM scores and GT was 0.84, with reader 1 having a correlation of 0.79 and reader 2 a correlation of 0.82. The correlation between average WM scores and GT was 0.82 and 0.85 for DM-affected and non-DM groups, respectively. With the use of the logarithm of GT, the correlations with average WM scores improved to 0.85 for the entire cohort (0.77 for reader 1 and 0.86 for reader 2) and 0.845 for the DM-affected group and 0.86 for the non-DM group. All reported correlation values were statistically significant ( $P \leq .0001$ ).

### **LST Versus GT**

On-line Fig 2 is a graph of the LST  $k$ -threshold versus correlation with GT for the entire cohort. Correlation values ranged from 0.62–0.81 for the thresholds considered. Maximum correlation for the full sample was 0.87, corresponding to  $k = 0.25$ . For the non-DM group, maximum correlation was 0.94 observed at  $k = 0.15$ . For the DM-affected group, the maximum correlation was 0.83, corresponding to  $k = 0.25$ . The GT correlation performance of the LST was not significantly different from subjective WM scores (Steiger  $Z = 0.8$ ,  $P < .4$  for raw GT and  $Z = 1.4$ ,  $P < .15$  for the log-transformed data).

### **LST Versus Subjective WM Lesion Scores**

Correlation values ranged from 0.59–0.65 for the threshold values considered. Maximum correlation was 0.74, which was observed when  $k = 0.15$  in the full sample (On-line Fig 2). For the non-DM group, maximum correlation was 0.76, which was observed at the same threshold of  $k = 0.15$ . For the DM-affected group, maximum correlation was 0.74, corresponding to a  $k$ -threshold of 0.2. The threshold value of 0.25 provided correlations of 0.73, 0.74, and 0.74 for the full sample, the non-DM group, and the DM-affected group, respectively. Correlation values were similar with the use of log-transformed values.

### **GT Manual Segmentation**

Paired Spearman correlation between manual segmentation raters, the final consensus GT volume, and the LST were all very high ( $\rho = 0.91$  between first and second rater,  $\rho = 0.96$  between first rater and GT,  $\rho = 0.98$  between second rater and GT,  $\rho = 0.92$  between first rater and LST,  $\rho = 0.8$  between second rater and LST, and  $\rho = 0.87$  between GT and LST), with  $P < .001$  for all comparisons. Although the inter-rater correlations for manual segmentation were high, mean  $\pm$  SD (median) of lesion volumes reported in units of milliliters were more widely spaced between raters: GT and LST with  $2.43 \pm 3.97$  (0.86) for rater 1,  $3.65 \pm 5.69$  (1.2) for rater 2,  $4.47 \pm 6.48$  (1.83) for GT, and  $2.45 \pm 4.59$  (0.38) for the LST, which suggests high inter-rater variability. The GT mean  $\pm$  SD TLV for the full sample was  $4.47 \pm 6.48$ . The distribution of WM TLV was heavily skewed toward values  $< 1$  mL (On-line Fig 3), with a minor secondary peak at 10 mL. The mean  $\pm$  SD TLV for the DM-affected group was  $4.42 \pm 4.62$ . Mean  $\pm$  SD TLV for the non-DM group was  $4.52 \pm 7.13$ . There was no statistically significant difference in TLV between groups. On-line Fig 4 is a plot of GT TLV versus LST TLV at a  $k$ -threshold of 0.25, demonstrating a strong linear relationship ( $R^2 = 0.76$ ).

On-line Fig 5 is a plot of GT TLV versus average WM scores demonstrating a nonlinear relationship for the subjective scale. To perform nonlinear fitting of these data, the WM scores were remapped from 0–9 to 1–10, and 2 data points with zero GT TLV were excluded. Logarithmic, polynomial, and power law relationships all provided better fits than a linear fit. The highest  $R^2$  (0.72) was provided by a logarithmic fit. Plotting WM scores versus  $\log(\text{GT TLV})$  demonstrated a strong linear relationship ( $R^2 = 0.73$ ).

## DISCUSSION

The LST was originally developed and evaluated for multiple sclerosis. Here, we validate its use for TLV measurement in subjects with DM, relative to subjective rating scales. The pathophysiologic mechanisms leading to visible MR imaging WM changes in DM are very different from those in multiple sclerosis. In multiple sclerosis, the prototypic hallmark is focal demyelination with varying degrees of gliosis and inflammation.<sup>16</sup> The MR imaging FLAIR appearance is typically that of focal well-demarcated round or ovoid lesions. In contrast, WM lesions in the elderly, or leukoaraiosis, tend to be more diffuse, with pathophysiology related to endothelial dysfunction and development of small-vessel ischemia.<sup>1,17–19</sup> In this regard, diabetic populations provide an important validation of the LST methodology that can potentially be extended to other populations in which WM lesion burden relates to microvascular disease. Additionally, we examined a relatively large cohort of non-DM siblings, providing a validation in a normal elderly population.

### **LST Versus Subjective WM Lesion Scores**

We demonstrate the LST to be comparable to subjective WM scores for determining severity of WM lesion load in a population with DM. A high degree of correlation was observed between TLV computed by use of the LST and GT manual segmentation. LST achieved a maximum correlation of 0.87, corresponding to a  $k$ -threshold of 0.25, and appeared robust in its segmentation performance, within a range of  $k$ -thresholds from 0.2–0.4, all demonstrating similar correlations. In comparison, the subjective WM scoring demonstrated slightly weaker correlation with GT, achieving a 0.84 correlation. This improved slightly to 0.85 by use of the log of the GT TLV. Additionally, the subjective WM scores demonstrated a nonlinear relationship to GT TLV. This is not surprising because the amount of visible WM disease increases substantially over the range of scores. That is, near total involvement of the brain WM for a grade of 9 is much greater in volume than 10 times the few lesions identified for a grade of 1. The use of a logarithmic transformation of the GT TLV provided a clear linear relationship to the subjective WM lesion scores. This finding has important implications for studies that use the subjective WM lesion rating scale. Studies that use the subjective WM lesion rating scale with standard statistical regression models violate assumptions of linearity and potentially affect the validity or significance of the results. The assumptions required for use of parametric testing (eg, Pearson correlation analysis) in this evaluation were fulfilled through log transform of the data. Alternatively, nonparametric testing can be used when these assumptions are not met. Repeating these analyses by use of the Spearman rank

correlation test and Kendall  $\tau$  again demonstrated higher values for the LST than subjective WM scores, but the differences did not achieve significance. The Pearson correlation, however, provides a more complete assessment of the associations between variables when the underlying assumptions are attained.

The  $k$ -threshold corresponding to the maximum correlation between subjective scoring and LST was lower than that for LST and GT (0.15 versus 0.25). The lower  $k$  value in the LST corresponds to a more relaxed threshold for detection of WM lesions. This suggests that subjective ratings overestimate the true degree of WM disease. The degree of reader bias toward overestimation may be greater at the lower disease burden range, which was typical of our sample.

### **LST Versus GT**

LST achieved a maximum  $R^2$  of 0.69 at a  $k$ -threshold of 0.25 in the sample with DM. In contrast, the LST achieved a maximum  $R^2$  of 0.94 and optimum  $k$ -threshold of 0.3 in the recent evaluation of multiple sclerosis.<sup>9</sup> The performance difference between DM and multiple sclerosis probably is an effect of disease severity. In the multiple sclerosis evaluation, there was greater disease burden, with TLV extending to >50 mL, compared with <35 mL for our DM population. More importantly, the performance in the multiple sclerosis population improved with increasing lesion volume, ranging from a mean Dice coefficient of 0.67 for lesion volumes <5 mL to 0.85 for lesions volume >15 mL. The multiple sclerosis evaluation did not appear to have a significant number of subjects with TLV <1 mL (if any), whereas for our population, most subjects had TLV <1 mL. Thus, the difference in performance for our group probably reflects disease severity, with the LST performing less optimally at low disease burdens, rather than a difference in lesion detectability between populations.

### **Automated Segmentation in Diabetes**

Although automated WM lesion detection is an area of active investigation, there have been very few studies validating tools in a diabetic population. Jongen et al<sup>20</sup> described a  $k$ -nearest neighboring clustering algorithm used in a study of subjects with diabetes. de Bresser et al<sup>21</sup> used the same algorithm in a separate study of subjects with diabetes and white matter lesion load. Tiehuis et al<sup>22</sup> also used the same algorithm in a study of cognitive function, vascular disease and diabetes, and, in another study, showed that it performs favorably compared with subjective rating scales with reference to cognitive assessments.<sup>23</sup> For all of these studies, performance of the described algorithm was previously evaluated by using a leave-on-out cross-validation procedure, achieving a similarity index of 0.8.<sup>24</sup> This validation, however, was performed only on 10 elderly subjects with a history of vascular disease and not specifically on patients with diabetes. A recently described method with the use of support vector machines was evaluated on a subset of 45 subjects from a larger study on the treatment of diabetes.<sup>25</sup> A single rater was used as the reference standard, with 10 subjects used for training and the remaining 35 for testing. This method demonstrated a high sensitivity (>0.9) and a specificity of ~0.85. Interestingly, this study had a second manual rater but only used the first rater as the reference

standard, possibly because of their reported large inter-rater variability. In comparison to these studies, our study provides a more direct evaluation of lesion segmentation in diabetes, including a large sample size, and a more rigorous approach to ground-truth determination.

### **WM Disease and Diabetes**

The LST performance was very similar between DM-affected and unaffected individuals, achieving similar maximum correlations and optimum  $k$ -thresholds. There was no significant difference in degree of WM lesion load between affected and unaffected groups, by use of any of the metrics (WM scores, LST, or GT). Whereas there is a convincing relationship between DM and lacunar infarcts and brain atrophy, the association with WM hyperintensities on conventional MR imaging is less clear.<sup>26</sup> There has been recent evidence suggesting that DM is an independent risk factor for deep WM lesions in the elderly.<sup>27</sup> Additionally, voxel-wise analyses of diffusion tensor imaging and fractional anisotropy have demonstrated early changes in white matter microstructural properties that were associated with diabetes duration.<sup>28</sup> Our sample may not have been large enough to detect a between-group difference. Alternatively, the effects of aging may be a greater contributor to the presence of visible WM disease than DM. It should be noted that our DM population had very few subjects with WM scores  $>5$ , and none were  $>7$ . We drew a random sample from the Diabetes Heart Study, with WM disease burdens probably reflecting the distribution of WM disease in the general DM population. Conclusions about diabetes and WM disease should not be made on the basis of this study because we did not control for a variety of confounding effects, including disease duration, co-morbidities, and medications.

### **Limitations**

No subject had WM scores  $>7$  or TLV  $>35$  mL. This limits evaluation at the extreme end of disease burden. Also, our population was skewed toward the lower end of disease burdens, with most having TLV  $<1$  mL. Although this is a limitation in terms of disease distribution, it is also probably reflective of the true disease burden and incidence of WM disease in the general population. One critical limitation is generic to all studies of WM disease burden, which is that there is no accepted reference standard. Manual delineation by experienced readers comes closest to what most would accept as a reference standard. The laborious nature of manual WM segmentation makes it generally impractical to have multiple raters. Semi-automated methodologies to facilitate the procedure can introduce bias through predetermination of potential lesion borders. Even with multiple readers, some readers are typically more accurate (or meticulous). These limitations may be mitigated by machine learning approaches that can weight more accurate readers more heavily in the determination of GT. We attempted to address these potential biases in GT segmentation with the use of a multi-tiered manual segmentation approach with the final consensus manual segmentation performed by experienced neuroradiologists. This is a time-intensive and laborious approach but allows confidence in the quality of the GT determination.

### **CONCLUSIONS**

We validate the use of the LST for determination of TLV in a diabetic population and demonstrate that it performs as well compared with GT as a widely used subjective WM lesion rating scale. Additionally, we identify an optimal  $k$ -threshold of 0.25, with robust performance between 0.2–0.4 in this population. The LST is a readily available substitute for subjective WM lesion scoring in studies of diabetes and other populations prone to leukoariosis. Studies that use subjective WM lesion scores should be cognizant of violations in assumptions of linearity for standard statistical models with the use of this scale.

Disclosures: Joseph Maldjian—RELATED: Grant: NIH NS058700 and NS0075107,\* Comments: NIH R01 grant funding for data collection. Christopher Whitlow—RELATED: Grant: NIH\*; UNRELATED: Grants/Grants Pending: NIH.\* Clayton Vandergiff—RELATED: Grant: NIH.\* Jasmin Divers—RELATED: Grant: NINDS RO1 NS075107. Barry Freedman—RELATED: Grant: NIH\* (\*money paid to institution).

### **REFERENCES**

1. Brown WR, Moody DM, Thore CR, et al. **Apoptosis in leukoariosis.** *AJNR Am J Neuroradiol* 2000;21:79–82
2. Murray AD, Staff RT, Shenkin SD, et al. **Brain white matter hyperintensities: relative importance of vascular risk factors in nondemented elderly people.** *Radiology* 2005;237:251–57
3. DeBette S, Markus HS. **The clinical importance of white matter hyperintensities on brain magnetic resonance imaging: systematic review and meta-analysis.** *BMJ* 2010;341:c3666
4. Prins ND, van Dijk EJ, den Heijer T, et al. **Cerebral white matter lesions and the risk of dementia.** *Arch Neurol* 2004;61:1531–34
5. Kuller LH, Longstreth WT Jr, Arnold AM, et al. **White matter hyperintensity on cranial magnetic resonance imaging: a predictor of stroke.** *Stroke* 2004;35:1821–25
6. DeBette S, Beiser A, DeCarli C, et al. **Association of MRI markers of vascular brain injury with incident stroke, mild cognitive impairment, dementia, and mortality: the Framingham Offspring Study.** *Stroke* 2010;41:600–06
7. Manolio TA, Kronmal RA, Burke GL, et al. **Magnetic resonance abnormalities and cardiovascular disease in older adults: the Cardiovascular Health Study.** *Stroke* 1994;25:318–27
8. Yue NC, Arnold AM, Longstreth WT Jr, et al. **Sulcal, ventricular, and white matter changes at MR imaging in the aging brain: data from the Cardiovascular Health Study.** *Radiology* 1997;202:33–39
9. Schmidt P, Gaser C, Arsic M, et al. **An automated tool for detection of FLAIR-hyperintense white-matter lesions in multiple sclerosis.** *Neuroimage* 2012;59:3774–83
10. Bowden DW, Cox AJ, Freedman BI, et al. **Review of the Diabetes Heart Study (DHS) family of studies: a comprehensively examined sample for genetic and epidemiological studies of type 2 diabetes and its complications.** *Rev Diabet Stud* 2010;7:188–201
11. Divers J, Hugenschmidt C, Sink KM, et al. **Cerebral white matter hyperintensity in African Americans and European Americans with type 2 diabetes.** *J Stroke Cerebrovasc Dis* 2013;22:e46–52
12. Ashburner J, Friston KJ. **Voxel-based morphometry: the methods.** *NeuroImage* 2000;11:805–21
13. Rorden C, Karnath HO, Bonilha L. **Improving lesion-symptom mapping.** *J Cogn Neurosci* 2007;19:1081–88
14. Fisher RA. **Frequency distribution of the values of the correlation coefficient in samples from an indefinitely large population.** *Biometrika* 1915;10:507–21
15. Steiger JH. **Tests for comparing elements of a correlation matrix.** *Psychol Bull* 1980;87:245–51
16. Filippi M, Rocca MA, Barkhof F, et al. **Association between pathological and MRI findings in multiple sclerosis.** *Lancet Neurol* 2012;11:349–60
17. Brown WR, Moody DM, Challa VR, et al. **Apoptosis in leukoariosis lesions.** *J Neurol Sci* 2002;203–204:169–71

18. Grueter BE, Schulz UG. **Age-related cerebral white matter disease (leukoaraiosis): a review.** *Postgrad Med J* 2012;88:79–87
19. Knottnerus IL, Ten Cate H, Lodder J, et al. **Endothelial dysfunction in lacunar stroke: a systematic review.** *Cerebrovasc Dis* 2009; 27:519–26
20. Jongen C, van der Grond J, Kappelle LJ, et al. **Automated measurement of brain and white matter lesion volume in type 2 diabetes mellitus.** *Diabetologia* 2007;50:1509–16
21. de Bresser J, Tiehuis AM, van den Berg E, et al. **Progression of cerebral atrophy and white matter hyperintensities in patients with type 2 diabetes.** *Diabetes Care* 2010;33:1309–14
22. Tiehuis AM, Mali WP, van Raamt AF, et al. **Cognitive dysfunction and its clinical and radiological determinants in patients with symptomatic arterial disease and diabetes.** *J Neurol Sci* 2009; 283:170–74
23. Tiehuis AM, Vincken KL, Mali WP, et al. **Automated and visual scoring methods of cerebral white matter hyperintensities: relation with age and cognitive function.** *Cerebrovasc Dis* 2008;25:59–66
24. Anbeek P, Vincken KL, van Bochove GS, et al. **Probabilistic segmentation of brain tissue in MR imaging.** *Neuroimage* 2005;27:795–804
25. Lao Z, Shen D, Liu D, et al. **Computer-assisted segmentation of white matter lesions in 3D MR images using support vector machine.** *Acad Radiol* 2008;15:300–13
26. van Harten B, de Leeuw FE, Weinstein HC, et al. **Brain imaging in patients with diabetes: a systematic review.** *Diabetes Care* 2006;29:2539–48
27. van Harten B, Oosterman JM, Potter van Loon BJ, et al. **Brain lesions on MRI in elderly patients with type 2 diabetes mellitus.** *Eur Neurol* 2007;57:70–74
28. Hsu JL, Chen YL, Leu JG, et al. **Microstructural white matter abnormalities in type 2 diabetes mellitus: a diffusion tensor imaging study.** *Neuroimage* 2012;59:1098–105

# Potential Role of Preoperative Conventional MRI Including Diffusion Measurements in Assessing Epidermal Growth Factor Receptor Gene Amplification Status in Patients with Glioblastoma

R.J. Young, A. Gupta, A.D. Shah, J.J. Graber, A.D. Schweitzer, A. Prager, W. Shi, Z. Zhang, J. Huse, and A.M.P. Omuro

## ABSTRACT

**BACKGROUND AND PURPOSE:** Epidermal growth factor receptor amplification is a common molecular event in glioblastomas. The purpose of this study was to examine the potential usefulness of morphologic and diffusion MR imaging signs in the prediction of epidermal growth factor receptor gene amplification status in patients with glioblastoma.

**MATERIALS AND METHODS:** We analyzed pretreatment MR imaging scans from 147 consecutive patients with newly diagnosed glioblastoma and correlated MR imaging features with tumor epidermal growth factor receptor amplification status. The following morphologic tumor MR imaging features were qualitatively assessed: 1) border sharpness, 2) cystic/necrotic change, 3) hemorrhage, 4) T2-isointense signal, 5) restricted water diffusion, 6) nodular enhancement, 7) subependymal enhancement, and 8) multifocal discontinuous enhancement. A total of 142 patients had DWI available for quantitative analysis. ADC maps were calculated, and the  $ADC_{mean}$ ,  $ADC_{min}$ ,  $ADC_{max}$ ,  $ADC_{ROI}$ , and  $ADC_{ratio}$  were measured.

**RESULTS:** Epidermal growth factor receptor amplification was present in 60 patients (40.8%) and absent in 87 patients (59.2%). Restricted water diffusion correlated with epidermal growth factor receptor amplification ( $P = .04$ ), whereas the other 7 morphologic MR imaging signs did not ( $P > .12$ ). Quantitative DWI analysis found that all ADC measurements correlated with epidermal growth factor receptor amplification, with the highest correlations found with  $ADC_{ROI}$  ( $P = .0003$ ) and  $ADC_{mean}$  ( $P = .0007$ ).

**CONCLUSIONS:** Our results suggest a role for diffusion MR imaging in the determination of epidermal growth factor receptor amplification status in glioblastoma. Additional work is necessary to confirm these results and isolate new imaging biomarkers capable of noninvasively characterizing the molecular status of these tumors.

**ABBREVIATIONS:** EGFR = epidermal growth factor receptor; GRE = gradient recalled-echo

The prognosis of patients with glioblastoma, the most common primary brain tumor, remains dismal, with a median overall survival duration of 16–17 months.<sup>1</sup> Significant advances have recently been made toward a better understanding of the molecular mechanisms underlying gliomagenesis, however, with the ultimate goal of improving outcomes. Glioblastoma was the first human cancer sequenced by The Cancer Genome Atlas network effort,<sup>2</sup> resulting in a comprehensive characterization of the mutational spectrum of this type of tumor. On the basis of integrated

genomic analysis, molecular classifications have been proposed with the intent of providing more uniform tumor subclasses from a biologic standpoint.<sup>3,4</sup> Continued genomic sequencing efforts are expected to have expanding roles in the selection of patients for clinical trials and the development of more individualized and specific targeted therapies.

Activation of the epidermal growth factor receptor (EGFR) pathway is one of the most frequent molecular events in glioblastomas, with EGFR overexpression or amplification observed in up to 50% of patients.<sup>5–7</sup> The EGFR gene is located on chromosome 7p12 and is more commonly amplified in primary glioblastoma than in secondary glioblastoma.<sup>8</sup> Activation of EGFR pathways is associated with increased motility, adhesion, invasion, and proliferation of tumor cells, as well as inhibition of apoptosis and induction of angiogenesis.<sup>9,10</sup> High-level EGFR amplification is a hallmark of the so-called Classical glioblastoma subtype, found in up to 97% of patients in that subgroup.<sup>3</sup>

DWI has correlated with cellular attenuation and gained increasing use in the evaluation of brain tumors, including glioblastoma.<sup>11–20</sup> The role of DWI in the prediction of EGFR amplifica-

Received December 31, 2012; accepted after revision March 12, 2013.

From the Departments of Radiology (R.J.Y., A.D. Shah, A.D. Schweitzer, A.P.), Neurology (J.J.G., A.M.P.O.), Epidemiology and Biostatistics (W.S., Z.Z.), and Pathology (J.H.) and Brain Tumor Center (R.J.Y., A.M.P.O.), Memorial Sloan-Kettering Cancer Center, New York, New York; and Department of Radiology (A.G.), Weill Cornell Medical College/New York Presbyterian Hospital, New York, New York.

R.J.Y. and A.G. co-drafted the original manuscript together and contributed equally as co-first authors. Z.Z. and W.S. performed statistical analysis.

Please address correspondence to Robert J. Young, MD, Department of Radiology, Memorial Sloan-Kettering Cancer Center, 1275 York Ave, MRI-1156, New York, NY 10065; e-mail: youngr@mskcc.org

<http://dx.doi.org/10.3174/ajnr.A3604>

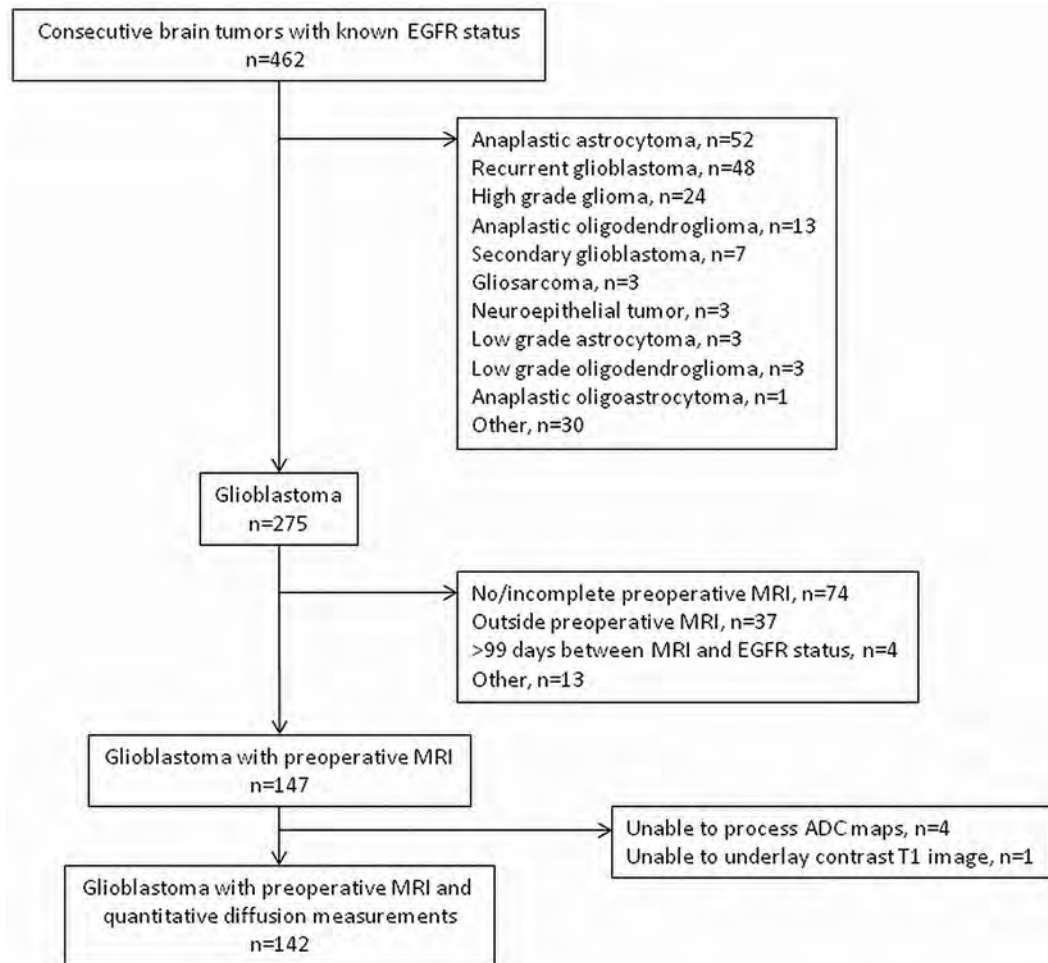


**FIG 1.** Main patient cohort.

tion status, however, has not been previously investigated. We hypothesized that the increased tumor cell proliferation and survival mediated by EGFR amplification will be measurable by DWI as restricted water diffusion. The purpose of this study was to investigate the potential role of morphologic and diffusion MR imaging features in the prediction of EGFR amplification status in patients newly diagnosed with glioblastoma.

## MATERIALS AND METHODS

### Standard Protocol Approvals, Registrations, and Patient Consents

This retrospective study was granted a Waiver of Informed Consent by the local institutional review board. The study was approved by the hospital privacy board and was compliant with Health Insurance Portability and Accountability Act regulations.

### Patients

We retrospectively searched a hospital data base for patients newly diagnosed with glioblastoma with known EGFR amplification status treated between September 1, 2008, and October 31, 2011. As summarized in Fig 1, we determined the main patient cohort of 147 consecutive patients after applying the following inclusion criteria: 1) known EGFR amplification status; 2) pathologic diagnosis of glioblastoma according to revised World Health Organization criteria after biopsy, subtotal resection, or gross to-

tal resection; and 3) preoperative conventional brain MR imaging. Charts were reviewed to determine overall survival.

### Conventional MR Imaging Parameters

MR imaging was performed with 1.5T (Signa Excite, HDx; GE Healthcare, Milwaukee, Wisconsin) and 3T magnets (Discovery 750; GE Healthcare). We acquired all images by using 5-mm section thickness and no intersection gap. The standard preoperative imaging protocol consisted of sagittal and axial T1-weighted images; axial T2-weighted images; axial gradient recalled-echo (GRE) or SWI; axial DWI with ADC maps; and contrast coronal, sagittal, and axial T1-weighted images. DWI was performed with single-shot echo-planar imaging by use of acquisitions at  $b$ -value = 0  $s/mm^2$  and  $b$ -value = 1000  $s/mm^2$ . Gadopentetate dimeglumine (Magnevist; Bayer HealthCare Pharmaceuticals, Wayne, New Jersey) was injected through a peripheral venous catheter (18–21 gauge) at doses standardized by patient body weight (0.2 mL/kg body weight, to a maximum of 20 mL). The same dose of contrast was administered for both 1.5T and 3T scans.

### Morphologic MR Imaging Signs

Two board-certified radiologists (one with 7 years of experience, and the other with 13 years of experience and holding a Certificate of Added Qualification in neuroradiology) independently analyzed the

MR imaging scans while blinded to the EGFR amplification status. The readers scored 8 different MR imaging signs and resolved disagreements by consensus. Each conventional MR imaging was scored in a binary fashion according to the presence or absence of the following morphologic signs: 1) border sharpness, 2) cystic/necrotic change, 3) hemorrhage, 4) T2-isointense signal, 5) restricted water diffusion, 6) nodular enhancement, 7) subependymal enhancement, and 8) multifocal discontinuous enhancement. Border sharpness was visually determined by inspection of the enhancing margins of the tumor on contrast T1-weighted images. We evaluated the presence of hemorrhage by inspecting SWI ( $n=74$ ); GRE ( $n=31$ ); or, if neither available, by inspecting the  $b$ -value = 0 DWI ( $n=42$ ). The hemorrhage-sensitive GRE and SWI sequences were being incorporated into our standard imaging protocols during the study period, with SWI acquired in all cases since early 2011. Restricted water diffusion was determined by assessment of hyperintense areas on  $b$ -value = 1000  $s/mm^2$  DWI that were confirmed as hypointense on ADC images, for exclusion of studies where hemorrhage, T2 shinethrough effects, or artifacts might mimic restricted water diffusion. To replicate the usual clinical practice, we qualitatively reviewed all studies at a standard 5-panel PACS station (Centricity Radiology, GE Healthcare).

### Quantitative DWI Analysis

The quantitative DWI analysis and ADC measurements were performed by a trained operator (with 6 months of experience) under the direct supervision of a board-certified radiologist with a Certificate of Added Qualification in neuroradiology (with 13 years of experience), who verified the ROIs in all patients. The quantitative analyses were performed while blinded to the patient EGFR amplification status and the recorded morphologic MR imaging signs (including visual assessments of restricted water diffusion). Each scan was transferred to an off-line commercially available workstation and processed by use of commercially available software (FuncTools 4.6 on Advantage Workstation; GE Healthcare) to calculate ADC images from the DWI. The contrast T1-weighted images were selected as the underlay for the ADC images, and the section containing the maximal contrast-enhancing portion of the tumor was chosen. An ROI was manually drawn around the entire contrast-enhancing tumor while deliberately excluding blood vessels and areas of cystic, necrotic, and hemorrhagic change that might affect ADC values. The ROI was then mapped to the corresponding ADC images, and measurements of  $ADC_{mean}$ ,  $ADC_{min}$ , and  $ADC_{max}$  from that ROI were recorded. In addition,  $\leq 4$  small circular ROIs ( $50$ – $75$   $mm^2$ ) were manually placed over solid areas of the enhancing tumor that also displayed restricted water diffusion to select the maximal ADC hypointensity, and the minimal value was recorded as  $ADC_{ROI}$ . This is a standard technique that has been described as highly reliable and reproducible for ROI measurements.<sup>21,22</sup> We also obtained  $ADC_{ratio}$ s by dividing  $ADC_{ROI}$  by  $ADC_{normal}$  placed in the normal contralateral brain. Quantitative DWI analyses were performed in 142 scans; 5 scans (all in patients without EGFR amplification) were discarded because of technical errors in measurement of ADC, though qualitative analyses were performed.

### EGFR Analysis

EGFR amplification status was determined by interphase/nuclear fluorescence in situ hybridization techniques on paraffin sections.

**Table 1: Characteristics of patients**

	Total
No. of patients	147
Median age, y (age range)	65.1 (13.8–83.4)
Sex (%)	
Female	66 (44.9)
Male	81 (55.1)
Extent of subsequent surgery (%)	
Biopsy	19 (12.9)
Subtotal resection	84 (57.1)
Gross total resection	44 (29.9)

**Table 2: Qualitative analysis of morphologic MR imaging signs ( $n=147$ )**

MR Imaging Sign	EGFR Status*		P Value
	Not Amplified ( $n=87$ )	Amplified ( $n=60$ )	
Sharp borders			.23
Absent	45 (52)	37 (62)	
Present	42 (48)	23 (38)	
Cystic and/or necrotic			.12
Absent	2 (2)	5 (8)	
Present	85 (98)	55 (92)	
T2 isointense			.38
Absent	74 (85)	54 (90)	
Present	13 (15)	6 (10)	
Diffusion restricted			.04
Absent	68 (79)	38 (63)	
Present	18 (21)	22 (37)	
Hemorrhage			.87
Absent	36 (41)	24 (40)	
Present	51 (59)	36 (60)	
Subependymal enhancement			.58
Absent	74 (85)	49 (82)	
Present	13 (15)	11 (18)	
Multifocal			.52
Absent	58 (67)	43 (72)	
Present	29 (33)	17 (28)	

\* Reported as  $n$  (%) with  $P$  values derived from the  $\chi^2$  test or the Fisher exact test.

Per tissue sample, a total of 200 cells were analyzed and the results reported as the highest level of EGFR amplification in chromosome copies per cell. EGFR amplification was defined as  $\geq 10$  copies per cell.

### Statistical Analysis

Univariate analysis by the  $\chi^2$  test or the Fisher exact test was performed to determine the relative usefulness of the morphologic MR imaging signs in the prediction of EGFR amplification status. The Wilcoxon rank sum test was performed to evaluate the quantitative ADC values. Significance was set to  $P < .05$ .

## RESULTS

Demographic and patient information for the 147 main cohort participants are summarized in Table 1. A total of 60 patients (40.8%) were determined to have high levels of EGFR amplification, whereas 87 (59.2%) did not. The median interval between the MR imaging scan and surgery was 4 days (standard deviation, 10 days).

### Morphologic MR Imaging Signs

The morphologic MR imaging results are summarized in Table 2. All patients in the cohort had preoperative morphologic MR imaging available for qualitative analysis. Restricted water diffusion

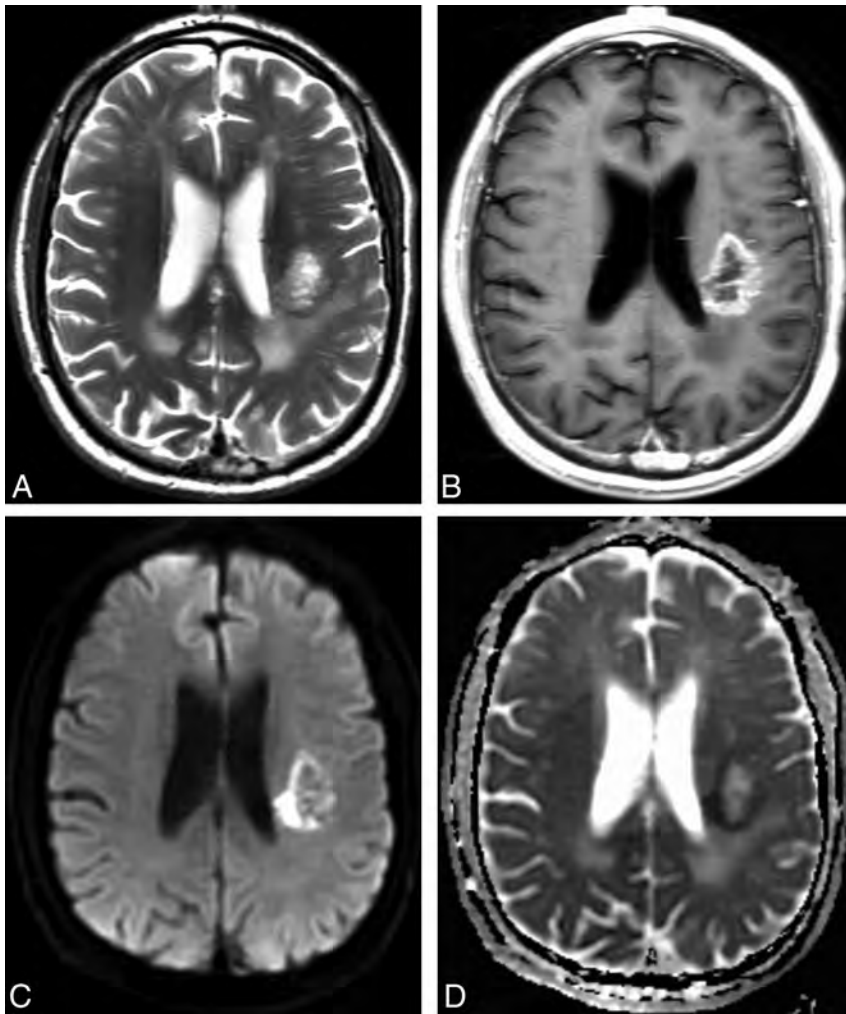


**FIG 2.** Representative example of restricted water diffusion in an EGFR-amplified tumor. Axial T2-weighted (A) and contrast T1-weighted (B) images show a heterogeneously enhancing glioblastoma in the left posterior corona radiata. DWI (C) shows hyperintense peripheral restricted water diffusion that is confirmed on the ADC image (D) with a hypointense signal, and corresponds to the enhancing fraction seen in (B).  $ADC_{mean}$  measurement of the enhancing fraction was  $0.13 \times 10^{-3} \text{ mm}^2/\text{s}$ . Fluorescence in situ hybridization analysis revealed high-level EGFR amplification with 98% of 200 analyzed cells showing  $> 20$  signals for EGFR.

occurred in 37% of patients with EGFR amplification and in 21% of patients without EGFR amplification ( $P = .04$ ). A representative case is shown in Fig 2. The related sensitivity (36.7%; 95% CI, 24.9%–50.2%) and specificity (79.1; 95% CI, 68.7%–86.8%), however, were moderate with area under the curve for the receiver operating characteristic curve = 0.579. The remaining 7 morphologic MR imaging signs were not significant ( $P > .12$ ).

#### Quantitative DWI Analysis

Lower ADC values were found in EGFR-amplified tumors with all metrics showing  $P < .01$ , as summarized in Table 3. The highest correlations were found for  $ADC_{ROI}$  ( $P = .0003$ ) and  $ADC_{mean}$  ( $P = .0007$ ). The predictive power was moderate, with the receiver operating characteristic analysis showing a maximal area under the curve for  $ADC_{ROI} = 0.680$ .

#### DISCUSSION

The use of MR imaging–based parameters for noninvasive tumor molecular characterization is an emerging field in neuroimaging.<sup>23–30</sup> By providing information about the molecular status of

tumors when tissue is not available for analysis, molecular characterization may have direct implications for management and potentially provide therapeutic value. Imaging parameters may also provide insights into the biologic behavior of tumors and information on hypoxia, cell attenuation, and angiogenesis, as related to different tumor molecular subtypes. In this study, we focused on EGFR amplification, one of the most common molecular alterations in glioblastomas and a hallmark of the classic glioblastoma subtype. Approximately 40% of our patients demonstrated EGFR amplification, which is in line with a previous study reporting EGFR amplification in up to 50% of patients with glioblastoma.<sup>31</sup> We found that restricted water diffusion correlated with EGFR amplification as assessed by quantitative analysis at a dedicated postprocessing workstation ( $P = .01$  to  $.0003$ ), as well as qualitative visual analysis at a clinical PACS reading station ( $P = .04$ ). These data suggest a potential role for diffusion analysis in the prediction of EGFR amplification status in glioblastoma. Aside from restricted water diffusion, we did not find other commonly reported imaging characteristics to be useful in predicting EGFR amplification.

The quantitative ADC values correlated more highly ( $P = .01$  to  $P = .0003$ ) than the qualitative visual inspection of DWI and ADC images ( $P = .04$ ). The ADC measurements confirmed that restricted water diffusion correlated with EGFR amplification. Selection of the

single maximal abnormality ( $ADC_{ROI}$ ) after placement of multiple small ROIs outperformed a normalized ratio ( $ADC_{ratio}$ ) and segmentation of the enhancing tumor ( $ADC_{mean}$ ,  $ADC_{min}$ ,  $ADC_{max}$ ). We did not detect any significant correlations between the morphologic MR imaging tumor characteristics and EGFR amplification. Previous studies,<sup>23,32</sup> which have used sophisticated texture analysis methods at dedicated postprocessing workstations, have been able to correlate some morphologic MR imaging metrics. For example, Aghi et al<sup>32</sup> concluded that the ratio of T2-bright volume to T1-enhancing volume and T1 and T2 border sharpness coefficients were useful predictors for EGFR amplification status. In a similar fashion, Diehn et al<sup>23</sup> reported on the usefulness of a ratio of contrast-enhancing tumor to necrotic tumor in the prediction of EGFR overexpression. The purpose of our morphologic MR imaging analysis was to isolate imaging features that are commonly described in radiology reports for usual clinical practice after visual analysis at a PACS workstation without any additional postprocessing steps.

**Table 3: Quantitative analysis of ADC correlation with EGFR (n=142)**

	EGFR Status*		P Value	AUC
	Not Amplified (n=82)	Amplified (n=60)		
ADC <sub>mean</sub>	1.27 (0.90–1.97)	1.15 (0.11–1.70)	.0007	0.667
ADC <sub>min</sub>	0.90 (0.16–8.38)	0.83 (0.51–1.23)	.01	0.624
ADC <sub>max</sub>	2.11 (1.22–3.28)	1.77 (0.86–3.01)	.005	0.639
ADC <sub>ROI</sub>	1.06 (0.56–1.59)	0.93 (0.67–1.30)	.0003	0.680
ADC <sub>ratio</sub>	1.37 (0.13–2.33)	1.22 (0.77–1.95)	.003	0.645

Note:—AUC indicates area under the curve.

\* Reported as median (range)  $\times 10^{-3}$  mm<sup>2</sup>/s with P values by the Wilcoxon rank sum test.

Increased EGFR amplification has been associated with increasing levels of tumor proliferation, angiogenesis, and invasiveness.<sup>5,33</sup> The mechanisms for restricted water diffusion are complex, with increased cellularity such as in lymphoma suggested to be the most important factor.<sup>34</sup> Restricted water diffusion has also been well correlated with ischemia and cytotoxic edema; it is unclear if restricted water diffusion occurs because of increases in tumor cellularity or ischemia, or both.<sup>15,35,36</sup> Many tumors including glioblastoma overexpress hypoxia-inducible transcription factor-2 alpha, a powerful driver of oncogenesis that helps modulate the downstream EGFR-signaling pathway.<sup>36-38</sup> The relationship between EGFR and tumor ischemia is further complicated by studies suggesting a protective effect of EGFR inhibition on hypoxic tumor cells that has limited the efficacy of the EGFR inhibitors in clinical trials.<sup>39,40</sup> The patients in the current study all had untreated glioblastoma, which precludes treatment-related confounders such as radiation, antiangiogenic therapy, and EGFR inhibitor therapy on diffusion characteristics. Although this area requires further study, we suggest that tumor cellularity and ischemia probably both play a role in causing increased restricted water diffusion with EGFR amplification.

Several potential applications are available for predicting EGFR amplification status in patients with glioblastoma. The first relates to work from The Cancer Genome Atlas Research Network,<sup>3</sup> which proposes the molecular classification of glioblastomas into Classical, Mesenchymal, Proneural, and Neural subtypes on the basis of gene expression aberrations of EGFR, NF1, and PDGFRA/IDH1. Of these, EGFR amplification was observed in 97% of the Classical subtype and less commonly in the other subtypes,<sup>3</sup> indicating that the noninvasive imaging profiling of EGFR amplification may have a role in predicting the Classical vs other subtypes. Designating the Classical subtype is important for clinical decision-making, as this information may help predict patient prognosis and patterns of tumor progression, particularly when combined with imaging-based biomarkers.<sup>4,28</sup> Second, despite the promising but tempered efficacy of early-generation EGFR tyrosine kinase inhibitors such as erlotinib, gefitinib, and vandetanib,<sup>41-45</sup> it is possible that subsequent EGFR inhibitors will provide durable improvements in outcome. Recent comparisons to non-small-cell lung cancer have shown that efficacy correlates with higher EGFR receptor binding-site occupancies,<sup>25,46-49</sup> suggesting avenues for development of future EGFR inhibitors to use in selected glioblastomas. Therefore, the importance of EGFR amplification status may grow with the development of newer treatments. Third, studies have suggested that serial imaging with ADC analysis and quantification may be useful

to document response to treatment,<sup>50,51</sup> though this has not been performed with EGFR inhibitor studies. Following EGFR amplification status during treatment with a targeted chemotherapeutic agent may provide insight into the efficacy of the treatment and subsequent treatment-induced changes in the tumor.

One potential limitation of our investigation is its retrospective nature. By

examining preoperative conventional MR imaging scans in treatment-naïve primary glioblastomas, however, we present a homogeneous patient population from which correlations with EGFR amplification status are made. A second potential limitation was the ROI technique used to quantify the presence or absence of restricted water diffusion. Because our study was retrospective in that the exact sites of pathologic analysis were not recorded, it is possible that the measured levels of EGFR amplification did not directly reflect the maximal diffusion abnormalities measurements. Further study with locus-specific radiologic-histopathologic correlation would help clarify this relationship. The intratumoral cell-to-cell variability of EGFR expression has also been described as relatively low,<sup>31</sup> suggesting that the observed correlations accurately reflect the relationship between EGFR expression and restricted water diffusion. Third, there was no consensus definition of EGFR amplification.<sup>31,52</sup> We defined EGFR amplification as  $\geq 10$  copies per cell after discussion with experienced neuro-oncologists, neuropathologists, neurosurgeons, and neuroradiologists at a National Cancer Institute–designated Comprehensive Cancer Center. This does not take into account the number of cells containing the gene amplification and may not be representative of the entire tumor; however, this relatively conservative interpretation is consistent with standard clinical and research practice at our institution and around the country.

## CONCLUSIONS

Our study suggests possible usefulness for DWI to predict EGFR amplification status in patients with glioblastoma. EGFR status information may be useful in the prediction of Classical subtype glioblastomas. Imaging has potential value for patients in whom multiple genetic and molecular analyses may be difficult or infeasible, such as when tissue is not available for study. Further research with locus-specific histopathologic correlations and follow-up after patient treatment may help us to fully explore the prognostic value and underlying physiologic basis of restricted water diffusion in EGFR amplification.

## ACKNOWLEDGMENT

We thank Ms. Judith A. Lampron for her expert editorial advice.

Disclosures: Robert Young—UNRELATED: Consultancy; ICON Medical Imaging, Comments: Blinded independent reviewer. Jerome Graber—UNRELATED: Payment for Lectures (including service on Speaker Bureaus); Speaker bureau for Biogen Idec; Other: Participation in market research studies for Olson Online Systems. Alisa Prager—UNRELATED: Grants/Grants Pending; MSKCC, NCI, Medical Student Summer Research Fellowship Program.\* Antonio Omuro—UNRELATED: Consultancy; Roche, Novocure. \*Money paid to institution.

## REFERENCES

1. Stupp R, Mason WP, van den Bent MJ, et al. Radiotherapy plus concomitant and adjuvant temozolomide for glioblastoma. *N Engl J Med* 2005;352:987–96
2. Hu LS, Eschbacher JM, Heiserman JE, et al. Reevaluating the imaging definition of tumor progression: perfusion MRI quantifies recurrent glioblastoma tumor fraction, pseudoprogression, and radiation necrosis to predict survival. *Neuro Oncol* 2012;14:919–30
3. Verhaak RG, Hoadley KA, Purdom E, et al. Integrated genomic analysis identifies clinically relevant subtypes of glioblastoma characterized by abnormalities in PDGFRA, IDH1, EGFR, and NF1. *Cancer Cell* 2010;17:98–110
4. Phillips HS, Kharbanda S, Chen R, et al. Molecular subclasses of high-grade glioma predict prognosis, delineate a pattern of disease progression, and resemble stages in neurogenesis. *Cancer Cell* 2006;9:157–73
5. Lal A, Glazer CA, Martinson HM, et al. Mutant epidermal growth factor receptor up-regulates molecular effectors of tumor invasion. *Cancer Res* 2002;62:3335–39
6. Mazzoleni S, Politi LS, Pala M, et al. Epidermal growth factor receptor expression identifies functionally and molecularly distinct tumor-initiating cells in human glioblastoma multiforme and is required for gliomagenesis. *Cancer Res* 2010;70:7500–13
7. Schlegel J, Merdes A, Stumm G, et al. Amplification of the epidermal-growth-factor-receptor gene correlates with different growth behaviour in human glioblastoma. *Int J Cancer* 1994;56:72–77
8. Ohgaki H, Kleihues P. Genetic pathways to primary and secondary glioblastoma. *Am J Pathol* 2007;170:1445–53
9. Halatsch ME, Schmidt U, Behnke-Mursch J, et al. Epidermal growth factor receptor inhibition for the treatment of glioblastoma multiforme and other malignant brain tumours. *Cancer Treat Rev* 2006;32:74–89
10. Ramis G, Thomas-Moya E, Fernandez de Mattos S, et al. EGFR inhibition in glioma cells modulates Rho signaling to inhibit cell motility and invasion and cooperates with temozolomide to reduce cell growth. *PLoS One* 2012;7:e38770
11. Barajas RF Jr, Rubenstein JL, Chang JS, et al. Diffusion-weighted MR imaging derived apparent diffusion coefficient is predictive of clinical outcome in primary central nervous system lymphoma. *AJNR Am J Neuroradiol* 2010;31:60–66
12. Bulakbasi N, Guvenc I, Onguru O, et al. The added value of the apparent diffusion coefficient calculation to magnetic resonance imaging in the differentiation and grading of malignant brain tumors. *J Comp Assist Tomogr* 2004;28:735–46
13. Calli C, Kitis O, Yunten N, et al. Perfusion and diffusion MR imaging in enhancing malignant cerebral tumors. *Eur J Radiol* 2006;58:394–403
14. Castillo M, Smith JK, Kwock L, et al. Apparent diffusion coefficients in the evaluation of high-grade cerebral gliomas. *AJNR Am J Neuroradiol* 2001;22:60–64
15. Gupta A, Young RJ, Karimi S, et al. Isolated diffusion restriction precedes the development of enhancing tumor in a subset of patients with glioblastoma. *AJNR Am J Neuroradiol* 2011;32:1301–06
16. Mills SJ, Soh C, Rose CJ, et al. Candidate biomarkers of extravascular extracellular space: a direct comparison of apparent diffusion coefficient and dynamic contrast-enhanced MR imaging-derived measurement of the volume of the extravascular extracellular space in glioblastoma multiforme. *AJNR Am J Neuroradiol* 2010;31:549–53
17. Young RJ, Gupta A, Shah AD, et al. Potential utility of conventional MRI signs in diagnosing pseudoprogression in glioblastoma. *Neurology* 2011;76:1918–24
18. Barajas RF Jr, Phillips JJ, Parvataneni R, et al. Regional variation in histopathologic features of tumor specimens from treatment-naive glioblastoma correlates with anatomic and physiologic MR imaging. *Neuro Oncol* 2012;14:942–54
19. Pope WB, Kim HJ, Huo J, et al. Recurrent glioblastoma multiforme: ADC histogram analysis predicts response to bevacizumab treatment. *Radiology* 2009;252:182–89
20. Lee EJ, terBrugge K, Mikulis D, et al. Diagnostic value of peritumoral minimum apparent diffusion coefficient for differentiation of glioblastoma multiforme from solitary metastatic lesions. *AJR Am J Roentgenol* 2011;196:71–76
21. Wetzel SG, Cha S, Johnson G, et al. Relative cerebral blood volume measurements in intracranial mass lesions: interobserver and intraobserver reproducibility study. *Radiology* 2002;224:797–803
22. Law M, Young R, Babb J, et al. Histogram analysis versus region of interest analysis of dynamic susceptibility contrast perfusion MR imaging data in the grading of cerebral gliomas. *AJNR Am J Neuroradiol* 2007;28:761–66
23. Diehn M, Nardini C, Wang DS, et al. Identification of noninvasive imaging surrogates for brain tumor gene-expression modules. *Proc Natl Acad Sci U S A* 2008;105:5213–18
24. Carrillo JA, Lai A, Nghiemphu PL, et al. Relationship between tumor enhancement, edema, IDH1 mutational status, MGMT promoter methylation, and survival in glioblastoma. *AJNR Am J Neuroradiol* 2012;33:1349–55
25. Bruzzone MG, Eoli M, Cuccarini V, et al. Genetic signature of adult gliomas and correlation with MRI features. *Expert Rev Molecular Diagn* 2009;9:709–20
26. Tykocinski ES, Grant RA, Kapoor GS, et al. Use of magnetic perfusion-weighted imaging to determine epidermal growth factor receptor variant III expression in glioblastoma. *Neuro Oncol* 2012;14:613–23
27. Gupta A, Omuro AM, Shah AD, et al. Continuing the search for MR imaging biomarkers for MGMT promoter methylation status: conventional and perfusion MRI revisited. *Neuroradiology* 2012;54:641–43
28. Jain R, Poisson L, Narang J, et al. Genomic mapping and survival prediction in glioblastoma: molecular subclassification strengthened by hemodynamic imaging biomarkers. *Radiology* 2013;267:212–20
29. Pope WB, Mirsadraei L, Lai A, et al. Differential gene expression in glioblastoma defined by ADC histogram analysis: relationship to extracellular matrix molecules and survival. *AJNR Am J Neuroradiol* 2012;33:1059–64
30. Jain R, Poisson L, Narang J, et al. Correlation of perfusion parameters with genes related to angiogenesis regulation in glioblastoma: a feasibility study. *AJNR Am J Neuroradiol* 2012;33:1343–48
31. Choi BD, Archer GE, Mitchell DA, et al. EGFRvIII-targeted vaccination therapy of malignant glioma. *Brain Pathol* 2009;19:713–23
32. Aghi M, Gaviani P, Henson JW, et al. Magnetic resonance imaging characteristics predict epidermal growth factor receptor amplification status in glioblastoma. *Clin Cancer Res* 2005;11:8600–05
33. Goldman CK, Kim J, Wong WL, et al. Epidermal growth factor stimulates vascular endothelial growth factor production by human malignant glioma cells: a model of glioblastoma multiforme pathophysiology. *Mol Biol Cell* 1993;4:121–33
34. Kono K, Inoue Y, Nakayama K, et al. The role of diffusion-weighted imaging in patients with brain tumors. *AJNR Am J Neuroradiol* 2001;22:1081–88
35. Schaefer PW, Grant PE, Gonzalez RG. Diffusion-weighted MR imaging of the brain. *Radiology* 2000;217:331–45
36. Rieger J, Bähr O, Müller K, et al. Bevacizumab-induced diffusion-restricted lesions in malignant glioma patients. *J Neurooncol* 2010;99:49–56
37. Wang X, Schneider A. HIF-2alpha-mediated activation of the epidermal growth factor receptor potentiates head and neck cancer cell migration in response to hypoxia. *Carcinogenesis* 2010;31:1202–10
38. Franovic A, Holterman CE, Payette J, et al. Human cancers converge at the HIF-2alpha oncogenic axis. *Proc Natl Acad Sci U S A* 2009;106:21306–11
39. Ronellenfitch MW, Brucker DP, Burger MC, et al. Antagonism of the mammalian target of rapamycin selectively mediates metabolic effects of epidermal growth factor receptor inhibition and protects human malignant glioma cells from hypoxia-induced cell death. *Brain* 2009;132:1509–22
40. Steinbach JP, Klumpp A, Wolburg H, et al. Inhibition of epider-

- mal growth factor receptor signaling protects human malignant glioma cells from hypoxia-induced cell death. *Cancer Res* 2004;64:1575–78
41. Kesavabhotla K, Schlaff CD, Shin B, et al. **Phase I/II study of oral erlotinib for treatment of relapsed/refractory glioblastoma multiforme and anaplastic astrocytoma.** *J Exp Ther Oncol* 2012;10:71–81
  42. Prados MD, Chang SM, Butowski N, et al. **Phase II study of erlotinib plus temozolomide during and after radiation therapy in patients with newly diagnosed glioblastoma multiforme or gliosarcoma.** *J Clin Oncol* 2009;27:579–84
  43. Brandes AA, Franceschi E, Tosoni A, et al. **Epidermal growth factor receptor inhibitors in neuro-oncology: hopes and disappointments.** *Clin Cancer Res* 2008;14:957–60
  44. Wachsberger PR, Lawrence YR, Liu Y, et al. **Epidermal growth factor receptor expression modulates antitumor efficacy of vandetanib or cediranib combined with radiotherapy in human glioblastoma xenografts.** *Int J Radiat Oncol Biol Phys* 2012;82:483–91
  45. Kreisl TN, McNeill KA, Sul J, et al. **A phase I/II trial of vandetanib for patients with recurrent malignant glioma.** *Neuro Oncol* 2012;14:1519–26
  46. Barkovich KJ, Hariono S, Garske AL, et al. **Kinetics of inhibitor cy-**
  - cling underlie therapeutic disparities between EGFR-driven lung and brain cancers.** *Cancer Discov* 2012;2:450–57
  47. Mellinghoff IK, Wang MY, Vivanco I, et al. **Molecular determinants of the response of glioblastomas to EGFR kinase inhibitors.** *N Engl J Med* 2005;353:2012–24
  48. Haas-Kogan DA, Prados MD, Tihan T, et al. **Epidermal growth factor receptor, protein kinase B/Akt, and glioma response to erlotinib.** *J Natl Cancer Inst* 2005;97:880–87
  49. Park JH, Lemmon MA. **Occupy EGFR.** *Cancer Discov* 2012;2:398–400
  50. Hamstra DA, Galban CJ, Meyer CR, et al. **Functional diffusion map as an early imaging biomarker for high-grade glioma: correlation with conventional radiologic response and overall survival.** *J Clin Oncol* 2008;26:3387–94
  51. Moffat BA, Chenevert TL, Lawrence TS, et al. **Functional diffusion map: A noninvasive MRI biomarker for early stratification of clinical brain tumor response.** *Proc Natl Acad Sci U S A* 2005;102:5524–29
  52. El Naqa I, Grigsby P, Apte A, et al. **Exploring feature-based approaches in PET images for predicting cancer treatment outcomes.** *Pattern Recognit* 2009;42:1162–71

# Prediction of Pseudoprogression in Patients with Glioblastomas Using the Initial and Final Area Under the Curves Ratio Derived from Dynamic Contrast-Enhanced T1-Weighted Perfusion MR Imaging

C.H. Suh, H.S. Kim, Y.J. Choi, N. Kim, and S.J. Kim



## ABSTRACT

**BACKGROUND AND PURPOSE:** Dynamic contrast-enhanced T1-weighted perfusion MR imaging is much less susceptible to artifacts, and its high spatial resolution allows accurate characterization of the vascular microenvironment of the lesion. The purpose of this study was to test the predictive value of the initial and final area under the time signal-intensity curves ratio derived from dynamic contrast-enhanced perfusion MR imaging to differentiate pseudoprogression from early tumor progression in patients with glioblastomas.

**MATERIALS AND METHODS:** Seventy-nine consecutive patients who showed new or enlarged, contrast-enhancing lesions within the radiation field after concurrent chemoradiotherapy were assessed by use of conventional and dynamic contrast-enhanced perfusion MR imaging. The bimodal histogram parameters of the area under the time signal-intensity curves ratio, which included the mean area under the time signal-intensity curves ratio at a higher curve ( $mAUCR_H$ ), 3 cumulative histogram parameters ( $AUCR_{50}$ ,  $AUCR_{75}$ , and  $AUCR_{90}$ ), and the area under the time signal-intensity curves ratio at mode ( $AUCR_{mode}$ ), were calculated and correlated with the final pathologic or clinical diagnosis. The best predictor for differentiation of pseudoprogression from early tumor progression was determined by receiver operating characteristic curve analyses.

**RESULTS:** Seventy-nine study patients were subsequently classified as having pseudoprogression ( $n=37$ , 46.8%) or early tumor progression ( $n=42$ , 53.2%). There were statistically significant differences of  $mAUCR_H$ ,  $AUCR_{50}$ ,  $AUCR_{75}$ ,  $AUCR_{90}$ , and  $AUCR_{mode}$  between the 2 groups ( $P < .0001$ , each). Receiver operating characteristic curve analyses showed the  $mAUCR_H$  to be the best single predictor of pseudoprogression, with a sensitivity of 90.1% and a specificity of 82.9%.  $AUCR_{50}$  was found to be the most specific predictor of pseudoprogression, with a sensitivity of 87.2% and a specificity of 83.1%.

**CONCLUSIONS:** A bimodal histogram analysis of the area under the time signal-intensity curves ratio derived from dynamic contrast-enhanced perfusion MR imaging can be a potential, noninvasive imaging biomarker for monitoring early treatment response in patients with glioblastomas.

**ABBREVIATIONS:** AUCR = area under the time signal intensity curves ratio; CCRT = concurrent chemoradiotherapy; DCE = dynamic contrast-enhanced; EES = extravascular extracellular space; ETP = early tumor progression; FAUC = final area under the time signal-intensity curve; IAUC = initial area under the time signal-intensity curve; Ve = volume fraction of extracellular extravascular space

Differentiation of treatment-related change including pseudoprogression from early tumor progression (ETP) is a common yet diagnostic challenge in neuro-oncology practice,

because increased leakage of contrast agent through blood-brain barrier disruption can be produced by both tumor neovessels and treatment-related injury.<sup>1,2</sup> Dynamic susceptibility-weighted contrast-enhanced perfusion MR imaging has made it possible to distinguish tumor recurrence from radiation necrosis by use of relative cerebral blood volume maps.<sup>3</sup> Recently, Hu et al<sup>4</sup> proposed that multiparametric MR imaging analysis may be a promising approach to identify the distribution of radiation necrosis. The results of <sup>18</sup>F-FDG-PET in the differentiation of recurrent glioblastomas from radiation necrosis have been mixed.<sup>5</sup>

Compared with DSC T2\*-weighted perfusion MR imaging, dynamic contrast-enhanced (DCE) T1-weighted perfusion MR imaging is much less susceptible to artifacts, and its high spatial

Received January 22, 2013; accepted after revision March 24.

From the Department of Radiology, Research Institute of Radiology, Asan Medical Center, University of Ulsan College of Medicine, Seoul, South Korea.

This study was supported by the Basic Science Research Program through the National Research Foundation of Korea, funded by the Ministry of Education, Science and Technology (grant 2009-0076988).

Please address correspondence to Ho Sung Kim, MD; Department of Radiology, Research Institute of Radiology, Asan Medical Center, University of Ulsan, College of Medicine, 86, Asanbyeongwon-gil, Songpa-gu, Seoul, 138-736, South Korea; e-mail: radhskim@gmail.com

Indicates open access to non-subscribers at www.ajnr.org

<http://dx.doi.org/10.3174/ajnr.A3634>

resolution allows accurate characterization of the vascular microenvironment of the lesion.<sup>6</sup> Model-based pharmacokinetic DCE parameters are “quantitative” insofar as their potential to measure true physiologic mechanisms, such as blood flow and endothelial permeability. However, this potential is difficult to realize in practice because of several challenges, including parameter coupling, measuring the arterial input function, water exchange, and model fit instability.<sup>7</sup> In many cases, correlation with tumor stage and response to treatment can be more easily, perhaps even more reproducibly, obtained by use of “semiquantitative” model-free parameters such as the initial area under the time signal-intensity curve (IAUC),<sup>8</sup> which do not require an arterial input function measurement and are immune to fit failures on noisy data. Their main limitation, however, is lack of a clear biologic association. The ideal DCE MR imaging analysis would feature the robustness and “biologic relevance” from both model-based and model-free approaches.

In the present study, we propose a more specific area under the time signal-intensity curve–derived parameter (initial and final area under the time signal-intensity curves ratio [AUCR]) dedicated to posttreatment glioblastoma, which represents both initial contrast wash-in into extravascular extracellular space (EES) and contrast retention within EES. Our hypothesis was that the IAUC probably reflects the degree of early leakage of contrast agent into the EES and the final area under the time signal-intensity curve (FAUC) provides insight into increased EES associated with decreased tumor cellularity and more tissue damage in pseudoprogression. We tried to validate the AUCR by comparison with clinicopathologic results of posttreatment glioblastomas. This choice was dictated by our desire to minimize the dependence on pharmacokinetic modeling. We also applied a 2-component mixture normal distribution to yield better-fitting curves of histograms<sup>9</sup> because perfusion histograms in glioblastomas are usually asymmetric, generally broad, and occasionally dual peaked. The purpose of this study was to test the predictive value of the bimodal histogram parameters of AUCR derived from DCE perfusion MR imaging in the differentiation of pseudoprogression from ETP in patients with newly diagnosed glioblastomas.

## MATERIALS AND METHODS

Our institutional review board approved this retrospective study and waived the informed consent requirement.

### Patients

A retrospective review of the data base of our institution identified 572 consecutive patients who underwent an MR imaging study for pretreatment and posttreatment glioma evaluation between December 2007 and July 2012. Among these patients, 79 were included as our study patient group according to the following criteria: 1) they had been pathologically confirmed as having glioblastomas before standard glioblastoma treatment; 2) they underwent concurrent chemoradiotherapy (CCRT) after surgical resection; 3) they demonstrated new or progressively enlarged enhancing lesions seen on the first follow-up MR images, including DCE perfusion MR images, within 4–5 weeks after the end of

concurrent chemoradiotherapy; 4) they did not have corticosteroid administration at the time of the DCE MR imaging; 5) they had adequate image acquisition and quality without patient motion and susceptibility artifacts; and 6) they underwent more than 2 subsequent follow-up MR studies. The size criterion for enlarged contrast-enhancing lesions was an increase of a measurable (> 1 cm) enhancing lesion by more than 25% in the sum of the products of perpendicular diameters between the pre-CCRT and first post-CCRT MR images. This criterion was modified from the Response Assessment in Neuro-Oncology (RANO) criteria for progressive disease more than 12 weeks after completion of CCRT. A total of 20 patients with treatment-naïve glioblastomas and who also underwent DCE T1-weighted perfusion MR imaging were enrolled as the control group. Because the AUCR was a new imaging parameter derived from a time-normalized signal intensity curve of the DCE study, we needed reference AUCR values only in our institution. The patients with treatment-naïve glioblastomas that had been pathologically confirmed and had not had any postsurgical artifacts could provide reference AUCR values in our institution. There was no overlap in the patient group and the control group. The study patient accrual process is summarized in Fig 1.

Pathologic analysis after second-look surgery categorized patients into an ETP group ( $n=17$ ) and a pseudoprogression group ( $n=7$ ). If second-look surgery was not available, the clinicoradiologic diagnosis of ETP ( $n=25$ ) or pseudoprogression ( $n=30$ ) was made by consensus of a neuro-oncologist and a neuroradiologist after complete chart and imaging review. The diagnosis of pseudoprogression was made if no change in treatment was required for a minimum of 6 months from the end of CCRT. This definition allows for the mild increase of the contrast-enhancing lesions compared with the usual decrease or stabilization, as long as no treatment change occurred during this period. The final diagnosis of ETP was made if a steady increase in enhancement on more than 2 subsequent follow-up MR imaging studies with an interval of 2–3 months, and clear clinical deterioration that was not attributable to concurrent medication or comorbid conditions, prompted a change in treatment.<sup>10</sup>

Of the 79 study patients, 36 were men (mean age, 49.5 years; age range, 35–69 years) and 43 were women (mean age, 52.9 years; range, 25–69 years), with an overall mean age of 51.2 years (age range, 25–69 years). Of the 20 control patients, 12 were men and 8 were women, with an overall mean age of 47.9 years (age range, 34–58 years).

### Imaging Protocol

Conventional and DCE perfusion MR imaging were performed by use of a 3T system (Achieva; Philips Healthcare, Best, the Netherlands) with an 8-channel sensitivity-encoding head coil. 3D gradient-echo data with 21 sections were obtained before, during, and after administration of a standard dose of 0.1 mmol (0.2 mL)/kg of gadoterate meglumine (Dotarem; Guerbet, Aulnay-sous-Bois, France) per kilogram of patient body weight (average total volume, 13.7 mL; range, 12–15 mL) and at a rate of 4 mL/s by

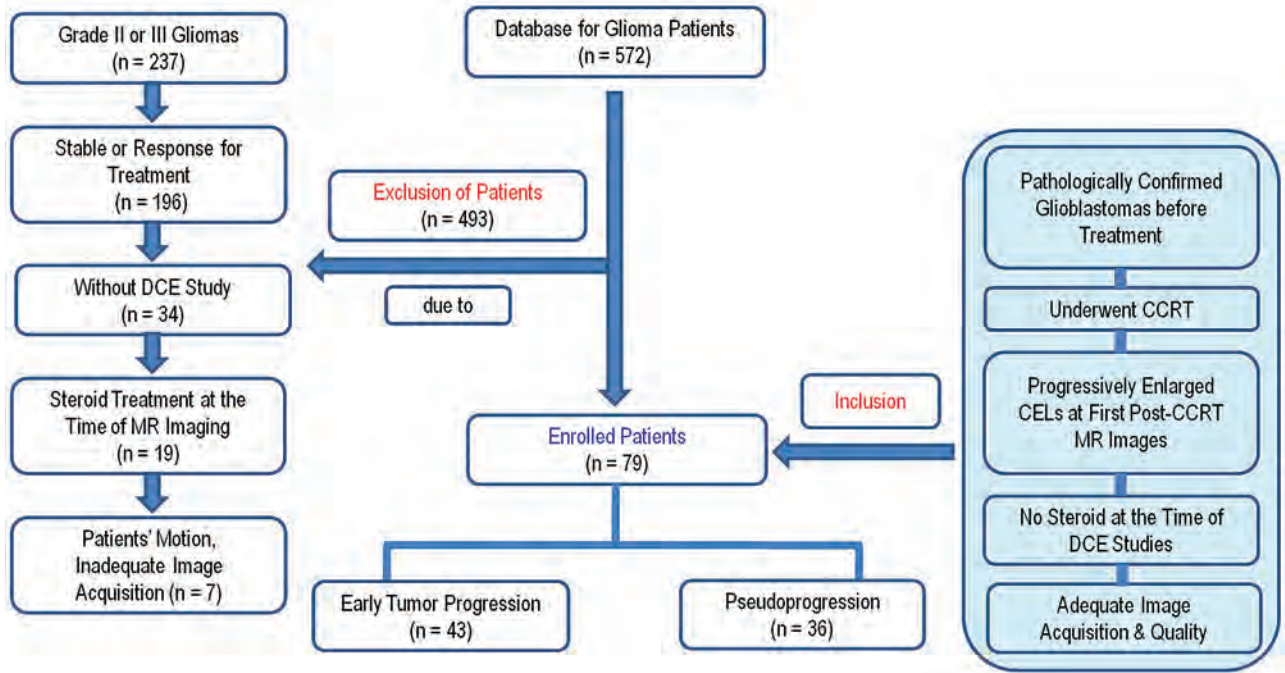


FIG 1. Flowchart of the study population. CEL, contrast-enhancing lesion.

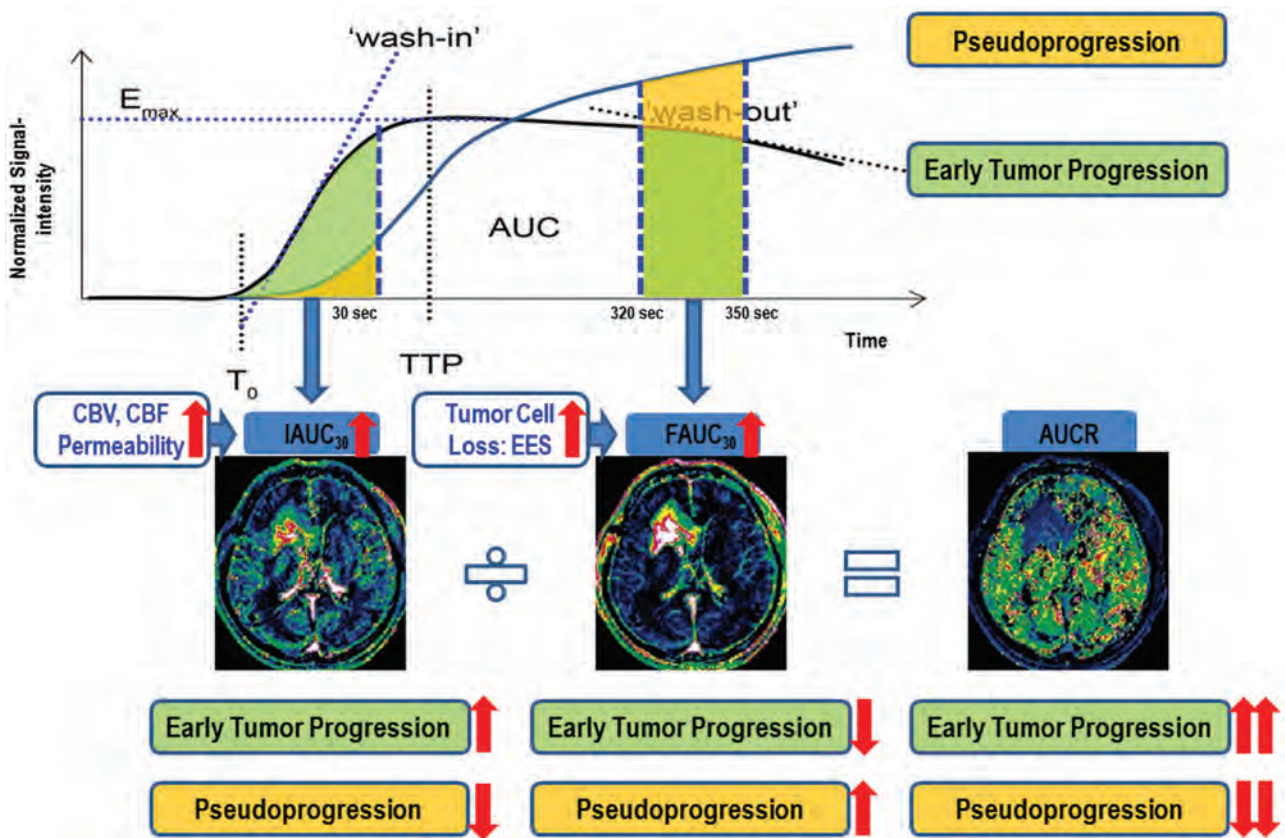
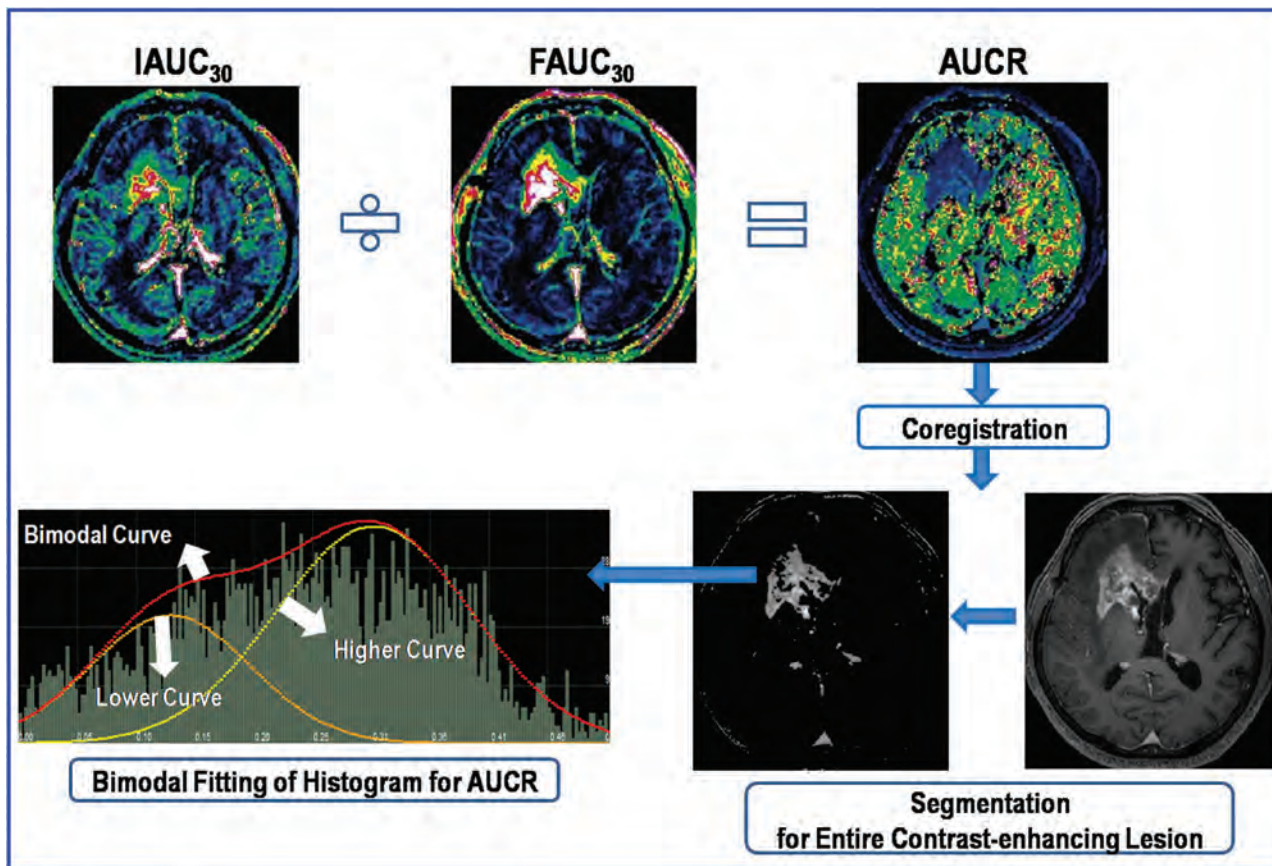


FIG 2. Illustration for calculating the AUCR from DCE perfusion MR imaging and the flowchart of our hypothesis.

use of an MR imaging-compatible power injector (Spectris; Medrad, Indianola, Pennsylvania). The dynamic acquisition was performed with a temporal resolution of 3.52 seconds, and contrast was administered after 10 baseline dynamics (total: 120 dynamics). The

detailed imaging parameters for DCE perfusion MR imaging were a section thickness of 4 mm with no gap; spatial in-plane resolution,  $184 \times 186$  mm; TR, 6.4 ms; TE, 3.1 ms; flip angle,  $15^\circ$ ; field of view, 23 cm; and total acquisition time, 6 minutes and 41 seconds.



**FIG 3.** Illustration of the step for calculating the AUCR and its histogram.

### Image Processing

All imaging data were transferred from the MR scanner to an independent personal computer for quantitative DCE perfusion analysis. Perfusion parametric maps were obtained by use of a commercial software package (nordicICE; NordicNeuroLab, Bergen, Norway), and in-house software developed by Matlab 2010b (MathWorks, Natick, Massachusetts). For DCE MR imaging, motion correction was done to correct a rigid body motion to the time-series data before the DCE dynamic curve analysis. On the time-signal intensity curve, signal intensity was normalized to the maximal value as the percent change of signal intensity. The  $IAUC_{30}$  was defined as the trapezoidal integration of the normalized signal intensity curve from the onset of enhancement to 30 seconds thereafter in the segmented contrast-enhancing voxels. This approach provides a measurement of the initial arrival of contrast agent in the tissue of interest after intravenous bolus administration that reflects blood flow, vascular permeability, and the fraction of interstitial space.<sup>11</sup> The determination of the initial 30 seconds was based on our observation that initial contrast agent wash-in was usually achieved during the first 30 seconds postcontrast agent arrival.  $FAUC_{30}$  was defined as the trapezoidal integration of the normalized signal intensity curve between 320 and 350 seconds after the onset of enhancement in the same enhancing voxels with  $IAUC_{30}$ . As shown by a previous study,<sup>7</sup>  $IAUC_{ve}$  (similar parameter with  $FAUC_{30}$ ) could be a correlate of volume fraction of extracellular extravascular space ( $V_e$ ). Cheng<sup>7</sup> chose an interval of  $IAUC_{ve}$  beyond the vascular phase

when contrast distribution is relatively stable to minimize flow and related vascular contributions. However, this author proposed that if signal-to-noise ratio permits,  $IAUC_{ve}$  should be computed at yet later times to improve correlation with  $V_e$ . We chose an interval between 320 and 350 seconds after the onset of enhancement to maximize the difference of  $FAUC_{30}$  between ETP and pseudoprogession groups. Thus, the  $FAUC_{30}$  could represent the amount of contrast agent leakage within the EES, and the increased  $FAUC_{30}$  could be explained by the increased EES associated with decreased tumor cellularity and more tissue damage in pseudoprogession (Fig 2). An experienced neuroradiologist (H.S.K. with 8 years of experience in neuro-oncologic imaging) specified the range of the prebolus, wash-in, and the last images used to estimate the  $IAUC_{30}$  and  $FAUC_{30}$ . Outlier values, which could occur from unstable curve-fitting conditions with a noisy input signal, were removed from the output maps by setting the outlier pixels equal to the maximum of the “normal” pixel range. Finally, the ratio of  $IAUC_{30}$  and  $FAUC_{30}$  (AUCR) was calculated within the same contrast-enhancing lesions on a voxel-by-voxel basis (Fig 2).

Model-based DCE parameters were obtained with a 2-compartment pharmacokinetic model by use of permeability software (PRIDE, Philips Healthcare) with the interactive data language (IDL, RSI) in the 20 treatment-naïve control patients. The rate of forward leakage can be produced as  $K^{trans}$  on the basis of the model.

**Table 1: Comparison of study patient demographic data**

Variables	Pseudoprogression	ETP
No. of male patients (%)	17 (45.9)	19 (45.2)
No. of female patients (%)	20 (54.1)	23 (54.8)
Age (y) <sup>a</sup>	48.5 ± 9.1	52.6 ± 8.5
Mean KPS <sup>a</sup>	93.0 ± 5.9	92.4 ± 6.3
Tumor volume (cm <sup>3</sup> ) <sup>a</sup>	50.2 ± 17.1	55.9 ± 22.12
Surgical extent before CCRT		
Biopsy	3	6
Subtotal resection	17	17
Gross total resection	17	19
Mean radiation dose (at CCRT, Gy)	59.5	59.7
Mean interval between CCRT and new or enlarging contrast-enhancing lesion (d)	31.2	29.7
MGMT promoter status (methylated/unmethylated)	10/4	7/12

**Note:**—KPS indicates Karnofsky performance status; MGMT, O(6)-methylguanine methyltransferase.

<sup>a</sup>Data are mean ± SD.

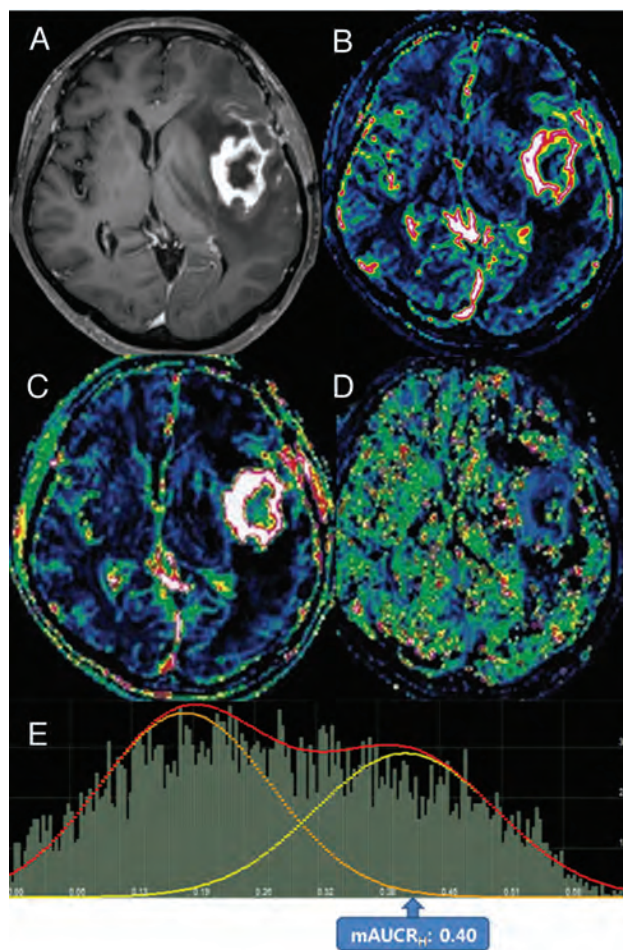


**FIG 4.** Images obtained in a 67-year-old woman with posttreatment glioblastoma who had ETP. Contrast-enhanced, T1-weighted imaging (A) performed 4 weeks after concomitant chemoradiotherapy showed a necrotic, contrast-enhancing mass centered in the left insula. The IAUc<sub>30</sub> (B) and FAUC<sub>30</sub> (C) maps derived from dynamic contrast-enhanced, T1-perfusion MR imaging. B, A visual increase of the IAUc<sub>30</sub> value was noted in the medial aspect of the contrast-enhancing lesion. The AUCR map (D) and its bimodal histogram (E) showed increases in bimodal histogram parameters indicating ETP.

For quantitative analysis, the experienced neuroradiologist (H.S.K.) segmented the contrast-enhancing lesion volumes on 3D postcontrast, T1-weighted images according to a semiautomated,

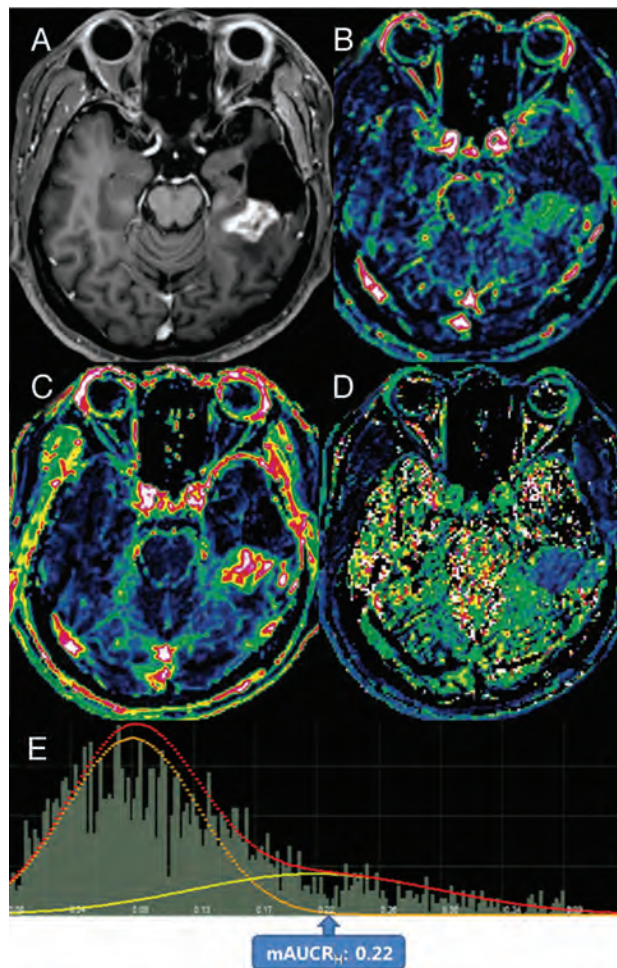


**FIG 5.** Images obtained in a 56-year-old man with posttreatment glioblastoma who had pseudoprogression. Contrast-enhanced T1-weighted imaging (A) obtained 3 weeks after concomitant chemoradiotherapy showed a necrotic, contrast-enhancing mass posterior to the surgical cavity of the left temporal lobe. The IAUc<sub>30</sub> (B) and FAUC<sub>30</sub> (C) maps derived from dynamic contrast-enhanced, T1-perfusion MR imaging. In B, a visual decrease of the IAUc<sub>30</sub> value was noted in the entire contrast-enhancing lesion. The AUCR map (D) and its bimodal histogram (E) showed a decrease in the mean value of the higher curve, thus indicating pseudoprogression.

adaptive thresholding technique by using the commercial software (nordicICE). The segmentation function was automatically performed according to the segmentation threshold, which was based on the pixel range of T1-signal intensity and was determined by the operator to visually exclude macroscopic necrosis, cysts, and normal vessels. The resulting segmented enhancing tumor volumes were verified by the experienced neuroradiologist (H.S.K.), who was blinded to the clinical outcome, and they were coregistered and mapped to the AUCR maps. The AUCR values calculated on a pixel-by-pixel basis for the segmented enhancing volume were used for histogram analysis (Fig 3).

Because perfusion histograms are often bimodal or skewed, we used a 2-mixture normal distribution to provide optimal fitting.<sup>9</sup> We then generated the mean for the higher peak (mean AUCR at a higher curve, mAUCR<sub>H</sub>). We also measured the AUCR at mode (AUCR<sub>mod</sub>). For the cumulative AUCR histogram parameters, the 50th (AUCR<sub>50</sub>), 75th (AUCR<sub>75</sub>), and 90th (AUCR<sub>90</sub>) percen-

**Table 2: Multiple comparison test (*P* value) of the AUCR histogram parameters in the early tumor progression, pseudoprogression, and control groups**

	AUCR <sub>50</sub>	AUCR <sub>75</sub>	AUCR <sub>90</sub>	AUCR <sub>mode</sub>	mAUCR <sub>H</sub>
Pseudoprogression vs ETP group	<.0001	<.0001	<.0001	<.0001	<.0001
Pseudoprogression vs control group	<.0001	<.0001	<.0001	<.0001	<.0001
ETP vs control group	.557	.572	.771	.752	.747

**Note:**—AUCR indicates area under the time signal-intensity curve ratio; AUCR<sub>50</sub>, 50 percentile cutoff value of AUCR; AUCR<sub>75</sub>, 75 percentile cutoff value of AUCR; AUCR<sub>90</sub>, 90 percentile cutoff value of AUCR; AUCR<sub>mode</sub>, AUCR at mode; mAUCR<sub>H</sub>, mean of the higher curve of AUCR.

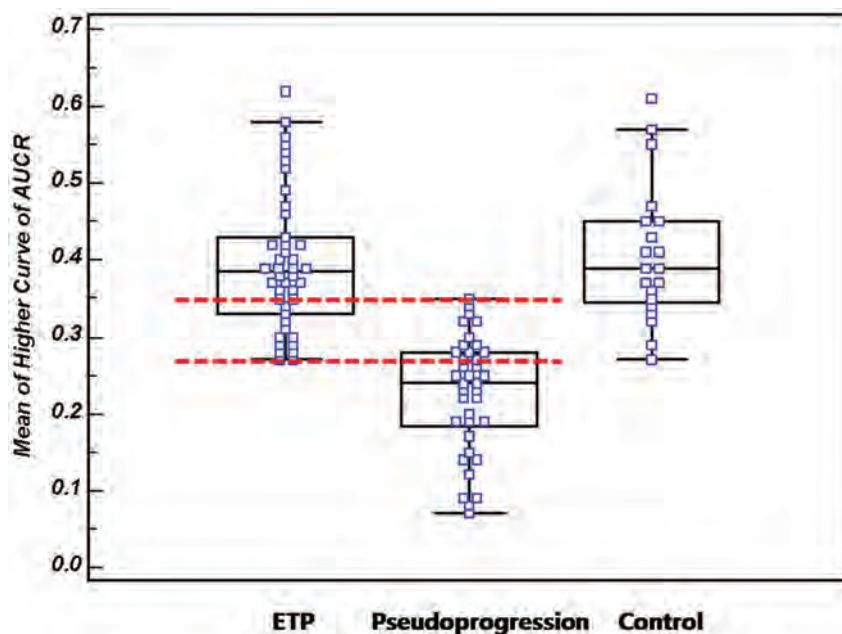


**FIG 6.** A box-and-whisker with scatterplots shows the mAUCR<sub>H</sub> of the ETP, pseudoprogression, and control groups. A clear difference between the ETP group and the pseudoprogression group can be seen ( $P < .0001$ ); however, an overlap zone is visible between an mAUCR<sub>H</sub> of 0.27 and 0.35 (interval between dotted lines).

tiles were derived (the  $n$ th percentile is the point at which  $n\%$  of the voxel values that form the histogram is found to the left).<sup>12</sup>

### Statistical Analysis

All data were expressed as mean  $\pm$  SD. The significant differences among the various, model-free parameters derived from the pseudoprogression group, the ETP group, and the control group, were assessed by 1-way ANOVA as the first test. If the overall  $P$  value was .05 or less, Bonferroni multiple comparison was used as a post hoc test. All  $P$  values were adjusted with Bonferroni correction for multiple comparisons.

In the receiver operating characteristic curves analysis, the cutoff points, which were determined by maximizing the sum of the sensitivity and specificity, were calculated to differentiate pseudoprogression from ETP. Areas under the receiver operating characteristic curves ( $A_z$ ), which were computed by use of the selected DCE parameters, were compared according to the method of DeLong et al.<sup>13</sup> Correlation between the AUCR and the  $K^{trans}$  was made by use of the Spearman correlation analysis.  $P$  values  $< .05$  were considered to indicate statistically significant differences.

## RESULTS

The mean time for postprocessing of the AUCR histogram, including curve fitting, was 7 minutes and 12 seconds. The O(6)-

methylguanine methyltransferase methylation status was obtained in 33 of 79 study patients through chart review. However, in our small patient study, the O(6)-methylguanine methyltransferase methylation status was not significantly different between the 2 groups. Descriptive statistics regarding the clinical and imaging parameters obtained in both the pseudoprogression and ETP groups are summarized in Table 1.

### Visual and Quantitative Analysis of the AUCR Histogram Parameters

The bimodal histograms of AUCR in ETP showed a higher relative frequency at the high AUCR value compared with pseudoprogression, thus resulting in substantial divergence between pseudoprogression and ETP at the high end of the cumulative histograms. The left-sided skewing and platykurtosis of the cumulative histogram of AUCR were more obvious in ETP than in pseudoprogression, which correlates well with the significant

difference in mAUCR<sub>H</sub>, AUCR<sub>50</sub>, AUCR<sub>75</sub>, AUCR<sub>90</sub>, and AUCR<sub>mode</sub> between the 2 groups (Figs 4 and 5).

All of the AUCR histogram parameters showed statistically significant differences between the pseudoprogression group and the ETP group (Table 2), with the ETP group showing higher AUCR histogram parameters. Although the mAUCR<sub>H</sub> showed a clear difference between the ETP group and the pseudoprogression group ( $P < .0001$ ), an overlap zone was visible between an mAUCR<sub>H</sub> of 0.27 and 0.35 (Fig 6). Significant differences in all of the AUCR histogram parameters were observed between the control group and the pseudoprogression group in which the cumulative histograms revealed that the mAUCR<sub>H</sub>, AUCR<sub>50</sub>, AUCR<sub>75</sub>, AUCR<sub>90</sub>, and AUCR<sub>mode</sub> differed significantly. However, no significant differences were observed in any of the AUCR histogram parameters between the control group and the ETP group (Table 2, Figs 6 and 7).

### Diagnostic Performance of the AUCR Histogram Parameters and Correlation with $K^{trans}$

Each parameter was evaluated individually for its discriminative ability by use of receiver operating characteristic analysis (Table 3). mAUCR<sub>H</sub> was the single best predictor for classification ( $A_z = .901$ ). The optimal cutoff value of mAUCR<sub>H</sub> for the prediction of pseudoprogression was 0.31, with a sensitivity of 90.1% and a

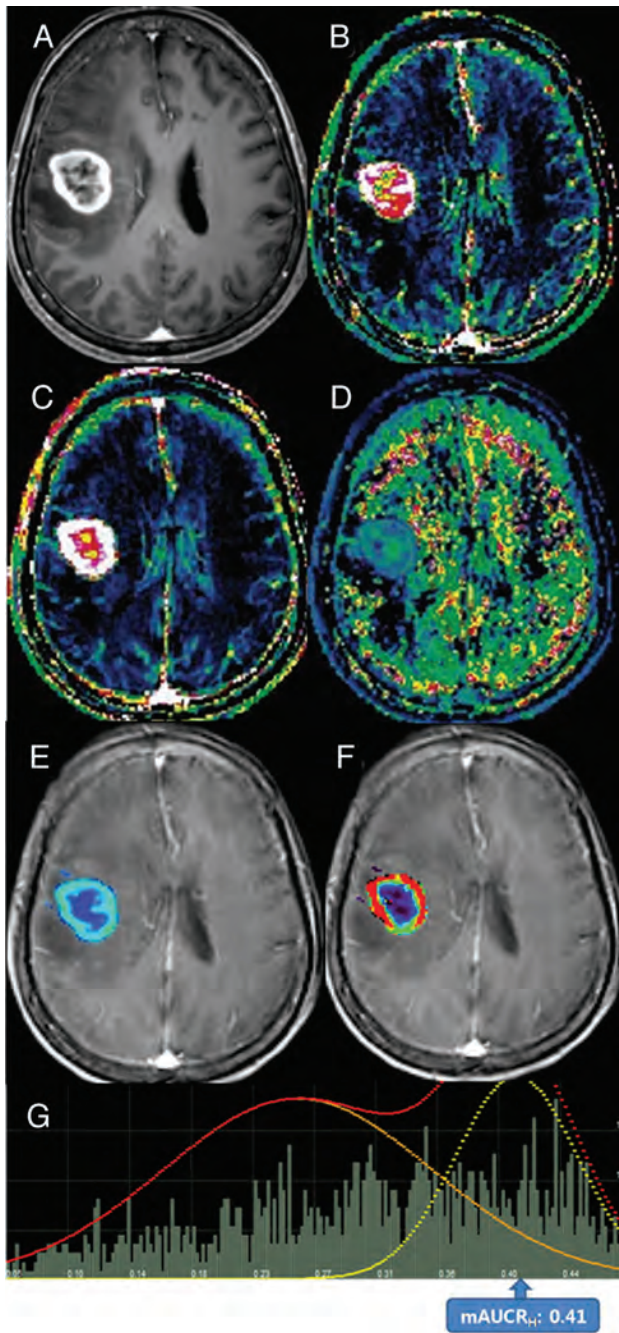


**FIG 7.** Images obtained in a 58-year-old woman with pathologically confirmed treatment-naïve glioblastoma. Contrast-enhanced, T1-weighted image obtained before surgery. *A*, The image showed a necrotic, contrast-enhancing mass in the right frontal lobe. *B*,  $IAUC_{30}$  (*B*) and  $FAUC_{30}$  (*C*) maps derived from dynamic contrast-enhanced, T1-perfusion MR imaging. *B*, A visual increase of the  $IAUC_{30}$  value was noted in the entire contrast-enhancing lesion. The  $AUCR$  (*D*),  $K^{trans}$  (*E*),  $V_e$  (*F*) maps, and  $AUCR$  bimodal histogram (*G*) are shown. *F*, The distribution of visually high  $K^{trans}$  corresponded with that of the  $IAUC_{30}$  map. *G*, An  $AUCR$  histogram showed increases in bimodal histogram parameters similar with those of ETP.

specificity of 82.9%.  $AUCR_{50}$  was found to be the most specific predictor of pseudoprogression, with a sensitivity of 87.2% and a specificity of 83.1% by use of a cutoff value of 0.19. Receiver operating characteristic curve analysis indicated that the diagnostic models on the basis of all of the  $AUCR$  histogram parameters had a statistically significant *P* value.

A scatterplot of maximal  $K^{trans}$  against  $mAUCR_H$  in 20 patients with treatment-naïve glioblastoma showed a significant correlation between the model-based and model-free parameters ( $r = 0.730$ ;  $P = .0003$ ; 95% confidence interval = 0.425–0.886).

## DISCUSSION

In this study, we chose 2 variables— $IAUC_{30}$  and  $FAUC_{30}$ —to describe the shape of the dynamic time–signal intensity curve. This choice was dictated by our desire to minimize the dependence on pharmacokinetic modeling.<sup>14</sup> We found that all of the  $AUCR$  histogram parameters could distinguish retrospectively whether a progressively enhancing lesion was caused by ETP or by pseudoprogression. Our results might be explained by the fact that the  $IAUC_{30}$  depends mostly on the blood flow as well as the total vascular surface area exposed to the contrast agent; therefore, ETP has a prominent  $IAUC_{30}$  on the basis of hypervascularity and neoangiogenesis. In addition,  $FAUC_{30}$  in the pseudoprogression group could be increased by greater retention of contrast agent in the EES because of less tumor cellularity and more tissue damage. Our results are also consistent with what has been described previously by Narang et al,<sup>15</sup> who used the  $IAUC$  at 60 seconds ( $IAUC_{60}$ ) in the initial vascular phase to successfully differentiate tumor progression from radiation necrosis. Contrary to this previous study,<sup>15</sup> we chose  $IAUC_{30}$  instead of  $IAUC_{60}$ . Determination of the initial 30 seconds for  $IAUC$  was based on our observation that initial contrast agent wash-in was usually achieved during the first 30-second postcontrast agent arrival.

Compared with a DCE MR study, a DSC study is more sensitive to susceptibility artifacts mainly associated with surgery- or radiation-induced hemorrhage, and its low spatial-resolution limits offer accurate characterization of the spatial distribution of brain tumor vessels. In addition, the  $T2^*$  contrast agent leakage effects, which depend on the attenuation and spatial distribution of tumor cells within the EES, can lead to an additional susceptibility calibration factor. Even without contrast agent extravasation, the estimation of  $T2^*$  parameters is confounded by the complicated relationship between the signal intensity and contrast agent concentration, as the vascular susceptibility calibration factor is known to vary across tissues with differing vascular geometries and architecture.<sup>16</sup> Recently, Larsen et al<sup>17</sup> reported that cerebral blood volume measurements by DCE MR imaging gave results very similar to FDG-PET regarding differentiation between tumor recurrence and radiation necrosis.

Although pharmacokinetic modeling (eg, Tofts) is the ideal approach, its “quantitative” potential is often undermined when a few conditions and assumptions are unmet. For example, an arterial input function is required, but its rapid and accurate measurement is challenging, and a visible vessel without inflow artifacts or partial-volume effects may not be available in the anatomic region of interest.<sup>7</sup>  $IAUC$  during a given time is a model-free parameter that describes the initial uptake of contrast agent in a tissue of interest. It has advantages in that it does not require arterial input function measurement, is unlikely to be influenced significantly by variations in scanner and sequence type, and does not rely on complex postprocessing pharmacokinetic modeling techniques.<sup>11</sup> However, model-free parameters lack a clear biologic association because they are “mixed” mea-

**Table 3: Diagnostic performance of the AUCR histogram parameters for differentiating ETP from pseudoprogression**

Parameter	A <sub>z</sub> Value <sup>ab</sup>	Sensitivity (%)	Specificity (%)	PPV (%)	NPV (%)	Cutoff Value
AUCR <sub>50</sub>	0.871 (0.757–0.939)	87.2	83.1	84.3	81.1	0.19
AUCR <sub>75</sub>	0.842 (0.741–0.922)	82.6	81.1	80.9	78.2	0.25
AUCR <sub>90</sub>	0.879 (0.772–0.949)	89.6	81.7	85.0	87.1	0.34
AUCR <sub>mode</sub>	0.791 (0.677–0.892)	73.1	79.7	79.1	72.5	0.16
mAUCR <sub>H</sub>	0.901 (0.791–0.976)	90.1	82.9	87.5	87.9	0.31

**Note:**—NPV indicates negative predictive value; PPV, positive predictive value.

<sup>a</sup> A<sub>z</sub> indicates the largest area under the receiver operating characteristic curve.

<sup>b</sup> Numbers in parentheses are 95% confidence intervals.

tures of tissue blood flow and vascular permeability, as well as an indirect measure of the EES. Although Evelhoch<sup>14</sup> suggested that it was related to blood flow, vessel permeability, and interstitial space, its physiologic meaning was investigated by Walker-Samuel et al,<sup>18</sup> who showed that the IAUC correlated intractably with  $K^{trans}$ , EES volume, and plasma volume. Their results revealed that the IAUC could be made to track  $K^{trans}$  or EES volume, but only under specific conditions and within a narrow range of physiologic values. We proposed a modified area under the time signal-intensity curve-derived DCE parameter (AUCR) dedicated to posttreatment glioblastoma, which retains the advantages of model-free approaches. We tried to validate the AUCR by comparison with clinicopathologic results of posttreatment glioblastomas and found that all of the AUCR histogram parameters were significantly different between the ETP group and the pseudoprogression group.

However, we did not directly compare the diagnostic accuracy of AUCR with model-based DCE parameters, such as  $K^{trans}$ , in the same patients with posttreatment glioblastomas because of incomplete arterial input function sampling. However, compared with a recently published report,<sup>19</sup> the sensitivity and specificity of AUCR were comparable to those of model-based DCE parameters and were higher than those of conventional IAUC in the differentiation of tumor from radiation necrosis. Moreover, the correlation of AUCR with  $K^{trans}$  was significantly high in 20 patients with treatment-naïve glioblastomas, who were eligible for relatively rapid arterial input function sampling.

Because AUCR histograms in posttreatment glioblastomas were often skewed, broad, and occasionally dual peaked, a 2-component mixture normal distribution was selected to model their shape, as proposed by Pope et al<sup>9</sup> by use of ADC histograms in recurrent glioblastoma. One potential explanation for this observation is that some areas of contrast-enhancing lesion may have predominant tumor and limited treatment-related change resulting in a prominent higher AUCR histogram curve, whereas other areas of contrast-enhancing lesion are composed of predominant treatment-related change and a limited tumor-generating prominent lower AUCR curve. However, a great deal of information seems to be lost on the presence of both pseudoprogression and tumor in the same patient if only the histograms are evaluated. In our present study, we found the same overlap of mAUCR<sub>H</sub> range between the ETP group and the pseudoprogression group, which might be attributable to the coexistence of viable tumor cells and treatment effects. As reported by Hu et al<sup>21</sup>, they can diagnose small isolated enhancing foci and identify histologically distinct subregions within large enhancing lesions by applying accurate threshold values determined by direct correlation between histopathologic features and DSC measurements. Future studies di-

rectly correlating AUCR with histopathologic patterns in ETP and pseudoprogression samples may clarify underlying pathophysiologic mechanisms.

Our study had several limitations. First, because the model's assumptions with IAUC<sub>30</sub> and FAUC<sub>30</sub> ignored multiple other effects, such as edema, back-pressure, and transport, all of which varied with tumor grade, the equations could only measure flow rates and not true permeability.<sup>20</sup> Second, our AUCR histogram parameters showed relatively lower specificity for differentiating ETP from treatment-related change compared with a previous DSC study, which was a well-designed prospective study that used image-guided neuronavigation during surgical resection to directly correlate specimen histopathologic patterns with localized DSC measurements.<sup>21</sup> Third, using the histogram analysis of AUCR values to evaluate for ETP vs pseudoprogression in a binary fashion does not provide for the clinical reality that pseudoprogression and tumor regrowth often occur together. Hu et al<sup>21</sup> proposed that diagnosing small isolated enhancing foci and identifying histologically distinct subregions within large enhancing lesions could be achieved by applying accurate threshold values derived from direct correlation between tissue-specimen histopathologic patterns and DSC measurements. Further studies using direct correlation between histopathologic features and AUCR is needed to make our results more convincing. Finally, our method required multiple postprocessing steps. A simpler measurement, perhaps with region-of-interest analysis, would be better suited to clinical practice. In addition, the quantitative analysis required thresholding the image in a semiautomated fashion to ensure that the entire enhancing tumor volume is included, which suggests the need for physician oversight and limiting the ability of technologists to apply this technique independently in clinical practice.

## CONCLUSIONS

A bimodal histogram analysis of AUCR can be used as a potential noninvasive imaging biomarker to monitor the early treatment response in patients with newly diagnosed glioblastomas.

## REFERENCES

1. Gasparetto EL, Pawlak MA, Patel SH, et al. **Posttreatment recurrence of malignant brain neoplasm: accuracy of relative cerebral blood volume fraction in discriminating low from high malignant histologic volume fraction.** *Radiology* 2009;250:887–96
2. Chamberlain MC. **Pseudoprogression in glioblastoma.** *J Clin Oncol* 2008;26:4359; author reply 4360
3. Fatterpekar GM, Galheigo D, Narayana A, et al. **Treatment-related change versus tumor recurrence in high-grade gliomas: a diagnostic conundrum—use of dynamic susceptibility contrast-enhanced (DSC) perfusion MRI.** *AJR Am J Roentgenol* 2012;198:19–26

4. Hu X, Wong KK, Young GS, et al. **Support vector machine multiparametric MRI identification of pseudoprogression from tumor recurrence in patients with resected glioblastoma.** *J Magn Reson Imaging* 2011;33:296–305
5. Nishashi T, Dahabreh IJ, Terasawa T. **Diagnostic accuracy of PET for recurrent glioma diagnosis: a meta-analysis.** *AJNR Am J Neuroradiol* 2013;34:944–50
6. Roberts C, Issa B, Stone A, et al. **Comparative study into the robustness of compartmental modeling and model-free analysis in DCE-MRI studies.** *J Magn Reson Imaging* 2006;23:554–63
7. Cheng HL. **Improved correlation to quantitative DCE-MRI pharmacokinetic parameters using a modified initial area under the uptake curve (mIAUC) approach.** *J Magn Reson Imaging* 2009;30:864–72
8. Liu G, Rugo HS, Wilding G, et al. **Dynamic contrast-enhanced magnetic resonance imaging as a pharmacodynamic measure of response after acute dosing of AG-013736, an oral angiogenesis inhibitor, in patients with advanced solid tumors: results from a phase I study.** *J Clin Oncol* 2005;23:5464–73
9. Pope WB, Kim HJ, Huo J, et al. **Recurrent glioblastoma multiforme: ADC histogram analysis predicts response to bevacizumab treatment.** *Radiology* 2009;252:182–89
10. Wen PY, Macdonald DR, Reardon DA, et al. **Updated response assessment criteria for high-grade gliomas: response assessment in neuro-oncology working group.** *J Clin Oncol* 2010;28:1963–72
11. Evelhoch JL, LoRusso PM, He Z, et al. **Magnetic resonance imaging measurements of the response of murine and human tumors to the vascular-targeting agent ZD6126.** *Clin Cancer Res* 2004;10:3650–57
12. Tozer DJ, Jager HR, Danchaivijitr N, et al. **Apparent diffusion coefficient histograms may predict low-grade glioma subtype.** *NMR Biomed* 2007;20:49–57
13. DeLong ER, DeLong DM, Clarke-Pearson DL. **Comparing the areas under two or more correlated receiver operating characteristic curves: a nonparametric approach.** *Biometrics* 1988;44:837–45
14. Evelhoch JL. **Key factors in the acquisition of contrast kinetic data for oncology.** *J Magn Reson Imaging* 1999;10:254–59
15. Narang J, Jain R, Arbab AS, et al. **Differentiating treatment-induced necrosis from recurrent/progressive brain tumor using nonmodel-based semiquantitative indices derived from dynamic contrast-enhanced T1-weighted MR perfusion.** *Neuro Oncol* 2011;13:1037–46
16. Kiselev VG. **On the theoretical basis of perfusion measurements by dynamic susceptibility contrast MRI.** *Magn Reson Med* 2001;46:1113–22
17. Larsen VA, Simonsen HJ, Law I, et al. **Evaluation of dynamic contrast-enhanced T1-weighted perfusion MRI in the differentiation of tumor recurrence from radiation necrosis.** *Neuroradiology* 2013;55:361–69
18. Walker-Samuel S, Leach MO, Collins DJ. **Evaluation of response to treatment using DCE-MRI: the relationship between initial area under the gadolinium curve (IAUGC) and quantitative pharmacokinetic analysis.** *Phys Med Biol* 2006;51:3593–602
19. Bisdas S, Naegele T, Ritz R, et al. **Distinguishing recurrent high-grade gliomas from radiation injury: a pilot study using dynamic contrast-enhanced MR imaging.** *Acad Radiol* 2011;18:575–83
20. Levy LM. **What is right about MRI permeability studies.** *AJNR Am J Neuroradiol* 2005;26:3–4
21. Hu LS, Baxter LC, Smith KA, et al. **Relative cerebral blood volume values to differentiate high-grade glioma recurrence from posttreatment radiation effect: direct correlation between image-guided tissue histopathology and localized dynamic susceptibility-weighted contrast-enhanced perfusion MR imaging measurements.** *AJNR Am J Neuroradiol* 2009;30:552–58

# Higher Rates of Decline for Women and Apolipoprotein E $\epsilon$ 4 Carriers

D. Holland, R.S. Desikan, A.M. Dale, and L.K. McEvoy, for the Alzheimer's Disease Neuroimaging Initiative



## ABSTRACT

**BACKGROUND AND PURPOSE:** Age and the *apolipoprotein E*  $\epsilon$ 4 allele are well-known risk factors for Alzheimer disease, but whether female sex is also a risk factor remains controversial. It is also unclear how these risk factors affect rates of structural brain and clinical decline across the spectrum of preclinical to clinical Alzheimer disease. Our objective is to estimate the effects of *apolipoprotein E*  $\epsilon$ 4 and sex on age-specific rates of morphometric and clinical decline in late-onset sporadic Alzheimer disease.

**MATERIALS AND METHODS:** With the use of linear mixed-effects models, we examined the effect of age, *apolipoprotein E*  $\epsilon$ 4, and sex on longitudinal brain atrophy and clinical decline among cognitively normal older individuals and individuals with mild cognitive impairment and Alzheimer disease (total = 688). We also evaluated the relationship between these effects and CSF biomarkers of Alzheimer disease pathology.

**RESULTS:** *Apolipoprotein E*  $\epsilon$ 4 significantly accelerated rates of decline, and women in all cohorts had higher rates of decline than men. The magnitude of the sex effect on rates of decline was as large as those of  $\epsilon$ 4, yet their relationship to measures of CSF biomarkers were weaker.

**CONCLUSIONS:** These results indicate that in addition to *apolipoprotein E*  $\epsilon$ 4 status, diagnostic and therapeutic strategies should take into account the effect of female sex on the Alzheimer disease process.

**ABBREVIATIONS:** AD = Alzheimer disease; ADAS-Cog = cognitive subscale of the Alzheimer Disease Assessment Scale; ADNI = Alzheimer's Disease Neuroimaging Initiative; APOE = *apolipoprotein E*; CDR-SB = Clinical Dementia Rating Scale, sum of boxes; HC = cognitively healthy elderly; MCI = mild cognitive impairment; MMSE = Mini-Mental State Examination; NFT = neurofibrillary tangle; p- $\tau$  = phosphorylated  $\tau$

The clinical presentation of Alzheimer disease (AD) is not uniform across individuals: in addition to atypical presentations<sup>1,2</sup> of AD, recent results show that the disease also presents differently in older compared with younger patients.<sup>3,4</sup> It is unclear, however, whether common genetic risk variants and sex also affect how the disease manifests and progresses.

In the United States, two-thirds of AD cases are women,<sup>5</sup> but because women live longer than men and older age is a known risk factor for AD, there remains controversy over whether women are

at greater risk of development of AD than men. Several large epidemiology studies have found evidence of higher age-specific rates of incidence<sup>6-10</sup> and prevalence<sup>11</sup> of AD in women compared with men, though other studies have found no difference.<sup>12,13</sup> Elderly women, however, have higher amounts of AD pathology than elderly men,<sup>14</sup> and women with AD perform more poorly than men on cognitive assessment.<sup>15</sup> Assessing sex differences in age-specific cognitive and structural rates of decline may help elucidate this controversy.

The strongest known common genetic risk factor for sporadic AD is the *apolipoprotein E* (APOE)  $\epsilon$ 4 allele.<sup>16,17</sup> APOE  $\epsilon$ 4 increases the age-specific risk of development of AD in a dose-dependent manner<sup>18,19</sup> and lowers the age of onset.<sup>18,20</sup> Recently, we showed<sup>3</sup> that rates of both cognitive and structural decline decreased with age in individuals with mild cognitive impairment (MCI) and AD, but increased with age for the cognitively healthy elderly. Because  $\epsilon$ 4 lowers the age of onset, age differences in rates of decline may have arisen partially from differences in  $\epsilon$ 4 prevalence with age. Thus, to better understand AD biomarker trajectories, it is important to assess simultaneously the effects of  $\epsilon$ 4 and

Received February 14, 2013; accepted after revision March 21.

From the Departments of Neurosciences (D.H., A.M.D., L.K.M.) and Radiology (R.S.D., A.M.D.), University of California, San Diego, La Jolla, California.

This research was supported by NIH grants R01AG031224, R01AG22381, U54NS056883, P50NS22343, and P50MH081755 (A.M.D.); NIA K01AG029218 (L.K.M.); NIH-NIBIB T32 EB005970 (R.S.D.).

Please address correspondence to Dominic Holland, PhD, 8950 Villa La Jolla Dr, Suite C101, La Jolla CA 92037; e-mail: dominic.holland@gmail.com

Indicates open access to non-subscribers at www.ajnr.org

Indicates article with supplemental on-line appendix.

<http://dx.doi.org/10.3174/ajnr.A3601>

**Table 1: Demographic data for participants with longitudinal structural and clinical measures**

Diagnostic Group	$\epsilon 4^-$				$\epsilon 4^+$			
	Male		Female		Male		Female	
	N	Age, y (SD)	N	Age, y (SD)	N	Age, y (SD)	N	Age, y (SD)
HC	70	75.87 (4.63)	67	76.84 (4.94)	26	76.63 (5.42)	25	75.67 (3.13)
MCI <sup>a</sup>	74	78.52 (5.96)	42	78.70 (4.08)	102	76.07 (5.42)	55	73.64 (5.34)
MCIc <sup>b</sup>	23	78.53 (5.50)	12	78.95 (3.81)	45	75.51 (5.28)	30	72.76 (4.97)
AD <sup>c</sup>	13	75.51 (5.70)	13	78.52 (4.21)	42	75.52 (5.90)	37	75.09 (5.07)

**Note:**—N indicates number of participants. Values are mean (standard deviation, SD). MCIc = MCI converters to AD.

<sup>a</sup>MCI:  $\epsilon 4^+$  women are significantly younger than all other groups (all  $P < .01$ );  $\epsilon 4^+$  men are significantly younger than  $\epsilon 4^-$  men and  $\epsilon 4^-$  women ( $P < .01$ ).

<sup>b</sup>MCIc:  $\epsilon 4^+$  women are significantly younger than all other groups (all  $P < .05$ );  $\epsilon 4^+$  men are significantly younger than  $\epsilon 4^-$  men and  $\epsilon 4^-$  women ( $P < .05$ ).

<sup>c</sup>AD:  $\epsilon 4^+$  women are significantly younger than  $\epsilon 4^-$  women ( $P < .05$ ).

age, as well as those of sex, on rates of clinical and structural decline.

We analyzed baseline and longitudinal data from cognitively healthy elderly (HC), MCI, and mild AD cohorts, age 65–90 years. We investigated the effects of  $\epsilon 4$  status and sex on cognitive and structural rates of change, and assessed whether such effects could be explained by baseline CSF concentrations of  $A\beta_{1-42}$  and the neurodegeneration-associated  $\tau$  and phosphorylated  $\tau_{181p}$  (p- $\tau$ ) proteins.

## MATERIALS AND METHODS

### Participants

We examined participants from the Alzheimer's Disease Neuroimaging Initiative (ADNI, www.adni-info.org). Participant enrollment criteria, MR image acquisition, and CSF collection and analysis methods are provided in the On-line Appendix.

We evaluated 688 participants, age  $\geq 65$  years at baseline, who had longitudinal cognitive evaluations: 211 HC, 333 patients with MCI, and 144 patients with AD. Of these, 188 HC, 273 patients with MCI, and 105 patients with AD also had longitudinal structural MR imaging data (Table 1). Longitudinal evaluations were performed at 6- or 12-month intervals for up to 24 (AD) or 36 (HC and MCI) months. The research protocol was approved by each local institutional review board, and written informed consent was obtained from each participant.

### MR Image Processing

We quantified anatomical regional change in serial MR imaging with the use of Quarc.<sup>21,22</sup> We analyzed data from all available time points that passed local quality control (total = 2244). Images that had degradation caused by motion, technical problems, significant clinical abnormalities (eg, hemispheric infarction), or changes in scanner vendor during the time series were excluded.<sup>23</sup> We examined rates of change in medial and lateral temporal lobe structures affected in early AD<sup>24-26</sup> and in whole-brain volume.

### Genetic, CSF, and Clinical Measures

We grouped participants with respect to sex and APOE  $\epsilon 4$  status (none,  $\epsilon 4^-$ , versus at least 1  $\epsilon 4$  allele,  $\epsilon 4^+$ ) (Table 1 and On-line Table 7). Baseline CSF data were available on approximately half of the ADNI participants. All participants were scored for Clinical Dementia Rating Scale, sum of boxes (CDR-SB),<sup>27,28</sup> cognitive subscale of the Alzheimer Disease Assessment Scale (ADAS-Cog),<sup>29,30</sup> and Mini-Mental State Examination (MMSE)<sup>31</sup> at each visit.

### Mixed-Effects Modeling

Longitudinal cognitive and structural MR imaging atrophy outcomes ( $Y_{ij}$ ) represent change with respect to baseline. This is expressed as the difference in test scores for cognitive measures and as a percentage of baseline size for cortical thickness change and region of interest volume change.

With the use of all available time points per participant, we investigated the dependence of atrophy rate and rate of clinical decline on  $\epsilon 4$  status and sex by use of a linear mixed-effects model,<sup>32</sup> controlling for baseline age, education, and, in the case of atrophy, baseline clinical severity. For each diagnostic group, the longitudinal outcome measurement  $Y_{ij}$  at time  $t_{ij}$  for participant  $i$  at follow-up time point  $j$  is

$$1) \quad Y_{ij} = (b_0 + \beta_{0i})t_{ij} + b_{\text{Cog}}C_{it_{ij}} + b_{\text{Edu}}D_{it_{ij}} + b_{\text{Age}}A_{it_{ij}} + b_{\text{APOE}}E_{it_{ij}} + b_{\text{Sex}}S_{it_{ij}} + \epsilon_{ij}$$

Here,  $b_0$ ,  $b_{\text{Cog}}$ ,  $b_{\text{Edu}}$ ,  $b_{\text{Age}}$ ,  $b_{\text{APOE}}$ , and  $b_{\text{Sex}}$  are group regression parameters to be determined;  $C_i$ ,  $D_i$ ,  $A_i$ ,  $E_i$ , and  $S_i$  are covariates for participant  $i$ , respectively, mean-centered baseline clinical severity as measured by ADAS-Cog (for atrophic measures only:  $C_i = 0$  when  $Y_{ij}$  is a cognitive measure), mean-centered educational level (years of education), mean-centered baseline age,  $\epsilon 4$  status ( $E_i = 0$  for  $\epsilon 4^-$ ,  $E_i = 1$  for  $\epsilon 4^+$ ), and sex status ( $S_i = 0$  for male,  $S_i = 1$  for female); and  $\epsilon_{ij}$  is the within-participant error, assumed to be independent and identically normally distributed with zero mean and variance  $\sigma_e^2$ . The first term on the right side of Eq. (1) incorporates mixed effects, allowing for different participant-specific rates of change:  $b_0$  is the group fixed effect slope and  $\beta_{0i}$  is the corresponding between-participant random effect slope, with zero mean, assumed to be normally distributed with variance  $\sigma_0^2$ . Subsequent covariate terms involve fixed effects only. We estimated the model parameters (including  $\sigma_0$  and  $\sigma_e$ ) by use of the Matlab (R2009b) function nlmeFit (MathWorks, Natick, Massachusetts). A follow-up set of analyses incorporated additional terms in Equation 1 for baseline CSF  $A\beta$  and p- $\tau$  concentrations to assess whether  $\epsilon 4$  or sex effects could be explained by CSF biomarker values.

## RESULTS

### Rates of Decline in Healthy Controls

Table 2 shows the effects of age,  $\epsilon 4$  status, and sex on rates of atrophy and clinical decline in HCs. For all brain regions, HC participants showed significant decline over time. The annual rate of change, expressed as a percentage of baseline size, ranged from  $-0.39\%$ /year for the entorhinal cortex to  $-0.64\%$ /year for the hippocampus (Table 2,  $b_0$  column). Older age at baseline was associated with a higher rate of change in medial temporal lobe

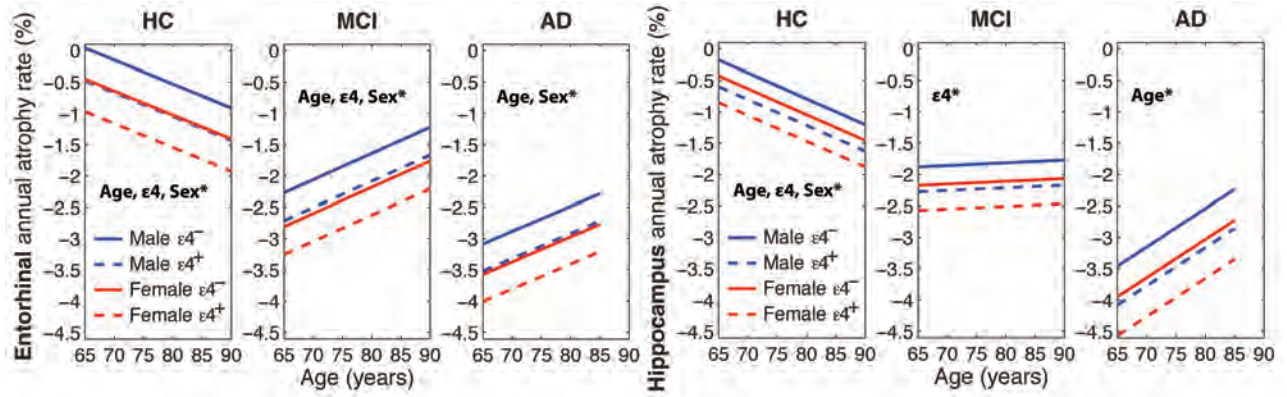


**FIG 1.** Entorhinal and hippocampal annual atrophy rates with respect to age for HC, MCI, and AD participants at their group mean educational level and cognitive performance. Where significant, effects of age (slope),  $\epsilon 4$  and sex (shifts along y-axis) are noted by \*. Also see Tables 2–4.

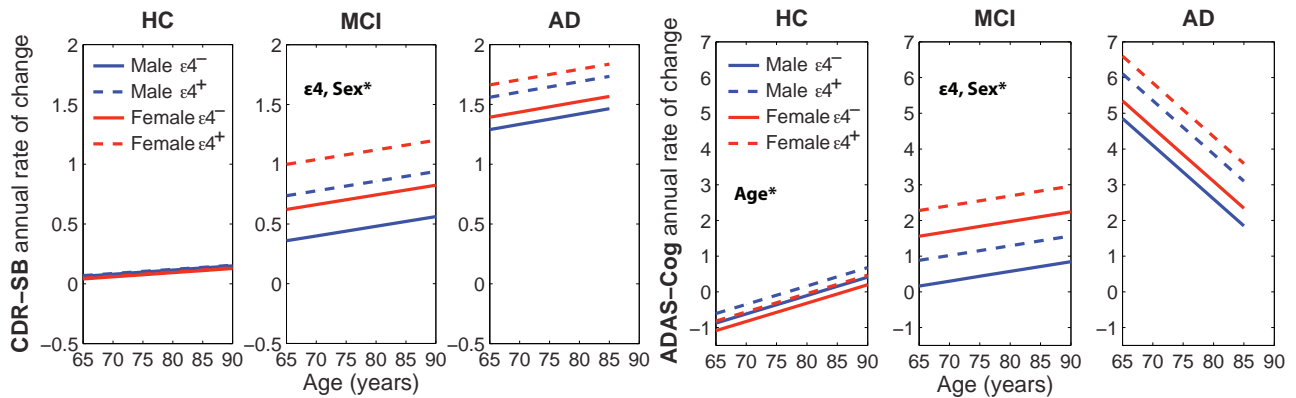


**FIG 2.** Annual rates of cognitive decline, measured with CDR-SB and ADAS-Cog, with respect to age for HC, MCI, and AD participants at their group mean educational level. Where significant, effects of age (slope),  $\epsilon 4$  and sex (shifts along y-axis) are noted by \*. Also see Tables 2–4.

structures, with an additional 0.04%/year loss in the hippocampus, entorhinal cortex, and amygdala for each additional year of age above the group mean (Table 2,  $b_{Age}$  column). The presence of an  $\epsilon 4$  allele showed a large effect on annual rate of change in the same medial temporal regions, contributing an additional  $-0.42\%/year$  loss in the hippocampus,  $-0.52\%/year$  loss in the entorhinal cortex, and  $-0.63\%/year$  loss in the amygdala (Table 2,  $b_{APOE}$  column).

Sex significantly affected rate of change (Table 2,  $b_{Sex}$  column), with women showing higher rates of change than men for the hippocampus (an additional  $-0.25\%/year$ ), the entorhinal cortex ( $-0.49\%/year$ ), and the amygdala ( $-0.53\%/year$ ).

In contrast to the strong effects of  $\epsilon 4$  and sex on medial temporal atrophy rates, we did not find a significant association between these factors and rate of decline on any of the clinical measures in HCs.

The effects of age,  $\epsilon 4$ , and sex on rates of decline in the entorhinal cortex and hippocampus are shown in Fig 1 for the HC, MCI, and AD cohorts, at the group average ages, educational levels, and ADAS-Cog scores. Fig 2 shows the effects of age,  $\epsilon 4$ , and sex on rates of decline in CDR-SB and ADAS-Cog for the 3 cohorts, at the group average ages and educational levels.

#### Rates of Decline in MCI

Table 3 shows the effects of age,  $\epsilon 4$  status, and sex on atrophy rates and rates of clinical decline in the MCI cohort. With the exception

of the hippocampus and amygdala, increased age was associated with a slower rate of decline ( $b_{Age}$  coefficients are positive) for all brain regions examined. Significant effects of  $\epsilon 4$  status were observed for all medial temporal lobe structures and for the inferior parietal cortex, with the additive effect of  $\epsilon 4$  on annual atrophy rate ranging from  $-0.28\%/year$  to  $-0.94\%/year$ . Independent of  $\epsilon 4$ , sex significantly affected rate of change in all brain regions examined, except for the hippocampus: Women atrophied faster than did men, with the magnitude of the additive effect exceeding that of the  $\epsilon 4$  effect.

Significant  $\epsilon 4$  additive contributions to rates of cognitive decline were found for CDR-SB (0.38 points/year), ADAS-Cog (0.72 points/year), and MMSE ( $-0.81$  points/year), whereas effects of female sex were significant for CDR-SB (0.26 points/year) and ADAS-Cog (1.40 points/year).

#### Rates of Decline in AD

Table 4 shows the effects of age,  $\epsilon 4$  status, and sex on rates of atrophy and clinical decline in AD participants. The effect of age on rates of change was significant for all brain regions examined, with increased age associated with lower rates of decline. The additive contribution to rate of decline for  $\epsilon 4$  was significant only for the amygdala ( $-0.91\%/year$ ) but showed a trend toward significance for the hippocampus and entorhinal cortex. Significant sex effects were found for all regions except for the hippocampus and amygdala, with women having higher rates of decline. There were

**Table 2: Effects of age, APOE ε4, and sex on rates of change in HC**

HC Measure	b <sub>0</sub>	b <sub>Cog</sub>	b <sub>Edu</sub>	b <sub>Age</sub> (SE; P)	b <sub>APOE</sub> (SE; P)	b <sub>Sex</sub> (SE; P)
Hippocampus	-0.64 <sup>a</sup>	-0.06 <sup>a</sup>	-0.04 <sup>a</sup>	-0.04 <sup>a</sup> (.01; .002)	-0.42 <sup>a</sup> (.13; .002)	-0.25 <sup>a</sup> (.13; .044)
Amygdala	-0.41 <sup>a</sup>	-0.03	-0.05	-0.04 <sup>a</sup> (.02; .028)	-0.63 <sup>a</sup> (.16; 1 × 10 <sup>-4</sup> )	-0.53 <sup>a</sup> (.15; 5 × 10 <sup>-4</sup> )
Entorhinal	-0.39 <sup>a</sup>	-0.04	-0.05	-0.04 <sup>a</sup> (.02; .025)	-0.52 <sup>a</sup> (.17; .003)	-0.49 <sup>a</sup> (.16; .002)
Inferior parietal	-0.50 <sup>a</sup>	0.00	-0.01	-0.01 (.01; .5)	-0.14 (.10; .2)	0.03 (.10; .8)
Middle temporal	-0.61 <sup>a</sup>	-0.02	-0.02	0.00 (.01; .7)	-0.19 (.12; .1)	-0.02 (.11; .9)
Med-orbito-frontal	-0.48 <sup>a</sup>	-0.03 <sup>a</sup>	-0.01	-0.01 (.01; .5)	-0.18 <sup>a</sup> (.09; .050)	-0.03 (.09; .8)
Whole brain	-0.41 <sup>a</sup>	0.00	-0.01	0.00 (.01; .8)	-0.08 (.06; .2)	-0.03 (.06; .7)
CDR-SB	0.10 <sup>a</sup>	-	-0.01	0.00 (.00; .4)	0.01 (.05; .9)	-0.02 (.04; .6)
ADAS-Cog	-0.29 <sup>a</sup>	-	-0.04	0.05 <sup>a</sup> (.02; .008)	0.27 (.20; .2)	-0.21 (.18; .2)
MMSE	0.02	-	-0.02	-0.02 <sup>a</sup> (.01; .009)	-0.14 (.08; .1)	-0.06 (.08; .4)

**Note:**—b-Values are coefficients in Equation 1; for structural measures, units are annual thickness or volume change as a percentage of baseline size (%/year), and for cognitive measures they are annual score change, per ADAS-Cog unit in the case of b<sub>Cog</sub>, and per year in the case of b<sub>Edu</sub> and b<sub>Age</sub>. ROIs: N = 188; mean age = 76.30 years; mean ADAS-Cog = 6.17; mean years education = 16.02. Clinical: N = 211; mean age = 76.35 years; mean years education = 16.03. SE indicates standard error; Med-orbito-frontal, medial orbito-frontal cortex.

<sup>a</sup> Values significant at P ≤ .05.

Values in the b<sub>0</sub> column show the expected rate of change for an APOE ε4—negative male subject of mean age, mean education, and with a mean level of cognitive function. The remaining columns show the additional rate of change caused by the other factors of interest, and the amount of change experienced by a given individual can be calculated on the basis of the sum of the relevant coefficients. For example, for hippocampal atrophy, each point above the mean baseline ADAS-Cog score contributes an additional 0.06% to the annual atrophy rate; each year of education below the mean contributes an additional 0.04% to annual atrophy rate, as does each year of age above the mean at baseline; presence of an APOE ε4 allele contributes an additional 0.42% to rate of decline, and female sex contributes an additional 0.25%. Thus, an APOE ε4+ female subject, of mean age, education, and cognitive function at baseline, would show a hippocampal atrophy rate of 1.31% (0.64 + 0.42 + 0.25).

**Table 3: Effects of age, APOE ε4, and sex on rates of change in MCI**

MCI Measure	b <sub>0</sub>	b <sub>Cog</sub>	b <sub>Edu</sub>	b <sub>Age</sub> (SE; P)	b <sub>APOE</sub> (SE; P)	b <sub>Sex</sub> (SE; P)
Hippocampus	-1.83 <sup>a</sup>	-0.13 <sup>a</sup>	0.03	0.00 (.02; .8)	-0.40 <sup>a</sup> (.20; .045)	-0.29 (.20; .1)
Amygdala	-1.57 <sup>a</sup>	-0.15 <sup>a</sup>	0.01	0.03 (.02; .1)	-0.94 <sup>a</sup> (.21; 7 × 10 <sup>-6</sup> )	-0.98 <sup>a</sup> (.21; 2 × 10 <sup>-6</sup> )
Entorhinal	-1.78 <sup>a</sup>	-0.12 <sup>a</sup>	0.00	0.04 <sup>a</sup> (.02; .006)	-0.44 <sup>a</sup> (.17; .011)	-0.54 <sup>a</sup> (.17; .002)
Inferior parietal	-0.91 <sup>a</sup>	-0.08 <sup>a</sup>	0.02	0.06 <sup>a</sup> (.01; 2 × 10 <sup>-6</sup> )	-0.28 <sup>a</sup> (.14; .040)	-0.40 <sup>a</sup> (.14; .004)
Middle temporal	-1.40 <sup>a</sup>	-0.11 <sup>a</sup>	0.00	0.07 <sup>a</sup> (.02; 9 × 10 <sup>-6</sup> )	-0.28 (.18; .1)	-0.52 <sup>a</sup> (.17; .003)
Med-orbito-frontal	-0.78 <sup>a</sup>	-0.04 <sup>a</sup>	0.04 <sup>a</sup>	0.02 <sup>a</sup> (.01; .023)	0.03 (.11; .8)	-0.24 <sup>a</sup> (.11; .026)
Whole brain	-0.74 <sup>a</sup>	-0.04 <sup>a</sup>	0.01	0.02 <sup>a</sup> (.01; 4 × 10 <sup>-4</sup> )	-0.09 (.08; .2)	-0.17 <sup>a</sup> (.08; .22)
CDR-SB	0.46 <sup>a</sup>	-	0.01	0.01 (.01; .4)	0.38 <sup>a</sup> (.11; 6 × 10 <sup>-4</sup> )	0.26 <sup>a</sup> (.11; .021)
ADAS-Cog	0.49 <sup>a</sup>	-	0.00	0.03 (.03; .3)	0.72 <sup>a</sup> (.31; .022)	1.40 <sup>a</sup> (.32; 2 × 10 <sup>-5</sup> )
MMSE	-0.35 <sup>a</sup>	-	0.02	0.02 (.02; .4)	-0.81 <sup>a</sup> (.20; 4 × 10 <sup>-5</sup> )	-0.34 (.20; .1)

**Note:**—See Table 2 for units and key.

<sup>a</sup> Values significant at P ≤ .05.

ROIs: N = 273; mean age = 76.65 years; mean ADAS-Cog = 11.68; mean years education = 15.61. Cognitive: N = 211; mean age = 76.84 years; mean years education = 15.63.

**Table 4: Effects of age, APOE ε4, and sex on rates of change in AD**

AD Measure	b <sub>0</sub>	b <sub>Cog</sub>	b <sub>Edu</sub>	b <sub>Age</sub> (SE; P)	b <sub>APOE</sub> (SE; P)	b <sub>Sex</sub> (SE; P)
Hippocampus	-2.80 <sup>a</sup>	-0.06 <sup>a</sup>	0.03	0.06 <sup>a</sup> (.03; .028)	-0.62 (.35; .08)	-0.49 (.30; .1)
Amygdala	-2.73 <sup>a</sup>	-0.05	0.06	0.06 <sup>a</sup> (.03; .043)	-0.91 <sup>a</sup> (.36; .012)	-0.41 (.31; .2)
Entorhinal	-2.65 <sup>a</sup>	-0.04	-0.02	0.04 <sup>a</sup> (.02; .045)	-0.43 (.25; .09)	-0.49 <sup>a</sup> (.22; .025)
Inferior parietal	-1.68 <sup>a</sup>	-0.06 <sup>a</sup>	-0.03	0.15 <sup>a</sup> (.02; <10 <sup>-6</sup> )	-0.25 (.24; .3)	-0.69 <sup>a</sup> (.21; .001)
Middle temporal	-2.48 <sup>a</sup>	-0.10 <sup>a</sup>	-0.05	0.17 <sup>a</sup> (.02; <10 <sup>-6</sup> )	-0.30 (.29; .3)	-0.88 <sup>a</sup> (.25; .001)
Med-orbito-frontal	-0.96 <sup>a</sup>	-0.02	-0.02	0.05 <sup>a</sup> (.02; .008)	0.04 (.24; .9)	-0.64 <sup>a</sup> (.21; .002)
Whole brain	-0.97 <sup>a</sup>	-0.04 <sup>a</sup>	-0.01	0.06 <sup>a</sup> (.01; <10 <sup>-6</sup> )	-0.19 (.14; .2)	-0.38 <sup>a</sup> (.12; .002)
CDR-SB	1.39 <sup>a</sup>	-	0.11 <sup>a</sup>	0.01 (.03; .8)	0.27 (.33; .4)	0.10 (.29; .7)
ADAS-Cog	3.20 <sup>a</sup>	-	0.29	-0.15 (.08; .069)	1.25 (.98; .2)	0.49 (.89; .6)
MMSE	-1.97 <sup>a</sup>	-	-0.16	0.13 <sup>a</sup> (.05; .007)	-0.20 (.57; .7)	0.03 (.52; 1.0)

**Note:**—See Table 2 for units and key.

<sup>a</sup> Values significant at P ≤ .05.

ROIs: N = 105; mean age = 75.74 years; mean ADAS-Cog = 18.49; mean years education = 14.83. Cognitive: N = 144; mean age = 75.99 years; mean years education = 14.70.

no significant effects of ε4 status or sex on rate of decline on any of the cognitive measures.

#### Effects of APOE ε4 and Sex on Baseline CSF and Clinical Measures

Controlling for age and sex, ε4 carriers showed significantly lower CSF Aβ concentrations than noncarriers, with the magnitude of the effect decreasing from HC to patients with MCI to those with AD (Fig 3 and On-line Table 5A). Relative to noncarriers, ε4

carriers showed significantly higher CSF concentrations of τ and p-τ in the HC and MCI cohorts, but no significant differences were found for these biomarkers in the AD cohort.

Controlling for age and ε4 status, there were no significant effects of sex on CSF Aβ or p-τ concentrations in any of the cohorts (Fig 3 and On-line Table 5A). For τ, the effect of sex approached significance for the MCI cohort only (P = .060), with women showing higher τ concentrations than men.

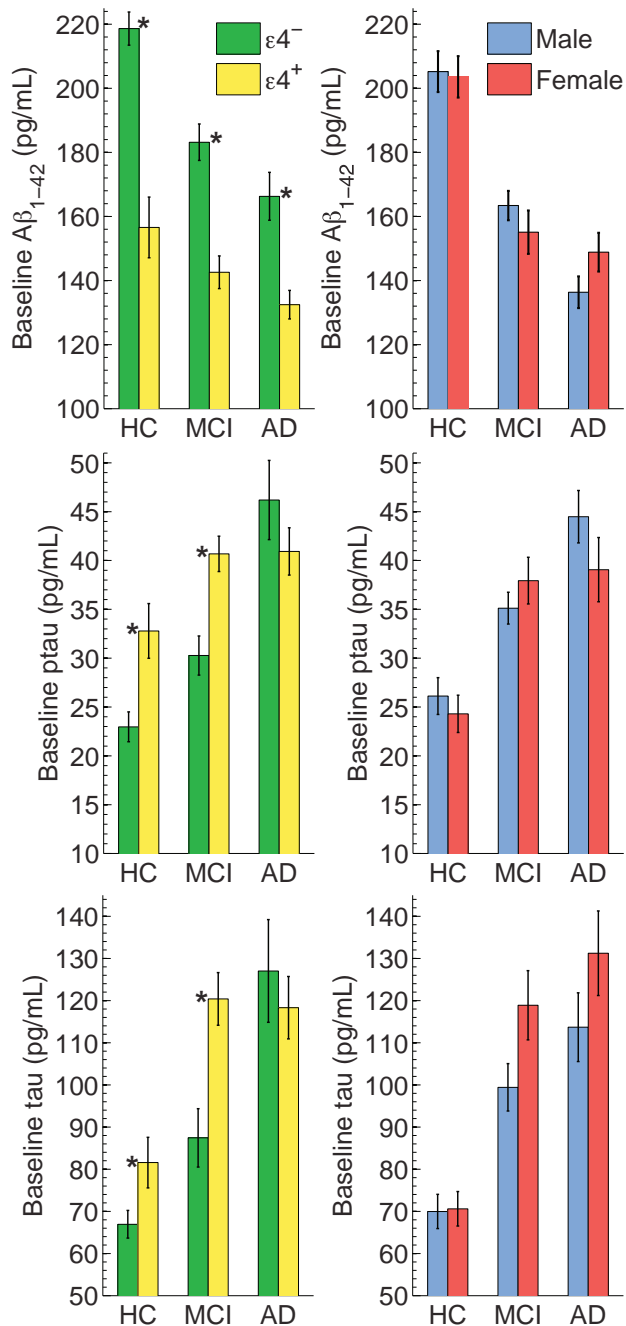


**FIG 3.** Baseline CSF values for A $\beta$ , p- $\tau$ , and  $\tau$ , by  $\epsilon 4$  status (left) and sex (right) for the HC, MCI, and AD cohorts. Numeric values are in On-line Table 5A. \*Significant differences.

Controlling for age and sex, performance on the clinical tests was significantly affected by  $\epsilon 4$  status in MCI participants only, with carriers showing worse performance than noncarriers for CDR-SB and ADAS-Cog, and showing a trend for worse performance on MMSE (On-line Table 5A and On-line Fig 1). Controlling for age and  $\epsilon 4$  status, no sex differences were found on the clinical tests in the patient cohorts, though MCI showed a trend toward significance for MMSE ( $P = .072$ ), with women performing more poorly.

#### Effects of Baseline CSF A $\beta$ and p- $\tau$ on Rates of Decline

With A $\beta$  in the model, significant effects of  $\epsilon 4$  and sex remained for MCI and AD participants, signifying that APOE  $\epsilon 4$  exerts an

effect on atrophy rate in AD independent of its relation to A $\beta$  (On-line Tables 3A–C). For HCs, however, there were no significant effects of  $\epsilon 4$  with CSF A $\beta$  in the model. Adding an additional term for p- $\tau$  concentrations did not alter these results (On-line Tables 4A–C), but this term was found to be significant in MCI for the amygdala, entorhinal cortex, ADAS-Cog, and MMSE, and in AD for the entorhinal cortex, rendering the A $\beta$  term insignificant for all measures.

#### DISCUSSION

Our results show that changes in brain structure and function related to aging and AD do not progress uniformly across individuals but instead depend on age, sex, and APOE  $\epsilon 4$  status. Age differences in progressive atrophy and clinical decline, whereby older patients with MCI and AD decline at a slower rate than younger patients but older healthy adults decline at a faster rate than younger healthy adults, have been previously reported.<sup>3,33</sup> However, our finding that sex differences in atrophy rates are as large as differences associated with the well-known genetic risk factor, APOE  $\epsilon 4$ , is novel, and has important implications for clinical practice, therapeutics research, and for advancing mechanistic understanding of AD.

The results showed that in all stages, from healthy aging through AD dementia, women had higher rates of brain atrophy than men, and the magnitude of the sex differences was at least as large as the magnitude of the APOE  $\epsilon 4$  effects. In HCs, sex differences were restricted to the medial temporal areas first affected in AD. In MCI and AD, the sex differences were more widespread, with weaker effects observed in medial temporal areas than in other brain regions. Additionally in MCI, in women compared with men, higher rates of atrophy were accompanied by higher rates of clinical decline.

These findings are consistent with prior large epidemiology studies<sup>5-7,11,34</sup> that showed higher rates of prevalence and incidence of AD in women than in men, with the differences between men and women comparable in magnitude to those between  $\epsilon 4$  carriers and noncarriers. They are also consistent with a recent meta-analysis that found lower cognitive performance for women than men diagnosed with AD.<sup>15</sup> A neuropathologic study<sup>35</sup> showed that women, especially if  $\epsilon 4$  carriers, are at higher risk of both neurofibrillary tangle (NFT) and amyloid plaque neuropathology than men in the earliest stages of AD (NFT stages I–III<sup>26</sup>).

One possible explanation for the sex differences in HCs, in which women showed faster rates of atrophy in medial temporal areas, is that the HC women may be showing early signs of AD-related neurodegeneration. However, the lack of sex differences in baseline CSF biomarkers of AD pathology in HCs does not support this view. The finding that CSF biomarkers did not explain the faster rates of decline occurring in women in any of the diagnostic groups suggests that other factors must be contributing to the sex differences. It has been argued that estrogens stimulate  $\alpha$ -secretase activity and thus enhance nonamyloidogenic processing of amyloid- $\beta$  precursor protein<sup>36,37</sup>; the diminution in estrogen levels after menopause would then contribute to higher levels of AD pathology and poorer cognitive performance in women than in men. However, further research is needed to elucidate the basis of the observed sex differences.

The *APOE*  $\epsilon 4$  effects observed in the present study on longitudinal rates of change across cohorts are consistent with the elevated burdens of amyloid and  $\tau$  pathology observed for  $\epsilon 4$  carriers compared with noncarriers at baseline. These baseline differences in CSF biomarkers between carriers and noncarriers agree with earlier reports<sup>38,39</sup> and with neuropathologic findings that  $\epsilon 4$  was associated with greater senile plaque and neurofibrillary tangle pathology in the elderly.<sup>14</sup> *APOE*  $\epsilon 4$  has further been associated with a higher plaque stage for a given age and allocortical NFT stage (Braak stages I–III, which correspond roughly with HC and early MCI) for  $\epsilon 4$  carriers compared with noncarriers, whereas at the later isocortical NFT stages (corresponding to late MCI and dementia),  $\epsilon 4$  gene dose was not an important predictor of pathology burden,<sup>35,40</sup> suggesting that  $\epsilon 4$  might exert its strongest effects in the prodromal stages of AD. Recently, Koffie et al<sup>41</sup> have shown that the  $\epsilon 4$  gene increases the amount of the synaptotoxic oligomeric  $A\beta$  in neuropil and its colocalization at synapses, even in nondemented control subjects, leading to synaptic injury and loss, a strong correlate of cognitive decline.<sup>42</sup> Our results showing elevated atrophy in  $\epsilon 4$  carriers generally, and our finding of marginally significant higher atrophy rates in prodementia stages of AD for the medial orbito-frontal cortex<sup>43</sup> and inferior parietal lobule, sites of early amyloid deposition,<sup>26</sup> are consistent with these neuropathologic findings.

How  $\epsilon 4$  affects rates of cognitive decline across the preclinical, prodromal, and dementia stages of AD has been unclear,<sup>20,44,45</sup> but some studies have suggested that the effect of  $\epsilon 4$  is stronger in the earlier phases of the disorder.<sup>39,46,47</sup> Our results suggest that the accelerating effect of  $\epsilon 4$  on rates of decline diminishes with advancing disease stage, which comports with an earlier finding that  $\epsilon 4$  gene dose does not have a significant effect on the duration of AD,<sup>20</sup> and supports the hypothesis that as neurodegeneration advances, it becomes increasingly independent of initiating events.<sup>48</sup>

This study has several limitations: The ADNI sample is not representative of the general population, and there was sex bias in MCI enrollment, with men outnumbering women. The HC and AD cohorts, however, showed more balanced sex representation. Because similar sex effects were observed across groups, they are unlikely to have arisen from enrollment bias. There is insufficient information within ADNI to address issues of whether history of hormone replacement therapy or number of years since menopause may have influenced the observed sex differences. Finally, statistical power was limited with respect to analyses of CSF biomarker data. Larger population-based studies that can systematically address hormonal issues, and other medical issues that may differ between the sexes, are needed to elucidate the basis of the observed sex differences in rate of atrophy and cognitive decline.

## CONCLUSIONS

Our results show that women and *APOE*  $\epsilon 4$  carriers in ADNI have higher rates of decline in normal aging, MCI, and AD, and that these effects are not fully explained by baseline CSF concentrations of AD-related proteins. Because two-thirds of AD cases in the United States are women, and because the higher rates of decline in women compared with men were at least as large as those related to the major genetic risk factor, *APOE*  $\epsilon 4$ , it is of

particular importance that sex differences in rates of decline in aging and AD be taken into account in the clinical setting and in therapeutics research. Greater understanding of the mechanistic basis of these differences likely will facilitate further understanding of AD etiology.

Disclosures: Dominic Holland—RELATED: Grant: NIH NIA,\* Comments: This research was supported by NIH grants R01AG031224, R01AG22381, U54NS056883, P50NS22343, and P50MH081755 (A.M.D.); NIA K01AG029218 (LKM); NIH-NIBIB T32 EB005970 (RSD); UNRELATED: Grants/Grants Pending: NIH\*; Patents (planned, pending or issued): UCSD,\* Comments: A patent application for Quarc, a method to quantify anatomical regional change developed at UCSD, has been filed through the UCSD Technology Transfer Office ("Longitudinal registration of anatomy in magnetic resonance imaging"; Application number: 12/742,642; Publication number: US 2010/0259263 A1). Rahul Desikan—RELATED: Grant: T32 EB005970,\* Comments: NIH Training Grant. Anders Dale—RELATED: Grant: UCSD,\* Comments: Numerous NIH grants as PI and Co-I; UNRELATED: Grants/Grants Pending: UCSD\*; Patents (planned, pending or issued): UCSD,\* MGH,\* Comments: I am an inventor of a provisional patent on Restriction Spectrum Imaging, and other issued patents in the areas of MRI acquisition and post-processing; Stock/Stock Options: CorTechs Labs Inc. Comments: I am a founder and hold equity in CorTechs Labs, Inc, and also serve on its Scientific Advisory Board. The terms of this arrangement have been reviewed and approved by UCSD in accordance with its conflict-of-interest policies; Other: UCSD\* Comments: I am the principal investigator of a research agreement between UCSD and General Electric Medical Systems. Linda McEvoy—RELATED: Grant: National Institute on Aging,\* Comments: Grant support from K01AG029218, R01AG22381; Support for Travel to Meetings for the Study or Other Purposes: National Institute on Aging,\* Comments: Grants listed above used to support presentation of data at 2012 Alzheimer's Association International conference (\*money paid to institution).

A.M.D. is a founder and holds equity in CorTechs Labs, Inc, and also serves on its Scientific Advisory Board. The terms of this arrangement have been reviewed and approved by the University of California, San Diego, in accordance with its conflict of interest policies. McEvoy's spouse is President of CorTechs Labs, Inc.

Data used in preparation of this article were obtained from the ADNI database (adni.loni.ucla.edu). As such, the investigators within the ADNI contributed to the design and implementation of ADNI and/or provided data but did not participate in analysis or writing of this report. A complete listing of ADNI investigators can be found at: [http://adni.loni.ucla.edu/wp-content/uploads/how\\_to\\_apply/ADNI\\_Acknowledgement\\_List.pdf](http://adni.loni.ucla.edu/wp-content/uploads/how_to_apply/ADNI_Acknowledgement_List.pdf).

## REFERENCES

- Duker AP, Espay AJ, Wszolek ZK, et al. **Atypical motor and behavioral presentations of Alzheimer disease: a case-based approach.** *Neurologist* 2012;18:266–72
- Murray ME, Graff-Radford NR, Ross OA, et al. **Neuropathologically defined subtypes of Alzheimer's disease with distinct clinical characteristics: a retrospective study.** *Lancet Neurol* 2011;10:785–96
- Holland D, Desikan RS, Dale AM, et al. **Rates of decline in Alzheimer disease decrease with age.** *PLoS One* 2012;7:e42325
- van der Flier WM, Pijnenburg YA, Fox NC, et al. **Early-onset versus late-onset Alzheimer's disease: the case of the missing APOE varepsilon4 allele.** *Lancet Neurol* 2011;10:280–88
- Alzheimer's Association. 2013 Alzheimer's disease facts and figures. *Alzheimers Dement* 2013;9:208–45
- Miech RA, Breitner JC, Zandi PP, et al. **Incidence of AD may decline in the early 90s for men, later for women: the Cache County study.** *Neurology* 2002;58:209–18
- Farrer LA, Cupples LA, Haines JL, et al. **Effects of age, sex, and ethnicity on the association between apolipoprotein E genotype and Alzheimer disease: a meta-analysis: APOE and Alzheimer Disease Meta Analysis Consortium.** *JAMA* 1997;278:1349–56
- Seshadri S, Wolf PA, Beiser A, et al. **Lifetime risk of dementia and Alzheimer's disease: the impact of mortality on risk estimates in the Framingham Study.** *Neurology* 1997;49:1498–504
- Andersen K, Launer LJ, Dewey ME, et al. **Gender differences in the incidence of AD and vascular dementia: the EURODEM Studies: EURODEM Incidence Research Group.** *Neurology* 1999;53:1992–97

10. Plassman BL, Langa KM, McCammon RJ, et al. **Incidence of dementia and cognitive impairment, not dementia in the United States.** *Ann Neurol* 2011;70:418–26
11. Breitner JC, Wyse BW, Anthony JC, et al. **APOE-epsilon4 count predicts age when prevalence of AD increases, then declines: the Cache County Study.** *Neurology* 1999;53:321–31
12. Barnes LL, Wilson RS, Schneider JA, et al. **Gender, cognitive decline, and risk of AD in older persons.** *Neurology* 2003;60:1777–81
13. Hebert LE, Scherr PA, McCann JJ, et al. **Is the risk of developing Alzheimer's disease greater for women than for men?** *Am J Epidemiol* 2001;153:132–36
14. Ghebremedhin E, Schultz C, Thal DR, et al. **Gender and age modify the association between APOE and AD-related neuropathology.** *Neurology* 2001;56:1696–701
15. Irvine K, Laws KR, Gale TM, et al. **Greater cognitive deterioration in women than men with Alzheimer's disease: a meta analysis.** *J Clin Exp Neuropsychol* 2012;34:989–98
16. Corder EH, Saunders AM, Strittmatter WJ, et al. **Gene dose of apolipoprotein E type 4 allele and the risk of Alzheimer's disease in late onset families.** *Science* 1993;261:921–23
17. Verghese PB, Castellano JM, Holtzman DM. **Apolipoprotein E in Alzheimer's disease and other neurological disorders.** *Lancet Neurol* 2011;10:241–52
18. Sando SB, Melquist S, Cannon A, et al. **APOE epsilon 4 lowers age at onset and is a high risk factor for Alzheimer's disease: a case control study from central Norway.** *BMC Neurol* 2008;8:9
19. Khachaturian AS, Corcoran CD, Mayer LS, et al. **Apolipoprotein E epsilon4 count affects age at onset of Alzheimer disease, but not lifetime susceptibility: the Cache County Study.** *Arch Gen Psychiatry* 2004;61:518–24
20. Corder EH, Saunders AM, Strittmatter WJ, et al. **Apolipoprotein E, survival in Alzheimer's disease patients, and the competing risks of death and Alzheimer's disease.** *Neurology* 1995;45:1323–28
21. Holland D, McEvoy LK, Dale AM. **Unbiased comparison of sample size estimates from longitudinal structural measures in ADNI.** *Hum Brain Mapp* 2012;33:2586–602
22. Holland D, Dale AM. **Nonlinear registration of longitudinal images and measurement of change in regions of interest.** *Med Image Anal* 2011;15:489–97
23. Holland D, McEvoy LK, Desikan RS, et al. **Enrichment and stratification for pre-dementia Alzheimer disease clinical trials.** *PLoS One* 2012;7:e47739
24. Arriagada PV, Marzloff K, Hyman BT. **Distribution of Alzheimer-type pathologic changes in nondemented elderly individuals matches the pattern in Alzheimer's disease.** *Neurology* 1992;42:1681–88
25. Arnold SE, Hyman BT, Flory J, et al. **The topographical and neuro-anatomical distribution of neurofibrillary tangles and neuritic plaques in the cerebral cortex of patients with Alzheimer's disease.** *Cereb Cortex* 1991;1:103–16
26. Braak H, Braak E. **Frequency of stages of Alzheimer-related lesions in different age categories.** *Neurobiol Aging* 1997;18:351–57
27. Williams MM, Storandt M, Roe CM, et al. **Progression of Alzheimer's disease as measured by Clinical Dementia Rating Sum of Boxes scores.** *Alzheimers Dement* 2013;9(1 Suppl):S39–44
28. Morris JC. **The Clinical Dementia Rating (CDR): current version and scoring rules.** *Neurology* 1993;43:2412–14
29. Rosen WG, Mohs RC, Davis KL. **A new rating scale for Alzheimer's disease.** *Am J Psychiatry* 1984;141:1356–64
30. Rockwood K, Fay S, Gorman M, et al. **The clinical meaningfulness of ADAS-Cog changes in Alzheimer's disease patients treated with donepezil in an open-label trial.** *BMC Neurol* 2007;7:26
31. Folstein MF, Folstein SE, McHugh PR. **"Mini-mental state": a practical method for grading the cognitive state of patients for the clinician.** *J Psychiatr Res* 1975;12:189–98
32. Fitzmaurice GM, Laird NM, Ware JH. *Applied Longitudinal Analysis.* Hoboken, New Jersey: Wiley; 2011
33. Bernick C, Cummings J, Raman R, et al. **Age and rate of cognitive decline in Alzheimer disease: implications for clinical trials.** *Arch Neurol* 2012;69:901–05
34. Plassman BL, Langa KM, Fisher GG, et al. **Prevalence of dementia in the United States: the aging, demographics, and memory study.** *Neuroepidemiology* 2007;29:125–32
35. Corder EH, Ghebremedhin E, Taylor MG, et al. **The biphasic relationship between regional brain senile plaque and neurofibrillary tangle distributions: modification by age, sex, and APOE polymorphism.** *Ann N Y Acad Sci* 2004;1019:24–28
36. Yaffe K, Haan M, Byers A, et al. **Estrogen use, APOE, and cognitive decline: evidence of gene-environment interaction.** *Neurology* 2000;54:1949–54
37. Xu H, Gouras GK, Greenfield JP, et al. **Estrogen reduces neuronal generation of Alzheimer beta-amyloid peptides.** *Nat Med* 1998;4:447–51
38. Prince JA, Zetterberg H, Andreasen N, et al. **APOE epsilon4 allele is associated with reduced cerebrospinal fluid levels of Abeta42.** *Neurology* 2004;62:2116–18
39. Kester MI, Blankenstein MA, Bouwman FH, et al. **CSF biomarkers in Alzheimer's disease and controls: associations with APOE genotype are modified by age.** *J Alzheimers Dis* 2009;16:601–07
40. Walker LC, Pahnke J, Madauss M, et al. **Apolipoprotein E4 promotes the early deposition of Abeta42 and then Abeta40 in the elderly.** *Acta Neuropathol* 2000;100:36–42
41. Koffie RM, Hashimoto T, Tai HC, et al. **Apolipoprotein E4 effects in Alzheimer's disease are mediated by synaptotoxic oligomeric amyloid-beta.** *Brain* 2012;135:2155–68
42. DeKosky ST, Scheff SW. **Synapse loss in frontal cortex biopsies in Alzheimer's disease: correlation with cognitive severity.** *Ann Neurol* 1990;27:457–64
43. Van Hoesen GW, Parvizi J, Chu CC. **Orbitofrontal cortex pathology in Alzheimer's disease.** *Cereb Cortex* 2000;10:243–51
44. Saunders AM. **Apolipoprotein E and Alzheimer disease: an update on genetic and functional analyses.** *J Neuropathol Exp Neurol* 2000;59:751–58
45. Growdon JH, Locascio JJ, Corkin S, et al. **Apolipoprotein E genotype does not influence rates of cognitive decline in Alzheimer's disease.** *Neurology* 1996;47:444–48
46. Cosentino S, Scarmeas N, Helzner E, et al. **APOE epsilon 4 allele predicts faster cognitive decline in mild Alzheimer disease.** *Neurology* 2008;70:1842–49
47. Juva K, Verkkoniemi A, Viramo P, et al. **APOE epsilon4 does not predict mortality, cognitive decline, or dementia in the oldest old.** *Neurology* 2000;54:412–15
48. Hyman BT. **Amyloid-dependent and amyloid-independent stages of Alzheimer disease.** *Arch Neurol* 2011;68:1062–64

# Changes of Pituitary Gland Volume in Kennedy Disease

C.C. Pieper, I.K. Teismann, C. Konrad, W.L. Heindel, and H. Schiffbauer



## ABSTRACT

**BACKGROUND AND PURPOSE:** Kennedy disease is a rare X-linked neurodegenerative disorder caused by a CAG repeat expansion in the first exon of the androgen-receptor gene. Apart from neurologic signs, this mutation can cause a partial androgen insensitivity syndrome with typical alterations of gonadotropic hormones produced by the pituitary gland. The aim of the present study was therefore to evaluate the impact of Kennedy disease on pituitary gland volume under the hypothesis that endocrinologic changes caused by partial androgen insensitivity may lead to morphologic changes (ie, hypertrophy) of the pituitary gland.

**MATERIALS AND METHODS:** Pituitary gland volume was measured in sagittal sections of 3D T1-weighted 3T-MR imaging data of 8 patients with genetically proven Kennedy disease and compared with 16 healthy age-matched control subjects by use of Multitracer by a blinded, experienced radiologist. The results were analyzed by a univariate ANOVA with total brain volume as a covariant. Furthermore, correlation and linear regression analyses were performed for pituitary volume, patient age, disease duration, and CAG repeat expansion length. Intraobserver reliability was evaluated by means of the Pearson correlation coefficient.

**RESULTS:** Pituitary volume was significantly larger in patients with Kennedy disease ( $636 [\pm 90] \text{ mm}^3$ ) than in healthy control subjects ( $534 [\pm 91] \text{ mm}^3$ ) ( $P = .041$ ). There was no significant difference in total brain volume ( $P = .379$ ). Control subjects showed a significant decrease in volume with age ( $r = -0.712, P = .002$ ), whereas there was a trend to increasing gland volume in patients with Kennedy disease ( $r = 0.443, P = .272$ ). Gland volume correlated with CAG repeat expansion length in patients ( $r = 0.630, P = .047$ ). The correlation coefficient for intraobserver reliability was 0.94 ( $P < .001$ ).

**CONCLUSIONS:** Patients with Kennedy disease showed a significantly higher pituitary volume that correlated with the CAG repeat expansion length. This could reflect hypertrophy as the result of elevated gonadotropic hormone secretion caused by the androgen receptor mutation with partial androgen insensitivity.

**ABBREVIATIONS:** KD = Kennedy disease; AR = androgen receptor; LH = lutropin; FSH = follicle-stimulating hormone; SHBG = sex hormone-binding globulin

Spinobulbar muscular atrophy (Kennedy disease [KD]) is a rare X-linked neurodegenerative disorder of mainly spinal and bulbar motoneurons. It is caused by a CAG repeat expansion in the first exon of the androgen receptor (AR). Apart from typical neurologic signs such as a progressive wasting of proximal muscles and bulbar symptoms, this mutation causes a partial andro-

gen insensitivity syndrome in >80% of patients, with gynecomastia being the most prominent symptom.<sup>1-3</sup>

Androgen insensitivity syndromes are typically associated with normal or elevated testosterone and estrogen levels, with elevated lutropin (LH) and sex hormone-binding globulin (SHBG) levels. This pattern can also be found in patients with KD.<sup>3</sup>

Battaglia et al<sup>4</sup> described a case of a 59-year-old patient with KD who presented with typical endocrine symptoms, but without any apparent physical signs of neurodegeneration.

The pituitary gland is known to produce hormones such as LH, which control the activity of other endocrine glands.

Because of high spatial and contrast resolution, MR imaging is currently the technique best suited to examine the pituitary gland.<sup>5-8</sup> The normal size of the gland in a healthy adult is approximately 5–10 mm in height, 10 mm in length, and 10–15 mm in width.<sup>9</sup>

Received December 31, 2012; accepted after revision February 25, 2013.

From the Department of Radiology (C.C.P.), University of Bonn, Germany; Departments of Radiology (C.C.P., W.L.H., H.S.) and Neurology (I.K.T.), University of Muenster, Germany; and Department of Psychiatry and Psychotherapy (C.K.), University of Marburg, Germany.

Please address correspondence to Hagen Schiffbauer, MD, Diagnostic Imaging Center Muenster, Loerstr 19, 48143 Muenster, Germany; e-mail: schiffbauer@uni-muenster.de

 Indicates article with supplemental on-line figures

<http://dx.doi.org/10.3174/ajnr.A3591>

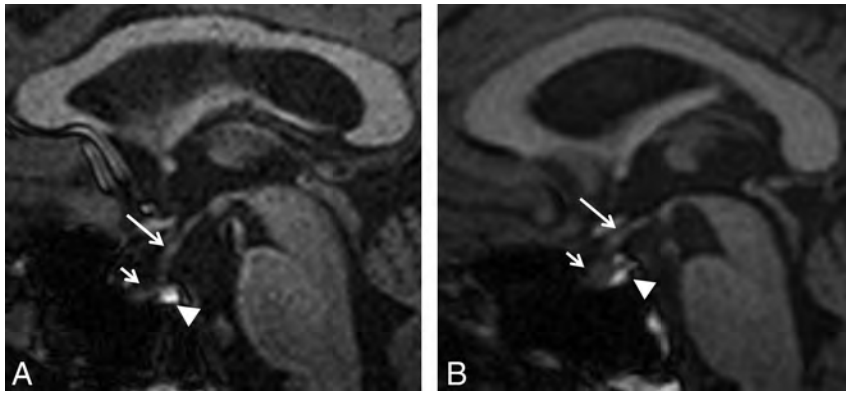


**FIG 1.** T1-weighted MR imaging shows midsagittal section of a normal subject, 57 years of age (A), and a patient of the same age with Kennedy disease (B). Infundibulum (long arrow), anterior lobe (short arrow), and posterior lobe (arrowhead) of the pituitary gland are shown.

All patients had dysphagia and 4 of 8 had dysarthria, as signs of bulbar neuron involvement.

Signs of partial androgen insensitivity were present in all patients. Six of 8 presented with severe gynecomastia. One patient had erectile dysfunction, and 4 of 8 fathered children. Hormone levels were determined in 2 patients previous to the first MR imaging examination, which showed elevated testosterone of 12.47 ng/mL (normal values <7.99 ng/mL) and SHBG in one patient and values at the upper limit of the normal range for testosterone and LH in the other.

### Pituitary gland volumetry

	Mean	F	P
Total brain volume			
Patients	1134 ( $\pm 69$ ) voxel	0.81	.379
Control subjects	1121 ( $\pm 83$ ) voxel		
Pituitary gland volume			
Measurement 1			
Patients	636 ( $\pm 90$ ) mm	3.72	.041
Control subjects	534 ( $\pm 91$ ) mm		
Measurement 2			
Patients	647 ( $\pm 98$ ) mm	5.10	.016
Control subjects	531 ( $\pm 84$ ) mm		

**Note.**—Results of the univariate ANOVA with total brain volume as covariant (*F* value: variance of the group means/mean of the within-group variances). Results are considered statistically significant in cases of  $P < .05$ .

It is well established that dysfunctions such as primary hypothyroidism leading to elevated thyroid-stimulating hormone levels are associated with an enlargement of the pituitary gland.<sup>10</sup>

The aim of the present study was to evaluate the impact of KD on the volume of the pituitary gland as measured by MR imaging under the hypothesis that the described changes in gonadotropic hormone levels in KD can lead to morphologic changes, namely, hypertrophy of the pituitary gland. To the best of our knowledge, this is the first study to examine the volume of the pituitary gland in patients with KD.

## MATERIALS AND METHODS

### Patients

The patient group consisted of 8 men (age, 44–73 years; mean, 53.8) with genetically proven KD with no neurologic comorbidity. The control group included 16 age-matched healthy men (42–77 years; mean, 54.4). Informed consent was obtained from each subject. The study was approved by the local ethics committee.

All patients were clinically examined at the Department of Neurology.

All 8 patients showed typical symptoms of KD reflecting neurodegeneration. Disease duration ranged from 2–19 years (mean,  $10.5 \pm 6.2$  years). Muscle weakness was present in 100% to different degrees. Muscular atrophy and fasciculations were most prominent in the tongue in 6 of 8 and 7 of 8 patients, respectively.

### Data Acquisition

MR imaging examinations were performed on a 3T Gyroscan Intera (Philips, Best, the Netherlands) with a transmit-receiver head coil. A 3D T1-weighted turbo-field-echo sequence was used for pituitary gland volumetry (matrix,  $512 \times 512$ ; FOV,  $256 \times 256$  mm<sup>2</sup>; TR, 7.4 ms; TE, 3.4 ms; 320 contiguous sagittal sections; section thickness, 0.5 mm; voxel size,  $0.5 \times 0.5 \times 0.5$  mm<sup>3</sup>, flip angle, 9°).

Pituitary gland volume was measured in sagittal sections by use of Multitracer (LONI Software, version 1.0; <http://www.loni.ucla.edu/Software/MultiTracer>)<sup>11</sup> by a blinded, experienced radiologist (Fig 1A–B). Measurements were repeated in the same fashion after 4 to 6 weeks.

### Statistical Analysis

The volumetric data were analyzed by a univariate ANOVA with total brain volume as a covariant in a group comparison of patients and control subjects by use of SPSS 17.0 (IBM, Armonk, New York). Patient data, namely, pituitary volume, patient age, disease duration, and CAG repeat expansion length, were then also entered into a linear regression model.

Furthermore, a 2-tailed correlation analysis between pituitary gland volume and age of patients and control subjects, as well as a 1-tailed analysis for CAG repeat length in patients was performed.

Intraobserver reliability was evaluated with use of the Pearson correlation coefficient.

## RESULTS

Patients with KD had a mean pituitary volume of  $636 (\pm 90)$  mm<sup>3</sup>, whereas healthy control subjects had a volume of  $534 (\pm 91)$  mm<sup>3</sup>, respectively. Statistical analysis showed pituitary volume to be significantly higher in patients with KD than in healthy control subjects ( $P = .041$ ). There was no significant difference in total brain volume ( $P = .379$ ) (Table 1 and On-line Fig 1).

The correlation analysis showed that in healthy control subjects, pituitary gland volume was significantly lower in older individuals (Pearson correlation coefficient  $r = -0.712$ ,  $P = .002$ ), whereas patients with KD showed a trend toward increasing gland volume with age ( $r = 0.443$ ) but without reaching statistical significance ( $P = .272$ ) (On-line Fig 2).

Gland volume also correlated significantly with CAG repeat expansion length in the patient group ( $r = 0.630$ ,  $P = .047$ ) (On-Line Fig 3).

Multiple linear regression showed that the CAG repeat expansion length was the only predictor of pituitary volume. Patient age and disease duration were excluded from the model and therefore were not predictive factors of pituitary volume in KD.

The overall Pearson correlation for intraobserver reliability was 0.94 ( $P < .001$ ), which is generally considered to reflect an excellent reproducibility.

## DISCUSSION

In patients with KD, neurodegeneration has been attributed to a CAG repeat expansion in the AR. This mutation leads to intranuclear accumulation of AR, which can induce transcriptional dysfunction (toxic gain of function) causing cell death resulting in neurologic symptoms, whereas partial androgen insensitivity, on the other hand, appears to be caused by a loss of function from the same mutation in the first exon of the AR.<sup>12-14</sup> This loss of function leads to endocrine disturbances with symptoms such as gynecomastia, testicular atrophy with reduced fertility, diabetes mellitus, or hypercholesterolemia.<sup>1,15-17</sup> Our work is in line with previous reports on endocrinologic changes in patients with KD, with 6 of 8 patients presenting with gynecomastia, 1 patient presenting with erectile dysfunction, and 2 patients presenting with proven high testosterone levels. For instance, Dejager et al<sup>3</sup> reported that >80% of cases presented with physical signs of androgen insensitivity, especially gynecomastia, undermasculinization, testicular hypotrophy, and reduced fertility, in a survey of 22 patients with KD. In most patients, gynecomastia was apparent before neurologic symptoms appeared; 50% showed additional signs of hypoandrogenicity such as erectile dysfunction and decreased sexual interest. As many as 86% exhibited a hormone profile indicative of partial androgen insensitivity. These changes slowly progressed over time.<sup>3</sup> This evidence is corroborated by a large cohort of patients with KD in Japan in which Atsuta et al<sup>18</sup> evaluated laboratory data in 61 cases. They stressed that even in older patients, testosterone levels remained high but decreased slightly with age.<sup>18</sup>

From the pathophysiologic point of view, testosterone normally inhibits LH and follicle-stimulating hormone (FSH) secretion through effects both on the hypothalamus and the pituitary gland.<sup>19</sup> In patients with KD, partial androgen insensitivity frequently leads to high testosterone levels with elevated LH levels and hyper-responsiveness of LH to gonadotropin-releasing hormone as a possible sign of a larger stock of LH caused by a lack of suppressive effects of testosterone on the pituitary gland itself.<sup>3,20</sup> Furthermore, the suppressive effect of synthetic androgens on testosterone levels, LH, and FSH is reduced in patients with KD, which suggests a weakened effect of androgens on the pituitary gland as a possible cause.<sup>21</sup>

LH and FSH are produced in the pituitary gland, which we investigated in the present study by means of high-field 3T MR imaging. The volume of the pituitary gland was significantly larger in patients with KD than in control subjects. It is known that pituitary gland size reflects hormonal secretion. An increase of LH and FSH at puberty, for example, leads to further enlarge-

ment.<sup>22,23</sup> Volume also increases steadily with age in healthy subjects, in women up to a peak in the second decade and in men in the third decade.<sup>24</sup> It could also be shown that high concentrations of gonadotropic hormones induced by the age-related drop in circulating gonadal steroids in climacteric women correlated with an increase of pituitary height. In men, pituitary height declines steadily after reaching the peak in the third decade.<sup>25</sup>

Although many studies could show that changes in pituitary dimensions predominantly affect the height of the gland,<sup>25</sup> more recent studies also used a direct volumetric approach by use of 2D or 3D MR images.<sup>26,27</sup>

We therefore hypothesized that the lack of suppressive effects of testosterone on the pituitary gland in KD causing hypersecretion of LH may also lead to morphologic changes of the gland in KD.

Our analysis showed that patients with KD had a significantly higher pituitary volume as compared with normal, age-matched individuals, whereas there was no difference in total brain volume. This could reflect a hypertrophy of the pituitary gland as the result of elevated gonadotropic hormone secretion caused by the AR receptor mutation with partial androgen insensitivity.

Furthermore, patients with KD showed a trend to increasing gland volume in older patients, whereas control subjects showed a statistically significant decrease in volume. These findings are in line with previous studies on healthy individuals.<sup>24,25</sup> These changes may reflect an ongoing process of gland hypertrophy over time and duration of the disease.

We also found larger pituitary gland volumes in patients with longer CAG repeat expansions. This is in line with the findings of Dejager et al,<sup>3</sup> who described a significant association of the number of CAG repeats and endocrine changes, age of onset of gynecomastia, and laboratory findings.

In our data, CAG repeat expansion length also proved to be the only independent predictor of pituitary volume in patients with KD, whereas other factors such as patient age and disease duration were not predictive of pituitary volume. It seems likely, therefore, that the significant association of CAG repeat expansion length and clinical parameters found by Dejager et al<sup>3</sup> is also reflected in the morphologic changes of the pituitary gland with even larger volumes in patients with longer CAG repeats. Patient age and disease duration alone were not sufficient to explain increasing gland volume.

There are limitations of the present study that must be observed. Laboratory findings concerning hormone levels at the time of the MR imaging were available in 2 patients with KD, showing elevated testosterone and SHBG levels. The endocrine changes described by Dejager et al<sup>3</sup> must be expected in our collective of patients with genetically proved KD as well, especially because physical signs of androgen insensitivity were present in all cases. However, a connection between elevated hormone secretion and gland hypertrophy in KD could only be assumed, and further research with a full endocrine assessment is warranted.

## CONCLUSIONS

In summary, we describe a significant increase of pituitary gland volume in patients with KD as compared with healthy individuals, previously not reported, as well as a positive correlation of gland

size and CAG repeat expansion length. This could reflect hypertrophy of the pituitary gland as the result of elevated gonadotropic hormone secretion caused by the CAG repeat expansion in the AR with partial androgen insensitivity.

## REFERENCES

- Kennedy WR, Alter M, Sung JH. **Progressive proximal spinal and bulbar muscular atrophy of late onset: a sex-linked recessive trait.** *Neurology* 1968;18:671–80
- Sobue G, Hashizume Y, Mukai E, et al. **X-linked recessive bulbospinal neuronopathy: a clinicopathological study.** *Brain* 1989;112(Pt 1):209–32
- Dejager S, Bry-Gauillard H, Bruckert E, et al. **A comprehensive endocrine description of Kennedy's disease revealing androgen insensitivity linked to CAG repeat length.** *J Clin Endocrinol Metab* 2002;87:3893–901
- Battaglia F, Le Galudec V, Cossee M, et al. **Kennedy's disease initially manifesting as an endocrine disorder.** *J Clin Neuromuscul Dis* 2003;4:165–67
- Castillo M. **Pituitary gland: development, normal appearances, and magnetic resonance imaging protocols.** *Top Magn Reson Imaging* 2005;16:259–68
- Rennert J, Doerfler A. **Imaging of sellar and parasellar lesions.** *Clin Neurol Neurosurg* 2007;109:111–24
- Miki Y, Matsuo M, Nishizawa S, et al. **Pituitary adenomas and normal pituitary tissue: enhancement patterns on gadopentetate-enhanced MR imaging.** *Radiology* 1990;177:35–38
- Portman O, Flemming S, Cox JP, et al. **Magnetic resonance imaging of the normal pituitary gland using ultrashort TE (UTE) pulse sequences (REV 1.0).** *Neuroradiology* 2008;50:213–20
- Amar AP, Weiss MH. **Pituitary anatomy and physiology.** *Neurosurg Clin N Am* 2003;14:11–23
- Kuroiwa T, Okabe Y, Hasuo K, et al. **MR imaging of pituitary hypertrophy due to juvenile primary hypothyroidism: a case report.** *Clin Imaging* 1991;15:202–05
- Woods RP. **Multitracer: a Java-based tool for anatomic delineation of grayscale volumetric images.** *Neuroimage* 2003;19:1829–34
- Parodi S, Pennuto M. **Neurotoxic effects of androgens in spinal and bulbar muscular atrophy.** *Front Neuroendocrinol* 2011;32:416–25
- Fischbeck KH. **Polyglutamine expansion neurodegenerative disease.** *Brain Res Bull.* 2001;56:161–63
- Merry DE. **Molecular pathogenesis of spinal and bulbar muscular atrophy.** *Brain Res Bull* 2001;56:203–07
- Barkhaus PE, Kennedy WR, Stern LZ, et al. **Hereditary proximal spinal and bulbar motor neuron disease of late onset: a report of six cases.** *Arch Neurol* 1982;39:112–16
- Harding AE, Thomas PK, Baraitser M, et al. **X-linked recessive bulbospinal neuronopathy: a report of ten cases.** *J Neurol Neurosurg Psychiatry* 1982;45:1012–19
- Thomas PS Jr, Fraley GS, Damian V, et al. **Loss of endogenous androgen receptor protein accelerates motor neuron degeneration and accentuates androgen insensitivity in a mouse model of X-linked spinal and bulbar muscular atrophy.** *Hum Mol Genet* 2006;15:2225–38
- Atsuta N, Watanabe H, Ito M, et al. **Natural history of spinal and bulbar muscular atrophy (SBMA): a study of 223 Japanese patients.** *Brain* 2006;129(Pt 6):1446–55
- Shekter CB, Matsumoto AM, Bremner WJ. **Testosterone administration inhibits gonadotropin secretion by an effect directly on the human pituitary.** *J Clin Endocrinol Metab* 1989;68:397–401
- Ahmed SF, Cheng A, Hughes IA. **Assessment of the gonadotrophin-gonadal axis in androgen insensitivity syndrome.** *Arch Dis Child* 1999;80:324–29
- Sobue G, Doyu M, Morishima T, et al. **Aberrant androgen action and increased size of tandem CAG repeat in androgen receptor gene in X-linked recessive bulbospinal neuronopathy.** *J Neurol Sci* 1994;121:167–71
- Elster AD, Chen MY, Williams DW 3rd, et al. **Pituitary gland: MR imaging of physiologic hypertrophy in adolescence.** *Radiology* 1990;174(3 Pt 1):681–85
- Shinkawa O, Furuhashi N, Fukaya T, et al. **Changes of serum gonadotropin levels and sex differences in premature and mature infant during neonatal life.** *J Clin Endocrinol Metab* 1983;56:1327–31
- Ikram MF, Sajjad Z, Shokh IS, et al. **Pituitary gland volume on magnetic resonance imaging: normative observations.** *Pak J Neurol Sci* 2007;2:141–44
- Tsunoda A, Okuda O, Sato K. **MR height of the pituitary gland as a function of age and sex: especially physiological hypertrophy in adolescence and in climacterium.** *AJNR Am J Neuroradiol* 1997;18:551–54
- Renz DM, Hahn HK, Schmidt P, et al. **Accuracy and reproducibility of a novel semi-automatic segmentation technique for MR volumetry of the pituitary gland.** *Neuroradiology* 2011;53:233–44
- Roldan-Valadez E, Garcia-Ulloa AC, Gonzalez-Gutierrez O, et al. **3D volumetry comparison using 3T magnetic resonance imaging between normal and adenoma-containing pituitary glands.** *Neurol India* 2011;59:696–99

# Stroke-Like Migraine Attacks after Radiation Therapy (SMART) Syndrome Is Not Always Completely Reversible: A Case Series

D.F. Black, J.M. Morris, E.P. Lindell, K.N. Krecke, G.A. Worrell, J.D. Bartleson, and D.H. Lachance



## ABSTRACT

**SUMMARY:** We retrospectively reviewed clinical and imaging findings in 11 patients with stroke-like migraine attacks after radiation therapy (SMART) syndrome to better understand this disorder previously thought to be reversible. Six men and 5 women had complex bouts of neurologic impairment beginning, on average, 20 years after cerebral irradiation. All had characteristic, unilateral gyriform enhancement on MR imaging that developed within 2–7 days and typically resolved in 2–5 weeks. Unlike prior reports, 45% had incomplete neurologic recovery manifesting as dysphasia, cognitive impairment, or hemiparesis. The remaining 55% recovered completely over an average of 2 months. Three of 11 patients developed cortical laminar necrosis. Brain biopsies in 4 of 11 did not demonstrate a specific pathologic substrate. These additional 11 patients contribute to the understanding of variability in stroke-like migraine attacks after radiation therapy syndrome, which often but not uniformly manifests with headaches and seizures, demonstrates a typical evolution of imaging findings, and may result in permanent neurologic and imaging sequelae.

**ABBREVIATIONS:** SMART = stroke-like migraine attacks after radiation therapy; CLN = cortical laminar necrosis; CJD = Creutzfeldt-Jakob disease; PIPG = peri-ictal pseudoprogression

Stroke-like migraine attacks after radiation therapy (SMART) is a syndrome presumed to be a delayed complication of whole-brain irradiation wherein patients have recurrent attacks of complex neurologic signs and symptoms, often including headache and seizures that start many years after radiation therapy and demonstrate characteristic imaging findings.<sup>1–5</sup> Patients may or may not have an antecedent history of migraine headaches or seizures. Attacks are typically subacute in onset and involve stroke-like deficits such as homonymous hemianopsia, hemiplegia, aphasia, and/or seizures. In all reported cases thus far, symptoms have been debilitating but ultimately resolve completely, usually after weeks. MR imaging findings that correlate with these clinical manifestations include unilaterally increased T2 signal within temporal, parietal, or occipital cortices and an exuberant, thick, gyral cortical gray matter enhancement that disappears as symptoms resolve. The MR imaging findings do not respect vascular borders.

Although SMART appears to be a delayed consequence of re-

mote cerebral irradiation, the pathophysiology is unknown and pathologic specimens have not been previously reported.

Between March 1, 2006, and March 1, 2012, the authors observed 11 patients in their daily practice who met the proposed diagnostic criteria for SMART and underwent head MR imaging while symptomatic.<sup>1</sup> We obtained approval from our internal review board to retrospectively report the clinical, pathologic, and imaging findings of these patients.

## Case Series

The 11 subjects ranged in age from 37–60 years (mean, 50 years) at the time of diagnosis with SMART. All had received cerebral irradiation for various indications many years before onset of the clinical syndrome (Table 1). Table 2 describes the frequency of their presenting signs and symptoms. Each patient was retrospectively included in this study only after completing a comprehensive neurologic and medical evaluation at our institution that excluded other alternative diagnostic possibilities. Interval between radiation therapy and SMART diagnosis ranged from 6–30 years (mean, 20), and the average age at the time of radiation therapy was 30 years. Six patients (55%) had more than 1 SMART episode. Five patients (45%) had a seizure history before SMART episodes, 8 (72%) patients had interictal epileptiform activity recorded on EEG, 4 (36%) had focal electrographic seizures recorded, and 2 patients had only focal slowing (Table 3). Four patients (37%) had recurrent severe migrainous headaches before SMART episodes,

Received January 4, 2013; accepted after revision March 4.

From the Departments of Radiology (D.F.B., J.M.M., E.P.L., K.N.K.) and Neurology (G.A.W., J.D.B., D.H.L.), Mayo Clinic, Rochester, Minnesota.

Paper previously presented at: Annual Meeting of the American Society of Neuro-radiology, April 23, 2012; New York, New York.

Please address correspondence to David F. Black, MD, Mayo Clinic, E2 Radiology, 200 First St SW, Rochester, MN 55905; e-mail: black.david@mayo.edu

<http://dx.doi.org/10.3174/ajnr.A3602>

**Table 1: Summary of demographics for patients with SMART**

Patient	Radiation Indication	Interval, y	Age at Diagnosis, y	Seizures	Seizure	Headache	Headache	Therapies Used
				Before	With	Before	With	
1	Pituitary lesion	22	60	?	Y	N	N	Phenytoin, levetiracetam
2	Pineal tumor	30	42	Y	N	?	Y	Corticosteroids
3	Astrocytoma	32	44	N	N	?	Y	Verapamil, phenytoin
4	Oligoastrocytoma	14	53	Y	Y	N	N	Phenytoin, levetiracetam
5	Dysgerminoma	19	50	N	N	Y	Y	Corticosteroids
6	Fibrillary astrocytoma	13	45	Y	Y	N	N	Levetiracetam, valproate, corticosteroids
7	Astroblastoma	27	58	Y	N	N	Y	Phenytoin, aspirin
8	Lymphoma	16	37	N	Y	Y	Y	Levetiracetam, verapamil, aspirin
9	Oligoastrocytoma	10	50	N	Y	Y	Y	Levetiracetam, verapamil, corticosteroids
10	Metastatic melanoma	6	50	Y	Y	N	Y	Levetiracetam, verapamil, corticosteroids
11	Brain stem glioma	30	58	N	Y	Y	Y	Levetiracetam, verapamil

**Note:**—"Interval" indicates the interval in years between radiotherapy and the diagnosis of SMART. "Seizures before" and "Seizure with," "Headache before" and "Headache with" refer to symptoms preceding initiation and during SMART episodes, respectively.

**Table 2: SMART presenting signs and symptoms**

Signs and Symptoms	No. of Cases	%
Interictal epileptiform activity, electrographic seizures, or clinical seizure activity <sup>a</sup>	9/11	82
Headache	8/11	73
Speech disturbance	7/11	64
Visual field defect	7/11	64
Altered mentation	5/11	45
Hemiparesis	5/11	45
Hemisensory change	2/11	18

<sup>a</sup>Interictal epileptiform spikes, sharp waves, electrographic seizures, or witnessed seizure. One of the patients without EEG interictal epileptiform activity had a witnessed convulsion.

**Table 3: EEG results during SMART symptoms**

Patient	EEG Results
1	Electrographic seizure activity over the right temporal region
2	Potentially epileptogenic discharges over the left temporal region
3	Potentially epileptogenic discharges over bilateral temporal regions
4	Electrographic seizure activity over the left temporal region
5	Focal slowing over the right hemisphere
6	Electrographic seizure activity over the left temporal region
7	Focal slowing over the left occipito-parietal region
8	Potentially epileptogenic discharges over the right frontal region (note: left temporo-parietal MRI changes)
9	Potentially epileptogenic discharges over the midline, right parietal, and bilateral temporal regions
10	Electrographic seizure activity over the right parietal region
11	No potentially epileptogenic activity on EEG but had witnessed generalized seizure

**Note:**—Eight patients (72%) had epileptiform activity recorded with EEG and 4 (36%) had focal electrographic seizures recorded.

and 8 (73%) had migraine-like headaches as part of their SMART presentation.

All patients demonstrated the typical gyriform, unilateral cortical gadolinium enhancement with minimal leptomeningeal enhancement that is characteristic of SMART as well as the correlative abnormal T2 and FLAIR signal with mild mass effect (Fig 1).

Although the radiation dose received was not known in most cases, we believe that the MR imaging findings were in regions that were included in the radiation ports. There was prominent involvement of the temporo-parietal and occipital lobes with relative sparing of the frontal lobes in all cases. Gyriform enhancement began 2–7 days after the initiation of neurologic signs and symptoms and typically resolved in 2–5 weeks but lasted from 11–84 days. Gadolinium T1-weighted images demonstrated the most conspicuous findings followed by FLAIR images.

Three patients (27%) developed cortical laminar necrosis (CLN) involving the same regions seen to enhance (Table 2). In case 2, CLN developed 17 days after symptoms began (Fig 2). No diffusion restriction was evident in the regions of enhancement or CLN.

The clinical course in cases 1, 9, and 10 was complicated by a superimposed cerebral infarction and symptoms of stroke (Figs 3 and 4). Each of these infarctions occurred within a subregion of the more typical changes of SMART in the right occipital lobe. In patients 1 and 9, right occipital infarctions were discovered in regions of resolved gyriform enhancement that had been present 7 and 9 days previously, respectively. There had been no evidence of restricted diffusion on the prior examinations. Patient 10 presented with a generalized seizure and had a new right occipital infarct with adjacent gyriform enhancement and cortical edema in the right temporoparietal and occipital lobes. Patients 9 and 10 went on to have full clinical recovery documented in the medical record. The residual deficits in patient 1 were not anatomically correlated to the region of infarction.

Patient 1 was initially diagnosed with Creutzfeldt-Jakob Disease (CJD) because of an elevated CSF 14–3–3 protein, but, over the next month, her neurologic status improved and she was able to walk short distances. Eventually, she was able to return home, though she required greater assistance from her husband with activities of daily living. She had no new neurologic difficulties for the next 5 years of follow-up.

Five patients (45%) demonstrated various degrees of multiple magnetic susceptibility foci most compatible with cavernomas, probably a consequence of prior radiation therapy.

Various medications were used in the care of these patients, most commonly levetiracetam, which appeared to improve sei-

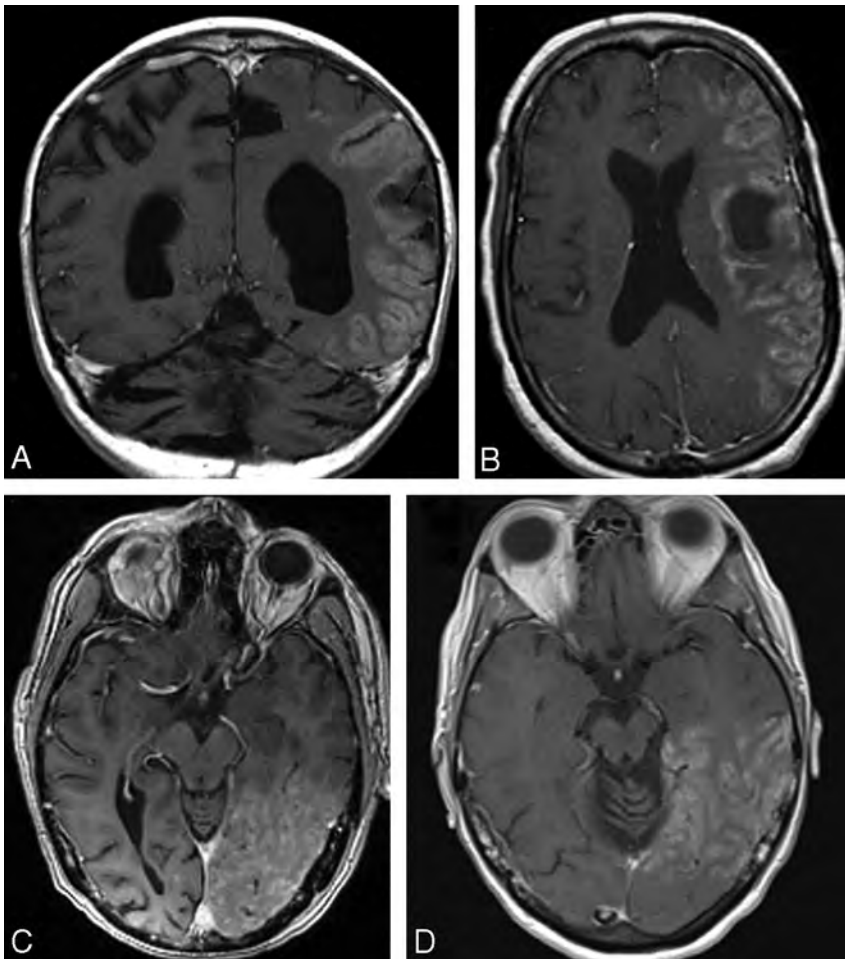


**FIG 1.** A, Patient 3; B, patient 4; C, patient 7; D, patient 11. T1-weighted images with gadolinium enhancement demonstrate typical patterns of enhancement seen in SMART.

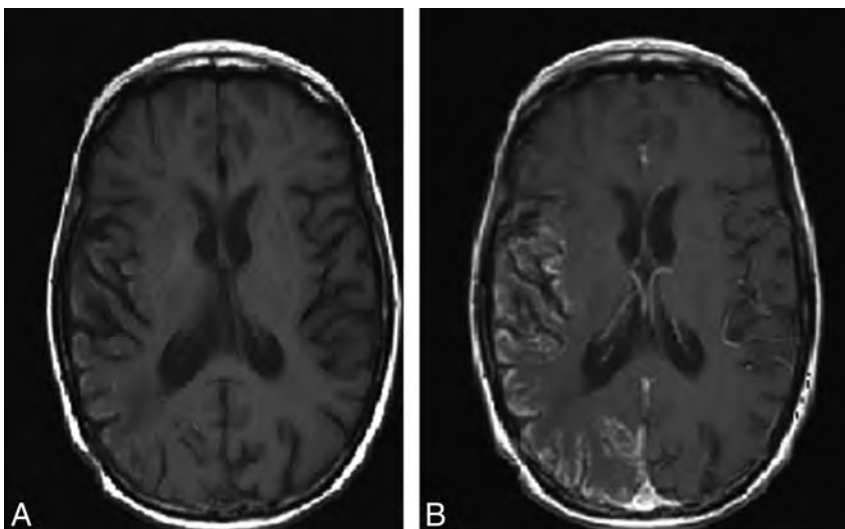


**FIG 2.** Patient 2. A, T1-weighted image without gadolinium demonstrates typical findings of right temporoparietal cortical laminar necrosis on day 17 of symptoms. B, T1-weighted image with gadolinium demonstrates concordant unilateral gyriform enhancement on the same examination.

zure control in several patients. Patient 2 was treated with a 3-month steroid taper and began to improve within the first week, though she did not return to her baseline. Three patients (patients

1, 2, and 5) had transient problems with sodium and water balance during their symptoms.

Four patients (36%) had brain biopsies because of concerns of tumor recurrence. All demonstrated mild, nonspecific gliosis without a specific pathologic substrate for SMART or evidence of recurrent tumor.

Six patients (55%) recovered completely back to their antecedent clinical baseline, with recovery taking 1.5–2.5 months (mean, 2). Five patients (45%) showed gradual but incomplete recovery with residual deficits most often including dysphasia, cognitive impairment, and mild hemiparesis (Table 4).

## DISCUSSION

This series provides several new insights into the poorly understood and possibly under-recognized syndrome of SMART. Prior publications described a benign natural history with complete return to clinical baseline; however, in this series, 45% of patients had incomplete clinical recovery. All the patients in this series met the proposed diagnostic criteria of SMART, except for this unexpected incomplete recovery.<sup>1</sup> Permanent imaging sequelae from SMART were demonstrated in 27%, with MR imaging findings typical of cortical laminar necrosis developing as early as 17 days after symptom onset.

We demonstrated that the thick gyriform cortical enhancement characteristic of SMART develops only after 2–7 days, typically resolves in 14–35 days, but may last between 11–84 days. Diffusion-weighted abnormalities were minimal and primarily demonstrated T2 shine through without convincing evidence of restricted diffusion except in the 3 cases that had superimposed infarcts. The small occipital infarcts seen in patients 1 and 9 occurred after the more typical changes of gyral edema and enhancement had resolved, again suggesting that the mechanisms causing SMART are complex. A process driven by some form of cerebral hyperexcitability with impaired autoregulatory parameters and endothelial damage occurring

as a consequence of remote radiation therapy seems plausible. Stabilizing seizure threshold and vascular reactivity are logical therapeutic interventions to consider.

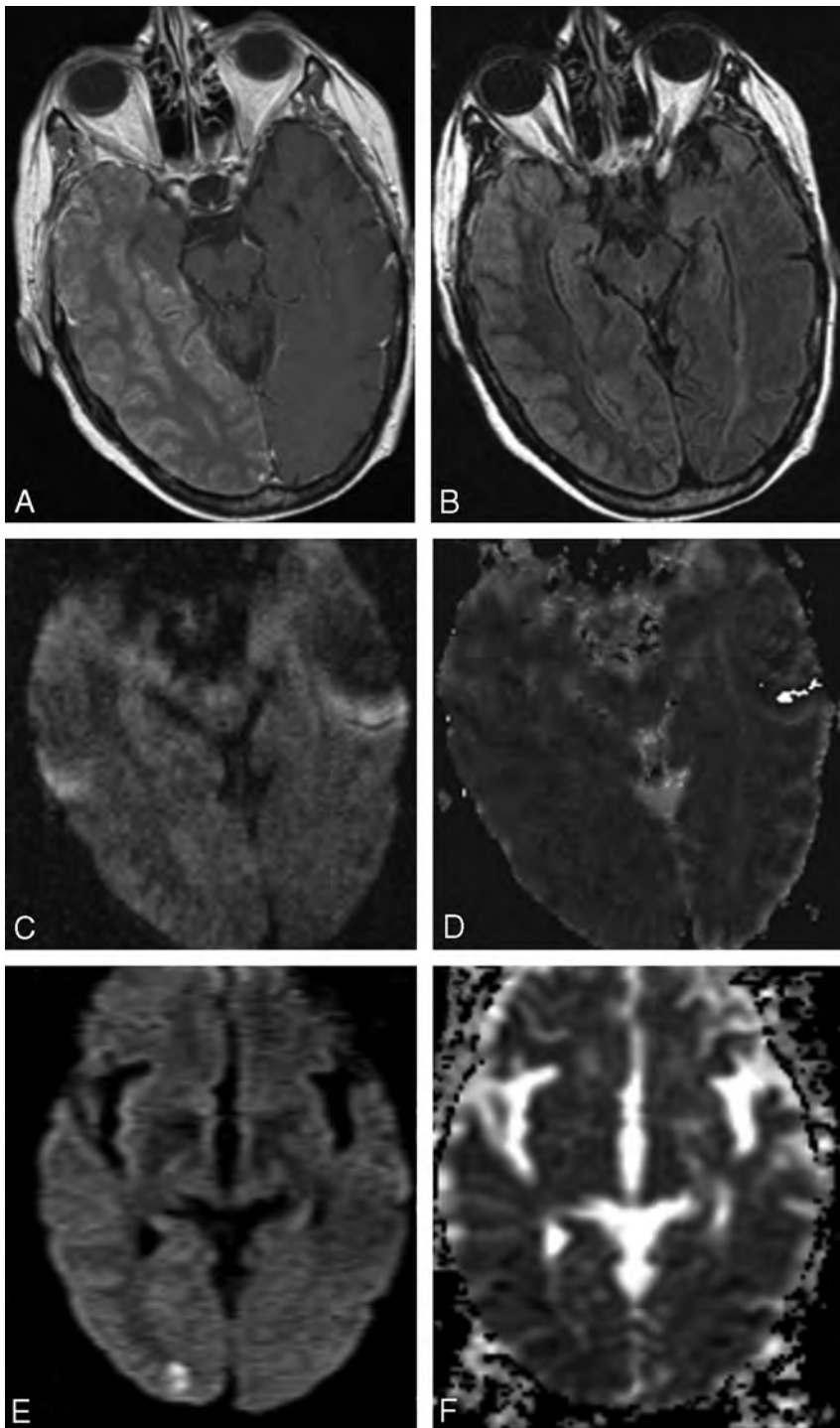


**FIG 3.** Patient 1. *A*, Gadolinium-enhanced T1 image demonstrating characteristic unilateral, thick gyriform enhancement during an episode of SMART. *B*, FLAIR sequence showing gyral T2 signal that corresponds to the regions of enhancement. *C* and *D*, Diffusion-weighted sequence and ADC map demonstrate no convincing diffusion restriction upon initial presentation until 7 days later (*E* and *F*), when enhancement resolved but a new right occipital infarction was found.

The pathologic substrate for SMART is unknown, and biopsy in 4 of the 11 patients (36%) failed to demonstrate pathologic etiology. Also, 3 of 11 patients in this series had comorbid problems with high or low sodium or diabetes insipidus, but to what extent this may have contributed is not known.

activity could explain cortical edema and impaired blood-brain barrier integrity with persisting contrast enhancement for days to weeks while patients' symptoms outlast any particular seizure activity and, at times, become permanent with evidence of cortical laminar necrosis.

Similar to previous reports, the interval between radiation and SMART diagnosis was on average 20 years, with an average age at diagnosis of 50.<sup>1,3</sup> All patients had somatosensory findings, 82% had various levels of evidence of seizure activity temporally and spatially correlated with imaging findings, 73% had migraine-like headaches, and all had unilateral, thick gyriform enhancement during their symptoms.

Limitations of this series include its retrospective nature. We did not actively recruit suspected cases but simply came across them during our daily practice. We saw 1–2 cases per year at our tertiary care center. Many of the subjects had received radiation therapy many years previously at other institutions; thus, radiation doses were largely unknown, though the radiation ports probably included regions affected by SMART in all cases.

Inherent to their history of cerebral irradiation and tumor, patients with SMART may have seizures as a premorbid condition and possible contributor to their neurologic problems. Many reports have demonstrated that nonconvulsive status epilepticus or frequent partial seizures may produce transient cortical edema, T2 hyperintensity, leptomeningeal or cortical enhancement, and permanent sequelae, including cortical laminar necrosis.<sup>6–9</sup> Postictal MR imaging findings in patients without prior radiation therapy appear different from SMART, suggesting that SMART may represent a unique syndrome with a complex poorly understood pathophysiology occurring in a subset of patients long after radiation therapy.<sup>10,11</sup>

It may be that seizures in patients with SMART strain an already impaired brain because of the chronic endothelial vascular damage caused by remote radiation, and this “double hit” produces infarction in some instances in the affected cortical areas. Whether seizures initiate or are a consequence of SMART, the combination of radiation-induced vascular damage and clinical and subclinical seizure activity

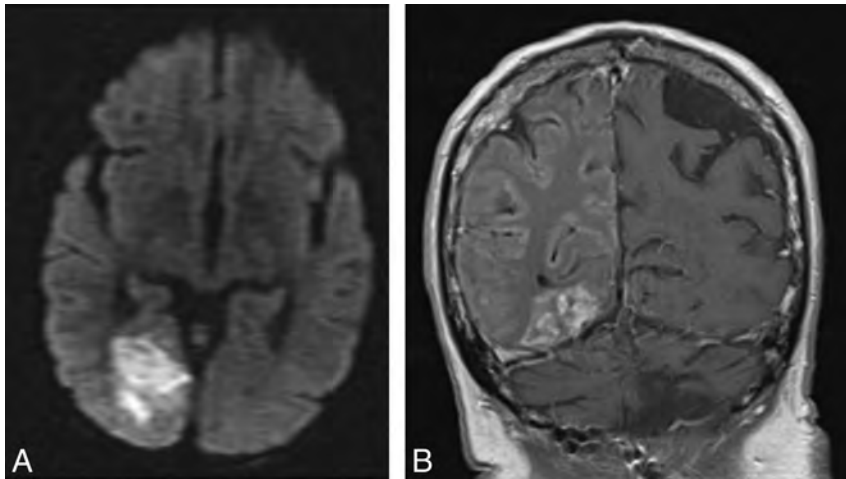


**FIG 4.** Patient 10. A, Acute right occipital infarction with restricted diffusion. B, T1 gadolinium-enhanced coronal image demonstrates the subacute enhancement of the infarction with more extensive gyral enhancement throughout the right temporoparietal region. Postoperative changes in the left cerebellum from prior melanoma resection.

**Table 4: Correlations between Radiologic Findings, Biopsy, and Recovery**

Patient	CLN	DWI	Biopsy	Stroke	Recovery
1	N	N	Y	Y	Incomplete
2	Y	N	N	N	Incomplete
3	N	N	N	N	2 mo
4	N	N	N	N	1–2 mo
5	Y	N	Y	N	Incomplete
6	N	N	N	N	2.5 mo
7	N	N	Y	N	Incomplete
8	N	N	Y	N	Incomplete
9	N	N	N	Y	2 mo
10	Y	Y	N	Y	2.5 mo
11	N	N	N	N	2 mo

**Note:**—“Y” and “N” indicate “Yes” or “No,” respectively. DWI indicates whether restricted diffusion was seen in the region of abnormal gyral edema and enhancement on the initial MR images (patients 1 and 9 subsequently had small foci of restricted diffusion after the other findings resolved). The stroke column indicates whether a stroke occurred during the same symptomatic epoch as the SMART symptoms.

Reports of what has been subsequently termed peri-ictal pseudoprogression (PIPG) demonstrate MR imaging findings similar to SMART but highlight absence of headache, less significant neurologic impairment, and more rapid clinical recovery as differentiating aspects.<sup>12</sup> Although PIPG probably represents the same spectrum of phenomena as SMART, reported cases tend to show more meningeal enhancement than the cortical enhancement seen in SMART.

Endothelial damage may also explain the interplay between too much or too little synaptic activity producing the migrainous headaches that occur in some patients with SMART as well as the unilaterality of the imaging findings that are similar to those reported in familial hemiplegic migraine.<sup>13</sup> Cha et al<sup>14</sup> reported identical twins with hemiplegic migraine without evidence of seizures who had MR imaging findings identical to SMART, though no history of radiation was mentioned. Therefore, vascular endothelial damage complicating radiation therapy may lower the threshold required to develop episodic symptoms of a hyperexcitable nervous system similar to the postulated mechanism of hemiplegic migraine and could contribute to the expression of symptoms consistent with migraine in these cases. Furthermore,

it is plausible to consider that this syndrome occurs in individuals who survive radiation therapy and have a genetic predisposition similar to hemiplegic migraine.

Rapid control of seizure activity, if present, is important in treating patients with SMART. Intravenous fosphenytoin, oral or intravenous levetiracetam, and a short course of high-dose corticosteroids appear to be candidates for treatment.<sup>15</sup> Because of the ischemic nature of the MR imaging findings that can progress to cortical laminar necrosis, verapamil appears to be an intuitive, though unproven, therapeutic option that may have the benefit of also preventing headaches. Although also unproven, some form of antiplatelet therapy or even statin therapy seem to be

intuitive potential treatment options.

The possibility of recurrent tumor or loss of seizure control as a cause of symptoms is omnipresent in patients with prior radiation for brain tumors, and ongoing aggressive surveillance is required. Awareness and recognition of SMART syndrome signs, symptoms, imaging findings, and recurrent attacks should serve to guard against rendering an incorrect dire prognosis and prevent aggressive interventions such as brain biopsy or cerebral angiography. All 4 patients who underwent biopsy in this series experienced incomplete recovery, and only 1 of the 7 patients who did not undergo biopsy had an incomplete recovery. It should be noted that no new signs or symptoms were temporally correlated with the biopsy procedures; thus, the relation between biopsy and clinical outcome is unknown. It is unclear why the 14–3–3 protein was elevated in patient 1, who ultimately did not have CJD, but false-positives have been found with other nonspecific encephalopathies, especially with ischemia.<sup>16</sup>

For appropriate diagnosis and treatment, it is important for clinicians and radiologists to be aware of the characteristic imaging findings of SMART as well as their temporal evolution, the association with seizures, the possibility of permanent sequelae, and the lack of benefit and possible detriment from brain biopsy.

## REFERENCES

- Black DF, Bartleson JD, Bell ML, et al. **SMART: stroke-like migraine attacks after radiation therapy.** *Cephalalgia* 2006;26:1137–42
- Bartleson JD, Krecke KN, O'Neill BP, et al. **Reversible, stroke-like migraine attacks in patients with previous radiation therapy.** *Neuro-Oncology* 2003;2:121–27
- Pruitt A, Dalmau J, Detre J, et al. **Episodic neurologic dysfunction with migraine and reversible imaging findings after radiation.** *Neurology* 2006;67:676–78
- Partap S, Walker M, Longstreth WT, et al. **Prolonged but reversible migraine-like episodes long after cranial irradiation.** *Neurology* 2006;66:1105–07
- Cordato DJ, Brimage P, Masters LT, et al. **Post-cranial irradiation syndrome with migraine-like headaches, prolonged and revers-**

- ible neurological deficits and seizures. *J Clin Neurosci* 2006;13:586–90
6. Cohen-Gadol AA, Britton JW, Worrell GA, et al. **Transient cortical abnormalities on magnetic resonance imaging after status epilepticus: case report.** *Surg Neurol* 2004;61:479–82
  7. Sammaritano M, Andermann F, Melanson D, et al. **Prolonged focal cerebral edema associated with partial status epilepticus.** *Epilepsia* 2007;26:334–39
  8. Donaire A, Carreno M, Gomez B, et al. **Cortical laminar necrosis related to prolonged focal status epilepticus.** *J Neurol Neurosurg Psychiatry* 2006;77:104–06
  9. Henry TR, Drury I, Brunberg JA, et al. **Focal cerebral magnetic resonance changes associated with partial status epilepticus.** *Epilepsia* 1994;35:35–41
  10. Hormigo A, Liberato B, Lis E, et al. **Nonconvulsive status epilepticus in patients with cancer.** *Arch Neurol* 2004;61:362–65
  11. Quan D, Hackney DB, Pruitt AA, et al. **Transient MRI enhancement in a patient with seizures and previously resected glioma: use of MRS.** *Neurology* 1999;53:211–13
  12. Rheims S, Ricard D, van den Bent M, et al. **Peri-ictal pseudoprogression in patients with brain tumor.** *Neuro-Oncology* 2011;13:775–82
  13. Black DF, Kung S, Sola CL, et al. **Familial hemiplegic migraine, neuropsychiatric symptoms, and Erdheim-Chester.** *Dis Headache* 2004;44:911–15
  14. Cha Y-H, Millett D, Kane M, et al. **Adult-onset hemiplegic migraine with cortical enhancement and oedema.** *Cephalalgia* 2007;27:1166–70
  15. Abend NS, Florance N, Finkel RS, et al. **Intravenous levetiracetam terminates refractory focal status epilepticus.** *Neurocrit Care* 2009;10:83
  16. Collins S, Boyd A, Fletcher A, et al. **Creutzfeldt-Jakob disease: diagnostic utility of 14–3–3 protein immunodetection in cerebrospinal fluid.** *J Clin Neurosci* 2000;7:203–08

# Sex Differences in Resting-State Functional Connectivity in Multiple Sclerosis

K.A. Koenig, M.J. Lowe, J. Lin, K.E. Sakaie, L. Stone, R.A. Bermel, E.B. Beall, S.M. Rao, B.D. Trapp, and M.D. Phillips



## ABSTRACT

**BACKGROUND AND PURPOSE:** Multiple studies have demonstrated evidence of sex differences in patients with MS, including differences in disease progression, cognitive decline, and biologic markers. This study used functional connectivity MRI to investigate sex differences in the strength of functional connectivity of the default mode network in patients with MS and healthy control subjects.

**MATERIALS AND METHODS:** A total of 16 men and 16 women with MS and 32 age- and sex-matched healthy control subjects underwent a whole-brain resting-state functional connectivity MRI scan. A group-based seed in the posterior cingulate was used to create whole-brain correlation maps. A  $2 \times 2$  ANOVA was used to assess whether disease status and sex affected the strength of connectivity to the posterior cingulate.

**RESULTS:** Patients with MS showed significantly stronger connectivity from the posterior cingulate to the bilateral medial frontal gyri, the left ventral anterior cingulate, the right putamen, and the left middle temporal gyrus ( $P < .0005$ ). In the left dorsal lateral prefrontal cortex, female patients showed significantly stronger connectivity to the posterior cingulate cortex compared with female control subjects ( $P = 3 \times 10^{-4}$ ), and male control subjects showed stronger posterior cingulate cortex–left dorsal lateral prefrontal cortex connectivity in comparison to female control subjects ( $P = .002$ ). Male patients showed significantly weaker connectivity to the caudate compared with female patients ( $P = .004$ ).

**CONCLUSIONS:** Disease status and sex interact to produce differences in the strength of functional connectivity from the posterior cingulate to the caudate and the left dorsal lateral prefrontal cortex.

**ABBREVIATIONS:** ACC = anterior cingulate cortex; DMN = default mode network; fcMRI = functional connectivity MRI; DLPFC = dorsal lateral prefrontal cortex; MNI = Montreal Neurological Institute; PCC = posterior cingulate cortex

There have been numerous reports of sex differences in patients with the neurodegenerative disorder MS. It has long been known that women are more likely to have MS than men, and recent reports have found a widening sex gap in diagnosis.<sup>1-3</sup> Although sex has a less dramatic effect on disease progression and clinical outcomes, several studies have reported more severe symptoms and faster progression in men.<sup>4-7</sup> The underlying processes thought to be involved in the development and progression of MS demonstrate significant sex differences. For example, male

and female patients with MS have shown differences in the markers of autoimmune function,<sup>8-10</sup> and there has been extensive research on the effects of sex hormones on disease progression, particularly during and after pregnancy.<sup>11,12</sup> There is evidence that fluctuations in hormone levels can affect tissue damage in the brain<sup>13</sup>; these observations have prompted research on the use of sex hormones as a treatment for MS.<sup>14,15</sup> It is unclear, however, whether there are sex differences in conventional MR imaging measures of disease status. One review concluded that sex does not appear to affect conventional MR imaging measures,<sup>16</sup> whereas other research has found increased gray matter atrophy and decreased development of T2-weighted lesions in men and increased white matter atrophy in women.<sup>17-19</sup> Recently, sex differences in expression levels of markers involved in demyelination were found in an animal model of MS.<sup>20</sup>

The measure of low-frequency blood oxygen level–dependent signal fluctuations in a patient at rest, referred to as resting-state functional connectivity MRI (fcMRI), is thought to capture information about intrinsic functional networks in the brain.<sup>21</sup> Pa-

Received December 17, 2012; accepted after revision March 16, 2013.

From the Imaging Institute (K.A.K., M.J.L., J.L., K.E.S., E.B.B., M.D.P.); Neurological Institute (L.S., R.A.B.); Scler Center for Cognitive Neuroimaging, Neurological Institute (S.M.R.); and Department of Neurosciences (B.D.T.), The Cleveland Clinic, Cleveland, Ohio.

This work was supported by grants from the National Multiple Sclerosis Society and the National Institutes of Health (NS035058).

Please address correspondence to Katherine A. Koenig, PhD, Imaging Institute, Cleveland Clinic, 9500 Euclid Ave, U15, Cleveland, OH 44195; e-mail: koenigk@ccf.org

Indicates open access to non-subscribers at www.ajnr.org

<http://dx.doi.org/10.3174/ajnr.A3630>

**Table 1: Demographic information**

Characteristic	Female Control Subjects (n = 16)	Female Patients (n = 16)	Male Control Subjects (n = 16 <sup>a</sup> )	Male Patients (n = 16)
Mean age, y (SD)	42.25 (9.4)	42.38 (9.5)	41.81 (9.6)	40.94 (8.9)
Mean education, y (SD)	16.44 (1.3)	15.00 (2.6)	16.81 (3.7)	16.3 (2.9)
Median EDSS (range)	NA	2 (1–3.5)	NA	1.5 (1–6)
Median disease duration (range)	NA	8 (1–24)	NA	6.5 (1–29)
Disease phenotype	NA	16 RR	NA	14 RR/2 SP
Mean cognitive task scores (SD)				
Symbol Digit Modalities Test	64.50 (10.1)	59.38 (9.0)	61.55 (12.3)	59.88 (8.5)
Paced Auditory Serial Addition Test	51.81 (8.6)	49.44 (9.8)	51.73 (7.5)	54.25 (6.4)
California Verbal Learning Test	53.69 (10.7)	56.25 (12.1)	54.09 (12.9)	49.06 (11.4)
Brief Visuospatial Memory Test–Revised	26.56 (3.9)	25.31 (4.7)	27.18 (5.1)	26.81 (5.2)
Controlled Word Association Test	44.44 (9.3)	47.13 (10.9)	45.36 (7.1)	45.94 (8.3)
Motion characteristics, mm				
Mean (SD)	0.275 (0.10)	0.290 (0.09)	0.309 (0.11)	0.254 (0.07)
Peak (SD)	0.629 (0.36)	0.724 (0.45)	0.742 (0.37)	0.555 (0.30)

**Note:**—RR indicates relapse–remitting; SP, secondary–progressive; NA, not applicable; EDSS, Expanded Disability Status Scale.

<sup>a</sup>n = 11 for male control subjects on all cognitive tasks.

tients with MS show differences in both the pattern and magnitude of fcMRI values, and there is some indication that these changes are related to the level of disease burden and cognitive deficits.<sup>20,22–26</sup> In particular, connectivity between the posterior cingulate and other structures in the default mode network has shown a relationship with cognition.<sup>23,27</sup>

It is unclear whether fcMRI values are affected by sex. One study found no differences between men and women in a sample of more than 600 participants,<sup>28</sup> whereas another study in a similar sample found higher fcMRI values in the default mode network, the left inferior frontal gyrus, and bilateral basal ganglia in women and higher fcMRI values in motor and sensory networks in men.<sup>29</sup> Other studies have found higher fcMRI values in the parietal, insular, and occipital regions in men; higher connectivity in the frontal and temporal regions, posterior cingulate, and parietal lobe in women; greater hemispheric asymmetry in men; and higher overall internetwork connectivity in men.<sup>29–33</sup>

Two studies have specifically assessed the effect of sex on fcMRI values in patients with MS. In a study that used synchronization likelihood and graph analysis, healthy men showed significantly higher synchronization and network efficiency when compared with healthy women, whereas men with MS had lower synchronization levels and reduced network efficiency compared with healthy men.<sup>34</sup> In contrast, Schoonheim et al<sup>25</sup> found higher synchronization in men with MS compared with healthy men when these factors were assessed with magnetoencephalography.

The default mode network (DMN) is a well-characterized resting-state network, comprising portions of the anterior (ACC) and posterior cingulate (PCC), precuneus, inferior parietal lobules, and prefrontal cortex.<sup>35</sup> Although the DMN is most active during a “resting” state, many studies have shown a relationship between DMN characteristics, cognitive performance, and disease status.<sup>23,26,36</sup> Compared with control subjects, patients with MS show decreases in DMN connectivity in the left medial prefrontal cortex, left precentral gyrus, right inferior frontal gyrus, left inferior temporal gyrus, and the ACC.<sup>23,26,37</sup> The ACC and left medial prefrontal cortex have shown a relationship with cognitive performance in MS, with better performance leading to increased DMN activity.<sup>26</sup> Several regions have shown increased DMN connectivity in patients with MS, including the right inferior parietal

lobule and the lateral regions of the PCC.<sup>23</sup> Although the DMN has shown a clear relationship to disease status in MS, to date no studies have examined sex differences.

In the present study, we used a seed-based approach to assess sex differences among patients with MS and control subjects in fcMRI of the whole brain to the posterior cingulate, a primary node in the DMN. A seed-based approach allows investigation of the DMN while also allowing investigation of peripherally related regions that may be involved in disease processes. We also considered the relationships among cognitive function, sex, and functional connectivity in MS. We found regional variations in the strength of connectivity to the PCC in patients with MS, and we found sex- and disease-status interactions in connectivity to the right caudate and left dorsal lateral prefrontal cortex (DLPFC).

## MATERIALS AND METHODS

From a larger dataset of patients with MS and control subjects, on the basis of being able to make an age- and sex-matched subsample, we selected 32 patients with MS and 32 healthy control subjects. Participants with MS were diagnosed by use of the International Panel Criteria for MS, with the diagnosis confirmed by a neurologist at the time of participation.<sup>38</sup> There were equal numbers of men and women in both samples (Table 1). All study participants were scanned by use of a 12-channel receive-only head coil on a Trio 3T scanner (Siemens, Erlangen, Germany). All participants used a bite bar during the scanning session to restrict head motion. After informed consent was given, the study participants were scanned in a single session by use of the following Cleveland Clinic Institutional Review Board–approved protocol:

Scan 1: Whole-brain T1 MPRAGE: 120 axial sections; thickness, 1.2 mm; FOV 256 × 256 mm; TI/TE/TR/flip angle, 900/1.71/1900 ms/8°; matrix, 256 × 128; band width, 62 kHz.

Scan 2: Whole-brain resting-state fcMRI study, with eyes closed: 132 repetitions of 31 4-mm-thick axial sections (no gap); matrix, 128 × 128; in-plane resolution, 2 × 2 mm; TE/TR/flip angle, 29/2800 ms/80°; FOV, 256 × 256 mm<sup>2</sup>; band width, 1954 Hz/pixel.

## Image Postprocessing

Functional connectivity data were postprocessed as follows: Cardiac and respiratory fluctuations, measured during

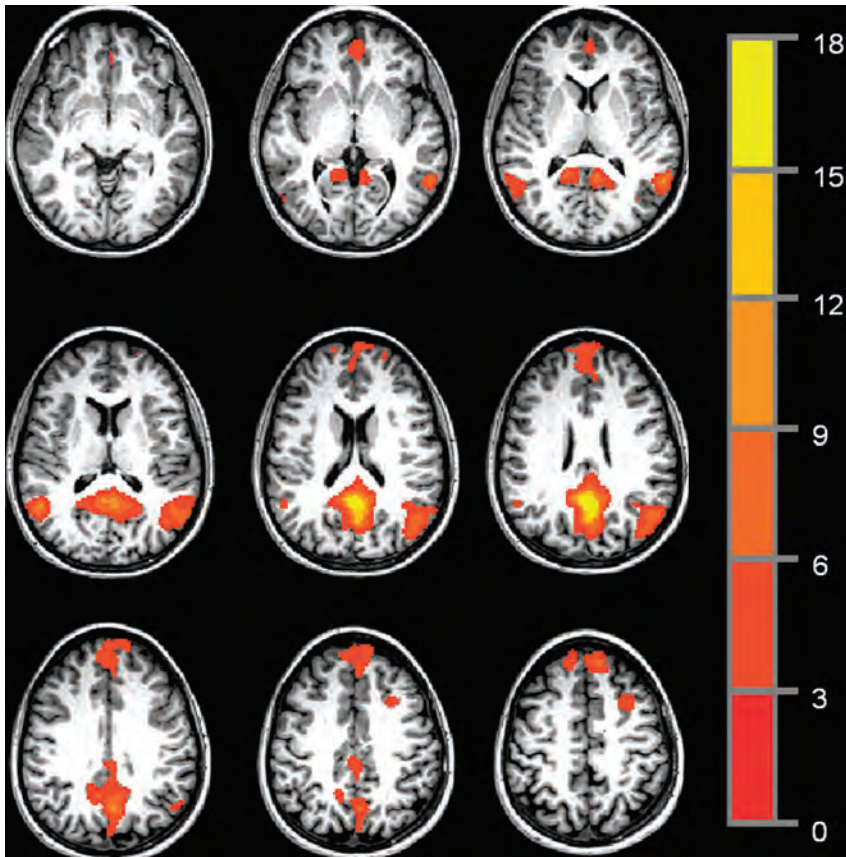


**FIG 1.** Representative single-participant PCC functional connectivity map, thresholded at  $P = .005$ , cluster size = 36, for an effective voxelwise  $P$  of  $1 \times 10^{-7}$ .

scanning, were regressed out at the voxel level with the use of RETROICOR.<sup>39</sup> Data were retrospectively motion-corrected by use of the AFNI (<http://afni.nimh.nih.gov/afni/>) program 3dvolreg, and output from 3dvolreg was used to identify and regress signal fluctuations that corresponded to voxel-level displacement.<sup>40</sup> Data were spatially filtered with a Hamming filter, temporally filtered to remove fluctuations  $>0.08$  Hz, and smoothed by use of the AFNI program 3dmerge with a 6-mm kernel.<sup>40</sup>

#### **Volumetric Analysis**

Tissue volume was estimated with the FSL (<http://www.fmrib.ox.ac.uk/fsl>) program SIENAX.<sup>41,42</sup> With the use of the T1 volume, SIENAX first applies an affine registration to Montreal Neurological Institute (MNI) 152 space to obtain a volumetric scaling factor.<sup>43,44</sup> Total gray matter, white matter, and CSF are calculated by means of tissue segmentation and are then normalized for head size by means of the scaling factor.<sup>45</sup> Segmentation maps were visually inspected to ensure accuracy, and a 2-way ANOVA and Tukey honest significance test were used to calculate between-group differences for gray and white matter volumes.<sup>46</sup>

#### **Image Analysis**

The AFNI tool InstaCorr was used to identify a seed for fMRI analysis.<sup>47</sup> This tool can be used to create individual fMRI maps on the basis of a given seed voxel and can determine how strongly

voxels are related to an fMRI network of interest. In the current study, a subset of 15 patients and 15 matched control subjects was used in a preliminary analysis to identify the midline PCC region of interest. For each of the 30 participants, InstaCorr was used to manually select the posterior cingulate voxel that had the highest correlation with traditional DMN regions, including the ACC, inferior parietal lobules, and medial prefrontal cortex. One-voxel PCC ROIs in native space were aligned to the anatomic volume by use of the AFNI program align\_epi\_anat.py,<sup>48</sup> and were then transferred to common space by use of a 12-degree of freedom affine coregistration to the MNI template.<sup>49</sup> Through manual inspection, it was determined that the spatial variation in MNI space was small enough across all 30 participants to justify generalizing a group-based region of interest to the entire sample of 32 patients and 32 control subjects. It was verified that a 4-mm diameter sphere at  $[1 -43 16]$  was sufficient to encompass the location of the PCC region of interest in all 30 of the tested participants. The 4-mm diameter sphere represents an estimate of the location of the PCC node of the default mode network and served as our fMRI seed for the re-

mainder of the analysis.

To avoid issues of resampling, PCC functional connectivity maps were created in native space. The group-based PCC ROI was warped into native space for each of the 64 participants and manually inspected to ensure that the transformation to native space resulted in placement of the ROI within the PCC. Any voxels included in the ROI that were not within PCC were excluded from the analysis. Through the use of Matlab (MathWorks, Natick, Massachusetts), a resting-state reference time-series was produced by taking the linearly detrended average time-series of all voxels in the PCC ROI, and a cross-correlation was calculated between the reference time-series and the linearly detrended resting-state time-series on a voxel-by-voxel basis.<sup>46</sup> The correlation was converted to a Student  $t$ , and the distribution was then normalized to unit variance and zero mean.<sup>50</sup> The resulting map indicates the strength of connection to the reference time-series in the PCC ROI. Fig 1 shows a representative single-participant PCC functional connectivity map, thresholded at  $P = .0005$ , with a cluster size of 36, for an effective voxelwise  $P$  of  $1 \times 10^{-7}$ .

Participants were then divided into 4 age-matched groups: male control subjects, female control subjects, male patients, and female patients (Table 1). Connectivity maps from the 32 patients and their matched healthy control subjects were transferred to MNI space and entered into a 2-way ANOVA by use of the AFNI program 3danova2.<sup>40</sup> The categories for the ANOVA were sex and

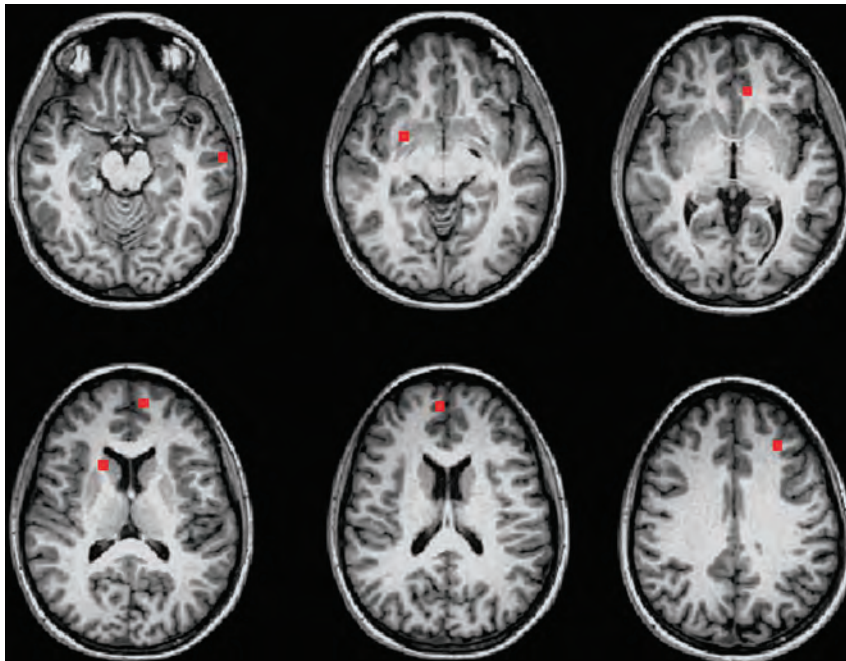


**FIG 2.** Nine-voxel in-plane ROIs centered at the voxel of highest significance for each region showing significant group differences in a 2-way ANOVA ( $P = 1 \times 10^{-5}$ ).

disease status. The resulting maps were thresholded at  $P = .01$  with a cluster size of 74, for an effective voxelwise  $P$  of  $1 \times 10^{-5}$ . In MNI space, a 9-voxel in-plane ROI was centered at the voxel of highest significance for each region identified in the ANOVA (Fig 2). To obtain individual subject fcMRI measures for post hoc analysis, ROIs for regions identified in the ANOVA were transferred to native space, aligned to the PCC fcMRI map, and visually inspected to ensure placement within the structure of interest. The mean values of connectivity to the PCC in significant ROIs were compared in a post hoc analysis by use of paired Student  $t$  tests and Tukey range test for correction of multiple comparisons.<sup>46</sup>

### Behavioral Data

All participants completed 5 cognitive tests, with the exception of 4 male control subjects. These 4 male control subjects were included in the fcMRI analysis but were not included in the cognitive performance/fcMRI comparison because of missing cognitive test data. The tests included measures of verbal and spatial memory (the California Verbal Learning Test-II and the Brief Visuospatial Memory Test-Revised), speed of processing and sustained attention (the Paced Auditory Serial Addition Test, 3 second administration and the oral version of the Symbol Digit Modalities Test), and verbal fluency (the Controlled Word Association Test). In addition, all participants were rated by a trained clinician on the Expanded Disability Status Scale.<sup>51</sup>

## RESULTS

### Demographics

Thirty-two patients with MS and 32 healthy control subjects were divided into 4 age-matched groups on the basis of sex (Table 1). Groups showed no differences in age or education, and the male

and female patient groups showed no differences in Expanded Disability Status Scale or disease duration.

### Behavioral Data

For each test, all study patients scored within 2 standard deviations of the mean performance of healthy control subjects. Raw score mean and standard deviation for each test are reported in Table 1. For group comparisons and correlation with imaging measures, cognitive measures were corrected on the basis of available norms. Both California Verbal Learning Test-II and Brief Visuospatial Memory Test-Revised total recall scores were converted to  $t$ -scores on the basis of age-corrected norms.<sup>52,53</sup> Raw scores for the oral Symbol Digit Modalities Test and the Controlled Word Association Test were converted to  $z$ -scores by means of norms corrected for age and level of education.<sup>54,55</sup> Paced Auditory Serial Addition Test raw scores were converted to  $z$ -scores by means of norms corrected for level of education.<sup>56</sup>

Unpaired Student  $t$  tests were used to compare cognitive performance. No significant differences in cognitive performance were found between patients and control subjects or between sexes.

### Volumetric Analysis

In a 2-way ANOVA, white matter differences were significant in both the disease and sex conditions, with no significant interaction effect. Although patients showed lower white matter volume as compared with control subjects ( $P = 9 \times 10^{-4}$ ), when all female participants (patient and control) were compared with all male participants, female participants showed significantly less white matter overall ( $P = 1 \times 10^{-4}$ ). The difference in white matter volume between sexes was greater in control subjects ( $P = 6 \times 10^{-4}$ ) than in patients ( $P = .033$ ). The opposite pattern emerged for gray matter. In the 2-way ANOVA, gray matter showed significance only in the sex condition ( $P = 3 \times 10^{-3}$ ), in which female participants showed higher gray matter volume as compared with male participants. The difference between sexes was of similar magnitude in control subjects ( $P = .035$ ) and patients ( $P = .017$ ).

### Motion

All functional connectivity datasets were assessed for motion by use of mean peak-to-peak displacement. Participants with a mean peak-to-peak displacement  $>0.4$  mm were flagged for visual inspection of the fcMRI time-series and subsequent correlation maps. Data from 3 patients and 3 control subjects were flagged for inspection. No evidence of motion-related artifact, including rings of correlation around the outside of the head, correlation in the ventricles, and rapid correlation pattern changes from section to section (a consequence of motion in an interleaved style acquisition), was found. On the basis of these criteria, no participants

**Table 2: Mean fcMRI values for MS and healthy control groups, by sex**

Region	MNI Coordinates	Mean fcMRI Value (SD)						P Value <sup>a</sup>
		Female Control Subjects	Female Patients	Male Control Subjects	Male Patients	All Control Subjects	All Patients	
Left medial frontal gyrus	[-7 61 3.8]	0.432 (0.773)	1.768 (1.833)	-0.044 (0.899)	1.050 (0.857)	0.194 (0.860)	1.409 (1.454)	.0001
Right medial frontal gyrus	[7 59 7.4]	1.292 (1.057)	2.317 (1.352)	1.101 (1.543)	2.367 (1.076)	1.197 (1.305)	2.342 (1.202)	.0005
Left anterior cingulate	[-7 40 -11.8]	-0.094 (0.471)	0.510 (1.017)	-0.430 (0.509)	0.603 (1.145)	-0.262 (0.512)	0.556 (1.066)	.0002
Right putamen	[27 10 -15.4]	-0.550 (0.913)	0.436 (0.681)	-0.339 (0.735)	0.237 (0.689)	-0.445 (0.823)	0.336 (0.681)	.0001
Left middle temporal gyrus	[-56 -4 -23.8]	0.376 (0.404)	0.991 (1.010)	0.162 (0.332)	1.253 (1.142)	0.269 (0.380)	1.122 (1.068)	.0001
Left DLPFC	[-25 40 19.4]	-0.986 (0.660)	-0.147 (0.809)	-0.194 (0.637)	0.848 (0.830)	-0.590 (0.754)	-0.497 (0.881)	NS
Right caudate	[19 24 3.8]	-0.642 (0.909)	0.210 (0.651)	0.094 (0.818)	-0.463 (0.612)	-0.274 (0.929)	-0.127 (0.710)	NS

Note:—NS indicates not significant.

<sup>a</sup>P values for control subject and patient comparisons.

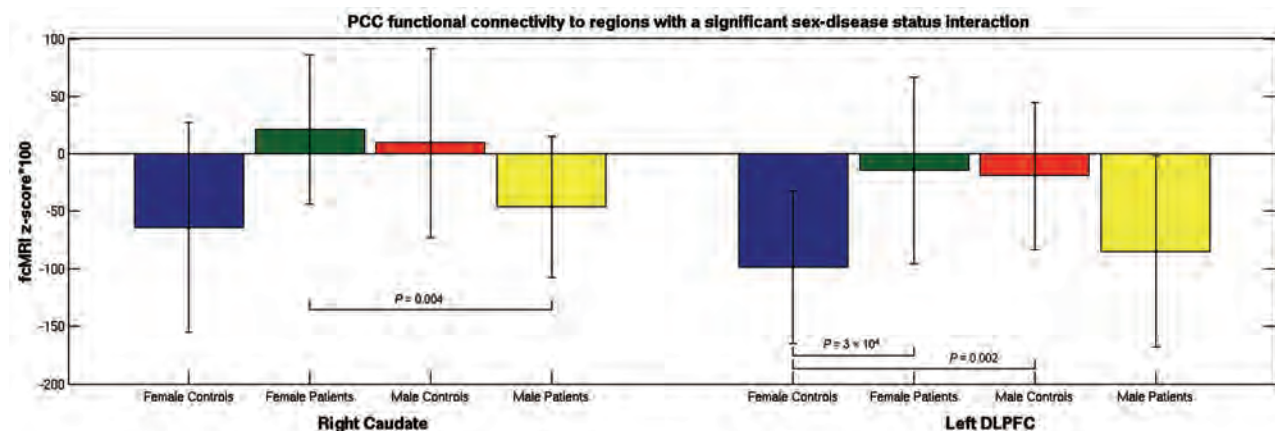


**FIG 3.** Mean functional connectivity to the PCC for regions that showed a sex-disease status.

were excluded because of motion. No significant differences in motion characteristics were found between patients and control subjects or between sexes (Table 1).

### Functional Connectivity

The voxelwise 2-way ANOVA showed significant differences in strength of connectivity to the PCC between patients and control subjects in the bilateral medial frontal gyri, the left ventral anterior cingulate, the right putamen, and the left middle temporal gyrus ( $P < 1 \times 10^{-5}$ ). Analysis of the sex/disease status interaction demonstrated a significant difference between groups in the right caudate ( $P = 4 \times 10^{-4}$ ) and the left middle frontal gyrus (specifically the left DLPFC) ( $P = 2 \times 10^{-4}$ ). There were no significant differences between regions on the basis of sex alone.

In the post hoc comparison, the bilateral medial frontal gyri, left ventral anterior cingulate, right putamen, and left middle temporal gyrus showed significant differences between the full patient and control groups ( $P < 5 \times 10^{-4}$ ) (Table 2). The right caudate and left DLPFC showed a disease status/sex interaction effect (Fig 3). These regions were compared by use of 4 *t* tests: 1) female patient versus female control; 2) male patient versus male control; 3) male patient versus female patient; and 4) male control versus female control. In the right caudate, male patients showed significantly weaker connectivity to the PCC compared with female patients ( $P = .004$ ). In the left DLPFC, female patients showed significantly stronger connectivity to the PCC compared with female control subjects ( $P = 3 \times 10^{-4}$ ). Control subjects also

showed a significant difference, with male subjects showing stronger PCC–left DLPFC connectivity in comparison with female subjects ( $P = .002$ ).

To rule out caudate atrophy as a cause of between-sex differences, we used the FreeSurfer image analysis suite (<http://surfer.nmr.mgh.harvard.edu>) to automatically segment the right and left caudate.<sup>57,58</sup> After manual inspection for accuracy, caudate volumes were corrected for head size and a 2-way ANOVA was used to compare volumes among the 4 groups. Disease status showed a significant effect on the left side only, with patients showing significantly smaller volumes than control subjects ( $P = .327$ ). Neither right nor left caudate volume correlated with connectivity measures.

In regions that showed differences between the patient and control groups, connectivity was compared with overall gray and white matter volume by use of a Pearson correlation. Connectivity values did not correlate with overall gray or white matter volumes in the control group. In patients, overall gray matter volume was positively associated with increased connectivity between the PCC and the left middle temporal gyrus ( $r = -0.5297, P = .001$ ). There were no correlations between fcMRI and cognition in any of the groups, and patients did not show correlations between connectivity measures and disease duration.

### DISCUSSION

The present study demonstrated that specific fcMRI differences between patients with MS and control subjects are influenced by

sex and disease status. The bilateral medial frontal gyri, right putamen, left anterior cingulate, and left middle temporal gyrus appear to have clear patient/control effects in both sexes, whereas differences in the left middle frontal gyrus and the right caudate are dependent on sex interactions.

In the present study, sex effects were most obvious in the left DLPFC and the right caudate. Although the levels of connectivity were low overall, the patterns of connectivity were opposite for male/female control subjects and patients in both regions. In the caudate, sex differences were significant in patients but not in healthy control subjects. The caudate is a frequent site of gray matter atrophy in MS,<sup>59</sup> and there is some indication that men experience a greater level of gray matter atrophy.<sup>17</sup> Although we did find that patients had a decrease in left caudate volume, we did not find that caudate volumes differed by sex. Both this finding and the use of a small, targeted ROI, manually inspected for placement, greatly diminish potential effects of atrophy and partial voluming on fcMRI measures.

Female control subjects and female patients had a significant difference in fcMRI values in the left DLPFC; this area was also the only region to demonstrate sex differences in connectivity between healthy control subjects. Previous studies have found that atrophy in the DLPFC may be linked to cognitive decline and alterations in functional activation in MS.<sup>60-62</sup> In our study, increased connectivity to the DLPFC was seen in female patients only, with male patients showing a weaker connectivity similar to that of female control subjects. In contrast, male control subjects demonstrated stronger connectivity to the DLPFC than did female control subjects, with values similar to those of female patients. Although it is difficult to directly compare this finding to the results of previous studies of sex differences in fcMRI, our use of a seed-based region of interest in the PCC is similar to that of Biswal et al,<sup>32</sup> whose work also found stronger connectivity to the left middle frontal gyrus in men.

We also found sex and disease effects in an analysis of white and gray matter volumes, corrected for head size. In patient and control groups, overall white matter volume was lower in women than in men, whereas overall gray matter volume was higher, a finding in line with a number of previous studies.<sup>63,64</sup> Patients with MS showed lower white matter volume than that in control subjects but showed no difference in gray matter volumes. Both gray and white matter volume loss is a common finding in MS,<sup>65</sup> though it has been suggested that gray matter loss is more closely associated with increased levels of disability.<sup>66</sup> Although we did find that fcMRI of the PCC–left middle temporal gyrus was related to gray matter loss in patients, the finding of equivalent gray matter and the lack of correlations between cognition and fcMRI measures in patients may be the result of the lack of cognitive impairment in our patient group. In a study of control subjects and both cognitively preserved and cognitively impaired patients with MS, Bonavita et al<sup>23</sup> found that patients showed lower connectivity in the anterior and midline posterior cingulate compared with healthy control subjects, with increased connectivity at the boundaries of the posterior cingulate and in parieto-occipital regions. The investigators also found a positive relationship between cognitive ability and fcMRI values in the anterior cingulate in cognitively preserved patients, whereas a negative relationship

was observed between cognitive ability and fcMRI values in the PCC in cognitively impaired patients. These data and similar results from a study by Rocca et al<sup>26</sup> suggest that a sample without cognitively impaired patients may not fully capture links between fcMRI and cognition. Although our population is not significantly impaired, we already see a number of changes in functional connectivity. Ideally, a longitudinal study of patients with MS could verify which imaging changes precede cognitive decline and which changes are the result of further disease progression.

The dataset used in the current study was small, and although male and female patients with MS were matched with control subjects for age, sex, education, and Expanded Disability Status Scale, lesion load or other measures of disability may have affected the results. A larger sample is necessary to further assess sex differences in MS and to clarify the relationships among sex, disease progression, cognitive decline, and potential imaging markers such as fcMRI.

## CONCLUSIONS

Our results suggest that female and male patients with MS have differences in the strength of functional connectivity from the posterior cingulate to the caudate and the DLPFC. This finding builds on the growing evidence of sex differences in MS and should serve as a reminder that sex differences must be taken into account in MS research.

## ACKNOWLEDGMENTS

The authors thank John Cowan, Tami Gaebelein, Sarah Gallucci, Blessy Mathews, Katie Murphy, and Derrek Tew for their contributions to this work.

Disclosures: Katherine Koenig—RELATED: Grant: National Multiple Sclerosis Society,\* NIH,\* Comments: NMSS RG 4110-A-two “fMRI & DTI Evaluation of Hippocampal Damage and Episodic Memory Loss in MS”; NIH R01NS035058 “Pathogenesis of demyelination of MS Brains”; UNRELATED: Grants/Grants Pending: CHDI Foundation.\* Mark Lowe—RELATED: Grant: National Multiple Sclerosis Society.\* Jian Lin—UNRELATED: Grants/Grants Pending: NIH,\* National Multiple Sclerosis Society,\* Lincy Foundation.\* Ken Sakaie—RELATED: Grant: National Institutes of Health,\* National Multiple Sclerosis Society.\* Robert Bermeil—UNRELATED: Consultancy: Biogen Idec, Novartis, Teva Astellas, Questcor. Erik Beall—RELATED: Grant: “Enhancing the PESTICA Toolkit: Open-Source Physiologic Noise Detection and Removal” 1R03EB012968–01A1, PI, 25%\*; “Functional MRI of Human Brain Language Systems” 2R01NS035929–10A1, Co-I, 10%\*; Stephen Rao—UNRELATED: Consultancy: Novartis, Genzyme, Biogen Idec; Grants/Grants Pending: NIH,\* CHDI Foundation,\* DoD,\* National MS Society\*; Payment for Manuscript Preparation: Biogen Idec, Novartis; Royalties: American Psychological Association. Bruce Trapp—RELATED: Grant: NIH,\* Comments: Pathogenesis in Demyelination of MS Brains R01NS035058; UNRELATED: Consultancy: Renovo Neural, Biogen Idec, Teva, Novartis Pharmaceuticals; Payment for Lectures (including service on speakers bureaus): EMD Serono. Michael Phillips—RELATED: Grant: National Multiple Sclerosis Society; Support for Travel to Meetings for the Study or Other Purposes: National Multiple Sclerosis Society\*; UNRELATED: Grants/Grants Pending: National Multiple Sclerosis Society (\*money paid to institution).

## REFERENCES

1. Debouverie M, Pittion-Vouyovitch S, Louis S, et al. **Increasing incidence of multiple sclerosis among women in Lorraine, Eastern France.** *Mult Scler* 2007;13:962–67
2. Celius E, Vandvik B. **Multiple sclerosis in Oslo, Norway: prevalence on 1 January 1995 and incidence over a 25-year period.** *Eur J Neurol* 2001;8:463–69
3. Orton S, Herrera B, Yee I, et al. **Sex ratio of multiple sclerosis in Canada: a longitudinal study.** *Lancet Neurol* 2006;5:932–36

4. Bove R, Healy B, Augustine A, et al. **Effect of gender on late-onset multiple sclerosis.** *Mult Scler* 2012;18:1472–79
5. Khaleeli Z, Ciccirelli O, Manfredonia F, et al. **Predicting progression in primary progressive multiple sclerosis: a 10-year multicenter study.** *Ann Neurol* 2008;63:790–93
6. Runmarker B, Andersen O. **Prognostic factors in a multiple sclerosis incidence cohort with twenty-five years of follow-up.** *Brain* 1993;116:117–34
7. Koutsis G, Evangelopoulos M, Andreadou E, et al. **The onset of multiple sclerosis in Greece: a single-center study of 1,034 consecutive patients.** *Eur Neurol* 2010;63:350–56
8. Menon R, Di Dario M, Cordiglieri C, et al. **Gender-based blood transcriptomes and interactomes in multiple sclerosis: involvement of SPI dependent gene transcription.** *J Autoimmun* 2012;38:J144–55
9. Zoccollella S, Tortorella C, Iaffaldano P, et al. **Low serum urate levels are associated to female gender in multiple sclerosis patients.** *PLoS One* 2012;7:e40608
10. Greer JM, Csurhes PA, Pender MP, et al. **Effect of gender on T-cell proliferative responses to myelin proteolipid protein antigens in patients with multiple sclerosis and controls.** *J Autoimmun* 2004;22:345–52
11. D'hooghe MB, Haentjens P, Nagels G, et al. **Menarche, oral contraceptives, pregnancy and progression of disability in relapsing onset and progressive onset multiple sclerosis.** *J Neurol* 2012;259:855–61
12. Kipp M, Amor S, Krauth R, et al. **Multiple sclerosis: neuroprotective alliance of estrogen–progesterone and gender.** *Front Neuroendocrinol* 2012;33:1–16
13. Tomassinia V, Pozzilli C. **Sex hormones, brain damage and clinical course of multiple sclerosis.** *J Neurol Sci* 2009;286:35–39
14. Sicotte NL, Liva SM, Kluth R, et al. **Treatment of multiple sclerosis with the pregnancy hormone estriol.** *Ann Neurol* 2002;52:421–28
15. Ziehn M, Avedisian A, Dervin S, et al. **Estriol preserves synaptic transmission in the hippocampus during autoimmune demyelinating disease.** *Lab Invest* 2012;92:1234–45
16. Fazekas F, Enzinger C, Wallner-Blazek M, et al. **Gender differences in MRI studies on multiple sclerosis.** *J Neurol Sci* 2009;286:28–30
17. Antulov R, Weinstock-Guttman B, Cox J, et al. **Gender-related differences in MS: a study of conventional and nonconventional MRI measures.** *Mult Scler* 2009;15:345–54
18. Li D, Zhao G, Paty D, et al. **Randomized controlled trial of interferon-beta-1a in secondary progressive MS: MRI results.** *Neurology* 2001;56:1505–13
19. Riccitelli G, Rocca M, Pagani E, et al. **Mapping regional grey and white matter atrophy in relapsing-remitting multiple sclerosis.** *Mult Scler* 2012;18:1027–37
20. Massella A, D'Intino G, Fernández M, et al. **Gender effect on neurodegeneration and myelin markers in an animal model for multiple sclerosis.** *BMC Neurosci* 2012;13:1–14
21. Biswal B, Yetkin FZ, Haughton VM, et al. **Functional connectivity in the motor cortex of resting human brain using echo-planar MRI.** *Magn Reson Med* 1995;34:537–41
22. Faivre A, Rico A, Zaaraoui W, et al. **Assessing brain connectivity at rest is clinically relevant in early multiple sclerosis.** *Mult Scler* 2012;18:1251–58
23. Bonavita S, Gallo A, Sacco R, et al. **Distributed changes in default-mode resting-state connectivity in multiple sclerosis.** *Mult Scler* 2011;17:411–22
24. Parisi L, Rocca M, Valsasina P, et al. **Cognitive rehabilitation correlates with the functional connectivity of the anterior cingulate cortex in patients with multiple sclerosis.** *Brain Imaging Behav* 2012 Apr 19 [Epub ahead of print]
25. Schoonheim M, Geurts J, Landi D, et al. **Functional connectivity changes in multiple sclerosis patients: a graph analytical study of MEG resting state data.** *Hum Brain Mapp* 2013;34:52–61
26. Rocca M, Valsasina P, Absinta M, et al. **Default-mode network dysfunction and cognitive impairment in progressive MS.** *Neurology* 2010;74:1252–59
27. Hawellek D, Hipp J, Lewis C, et al. **Increased functional connectivity indicates the severity of cognitive impairment in multiple sclerosis.** *Proc Natl Acad Sci U S A* 2011;108:19066–71
28. Segall J, Allen E, Jung R, et al. **Correspondence between structure and function in the human brain at rest.** *Front Neuroinform* 2012;6:1–17
29. Allen E, Erhardt E, Damaraju E, et al. **A baseline for the multivariate comparison of resting-state networks.** *Front Syst Neurosci* 2011;5:1–23
30. Filippi M, Valsasina P, Misci P, et al. **The organization of intrinsic brain activity differs between genders: a resting-state fMRI study in a large cohort of young healthy subjects.** *Hum Brain Mapp* 2013;34:1330–43
31. Tian L, Wang J, Yan C, et al. **Hemisphere- and gender-related differences in small-world brain networks: a resting-state functional MRI study.** *Neuroimage* 2011;54:191–202
32. Biswal B, Mennes M, Zuo X, et al. **Toward discovery science of human brain function.** *Proc Natl Acad Sci U S A* 2010;107:4734–39
33. Liu H, Stufflebeam S, Sepulcre J, et al. **Evidence from intrinsic activity that asymmetry of the human brain is controlled by multiple factors.** *Proc Natl Acad Sci U S A* 2009;106:20499–503
34. Schoonheim M, Hulst H, Landi D, et al. **Gender-related differences in functional connectivity in multiple sclerosis.** *Mult Scler* 2012;18:164–73
35. Raichle M, MacLeod A, Snyder A, et al. **A default mode of brain function.** *Proc Natl Acad Sci U S A* 2001;98:676–82
36. Anticevic A, Cole M, Murray J, et al. **The role of default network deactivation in cognition and disease.** *Trends Cogn Sci* 2012;16:584–92
37. Rocca M, Valsasina P, Martinelli V, et al. **Large-scale neuronal network dysfunction in relapsing-remitting multiple sclerosis.** *Neurology* 2012;79:1449–57
38. McDonald W, Compston A, Edan G, et al. **Recommended diagnostic criteria for multiple sclerosis: guidelines from the International Panel on the Diagnosis of Multiple Sclerosis.** *Ann Neurol* 2001;50:121–27
39. Glover G, Li T, Ress D. **Image-Based Method for Retrospective Correction of Physiological Motion Effects in fMRI: RETROICOR.** *Magn Reson Med* 2000;44:162–67
40. Cox R. **AFNI: software for analysis and visualization of functional magnetic resonance neuroimages.** *Comput Biomed Res* 1996;29:162–73
41. Smith SM, Zhang Y, Jenkinson M, et al. **Accurate, robust and automated longitudinal and cross-sectional brain change analysis.** *NeuroImage* 2002;17:479–89
42. Smith SM, Jenkinson M, Woolrich MW, et al. **Advances in functional and structural MR image analysis and implementation as FSL.** *NeuroImage* 2004;23:208–19
43. Jenkinson M, Smith SM. **A global optimisation method for robust affine registration of brain images.** *Med Image Anal* 2001;5:143–56
44. Jenkinson M, Bannister PR, Brady JM, et al. **Improved optimisation for the robust and accurate linear registration and motion correction of brain images.** *NeuroImage* 2002;17:825–41
45. Zhang Y, Brady M, Smith M. **Segmentation of brain MR images through a hidden Markov random field model and the expectation maximization algorithm.** *IEEE Trans Med Imaging* 2001;20:45–57
46. MATLAB. *Version 7.4.0 (R2007a)*. Natick, Massachusetts: The MathWorks Inc; 2007
47. Cox R, Saad Z. **Surfing the connectome: InstaCorr in AFNI and SUMA.** *Second Biennial International Conference on Resting-State Functional Brain Connectivity*. Milwaukee, Wisconsin; September 16–19, 2010
48. Saad Z, Glen D, Chen G, et al. **A new method for improving functional-to-structural alignment using local Pearson correlation.** *NeuroImage* 2009;44:839–48
49. Beall E, Lowe M. **Isolating physiologic noise sources with independently determined spatial measures.** *NeuroImage* 2007;37:1286–300
50. Lowe M, Mock B, Sorenson J. **Functional connectivity in single and**

- multislice echoplanar imaging using resting-state fluctuations.** *NeuroImage* 1998;7:119–32
51. Kurtzke J. **Rating neurologic impairment in multiple sclerosis: an expanded disability status scale (EDSS).** *Neurology* 1983;33:1444–52
  52. Delis D, Kramer J, Kaplan E, et al. *California Verbal Learning Test—Second Edition.* San Antonio, Texas: Psychological Corporation; 2000
  53. Benedict R. *Brief Visuospatial Memory Test—Revised Professional Manual.* Odessa, Florida: Psychological Assessment Resources; 1997
  54. Smith A. *Symbol Digit Modalities Test: Manual.* Los Angeles: Western Psychological Services; 1982
  55. Tombaugh T, Kozak J, Rees L. **Normative data stratified by age and education for two measures of verbal fluency: FAS and animal naming.** *Arch Clin Neuropsychol* 1999;14:167–77
  56. Rao S. *A Manual for the Brief, Repeatable Battery of Neuropsychological Tests in Multiple Sclerosis.* Milwaukee: Medical College of Wisconsin; 1990
  57. Fischl B, Salat D, Busa E, et al. **Whole brain segmentation: automated labeling of neuroanatomical structures in the human brain.** *Neuron* 2002;33:341–55
  58. Fischl B, Salat D, van der Kouwe A, et al. **Sequence-independent segmentation of magnetic resonance images.** *NeuroImage* 2004;23: S69–84
  59. Bermel R, Innus M, Tjoa C, et al. **Selective caudate atrophy in multiple sclerosis: a 3D MRI parcellation study.** *NeuroReport* 2003;14: 335–39
  60. Nocentini U, Bozzali M, Spanò B, et al. **Exploration of the relationships between regional grey matter atrophy and cognition in multiple sclerosis.** *Brain Imaging Behav* 2012 May 15 [Epub ahead of print]
  61. Morgen K, Sammer G, Courtney S, et al. **Distinct mechanisms of altered brain activation in patients with multiple sclerosis.** *NeuroImage* 2007;37:937–46
  62. Tekok-Kilic A, Benedict R, Weinstock-Guttman B, et al. **Independent contributions of cortical gray matter atrophy and ventricle enlargement for predicting neuropsychological impairment in multiple sclerosis.** *NeuroImage* 2007;36:1294–300
  63. Gur R, Turetsky B, Matsui M, et al. **Sex differences in brain gray and white matter in healthy young adults: correlations with cognitive performance.** *J Neurosci* 1999;19:4065–72
  64. Allen J, Damasio H, Grabowski T, et al. **Sexual dimorphism and asymmetries in the gray-white composition of the human cerebrum.** *NeuroImage* 2003;18:880–94
  65. Grassiot B, Desgranges B, Eustache F, et al. **Quantification and clinical relevance of brain atrophy in multiple sclerosis: a review.** *J Neurol* 2009;256:1397–412
  66. Sanfilipo M, Benedict R, Sharma J, et al. **The relationship between whole brain volume and disability in multiple sclerosis: a comparison of normalized gray vs white matter with misclassification correction.** *NeuroImage* 2005;26:1068–77

# Reduced Mortality and Severe Disability Rates in the SENTIS Trial

P.D. Schellinger, A. Shuaib, M. Köhrmann, D.S. Liebeskind, T. Jovin, M.D. Hammer, S. Sen, D.Y. Huang, S. Solander, R. Gupta, R.R. Leker, and J.L. Saver, for the SENTIS Trial Investigators



## ABSTRACT

**BACKGROUND AND PURPOSE:** The Safety and Efficacy of NeuroFlo Technology in Ischemic Stroke trial showed a trend for reduced all-cause mortality and positive secondary safety end point outcomes. We present further analyses of the mortality and severe disability data from the Safety and Efficacy of NeuroFlo Technology in Ischemic Stroke trial.

**MATERIALS AND METHODS:** The Safety and Efficacy of NeuroFlo Technology in Ischemic Stroke trial was a multicenter, randomized, controlled trial that evaluated the safety and effectiveness of the NeuroFlo catheter in patients with stroke. The current analysis was performed on the as-treated population. All-cause and stroke-related mortality rates at 90 days were compared between groups, and logistic regression models were fit to obtain ORs and 95% CIs for the treated versus not-treated groups. We categorized death-associated serious adverse events as neurologic versus non-neurologic events and performed multiple logistic regression analyses. We analyzed severe disability and mortality by outcomes of the mRS. Patient allocation was gathered by use of a poststudy survey.

**RESULTS:** All-cause mortality trended in favor of treated patients (11.5% versus 16.1%;  $P = .079$ ) and stroke-related mortality was significantly reduced in treated patients (7.5% versus 14.2%;  $P = .009$ ). Logistic regression analysis for freedom from stroke-related mortality favored treatment (OR, 2.41; 95% CI, 1.22, 4.77;  $P = .012$ ). Treated patients had numerically fewer neurologic causes of stroke-related deaths (52.9% versus 73.0%;  $P = .214$ ). Among the 90-day survivors, nominally fewer treated patients were severely disabled (mRS 5) (5.6% versus 7.5%; OR, 1.72; 95% CI, 0.72, 4.14;  $P = .223$ ). Differences in allocation of care did not account for the reduced mortality rates.

**CONCLUSIONS:** There were consistent reductions in all-cause and stroke-related mortality in the NeuroFlo-treated patients. This reduction in mortality did not result in an increase in severe disability.

**ABBREVIATIONS:** SENTIS = Safety and Efficacy of NeuroFlo Technology in Ischemic Stroke; NIHSS = National Institutes of Health Stroke Scale Score

Recently, the primary results of the Safety and Efficacy of NeuroFlo Technology in Ischemic Stroke (SENTIS) trial have been published.<sup>1</sup> NeuroFlo therapy involves partial occlusion of

the abdominal aorta that results in a prompt increase in blood volume above the partial occlusion and has been shown to specifically increase CBF by diverting blood flow from the lower limbs to the brain.<sup>2</sup> Preclinical studies in animal models and imaging studies in patients indicate that this intervention creates a substantial increase in CBF that persists beyond deflation and removal of the NeuroFlo device without an increase in intracerebral hemorrhages.<sup>1,3</sup> A feasibility study in 25 patients with ischemic stroke treated up to 24 hours after symptom onset also showed no parenchymal hematomas and no symptomatic intracerebral hemorrhages.<sup>4</sup> For an extensive review of the literature and mode of action, we refer to a recent review by Liebeskind et al.<sup>5</sup>

SENTIS was a prospective, randomized, multicenter trial to evaluate the safety and efficacy of CBF augmentation in patients with acute ischemic stroke who were able to have NeuroFlo treatment initiated within 14 hours of the onset of symptoms. SENTIS was the first randomized trial of an interventional device for stroke with a primary clinical outcomes end point, a global dis-

Received January 8, 2013; accepted after revision March 21.

From JW Klinikum (P.D.S.), Minden, Germany; University of Alberta (A.S.), Edmonton, Alberta, Canada; Universitätsklinikum Erlangen (M.K.), Erlangen, Germany; University of California, Los Angeles (D.S.L., J.L.S.), Los Angeles, California; University of Pittsburgh Medical Center (T.J., M.D.H.), Pittsburgh, Pennsylvania; St Thomas Hospital (S.Sen), Nashville, Tennessee; University of South Carolina (D.Y.H.), Columbia, South Carolina; University of North Carolina (S.Solander), Chapel Hill, North Carolina; Emory University (R.G.), Atlanta, Georgia; and Hadassah Hebrew University Medical Center (R.R.L.), Jerusalem, Israel.

Clinical Trial Registration Information: URL: <http://clinicaltrials.gov>. Unique identifier: NCT00119717.

Please address correspondence to Peter D. Schellinger, MD, PhD, FESO, Johannes Wesling Klinikum Minden, Departments of Neurology and Neurogeriatrics, Hans-Nolte-Str 1, D-32429 Minden, Germany; e-mail: [peter.schellinger@muehlenkreiskliniken.de](mailto:peter.schellinger@muehlenkreiskliniken.de)

Indicates open access to non-subscribers at [www.ajnr.org](http://www.ajnr.org)

Evidence-Based Medicine Level 1.

<http://dx.doi.org/10.3174/ajnr.A3613>

ability outcome assessment that is based on an excellent outcome on a combination of several scales (Barthel Index, National Institutes of Health Stroke Scale Score [NIHSS], mRS, and Glasgow Outcome Scale). In the intent-to-treat analysis, the SENTIS results did not achieve statistical significance for the primary efficacy end point: (OR, 1.17; 95% CI, 0.81–1.67;  $P = .407$ ). The primary safety end point was met: There was no difference in serious adverse events between groups ( $P = .923$ ). A statistical trend for all-cause mortality and positive secondary safety end point outcomes was observed.<sup>1</sup> Additionally, post hoc analyses have shown positive results, especially with regard to stroke-related mortality. In this report, we present further analyses of the mortality and severe disability data from the SENTIS trial.

## MATERIALS AND METHODS

For detailed methods of the trial, we refer to the original publication of the SENTIS trial (ClinicalTrials.gov, No. NCT00119717).<sup>1</sup> The trial was funded by CoAxia. All authors vouch for the accuracy and completeness of the data and analysis. All authors had access to all the data in the study and had final responsibility for submission of this publication.

Briefly, patients who met all of the enrollment criteria and provided written consent were allocated to NeuroFlo treatment with standard medical management (treatment) or standard medical management alone (control) through the use of a 1:1 randomization scheme that was stratified by site, baseline NIHSS, and the time from symptom onset. All patients were followed for safety and efficacy through 90 days; formal clinical assessments were performed at 6 and 24 hours and at 4 (or hospital discharge, if earlier), 30, and 90 days. The final 90-day assessment was blinded. Follow-up cranial CT imaging was performed at 24 hours and, in cases of neurologic worsening, at any time up to 90 days. Additionally, a poststudy survey was completed to gather information on patient treatment unit allocation (admission to neuro/stroke intensive care unit, other intensive care unit, stroke unit, or general unit) and the presence of “do not resuscitate”/“do not intubate,” and “comfort care only” orders.

### Statistical Analyses

All analyses were performed on the “modified as-treated” population.<sup>1</sup> Standard summary statistics were calculated for all study variables. Categorical variables were summarized by the use of frequency distributions and 95% CIs.

The proportions of patients with all-cause and stroke-related mortality were compared between groups by use of a Cochran-Mantel-Haenszel test, stratified by age and baseline NIHSS. Logistic regression models were also fit for all-cause and stroke-related mortality to obtain an OR and 95% CI for the treated versus not-treated comparison. Kaplan-Meier curves for stroke-related mortality were provided, along with estimates at specific time points (4, 30, 60, and 90 days) and their associated 95% CIs.

We qualitatively reviewed the serious adverse events related to deaths categorized into neurologic versus non-neurologic events and performed multiple logistic regression analyses for influence of baseline stroke severity (NIHSS) and allocation of treatment location/unit.

We analyzed the severe disability and mortality data by dichotomized (mRS 0–4 versus 5), tetrachotomized (mRS 0–2, 3–4, 5, 6), and full-scale (mRS 0, 1, 2, 3, 4, 5, 6) outcomes of the mRS.

All statistical tests, including those comparing the treatment groups for mortality, stroke-related mortality, and allocation to treatment location, are 2-sided. Statistical analyses were conducted in SAS version 9.1 or above (SAS Institute, Cary, North Carolina).

## RESULTS

Between October 2005 and January 2010, 515 patients were enrolled in the SENTIS trial at 68 centers. A total of 257 patients were randomly assigned to the control group and 258 patients were randomly assigned to the treatment group (intention-to-treat population). Twenty-eight patients randomly assigned to treatment were excluded because of prespecified criteria, 5 patients randomly assigned to treatment did not receive treatment, and 1 patient randomly assigned to the control group received NeuroFlo treatment (both were protocol deviations), resulting in 261 not-treated patients and 226 treated patients in the “modified as-treated” analysis.<sup>1</sup>

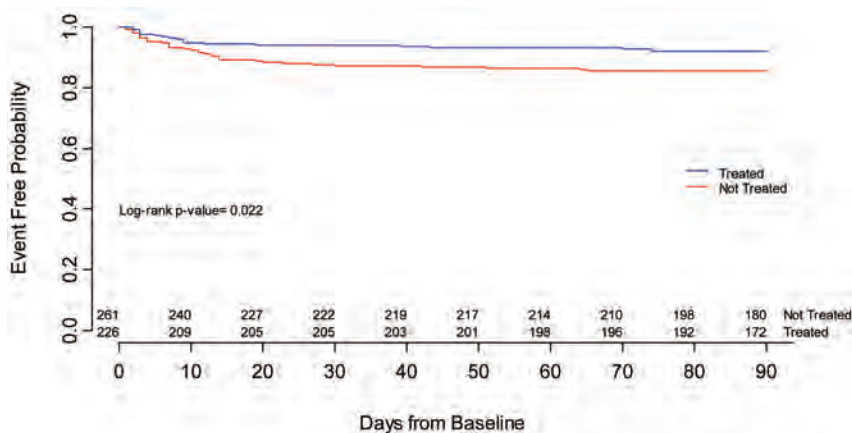
### Mortality

All-cause mortality rates (intention to treat: 11.2% versus 16.3%; OR, 1.60; 95% CI, 0.91–2.83;  $P = .086$ ; modified intention to treat: 11.3% versus 16.3%; OR, 1.56; 95% CI, 0.87–2.80;  $P = .087$ ), and stroke-related mortality (intention to treat: 7.8% versus 14.4%; OR, 2.45; 95% CI, 1.25–4.79;  $P = .009$ ; modified intention to treat: 7.4% versus 14.4%; OR, 2.53; 95% CI, 1.25–5.09;  $P = .010$ ) rates did not differ between the intention to treat, modified intention to treat, and the from here on presented “modified as-treated” populations in treatment versus control patients.

As reported in the primary results, all-cause mortality (“modified as-treated”) trended in favor of treated patients ( $P = .079$ ); by the 90-day follow-up visit, 11.5% (26/226) in the treated group and 16.1% (42/261) in the not-treated group had died.<sup>1</sup> Stroke-related mortality differed significantly between groups, again in favor of treated patients: 7.5% (17/226) treated versus 14.2% (37/261) not treated (95% CI –12.1, –1.2;  $P = .009$ ). Most (85%) of the stroke-related deaths occurred within 30 days of the index stroke. The logistic regression analysis for freedom from stroke-related mortality, adjusted by baseline NIHSS and age, favored treatment, with an OR of 2.41 (95% CI, 1.22, 4.77;  $P = .012$ ). Fig 1 shows the Kaplan-Meier curve for freedom from stroke-related mortality.

### Primary Causes of Stroke-Related Deaths

For a full listing and definitions of stroke-related versus not stroke-related mortality, see Table 4 of the original SENTIS publication.<sup>1</sup> Although the absolute numbers for each cause of stroke-related death were too few for any differences between arms to reach statistical significance, treated patients numerically had fewer stroke-related deaths for all causes except renal causes. Most notably, stroke-related deaths from neurologic causes (eg, bleeding, stroke progression, edema, new strokes) were numerically fewer in treated versus not-treated patients (treated: 9/17, 52.9%; non-treated: 27/37, 73.0%;  $P = .214$ ) as opposed to other reasons for death (eg, cardiac, renal, pulmonary, multi-organ failure, sepsis).



Time-point	Treated N=226			Not-treated N=261		
	Events (N)	Cumulative Events (N)	Event Free Rate (%) [95% CI]	Events (N)	Cumulative Events (N)	Event Free Rate (%) [95% CI]
4-Days	5	5	97.8 (94.7-99.1)	12	12	95.4 (92.0-97.4)
30-Days	8	13	94.1 (90.1-96.5)	21	33	87.2 (82.5-90.8)
60-Days	2	15	93.2 (89.0-95.8)	2	35	86.4 (81.6-90.1)
90-Days	2	17	92.2 (87.8-95.1)	2	37	85.6 (80.7-89.4)

The Greenwood's formula was used to calculate the 95% confidence interval for the Kaplan-Meier estimates for survival for each randomization group.

FIG 1. Kaplan-Meier curve: Freedom from stroke-related mortality.

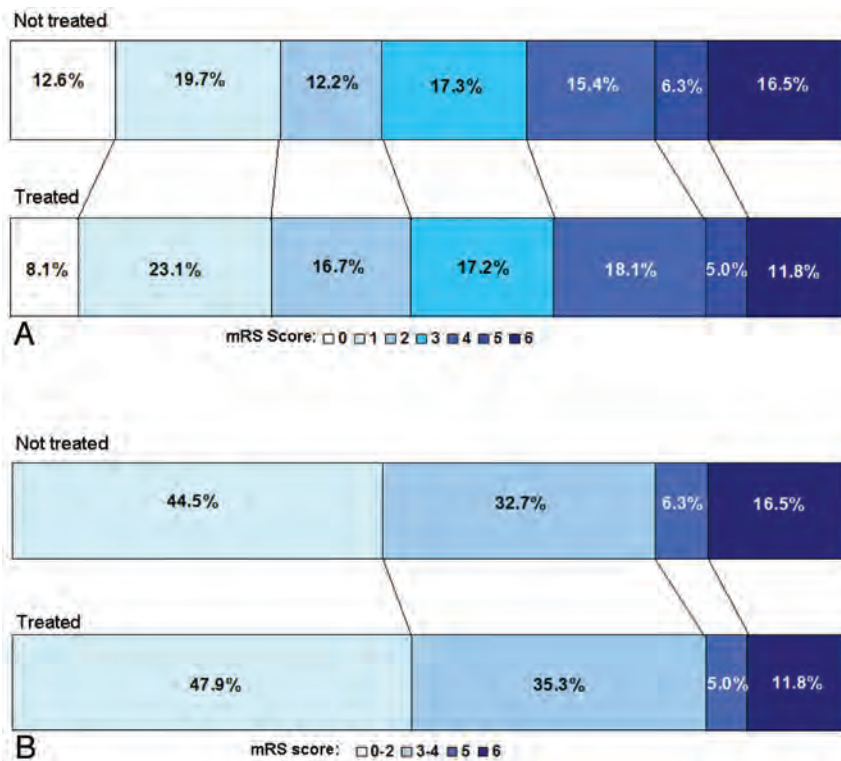


FIG 2. Modified Rankin shift for SENTIS as-treated population. \*Values within the shift analysis are based on 90-day evaluable patients.

### Severe Disability

The trend toward reduced all-cause mortality, mainly driven by a significantly reduced stroke-related mortality, did not come at the cost of an increased rate of severe disability. Among the survivors

at the 90-day follow-up, fewer of the treated (5.6%, 11/195) patients than the control patients (7.5%, 16/212) were severely disabled (mRS score = 5). The absolute difference (1.9%) was not statistically significant in either univariate or multivariate analyses (OR, 0.58; 95% CI, 0.24, 1.39;  $P = .223$ ). As shown in Fig 2, compared with the not-treated group, the treated group had more patients in the lower range of the mRS scores and fewer with scores that indicate death (mRS 6) and severe disability (mRS 5). This suggests that after NeuroFlo treatment, patients who may have otherwise died (mRS 6) or been severely disabled (mRS 5) were more likely to survive with moderate or mild disability. Additionally, patients who may have been moderately disabled (mRS 3–4) were shifted toward an independent outcome (mRS 0–2).

### First Site of Care

A total of 437 of 515 (85%) poststudy surveys were returned with evaluable data regarding first site of care; 204 of 226 for treated patients and 233 of 261 for control patients. The survey suggested differences in the first site of care between treatment arms with nominally more treated patients admitted before the procedure to a stroke- or neuro-intensive care unit than not-treated patients (Table 1). When all intensive care units were combined, the numbers were significant, with an absolute difference of 13.5% (60.3% versus 46.8%,  $P = .005$ ). Conversely, more patients from the not-treated arm were admitted to general wards as their first site of care. When these variables were included in the multivariate analysis, first site of care was not a predictor of mortality, stroke-related mortality, or independent outcome categorized as mRS 0–2 versus 3–6. Furthermore, when the outcome of all-cause mortality is analyzed by the first site of care, the treated group had lower rates of mortality (8.5–23.1%) than the not-treated group (14.4–20.6%) for all sites of care except for general unit (treated, 23.1% versus not treated, 20.6%;  $P = 1.000$ ) (Table 2). Similarly, the stroke-related mortality rate was also nominally lower in the treated group (7.3–15.4%) compared with the not-treated group (11.1–17.7%) for all first sites of care except general unit (treated, 15.4% versus not treated,

**Table 1: First site of care**

First Site of Care	Treated	Not Treated	P Value (Fisher Exact)
	N = 204	N = 233	
	n = 25	n = 38	
Neuro/Stroke ICU	40.2% (82/204)	32.2% (75/233)	.090
Other ICU	20.1% (41/204)	14.6% (34/233)	.162
Stroke unit	33.3% (68/204)	38.6% (90/233)	.273
General unit	6.4% (13/204)	14.6% (34/233)	.008
Any ICU <sup>a</sup>	60.3% (123/204)	46.8% (109/233)	.005

**Note:**—N indicates total number of surveys received with evaluable data for first site of care; n, number of patients with evaluable surveys who died.

<sup>a</sup> Any ICU is the combination of the Neuro/Stroke ICU and Other ICU.

**Table 2: All-cause mortality rate by first site of care**

First Site of Care	Treated	Not Treated	P Value (Fisher Exact)
	N = 204	N = 233	
	n = 25	n = 38	
Neuro/Stroke ICU	8.5% (7/82)	16.0% (12/75)	.220
Other ICU	14.6% (6/41)	17.7% (6/34)	.760
Stroke unit	13.2% (9/68)	14.4% (13/90)	1.000
General unit	23.1% (3/13)	20.6% (7/34)	1.000
Total mortality rate	12.3%	16.3%	.275

**Note:**—N indicates total number of surveys received with evaluable data for first site of care; n, number of patients with evaluable surveys who died.

**Table 3: Stroke-related mortality rate by first site of care**

First Site of Care	Treated	Not Treated	P Value (Fisher Exact)
	N = 204	N = 233	
	n = 17	n = 33	
Neuro/Stroke ICU	7.3% (6/82)	16.0% (12/75)	.131
Other ICU	7.3% (3/41)	17.7% (6/34)	.285
Stroke unit	8.8% (6/68)	11.1% (10/90)	.792
General unit	15.4% (2/13)	14.7% (5/34)	1.000
Total stroke-related mortality rate	8.3%	14.2%	.070

**Note:**—N indicates total number of surveys received with evaluable data for first site of care; n, number of patients with evaluable surveys who died of stroke-related causes.

14.7%;  $P = 1.000$ ) (Table 3). Therefore, the differences in allocation of care do not account for the reduced mortality rates among the treated patients.

### Do Not Resuscitate/Do Not Intubate and Withdrawal of Care Orders

The numbers for do not resuscitate/intubate, and comfort care orders did not differ between treatment and control patients: 10.3% (21/204) versus 11.7% (28/239) (Fisher exact test,  $P = .652$ ), and 6.9% (14/204) versus 10.5% (25/239) ( $P = .239$ ). Death was highly associated with the presence of these orders (OR, 22.96; 95% CI, 8.5, 62.3;  $P < .0001$ ) and comfort care orders (OR, 77.33; 95% CI, 23.3, 218.5;  $P < .0001$ ). The median number of days between initiation of the orders and death was 2.0 days for do not resuscitate/intubate orders and 2.5 days for comfort care orders; there was no difference between treated and not-treated patients.

## DISCUSSION

The SENTIS trial tested the clinical efficacy and safety of the NeuroFlo device, which, by increasing cerebral blood flow to ischemic brain, was hypothesized to lead to reduced morbidity and

mortality in patients with acute stroke treated within 14 hours after onset of symptom.<sup>1</sup> SENTIS established safety for the NeuroFlo procedure but missed statistical significance for the primary clinical outcome end point. While the use of the global outcome end point and also dichotomized end points of the mRS have been a matter of recent debate,<sup>6–8</sup> the currently favored mRS shift analysis over the full range of the ordinal scale did not render a different trial result.<sup>1</sup> An intriguing and important observation in the SENTIS trial was a trend for reduced overall mortality. This reduction was driven by a significantly lower stroke-related mortality rate among treated patients. Death rates from stroke, stroke-related complications, and new strokes were all nominally lower in the treated patients. Notably, the reduction in the death rate was not accompanied by an increase in the proportion of patients who were severely disabled. Additionally, these findings were not related to the first site of care or withdrawal of care in treated versus not-treated patients.

Albeit dealing with post hoc analyses, these results shed more light on the findings from SENTIS. It is apparent that the trend in reduced all-cause mortality was for the most part a result of reduced stroke-related mortality. Hemodynamic augmentation by partial aortic occlusion results in a varying increase of CBF by approximately 30%, an effect that lasts beyond the procedure itself.<sup>5</sup> Although further analysis of the acquired imaging data are necessary, this may lead to improved collateral flow to ischemic penumbral brain and thereby reduce infarct size in treated patients as compared with control subjects. Stroke size has been repeatedly established as a predictor for outcome and mortality.<sup>9–12</sup> Both direct stroke-related complications (eg, space-occupying infarction with increased intracranial pressure, edema) and secondary disability-associated complications (eg, deep venous thrombosis, infections, aspiration) may be reduced as a result of a smaller final infarct size. Although SENTIS was not powered to detect the effect on overall clinical outcome measured with the mRS, the mortality findings are encouraging and may be useful in designing further studies. Some of the promising approaches with other acute stroke treatments that have been studied in pilot trials are the use of partial aortic occlusion as an adjunct to standard rtPA (FastFlo)<sup>3</sup> and in extended time windows (Flo24).<sup>4</sup> In both trials, feasibility and safety could be demonstrated. A larger NeuroFlo device with a central lumen has been developed, which could allow for intraarterial treatment and/or thrombectomy in parallel to partial aortic occlusion and flow improvement. The latter has not been tested in a pilot trial.

A frequently disputed ethical as well as economic issue is whether a therapeutic procedure reduces mortality at the cost of increasing severe disability in survivors.<sup>13</sup> In SENTIS, the reduction in mortality did not result in an increase in severe disability as measured by the mRS. This is not explained by a difference in the rate of serious adverse events between the 2 arms and illustrates an overall shift toward better outcomes in the treatment arm, an effect also observed in the hemicraniectomy trials.<sup>14</sup>

Potential confounding variables in assessing mortality outcomes in stroke trials are variability in admission to intensive care units and stroke units and variability in the application of do not resuscitate or intubate orders and compassionate care, a frequent phenomenon especially among victims of ischemic stroke and

hemorrhagic stroke.<sup>15</sup> It is theoretically possible, in interventional trials unblinded for the treatment arm and only blinded for the outcome assessment (PROBE design), that actively treated patients may more frequently receive specialized care and allocation to intensive care and stroke units, leading to self-fulfilling results. In a poststudy survey, we acquired further data regarding site of care and do not resuscitate/intubate orders not originally obtained for the SENTIS trial itself. There were no major differences with regard to treatment allocation or do not resuscitate/intubate orders; however, more patients treated with NeuroFlo were assigned to stroke units and neuro-intensive care units. This difference in first site of care may be due in part to standard of care procedures and hospital protocols that often require intensive care unit admission after any endovascular procedure. Despite the allocation imbalance, in treated patients, both the all-cause and stroke-related mortality rates were nominally lower in all but one allocation (general ward), where they were nearly identical. Finally, first treatment site was not an independent predictor of outcome in the multivariate analysis.

Among the limitations of our analyses are the inclusion of post hoc analyses and the use of a poststudy survey, though the latter was submitted for 85% of the study patients. Despite these limitations, we believe that the significant reduction in stroke-related mortality in the SENTIS trial is an indication of potential efficacy of the therapeutic approach. We did not find other explanations for this observation and therefore do not believe this to arise from confounds in sites of or intensity of care, though SENTIS was ultimately not powered for the predefined end point. We believe that the therapeutic approach of hemodynamic augmentation merits further study because the efficacy results are promising and safety is established.

## ACKNOWLEDGMENTS

The authors would like to thank the following: Lisa M. Thackeray, MS, of The Integra Group for statistical support; and Kay Zander, MA, and Ellen O'Malley, MS, of CoAxia, Inc, for valuable input, review, and editing of the manuscript.

Disclosures: Peter D. Schellinger—RELATED: Consulting Fee or Honorarium: CoAxia; Support for Travel to Meetings for the Study or Other Purposes: CoAxia; Fees for Participation in Review Activities, Such as Data Monitoring Boards, Statistical Analysis, Endpoint Committees, and the Like: CoAxia; UNRELATED: Board Membership: Boehringer Ingelheim, Cerevast; Consultancy: Boehringer Ingelheim, Cerevast; Payment for Lectures (including service on speakers bureaus): Boehringer Ingelheim, Cerevast. Ashfaq Shuaib—RELATED: Grant: CoAxia\*; Consulting Fee or Honorarium: CoAxia; Support for Travel to Meetings for the Study or Other Purposes: CoAxia; UNRELATED: Consultancy: Pfizer, BI, Sanofi, Bayer, AstraZeneca, Lundbeck, dPharm, Comments: Consultancy/advisory boards; Grants/Grants Pending: Lundbeck,\* dPharm,\* Asubio,\* Photothera,\* Brainsgate\*; Payment for Lectures (including service on speakers bureaus): AstraZeneca, Bayer, BI, Sanofi, Pfizer, Merck, dPharm, Asubio. Martin Köhrmann—RELATED: Consulting Fee or Honorarium: CoAxia; Support for Travel to Meetings for the Study or Other Purposes: CoAxia\*; UNRELATED: Board Membership: Boehringer Ingelheim; Payment for Lectures (including service on speakers bureaus): Boehringer Ingelheim, Bayer Healthcare, Novartis. David Liebeskind—RELATED: Grant: NIH.\* Comments: P50NS044378, K24NS072272, R13NS082049. Maxim Hammer—UNRELATED: Expert Testimony: Roetzel and Andress (a legal professional organization), Comments: I have provided medical expert testimony on stroke cases for legal firms. Souvik Sen—RELATED: Consulting Fee or Honorarium: Consultant fee from CoAxia, Inc (2 years ago); UNRELATED: Grants/Grants Pending: National Institutes of Health\*; Payment for Lectures (including service on speakers bureaus): Speakers bureau for Boehringer Ingelheim, Genentech, Sanofi-Synthelabo, and Bristol-Myers Squibb. Rishi Gupta—RELATED: Consulting Fee or Honorarium: CoAxia, Comments: less than \$5000 over

24 months; UNRELATED: Consultancy: Stryker Neurovascular (less than \$10,000 over 12 months), Covidien (less than \$10,000 over 12 months); OTHER RELATIONSHIPS: Associate Editor, *Journal of Neuroimaging*. Jeffrey L. Saver—RELATED: Grant: CoAxia\*; Consulting Fee or Honorarium: CoAxia\*; Support for Travel to Meetings for the Study or Other Purposes: CoAxia\*; UNRELATED: Consultancy: Grifols,\* Covidien,\* Lundbeck\*; Grants/Grants Pending: NIH-NINDS\*; OTHER RELATIONSHIPS: My employer, the University of California, has some patent rights on retrieval devices for stroke. I am not a party or beneficiary to the arrangements (\*money paid to institution). CoAxia, Inc, provided funding for the SENTIS Trial. Tudor Jovin, MD: TJ is employed by the University of Pittsburgh, Pittsburgh, Pennsylvania. The University received clinical trial payments based on the number of patients enrolled in the SENTIS trial from CoAxia. He has received honorarium from CoAxia for consulting work with the company; David Y. Huang, MD: DYH is employed by the University of North Carolina, Chapel Hill, North Carolina. The University received clinical trial payments based on the number of patients enrolled in the SENTIS trial from CoAxia. Sten Solander, MD: SS is employed by the University of North Carolina, Chapel Hill, North Carolina. The University received clinical trial payments based on the number of patients enrolled in the SENTIS trial from CoAxia. He has received consulting fees for consulting from CoAxia. Ronen R. Leker, MD: RRL is employed by the Hadassah-Hebrew University Medical Center, Jerusalem, Israel. Hadassah received clinical trial payments based on the number of patients enrolled in the SENTIS trial from CoAxia.

## REFERENCES

- Shuaib A, Bornstein NM, Diener HC, et al. **Partial aortic occlusion for cerebral perfusion augmentation: Safety and Efficacy of NeuroFlo in Acute Ischemic Stroke trial.** *Stroke* 2011;42:1680–90
- Hammer M, Jovin T, Wahr JA, et al. **Partial occlusion of the descending aorta increases cerebral blood flow in a nonstroke porcine model.** *Cerebrovasc Dis* 2009;28:406–10
- Emery DJ, Schellinger PD, Selchen D, et al. **Safety and feasibility of collateral blood flow augmentation after intravenous thrombolysis.** *Stroke* 2011;42:1135–37
- Hammer MD, Schwamm L, Starkman S, et al. **Safety and feasibility of NeuroFlo use in eight- to 24-hour ischemic stroke patients.** *Int J Stroke* 2012;7:655–61
- Liebeskind DS. **Aortic occlusion for cerebral ischemia: from theory to practice.** *Curr Cardiol Rep* 2008;10:31–36
- Schellinger PD, Bath PM, Lees KR, et al. **Assessment of additional endpoints for trials in acute stroke: what, when, where, in who?** *Int J Stroke* 2012;7:227–30
- Lees KR, Bath PM, Schellinger PD, et al. **Contemporary outcome measures in acute stroke research: choice of primary outcome measure.** *Stroke* 2012;43:1163–70
- Bath PM, Lees KR, Schellinger PD, et al. **Statistical analysis of the primary outcome in acute stroke trials.** *Stroke* 2012;43:1171–78
- Davis SM, Donnan GA, Parsons MW, et al. **Effects of alteplase beyond 3 h after stroke in the Echoplanar Imaging Thrombolytic Evaluation Trial (EPITHET): a placebo-controlled randomised trial.** *Lancet Neurol* 2008;7:299–309
- Thomalla GJ, Kucinski T, Schoder V, et al. **Prediction of malignant middle cerebral artery infarction by early perfusion- and diffusion-weighted magnetic resonance imaging.** *Stroke* 2003;34:1892–99
- Albers GW, Thijs VN, Wechsler L, et al. **Magnetic resonance imaging profiles predict clinical response to early reperfusion: the diffusion and perfusion imaging evaluation for understanding stroke evolution (DEFUSE) study.** *Ann Neurol* 2006;60:508–17
- Mlynash M, Lansberg MG, De Silva DA, et al. **Refining the definition of the malignant profile: insights from the DEFUSE-EPITHET pooled data set.** *Stroke* 2011;42:1270–75
- Juttler E, Schellinger PD, Aschoff A, et al. **Clinical review: therapy for refractory intracranial hypertension in ischaemic stroke.** *Crit Care* 2007;11:231
- Vahedi K, Hofmeijer J, Juettler E, et al. **Early decompressive surgery in malignant infarction of the middle cerebral artery: a pooled analysis of three randomised controlled trials.** *Lancet Neurol* 2007;6:215–22
- Steiner T, Mendoza G, De Georgia M, et al. **Prognosis of stroke patients requiring mechanical ventilation in a neurological critical care unit.** *Stroke* 1997;28:711–15

# Endovascular Treatment of Distal Anterior Cerebral Artery Aneurysms: Single-Center Experience and a Systematic Review

C.L. Sturiale, W. Brinjikji, M.H. Murad, H.J. Cloft, D.F. Kallmes, and G. Lanzino



## ABSTRACT

**SUMMARY:** In this study, a single center's experience of 20 patients and a systematic review and a meta-analysis of 16 studies, including 279 patients/aneurysms, assessed the safety and efficacy of endovascular treatment of distal anterior cerebral artery aneurysms. The authors conclude that endovascular treatment of distal anterior cerebral artery aneurysms is associated with high angiographic occlusion rates, but the complication rates are higher compared with other aneurysms in the circle of Willis.

**ABBREVIATIONS:** DACA = distal anterior cerebral artery; GOS = Glasgow Outcome Scale

Distal anterior cerebral artery (DACA) aneurysms are rare, representing approximately 1–9% of all intracranial aneurysms.<sup>1</sup> Endovascular treatment of these aneurysms presents a number of challenges. Earlier studies have reported high rates of arterial dissection, intraprocedural rupture, and incomplete occlusion rates for endovascular treatment of DACA aneurysms.<sup>2–5</sup> Despite these initial challenges, further refinements in endovascular techniques made coil embolization emerge as a promising therapeutic option for aneurysms at this location.<sup>6,7</sup> To clarify the safety and efficacy of endovascular treatment of DACA aneurysms, we report our experience in conjunction with a systematic review and meta-analysis of the literature.

## MATERIALS AND METHODS

After institutional review board approval, we performed a retrospective analysis of all consecutive adult patients who underwent attempted endovascular treatment of intracranial aneurysms involving the DACA at a tertiary referral center (Mayo Clinic, Rochester, Minnesota) between January 1999 and September 2012. All patients provided approval for the use of their medical records for retrospective analysis. Patients were identified through a search of angiographic reports and clinical records. The following data were collected for each patient: demographic characteristics, an-

giographic features, clinical presentation, and outcomes. Among the angiographic features, aneurysm size (maximum dimension as measured by 3D digital subtraction angiography), rupture status, location, and incidence of azygos variant were evaluated. The CT appearance of all patients with SAH was assessed by use of the Fisher scale, and the clinical status at admission for patients with subarachnoid hemorrhage was assessed by use of the Hunt and Hess Scale. Clinical outcome for all patients was assessed by use of the Glasgow Outcome Scale (GOS). Details about the endovascular procedure included use of adjuncts (balloon-assisted and stent-assisted coiling), intraprocedural complications, and degree of immediate angiographic occlusion.

## Outcomes and Complications

Radiologic outcomes for endovascular coiling were stratified into 3 levels, on the basis of the degree of angiographic aneurysm filling evaluated immediately after the completion of the endovascular procedure and at last follow-up: 1) complete occlusion (100%), defined as a lack of angiographic filling of the sac and the neck or nearly complete occlusion (>90%), defined as no filling of the sac but with small residual neck filling; 2) incomplete occlusion (<90%), defined as persistent angiographic filling of a portion(s) of the sac, and 3) failed occlusion, defined as an aneurysm that could not be embolized, without any coil introduced or left in the aneurysm. Studied periprocedural complications (within 30 days of treatment) included intraoperative rupture, parent artery occlusion, transient ischemic attack, vasospasm, and stroke.

## Literature Review

A comprehensive review of the literature was performed by use of the keywords “aneurysms” “pericallosal,” “distal anterior cerebral artery,” “DACA,” and “endovascular” to search the PubMed,

Received December 4, 2012; accepted after revision February 23, 2013.

From the Departments of Neurologic Surgery (C.L.S., G.L.), and Radiology (W.B., H.J.C., D.F.K.), and Center for Science of Healthcare Delivery (M.H.M.), Mayo Clinic College of Medicine, Rochester, Minnesota.

Please address correspondence to Giuseppe Lanzino, MD, Department of Neurologic Surgery, Mayo Clinic College of Medicine, Rochester, MN 55905; e-mail: Lanzino.Giuseppe@mayo.edu

 Indicates article with supplemental on-line tables.

<http://dx.doi.org/10.3174/ajnr.A3629>

Ovid MEDLINE, Ovid EMBASE, Scopus, and Web of Science data bases. All studies reporting patients with DACA aneurysms treated with endovascular therapy were selected. To be considered, studies had to be published in English, report more than 2 cases, and provide detailed information regarding perioperative and postoperative complications and aneurysm occlusion rates. The search strategy was developed and executed by a reference librarian and a methodologist with expertise in systematic reviews. For each study, we extracted the following information: aneurysm rupture status, immediate and delayed angiographic occlusion rates, procedural failure rates, morbidity, mortality, overall patient perioperative complication rate, iatrogenic aneurysm rupture, periprocedural stroke, vasospasm, and intraprocedural thrombosis/transient hemiparesis. In assessing overall patient perioperative complication rate, we determined the proportion of patients who had 1 or more of the following complications: iatrogenic aneurysm rupture, periprocedural stroke, vasospasm, and intraprocedural thrombosis/transient hemiparesis. For studies reporting clinical outcome according to the mRS, the equivalent score on GOS was calculated.

### Statistical Analysis

For our institutional case series, all statistical analyses were performed by use of the SAS-based statistical software package JMP 9.0 (www.jmp.com). Significant difference between continuous variables was assessed by a Student *t* test. From each study, we assessed the cumulative incidence (event rate) and 95% CI for each outcome. Event rates were pooled across studies by use of random-effects meta-analysis.<sup>8</sup> Heterogeneity across studies was evaluated by use of the *I*<sup>2</sup> statistic.<sup>9</sup>

## RESULTS

### Institutional Series

A total of 20 consecutive patients were included in our single-center series (18 women and 2 men). Three patients had an additional 7 aneurysms. Four of these associated aneurysms were observed and not treated because of the small size. Two patients underwent clip ligation and 1 patient underwent endovascular coil embolization for their associated aneurysms in separate sessions. Demographic, angiographic, and clinical features are summarized in On-line Table 1. The mean  $\pm$  SD age was 60.5  $\pm$  10.8 (range, 38–80 years). Eleven patients (55%) presented with SAH. In all cases, the DACA aneurysm was responsible for the SAH. Most aneurysms (19/20) were small (<10 mm in maximum diameter). The mean size of ruptured aneurysms was significantly smaller than unruptured aneurysms (4.3 versus 7.6 mm, *P* = .029). Endovascular coiling was completed successfully in every case. Immediate total/near-total angiographic obliteration was achieved in 85% of cases and was maintained at follow-up (16.6 months on average) in 69% (11/16) of patients. Two patients (10%) with partial occlusion at follow-up underwent surgical clipping. No patients underwent recoiling. Two patients (10%) had intraoperative aneurysm perforations that were controlled with additional coiling of the aneurysm. Both patients had previously ruptured aneurysms, and this procedural complication resulted in no morbidity. One patient (5%) had intraprocedural thrombus formation that was asymptomatic and treated with in-

travenous administration of abciximab (ReoPro). None of these periprocedural events resulted in permanent morbidity or mortality.

### Systematic Review

Two hundred forty-one articles were retrieved after the first literature search. Among these, 53 were selected by abstract review and analyzed in detail. Fifteen studies met our inclusion/exclusion criteria and are listed in On-line Table 2. Including our own experience, a total of 16 studies were included in this meta-analysis.<sup>1-7,10-17</sup> The total number of patients analyzed was 279 (259 from literature and 20 from our series). Fourteen studies with a total of 246 patients provided information regarding aneurysm rupture status; among them, 185 patients (75.2%) harbored ruptured aneurysms. The largest study had 41 patients and the smallest study had 4 patients.

### Endovascular Technique and Short-Term Angiographic Outcomes

The rate of total/near-total occlusion immediately after the endovascular procedure was 86% (95% CI = 75–92%) and the procedural failure rate was 8% (95% CI = 4–14%).

### Procedure-Related Complications

The overall rate of operative complications was 12% (95% CI = 8–18%). Procedure-related ischemia and iatrogenic rupture occurred in 5% (95% CI = 3–9%) and 7% (95% CI = 4–12%) of patients, respectively. Procedure-related permanent morbidity rate was 8% (95% CI = 5–13%).

### Long-Term Angiographic and Clinical Follow-Up

The rate of total/near-total (>95%) occlusion at mean follow-up was 78% (95% CI = 65–88%). A good clinical recovery (including both patients with ruptured and unruptured aneurysms) was reported in 75% (95% CI = 66–82%). The average duration of clinical follow-up was 13.47  $\pm$  8.73 months (mean follow-up duration reported in 12/16 of the studies). The rate of overall mortality at follow-up was 9% (95% CI = 6–14%) (On-line Table 3).

### Heterogeneity and Publication Bias

Statistical heterogeneity was low to moderate for most outcomes except for complete/near complete occlusion (immediate and at follow-up) and SAH occurrence (*I*<sup>2</sup>>50%). Data were limited and did not allow for additional quantitative analysis to explore causes of heterogeneity through subgroup analysis or evaluate for the presence of publication bias.

## DISCUSSION

In combining outcomes data from 16 studies, this systematic review provides representative data on aneurysm occlusion rates and complications associated with endovascular treatment of DACA aneurysms. We have demonstrated high rates of total/near total occlusion for DACA aneurysms treated with endovascular embolization. However, complications are not negligible, with procedure-related morbidity rates of 8%. Approximately 75% of the patients in this meta-analysis had SAH, which probably contributes to the relatively high mortality rates (9%) reported with endovascular treatment of DACA aneurysms.

Ruptured DACA aneurysms cause intracerebral hemorrhage (in addition to SAH) in more than one-half of cases and are associated with worse outcome after rupture when compared with aneurysms in other locations.<sup>18,19</sup> Complications associated with endovascular treatment of these aneurysms are not rare and probably related to a higher level of technical difficulty because of distal location, morphology (with frequent partial incorporation of the parent artery in the neck), and higher association with anatomic variations. These challenges may explain the relatively higher procedure-related complication rates compared with aneurysms in more common locations reported by some investigators.<sup>1-4</sup> Keston et al<sup>2</sup> demonstrated higher rates of periprocedural rupture and incomplete coiling of DACA aneurysms when compared with other circle of Willis aneurysms. In the International Study of Unruptured Intracranial Aneurysms (ISUIA), endovascular treatment of unruptured circle of Willis aneurysms was associated with a perioperative mortality rate of 2% and an overall morbidity/mortality rate of 9.3%.<sup>20</sup> In a series of 600 circle of Willis aneurysms, Brisman et al<sup>21</sup> reported an intraoperative rupture rate of 1%. In a systematic review of treatment of aneurysms of the MCA, a location that has traditionally been considered a difficult location for endovascular treatment, Brinjikji et al<sup>22</sup> demonstrated an intraoperative rupture rate of nearly 2% for unruptured aneurysms and 5% for ruptured aneurysms. In this series, combined procedure-related morbidity and mortality were 5% and 6% for unruptured and ruptured aneurysms, respectively. In our systematic review, the overall periprocedural rupture rate was nearly 7%, with a procedure related morbidity rate of 8%, markedly higher than that reported for treatment of other circle of Willis aneurysms.

Early case series of coiling for ruptured pericallosal aneurysms reported low success rates and high technical difficulty.<sup>3,19</sup> Pierot et al<sup>4</sup> reported a coiling success rate of only 25% (2/8 patients) and concluded that endovascular therapy was at best an adjunct to surgery.<sup>4</sup> However, with refinement of endovascular therapy, subsequent case series have reported higher technical success rates.<sup>3,15,17</sup> In a recently published series of 22 patients with DACA aneurysms by Cavalcanti et al,<sup>23</sup> complete/near complete occlusion rate was 95% and 1 patient had an intraoperative rupture. In their review of the literature, recently published series reported occlusion rates of 80–100%, with a procedural related morbidity rate of 9% and mortality rate of 9%. Intraoperative rupture in both their series and systematic review was approximately 5%. Our meta-analysis has similar outcomes compared with the systematic review by Cavalcanti et al<sup>23</sup>; we found aneurysmal occlusion rates of 86%, iatrogenic rupture rates of 7%, procedure-related morbidity rates of 8%, and mortality rates of 9%.

Although complication rates for endovascular treatment of DACA aneurysms remain a concern, previous studies have demonstrated that patients with ruptured pericallosal aneurysms have significantly better outcomes when treated with coiling over clipping. In a study of 86 patients (54 clipped and 32 coiled) harboring pericallosal aneurysms, Hui et al<sup>12</sup> demonstrated that patients with ruptured pericallosal aneurysms fared better with endovascular therapy, with a better chance of complete recovery. Surgical and endovascular treatments of unruptured pericallosal aneurysms have similar results and outcome.

Our study has several methodologic limitations. Primarily, the available evidence is observational, nonrandomized, and non-comparative. Data in the published literature are collected retrospectively and details such as stratification of outcomes by clinical status at admission are often lacking. In addition, it is difficult to differentiate procedure-related mortality from mortality secondary to complications of SAH. Thus, it is likely that mortality secondary to treatment of pericallosal aneurysms is lower than reported in this study. The quality of evidence (confidence) is limited because of imprecision, heterogeneity, and methodologic limitations with the use of the GRADE framework (Grading of Recommendations, Assessment, Development and Evaluation).<sup>24-26</sup> Our systematic review and case series has several strengths. We followed a comprehensive systematic review process and searched multiple data bases in an attempt to improve the precision of estimates derived from our own data. We believe that these results represent the best available evidence regarding endovascular treatment for aneurysms in an uncommon location. The outcomes reported here reflect an average incidence to be expected for this procedure across multiple settings and institutions.

## CONCLUSIONS

Endovascular coiling of DACA aneurysms is associated with immediate occlusion rates of 85% and a low recurrence rate at follow-up. However, endovascular treatment of DACA aneurysms is also associated with complication rates higher than those reported for endovascular treatment of aneurysms in other locations.

Disclosures: Harry J. Cloft—UNRELATED: Grants/Grants Pending: Cordis Endovascular.\* David Kallmes—UNRELATED: Consultancy: ev3,\* Medtronic,\* Codman\*; Grants/Grants Pending: ev3,\* MicroVention,\* Sequent,\* Codman\*; Payment for Lectures (including service on speakers bureaus): MicroVention\*; Royalties: UVA Patent Foundation\*; Payment for Development of Educational Presentations: ev3\*; Travel/Accommodations/Meeting Expenses Unrelated to Activities Listed: MicroVention.\* Giuseppe Lanzino—UNRELATED: Consultancy: Edge Therapeutics; Payment for Development of Educational Presentations: Covidien/ev3\*; Travel/Accommodations/Meeting Expenses Unrelated to Activities Listed: Boston Biomedica Associates, Comments: Investigator meeting; expenses covered by sponsor (\*money paid to institution).

## REFERENCES

- Carvi y Nieves MN. **The influence of configuration and location of ruptured distal cerebral anterior artery aneurysms on their treatment modality and results: analysis of our casuistry and literature review.** *Neurol Res* 2010;32:73–81
- Keston P, White PM, Horribine L, et al. **The endovascular management of pericallosal artery aneurysms.** *J Neuroradiol* 2004;31:384–90
- Menovsky T, van Rooij WJ, Sluzewski M, et al. **Coiling of ruptured pericallosal artery aneurysms.** *Neurosurgery* 2002;50:11–14
- Pierot L, Boulin A, Castaings L, et al. **Endovascular treatment of pericallosal artery aneurysms.** *Neurol Res* 1996;18:49–53
- Suzuki S, Kurata A, Yamada M, et al. **Outcomes analysis of ruptured distal anterior cerebral artery aneurysms treated by endosaccular embolization and surgical clipping.** *Interv Neuroradiol* 2011;17:49–57
- Tournade A, Riquelme C, Musacchio M, et al. **Endovascular treatment of berry intracranial aneurysms using a new detachable coil system (DCS ((R)): Detachable Coil System Cook).** *Interv Neuroradiol* 2001;7:93–102
- Waldenberger P, Petersen J, Chemelli A, et al. **Endovascular therapy of distal anterior cerebral artery aneurysms—an effective treatment option.** *Surg Neurol* 2008;70:368–77

8. DerSimonian R, Laird N. **Meta-analysis in clinical trials.** *Control Clin Trials* 1986;7:177–88
9. Higgins JP, Thompson SG, Deeks JJ, et al. **Measuring inconsistency in meta-analyses.** *BMJ* 2003;327:557–60
10. Darkhabani ZM, Lazzaro MA, Zaidat OO. **Pericallosal artery aneurysm treatment using Y-configuration stent-assisted coil embolization: a report of four cases.** *J Neurointerv Surg* 2012;4:459–62
11. Huang Q, Shen J, Xu Y, et al. **Endovascular treatment of ruptured distal anterior cerebral artery aneurysm.** *Neurol India* 2010;58:259–63
12. Hui FK, Schuette AJ, Moskowitz SI, et al. **Microsurgical and endovascular management of pericallosal aneurysms.** *J Neurointerv Surg* 2011;3:319–23
13. Hussain Z, Corkill RA, Kuker W, et al. **Distal aneurysms of the unpaired ACA: embryologic and therapeutic aspects.** *Neuroradiology* 2005;47:209–14
14. Nakai Y, Sonobe M, Takigawa T, et al. **Angiographical change of Guglielmi detachable coils: treated cerebral aneurysm in acute stage.** *Interv Neuroradiol* 2004;10(Suppl 1):161–66
15. Nguyen TN, Raymond J, Roy D, et al. **Endovascular treatment of pericallosal aneurysms.** *J Neurosurg* 2007;107:973–76
16. Pandey A, Rosenwasser RH, Veznedaroglu E. **Management of distal anterior cerebral artery aneurysms: a single institution retrospective analysis (1997–2005).** *Neurosurgery* 2007;61:909–16
17. Vora N, Thomas AJ, Gupta R, et al. **Endovascular treatment of distal anterior cerebral artery aneurysms: technical results and review of the literature.** *J Neuroimaging* 2010;20:70–73
18. de Sousa AA, Dantas FL, de Cardoso GT, et al. **Distal anterior cerebral artery aneurysms.** *Surg Neurol* 1999;52:128–35
19. Lehecka M, Lehto H, Niemela M, et al. **Distal anterior cerebral artery aneurysms: treatment and outcome analysis of 501 patients.** *Neurosurgery* 2008;62:590–601
20. Wiebers DO, Whisnant JP, Huston J 3rd, et al. **Unruptured intracranial aneurysms: natural history, clinical outcome, and risks of surgical and endovascular treatment.** *Lancet* 2003;362:103–10
21. Brisman JL, Niimi Y, Song JK, et al. **Aneurysmal rupture during coiling: low incidence and good outcomes at a single large volume center.** *Neurosurgery* 2005;57:1103–09
22. Brinjikji W, Lanzino G, Cloft HJ, et al. **Endovascular treatment of middle cerebral artery aneurysms: a systematic review and single-center series.** *Neurosurgery* 2011;68:397–402
23. Cavalcanti DD, Abla AA, Martirosyan NL, et al. **Endovascular management of distal ACA aneurysms: single-institution clinical experience in 22 consecutive patients and literature review.** *AJNR Am J Neuroradiol* 2013;34:1593–99
24. Guyatt GH, Oxman AD, Kunz R, et al. **GRADE guidelines 6: rating the quality of evidence—imprecision.** *J Clin Epidemiol* 2011;64:1283–93
25. Murad MH, Swiglo BA, Sidawy AN, et al. **Methodology for clinical practice guidelines for the management of arteriovenous access.** *J Vasc Surg* 2008;48:26S–30S
26. Balshem H, Helfand M, Schunemann HJ, et al. **GRADE guidelines, 3: rating the quality of evidence.** *J Clin Epidemiol* 2011;64:401–06

# Incidence of Microemboli and Correlation with Platelet Inhibition in Aneurysmal Flow Diversion

M.R. Levitt, B.V. Ghodke, D.K. Hallam, L.N. Sekhar, and L.J. Kim



## ABSTRACT

**SUMMARY:** Flow-diverting stents have been associated with embolic and hemorrhagic complications, but the rate of procedure-related microemboli is unknown. Using transcranial Doppler sonography, we measured the rate of microemboli in 23 patients treated with flow-diverting stents. Patients received preprocedural dual antiplatelet medications and intraprocedural heparinization. Point-of-care platelet reactivity testing was performed before the procedure, and nonresponders (>213 P2Y<sub>12</sub>/ADP receptor reactivity units) received additional thienopyridine. Transcranial Doppler sonography was performed within 12–24 hours. Microemboli were detected in 3 patients (13%), 2 of whom were initially nonresponders. There was no association between the presence of microemboli and procedural or neurologic complications, aneurysm size, number of stents, or procedure time. Eight procedures (34.8%) required additional thienopyridine for inadequate platelet inhibition, and 3 required further treatment for persistent nonresponse to point-of-care platelet reactivity testing. There were 6 technical and 2 postoperative complications; none were associated with inadequate platelet inhibition or microemboli. The combination of routine point-of-care platelet reactivity testing and postprocedural microembolic monitoring may help identify patients at risk for thromboembolic complications after flow-diverting stents.

**ABBREVIATIONS:** FDS = flow-diverting stent; PRT = point-of-care platelet reactivity testing; PRU = P2Y<sub>12</sub>/adenosine diphosphate receptor reactivity units; TCD = transcranial Doppler sonography

The use of a flow-diverting stent (FDS) such as the Pipeline Embolization Device (Covidien/ev3, Irvine, California) in the treatment of unruptured, wide-neck, or fusiform intracranial aneurysms has had promising results.<sup>1,2</sup> However, reports of significant complications have arisen, such as delayed intraparenchymal hemorrhage in the arterial distribution of the reconstructed vascular segment.<sup>3,4</sup> The mechanism for this complication is hypothesized as thromboembolic<sup>5</sup> (possibly from foreign materials<sup>6</sup>) or hemodynamic<sup>4</sup> in nature, though the definitive mechanism is unknown.

Transcranial Doppler sonography (TCD) can be used to detect intra-arterial microembolic signals, a high frequency of which is thought to be predictive of embolic stroke.<sup>7</sup> TCD has been applied

to detect the rate of microemboli after endovascular aneurysm coiling to identify and treat patients at risk for thromboembolic complications.<sup>8,9</sup> To our knowledge, the rate of microemboli after aneurysm treatment with a FDS has not been reported.

Dual antiplatelet therapy with aspirin and a thienopyridine (commonly clopidogrel) is used to prevent endovascular thrombotic complications, especially in cerebrovascular stent placement.<sup>10</sup> However, up to 66% of patients undergoing stent placement show resistance to clopidogrel (“nonresponders”), and a lesser proportion are resistant to aspirin.<sup>11–14</sup> Antiplatelet resistance has been associated with thromboembolic complications,<sup>10,11</sup> though the inhibition threshold and timing of platelet testing is controversial,<sup>15,16</sup> as is the pharmacologic management of nonresponders.<sup>17,18</sup>

The purpose of this study was to describe the incidence of microemboli on routine postprocedural TCD monitoring after FDS placement in a series of consecutive patients with unruptured aneurysms and to analyze the interaction between microemboli and platelet inhibition.

## CASE SERIES

All patients with unruptured aneurysms treated between August 2011 and October 2012 with a FDS were included. Confidential chart review was performed to collect pertinent data, including

Received November 12, 2012; accepted after revision March 14, 2013.

From the Departments of Neurological Surgery (M.R.L., B.V.G., D.K.H., L.N.S., L.J.K.) and Radiology (B.V.G., D.K.H., L.J.K.), University of Washington School of Medicine, Seattle, Washington.

Paper previously presented in part at: 2013 Joint American Association of Neurological Surgeons/Congress of Neurological Surgeons Cerebrovascular Section Annual Meeting, February 3–5, 2013; Honolulu, Hawaii.

Please address correspondence to Louis J. Kim, MD, Box 359924, Department of Neurological Surgery, Harborview Medical Center, 325 9th Ave, Seattle, WA 98104; e-mail: ljkim1@u.washington.edu

indicates article with supplemental on-line table

<http://dx.doi.org/10.3174/ajnr.A3627>

the following: 1) patient demographics (sex, age, body weight at the time of the intervention); 2) aneurysm characteristics (location, dome and neck size if nonfusiform), procedural characteristics (number and length of FDSs, need for aneurysm coils, total fluoroscopy time, immediate angiographic outcome [and follow-up angiography if available]), periprocedural thromboembolic and technical complications; 3) medications administered before and during hospitalization (heparin, aspirin, clopidogrel, prasugrel, proton-pump inhibitors); and 4) diagnostic testing before and during hospitalization (point-of-care platelet reactivity testing [PRT], microembolic monitoring with TCD, neurologic examination on admission and discharge).

Patients were placed on a standardized anticoagulation protocol including at least 5 days of preprocedural dual antiplatelet medications (aspirin, 325 mg, and clopidogrel, 75 mg daily, except 1 patient who was switched from clopidogrel to prasugrel, 10 mg daily, due to gastrointestinal bleeding). PRT was performed 2–24 hours before the procedure by using the VerifyNow point-of-care platelet assay (Accumetrics, San Diego California). This test measures the degree of platelet inhibition by both aspirin (in aspirin reactivity units) and thienopyridines (in P2Y<sub>12</sub>/ADP receptor reactivity units [PRU])<sup>19</sup>; inadequate inhibition was defined as  $\geq 550$  aspirin reactivity units or  $> 213$  PRU.<sup>16</sup> Nonresponders between 214 and 224 PRU were given an additional 150 mg of clopidogrel; all other nonresponders were given 300–600 mg at the discretion of the attending neurointerventionalist. PRT was repeated in nonresponders within 24 hours of the procedure, and those with continued poor response were switched to prasugrel, 10 mg daily, after a 60-mg loading dose.

All interventional procedures were performed with the patient under general anesthesia. All patients were given intravenous heparin after diagnostic angiography but before the start of intervention, and activated clotting time testing was performed. Additional heparin boluses were given to maintain an activated clotting time of  $> 250$ . After an immediate postprocedural non-contrast head CT, patients were admitted to the intensive care unit for 24 hours with hourly vital signs and neurologic examinations.

Routine microembolic monitoring with TCD was performed by experienced vascular technicians on the first postprocedure day (12–24 hours after the procedure), by using an M-mode color-coded TCD oriented along the axis of the artery distal to the treated aneurysm (for carotid aneurysms, the ipsilateral MCA; in vertebral aneurysms, the ipsilateral posterior cerebral artery). TCD was performed for at least 20 minutes, and the number of microembolic signals was recorded. Those patients with detected microemboli remained in the intensive care unit and received additional anticoagulation (described below) and a TCD examination the following day.

Statistical significance was defined as a *P* value  $< .05$ , with Student *t* testing for quantitative and Fisher exact and  $\chi^2$  testing for qualitative variables.

Twenty-two patients underwent 23 consecutive FDS procedures for 25 aneurysms during the study period. Patient and aneurysm characteristics are shown in the On-line Table. One patient was treated twice due to incomplete aneurysm obliteration on follow-up imaging, and one had 3 distinct aneurysms treated

during the same procedure. All patients were treated with the Pipeline Embolization Device; 3 patients also received placement of a single coil in the aneurysm dome during the procedure, and 1 received multiple coils. All patients demonstrated marked stagnation of blood flow into the treated aneurysms on immediate posttreatment angiography. Of the 8 patients with follow-up imaging, 5 demonstrated complete aneurysm obliteration and 3 had residual filling for which 1 required additional FDS placement.

Six patients had intraprocedural complications (26.1%) including 1 proximal ICA dissection from a guide catheter (treated with a single dose of abciximab with immediate angiographic resolution), 1 femoral artery dissection requiring balloon angioplasty, 2 incidents of stent narrowing on postdeployment angiography requiring balloon angioplasty, and 1 each of distal stent dislodging and foreshortening requiring an additional stent. There were no clinical sequelae from these complications, and no microemboli were seen in any of the 6 patients. There were 2 postprocedural complications (8.7%). One patient displayed a small area of contrast extravasation ipsilateral to the treated aneurysm on routine postprocedural CT and remained asymptomatic. Another patient had transient diplopia, which resolved on the first postprocedure day. Both patients demonstrated adequate response on preprocedural PRT and no microemboli on postprocedural TCD. There were no permanent neurologic deficits in any patient.

No patient demonstrated aspirin resistance, but 8 patients (34.8%) demonstrated clopidogrel resistance on preprocedural PRT and received additional clopidogrel. Three remained nonresponders and were switched to prasugrel, with response on subsequent PRT. The average PRU for responders was significantly lower than that for nonresponders (128.0 versus 246.1, *P*  $< .001$ ). There was no significant difference between responders and nonresponders on all other variables, including age, body weight, aneurysm diameter, neck size, dome-to-neck ratio, total fluoroscopy time, or concurrent proton-pump inhibitor use.

Microemboli were detected by TCD in 3 patients (13%), 2 of whom were nonresponders on initial PRT but none of whom required prasugrel. Patient 4 had received a 600-mg bolus of clopidogrel before the procedure for inadequate platelet response (PRU 232). After TCD demonstrated 183 emboli/h, daily clopidogrel was increased to 150 mg and heparin infusion was started. An urgent diagnostic angiogram showed no thrombus, stenosis, or dissection. No further microemboli were noted on subsequent daily TCD, and the heparin was discontinued. The patient was discharged home on postprocedure day 3 with a PRU of 212. Patient 13 (who was also treated with a single coil in the aneurysm dome during the FDS procedure) was a responder on PRT (PRU 177). He had 15 emboli/h and received an additional 150-mg bolus of clopidogrel followed by 150 mg daily. Subsequent TCD demonstrated no microemboli, and the patient was discharged home with a PRU of 208. Patient 20 was a nonresponder on initial PRT (PRU 223) and received an additional 150 mg of clopidogrel before the procedure; TCD showed 6 emboli/h. She was placed on 150 mg of clopidogrel daily and was discharged the next day when TCD demonstrated 3 emboli/h; PRU were 186. There were no transient or permanent neurologic deficits among any patient with microemboli. There was no significant interaction be-

tween the presence of microemboli and platelet responder status ( $P = .27$ ).

## DISCUSSION

We have reported the incidence of thromboemboli as detected by postprocedural TCD following FDS treatment of unruptured aneurysms. We did not observe any major embolic or hemorrhagic complications, but 13% of procedures resulted in detectable microemboli and the patients received additional anticoagulation. Thromboembolic complication rates of up to 9.3% were reported in large series using the Pipeline FDS,<sup>2,5,20</sup> while the reported rate in stent-assisted aneurysm coiling was 2.0%–7.4%.<sup>21–23</sup>

Embolic phenomena are common after aneurysm coiling, and asymptomatic DWI abnormalities were found in 61%–69% of patients on postprocedural MR imaging.<sup>24,25</sup> A comparison of single and dual antiplatelet agents during aneurysm coiling (including balloon or stent assistance, but not FDS) found no difference between regimens for symptomatic ischemic complications and asymptomatic postprocedural DWI abnormalities, except in the case of wide-neck aneurysms.<sup>26</sup> However, a reduction in the frequency and size of DWI lesions was found in patients receiving larger heparin boluses during aneurysm coiling.<sup>27</sup>

Microemboli detected with TCD are associated with stroke, especially at a rate of  $>10/h$ , in carotid disease<sup>28</sup> and aneurysm coiling in high-risk patients.<sup>9</sup> Schubert et al<sup>8</sup> used routine postprocedural TCD embolic monitoring in 123 aneurysm coiling procedures (not including FDS) and found microemboli in 8.1% of patients during monitoring between 12 and 24 hours postprocedure. Continuous heparinization lowered neurologic deficits and embolic counts significantly; embolic counts trended lower with clopidogrel use.

We found a higher rate of microemboli (13%) after FDS. Our study lacked the power to draw statistical conclusions regarding microembolic risk factors, but 2 of the 3 patients were nonresponders to clopidogrel before the procedure. We found no other demographic, anatomic, or procedural characteristics associated with emboli.

Platelet aggregation on the stent wall, exacerbated by a variable response to platelet inhibition, has been implicated in embolic complications from stent-placement procedures.<sup>11–13,29</sup> Rates of thrombosis-related complications among coronary interventional and neuroendovascular procedures appear higher in nonresponders.<sup>10,11,30</sup> A prospective study of patients undergoing coronary intervention found that the lack of response to antiplatelet agents was an independent risk factor for asymptomatic DWI lesions on postprocedural MR imaging.<sup>31</sup>

Antiplatelet resistance appears to be multifactorial. Genetic polymorphisms have been found in 25%–64% of patients with cardiovascular disease.<sup>17,30</sup> Genetic testing is not commercially available, so the genetic polymorphisms of our patient population are unknown. An association between the use of proton-pump inhibitors and reduced clopidogrel has been reported<sup>32</sup> but did not lead to increased rates of thrombosis in a large randomized trial.<sup>33</sup> We did not find a correlation between proton-pump inhibitor use and clopidogrel resistance or microemboli, though only 5 of 23 patients received proton-pump inhibitors. Finally,

higher body weight has been associated with clopidogrel resistance.<sup>34</sup> Our study did not find a significant difference between body weights of responders and nonresponders, though there was a trend toward clopidogrel resistance ( $P = .07$ ).

The periprocedural management of patients with inadequate platelet inhibition is controversial, and most neuroendovascular guidelines are extrapolated from cardiovascular studies. A meta-analysis<sup>35</sup> comparing loading doses of 300 or 600 mg of clopidogrel found fewer cardiovascular complications with a higher dose, but a large randomized trial showed no effect on thrombosis-related complications in nonresponders.<sup>36</sup> Some authors suggest a dose-dependent strategy based on genotype<sup>17</sup> or switching to prasugrel,<sup>37</sup> as we did if follow-up PRT inhibition was inadequate.

The implications of microemboli after FDS placement are not well understood. Delayed intraparenchymal hemorrhage in the same arterial distribution as a recently placed (1–14 days) FDS is a complication unique to FDSs compared with other stent-assisted neuroendovascular procedures, at rates of up to 8.5%.<sup>3</sup> Thromboemboli have been implicated in the pathogenesis of this complication,<sup>5</sup> which may be due to increased coverage or rigidity of FDS devices, procedural complexity, altered downstream hemodynamics, destabilization of the aneurysm wall, or a combination of factors.

Some authors have hypothesized that postprocedural thromboemboli can produce silent ischemic events with subsequent hemorrhagic conversion. A recent postmortem report of 3 patients with such delayed hemorrhages found foreign body embolic material obstructing the vessels in and around the hemorrhage; these materials were not found elsewhere in the brain.<sup>6</sup> The origin of this material is unclear but could be related to the FDS or equipment used in its deployment.

Postprocedural aneurysm rupture is another rare complication unique to FDSs.<sup>38</sup> Hemodynamic changes induced by FDS placement have been implicated in recent computational fluid dynamics studies.<sup>39</sup> Histologic examination of the wall of aneurysms with delayed rupture demonstrated necrosis in several studies,<sup>38,40</sup> suggesting that intra-aneurysmal thrombosis after FDS placement leads to excessive platelet degranulation and aneurysm wall degradation. Given the varied presentation of hemorrhagic complications reported after treatment with a FDS, the authors suspect that the etiologies may include thromboemboli.

This report has several limitations. First, this was an observational study with a small cohort ( $n = 23$ ) of almost exclusively anterior circulation aneurysms, without a control group. Second, reports are conflicting regarding the appropriate cutoff to define poor platelet inhibition. We used the results of Godino et al<sup>16</sup> ( $>213$  PRU) because they correlated well with flow cytometry, considered one of the criterion standard platelet response tests. However, other studies have used higher values<sup>36</sup> or instead considered the percentage of PRU compared with a baseline value.<sup>12,34</sup> Third, our anticoagulation protocol for the management of nonresponders has not been prospectively validated. Finally, microemboli detection by using TCD did not begin until 12–24 hours after the procedure; immediate postprocedural asymptomatic microemboli may have been missed.

## CONCLUSIONS

We observed a 13% rate of microemboli by using routine post-procedural TCD monitoring after FDS treatment of unruptured aneurysms in our small cohort. Overall, 34.8% of patients were nonresponders according to preprocedural PRT, including 2 of the 3 patients with microemboli. A combined approach of preprocedural PRT and postprocedural embolic monitoring may identify patients at risk of thromboembolic complications after treatment with a FDS.

Disclosures: Michael R. Levitt—UNRELATED: Grants/Grants Pending: National Institutes of Health,\* Volcano Co.\* Basavaraj V. Ghodke—UNRELATED: Other: Covidien, Comments: Proctor, under \$5000. Louis J. Kim—UNRELATED: Grants/Grants Pending: National Institutes of Health,\* Volcano Co.\* Consultancy: Aesculap Inc, Stock/Stock Options: SPI Surgical, Inc. \*Money paid to the institution.

## REFERENCES

1. Nelson PK, Lylyk P, Szikora I, et al. **The Pipeline embolization device for the intracranial treatment of aneurysms trial.** *AJNR Am J Neuroradiol* 2011;32:34–40
2. Briganti F, Napoli M, Tortora F, et al. **Italian multicenter experience with flow-diverter devices for intracranial unruptured aneurysm treatment with periprocedural complications—a retrospective data analysis.** *Neuroradiology* 2012;54:1145–52
3. Cruz JP, Chow M, O’Kelly C, et al. **Delayed ipsilateral parenchymal hemorrhage following flow diversion for the treatment of anterior circulation aneurysms.** *AJNR Am J Neuroradiol* 2012;33:603–08
4. Velat GJ, Fargen KM, Lawson MF, et al. **Delayed intraparenchymal hemorrhage following Pipeline embolization device treatment for a giant recanalized ophthalmic aneurysm.** *J Neurointerv Surg* 2012;4:e24
5. Fischer S, Vajda Z, Aguilar Perez M, et al. **Pipeline embolization device (PED) for neurovascular reconstruction: initial experience in the treatment of 101 intracranial aneurysms and dissections.** *Neuroradiology* 2012;54:369–82
6. Deshmukh V, Hu YC, McDougall CG, et al. **Histopathological assessment of delayed ipsilateral parenchymal hemorrhages after the treatment of paraclinoid aneurysms with the Pipeline embolization device.** In: *Proceedings of the Congress of Neurological Surgeons 2012 Annual Meeting*, Chicago, Illinois. October 6–10, 2012
7. King A, Markus HS. **Doppler embolic signals in cerebrovascular disease and prediction of stroke risk: a systematic review and meta-analysis.** *Stroke* 2009;40:3711–17
8. Schubert GA, Thome C, Seiz M, et al. **Microembolic signal monitoring after coiling of unruptured cerebral aneurysms: an observational analysis of 123 cases.** *AJNR Am J Neuroradiol* 2011;32:1386–91
9. Klötzsch C, Nahser HC, Henkes H, et al. **Detection of microemboli distal to cerebral aneurysms before and after therapeutic embolization.** *AJNR Am J Neuroradiol* 1998;19:1315–18
10. Müller-Schunk S, Linn J, Peters N, et al. **Monitoring of clopidogrel-related platelet inhibition: correlation of nonresponse with clinical outcome in supra-aortic stenting.** *AJNR Am J Neuroradiol* 2008;29:786–91
11. Lee DH, Arat A, Morsi H, et al. **Dual antiplatelet therapy monitoring for neurointerventional procedures using a point-of-care platelet function test: a single-center experience.** *AJNR Am J Neuroradiol* 2008;29:1389–94
12. Prabhakaran S, Wells KR, Lee VH, et al. **Prevalence and risk factors for aspirin and clopidogrel resistance in cerebrovascular stenting.** *AJNR Am J Neuroradiol* 2008;29:281–85
13. Pandya DJ, Fitzsimmons BF, Wolfe TJ, et al. **Measurement of antiplatelet inhibition during neurointerventional procedures: the effect of antithrombotic duration and loading dose.** *J Neuroimaging* 2010;20:64–69
14. Reavey-Cantwell JF, Fox WC, Reichwage BD, et al. **Factors associated with aspirin resistance in patients premedicated with aspirin and clopidogrel for endovascular neurosurgery.** *Neurosurgery* 2009;64:890–95, discussion 895–96
15. Ono T, Kaikita K, Hokimoto S, et al. **Determination of cut-off levels for on-clopidogrel platelet aggregation based on functional CYP2C19 gene variants in patients undergoing elective percutaneous coronary intervention.** *Thromb Res* 2011;128:e130–136
16. Godino C, Mendolicchio L, Figini F, et al. **Comparison of VerifyNow-P2Y12 test and Flow Cytometry for monitoring individual platelet response to clopidogrel: what is the cut-off value for identifying patients who are low responders to clopidogrel therapy?** *Thromb J* 2009;7:4
17. Mega JL, Hochholzer W, Frelinger AL, et al. **Dosing clopidogrel based on CYP2C19 genotype and the effect on platelet reactivity in patients with stable cardiovascular disease.** *JAMA* 2011;306:2221–28
18. Cuisset T, Quilici J, Cohen W, et al. **Usefulness of high clopidogrel maintenance dose according to CYP2C19 genotypes in clopidogrel low responders undergoing coronary stenting for non ST elevation acute coronary syndrome.** *Am J Cardiol* 2011;108:760–65
19. Malinin A, Pokov A, Spergling M, et al. **Monitoring platelet inhibition after clopidogrel with the VerifyNow-P2Y12(R) rapid analyzer: the VERify Thrombosis risk ASsessment (VERITAS) study.** *Thromb Res* 2007;119:277–84
20. McAuliffe W, Wycoco V, Rice H, et al. **Immediate and midterm results following treatment of unruptured intracranial aneurysms with the Pipeline embolization device.** *AJNR Am J Neuroradiol* 2012;33:164–70
21. Mocco J, Snyder KV, Albuquerque FC, et al. **Treatment of intracranial aneurysms with the Enterprise stent: a multicenter registry.** *J Neurosurg* 2009;110:35–39
22. Piotin M, Blanc R, Spelle L, et al. **Stent-assisted coiling of intracranial aneurysms: clinical and angiographic results in 216 consecutive aneurysms.** *Stroke* 2010;41:110–15
23. Fargen KM, Hoh BL, Welch BG, et al. **Long-term results of Enterprise stent-assisted coiling of cerebral aneurysms.** *Neurosurgery* 2012;71:239–44, discussion 244
24. Rordorf G, Bellon RJ, Budzik RE Jr, et al. **Silent thromboembolic events associated with the treatment of unruptured cerebral aneurysms by use of Guglielmi detachable coils: prospective study applying diffusion-weighted imaging.** *AJNR Am J Neuroradiol* 2001;22:5–10
25. Soeda A, Sakai N, Sakai H, et al. **Thromboembolic events associated with Guglielmi detachable coil embolization of asymptomatic cerebral aneurysms: evaluation of 66 consecutive cases with use of diffusion-weighted MR imaging.** *AJNR Am J Neuroradiol* 2003;24:127–32
26. Nishikawa Y, Satow T, Takagi T, et al. **Efficacy and safety of single versus dual antiplatelet therapy for coiling of unruptured aneurysms.** *J Stroke Cerebrovasc Dis* 2013;22:650–55
27. Lim Fat MJ, Al-Hazzaa M, Bussiere M, et al. **Heparin dosing is associated with diffusion weighted imaging lesion load following aneurysm coiling.** *J Neurointerv Surg* 2013;5:366–70
28. Markus HS, Droste DW, Kaps M, et al. **Dual antiplatelet therapy with clopidogrel and aspirin in symptomatic carotid stenosis evaluated using Doppler embolic signal detection: the Clopidogrel and Aspirin for Reduction of Emboli in Symptomatic Carotid Stenosis (CARESS) trial.** *Circulation* 2005;111:2233–40
29. Mazighi M, Saint Maurice JP, Bresson D, et al. **Platelet aggregation in intracranial stents may mimic in-stent restenosis.** *AJNR Am J Neuroradiol* 2010;31:496–97
30. Mega JL, Close SL, Wiviott SD, et al. **Genetic variants in ABCB1 and CYP2C19 and cardiovascular outcomes after treatment with clopidogrel and prasugrel in the TRITON-TIMI 38 trial: a pharmacogenetic analysis.** *Lancet* 2010;376:1312–19
31. Kim BJ, Lee SW, Park SW, et al. **Insufficient platelet inhibition is related to silent embolic cerebral infarctions after coronary angiography.** *Stroke* 2012;43:727–32

32. Gilard M, Arnaud B, Cornily JC, et al. **Influence of omeprazole on the antiplatelet action of clopidogrel associated with aspirin: the randomized, double-blind OCLA (Omeprazole Clopidogrel Aspirin) study.** *J Am Coll Cardiol* 2008;51:256–60
33. Bhatt DL, Cryer BL, Contant CF, et al. **Clopidogrel with or without omeprazole in coronary artery disease.** *N Engl J Med* 2010;363:1909–17
34. Drazin D, Choulakian A, Nuño M, et al. **Body weight: a risk factor for subtherapeutic antithrombotic therapy in neurovascular stenting.** *J Neurointerv Surg* 2011;3:177–81
35. Siller-Matula JM, Huber K, Christ G, et al. **Impact of clopidogrel loading dose on clinical outcome in patients undergoing percutaneous coronary intervention: a systematic review and meta-analysis.** *Heart* 2011;97:98–105
36. Price MJ, Berger PB, Teirstein PS, et al. **Standard- vs high-dose clopidogrel based on platelet function testing after percutaneous coronary intervention: the GRAVITAS randomized trial.** *JAMA* 2011;305:1097–105
37. Alexopoulos D, Dimitropoulos G, Davlouros P, et al. **Prasugrel overcomes high on-clopidogrel platelet reactivity post-stenting more effectively than high-dose (150-mg) clopidogrel: the importance of CYP2C19\*2 genotyping.** *JACC Cardiovasc Interv* 2011;4:403–10
38. Chow M, McDougall C, O’Kelly C, et al. **Delayed spontaneous rupture of a posterior inferior cerebellar artery aneurysm following treatment with flow diversion: a clinicopathologic study.** *AJNR Am J Neuroradiol* 2012;33:E46–51
39. Cebal JR, Mut F, Raschi M, et al. **Aneurysm rupture following treatment with flow-diverting stents: computational hemodynamics analysis of treatment.** *AJNR Am J Neuroradiol* 2011;32:27–33
40. Kulcsár Z, Houdart E, Bonafe A, et al. **Intra-aneurysmal thrombosis as a possible cause of delayed aneurysm rupture after flow-diversion treatment.** *AJNR Am J Neuroradiol* 2011;32:20–25

# Spontaneous Delayed Migration/Shortening of the Pipeline Embolization Device: Report of 5 Cases

N. Chalouhi, S.I. Tjoumakaris, L.F. Gonzalez, D. Hasan, P.J. Pema, G. Gould, R.H. Rosenwasser, and P.M. Jabbour

## ABSTRACT

**SUMMARY:** Five patients were found to have spontaneous delayed migration/shortening of their Pipeline Embolization Devices on follow-up angiography. The device migrated proximally in 4 patients and distally in 1 patient. One patient had a subarachnoid hemorrhage and died as a result of migration of the Pipeline Embolization Device, and another patient presented with complete MCA occlusion and was left severely disabled. Mismatch in arterial diameter between inflow and outflow vessels was a constant finding. Migration of the Pipeline Embolization Device was managed conservatively, with additional placement of the device, or with parent vessel occlusion. Obtaining complete expansion of the embolization device by using a longer device, increasing vessel coverage, using adjunctive aneurysm coiling, and avoiding dragging and stretching of the device are important preventive measures. Neurointerventionalists should be aware of this potentially fatal complication and take all necessary preventive measures.

**ABBREVIATIONS:** PED = Pipeline Embolization Device; SHA = superior hypophyseal artery

The Pipeline Embolization Device (PED; Covidien/ev3, Irvine, California) is a dedicated flow diverter designed to treat intracranial aneurysms. Recent series have shown the PED to be a reasonably safe and effective treatment.<sup>1-5</sup> The risks for intracranial hemorrhage, delayed aneurysm rupture, and thromboembolic events have been major concerns with this approach.<sup>1-3,6,7</sup> Additional complications are becoming evident, as the PED is increasingly used for an expanding population of patients with cerebral aneurysms. In this study, we report 5 cases of patients with spontaneous delayed migration or shortening of the PED and discuss the possible cause, implications, and management of this serious and potentially fatal complication.

## MATERIALS AND METHODS

Five patients treated with the PED in whom spontaneous delayed migration or shortening of their devices developed were prospectively identified. During the same period (from November 2010–January 2013), a total of 155 patients were treated with the PED at

our institution. The 5 cases of PED migration occurred late during the study period (second half of the cohort).

PEDs were deployed through a Marksman microcatheter (ev3, Irvine, California) by use of a triaxial guide-catheter system. The maximal diameter in the predicted landing zone was determined, and the PED was sized according to the width of the inflow vessel to avoid any endoleak. The expansion of the PED was documented under fluoroscopy or with additional DynaCT angiography (Siemens, Erlangen, Germany) at the operator's discretion.

## Representative Case Patients

**Patient 1.** A 50-year-old man with schizophrenia presented with an unruptured left MCA (M1) aneurysm discovered during work-up for severe cervical myelopathy. The aneurysm measured  $12.7 \times 11.6$  mm; the diameter of the inflow vessel was 3.2 mm, and the diameter of the outflow vessel was 2.5 mm. Given the aneurysm size, wide-neck morphologic feature, and the patient's categorical refusal of open surgery, the decision was made to treat the aneurysm with the PED. The patient was pretreated with aspirin and clopidogrel for 10 days. The patient was given a bolus of heparin, and activated clotting time was maintained at 2–3 times the baseline throughout the procedure. With use of a triaxial system, a  $3 \times 16$ -mm PED was deployed across the neck of the aneurysm, extending from the proximal superior division of the M2 segment to the mid-M1 segment (Fig 1). A control cerebral angiogram was performed and showed stasis within the aneurysm. Five months later, the patient presented to the emergency

Received January 31, 2013; accepted after revision March 20.

From the Department of Neurosurgery (N.C., S.I.T., L.F.G., G.G., R.H.R., P.M.J.), Thomas Jefferson University and Jefferson Hospital for Neuroscience, Philadelphia, Pennsylvania; Department of Neurosurgery (D.H.), University of Iowa, Iowa City, Iowa; and Department of Radiology (P.J.P.), Riverside Methodist Hospital, Columbus, Ohio.

Please address correspondence to Pascal M. Jabbour, MD, Associate Professor, Department of Neurological Surgery, Division of Neurovascular Surgery and Endovascular Neurosurgery, Thomas Jefferson University Hospital, 901 Walnut St, 3rd Floor, Philadelphia, PA 19107; e-mail: pascal.jabbour@jefferson.edu

<http://dx.doi.org/10.3174/ajnr.A3632>

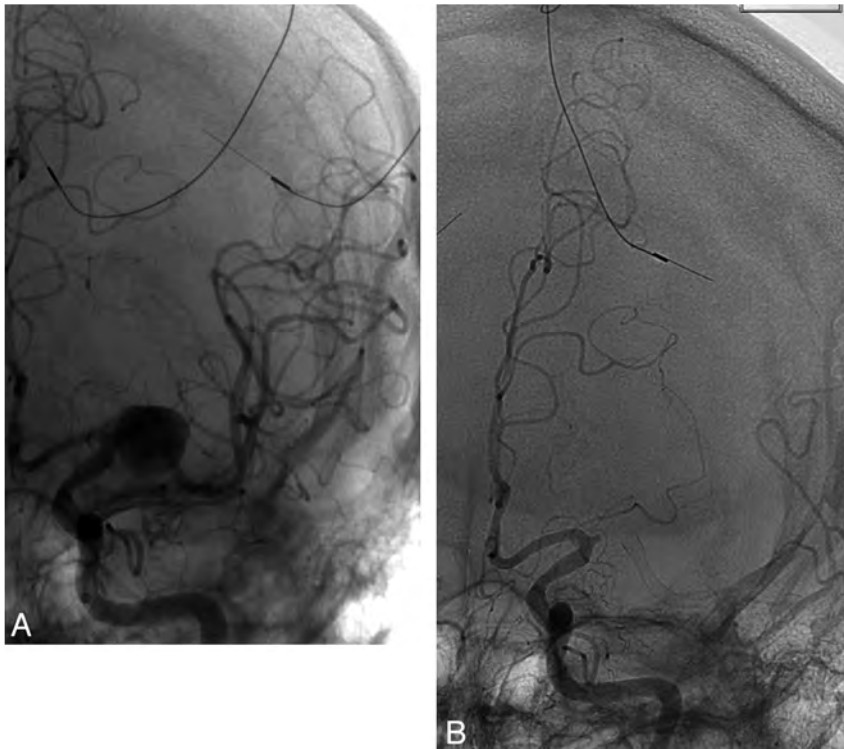


**FIG 1.** A, Angiogram after deployment of a PED extending from the proximal superior division of the M2 segment to the mid-M1 segment. B, Angiogram showing complete MCA occlusion 5 months later with distal PED migration.

department with an acute onset of right-sided hemiplegia. He had not been compliant with the antiplatelet therapy. A noncontrast head CT scan result was negative for hemorrhage, and CT angiography demonstrated complete occlusion of the M1. CT perfusion revealed a large area at risk, and the patient was transferred to the angiography suite for mechanical thrombectomy. A left ICA injection showed that the M1 segment of the MCA was completely occluded. It is interesting to note that the PED had migrated distally, with the proximal end of the device now within the aneurysm sac. There was no evidence of filling of the aneurysm. The procedure was aborted at this point because it was felt that blind navigation through the aneurysm sac would carry a high risk for aneurysm perforation. The patient remained hemiplegic and was discharged to rehabilitation.

**Patient 2.** A 46-year-old woman presented to our institution with a 1-year history of visual loss. A visual field test revealed right-sided homonymous hemianopsia, and MRA showed a giant left supraclinoid ICA aneurysm. Flow diversion was thought to be the most durable treatment of the aneurysm. The patient was premedicated with aspirin and clopidogrel (Plavix). On DSA, the aneurysm measured  $2.8 \times 2.3$  cm with no distinct neck; the inflow zone was slightly distal to the ophthalmic artery, and the outflow zone was posterolateral within the aneurysm. There was delayed filling of the anterior and middle cerebral arteries caused by aneurysmal blood steal. A  $4.25 \times 30$ -mm PED was deployed from the mid-M1 segment (diameter, 1.9 mm) to the proximal cavernous ICA (diameter, 3.8 mm) (Fig 2). Control angiography showed significant contrast stasis in the entire aneurysm with excellent filling of the ante-

rior and middle cerebral arteries. The patient was neurologically intact after the procedure, but on postoperative day 3 she experienced right-sided hemiplegia with severe headaches. A noncontrast head CT scan was performed emergently and showed extensive subarachnoid hemorrhage. She underwent emergent reversal of antiplatelet therapy with placement of a right frontal ventriculostomy and was taken for subsequent angiography. On DSA, there was evidence of proximal PED migration, with displacement of the distal limb of the device now located centrally within the aneurysm sac and diverting the flow jet directly into the dome of the aneurysm. There was also evidence of a new rupture site on the aneurysmal dome (facing the distal end of the device). Several coils were deployed inside the aneurysm, and the decision was made to deconstruct the parent artery to prevent a new catastrophic hemorrhage. The left ICA was successfully occluded with a combination of coils and Onyx 34 (ev3). A control cerebral angiogram showed no filling of the left ICA and aneurysm. Despite maximal medical intervention,

the patient experienced uncontrollable intracranial pressure and rapidly progressed to brain death.

**Patient 3.** A 41-year-old woman presented to our institution for evaluation and treatment of 2 incidentally discovered aneurysms arising from the left superior hypophyseal segment and the left cavernous segment of the ICA. The aneurysm of the superior hypophyseal artery (SHA) measured  $6.43 \times 6.97$  mm with a neck of 3.6 mm, and the cavernous aneurysm measured  $2.97 \times 3.63$  mm with a 3-mm neck. The diameter of the petrous segment of the ICA was 4.1 mm, and the diameter of the paraclinoid segment was 2.7 mm. The decision was made to treat both aneurysms with a flow-diversion technique by use of the PED. The patient was prescribed aspirin and clopidogrel. With use of a triaxial system, a  $4 \times 25$ -mm PED was deployed across the aneurysms without difficulty, extending from the paraclinoid segment of the ICA to the petrous segment (Fig 3). Control angiography demonstrated adequate PED placement with contrast stasis in the SHA aneurysm. DynaCT was subsequently performed, demonstrating adequate stent apposition to the vessel wall with covering of the necks of both aneurysms. The procedure and postoperative course were uneventful, and the patient was discharged on the following day. Follow-up angiography 4 months later showed that the distal portion of the PED had migrated slightly proximally, with the neck of the SHA aneurysm no longer covered by the device. There was complete filling of the SHA aneurysm, with no contrast stasis. The cavernous aneurysm had completely resolved. The patient was scheduled for subsequent embolization.

**Patient 4.** A 61-year-old woman with increasing retro-orbital pain from a large right cavernous ICA aneurysm underwent un-

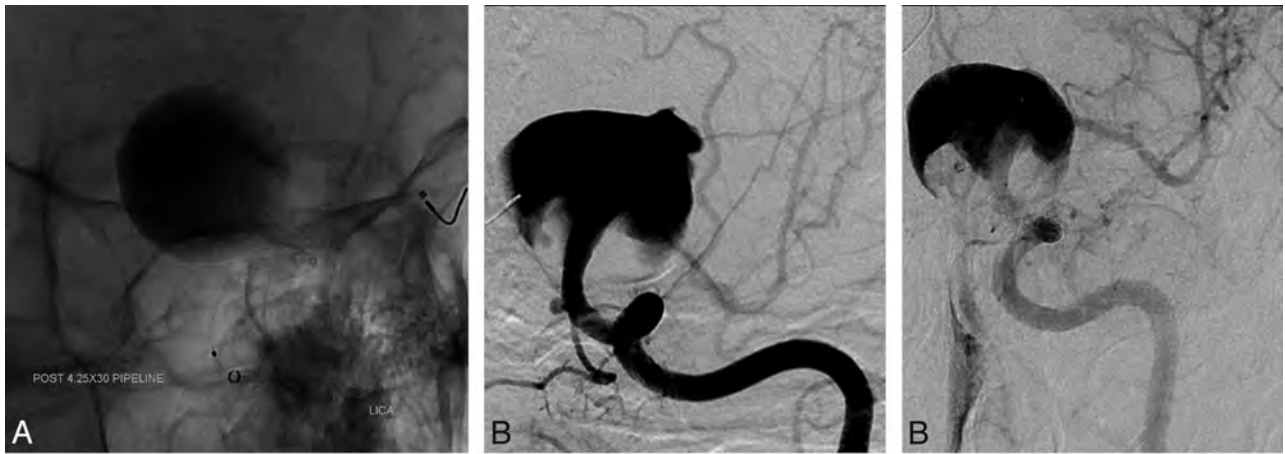


**FIG 2.** A, Angiogram showing a PED that was deployed from the mid-M1 segment to the proximal cavernous ICA. B, DSA showing proximal PED migration. Note the new rupture site on the aneurysmal dome facing the displaced PED. C, Noncontrast head CT scan on postoperative day 3 showing an extensive subarachnoid hemorrhage, with displacement of the distal limb of the device now located centrally within the aneurysmal sac.

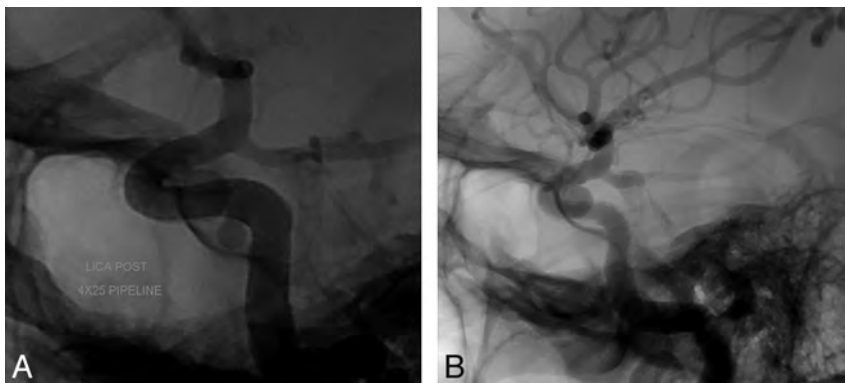
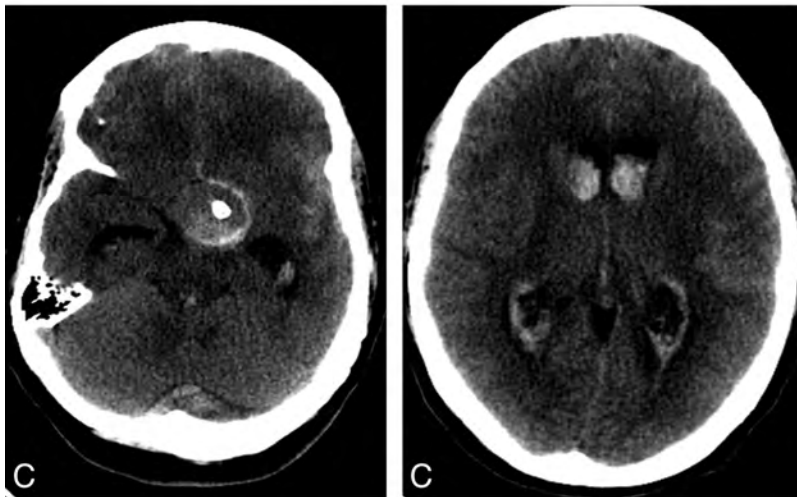


**FIG 3.** A, A PED is deployed across 2 aneurysms extending from the petrous segment to the paraclinoid segment of the ICA. B, Follow-up angiography 4 months later showing that the distal portion of the PED had migrated slightly proximally, with the neck of the SHA aneurysm no longer covered by the device.

eventful treatment of her aneurysm with the PED (Fig 4). There was significant mismatch in arterial diameter ( $> 1$  mm) between the inflow and outflow vessels. At 5 months after the procedure, the patient's symptoms recurred. On the 6-month follow-up angiography, there was proximal PED migration, with the distal end of the device projecting directly into the aneurysm and creating a jet of contrast against the aneurysm sac. A second, overlapping PED was successfully deployed within the first PED to cover the neck of the aneurysm. Six weeks later, the patient's symptoms

had completely resolved and a follow-up CT angiogram showed complete obliteration of the aneurysm.

**Patient 5.** A 71-year-old woman presented for treatment of a symptomatic aneurysm of the left cavernous ICA measuring 16.5 mm. The diameter of the inflow vessel was 4.4 mm, and the diameter of the outflow vessel was 4.2 mm. It was decided to treat the aneurysm with flow diversion. A  $4.5 \times 18$ -mm PED was deployed across the aneurysm without difficulty, extending from the immediate pregenu portion to the midvertical segment of the cavernous ICA. A control angiogram demonstrated contrast stasis within the aneurysm, with adequate stent apposition to the vessel wall. A subsequent angiogram 1 day later showed complete occlusion of the aneurysm. The postoperative course was uneventful, and the patient was discharged neurologically intact. She remained asymptomatic and returned 7 months later for follow-up angiography. On DSA, there was complete filling of the aneurysm sac and the PED had migrated proximally. The migration distance was 7.5 mm. A second, overlapping  $5 \times 30$ -mm PED was subsequently deployed beyond the first stent to bridge the neck of the aneurysm and disrupt the inflow jet.

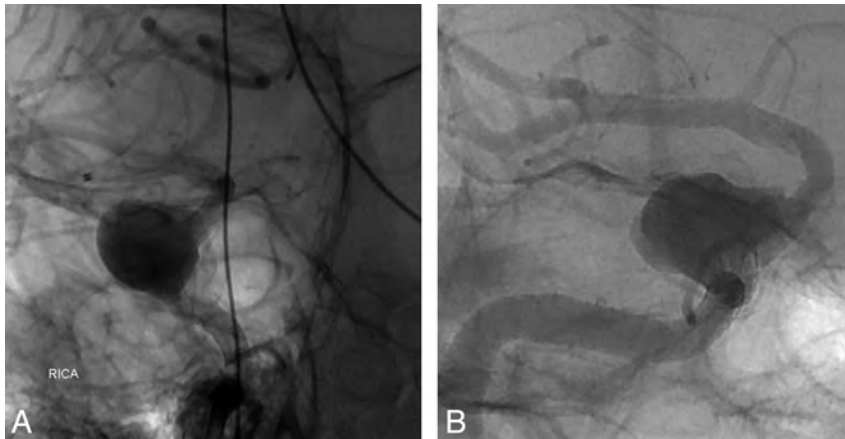


**FIG 4.** A, Angiogram showing the initial position of the PED; the distal end is at the clinoid segment. B, Angiogram showing proximal migration of the PED; the distal end of the device is now within the aneurysmal sac.

**PED migration characteristics**

Patient No.	Length of PED Extending to Aneurysm (mm)		Migration Distance (mm)	Migration of Proximal or Distal End of PED?
	Proximal to Aneurysm	Distal to Aneurysm		
1	7	6	9	Proximal
2	10	15	20	Distal
3	15	3	5	Distal
4	10	7	>10	Distal and proximal
5	13	3.5	7.5	Distal

**DISCUSSION**

Several groups have recently reported their experience with the PED. In most series, remarkably high rates of aneurysm occlusion were achieved at follow-up with an acceptable risk for major complications.<sup>1-5</sup> Some authors, based on favorable results from non-controlled series, have even recommended the PED as a first-line option for unruptured aneurysms.<sup>3</sup> Long-term safety results, however, are lacking and new complications have been emerging as neurointerventionalists accumulate experience with the device. The phenomenon of delayed migration or shortening of the PED has not been described in previously published series.

In this study, we have reported 5 cases of patients with spontaneous delayed migration or shortening of the PED (Table). In most cases, the PED migrated proximally (patients 2-5), and there was a significant difference in luminal diameter between inflow and outflow vessels. This may have produced a constant retrograde squeezing force at the distal end of the PED causing it to “watermelon-seed” backward into the aneurysm sac. Also, given the vertical position of the ICA, the weight of the device may have dragged the construct downward. The PED migration may also be at least in part the result of an “accordion effect,” a phenomenon of foreshortening of a device that was possibly stretched during deployment. This is particularly true in patients 1, 2, and 5 where the PED moved from its initial position because of device shortening rather than migration. In patient 1, the PED moved distally due to shortening because it was probably better anchored distally than it was proximally.

The incidence of spontaneous migration seems to be higher with the PED (5/155, 3.2%) than other self-expanding stents such

as the Neuroform (Stryker Neurovascular, Fremont, California) (no cases previously reported) or Enterprise (Codman & Shurtleff, Raynham, Massachusetts) (only 6 cases previously reported).<sup>8</sup> The PED is particularly vulnerable to the phenomenon of spontaneous migration because it is a low-porosity stent, which facilitates the transmission of a force exerted at one end of the device to the other end.<sup>9-10</sup> The migration of the PED is somewhat similar to the migration of Enterprise stents. Previous cases have involved Enterprise stents deployed from the midbasilar artery to the P1 segment of the posterior cerebral artery during treatment of basilar tip aneurysms.<sup>10-15</sup> The migration was primarily attributed to the

diameter difference between the basilar artery and the P1 segment of the posterior cerebral artery. Lubicz et al<sup>16</sup> previously described the delayed migration of a Silk stent (Balt Extrusion, Montmorency, France) in a patient with a giant saccular carotid ophthalmic aneurysm. The patient had a massive SAH as a result of the migration and died.

Our present series shows that PED migration can occur both early and late after treatment. In patient 2, the migration occurred within 72 hours. Conversely, in patient 4 the migration likely occurred several months after the initial intervention, as suggested by the recurrence of the patient’s symptoms at 5 months.

Although PED migration was uneventful in 3 patients, it was associated with fatal or severely disabling complications in 2 patients. In patient 2, the distal end of the PED migrated proximally into the aneurysm sac, creating a direct jet of blood against the aneurysm wall and precipitating aneurysm rupture. This occurrence is further supported by the observation that the rupture site on the aneurysmal dome was directly facing the distal end of the device. In patient 1, the patient presented with complete occlusion of the MCA, but it is not clear whether this event was related to the distal migration of the PED. Still, the device migration into the aneurysmal sac precluded any attempt at mechanical thrombolysis, and the procedure had to be aborted because of the high risk for iatrogenic aneurysm perforation (thus preventing potential neurologic recovery).

The following precautions should be taken to minimize the occurrence of spontaneous delayed PED migration or shortening, especially if there is a mismatch in diameter between inflow and outflow vessels:

1. Obtaining complete expansion of the PED with optimal vessel wall apposition. Accurate sizing of the PED is of utmost importance. DynaCT may be useful to confirm adequate apposition of the device to the vessel wall.
2. Using longer PEDs to prevent excessive foreshortening. In addition, the conveyance of retrograde forces is lower with longer stents.<sup>9,10</sup> Increasing vessel coverage proximally and/or distally to the aneurysm may also be helpful. A second stent can be deployed to increase vessel coverage when needed. One could

argue in retrospect that PED deployment was too proximal in patients 3 and 5 and was too distal in patient 1.

3. Avoidance of dragging of the PED to prevent foreshortening. Instead of going in distally and dragging the device proximally into the landing zone, it would be preferable to go directly into the landing zone to detach and deploy the device.
4. Avoidance of stretching of the PED during deployment to prevent the “accordion effect.”
5. Adjunctive aneurysm coiling, as this may prevent prolapse of the PED into the aneurysm for larger aneurysms.

We have recently applied these precautions, and we will assess in a future study whether they can lead to a significant decrease in the incidence of PED migration or shortening.

PED migration is best managed by placing additional PEDs to achieve complete coverage of the aneurysm and divert the blood flow away from the aneurysmal sac. A J-shaped guidewire is passed through the migrated stent and is navigated directly into the distal ICA. This is followed by deployment of 1 or more PEDs as necessary until the parent vessel is reconstructed. If the proximal part of the device has migrated into the aneurysmal sac and attempts to recatheterize the PED have failed, retrograde access of the PED is gained from the distal ICA through a microwire advanced from the basilar artery through the posterior communicating artery or from the contralateral ICA through the anterior communicating artery.<sup>17</sup> Endovascular parent vessel deconstruction or surgical ligation, when tolerated, is an alternative strategy to manage PED migration. In the setting of subarachnoid hemorrhage, as in patient 2, the goal of treatment is to obtain immediate occlusion of the aneurysmal sac and/or the parent vessel.

## CONCLUSIONS

Spontaneous delayed migration or shortening of the PED is a serious and potentially fatal complication. The device may migrate proximally or distally and result in aneurysmal rupture or thrombotic events. The migration may occur both early and late after treatment. Obtaining complete expansion of the PED by using longer PEDs, increasing vessel coverage, using adjunctive aneurysm coiling, and avoiding dragging and stretching of the PED are important preventive measures. Neurointerventionalists should be aware of this undesirable phenomenon and take all necessary preventive measures. If any concern arises regarding the position of the PED, early imaging follow-up may be indicated.

Disclosures: Stavropoula Tjoumakaris—UNRELATED: Consultancy: Stryker. Pascal Jabbour—UNRELATED: Consultancy: ev3, CNV.

## REFERENCES

1. Lylyk P, Miranda C, Ceratto R, et al. **Curative endovascular reconstruction of cerebral aneurysms with the Pipeline embolization**

- device: the Buenos Aires experience. *Neurosurgery* 2009;64:632–42; discussion 642–43; quiz N636
2. Saatci I, Yavuz K, Ozer C, et al. **Treatment of intracranial aneurysms using the Pipeline flow-diverter embolization device: a single-center experience with long-term follow-up results.** *AJNR Am J Neuroradiol* 2012;33:1436–46
3. Yu SC, Kwok CK, Cheng PW, et al. **Intracranial aneurysms: mid-term outcome of Pipeline embolization device—a prospective study in 143 patients with 178 aneurysms.** *Radiology* 2012;265:893–901
4. McAuliffe W, Wycoco V, Rice H, et al. **Immediate and midterm results following treatment of unruptured intracranial aneurysms with the Pipeline embolization device.** *AJNR Am J Neuroradiol* 2012;33:164–70
5. Nelson PK, Lylyk P, Szikora I, et al. **The Pipeline embolization device for the intracranial treatment of aneurysms trial.** *AJNR Am J Neuroradiol* 2011;32:34–40
6. Chitale R, Gonzalez LF, Randazzo C, et al. **Single center experience with Pipeline stent: feasibility, technique, and complications.** *Neurosurgery* 2012;71:679–91; discussion 691
7. O’Kelly CJ, Spears J, Chow M, et al. **Canadian experience with the Pipeline Embolization device for repair of unruptured intracranial aneurysms.** *AJNR Am J Neuroradiol* 2013;34:381–87
8. Prestigiacomo CJ. **Stent-assisted coiling for aneurysms and the phenomenon of stent migration: is it worth it?** *J Neurointerv Surg* 2010;2:351
9. Gao B, Malek AM. **Possible mechanisms for delayed migration of the closed cell–designed Enterprise stent when used in the adjunctive treatment of a basilar artery aneurysm.** *AJNR Am J Neuroradiol* 2010;31:E85–86
10. Lobotesis K, Gholkar A, Jayakrishnan V. **Early migration of a self-expanding intracranial stent: case report.** *Neurosurgery* 2010;67:E516–17
11. Dashti SR, Fiorella D, Toledo MM, et al. **Proximal migration and compaction of an Enterprise stent into a coiled basilar apex aneurysm: a posterior circulation phenomenon?** *J Neurointerv Surg* 2010;2:356–58
12. Lavine SD, Meyers PM, Connolly ES, et al. **Spontaneous delayed proximal migration of Enterprise stent after staged treatment of wide-necked basilar aneurysm: technical case report.** *Neurosurgery* 2009;64:E1012; discussion E1012
13. Kelly ME, Turner RD, Moskowitz SI, et al. **Delayed migration of a self-expanding intracranial microstent.** *AJNR Am J Neuroradiol* 2008;29:1959–60
14. Rodriguez GJ, Maud A, Taylor RA. **Another delayed migration of an Enterprise stent.** *AJNR Am J Neuroradiol* 2009;30:E57
15. Khatri R, Rodriguez GJ, Siddiq F, et al. **Early migration of a self-expanding intracranial stent after the treatment of a basilar trunk aneurysm: report of a second case.** *Neurosurgery* 2011;69:E513–15; author reply E515–17
16. Lubicz B, Collignon L, Raphaeli G, et al. **Flow-diverter stent for the endovascular treatment of intracranial aneurysms: a prospective study in 29 patients with 34 aneurysms.** *Stroke* 2010;41:2247–53
17. Hauck EF, Natarajan SK, Langer DJ, et al. **Retrograde trans-posterior communicating artery snare-assisted rescue of lost access to a foreshortened Pipeline embolization device: complication management.** *Neurosurgery* 2010;67:495–502

# CTA for Screening of Complicated Atherosclerotic Carotid Plaque—American Heart Association Type VI Lesions as Defined by MRI

M. Trelles, K.M. Eberhardt, M. Buchholz, A. Schindler, A. Bayer-Karpinska, M. Dichgans, M.F. Reiser, K. Nikolaou, and T. Saam



## ABSTRACT

**BACKGROUND AND PURPOSE:** High-resolution carotid MR imaging can accurately identify complicated American Heart Association lesion type VI plaques, which are characterized by thrombus, hemorrhage, or a ruptured fibrous cap. The purpose of this study is to evaluate whether CTA can be used as screening tool to predict the presence or absence of American Heart Association lesion type VI plaques as defined by high-resolution MR imaging.

**METHODS:** Fifty-one patients with suspected ischemic stroke or TIA with carotid CTA and carotid MR imaging performed within 14 days of the event/admission from April 2008 to December 2010 were reviewed. Vessels with stents or occlusion were excluded ( $n = 2$ ). Each carotid artery was assigned an American Heart Association lesion type classification by MR imaging. The maximum wall thickness, maximum soft plaque component thickness, maximum calcified component thickness, and its attenuation (if the soft plaque component thickness was  $>2$  mm) were obtained from the CTA.

**RESULTS:** The maximum soft plaque component thickness proved the best discriminating factor to predict a complicated plaque by MR imaging, with a receiver operating characteristic area under the curve of 0.89. The optimal sensitivity and specificity for detection of complicated plaque by MR imaging was achieved with a soft plaque component thickness threshold of 4.4 mm (sensitivity, 0.65; specificity, 0.94; positive predictive value, 0.75; and negative predictive value, 0.9). No complicated plaque had a soft tissue plaque thickness  $<2.2$  mm (negative predictive value, 1) and no simple (noncomplicated) plaque had a thickness  $>5.6$  mm (positive predictive value, 1).

**CONCLUSIONS:** Maximum soft plaque component thickness as measured by carotid CTA is a reliable indicator of a complicated plaque, with a threshold of 2.2 mm representing little to no probability of a complicated American Heart Association lesion type VI plaque.

**ABBREVIATIONS:** AHA-LT6 = American Heart Association type VI; IPH = intraplaque hemorrhage; HU = Hounsfield units

Macroangiopathic disease causes 20–30% of ischemic strokes, most occurring as the result of plaque rupture.<sup>1,2</sup> This percentage might even be higher, as a recent MR imaging study<sup>3</sup> suggested that a substantial portion of patients with cryptogenic strokes have ipsilateral complicated American Heart Association type VI (AHA-LT6) carotid plaques, characterized by intraplaque hemorrhage (IPH), thrombus, or a ruptured fibrous cap. These characteristics are currently identifiable on high-reso-

lution MR imaging of the carotid arteries<sup>4,5</sup> with improved sensitivity and specificity with the use of specialized high-resolution techniques.<sup>4,6-9</sup> Furthermore, several MR studies have demonstrated that AHA-LT6 plaques are related to increased risk of stroke independent of the severity of luminal stenosis.<sup>10,11</sup> High-resolution MR imaging of the carotid bifurcation, however, is time-consuming, requires specialized coils, and is not widely available.

Carotid sonography is often used as a first-line imaging technique to screen for the presence or absence of atherosclerosis, but this method is highly operator-dependent and provides limited information regarding plaque morphology and complications.<sup>12-14</sup> Operators usually focus on the degree of stenosis, and intima-media thickness measurements, plaque thickness, and morphology are not considered part of the routine sonography evaluation.

CT of the brain is commonly used as part of the routine clinical work-up in patients with suspected ischemic stroke or TIA. CTA

Received December 6, 2012; accepted after revision March 20, 2013.

From the Department of Radiology (M.T.), University of Texas Medical Branch, Galveston, Texas; and Institute for Clinical Radiology (K.M.E., M.B., A.S., M.F.R., K.N., T.S.) and Institute for Stroke and Dementia Research (A.B.-K., M.D.), Ludwig-Maximilians-University, Munich, Germany.

Please address correspondence to Tobias Saam, MD, Institute for Clinical Radiology, Ludwig-Maximilians-University Hospitals Munich, Pettenkofenstr. 8a, 80336 München, Germany; e-mail: mitrelle@utmb.edu

 Indicates article with supplemental on-line table

 Indicates article with supplemental on-line figure

<http://dx.doi.org/10.3174/ajnr.A3607>

of the circle of Willis and cervical carotid arteries is frequently performed concomitantly to evaluate for thrombus and to define the degree of carotid stenosis,<sup>15</sup> which is the only broadly accepted finding used to indicate endarterectomy.<sup>16-18</sup> Furthermore, carotid CTA provides high-resolution images of the carotid bulb to identify ulcerations<sup>19-21</sup> and it also provides information about aortic arch plaques, which have been associated with thromboembolic events.<sup>22</sup>

MDCT angiography is also able to differentiate between soft, mixed, and hard plaques, with questionable evaluation of fibrous tissue and lipid-rich necrotic core.<sup>23-25</sup> The use of Hounsfield units (HU) analysis for the identification of the components is limited secondary to overlap in HU values between different plaque components and the presence of artifacts from calcified plaque and the enhanced arterial lumen.<sup>26,27</sup> To date, CTA is not able to reliably identify complicated AHA-TL6 plaques, which are characterized by fibrous cap rupture, attached thrombus, or hemorrhage, and are the imaging findings most closely related with an increased clinical risk of stroke.<sup>11</sup> Thus, it would be beneficial to evaluate imaging characteristics found on CTA that would warrant obtaining a high-resolution MR imaging of the carotid bifurcation.

The purpose of this study is to evaluate whether carotid CTA can be used as a screening tool to predict the presence or absence of a complicated AHA-TL6 carotid bulb plaque with fibrous cap rupture, attached thrombus, or hemorrhage as defined by high-resolution MR imaging.

## MATERIALS AND METHODS

### Patient Selection

Patients with suspected ischemic stroke or TIA of the anterior circulation who had a carotid CTA and high-resolution carotid MR imaging performed within 14 days of the event or admission from April 2008 to December 2010 were included. Patients with imaging studies of insufficient quality and vessels with prior endarterectomy, stent, or occlusion were excluded. The study was approved by the local ethics committee, and all subjects gave written informed consent. CT brain imaging was routinely performed immediately after presentation to assess intracerebral hemorrhage and acute ischemic stroke.

### Imaging Protocols and Analysis

Because assessment of patients with stroke is performed by several units in our clinical center, scans were performed on various CT scanners: Bright Speed S (GE Healthcare, Milwaukee, Wisconsin), Aquilion (Toshiba Medical Systems, Tokyo, Japan), Somatom Definition Flash (Siemens, Erlangen, Germany), Somatom Definition AS+ (Siemens), and Sensation 64 (Siemens). All CTA images were obtained with coverage at least from the aortic arch to the cranium by use of the respective standard protocol parameters. Nonionic iodinated contrast material was applied intravenously, adjusted to patient weight (Ultravist 370; BayerSchering Pharma, Berlin, Germany, ie, 0.35–0.50 g iodine per kg body weight at an injection rate of 4.5–6 mL/s followed by 100 mL of saline at identical flow) (On-line Table).

Participants underwent high-resolution black-blood carotid MR imaging within a mean of 7.8 days after the CT scan. All

subjects were imaged by use of a previously published multi-sequence protocol<sup>24</sup> (TOF MR angiography, axial precontrast and postcontrast black-blood T1, proton attenuation, and T2WI sequences with fat saturation centered at the carotid bifurcation; best in-plane resolution,  $0.5 \times 0.5 \text{ mm}^2$ ) at 3T (Magnetom Verio, Siemens). To improve signal-to-noise performance and optimize spatial resolution, a dedicated 4-channel surface coil (Machnet B.V., Eelde, The Netherlands) was used for bilateral carotid scans. Gadolinium-DO3A-Butrol (Gadobutrol, Bayer Schering) of 0.1 mmol/kg (0.1 mL/kg) was given at a rate of 3 mL/s.

An experienced radiologist blinded to the MR imaging results (M.T.) reviewed the axial sections of the CTAs to obtain the following measurements: maximum plaque wall thickness, maximum thickness of soft plaque component, and maximum thickness of calcified plaque component (On-line Figure). If the soft plaque component thickness was  $>2 \text{ mm}$ , 2 oval ROIs were obtained from the plaque area measuring the mean, minimum, and maximum HU and the standard deviation. Window level settings were set at 800/200, though small adjustments were allowed. The ROI size was kept  $\geq 2 \text{ mm}^2$ . Superimposition of both ROIs was allowed in cases with small plaques. The ROIs were taken with care to include the area showing less attenuation, avoiding calcifications and the enhanced lumen. The presence of ulceration or thrombus was also noted. Ulcerations were defined as an out-pouching of contrast material  $>1 \text{ mm}$ .<sup>28</sup> For completeness, the percentage of stenosis obtained by the NASCET method was also calculated.

To assess for the reproducibility of the axial measurements, a second experienced radiologist (K.M.E.) who was blinded to the initial results repeated the measurements in the original axial sections in 20 patients (40 carotid arteries). Furthermore, to explore the potential of measurements in a plane orthogonal to the lumen and to exclude a systematic bias of the axial measurements, curved planar reformatted images of the same 20 patients were uploaded in a separate session on a dedicated workstation (IMPAX Volume Viewing 2.2; Agfa, Greenville, South Carolina) and all plaque thickness measurements were repeated in an orthogonal plane. An image-quality rating (4-point scale, 1 = nondiagnostic, 2 = moderate, 3 = good, 4 = excellent) was assigned to all MR images. The MR imaging data were classified according to the modified American Heart Association lesion type classification as previously defined by Cai et al<sup>29</sup> by 2 experienced radiologists (T.S. and K.N.) who were blinded to the CTA data. In the case of discrepancy, a consensus decision was made. Patients with image quality  $\geq 2$  by MR imaging were included. The presence of complications such as hemorrhage, fibrous cap rupture, ulceration, calcific nodule, or thrombus was also annotated.

### Statistical Analysis

Categorical variables are presented as percentages; continuous variables are presented as mean  $\pm 95\%$  confidence interval. Data analysis was performed by use of SPSS Statistics (Version 20; IBM, Armonk, New York). Graphs were constructed with the use of Excel (Version 14; Microsoft, Redmond, Washington). Continuous data were compared with the unpaired Student *t* test. Categorical data were compared by means of  $\chi^2$  test. Inter-reader and intermeasurement agreement (between measurements in the ax-

**Table 1: Patient characteristics**

	Study Population (n = 51)
Demographic	
Age, y	71.3 ± 0.9
Male sex	74%
Body mass index	26.0 ± 0.3
CT imaging	
Stenosis, % (NASCET)	26.7% ± 5.6%
Cardiovascular risk factors	
Smoker	25.5% (13)
Ex-smoker	41.2% (21)
Hypertension	76.5% (39)
Hypercholesterolemia	45.1% (23)
Diabetes	23.5% (12)
Coronary heart disease	13.7% (7)
Family history of cardiovascular events	31.4% (16)

Note:—Values are mean ± CI unless otherwise shown.

**Table 2: General plaque characteristics by MRI-derived AHA lesion type**

MRI-AHA Lesion Type	Maximum Wall Thickness	Maximum Soft Plaque Thickness	Maximum Hard Plaque Thickness	Minimum Density	Maximum Density	Mean Density	NASCET Percentage Stenosis
I-II	2.2 ± 0.6	1.8 ± 0.6	1.4 ± 0.8	38 ± NA <sup>a</sup>	197 ± NA <sup>a</sup>	82 ± NA <sup>a</sup>	0.0% ± NA <sup>a</sup>
III	3.7 ± 0.5	1.8 ± 0.8	3.0 ± 0.5	41 ± 18	224 ± 68	114 ± 29	15.1% ± 12.5%
IV-V	4.0 ± 0.3	2.9 ± 0.5	2.4 ± 0.5	14 ± 10	134 ± 21	59 ± 12	21.1% ± 8.0%
VI	5.3 ± 0.4	4.7 ± 0.5	2.5 ± 0.5	18 ± 9	143 ± 18	60 ± 12	46.3% ± 10.6%
VII	4.4 ± 0.7	1.1 ± 0.5	3.9 ± 0.5	31 ± 8	215 ± 33	91 ± 11	33.1% ± 14.0%
Total	4.2 ± 0.3	2.8 ± 0.4	2.7 ± 0.3	20 ± 6	152 ± 17	67 ± 9	26.7% ± 5.6%

Note:—Thickness is given in millimeters; density of the soft plaque component in Hounsfield units (HU) ± CI. AHA indicates American Heart Association.

<sup>a</sup> Only 1 HU measurement was obtained for AHA lesion type I/II, therefore no CIs are reported.

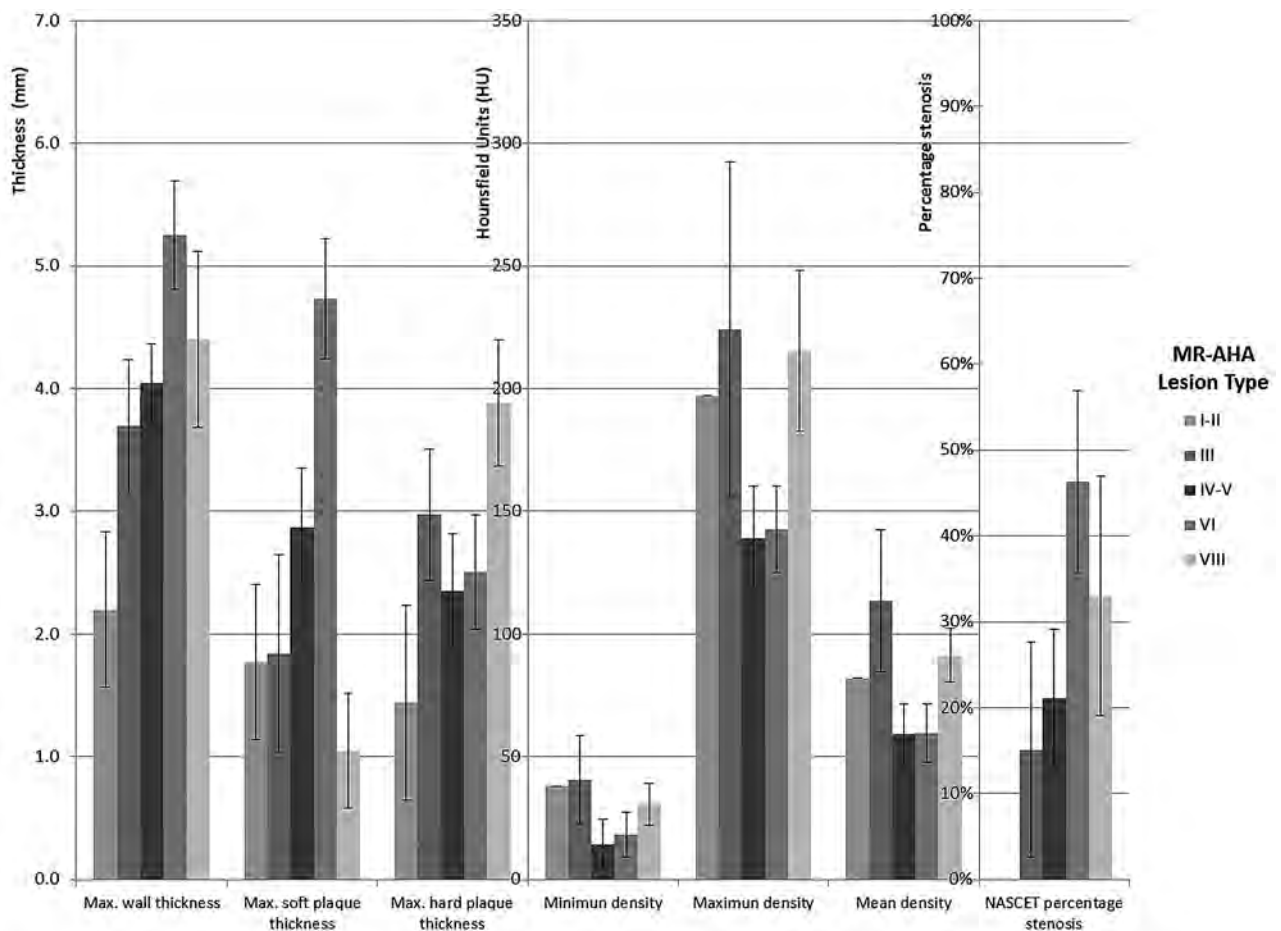


**FIG 1.** General plaque characteristics by MR imaging–derived American Heart Association lesion type. Thickness is given in centimeters, density in Hounsfield units, stenosis in percentage (%) ± confidence interval.

ial plane and a plane orthogonal to the vessel lumen) was determined by the intraclass correlation coefficient. A value of  $P < .05$  was considered statistically significant. Receiver operating characteristic curves were constructed to evaluate the ability of the different imaging characteristics to predict the presence of complicated plaque by MR imaging. The optimal sensitivity and specificity were calculated together with the area under the curve.

## RESULTS

### Patients

Fifty-four patients were included (mean age of 71 years, male/female ratio of 2.9/1). Three MR imaging scans (with 6 carotid vessels in total) were excluded because of insufficient image quality. One carotid vessel with a stent and 1 carotid vessel with total

occlusion were also excluded. This resulted in a total of 100 carotid vessels in 51 patients for analysis. Patient information is shown in Table 1.

### Carotid Plaque Lesion Type Classification

Twenty-three carotid arteries had a complicated AHA-LT6 by MR imaging, with the presence of IPH, thrombus, or a ruptured fibrous cap. Seven arteries were classified as type I, 14 as type III, 38 as type IV/V, and 18 as type VII plaques. No plaque was classified as a type VIII plaque; 67 of 100 vessels had a maximum thickness plaque component >2 mm and thus HU measurements were performed. All of the complicated plaques had a soft plaque thickness >2 mm and thus HU was measured.

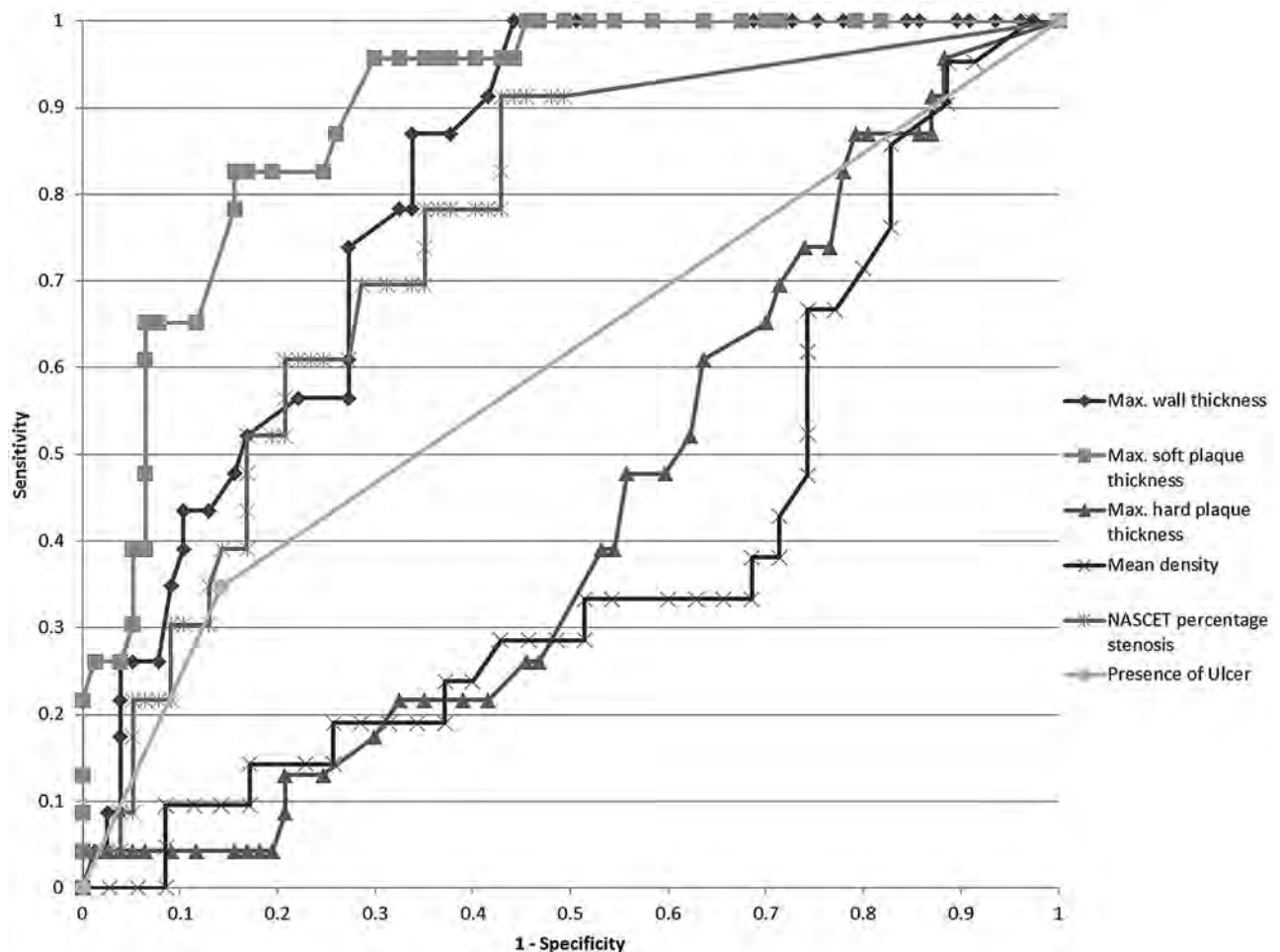
**Table 3: General plaque characteristics of noncomplicated versus complicated AHA-LT6 by MRI**

	AHA-LT6	Others	P Value
Maximum wall thickness	5.3 ± 0.4	3.9 ± 0.3	(<.001)
Maximum soft plaque thickness	4.7 ± 0.5	2.2 ± 0.3	(<.001)
Maximum hard plaque thickness	2.5 ± 0.5	2.7 ± 0.3	(.24)
Minimum density	18 ± 9	21 ± 9	(.36)
Maximum density	143 ± 18	162 ± 24	(.16)
Mean density	60 ± 12	72 ± 12	(.12)
NASCET percentage stenosis	46.3% ± 10.6%	20.5% ± 6.0%	(<.001)
Presence of ulcer	15.8% ± 19.5%	34.8% ± 7.8%	(.02)

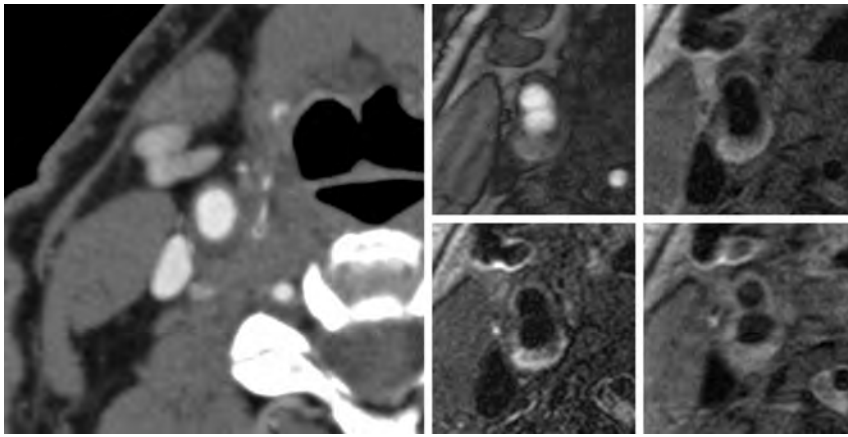
Note:—Thickness is given in millimeters; density in Hounsfield Units ± CI.

Table 2 and Fig 1 show the CTA-based plaque characteristics average results for the maximum plaque wall thickness, maximum thickness of soft plaque component, and maximum thickness of calcified plaque component as well as the average HU for the mean, maximum, and minimum densities and the average NASCET percentage stenosis according to the MR imaging-based assessment of the AHA lesion type. Confidence intervals are also reported. In general, maximum thickness and maximum soft plaque thickness increased from type I/II to type VI lesions and slightly decreased in type VII lesions, which are predominantly calcified. Therefore, the hard plaque component was largest in type VII lesions. Densities of the plaques were lower in the plaques with a lipid-rich necrotic core by MR imaging such as type IV/V and type VI compared with the lesions that were classified as predominantly fibrous by MR imaging, such as type III lesions or the soft component of type VII lesions ( $P = .02$ ). The average percentage of stenosis also increased from type I/II (nonstenotic), reaching a maximum with AHA-LT6. Lesion type VII showed a slight decrease in average percentage stenosis compared with AHA-LT6.

Table 3 compares complicated (AHA LT-6) and noncomplicated plaques. The average maximum thickness of the soft plaque component, the average maximum wall thickness, the NASCET



**FIG 2.** Receiver operating characteristic curves for the performance of the maximum wall thickness, maximum soft plaque thickness, maximum hard plaque thickness, mean attenuation NASCET percentage stenosis values, and presence of ulceration in screening for complicated AHA-LT6 plaques (area under the curve,  $0.810 \pm 0.084$ ,  $0.897 \pm 0.063$ ,  $0.433 \pm 0.123$ ,  $0.384 \pm 0.155$ ,  $0.756 \pm 0.106$ , and  $0.602 \pm 0.139$ , respectively).



**FIG 3.** CTA image through a complicated AHA-LT6 plaque in the right carotid artery at the carotid bifurcation shows a soft plaque with a mean attenuation of 16 HU (range, -7 to 46) and a thickness of the soft plaque component of 6 mm. TOF, T1, T2, and T1 postgadolinium images at the same level show a hyperintense plaque on all 4 weightings, which suggests the presence of type II IPH.

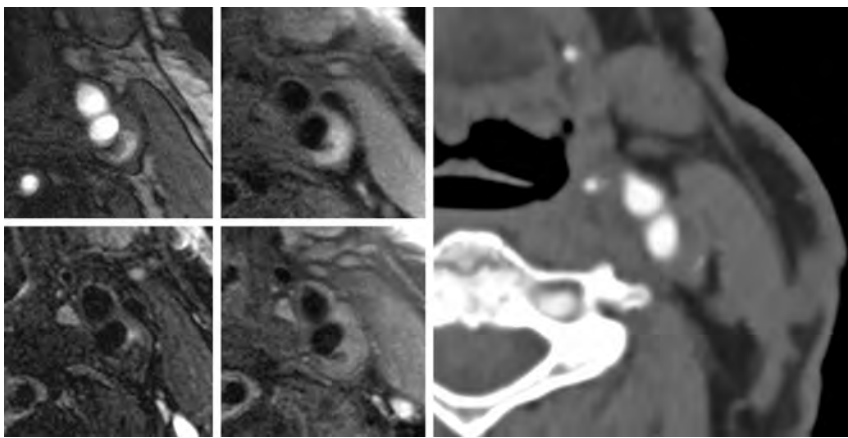


**FIG 4.** TOF, T1, T2, and T1 postgadolinium images of a complicated AHA-LT6 plaque in the left internal carotid artery. The plaque is hyperintense on TOF and T1WI and hypointense on T2WI, which suggests the presence of type I IPH. The CT image at the identical location shows a high attenuation soft plaque with a mean attenuation of 51 HU (range, 29–144) and a thickness of the soft plaque component of 8 mm.

percentage stenosis, and presence of ulcerations were significantly higher in complicated plaques compared with noncomplicated plaques ( $4.7 \pm 0.5$  versus  $2.2 \pm 0.3$  mm,  $P < .001$ ;  $5.3 \pm 0.4$  versus  $3.9 \pm 0.3$  mm,  $P < .001$ ;  $46.3\% \pm 10.6\%$  versus  $20.5\% \pm 6.0\%$ ,  $P < .001$ ; and  $15.8\% \pm 19.5\%$  versus  $34.8\% \pm 7.8\%$ ,  $P = .02$ , respectively). The mean the soft plaque component attenuation did not differ significantly between complicated and noncomplicated plaques ( $60 \pm 12$  versus  $72 \pm 12$  HU,  $P = .12$ ).

The maximum soft plaque thickness was the best single discriminating factor to predict a complicated plaque by MR imaging, with a relative receiver operating characteristic area under the curve of  $0.90 \pm 0.06$ . Maximum wall thickness, NASCET percentage stenosis, and presence of ulceration performed less adequately with receiver operating characteristic area under the curve of  $0.81 \pm 0.08$ ,  $0.76 \pm 0.11$ , and  $0.60 \pm 0.14$ , respectively. Hard plaque component thickness and HU measurements were not of diagnostic help. Utilization of maximum, minimum, and average HU values made no difference in the discriminatory

power. Fig 2 shows these multiple receiver operating characteristic curves. Although the presence of ulceration showed a statistically significant relationship with the presence of complicated AHA-LT6 plaques, it performed poorly from a clinical standpoint (sensitivity, 0.35; specificity, 0.86; positive predictive value, 0.42; and negative predictive value, 0.81).

Figs 3 and 4 show MR and CTA images of 2 complicated AHA-LT6 plaques by MR imaging. Although CTA images show plaques with distinct densities (16 versus 54 HU), MR imaging identifies IPH in both lesions representing complicated AHA-LT6 plaques.

Optimal sensitivity and specificity for detection of complicated plaque by MR imaging was achieved with a soft plaque component thickness threshold of 4.4 mm (sensitivity, 0.65; specificity, 0.94; positive predictive value, 0.75; and negative predictive value, 0.9). Furthermore, of the 42 arteries with a soft plaque thickness  $< 2.2$  mm, no complicated AHA-LT6 plaque was identified by MR imaging (negative predictive value, 1), and of the 5 arteries with a soft plaque thickness  $> 5.6$  mm all plaques were complicated AHA-LT6 plaques (positive predictive value, 1).

#### **Interreader and Intermeasurement Agreement**

The interreader intraclass correlation coefficient between reviewers 1 and 2 for axial measurements was 0.94 (0.89–

0.97), 0.64 (0.48–0.83), and 0.95 (0.91–0.98) for the measurements of maximum plaque wall thickness, maximum thickness of calcified plaque component, and maximum thickness of soft plaque component (Table 4). When axial measurements were compared with measurements obtained at an orthogonal plane to the lumen, the intraclass correlation coefficients were 0.86 (0.75–0.92), 0.80 (0.64–0.89), and 0.93 (0.87–0.96) for reader 1 and 0.93 (0.87–0.96), 0.69 (0.47–0.82), and 0.97 (0.94–0.98) for reader 2.

#### **DISCUSSION**

The current study demonstrates that an easy-to-obtain CTA measurement, the maximum width of the soft tissue component of the atherosclerotic plaque on CTA images, is well suited to screen for the presence of complicated AHA-LT6 plaques. The optimal sensitivity and specificity for detection of complicated plaque by MR imaging was achieved with a soft plaque component thickness threshold of 4.4 mm. More importantly, no plaque with a soft plaque component thickness  $< 2.2$  mm showed signs of compli-

**Table 4: Interreader and intermeasurement intraclass correlation coefficients for maximum wall, calcified plaque, and soft plaque thickness**

	Interreader Intraclass Correlation Coefficient	First Axial Reading versus Orthogonal Intraclass Correlation Coefficient	Second Axial Reading versus Orthogonal Intraclass Correlation Coefficient
Maximum wall thickness	0.94 (0.89–0.97)	0.86 (0.75–0.92)	0.93 (0.87–0.96)
Maximum calcified plaque thickness	0.69 (0.48–0.83)	0.80 (0.64–0.89)	0.69 (0.47–0.82)
Maximum soft plaque thickness	0.95 (0.91–0.98)	0.93 (0.87–0.96)	0.97 (0.94–0.98)

cation by MR imaging. Thus, this easy-to-obtain parameter may be used to screen for the presence of complicated AHA-LT6. Furthermore, all arteries with a soft plaque thickness >5.6 mm were complicated AHA-LT6 plaques, which suggests that this plaque thickness is a good indicator for the presence of complicated atherosclerotic lesions.

Recent studies have shown a strong correlation between the maximal wall thickness and risk for new carotid stroke.<sup>30,31</sup> This correlation could—at least in part—be explained by findings from our study, which suggest a strong correlation of all thickness measurements and presence of complicated AHA-LT6. This is also consistent with previous CTA studies that suggested a strong correlation between volumetric size of the soft plaque component and presence of ulceration<sup>28</sup> and between presence of ulceration and IPH as described by MR imaging.<sup>26</sup> However, we also showed that the maximum thickness of the soft plaque component performed better than the above-mentioned imaging characteristics in the prediction of a complicated AHA-LT6 plaque by MR imaging. This study reinforces that complications occur in the soft plaque component of the atherosclerotic plaque, and it can be assumed that the probability of finding a complication increases with the size of the soft plaque thickness.

A previous CTA/MR imaging comparison study showed that the attenuation of plaques with IPH is larger than the attenuation of plaques without IPH (47 versus 43 HU,  $P = .02$ ).<sup>26</sup> However, this study found a large overlap of HU of plaques with and without IPH, which suggests that HU measurements are not suited to identify complicated plaques. These findings are supported by our study, which did not show any significant differences in HU of complicated and noncomplicated plaques. Initially we had hypothesized that with the use of the minimal HU value obtained from the ROIs, we would be able to better differentiate hemorrhagic from lipid-rich necrotic core lesions; however, that was not supported by our data.

Interestingly, when all the lesion types containing a lipid-rich necrotic core were combined, those lesions had a significantly lower attenuation than lesions with predominantly fibrous tissue, such as lesion type III and the soft component of lesion type VII ( $P = .02$ ). This is consistent with a previous study by de Weert et al,<sup>23</sup> which showed that CT is able to differentiate lipid from fibrous tissue if lesions are not calcified. Although our study showed that CTA is able to differentiate between lipid and fibrous tissue in noncomplicated plaques, our findings also indicated that CTA is unable to differentiate between lipid-rich lesions with and without complications, thus limiting its clinical use to identify the vulnerable plaque.

Interreader agreement for the maximum soft plaque component thickness and maximum total vessel wall thickness was excellent, which indicates that these measurements are highly repro-

ducible. Although orthogonal vessel wall measurements are generally considered more accurate than axial measurements because they are not biased by vessel tortuosity, our results indicate excellent agreement between measurements in axial and orthogonal planes and no systematic difference. In our opinion, axial thickness measurements are preferable because they are less time-consuming and can be performed easily without postprocessing on a standard PACs work station. Thus, this measurement can be easily adopted into routine clinical practice.

### Limitations

Our patient population had a relatively large percentage of complicated plaques (23%). However, this is expected because all patients had a symptomatic TIA or ischemic stroke of the anterior circulation, and strong associations between AHA-LT6 and ischemic stroke have been reported recently.<sup>11</sup> Although efforts were made to reduce the time between studies, delay in obtaining the MR imaging may have generated confounding variables. However, on the basis of our experience and the experience of others with serial MR imaging, atherosclerotic changes over time are minimal.<sup>10,32</sup> We do not believe that this altered our results substantially. Of importance, in our clinic, patients with CTA-proven or sonography-proven significant carotid stenosis of >70% undergo carotid intervention within 24 hours and were thus excluded from our study.

### CONCLUSIONS

The maximum soft plaque component thickness as measured by carotid CTA has the best discriminatory power to predict the presence or absence of AHA-LT6. All plaques with a soft tissue component >5.6 mm were associated with complicated AHA-LT6 by MR imaging, whereas none of the plaques with a soft tissue component <2.2 mm showed a complicated AHA-LT6. Thus, 2.2-mm soft plaque thickness appears to be the ideal cutoff to exclude the presence of complicated AHA-LT6 plaque, though further studies are needed to confirm the reliability of the above stated thresholds. Of particular importance is to confirm that a larger soft plaque component size increases the probability of atherosclerotic plaque complications and thus the probability of clinical strokes.

Disclosures: Martin Dichgans—UNRELATED: Board Membership: Boehringer Ingelheim, EVER Pharma; Consultancy: Bayer, Boehringer Ingelheim, Heel, Bristol-Myers-Squibb; Grants/Grants Pending: EU FP7,\* DFG,\* DLR,\* Fondation Leducq,\* Vasc.Dem.Res.Found.,\* Jackstaedt,\* Corona\*; Payment for Manuscript Preparation: Georg Thieme, UpToDate, W. Kohlhammer, Tobias Saam—UNRELATED: Grants/Grants Pending: Deutsche Forschungsgemeinschaft (EXC158),\* Comments: "Grating-Based Phase Contrast Applied to Atherosclerotic Plaque Imaging using Compact X-Ray Sources"; Payment for Lectures (including service on speakers bureaus): MSD Sharp, DOHME GmbH, GlaxoSmithKline (\*money paid to institution).

## REFERENCES

1. Redgrave JN, Lovett JK, Gallagher PJ, et al. **Histological assessment of 526 symptomatic carotid plaques in relation to the nature and timing of ischemic symptoms: the Oxford plaque study.** *Circulation* 2006;113:2320–28
2. von Sarnowski B, Ludemann J, Volzke H, et al. **Common carotid intima-media thickness and Framingham risk score predict incident carotid atherosclerotic plaque formation: longitudinal results from the study of health in Pomerania.** *Stroke* 2010;41:2375–77
3. Freilinger TM, Schindler A, Schmidt C, et al. **Prevalence of nonstenosing, complicated atherosclerotic plaques in cryptogenic stroke.** *JACC Cardiovasc Imaging* 2012;5:397–405
4. Randoux B, Marro B, Koska F, et al. **Carotid artery stenosis: prospective comparison of CT, three-dimensional gadolinium-enhanced MR, and conventional angiography.** *Radiology* 2001;220:179–85
5. Cai J, Hatsukami TS, Ferguson MS, et al. **In vivo quantitative measurement of intact fibrous cap and lipid-rich necrotic core size in atherosclerotic carotid plaque: comparison of high-resolution, contrast-enhanced magnetic resonance imaging and histology.** *Circulation* 2005;112:3437–44
6. Leclerc X, Nicol L, Gauvrit JY, et al. **Contrast-enhanced MR angiography of supraaortic vessels: the effect of voxel size on image quality.** *AJNR Am J Neuroradiol* 2000;21:1021–27
7. Ouhlous M, Lethimonnier F, Dippel DW, et al. **Evaluation of a dedicated dual phased-array surface coil using a black-blood FSE sequence for high resolution MRI of the carotid vessel wall.** *J Magn Reson Imaging* 2002;15:344–51
8. Aoki S, Nakajima H, Kumagai H, et al. **Dynamic contrast-enhanced MR angiography and MR imaging of the carotid artery: high-resolution sequences in different acquisition planes.** *AJNR Am J Neuroradiol* 2000;21:381–85
9. Saam T, Ferguson MS, Yarnykh VL, et al. **Quantitative evaluation of carotid plaque composition by in vivo MRI.** *Arterioscler Thromb Vasc Biol* 2005;25:234–39
10. Takaya N, Yuan C, Chu B, et al. **Presence of intraplaque hemorrhage stimulates progression of carotid atherosclerotic plaques: a high-resolution magnetic resonance imaging study.** *Circulation* 2005;111:2768–75
11. Parmar JP, Rogers WJ, Mugler JP 3rd, et al. **Magnetic resonance imaging of carotid atherosclerotic plaque in clinically suspected acute transient ischemic attack and acute ischemic stroke.** *Circulation* 2010;122:2031–38
12. Alexandrov AV, Vital D, Brodie DS, et al. **Grading carotid stenosis with ultrasound: an interlaboratory comparison.** *Stroke* 1997;28:1208–10
13. Jahromi AS, Cina CS, Liu Y, et al. **Sensitivity and specificity of color duplex ultrasound measurement in the estimation of internal carotid artery stenosis: a systematic review and meta-analysis.** *J Vasc Surg* 2005;41:962–72
14. Saba L, Sanfilippo R, Montisci R, et al. **Vulnerable plaque: detection of agreement between multi-detector-row CT angiography and US-ECD.** *Eur J Radiol* 2011;77:509–15
15. Anzidei M, Napoli A, Zaccagna F, et al. **Diagnostic accuracy of colour Doppler ultrasonography, CT angiography and blood-pool-enhanced MR angiography in assessing carotid stenosis: a comparative study with DSA in 170 patients.** *Radiol Med* 2012;117:54–71
16. **Randomised trial of endarterectomy for recently symptomatic carotid stenosis: final results of the MRC European Carotid Surgery Trial (ECST).** *Lancet* 1998;351:1379–87
17. Barnett HJ, Taylor DW, Eliasziw M, et al. **Benefit of carotid endarterectomy in patients with symptomatic moderate or severe stenosis: North American Symptomatic Carotid Endarterectomy Trial Collaborators.** *N Engl J Med* 1998;339:1415–25
18. Halliday A, Mansfield A, Marro J, et al. **Prevention of disabling and fatal strokes by successful carotid endarterectomy in patients without recent neurological symptoms: randomised controlled trial.** *Lancet* 2004;363:1491–502
19. de Weert TT, Cretier S, Groen HC, et al. **Atherosclerotic plaque surface morphology in the carotid bifurcation assessed with multi-detector computed tomography angiography.** *Stroke* 2009;40:1334–40
20. Saba L, Caddeo G, Sanfilippo R, et al. **CT and ultrasound in the study of ulcerated carotid plaque compared with surgical results: potentialities and advantages of multidetector row CT angiography.** *AJNR Am J Neuroradiol* 2007;28:1061–66
21. Saba L, Caddeo G, Sanfilippo R, et al. **Efficacy and sensitivity of axial scans and different reconstruction methods in the study of the ulcerated carotid plaque using multidetector-row CT angiography: comparison with surgical results.** *AJNR Am J Neuroradiol* 2007;28:716–23
22. Furtado AD, Adraktas DD, Brasic N, et al. **The triple rule-out for acute ischemic stroke: imaging the brain, carotid arteries, aorta, and heart.** *AJNR Am J Neuroradiol* 2010;31:1290–96
23. de Weert TT, Ouhlous M, Meijering E, et al. **In vivo characterization and quantification of atherosclerotic carotid plaque components with multidetector computed tomography and histopathological correlation.** *Arterioscler Thromb Vasc Biol* 2006;26:2366–72
24. Wintermark M, Jawadi SS, Rapp JH, et al. **High-resolution CT imaging of carotid artery atherosclerotic plaques.** *AJNR Am J Neuroradiol* 2008;29:875–82
25. Saba L, Sanfilippo R, Pirisi R, et al. **Multidetector-row CT angiography in the study of atherosclerotic carotid arteries.** *Neuroradiology* 2007;49:623–37
26. U-King-Im JM, Fox AJ, Aviv RI, et al. **Characterization of carotid plaque hemorrhage: a CT angiography and MR intraplaque hemorrhage study.** *Stroke* 2010;41:1623–29
27. Walker LJ, Ismail A, McMeekin W, et al. **Computed tomography angiography for the evaluation of carotid atherosclerotic plaque: correlation with histopathology of endarterectomy specimens.** *Stroke* 2002;33:977–81
28. Saba L, Sanfilippo R, Sannia S, et al. **Association between carotid artery plaque volume, composition, and ulceration: a retrospective assessment with MDCT.** *AJR Am J Roentgenol* 2012;199:151–56
29. Cai JM, Hatsukami TS, Ferguson MS, et al. **Classification of human carotid atherosclerotic lesions with in vivo multicontrast magnetic resonance imaging.** *Circulation* 2002;106:1368–73
30. Saba L, Sanfilippo R, Pascalis L, et al. **Carotid artery wall thickness and ischemic symptoms: evaluation using multi-detector-row CT angiography.** *Eur Radiol* 2008;18:1962–71
31. Magge R, Lau BC, Soares BP, et al. **Clinical risk factors and CT imaging features of carotid atherosclerotic plaques as predictors of new incident carotid ischemic stroke: a retrospective cohort study.** *AJNR Am J Neuroradiol* 2013;34:402–09
32. Kwee RM, Truijman MT, van Oostenbrugge RJ, et al. **Longitudinal MRI study on the natural history of carotid artery plaques in symptomatic patients.** *PLoS One* 2012;7:e42472

# CT Perfusion Can Predict Overexpression of CXCL8 (Interleukin-8) in Head and Neck Squamous Cell Carcinoma

S.Y. Jo, P.I. Wang, J.E. Nör, E.L. Bellile, Z. Zhang, F.P. Worden, A. Srinivasan, and S.K. Mukherji



## ABSTRACT

**BACKGROUND AND PURPOSE:** Increased angiogenesis in head and neck squamous cell carcinoma correlates to more aggressive tumors with increased morbidity. Because both elevated blood flow and high serum CXCL8 levels are correlated with increased angiogenesis, our objective was to see if elevated blood flow measured with CT perfusion correlated with CXCL8 levels, thereby helping to identify candidates for targeted therapies that inhibit the Bcl-2 proangiogenic pathway associated with CXCL8.

**MATERIALS AND METHODS:** Seven patients with locally recurrent or metastatic head and neck squamous cell carcinoma were enrolled in the trial. These patients underwent CT perfusion and the following parameters were measured: blood volume, blood flow, capillary permeability, and MTT; relative values were calculated by dividing by normal-appearing muscle. Serum was drawn for CXCL8 enzyme-linked immunosorbent assay analysis in these patients.

**RESULTS:** There was a significant positive correlation between the CXCL8 levels and relative blood flow ( $r = 0.94; P = .01$ ). No correlation was found between CXCL8 and relative blood volume, relative capillary permeability, or relative MTT.

**CONCLUSIONS:** Relative blood flow may be useful as a surrogate marker for elevated CXCL8 in patients with head and neck squamous cell cancer. Patients with elevated relative blood flow may benefit from treatment targeting the Bcl-2 proangiogenic pathways.

**ABBREVIATIONS:** BF = blood flow; BV = blood volume; CP = capillary permeability; HNSCC = head and neck squamous cell carcinoma; VEGF = vascular endothelial growth factor

Studies in patients with cancer have found that increased blood flow on CT perfusion is correlated with angiogenesis and increased tumor vascularity, and increased tumor vascularity is associated with local recurrence and metastasis.<sup>1-7</sup> Therefore, increased blood flow on CTP suggests that a tumor is more aggressive and more likely to result in poor outcome.

A serum chemokine, CXCL8 or interleukin-8, also predicts poor patient survival because this pro-angiogenic chemokine

promotes metastasis by neutrophil infiltration and stimulates vascular endothelial cell proliferation, survival, and migration.<sup>8-10</sup> CXCL8 is an end-product of the vascular endothelial growth factor (VEGF) pathway, a key pathway for angiogenesis (Fig 1). Inhibition of the VEGF pathway is a widely pursued strategy to curtail angiogenesis, and at our institution, the experimental drug AT-101 is being used to inhibit Bcl-2, which is an upstream molecule in the VEGF pathway.<sup>11-13</sup>

Our goal was to see if CTP-derived parameters correlate with the level of CXCL8 in patient serum. Because CXCL8 is not currently clinically orderable, CTP could potentially serve as a surrogate marker for patient prognosis and/or anti-angiogenesis treatment patient selection.

## MATERIALS AND METHODS

### Human Subjects

Seven patients were prospectively enrolled in an institutional review board–approved phase II clinical trial of docetaxel (Taxotere) and the investigational drug AT-101 for locally recurrent or metastatic head and neck squamous cell carcinoma (HNSCC). The patients underwent both pretreatment CTP and serum measurements of CXCL8 before the initiation of AT-101. Inclusion

Received January 23, 2013; accepted after revision March 16.

From the Departments of Radiology (S.Y.J., A.S., P.I.W., S.K.M.), Otolaryngology (J.E.N.), and Medical Oncology (F.P.W.), and Cancer Center Biostatistics Unit (E.L.B.), University of Michigan Hospital, Ann Arbor, Michigan; and Angiogenesis Research Laboratory (J.E.N., Z.Z.), Department of Restorative Sciences, University of Michigan School of Dentistry, Ann Arbor, Michigan.

Support for this project was provided by grant P50-CA-97248 (University of Michigan Head and Neck SPORE) from the NIH/NCI and grant R01-DE23220 from the NIH/NIDCR.

Please address correspondence to Suresh K. Mukherji, MD, Department of Radiology, B2 Room A209, University of Michigan, 1500 East Medical Center Dr, Ann Arbor, MI 48109; e-mail: mukherji@umich.edu

Indicates open access to non-subscribers at [www.ajnr.org](http://www.ajnr.org)

Indicates article with supplemental on-line figure

<http://dx.doi.org/10.3174/ajnr.A3610>

criteria were men and nonpregnant, nonlactating women >18 years old, confirmed diagnosis of stage IVC (metastatic) or advanced, locally recurrent HNSCC not amenable to surgery or palliative radiation therapy.

### Serum Samples and Enzyme-Linked Immunosorbent Assay

After patient consent, peripheral blood was collected. Blood samples were incubated for 2 hours at room temperature for clot formation before centrifuging for 20 minutes at approximately 1000g. Then, serum was removed and either assayed immediately or aliquoted and stored at  $-80^{\circ}\text{C}$ .

Expression levels of CXCL8 were determined by enzyme-linked immunosorbent assay (Quantikine; R&D Systems, Minneapolis, Minnesota) according to the manufacturer's instructions. After the development of the colorimetric reaction, the optical attenuation was measured on a microplate spectrophotometer, Tecan GENios (MTX Lab Systems, Vienna, Virginia) at a wavelength of 450 nm; the concentration (pg/mL) was derived from optical density readings and a generated standard curve. Each sample was tested in triplicate wells.

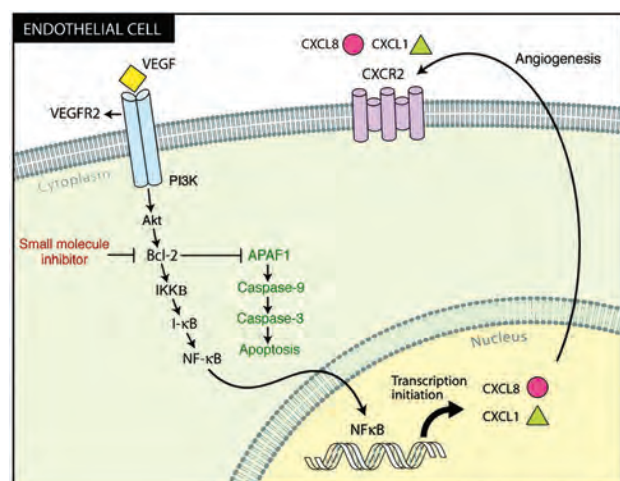


**FIG 1.** VEGF pathway for angiogenesis. Bcl-2, in the beginning of the pathway, is inhibited by a small molecule inhibitor, AT-101. The downstream serum marker CXCL8 is depicted by the red circle. Reprinted with permission from the American Association for Cancer Research: Karl E, Warner K, Zeitlin B, et al. Bcl-2 Acts in a Proangiogenic Signaling Pathway through Nuclear Factor- $\kappa$ B and CXC Chemokines. *Cancer Res* 2005;65:5063–69.

### CT Perfusion

All 7 patients underwent CTP (LightSpeed Ultra; GE Healthcare, Milwaukee, Wisconsin). The technique consisted of injecting 50 mL of nonionic contrast (4 mL/s; Ultravist 300; Bayer HealthCare Pharmaceuticals, Wayne, New Jersey). At 5 seconds into the injection, a cine acquisition was initiated with the following parameters: 120 kV and 60 mA. The cine images covered a 4-cm area, as 8 images were taken with a 5-mm section thickness per cine rotation. A region of interest was placed in the internal carotid artery to generate the contrast enhancement curve. A single observer (a fellowship-trained neuroradiologist with 20 years' experience in head and neck imaging), who was aware of the tumor site but unaware of CXCL8 levels, drew regions of interest (25–30 mm<sup>2</sup>) through the tumor and in normal-appearing muscle (Figs 2 and 3). Streak and other artifacts were avoided. The perfusion data were postprocessed by a deconvolution-based method into maps that represented blood volume (BV), blood flow (BF), capillary permeability (CP), and MTT, by use of the commercially available Perfusion-4 software package on an Advantage Windows Workstation (GE Healthcare).

The relative (r) CTP measures were calculated by dividing our BF, BV, CP, and MTT values by the normal-appearing tissue values to create the rBF, rBV, rMTT, and rCP.

### Statistics

Pearson and Spearman correlation coefficients were calculated to assess the relationship between the pretreatment serum CXCL8 values and CTP measures. Raw (BF, BV, MTT, CP) and relative (rBF, rBV, rMTT, rCP) CTP measures were analyzed.

Statistical significance of the correlations was computed by use of 2-sided exact tests. Values of  $P < .05$  were considered statistically significant. No corrections for multiple testing were used because of the exploratory nature of this preliminary analysis and because the CTP measures are unlikely to be independent. All statistical analysis was performed in SAS software version 9.3 (SAS Institute, Cary, North Carolina).

### RESULTS

Of the 7 patients, 86% were men (6/7), 71% had metastatic disease (5/7), 29% had locally recurrent disease (2/7), and 86% (6/7) had died of their disease since enrollment (3–16 months from enrollment). The average age was 59 years (range, 41–73 years), and

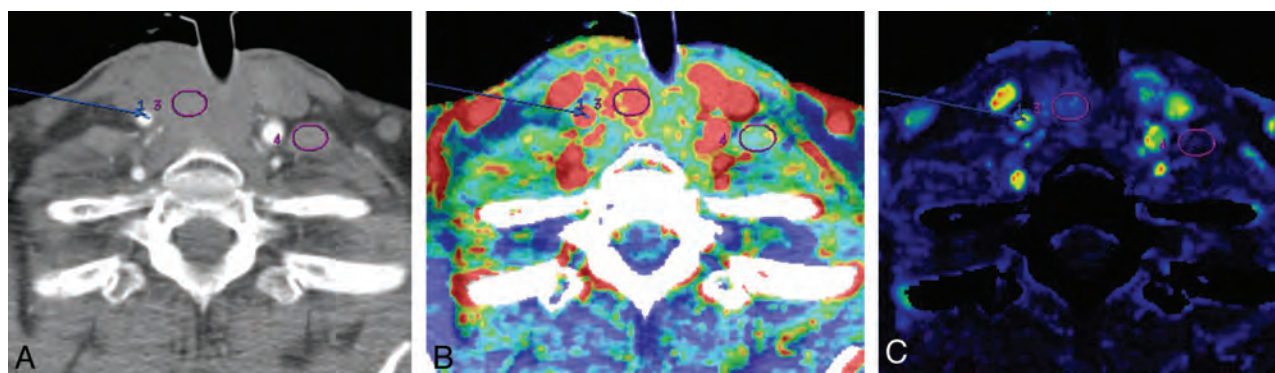


**FIG 2.** Peri-stomal recurrence of HNSCC (patient 5) in a 73-year-old woman. A, Base image shows arterial enhancement. Blue arrow points to the right internal carotid artery (for the arterial input signal). Circle 3 is within the tumor; circle 4 is in contralateral noninvolved musculature. B, Blood volume image shows that the region of interest (circle 3) was placed in solid non-necrotic tumor. C, Blood flow imaging shows minimally increased signal within the tumor bed (circle 3).

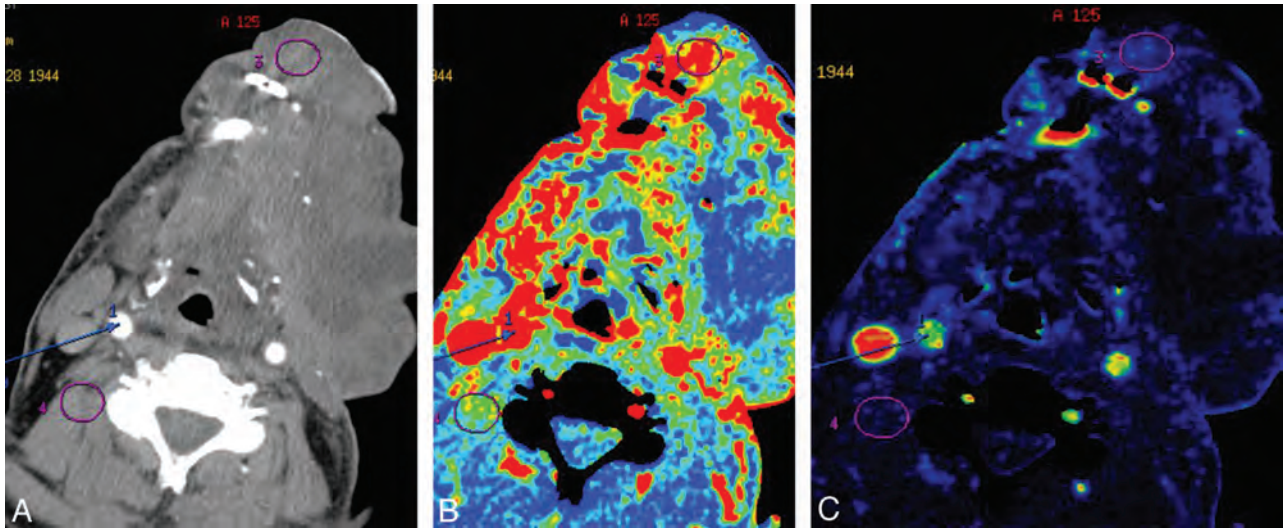


**FIG 3.** Floor-of-the-mouth HNSCC in a 67-year-old man (patient 2). A, Base image shows arterial enhancement. Blue arrow points to the right internal carotid artery (for the arterial input signal). Circle 3 is within the tumor; circle 4 is in noninvolved musculature. B, Blood volume image shows that the region of interest (circle 3) within the tumor was placed in solid non-necrotic tumor. C, Blood flow imaging shows minimally increased signal within the tumor bed (circle 3).

**Table 1: Patient data, tumor characteristics, and clinical course in 7 patients with advanced, treatment-resistant HNSCC**

Patient	Location	Race	Sex	Age	Metastatic Site	Tobacco	Clinical Course
1	Right nasal cavity	White	Male	54	n/a	None	Died
2	Left floor of mouth	White	Male	67	n/a	50 Pack-years	Died
3	Right parotid gland	African American	Male	68	Lung	30 Pack-years	Alive
4	Left oral tongue	White	Male	57	Lung, liver, lymph nodes, bone	None	Died
5	Peri-stomal	African American	Female	73	Lung	20 Pack-years	Died
6	Peri-stomal	White	Male	54	Lung	60 Pack-years	Alive
7	Left floor of mouth	White	Male	41	Lung, lymph nodes	15 Pack-years	Alive

71% (5/7) had significant smoking history. Patient demographics are summarized in Table 1.

Pearson correlation showed a statistically significant positive correlation between CXCL8 expression level and rBF ( $r = 0.94$ ,  $P = .01$ ; Fig 4). Spearman rank correlation coefficient also showed positive correlation between CXCL8 and rBF, though statistical significance was not reached ( $r = 0.61$ ,  $P = .17$ ). No significant correlation was found between CXCL8 and BV, rBV, CP, rCP, MTT, or rMTT as summarized in Table 2. The scatter plot for these variables can be seen in the On-line Figure. The mean, standard deviation, and range of the CTP parameters and CXCL8 expression levels in the 7 patients studied are summarized in Table 3.

## DISCUSSION

Angiogenesis is the mechanism by which new capillaries form from existing vasculature and is fundamental to normal tissue/organ growth and development.<sup>14</sup> Hypermitotic cellular activity requires the formation of new blood vessels, leading to tumor neovascularity.<sup>14</sup> Previous investigators have shown that tumors cannot expand  $>0.1$ – $0.2$  mm in size without the induction of angiogenesis.<sup>14</sup> Three of the primary activators of angiogenesis that promote endothelial proliferation are VEGF, CXCL1 (growth-related oncogene, GRO- $\alpha$ ), and CXCL8 (interleukin-8).<sup>15,16</sup> The expression of CXCL8 is activated by the nuclear factor- $\kappa$ B signaling pathway, which is controlled by a pro-angiogenic signaling molecule, Bcl-2.<sup>17</sup> Recent studies have shown that Bcl-2

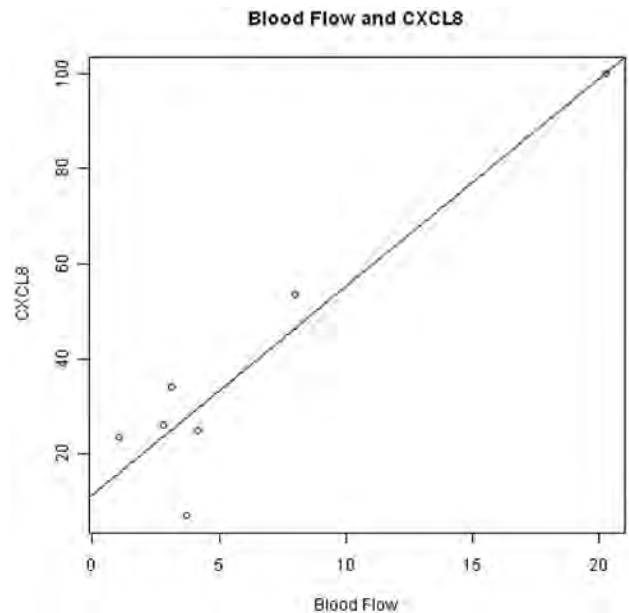


**FIG 4.** Scatterplot displays positive correlation between serum CXCL8 expression level (pg/mL) and rBF (mL/100 g per minute) in the 7 patients with advanced stage HNSCC.

is substantially upregulated in HNSCC compared with normal oral mucosal endothelial cells, which would suggest that HNSCC may have elevated levels of CXCL8.<sup>18</sup>

**Table 2: Pearson correlation between serum CXCL8 expression level and CTP parameters**

Parameter	CXCL8 Correlation Coefficient	P Value
BF	-0.16	.67
BV	0.22	.47
CP	-0.57	.19
MTT	-0.03	.92
rBF	0.94	.01
rBV	-0.14	.77
rCP	-0.07	.88
rMTT	0.18	.68

**Table 3: CTP and CXCL8 expression results in 7 patients**

Parameter	Mean ± SD	Range
CXCL8	38.46 ± 30.46	6.97–99.89
BF	74.08 ± 56.41	14.78–187.93
BV	22.56 ± 35.96	5.08–103.71
CP	48.07 ± 21.56	16.73–79.84
MTT	9.46 ± 2.08	7.34–13.81
rBF	6.18 ± 6.56	1.08–20.26
rBV	2.77 ± 0.87	1.31–3.72
rCP	3.31 ± 1.88	1.46–6.70
rMTT	1.12 ± 0.41	0.78–1.94

CXCL8 is known to be a promoter of angiogenesis and a regulator of cell growth and motility in HNSCC.<sup>18</sup> Overexpression of CXCL8 in HN4 cells (a primary HNSCC cell line with low endogenous CXCL8) increased cell growth and enhanced migration, whereas RNAi-mediated knockdown of CXCL8 expression in HN12 cells (a metastatic HNSCC cell line with elevated CXCL8) decreased proliferation and inhibited invasion through a basement membrane substrate.<sup>19</sup>

Our results show a significant linear positive correlation between patient serum CXCL8 levels and rBF values ( $r = 0.94$ ;  $P = .01$ ), which suggests that an association exists between serum biomarker CXCL8 and rBF values. This study further supports the growing concept that noninvasive imaging biomarkers can be predictive of molecular biomarkers. In HNSCC, CTP has been shown to predict microvascular attenuation and epidermal growth factor receptor overexpression and to correlate with patient outcomes in patients undergoing induction chemotherapy.<sup>1,20-22</sup>

This preliminary study suggests that CTP can predict the expression of small, biologically active proteins that are important end products on the VEGF proangiogenic pathway. The capability of CTP to predict levels of these angiogenic proteins suggests that CTP may help to identify highly vascular and more aggressive tumors through its ability to predict increased microvascular attenuation and the overexpression of CXCL8. Such tumors could be potential candidates for anti-angiogenic agents such as AT-101.

There are several limitations to our study. Our data were prospectively obtained in a small number of patients from a single institution. Statistical significance was tested by use of exact tests to address the issue of small sample size, but the potential for outliers to have heavy influence exists. We performed the same analysis excluding a potential outlier patient with the highest CXCL8 and rBF, and, as expected, we observed a weaker correlation than reported for all 7 patients. We could find no clinical reason for ex-

cluding this patient from our reported results but acknowledge that further study with a larger, more robust sample is necessary.

If future studies show that the correlation between CXCL8 and rBF holds in patients with all stages of HNSCC (not only stage IV as we describe), then CTP could become a useful, noninvasive tool for predicting treatment response. Because patients with HNSCC are routinely imaged to evaluate treatment response, CTP would provide complementary information to help guide therapy.

## CONCLUSIONS

Our preliminary results show a significant linear positive correlation with patient serum CXCL8 level and rBF values in advanced HNSCC, which suggests that an association exists between serum biomarker CXCL8 and rBF values.

Disclosures: Jacques Nör—RELATED: Grant: NIH,\* Comments: University of Michigan Head and Neck SPORE; UNRELATED: Grants/Grants Pending: Medimmune,\* Ascenta.\* Emily Bellile—RELATED: Grant: Head and Neck SPORE grant,\* Comments: Part of my salary is paid for through funds from the University of Michigan Head and Neck SPORE Grant. Francis Worden—UNRELATED: Expert Testimony: I was involved in reviewing a legal case for a woman in NC with an advanced laryngeal cancer. I provided a deposition and gave an expert testimony in court; Payment for Lectures (including service on Speakers Bureaus): Bristol-Myers-Squibb (\*money paid to institution).

## REFERENCES

- Ash L, Teknos TN, Gandhi D, et al. **Head and neck squamous cell carcinoma: CT perfusion can help noninvasively predict intratumoral microvessel density.** *Radiology* 2009;251:422–28
- Delrue L, Blanckaert P, Mertens D, et al. **Assessment of tumor vascularization in pancreatic adenocarcinoma using 128-slice perfusion computed tomography imaging.** *J Comput Assist Tomogr* 2011;35:434–38
- Afaq A, Akin O. **Imaging assessment of tumor response: past, present and future.** *Future Oncol* 2011;7:669–77
- Jiang HJ, Zhang ZR, Shen BZ, et al. **Quantification of angiogenesis by CT perfusion imaging in liver tumor of rabbit.** *Hepatobiliary Pancreat Dis Int* 2009;8:168–73
- Gleich LL, Biddinger PW, Pavelic ZP, et al. **Tumor angiogenesis in T1 oral cavity squamous cell carcinoma: role in predicting tumor aggressiveness.** *Head Neck* 1996;18:343–46
- Kupisz K, Chibowski D, Klatka J, et al. **Tumor angiogenesis in patients with laryngeal cancer.** *Eur Arch Otorhinolaryngol* 1999;256:303–05
- Lentsch EJ, Goudy S, Sosnowski J, et al. **Microvessel density in head and neck squamous cell carcinoma primary tumors and its correlation with clinical staging parameters.** *Laryngoscope* 2006;116:397–400
- Waugh DJ, Wilson C. **The interleukin-8 pathway in cancer.** *Clin Cancer Res* 2008;14:6735–41
- Trellakis S, Bruderek K, Dumitru CA, et al. **Polymorphonuclear granulocytes in human head and neck cancer: enhanced inflammatory activity, modulation by cancer cells and expansion in advanced disease.** *Int J Cancer* 2011;129:2183–93
- De Larco JE, Wuertz BR, Furcht LT. **The potential role of neutrophils in promoting the metastatic phenotype of tumors releasing interleukin-8.** *Clin Cancer Res* 2004;10:4895–900
- Pourgholami MH, Morris DL. **Inhibitors of vascular endothelial growth factor in cancer.** *Cardiovasc Hematol Agents Med Chem* 2008;6:343–47
- Liu Q, Wang HG. **Anti-cancer drug discovery and development: Bcl-2 family small molecule inhibitors.** *Commun Integr Biol* 2012;5:557–65

13. Zeitlin BD, Zeitlin IJ, Nor JE. **Expanding circle of inhibition: small-molecule inhibitors of Bcl-2 as anticancer cell and antiangiogenic agents.** *J Clin Oncol* 2008;26:4180–88
14. Carmeliet P, Jain RK. **Angiogenesis in cancer and other diseases.** *Nature* 2000;407:249–57
15. Mehrad B, Keane MP, Strieter RM. **Chemokines as mediators of angiogenesis.** *Thromb Haemost* 2007;97:755–62
16. Singh S, Sadanandam A, Singh RK. **Chemokines in tumor angiogenesis and metastasis.** *Cancer Metastasis Rev* 2007;26:453–67
17. Nor JE, Christensen J, Mooney DJ, et al. **Vascular endothelial growth factor (VEGF)-mediated angiogenesis is associated with enhanced endothelial cell survival and induction of Bcl-2 expression.** *Am J Pathol* 1999;154:375–84
18. Kaneko T, Zhang Z, Mantellini MG, et al. **Bcl-2 orchestrates a cross-talk between endothelial and tumor cells that promotes tumor growth.** *Cancer Res* 2007;67:9685–93
19. Christofakis EP, Miyazaki H, Rubink DS, et al. **Roles of CXCL8 in squamous cell carcinoma proliferation and migration.** *Oral Oncol* 2008;44:920–26
20. Hoefling NL, McHugh JB, Light E, et al. **Human papillomavirus, p16, and epidermal growth factor receptor biomarkers and CT perfusion values in head and neck squamous cell carcinoma.** *AJNR Am J Neuroradiol* 2013;34:1062–66
21. Zima A, Carlos R, Gandhi D, et al. **Can pretreatment CT perfusion predict response of advanced squamous cell carcinoma of the upper aerodigestive tract treated with induction chemotherapy?** *AJNR Am J Neuroradiol* 2007;28:328–34
22. Surlan-Popovic K, Bisdas S, Rumboldt Z, et al. **Changes in perfusion CT of advanced squamous cell carcinoma of the head and neck treated during the course of concomitant chemoradiotherapy.** *AJNR Am J Neuroradiol* 2010;31:570–75

# Differentiation of Recurrent Tumor and Posttreatment Changes in Head and Neck Squamous Cell Carcinoma: Application of High b-Value Diffusion-Weighted Imaging

I. Hwang, S.H. Choi, Y.-J. Kim, K.G. Kim, A.L. Lee, T.J. Yun, J.-h. Kim, and C.-H. Sohn



## ABSTRACT

**BACKGROUND AND PURPOSE:** High b-value DWI has been expected to have an additional diagnostic role and demonstrated some promising results in head and neck cancer. The aim of this study was to evaluate the diagnostic performance of DWI at a high b-value ( $b=2000$  s/mm<sup>2</sup>) compared with a standard b-value ( $b=1000$  s/mm<sup>2</sup>) and the ratio of ADC values of high and standard b-values for their ability to differentiate between recurrent tumor and posttreatment changes after the treatment of head and neck squamous cell carcinoma.

**MATERIALS AND METHODS:** A total of 33 patients diagnosed with head and neck squamous cell carcinoma were enrolled in the present study; all had contrast-enhancing lesions on follow-up MR imaging. All patients underwent single-shot echo-planar DWI at  $b=1000$  s/mm<sup>2</sup> and  $b=2000$  s/mm<sup>2</sup>, and corresponding ADC maps were generated (ADC<sub>1000</sub> and ADC<sub>2000</sub>, respectively). The mean ADC<sub>1000</sub>, ADC<sub>2000</sub>, and ADC<sub>ratio</sub> (ADC<sub>ratio</sub> = ADC<sub>2000</sub>/ADC<sub>1000</sub> × 100) values were evaluated within a manually placed ROI with contrast-enhanced T1-weighted images as references. For the statistical analysis, we performed a Student *t* test and multivariate logistic regression.

**RESULTS:** The mean ADC<sub>1000</sub> in recurrent tumor was significantly lower than that in posttreatment changes ( $P < .001$ ), whereas the mean ADC<sub>2000</sub> resulted in no significant difference ( $P = .365$ ). The mean ADC<sub>ratio</sub> was significantly higher in recurrent tumor than that in posttreatment changes ( $73.5 \pm 7.2\%$  vs  $56.9 \pm 8.8\%$ , respectively;  $P < .001$ ). Multivariate logistic regression analysis revealed that the ADC<sub>ratio</sub> was the only independently differentiating variable ( $P = .024$ ). The sensitivity, specificity, and accuracy of ADC<sub>ratio</sub> were 95.0%, 69.2%, and 84.8%, respectively, by use of the optimal cutoff value of 62.6%.

**CONCLUSIONS:** We suggest that the ADC<sub>ratio</sub> calculated from the ADC<sub>1000</sub> and ADC<sub>2000</sub> is a promising value for the differentiation of recurrent tumor and posttreatment changes in head and neck squamous cell carcinoma.

**ABBREVIATIONS:** ADC<sub>1000</sub> = ADC value calculated at  $b=0$  and 1000 s/mm<sup>2</sup>; ADC<sub>2000</sub> = ADC value calculated at  $b=0$  and 2000 s/mm<sup>2</sup>; ADC<sub>ratio</sub> = ratio of ADC<sub>2000</sub> over ADC<sub>1000</sub>; HNSCC = head and neck squamous cell carcinoma

Imaging surveillance after treatment of head and neck squamous cell carcinoma (HNSCC) is useful to detect residual or recurrent tumor, even when clinical recurrence is not suspected. In these patients, however, the multidisciplinary treatment with surgery, radiation therapy, and/or chemotherapy that improves pa-

tient survival and quality of life<sup>1,2</sup> complicates interpretation of posttreatment follow-up imaging studies because surgery can alter anatomy and radiation therapy and chemotherapy can result in edema and fibrosis. These posttreatment changes can mimic tumor recurrence, and sometimes it is difficult to distinguish these from residual or recurrent tumor on CT or MR images.<sup>3-5</sup>

DWI is based on the Brownian motion of water protons in the tissue, which is affected by the microstructure of tissue.<sup>6</sup> Several previous studies support the value of applying DWI in head and neck cancer for the differentiation and characterization of primary tumor, nodal staging, and the prediction of treatment response.<sup>6-12</sup> In addition, several promising studies have been reported on the usefulness of DWI in the discrimination between recurrent or residual tumor and posttreatment changes.<sup>12-14</sup> These studies have demonstrated that performing DWI and mea-

Received January 17, 2013; accepted after revision March 19.

From the Department of Radiology (I.H., S.H.C., A.L.L., T.J.Y., J.-h.K., C.-H.S.) Seoul National University College of Medicine, Seoul, Korea; Center for Nanoparticle Research (S.H.C.), Institute for Basic Science, and School of Chemical and Biological Engineering, Seoul National University, Seoul, Korea; and Biomedical Engineering Branch (Y.-J.K., K.G.K.), Division of Convergence Technology, National Cancer Center, Goyang-si, Gyeonggi-do, Korea.

This study was supported by a grant from the National R&D Program for Cancer Control, Ministry of Health & Welfare, Republic of Korea (1120300); the Korea Healthcare Technology R&D Projects, Ministry for Health, Welfare & Family Affairs (A112028); and the Research Center Program of IBS (Institute for Basic Science) in Korea.

Please address correspondence to Seung Hong Choi, MD, PhD, Department of Radiology, Seoul National University College of Medicine, Center for Nanoparticle Research, Institute for Basic Science, and School of Chemical and Biological Engineering, Seoul National University, 28, Yongon-dong, Chongno-gu, Seoul, 110-744, Korea; e-mail: verocay@snuh.org

Indicates open access to non-subscribers at [www.ajnr.org](http://www.ajnr.org)

<http://dx.doi.org/10.3174/ajnr.A3603>

asuring the ADC values may enable differentiation of residual or recurrent tumor from posttreatment changes.

In recent years, high b-value ( $b > 1000 \text{ s/mm}^2$ ) DWI was introduced along with improvements in MR imaging gradient technology. These high b-value techniques have demonstrated promising results in brain imaging compared with the standard b-value ( $b=1000 \text{ s/mm}^2$ ) DWI.<sup>15-17</sup> In head and neck cancer, a previous study introduced a ratio of the ADC values from high b-value and standard b-value DWI and suggested that it correlates with the maximal standardized uptake value from FDG-PET.<sup>18</sup> Another published study revealed that high b-value DWI is helpful in the differentiation of histologic grades in HNSCC.<sup>19</sup>

The aim of our present study was to evaluate the additional role and diagnostic performance of high b-value ( $b=2000 \text{ s/mm}^2$ ) DWI compared with standard b-value ( $b=1000 \text{ s/mm}^2$ ) DWI, and the ratio of ADC values from high and standard b-values for the differentiation between recurrent tumor and posttreatment changes after treatment of HSNCC.

## MATERIALS AND METHODS

### Study Population

Our hospital institutional review board approved this retrospective study, and the requirement for informed consent was waived. A total of 1331 patients with head and neck cancer underwent head and neck MR imaging in our institution between January 2010 and February 2012. Among them were 351 patients with pathologically confirmed HNSCC. After retrospectively reviewing the electronic medical records, we included 56 patients matching these inclusion criteria: 1) the patient underwent MR imaging with standard and high b-value DWI after treatment of HNSCC; 2) the term between the end of treatment and posttreatment imaging was longer than 6 weeks, to avoid very early posttreatment changes; 3) there was newly developed or increased enhancing portion on postcontrast T1-weighted images where recurrence was highly suspected or indeterminate; and 4) the lesion was large enough to measure on MR imaging (diameter  $\geq 5$  mm). A total of 23 patients were further excluded from our study population because of degradation of image quality (eg, susceptibility artifacts that distort the area of concern partly or completely) ( $n=15$ ), incomplete medical history because of loss to follow-up ( $n=7$ ), and a history of additional malignant disease outside of the head and neck area ( $n=1$ ). Finally, we included 33 patients (18 men, 15 women; mean age, 60.2 years; age range, 30–78 years). The primary tumor locations were the oral cavity ( $n=16$ ), oropharynx ( $n=4$ ), sinonasal cavity ( $n=5$ ), nasopharynx ( $n=3$ ), hypopharynx ( $n=2$ ), and external auditory canal ( $n=3$ ). Various surgical procedures or radiation therapy techniques were performed according to the disease extent and location, with the following treatments: surgery alone ( $n=9$ ); both chemotherapy and radiation therapy ( $n=7$ ); surgery and postoperative radiation therapy ( $n=13$ ); and a combination of chemotherapy, surgery, and radiation therapy ( $n=4$ ). In our institution, most of the patients treated for head and neck cancer are monitored with MR imaging routinely. Thirteen patients underwent MR imaging earlier than the scheduled date because of clinical suspicion of recurrence (eg, palpable mass or visible lesion on endoscopy; tumor recurrence in 12 patients, posttreatment changes in 1 patient). MR imaging was obtained in 1 patient because of a visible mass at the oral

cavity on physical examination; this was followed by MR imaging for 2 years without change, suggesting posttreatment change. All other patients underwent MR imaging as a routine follow-up technique.

### Determination of Recurrent Tumor vs Posttreatment Changes

Recurrent tumor and posttreatment changes were differentiated with clinical or histopathologic characterization as follows:

**Histopathologic Diagnosis.** We obtained the pathologic diagnosis by reviewing the institution electronic medical records. The institution pathologists, who had at least fellowship training in reading head and neck pathologic changes, made these pathology reports. Histopathologic evaluation was performed in 19 cases; 17 and 2 were confirmed as recurrent tumor and posttreatment changes, respectively. Pathologic diagnoses for those 2 patients were chronic hyperplastic candidiasis and chronic active inflammation, and these patients had no evidence of recurrence during subsequent follow-up at 22 months and at 15 months, respectively.

**Clinical Diagnosis.** In patients without histopathologic evaluation during follow-up, tumor recurrence was defined by clinical criteria. In 3 cases, recurrent tumors were clinically determined based on growth of an enhancing lesion by at least 20% or more on the subsequent follow-up image. Posttreatment lesions ( $n=11$ ) were clinically defined as no change or a decrease in size of the enhancing lesion and no other evidence of recurrence during at least 1 year of follow-up (mean follow-up time, 24 months; range, 15–39 months).

### MR Imaging Acquisition

All patients underwent MR imaging by use of a 1.5T MR imaging system (Signa Excite, HDx or HDxt; GE Healthcare, Milwaukee, Wisconsin) with an 8-channel head and neck coil. A transverse T1-weighted spin-echo sequence was performed with the following parameters: TR range, 550–560 ms; TE range, 10–12 ms; 30–36 sections; section thickness, 4 mm; intersection gap, 1.2 mm; FOV, 220  $\times$  220 mm; matrix, 320  $\times$  192; acquired signal, 1; and pixel resolution, 0.7  $\times$  1.1  $\times$  4.0 mm. The contrast-enhanced transverse T1-weighted spin-echo sequences with fat suppression were also acquired after the intravenous injection of 0.1 mmol/kg of gadopentetate dimeglumine (Magnevist; Bayer Schering Pharma, Berlin, Germany). Additional coronal and sagittal T1-weighted sequences were performed with identical imaging parameters after administration of contrast agent.

The single-shot echo-planar DWI was obtained in the transverse plane before contrast material injection at both the standard b-value ( $b=0$  and  $1000 \text{ s/mm}^2$ ) and high b-value ( $b=0$  and  $2000 \text{ s/mm}^2$ ) with the following parameters: TR range, 8000–10,000 ms and TE range, 61.6–77.6 ms (at  $b=1000 \text{ s/mm}^2$ ); TR range, 9325–12,000 ms and TE range, 73.8–90.4 ms (at  $b=2000 \text{ s/mm}^2$ ); 30–45 sections; section thickness, 4 mm; intersection gap, 1.2 mm; bandwidth, 1953 Hz/pixel; FOV, 240  $\times$  240 mm; matrix, 160  $\times$  160; acquired signal, 2; and pixel resolution, 1.5  $\times$  1.5  $\times$  4.0 mm. DWI data were acquired in 3 orthogonal directions and combined into a trace image. The average durations of DWI at  $b=0$  and  $1000 \text{ s/mm}^2$  and  $b=0$  and  $2000 \text{ s/mm}^2$  were 1 min 23 s and 2 min 50 s, respectively.

The corresponding ADC maps were automatically derived from the following equation on the Advantage workstation (GE Healthcare):  $\text{ADC} = -\ln[S(b)/S(0)]/b$ , where  $b$  is the diffusion-

**Table 1: Comparison of demographic and clinicopathologic features between recurrent tumor group and posttreatment changes group**

Characteristic	Patient Group		P Value
	Recurrent Tumor	Posttreatment Changes	
Mean age (y)	58.2 (range, 30–77)	63.2 (range, 44–78)	.288
Sex (M:F)	4:9	14:6	.038 <sup>a</sup>
Clinical suspicion of tumor recurrence <sup>b</sup>	60% (12)	0.7% (1)	.003 <sup>a</sup>
Mean ROI size (mm <sup>2</sup> )	170.59 ± 190.68	152.15 ± 203.65	.773
Interval between treatment and imaging (mo)	15.1 ± 16.0	10.4 ± 9.5	.342

<sup>a</sup> Fisher exact test.<sup>b</sup> Number of patients in parentheses.**Table 2: ADC values of the newly developed or increased enhancing portion and deep cervical muscles**

	Value (Mean ± SD)		P Value <sup>a</sup>
	Recurrent Tumor	Posttreatment Changes	
Newly detected or increased enhancing lesion			
ADC <sub>1000</sub> (10 <sup>-3</sup> mm <sup>2</sup> /s)	1.205 ± 0.244	1.649 ± 0.319	<.001
ADC <sub>2000</sub> (10 <sup>-3</sup> mm <sup>2</sup> /s)	0.878 ± 0.153	0.940 ± 0.235	.365
ADC <sub>ratio</sub> (%)	73.5 ± 7.2	56.9 ± 8.8	<.001
Deep cervical muscles			
ADC <sub>1000</sub> (10 <sup>-3</sup> mm <sup>2</sup> /s)	1.338 ± 0.103	1.301 ± 0.133	.371
ADC <sub>2000</sub> (10 <sup>-3</sup> mm <sup>2</sup> /s)	0.722 ± 0.128	0.724 ± 0.157	.967
ADC <sub>ratio</sub> (%)	53.9 ± 8.1	55.2 ± 7.8	.643

<sup>a</sup> Calculated using the 2-tailed independent Student *t* test.

weighting factor ( $b=1000$  or  $2000$  s/mm<sup>2</sup>), and  $S(b)$  and  $S(0)$  are the signal intensities with and without diffusion-sensitizing gradients, respectively.

### Image Analysis

MR images were reviewed on a PACS workstation monitor (m-view 5.4; Infinitt, Seoul, Korea). ADC ratio ( $ADC_{ratio} = ADC_{2000}/ADC_{1000} \times 100$ , where  $ADC_{1000}$  and  $ADC_{2000}$  are the ADC values of the DWI obtained with  $b=0$  and  $1000$  s/mm<sup>2</sup>, and  $b=0$  and  $2000$  s/mm<sup>2</sup>, respectively) maps were generated by use of pixel-by-pixel computation of ADC maps generated with in-house-developed software.

The images were reviewed by consensus between 2 investigators (I.H. and S.H.C. with 2 years and 10 years of experience in interpreting head and neck MR images, respectively), in which the investigators placed ROIs on the axial ADC<sub>1000</sub> maps with references of contrast-enhanced T1-weighted images obtained in 3 orthogonal planes. At the time of the interpretation session, the investigators were blinded to the final pathologic or clinical results. The ROIs were drawn on the most representative section of the ADC map, in which the size of the tumor was the largest or the conspicuity of the lesion was highest. The boundary of the ROI encompassed all of the visible tumor on that section of the ADC map corresponding to the contrast-enhanced T1-weighted images, but any necrotic portion and normal osseous structures were avoided to the fullest extent possible. Subsequently, the ROIs were copied onto the corresponding ADC<sub>2000</sub> and ADC<sub>ratio</sub> maps, respectively. The size of each ROI was also recorded.

In addition, ROI measurement from the deep cervical muscles was included for comparison as an internal control of normal soft tissue. On a section encompassing the largest areas of the deep cervical muscles, a large circular ROI was drawn on the ADC<sub>1000</sub> maps

and was subsequently copied to the corresponding ADC<sub>2000</sub> and ADC<sub>ratio</sub> maps, respectively.

### Statistical Analysis

All statistical analyses were performed with SPSS Statistics 19.0 for Windows (IBM, Armonk, New York). For all statistical analyses, a 2-tailed *P* value < .05 was considered to indicate a statistically significant difference. The 2-tailed independent Student *t* test was used to compare the clinicopathologic characteristics (eg, age, mean interval from completion of therapy to follow-up imaging, and the ROI size) and mean ADC values between the group with recurrent tumor and the group with posttreatment changes. In addition, the 2-tailed paired Student *t* test was used to assess the differences between the newly developed enhancing lesion and deep cervical muscles in each group. Multivariate binary logistic regression was performed to assess the most independently differentiating variable between ADC<sub>1000</sub>, ADC<sub>2000</sub>, and ADC<sub>ratio</sub>. Furthermore, a receiver operating characteristic curve was

drawn to investigate the optimal cutoff values for the parameters with statistical significance, of which sensitivity, specificity, and accuracy were also calculated.

## RESULTS

### Clinicopathologic Characteristics

In our study population, recurrent tumor was found in 20 patients and posttreatment changes were found in 13 patients. There were more male patients in the recurrent tumor group (M:F = 14:6) vs the posttreatment changes group (M:F = 4:9). In the recurrent tumor group, MR imaging was obtained mainly because of clinical suspicion of recurrence, whereas MR imaging was mostly performed in a routine follow-up manner in the group with posttreatment changes (Table 1). Otherwise, no significant difference was observed in mean age, mean ROI size, and mean interval from completion of therapy to follow-up imaging between the recurrent tumor group and the group with posttreatment changes (Table 1). The mean imaging follow-up time of the group with posttreatment changes was 23 months, and no patient had recurrence during the follow-up period.

### Comparison of ADC<sub>1000</sub>, ADC<sub>2000</sub>, and ADC<sub>ratio</sub> between Patients with Recurrent Tumor and Patients with Posttreatment Changes

Table 2 and Fig 1 summarize the mean ADC<sub>1000</sub>, ADC<sub>2000</sub>, and ADC<sub>ratio</sub> of the focal enhancing lesion vs the deep cervical muscles of the 2 groups. The mean ADC<sub>1000</sub> in the recurrent tumor group was significantly lower than that in the posttreatment change group ( $1.205$  vs  $1.649 \times 10^{-3}$  mm<sup>2</sup>/s, respectively;  $P < .001$ ). Similarly, the mean ADC<sub>2000</sub> also showed a lower value in the recurrent tumor group vs the posttreatment changes group, but without a statistically significant difference ( $0.878$  vs  $0.940 \times 10^{-3}$  mm<sup>2</sup>/s;  $P = .365$ ). The mean ADC<sub>ratio</sub> of the recurrent tu-

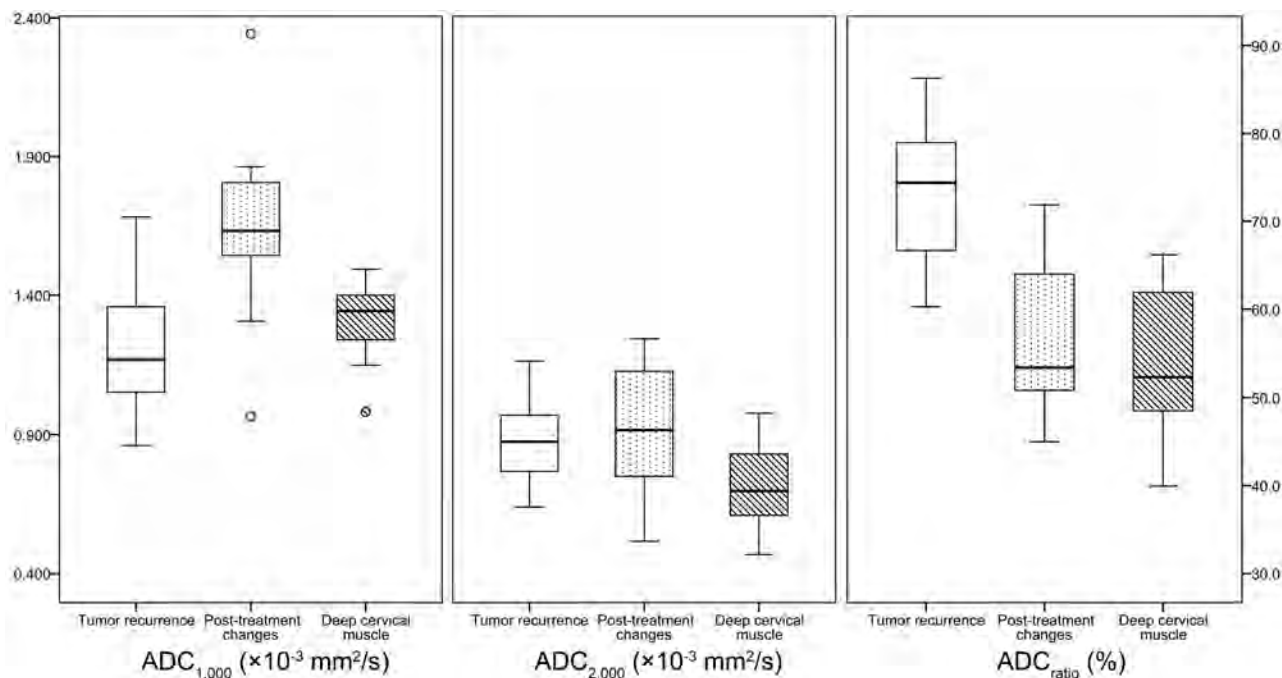


**FIG 1.** Box-and-whisker plots of the ADC values at the standard b-value ( $ADC_{1000}$ ), high b-value ( $ADC_{2000}$ ), and the ADC ratio ( $ADC_{ratio}$ ) in the newly detected enhancing lesion on the postcontrast T1-weighted image and deep cervical muscle (horizontal line = median values, bottom of the box: 25th percentile, top of the box = 75th percentile, whiskers = smallest or largest values except outliers, small circle = outliers).

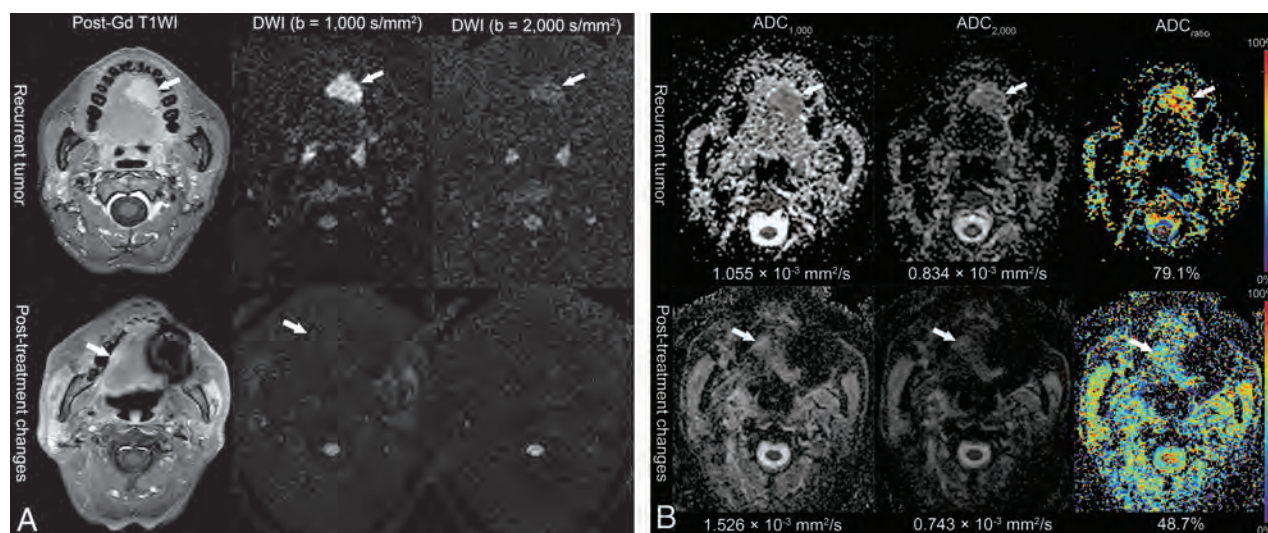


**FIG 2.** Representative MR images of the recurrent tumor (37-year-old woman, status post left partial glossectomy) and posttreatment changes (63-year-old woman, status post right hemiglossectomy and postoperative radiation therapy) from treated squamous cell carcinoma of the tongue. **A**, Postcontrast T1-weighted images and DWI with standard and high b-values. The recurrent tumor shows high signal intensity on the DWI in both standard and high b-values. In contrast, the signal intensity of posttreatment changes on the high-b-value DWI is not increased. **B**, Corresponding ADC maps show lower ADC values in the recurrent tumor than those in the posttreatment changes on the standard b-value DWI. Color-coded  $ADC_{ratio}$  maps demonstrate that the  $ADC_{ratio}$  is much increased in the recurrent tumor.

mor group was significantly higher than that of the posttreatment changes group (73.5% vs 56.9%, respectively;  $P < .001$ ).

No significant difference was observed between the recurrent tumor group and the posttreatment changes group in the mean  $ADC_{1000}$ ,  $ADC_{2000}$ , and  $ADC_{ratio}$  of the deep cervical muscles (Table 2).

The mean  $ADC_{ratio}$  of recurrent tumor was significantly higher than that of cervical muscles (73.5% vs 53.9%;  $P < .001$ ). However, the mean  $ADC_{ratio}$  of enhancing lesion because of post-

treatment changes was not significantly different from that of deep cervical muscles (56.9% vs 55.2%;  $P = .553$ ). Figure 2 shows representative MR images of the recurrent tumor group and the posttreatment changes group, respectively.

#### Multivariate Logistic Regression Analysis

The  $ADC_{1000}$  and  $ADC_{ratio}$  were significantly different variables to differentiate between recurrent tumor and posttreatment changes by the independent Student *t* test. Multivariate logistic

**Table 3: Diagnostic performances of the ADC<sub>1000</sub> and ADC<sub>ratio</sub>**

	Cutoff Value <sup>a</sup>	Sensitivity (%)	Specificity (%)	PPV (%)	NPV (%)	Accuracy (%)
ADC <sub>1000</sub>	$1.460 \times 10^{-3} \text{ mm}^2/\text{s}$	85.0 (17/20)	84.6 (11/13)	89.5 (17/19)	78.6 (11/14)	84.8 (28/33)
ADC <sub>ratio</sub>	62.6%	95.0 (19/20)	69.2 (9/13)	69.6 (16/23)	90.0 (9/10)	84.8 (28/33)

**Note:**—Raw data are in parentheses. NPV indicates negative predictive value; PPV, positive predictive value.

<sup>a</sup>Receiver operating characteristic curves were drawn to find the optimal cutoff values for the ADC<sub>1000</sub> and ADC<sub>ratio</sub>.

regression analysis with the ADC<sub>1000</sub> and ADC<sub>ratio</sub> as independent variables was constructed. The ADC<sub>ratio</sub> was the most independently differentiating variable ( $P = .024$ ), whereas the ADC<sub>1000</sub> was marginally insignificant ( $P = .051$ ).

### Optimal Cutoff Values and Diagnostic Performances

Receiver operating characteristic curves were drawn to find the optimal cutoff values for the ADC<sub>1000</sub> and ADC<sub>ratio</sub>. The optimal cutoff value for the ADC<sub>1000</sub> was  $1.460 \times 10^{-3} \text{ mm}^2/\text{s}$ . The sensitivity, specificity, and accuracy were 85.0% (17/20), 84.6% (11/13), and 84.8% (28/33), respectively. For the ADC<sub>ratio</sub>, the optimal cutoff value was 62.6%, and the sensitivity, specificity, and accuracy were 95.0% (19/20), 69.2% (9/13), and 84.8% (28/33), respectively. The summary of the diagnostic performance of each value is listed in Table 3.

### DISCUSSION

Our results demonstrate that the ADC value derived from the standard b-value DWI ( $b = 1000 \text{ s}/\text{mm}^2$ ) had a similar diagnostic performance compared with a previous study, and that the mean ADC<sub>1000</sub> in the posttreatment changes group was significantly higher than that of the recurrent tumor group.<sup>13</sup> The optimal cutoff value for the ADC<sub>1000</sub> to distinguish between recurrent tumor and postoperative changes ( $1.460 \times 10^{-3} \text{ mm}^2/\text{s}$ ) also correlated with a previous study ( $1.30 \times 10^{-3} \text{ mm}^2/\text{s}$ ).<sup>13</sup> These reproducible findings support the use of the standard b-value DWI on posttreatment follow-up imaging of HNSCC. On the other hand, the mean ADC<sub>2000</sub> itself was not significantly different between the 2 groups and did not have an additional diagnostic benefit. However, we did observe a significant difference in the mean ADC<sub>ratio</sub> between the recurrent tumor group and the posttreatment changes group ( $73.5 \pm 7.2\%$  vs  $56.9 \pm 8.8\%$ , respectively); multivariate logistic regression analysis showed that the ADC<sub>ratio</sub> vs the ADC<sub>1000</sub> was more useful for differentiating between the 2 groups.

The ADC value has been known to decrease when the b-value increases beyond  $1000 \text{ s}/\text{mm}^2$ , according to several previous reports.<sup>20-22</sup> The decrease in the observed ADC with an increasing b-value could be explained by the decay of biexponential signal intensity. In a human brain model, fast and slow diffusion components have been described.<sup>20,22</sup> Fast diffusion components are the main source of signal at a relatively low b-value, whereas the signal intensity is dominated by the slow diffusion component at a high b-value.<sup>23</sup> Increased cellularity in recurrent tumor leads to an increase in the intracellular water component, whereas posttreatment changes are composed of edema and inflammatory changes, increasing the proportion of easily diffusible extracellular water content.<sup>6,13</sup> Although the intracellular and extracellular water components are not exactly equal to the slow and fast diffusion components, respectively, they are considered corresponding components.<sup>20,24</sup> To evaluate the fast and slow diffusion components, DWI with multiple b-values has been studied with a biexponential fitting.<sup>25</sup> In our study, we calculated 2 ADC values

with a monoexponential model with 2 different b-values, and we adopted the ADC<sub>ratio</sub> as an alternative biomarker that represents the composition of the fast and slow diffusion components. Choi et al<sup>18</sup> hypothesized that by increasing the b-value from  $1000 \text{ s}/\text{mm}^2$  to  $2000 \text{ s}/\text{mm}^2$ , the ADC value would have a more substantial decrease in the fast diffusion component. As a result, the higher ADC<sub>ratio</sub> means that it contains more of the slow diffusion component and represents higher cellularity.<sup>18</sup> Therefore, our results show that the mean ADC<sub>ratio</sub> was much higher in the recurrent tumor group vs the posttreatment changes group.

Although the mean ADC<sub>2000</sub> also showed a lower value in the recurrent tumor compared with posttreatment changes, it was not statistically different between the 2 groups. A possible explanation is that the relative decrease of ADC<sub>1000</sub> to ADC<sub>2000</sub> was higher in the posttreatment changes group; therefore, the final ADC<sub>2000</sub> of the recurrent tumor group was similar to that of the posttreatment changes group. The differences between the ADC<sub>1000</sub> and ADC<sub>2000</sub> also could be influenced by different imaging parameters. However, Ogura et al<sup>26</sup> reported that a long TR ( $> 6000 \text{ ms}$ ) and short TE ( $< 100 \text{ ms}$ ) did not significantly influence the ADC values. Therefore, the influence of different imaging parameters was thought to be negligible in our study.

For comparison, we also investigated the ADC values from the deep cervical muscles as a normal soft tissue. With the increase in the b-value from  $1000$  to  $2000 \text{ s}/\text{mm}^2$ , the ADC value was also substantially decreased in muscle. The mean ADC ratio of the recurrent tumor group was significantly higher than that of the deep cervical muscles, which might prove beneficial for the detection of recurrent tumor by visual inspection in the ADC<sub>ratio</sub> maps.

The diagnostic yields of both ADC<sub>ratio</sub> and ADC<sub>1000</sub> in our present study was lower than those of the study by Abdel Razek et al,<sup>13</sup> in which they used only ADC<sub>1000</sub> maps. We believe that this finding might be the result of differences in study populations. The minimal size of the lesions was 1.5 cm in diameter in the study by Abdel Razek et al,<sup>13</sup> whereas our study included smaller lesions (eg, 5 mm).

In our study, 15 patients were excluded because of MR imaging artifacts or poor visualization of the lesion, and the proportion of artifacts in eligible patients was relatively high (26.8%). Although we optimized scanning parameters to reduce artifacts and maximize the signal-to-noise ratio, we found that the intrinsic limitations of single-shot echo-planar DWI in head and neck imaging (eg, heterogeneity of the tissue, a very low acquirable signal, movements, air-tissue boundaries, and surgical materials) were still challenging in interpreting the DWI.<sup>27</sup> To overcome the drawbacks of DWI, additional localized coverage imaging or zonally magnified oblique multisection (ZOOM; Siemens, Erlangen, Germany) echo-planar imaging could be performed.<sup>28</sup>

Our study had some limitations. One limitation was that we enrolled a small number of patients from a single center and performed retrospective analysis, which could lead to selection bias.

We tried to include all patients who met the inclusion criteria to minimize selection bias. In addition, we included HNSCC with various locations, treatment modalities, and intervals between last treatment and imaging, and this heterogeneity could limit the generalizability of our results. Although tumor location is related to prognosis,<sup>29</sup> we believed that any significant impact of tumor location relative to ADC values was unlikely.

Another limitation of our present study was that there were patients for whom we did not have histopathologic confirmation. Therefore, exact correlation of the ADC value or ADC<sub>ratio</sub> with histopathologic changes was limited, especially for the posttreatment changes group. In clinical settings, it is common practice to follow patients with complementary imaging modalities, such as FDG-PET, to ensure that the enhancing lesion identified by MR imaging is metabolically active before a biopsy is performed,<sup>30</sup> but this was not possible in the context of our study.

## CONCLUSIONS

We suggest that the ADC<sub>ratio</sub> calculated from ADC<sub>1000</sub> and ADC<sub>2000</sub> is a promising value to differentiate between recurrent tumor and posttreatment changes in HNSCC and may be marginally more useful than the ADC<sub>1000</sub> alone. High b-value DWI of the head and neck region is technically feasible and requires a relatively short additional scan time; therefore, high b-value DWI could be added to the posttreatment routine follow-up MR imaging to provide additional potentially helpful information in the detection of recurrent HNSCC.

Disclosures: Seung Hong Choi—RELATED: Grant: A grant from the National R&D Program for Cancer Control, Ministry of Health & Welfare, Republic of Korea (1120300),\* the Korea Healthcare Technology R&D Projects, Ministry for Health, Welfare & Family Affairs (A112028),\*\* \*Money paid to institution.

## REFERENCES

1. El-Deiry M, Funk GF, Nalwa S, et al. Long-term quality of life for surgical and nonsurgical treatment of head and neck cancer. *Arch Otolaryngol Head Neck Surg* 2005;131:879–85
2. Ang KK, Harris J, Garden AS, et al. Concomitant boost radiation plus concurrent cisplatin for advanced head and neck carcinomas: radiation therapy oncology group phase II trial 99–14. *J Clin Oncol* 2005;23:3008–15
3. Zbaren P, Caversaccio M, Thoeny HC, et al. Radionecrosis or tumor recurrence after radiation of laryngeal and hypopharyngeal carcinomas. *Otolaryngol Head Neck Surg* 2006;135:838–43
4. Nomayr A, Lell M, Sweeney R, et al. MRI appearance of radiation-induced changes of normal cervical tissues. *Eur Radiol* 2001;11:1807–17
5. Offiah C, Hall E. Post-treatment imaging appearances in head and neck cancer patients. *Clin Radiol* 2011;66:13–24
6. Wang J, Takashima S, Takayama F, et al. Head and neck lesions: characterization with diffusion-weighted echo-planar MR imaging. *Radiology* 2001;220:621–30
7. Srinivasan A, Dvorak R, Perni K, et al. Differentiation of benign and malignant pathology in the head and neck using 3T apparent diffusion coefficient values: early experience. *AJNR Am J Neuroradiol* 2008;29:40–44
8. Maeda M, Kato H, Sakuma H, et al. Usefulness of the apparent diffusion coefficient in line scan diffusion-weighted imaging for distinguishing between squamous cell carcinomas and malignant lymphomas of the head and neck. *AJNR Am J Neuroradiol* 2005;26:1186–92
9. Sumi M, Sakihama N, Sumi T, et al. Discrimination of metastatic cervical lymph nodes with diffusion-weighted MR imaging in patients with head and neck cancer. *AJNR Am J Neuroradiol* 2003;24:1627–34
10. Vandecaveye V, De Keyzer F, Vander Poorten V, et al. Head and neck squamous cell carcinoma: value of diffusion-weighted MR imaging for nodal staging. *Radiology* 2009;251:134–46
11. Kim S, Loevner L, Quon H, et al. Diffusion-weighted magnetic resonance imaging for predicting and detecting early response to chemoradiation therapy of squamous cell carcinomas of the head and neck. *Clin Cancer Res* 2009;15:986–94
12. King AD, Mo FK, Yu KH, et al. Squamous cell carcinoma of the head and neck: diffusion-weighted MR imaging for prediction and monitoring of treatment response. *Eur Radiol* 2010;20:2213–20
13. Abdel Razek AA, Kandeel AY, Soliman N, et al. Role of diffusion-weighted echo-planar MR imaging in differentiation of residual or recurrent head and neck tumors and posttreatment changes. *AJNR Am J Neuroradiol* 2007;28:1146–52
14. Vandecaveye V, De Keyzer F, Nuyts S, et al. Detection of head and neck squamous cell carcinoma with diffusion weighted MRI after (chemo)radiotherapy: correlation between radiologic and histopathologic findings. *Int J Radiat Oncol Biol Phys* 2007;67:960–71
15. Seo HS, Chang KH, Na DG, et al. High b-value diffusion (b = 3000 s/mm<sup>2</sup>) MR imaging in cerebral gliomas at 3T: visual and quantitative comparisons with b = 1000 s/mm<sup>2</sup>. *AJNR Am J Neuroradiol* 2008;29:458–63
16. Kang Y, Choi SH, Kim YJ, et al. Gliomas: histogram analysis of apparent diffusion coefficient maps with standard- or high-b-value diffusion-weighted MR imaging—correlation with tumor grade. *Radiology* 2011;261:882–90
17. Purroy F, Begue R, Quilez A, et al. Contribution of high-b-value diffusion-weighted imaging in determination of brain ischemia in transient ischemic attack patients. *J Neuroimaging* 2013;23:33–38
18. Choi SH, Paeng JC, Sohn CH, et al. Correlation of 18F-FDG uptake with apparent diffusion coefficient ratio measured on standard and high b value diffusion MRI in head and neck cancer. *J Nucl Med* 2011;52:1056–62
19. Yun TJ, Kim JH, Kim KH, et al. Head and neck squamous cell carcinoma: Differentiation of histologic grade with standard- and high-b-value diffusion-weighted MRI. *Head Neck* 2013;35:626–31
20. Clark CA, Le Bihan D. Water diffusion compartmentation and anisotropy at high b values in the human brain. *Magn Reson Med* 2000;44:852–59
21. DeLano MC, Cooper TG, Siebert JE, et al. High-b-value diffusion-weighted MR imaging of adult brain: image contrast and apparent diffusion coefficient map features. *AJNR Am J Neuroradiol* 2000;21:1830–36
22. Brugieres P, Thomas P, Maraval A, et al. Water diffusion compartmentation at high b values in ischemic human brain. *AJNR Am J Neuroradiol* 2004;25:692–98
23. Maier SE, Bogner P, Bajzik G, et al. Normal brain and brain tumor: multicomponent apparent diffusion coefficient line scan imaging. *Radiology* 2001;219:842–49
24. Sehny JV, Ackerman JJ, Neil JJ. Evidence that both fast and slow water ADC components arise from intracellular space. *Magn Reson Med* 2002;48:765–70
25. Roth Y, Tichler T, Kostenich G, et al. High-b-value diffusion-weighted MR imaging for pretreatment prediction and early monitoring of tumor response to therapy in mice. *Radiology* 2004;232:685–92
26. Ogura A, Hayakawa K, Miyati T, et al. Imaging parameter effects in apparent diffusion coefficient determination of magnetic resonance imaging. *Eur J Radiol* 2011;77:185–88
27. Thoeny HC, De Keyzer F, King AD. Diffusion-weighted MR imaging in the head and neck. *Radiology* 2012;263:19–32
28. Wheeler-Kingshott CA, Trip SA, Symms MR, et al. In vivo diffusion tensor imaging of the human optic nerve: pilot study in normal controls. *Magn Reson Med* 2006;56:446–51
29. Mehanna H, West CM, Nutting C, et al. Head and neck cancer—Part 2: Treatment and prognostic factors. *BMJ* 2010;341:c4690
30. Kubota K, Yokoyama J, Yamaguchi K, et al. FDG-PET delayed imaging for the detection of head and neck cancer recurrence after radiochemotherapy: comparison with MRI/CT. *Eur J Nucl Med Mol Imaging* 2004;31:590–95

# Optimized Cutoff Value and Indication for Washout Thyroglobulin Level According to Ultrasound Findings in Patients with Well-Differentiated Thyroid Cancer

J.Y. Jung, J.H. Shin, B.-K. Han, and E.Y. Ko

## ABSTRACT

**BACKGROUND AND PURPOSE:** Washout thyroglobulin provides evidence for metastatic or recurrent lesions. However, the cutoff value is still controversial. We investigated an optimized cutoff value and indication for the use of washout thyroglobulin from fine-needle aspiration in neck lymph nodes from preoperative or postoperative patients with well-differentiated thyroid cancers.

**MATERIALS AND METHODS:** A total of 177 lymph nodes from 161 patients underwent sonographically guided fine-needle aspiration cytology and washout thyroglobulin measurement and then underwent surgery and clinical follow-up. We assessed an optimized cutoff value of washout thyroglobulin for diagnosing metastasis and compared its diagnostic performance with that of washout thyroglobulin  $> 10$  ng/mL, the currently accepted cutoff value. We also analyzed diagnostic performances of fine-needle aspiration cytology alone and of the combination of fine-needle aspiration cytology and washout thyroglobulin on the basis of the presence or absence of suspicious ultrasonographic findings.

**RESULTS:** Of the 177 lymph nodes, 77 were metastases and 100 were benign. An optimized cutoff value for washout thyroglobulin was 1.8 ng/mL. The sensitivity and negative predictive value in diagnosing metastasis improved significantly with a cutoff value of 1.8 ng/mL compared with a cutoff value of 10 ng/mL ( $P = .0412$  for sensitivity,  $P = .0188$  for negative predictive value). In patients with suspicious ultrasonographic findings, applying washout thyroglobulin along with fine-needle aspiration cytology significantly enhanced the sensitivity and negative predictive value of fine-needle aspiration cytology performances to 100% and 100%, respectively ( $P = .0051$ , and  $P = .0088$ ). There was no difference in diagnostic performance between fine-needle aspiration cytology and the combination of the 2 methods in patients without suspicious ultrasonographic findings.

**CONCLUSIONS:** Applying the optimized cutoff value of washout thyroglobulin of 1.8 ng/mL in patients with suspicious ultrasonographic features facilitates the diagnostic evaluation of neck lymph nodes in both preoperative and postoperative patients with well-differentiated thyroid cancer.

**ABBREVIATIONS:** FNA = fine-needle aspiration; FNA-Tg = washout thyroglobulin; NPV = negative predictive value; PPV = positive predictive value; Tg = thyroglobulin; US = ultrasonography

High thyroglobulin (Tg) in a lymph node indicates metastatic disease in both preoperative and postoperative patients with thyroid cancer.<sup>1-4</sup> Although this value of washout Tg (FNA-Tg) from fine-needle aspiration (FNA) serves as an important standard for suspicious recurrent or metastatic lesions,<sup>5</sup> the cutoff value to define “high” is controversial.

In a previous report, investigators recommended that the threshold values for FNA-Tg levels be higher than 10 ng/mL if the

serum thyroglobulin level or the mean + 2 SDs in node-negative patients is not available for reference.<sup>6</sup> In real practice, some lymph nodes whose FNA-Tg values were  $< 10$  were tumor-involved, and the most useful cutoff value of FNA-Tg remains controversial. To increase the efficacy of the FNA-Tg measurement, one must find the standard value and the characteristics of lymph nodes for which FNA-Tg can promote more accurate results.

Generally, ultrasonography (US)-guided FNA cytology is applied to lymph nodes of patients with thyroid cancer on the basis of clinical or sonographic suspicion.<sup>7-9</sup> Although sampling can always be done on the basis of clinical concern or an unexpected US finding, it is not cost-effective to carry out FNA-Tg on all lesions; hence, it is imperative to clarify the distinctive US characteristic that would lead to effective performance of adjunctive FNA-Tg.

Received December 26, 2012; accepted after revision February 28, 2013.

From the Department of Radiology, Samsung Medical Center, Sungkyunkwan University School of Medicine, Seoul, Korea.

Please address correspondence to Jung Hee Shin, MD, Department of Radiology and Center for Imaging Science, Samsung Medical Center, Sungkyunkwan University School of Medicine, 50 Irwon-dong, Gangnam-gu, Seoul 135-710, Korea; e-mail: jhshin11@skku.edu

<http://dx.doi.org/10.3174/ajnr.A3687>

We investigated the optimal cutoff value and indication of FNA-Tg from FNA to aid the evaluation of neck lymph nodes in patients with preoperative or postoperative thyroid cancers.

## MATERIALS AND METHODS

### Patients

Our institutional review board approved this retrospective study and required neither patient approval nor informed consent for the review of images and medical records. All patients undergoing FNA cytology or surgery had previously received and filled out the informed consent before each procedure.

Between September 2009 and March 2010, two hundred twenty-four lymph nodes from 201 consecutive patients underwent US-guided FNA cytology and FNA-Tg from the aspiration. FNA was performed for patients with clinically suspicious nodes, dominant or enlarged nodes during routine pre-/postoperative surveillance, and/or abnormal nodes identified by another imaging technique. A total of 47 nodes were excluded due to the absence of a surgical excision or a follow-up. Thus 177 nodes from 161 patients with either a surgical excision or follow-up for at least 2 years were included in our study.

### Ultrasonography

We performed ultrasonographic evaluations by using a HDI 5000 or iU22 (Philips Healthcare, Bothell, Washington) connected with a 7- to 12-MHz linear-array transducer. The US examinations were performed by 1 of 6 radiologists, all of whom specialized in the performance and interpretation of thyroid US for a mean of 5 years (range, 1–10). Suspicious metastatic lymph nodes on US included those that were either not oval (taller-than-wide or round) or showed microcalcifications, cystic changes, hyperechoic cortices, or irregular margins.<sup>10</sup> We considered a US feature positive if at least 1 of these findings was shown. The size of the lymph node was measured as the largest diameter on US because the maximal axial short diameter can be subjective depending on the US operators; and describing the largest diameter of lymph nodes facilitated surgical identification of nodes and reduced confusion.

### Ultrasonography-Guided Fine-Needle Aspiration

Two-milliliter syringes with 23 gauge needles attached were used for US-guided FNA cytology. The aspirates were spread on frosted-end glass slides and were immediately fixed in 95% alcohol for both Papanicolaou and May Grunwald/Giemsa staining. In cases in which a patient had multiple lesions, we performed FNA cytology on the most suspicious or largest one. Only the most suspicious lesion from FNA-Tg measurement was chosen for evaluation. One of 7 experienced cytopathologists analyzed the slides. A typical adequate smear was one with 6 groups of >10 cells. Cytology for lesions was classified into 3 categories: malignant, benign, and inadequate. If the cytology showed hemosiderin-laden macrophages, we classified it as inadequate.

### Washout Thyroglobulin

We used serum thyroglobulin immunoradiometric assay CT (IRMA-1; Radim, Pomezia, Italy) to measure FNA-Tg from FNA specimens. Specimens were extracted by US-guided FNA cytology

**Table 1: Clinical, imaging, and cytopathologic characteristics of 177 lymph nodes**

Characteristics	Total (n = 177) (%)
Age (mean) (yr)	47 (range, 15–85)
Sex (female/male)	127:50
Mean lesion size (mean) (cm)	1.0 (range, 0.2–3.6)
Patient status	
Preoperative	81 (46)
Postoperative	96 (54)
Suspicious malignant US features	
Yes	109 (62)
No	68 (38)
Initial FNA	
Malignant	66 (37)
Benign	94 (53)
Inadequate	17 (10)
Final cytopathology	
Malignant	77 (44)
Benign	100 (56)
Reference standard	
Surgical excision	81 (46)
Follow-up	96 (54)

and smeared on the glass slides. The specimens remaining in the syringe and the needle were rinsed with 1 mL of normal saline and sent for the assays. The most useful cutoff value of FNA-Tg for differentiating metastasis/recurrence from benign lesions was assessed. We did not measure Tg antibodies because the clinical performance of FNA-Tg is unaffected by serum Tg antibodies.<sup>11</sup>

### Diagnostic Performances

The diagnostic performances included sensitivity, specificity, positive predictive value (PPV), negative predictive value (NPV), and accuracy. We treated inadequate cytology as negative for malignancy because inadequate cytology alone does not indicate surgical excision. The diagnostic performance of the new cutoff value was compared by using FNA-Tg > 10 ng/mL as a reference standard. The performances of FNA cytology and FNA cytology with FNA-Tg at the best cutoff value were compared according to US findings. We also assessed the diagnostic performance of US findings. We investigated each cutoff value of FNA-Tg in the preoperative and postoperative state.

### Statistical Analyses

The comparison of the diagnostic performances of FNA cytology and FNA cytology with FNA-Tg according with the presence or absence of suspicious US findings was analyzed by the McNemar test and Bennett method. The FNA-Tg receiver operating characteristic curve was developed by using MedCalc for Windows, Version 6.1 (MedCalc Software, Mariakerke, Belgium). The cutoff value, which maximizes the sum of the sensitivity plus specificity, was determined as the points in the upper left-hand corner. We considered a difference statistically significant with *P* values < .05.

## RESULTS

The clinical and cytopathologic characteristics of the 177 lymph nodes are summarized in Table 1. According to our final results, of the 177 lymph nodes, 77 (44%) were malignant and 100 (56%) were benign.

The best cutoff value for FNA-Tg was 1.8 ng/mL, at which the accuracy and the sum of sensitivity and specificity were highest. Sensitivity and NPV in diagnosing malignancy were significantly improved in FNA-Tg  $\geq$  1.8 ng/mL compared with FNA-Tg > 10 ng/mL ( $P = .0412$ ,  $P = .0188$ , respectively). Even though specificity and PPV were decreased by the new cutoff value, the  $P$  values were not significant ( $P = .4795$  and  $P = .2879$ , respectively) (Table 2).

A total of 109 (62%) of 177 lymph nodes had suspicious US findings in our study. The diagnostic performance of each US finding is shown in Table 3. When at least 1 of the US findings was positive, the sensitivity, specificity, PPV, NPV, and accuracy of US findings for the diagnosis of metastasis/recurrence was 96.1%, 65.0%, 67.9%, 95.6%, and 78.5%, respectively.

With the best cutoff value of 1.8 ng/mL, the overall diagnostic performance of FNA cytology with FNA-Tg was enhanced in sensitivity and NPV while specificity and PPV decreased compared with FNA cytology alone. The statistical difference in accuracy between the combination of the 2 methods and FNA cytology alone was insignificant. Additionally, in patients with suspicious US findings, the sensitivity and NPV of FNA cytology with FNA-Tg were better than those of FNA cytology alone ( $P = .0051$  and  $P = .0088$ ) (Fig 1). There was no difference in diagnostic performances between FNA cytology alone and FNA cytology with FNA-Tg in patients without suspicious US findings (Fig 2

**Table 2: Comparison between diagnostic performances of washout Tg  $\geq$  1.8 ng/mL and > 10 ng/mL**

%	Sensitivity	Specificity	PPV	NPV	Accuracy
Washout Tg > 10	88.3	96.0	94.4	91.4	92.7
Washout Tg $\geq$ 1.8	96.1	94.0	92.5	96.9	94.9
<i>P</i> value	.0412	.4795	.2879	.0188	.2888

**Table 3: Diagnostic performance of suspicious US findings for 177 lymph nodes<sup>a</sup>**

	Sensitivity	Specificity	PPV	NPV	Accuracy
Microcalcification	27.3 (21/77)	95.0 (95/100)	80.8 (21/26)	62.9 (95/151)	65.5 (116/177)
Cystic change	28.6 (22/77)	96.0 (96/100)	84.6 (22/26)	63.6 (96/151)	66.7 (118/177)
Hyperechoic cortex	42.9 (33/77)	89.0 (89/100)	75.0 (33/44)	66.9 (89/133)	68.9 (122/177)
Not oval shape	15.6 (12/77)	86.0 (86/100)	46.1 (12/26)	57.0 (86/151)	55.3 (98/177)
Irregular margin	26.0 (20/77)	95.0 (95/100)	80.0 (20/25)	62.5 (95/152)	65.0 (115/177)
At least 1 of US findings	96.1 (74/77)	65.0 (65/100)	67.9 (74/109)	95.6 (65/68)	78.5 (119/177)

<sup>a</sup> Data are percentages.

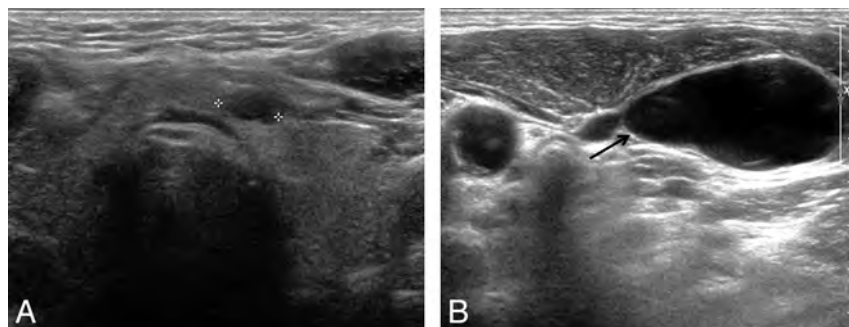


**FIG 1.** Ultrasonography of a 73-year-old man who had a small cystic nodule (A, cross) in the left thyroid gland and a suspicious cystic level VI lymph node (B, arrow). US-guided FNA cytology was performed on the small cystic thyroid nodule and the level VI cystic node, and the results were suspicious for papillary thyroid carcinoma from a nodule and a few pigmented macrophages from a lymph node. However, metastasis was considered due to the high FNA-Tg level of 1023 ng/mL. Final surgical pathology revealed a tiny papillary thyroid carcinoma of the left thyroid gland and nodal metastasis.

and Table 4). Therefore, FNA-Tg was not necessary in patients with no suspicious US features. We provide a flow chart from our results (Fig 3).

According to the initial FNA cytology results of 177 lymph nodes, 66 (37%) were malignant, 94 (53%) benign, and 17 (10%) inadequate.

Among the inadequate cytology cases, 8 were from too scanty cellular smear; 7, from hemosiderin-laden macrophages; 1, from mild atypical cells; and 1, from degenerated blood. Of the 17 inadequate cytology cases, 11 were identified with surgical excision and the other 6 were confirmed as well in US follow-up of 14 months. Ten (59%) malignant nodes were identified among 17 inadequate results. All 10 metastatic nodes had FNA-Tg levels higher than 1.8 ng/mL. The remaining 7 benign nodes demonstrated FNA-Tg values below 1.8 ng/mL.

Of 94 initial benign cytologic results, 8 (8.5%) nodes had FNA-Tg levels higher than 1.8. Two of the nodes with markedly high FNA-Tg (>1000) were due to remnant thyroid tissue misinterpreted as nodes, and 2 were pathologically confirmed as metastasis. FNA-Tg of the remaining 4 cases was slightly higher than 1.8 ng/mL.

Cytologic malignant lesions with FNA-Tg lower than 1.8 ng/mL were found in 4 (6%) of 66 cases. One of these 4 was negative for malignancy surgically and counted as false-positive FNA cytology. Subsequently, 3 of these 4 were confirmed as malignant surgically. However, these lesions showed a very low FNA-Tg ( $\leq$ 0.6).

The final pathology of 161 patients was papillary thyroid carcinoma for 160 and follicular thyroid carcinoma for 1. The best cutoff value of FNA-Tg in the preoperative and postoperative state was 1.8 and 1.9 ng/mL, respectively.

## DISCUSSION

Our results show that FNA-Tg can be an effective adjunct for diagnosing nodal metastasis in preoperative and postoperative patients with thyroid cancer when it is used in nodes with suspicious sonographic features. Furthermore, applying a cutoff value of 1.8 ng/mL facilitates improved sensitivity and NPV compared with the conventional standard (>10 ng/mL) when evaluating neck lymph nodes.

One prior report suggested that the most appropriate cutoff value of FNA-Tg is 1.1 ng/mL,<sup>12</sup> and another study yielded a cutoff value of 5 ng/mL.<sup>13</sup> The result of our study, 1.8 ng/mL, was between the 2 reports. Moreover, we demonstrate that the value of FNA-Tg was not useful in nodes without suggested suspicious US findings (Fig 3).

Given that a definitely abnormal serum Tg level in postoperative patients is above 2 ng/mL,<sup>14</sup> we hypothesized that the FNA-Tg from FNA specimens would have a similar threshold value. Many radiologists tend to confuse the FNA-Tg

cutoff, which is widely regarded as 10, and the serum Tg level cutoff, considered as 2, leading to an increased chance of misdiagnosis. Using our cutoff value, we think that such confusion



**FIG 2.** A 39-year-old female patient who underwent total thyroidectomy. The patient had a palpable lymph node (cross) in level V and no suspicious US feature. Even though the lymph node had inadequate FNA cytology due to a few hemosiderin-laden macrophage and lymphoid cells, it was considered benign because of its low FNA-Tg level. The node showed no changes in a 2-year follow-up. According to our results, there was no significant diagnostic enhancement of FNA-Tg in patients without suspicious US findings.

**Table 4: Comparison of diagnostic performances of FNA-C and FNA-C with FNA-Tg according to US features using washout Tg  $\geq 1.8^a$**

US Feature	Sensitivity	Specificity	PPV	NPV	Accuracy
Overall					
FNA-C	84.4	99.0	98.5	89.2	92.1
FNA-C+FNA-Tg	100	93.0	91.7	100	96.1
P value	.0015 <sup>b</sup>	.04123 <sup>b</sup>	.0235 <sup>b</sup>	.0011 <sup>b</sup>	.2386
Positive					
FNA-C	85.1	97.1	98.4	75.6	88.9
FNA-C+FNA-Tg	100	91.4	96.1	100	97.3
P value	.0051 <sup>b</sup>	.9590	.4149	.0088 <sup>b</sup>	.0530
Negative					
FNA-C	66.7	100	100	98.5	98.5
FNA-C+FNA-Tg	100	93.9	42.9	100	61.7
P value	1.0000	.1336	.02482	.3212	.3711

**Note:**—FNA-C indicates FNA cytology.

<sup>a</sup> Data other than P values are percentages.

<sup>b</sup> Significant.

between the 2 cutoffs could be reduced in a clinical setting. When we divided the patients into preoperative and postoperative states because there have been no specific mentioned reports, each cutoff value of FNA-Tg was close to 2.

It is important that suspicious sonographic features of lymph nodes in patients with thyroid cancer be well-defined so that unnecessary FNA cytology can be avoided. Clinical suspicion such as palpable or enlarged lymph nodes during routine pre-/postoperative US surveillance leads to aspiration. However, we learned that US findings take precedence over clinical suspicion. Our results showed the high performance of our sonographic criteria for lymph node metastases in patients with thyroid cancer with a sensitivity of 96.1%, specificity of 65.0, and accuracy of 78.5%. These rates were similar to the US performances of previous studies.<sup>15-17</sup> We did not include Doppler US features because lymph nodes with abnormal vascularity frequently already have abnormal gray-scale features. As a previous report suggested, an abnormal Doppler feature alone is problematic and should serve only as a complementary finding.<sup>17</sup>

The role of FNA-Tg is very valuable when cytology is inadequate. Even though cystic change identified on US featured the highest specificity at 96.0%—but a low sensitivity of 28.6%—in our results, cytology frequently showed a nondiagnostic result, such as a few hemosiderin-laden macrophages. The importance of the presence of macrophages in cystic lymph nodes has been emphasized in past research as well.<sup>18,19</sup> In our cases, 7 of 17 inadequate results featured macrophages, and consequently all (86%) except 1 were diagnosed as a malignancy. Therefore, FNA cytology with FNA-Tg performed on the lymph nodes that have cystic change by US findings can accurately evaluate the nodes and make up for the inadequate cytology.

Previous studies have already reported the accuracy of FNA

cytology with FNA-Tg in suspicious nodal metastases, having a sensitivity and specificity ranging from 84% to 100% and 85% to 95.4%, respectively.<sup>1,20</sup> By contrast, in the overall diagnostic performance of our study with FNA-Tg  $\geq 1.8$  ng/mL, consulting both FNA-Tg and FNA cytology increased the sensitivity and NPV to 100% but decreased the specificity and PPV, without any significant change in accuracy. The reason is that we considered the final result positive if the result of both or either of 2 methods was positive. Therefore, the sensitivity [true-positive/(true-positive + false-negative)] and NPV [true-negative/(true-negative + false-negative)] increased due to reduced false-negatives such as inadequate cytology, and the specificity [true-negative/(false-positive + true-negative)] and PPV [true-positive/(true-positive + false-positive)] decreased due to increased false-positives from the remnant thyroid tissue. The performance of FNA cytology itself was excellent in our institution (sensitivity

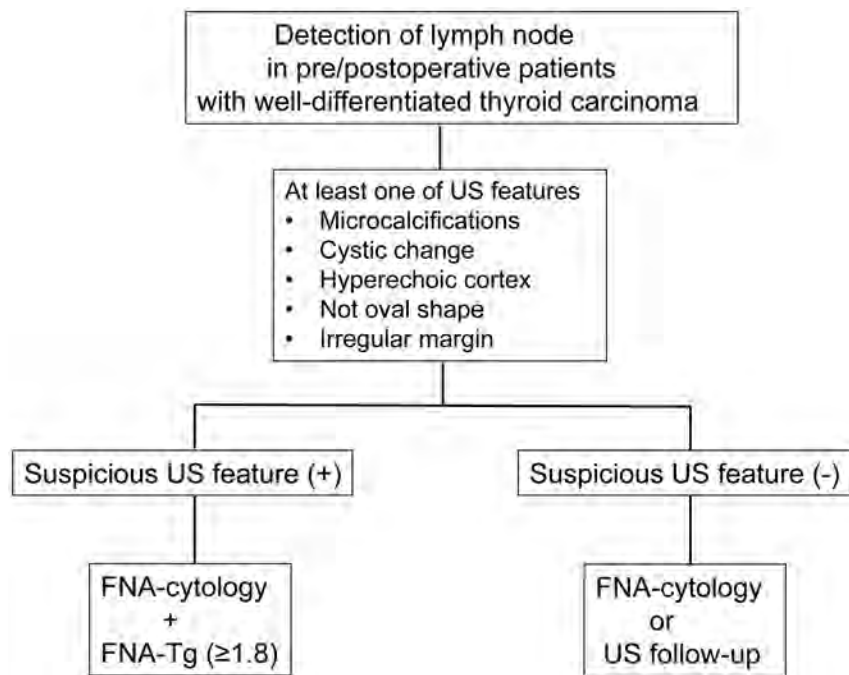


**FIG 3.** Flow chart of recommended management of clinically suspicious lymph nodes in patients with well-differentiated thyroid carcinoma from our results.

ity, 84.8%; specificity, 99.0%; and accuracy, 92.1%) and thus made the value of FNA-Tg underestimated. We think that FNA cytology with FNA-Tg would be more valuable for poor performers or beginners of FNA cytology.

There are several limitations in our study. Not all of the cases were confirmed pathologically. In addition, the device for measuring FNA-Tg varies from one institution to another. Therefore, the reliability of the results may require further investigation depending on the device used. Last, interobserver variability may exist when diagnosing suspicious malignant features on the basis of US.

## CONCLUSIONS

The optimal cutoff value of FNA-Tg in differentiating metastasis/recurrence from benign lesions in patients with thyroid cancer was 1.8 ng/mL. FNA cytology with FNA-Tg enhances diagnostic performance in lymph nodes with suspicious US features. Consequently, applying the optimal cutoff value and proper indication of FNA-Tg enhances diagnostic performances in the evaluation of neck lymph nodes for metastatic disease in both preoperative and postoperative patients with thyroid cancer.

## ACKNOWLEDGMENT

As a researcher and the first author, J.J.Y., a 12th grade student participated in this research and demonstrated her full contribution and brilliance.

## REFERENCES

1. Frasoldati A, Toschi E, Zini M, et al. **Role of thyroglobulin measurement in fine-needle aspiration biopsies of cervical lymph nodes in patients with differentiated thyroid cancer.** *Thyroid* 1999;9:105–11
2. Salmashioğlu A, Erbil Y, Citlak G, et al. **Diagnostic value of thyroglobulin measurement in fine-needle aspiration biopsy for detecting metastatic lymph nodes in patients with papillary thyroid carcinoma.** *Langenbecks Arch Surg* 2011;396:77–81
3. Baskin HJ. **Detection of recurrent papillary thyroid carcinoma by thyroglobulin assessment in the needle washout after fine-needle aspiration of suspicious lymph nodes.** *Thyroid* 2004;14:959–63
4. Sigstad E, Heilo A, Paus E, et al. **The usefulness of detecting thyroglobulin in fine-needle aspirates from patients with neck lesions using a sensitive thyroglobulin assay.** *Diagn Cytopathol* 2007;35:761–67
5. Sands NB, Karls S, Rivera J, et al. **Preoperative serum thyroglobulin as an adjunct to fine-needle aspiration in predicting well-differentiated thyroid cancer.** *J Otolaryngol Head Neck Surg* 2010;39:669–73
6. Kim MJ, Kim EK, Kim BM, et al. **Thyroglobulin measurement in fine-needle aspirate washouts: the criteria for neck node dissection for patients with thyroid cancer.** *Clin Endocrinol (Oxf)* 2009;70:145–51
7. Gharib H, Goellner JR. **Fine-needle aspiration biopsy of the thyroid: an appraisal.** *Ann Intern Med* 1993;118:282–89
8. Carmeci C, Jeffrey RB, McDougall IR, et al. **Ultrasound-guided fine-needle aspiration biopsy of thyroid masses.** *Thyroid* 1998;8:283–89
9. Danese D, Sciacchitano S, Farsetti A, et al. **Diagnostic accuracy of conventional versus sonography-guided fine-needle aspiration biopsy of thyroid nodules.** *Thyroid* 1998;8:15–21
10. Hahn SY, Shin JH, Han BK, et al. **Predictive factors related to the recurrence at US-guided fine needle aspiration in postoperative patients with differentiated thyroid cancer.** *Clin Endocrinol (Oxf)* 2011;74:270–75
11. Boi F, Baghino G, Atzeni F, et al. **The diagnostic value for differentiated thyroid carcinoma metastases of thyroglobulin (Tg) measurement in washout fluid from fine-needle aspiration biopsy of neck lymph nodes is maintained in the presence of circulating anti-Tg antibodies.** *J Clin Endocrinol Metab* 2006;91:1364–69
12. Giovannella L, Ceriani L, Suriano S. **Lymph node thyroglobulin measurement in diagnosis of neck metastases of differentiated thyroid carcinoma.** *J Thyroid Res* 2011; 2011:621839
13. Sohn YM, Kim MJ, Kim EK, et al. **Diagnostic performance of thyroglobulin value in indeterminate range in fine needle aspiration washout fluid from lymph nodes of thyroid cancer.** *Yonsei Med J* 2012;53:126–31
14. Cooper DS, Doherty GM, Haugen BR, et al. **Revised American Thyroid Association management guidelines for patients with thyroid nodules and differentiated thyroid cancer.** *Thyroid* 2009;19:1167–214
15. Kim E, Park JS, Son KR, et al. **Preoperative diagnosis of cervical metastatic lymph nodes in papillary thyroid carcinoma: comparison of ultrasound, computed tomography, and combined ultrasound with computed tomography.** *Thyroid* 2008;18:411–18
16. Rosário PW, de Faria S, Bicalho L, et al. **Ultrasonographic differentiation between metastatic and benign lymph nodes in patients with papillary thyroid carcinoma.** *J Ultrasound Med* 2005;24:1385–89
17. Ahuja A, Ying M. **Sonographic evaluation of cervical lymphadenopathy: is power Doppler sonography routinely indicated?** *Ultrasound Med Biol* 2003;29:353–59
18. Tseng FY, Hsiao YL, Chang TC. **Cytologic features of metastatic papillary thyroid carcinoma in cervical lymph nodes.** *Acta Cytol* 2002;46:1043–48
19. Koo JS, Kwak JY, Jung W, et al. **Importance of foamy macrophages only in fine needle aspirates to cytologic diagnostic accuracy of cystic metastatic papillary thyroid carcinoma.** *Acta Cytol* 2010;54:249–54
20. Lee MJ, Ross DS, Mueller PR, et al. **Fine-needle biopsy of cervical lymph nodes in patients with thyroid cancer: a prospective comparison of cytopathologic and tissue marker analysis.** *Radiology* 1993;187:851–54

# Automated Quantitation of the Posterior Scleral Flattening and Optic Nerve Protrusion by MRI in Idiopathic Intracranial Hypertension

N. Alperin, A.M. Bagci, B.L. Lam, and E. Sklar



## ABSTRACT

**BACKGROUND AND PURPOSE:** Subjective determination of the posterior sclera flattening and optic nerve protrusion in MRI is challenging because of the 3D nature of the globe morphology. This study aims to develop and compare quantitative measures of globe flattening and optic nerve protrusion with subjective rating, and assess relationships with papilledema grade and intraocular and CSF pressures.

**MATERIALS AND METHODS:** Data of 34 globes from 7 overweight female patients with idiopathic intracranial hypertension and 6 age- and weight-matched healthy female control subjects were assessed, as well as a subcohort of 4 of the patients with idiopathic intracranial hypertension who underwent follow-up MR imaging 2 weeks after lumbar puncture and initiation of treatment with acetazolamide. MR imaging examination included a 3D CISS sequence on 1.5T and 3T scanners with 0.6-mm isotropic resolution. Subjective ratings of globe flattening were obtained by experienced and inexperienced readers. Quantitative measures of globe flattening, nerve protrusion, and maximal deformation were derived by use of a 2D map of the distances from the globe center to the posterior wall.

**RESULTS:** Contingency coefficients for globe flattening agreements with subjective rating by the experienced and inexperienced readers were 0.72 and 0.56, respectively. Mean values of the 3 deformation measures were significantly poorer in the idiopathic intracranial hypertension group, with nerve protrusion demonstrating the strongest difference ( $P = .0002$ ). Nerve protrusion was most strongly associated with papilledema grade with a contingency coefficient of 0.74 ( $P = .01$ ), whereas globe flattening was negatively correlated with intraocular pressure ( $R = -0.75$ ,  $P < .0001$ ). Maximal deformation was negatively associated with CSF opening pressure ( $R = -0.86$ ,  $P = .0001$ ). After treatment, only the changes in nerve protrusion and maximal deformation were significant.

**CONCLUSIONS:** Automated measures of globe deformation improve reliability over subjective rating. Of the 2 globe deformation measures, nerve protrusion had the strongest predictive value for papilledema grade and had the highest sensitivity for assessment of treatment efficacy in idiopathic intracranial hypertension.

**ABBREVIATIONS:** IOP = intraocular pressure; IH = intracranial hypertension; IIH = idiopathic intracranial hypertension; LP = lumbar puncture; ICP = intracranial pressure; NP = nerve protrusion; GF = globe flatness; MD = maximal deformation

Flattening of the posterior sclera and inward protrusion of the optic nerve head are recognized MR imaging markers of intracranial hypertension (IH).<sup>1-5</sup> These findings have been reported primarily in idiopathic intracranial hypertension (IIH)<sup>1-3</sup> but also in secondary IH, including sinus thrombosis and nonthrombotic cases of

venous sinus occlusions.<sup>4</sup> Posterior sclera flattening has also been observed in astronauts after long-duration exposure to microgravity.<sup>5,6</sup> Occurrence rates of globe flattening and optic nerve protrusion in IIH and secondary IH are reported to be different. Work by Agid et al<sup>3</sup> assessing several cross-sectional neuroimaging signs seen in IIH suggests that posterior globe flattening has the strongest diagnostic value, with specificity of 100%, whereas optic nerve protrusion was not significantly associated with IIH. In contrast, Rohr et al<sup>4</sup> assessed similar signs in patients with secondary IH and reported specificity of 78% for globe flattening and 100% for optic disc protrusion. Both studies, however, used subjective visual inspection to determine the presence of flattening and optic nerve protrusion.

Determining the presence and degree of globe distortions in MR imaging by visual inspection is challenging because of the 3D nature of the globe morphology. In addition, impression of distortion can vary with imaging orientation.

Received February 5, 2013; accepted after revision March 19, 2013.

From the Department of Radiology (N.A., A.M.B., E.S.) and Bascom Palmer Eye Institute (B.L.L.), University of Miami, Miami, Florida.

Paper previously presented at: Annual Meeting of the American Society of Neuroradiology, May 20–23, 2013; San Diego, California.

This study was supported in part by the National Institutes of Health (R01NS052122).

Please address correspondence to Noam Alperin, PhD, Advanced Image Processing Laboratory, Department of Radiology, University of Miami, 1150 NW 14th St, Miami, FL 33136; e-mail: Nalperin@med.miami.edu

Indicates open access to non-subscribers at [www.ajnr.org](http://www.ajnr.org)

<http://dx.doi.org/10.3174/ajnr.A3600>

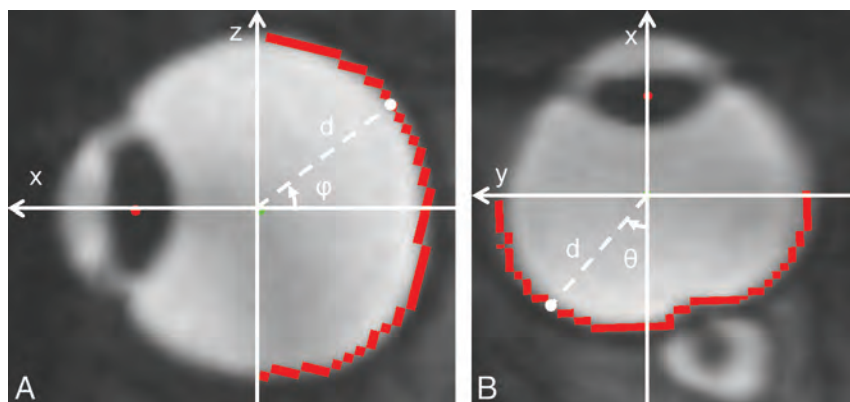


**FIG 1.** MR images of the globe reformatted in sagittal (A) and axial (B) planes. The coordinate system is defined by the center of mass of the lens and the globe (red and green points), respectively. The red contour marks the posterior sclera. Each point on the sclera is defined by the distance to the center of the orbit (dashed line), azimuth angle ( $\theta$ ), and the elevation angle ( $\varphi$ ).

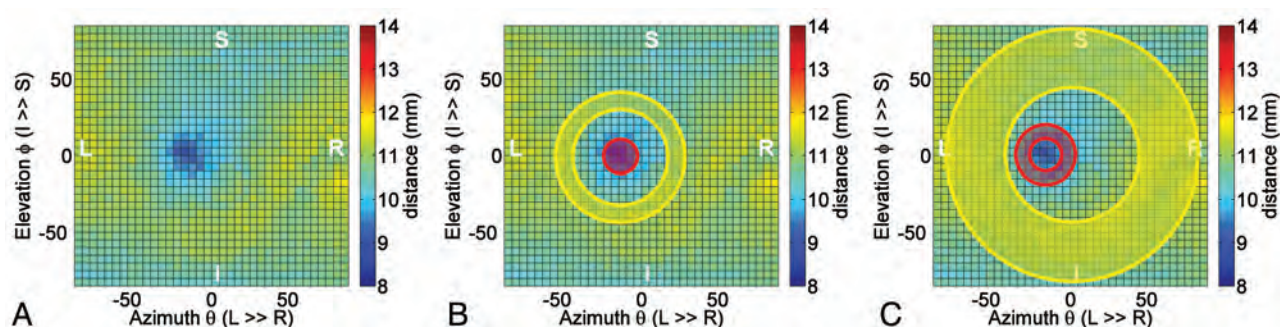


**FIG 2.** A 2D color-coded distance map visualizes distances between the center of the globe and points on the posterior sclera. The map represents the globe shown in Fig 1. The inward protrusion of the papilla is visualized as an off-center blue patch (A). The central (red) and peripheral (yellow) ROIs used for the derivation of NP and GF are shown in B and C, respectively. The angular boundaries of the central (papillar), peripapillar, and peripheral ROIs are  $0-10^\circ$ ,  $10-18^\circ$ , and  $40-80^\circ$ , respectively.

Flattening of the posterior sclera and inward protrusion of the optic papilla are often seen in patients with papilledema documented by funduscopy. Papilledema, or optic nerve head edema, is caused by increased CSF volume and pressure within the optic nerve sheath leading to axoplasmic flow stasis and subsequent ischemia.<sup>7,8</sup> The exact mechanism by which papilledema occurs is still debatable. Either mechanical or ischemic processes are currently the 2 competing theories.<sup>9</sup> A recent comprehensive review of MR imaging of papilledema and the visual pathway lists globe flattening and optic papilla protrusion among several findings commonly seen in papilledema.<sup>10</sup> However, because of a lack of quantitative measures of globe flattening and optic nerve protrusion, it is unknown whether papilledema grade is associated with the degrees of flattening and/or protrusion. Reliable quantification of flattening and protrusion may increase the diagnostic power of these markers and further elucidate the mechanism by which elevated intracranial pressure (ICP) causes papilledema.

An automated method for quantifying globe flattening and optic nerve protrusion is described in the present study. Measures obtained in patients with IIH and healthy control subjects were compared with subjective rating by experienced and inexperienced readers. Measurements were also tested for association with papilledema

grade, intraocular pressure (IOP), and CSF opening pressure. Finally, sensitivity for detection of changes after treatment was assessed.

## MATERIALS AND METHODS

### Study Participants

All study participants provided written informed consent approved by the institutional review board. MR imaging data of 34 globes were analyzed. The data were obtained from a cohort of 7 overweight women of childbearing age ( $30 \pm 12$  years; range, 17–44 years; mean body mass index,  $36 \pm 4$  kg/m<sup>2</sup>; range, 29–41 kg/m<sup>2</sup>) with a confirmed diagnosis of IIH as per the modified Dandy criteria<sup>11</sup> and 6 healthy age- and weight-matched female subjects ( $30 \pm 8$  years; range, 22–44 years; body mass index,  $37 \pm 6$  kg/m<sup>2</sup>; range, 31–49 kg/m<sup>2</sup>). A subcohort of 4 patients with IIH underwent a follow-up MR imaging scan approximately 2 weeks after lumbar puncture (LP) and initiation of treatment with acetazolamide.

Detailed neurologic symptoms and ophthalmologic assessments were obtained before diagnostic LP. Papilledema severity was classified by fundoscopic examination before and 2 weeks after LP, by use of the Frisen scale.<sup>12</sup> Bilateral papilledema was found in all patients with IIH (mean grade,  $2.0 \pm 1.0$ ; range, 1–4). Six of 7 patients reported moderate to severe headaches and vision-related problems, including

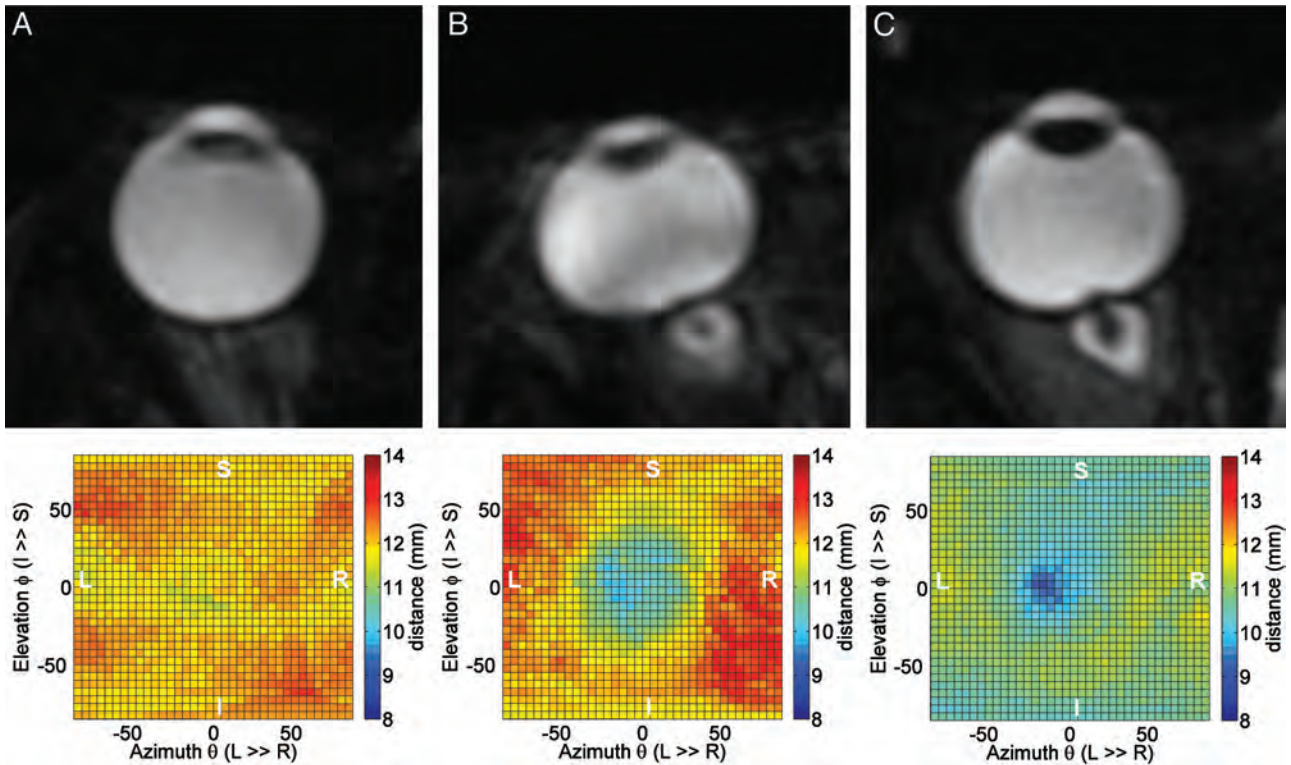


**FIG 3.** Reformatted MR images shown in axial plane for a normal globe (A), a flattened globe with minimal optic nerve protrusion (B), and a globe with minimal flattening and extensive optic nerve protrusion (C). Respective distance maps are shown in the bottom. The corresponding GF and NP values are (A) 0.97 and 0.97, (B) 0.86 and 0.91, and (C) 0.91 and 0.88.

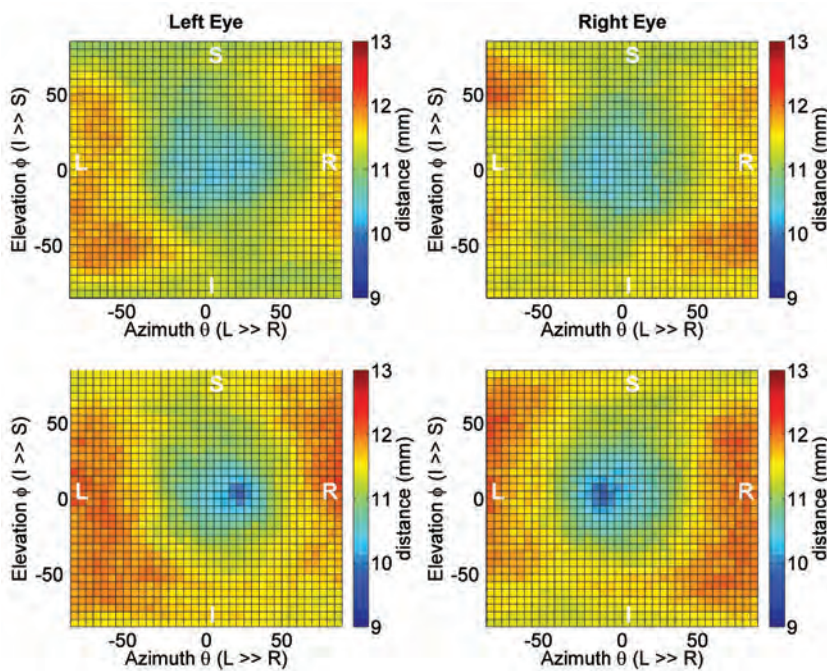


**FIG 4.** Average left and right eyes, 2D-distance maps obtained from the control cohort (upper row) and the IIH cohort (lower row). The presence of nerve protrusion is clearly seen in the maps from the IIH cohort.

blurriness, transient visual obscurations, and impaired peripheral vision. The mean opening pressure by LP was  $36.9 \pm 7.8$  cmH<sub>2</sub>O (range, 26–47 cmH<sub>2</sub>O). IOP was measured in the IIH and the control cohorts, with mean values of  $17.3 \pm 2.9$  mm Hg and  $12.6 \pm 1.5$  mm Hg, respectively.

1 = minimal flattening or deviation from circular shape at least in 1 plane, 2 = obvious flattening with apparent deviation from circular shape on both planes, and 3 = profound flattening of a large portion of the posterior wall.

### MR Imaging Scan Protocol

MR imaging scans were performed by use of 1.5T and 3T scanners (Symphony and Trio; Siemens, Erlangen, Germany). Quantitative assessment of the globes was obtained from a 3D CISS sequence (A) with an isotropic resolution of 0.6 mm and the following parameters: TR, 6.35 ms (5.42 ms for 3T); TE, 2.82 ms (2.43 for 3T); flip angle, 47° (34° for 3T); and bandwidth, 560 Hz/pixel (650 Hz/pix for 3T). Scan time was up to 3 minutes (2.5 for 3T).

### Subjective Assessment of Globe Flattening

Flattening of the posterior ocular wall was visually evaluated by an experienced reader (>25 years) and an inexperienced reader (<1 year), blinded to the clinical diagnosis. A second reading was obtained to assess intraobserver reliability. MR images were reformatted and reviewed in both axial and sagittal views. A 4-point rating was used, in which 0 = no flattening,

### Automated Measurements of Globe Deformity

The automated method for quantifying the 3D geometry of the posterior sclera includes 3 steps: 1) segmentation, 2) identification of a reference point (center of globe), and 3) generating a 2D map of the distances from the globe center to the posterior wall. First, the MR images are aligned to a common anatomic space by use of rigid linear registration<sup>13</sup> to ensure that both globes are located on the same axial plane. Reformatted images are then segmented by use of an expectation-maximization algorithm<sup>14</sup> to delineate the outside boundaries of the globe and the lens. The centers of mass of the globe and the lens are then identified and are used to define an orthogonal coordinate system in which the x-axis is the posterior-anterior orientation, or the optical axis, and the y-axis is oriented laterally from left to right, as shown in Fig 1. This framework is independent of the individual's gaze direction. Each point on the globe posterior wall is identified by use of 3 parameters:  $d$ , the distance in millimeters from the globe center;  $\theta$ , the azimuth angle (in the xy plane); and  $\varphi$ , the elevation angle (in the xz plane), where  $\theta$  and  $\varphi$  range from  $-90^\circ$  to  $+90^\circ$ . An example of a 2D distance map is shown in Fig 2A. The darker shades of blue indicate shorter distances from the center and the yellow and red shades represent longer distances. A 2D map of a perfectly spherical hemisphere will have a uniform color with a distance equal to its radius.

Three measures of globe deformation are calculated by using

**Table 1: Mean values of deformation measures for the control and IIH cohorts**

Measure	Control (n = 7)	IIH (n = 6)	P Value
NP	0.96 ± 0.013	0.91 ± 0.028	.00002
GF	0.93 ± 0.020	0.91 ± 0.022	.0035
MD	0.93 ± 0.021	0.88 ± 0.027	.00002

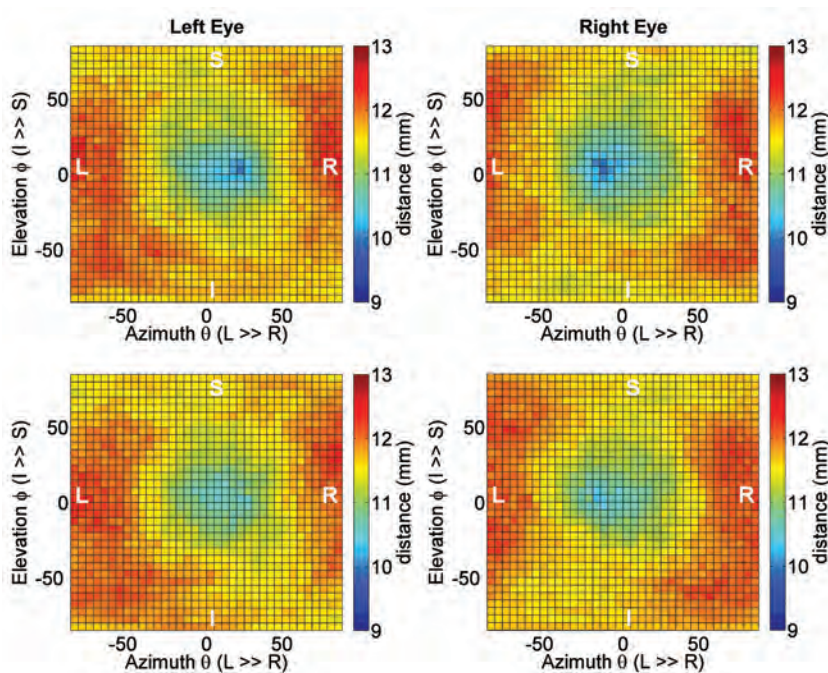


**FIG 5.** Pretreatment (upper row) and posttreatment (lower row) average distance maps of the patients with IIH who had a follow-up MR imaging scan ( $n = 4$ ). A significant reversal of the extent of the optic nerve protrusion is visualized in the posttreatment maps.

the distance map: 1) nerve protrusion (NP), depicting the extent of the nerve head protrusion; 2) globe flatness (GF), depicting the degree of flattening of the posterior wall, and 3) maximal deformation (MD), depicting the combined deformation due to the flattening and the nerve protrusion. Each measure is defined as the ratio of the mean distance within a central and a peripheral region in the 2D distance map. NP is obtained by use of circular and annular ROIs covering the optic nerve head and the peripapillary region, respectively. GF is obtained by use of an annular region of interest surrounding the nerve head and an annular region of interest centered at the optical axis and covering the peripheral section of the globe posterior hemisphere. The locations and extents of these regions are shown in Fig 2B and 2C, respectively. The MD measure, which assesses the combined distortion caused by nerve protrusion and globe flattening, is obtained by use of the central ROI of NP and the peripheral ROI of GF. In a perfectly spherical globe with no protrusion, all 3 measures have a value of 1. A lower value represents a larger inward deformation. Image analysis was implemented by use of Matlab (MathWorks, Natick, Massachusetts). Total computation time with the use of a personal computer was approximately 15 minutes.

### Statistical Methods

Interrater and intrarater agreements of the readers' visual ratings were assessed by use of the  $\kappa$  test.<sup>15</sup> Association between visual rating of flatness and GF were determined by means of frequency tables and  $\chi^2$  test, with the continuous GF discretized into 4 equally spaced intervals to match the visual rating scale. Differences between the computer-derived measures in the control and IIH cohorts were assessed by means of the unpaired  $t$  test. Differences between pretreatment and posttreatment were assessed by means of the paired  $t$  test. Receiver operating characteristic analysis

was applied to determine thresholds that best distinguish patients with IIH from control subjects. Associations between papilledema grade and the derived globe deformation measures were also determined by means of  $\chi^2$  test after discretizing of the deformation measures into 5 equally spaced intervals matching the Friszen scale. Finally, associations with IOP and opening CSF pressure during LP were tested by calculation of Pearson correlation coefficient. All statistical calculations were performed by use of MedCalc version 11.6 (MedCalc Software, Mariakerke, Belgium).

### RESULTS

The highest inter rater agreement between the experienced and inexperienced readers for the visual ratings of the globe flatness was moderate, with a weighted  $\kappa$  value of 0.46. The intrarater agreement for the experienced and inexperienced readers had a similar  $\kappa$  value

of 0.56 and 0.60, respectively. The GF measure was significantly associated with the visual ratings of flatness with maximal contingency coefficients of 0.72 and 0.57 for the experienced and inexperienced readers, respectively.

Examples demonstrating the relationship between the shape of the globe and the corresponding distance map for a nearly spherical globe, a flattened globe wall with minimal protrusion, and a globe with extensive protrusion with minimal flattening are shown in Fig 3.

Average right and left distance maps obtained separately for the control and IIH cohorts are shown in Fig 4. The presence of nerve protrusion is clearly seen in both eyes of the IIH cohort but not in the control. Nerve protrusion, globe flatness, and maximal deformation measures obtained in the 2 cohorts are summarized in Table 1. These measures were all significantly larger in the control compared with IIH group: NP,  $0.96 \pm 0.013$  versus  $0.91 \pm 0.028$  ( $P = .00002$ ); GF,  $0.93 \pm 0.020$  versus  $0.91 \pm 0.022$  ( $P = .003$ ); and MD,  $0.93 \pm 0.021$  versus  $0.88 \pm 0.027$  ( $P = .00002$ ), respectively.

The effect of treatment with acetazolamide on reversal of the eye globe deformation is clearly visualized in the average pretreatment and posttreatment distance maps from the subgroup of the 4 patients with IIH who underwent a follow-up MR. The pretreatment and posttreatment mean distance maps are shown in Fig 5. Pretreatment and posttreatment measures are summarized in Table 2. Interestingly, NP but not GF was significantly larger after treatment. MD was also significantly larger because it includes the effect of NP. Pre- and post-NP values were  $0.91 \pm 0.32$  and  $0.94 \pm 0.17$  ( $P = .036$ ), respectively. Pre- and post-GF values were  $0.90 \pm 0.21$  and  $0.92 \pm 0.23$  ( $P = .09$ ), respectively. Differences between pretreatment and posttreatment ratings by the 2 readers were not statistically significant.

The extent of nerve protrusion was significantly associated with papilledema grade, with a contingency coefficient of 0.74 and significance level of  $P = .01$ . In contrast, the flatness measure association with papilledema grade was not statistically significant (contingency coefficient = 0.504,  $P = .8$ ). Whereas the NP mea-

sure was more strongly associated with papilledema grade, the GF measure was more strongly associated with IOP. A strong negative correlation with an  $R$  value of  $-0.76$ , with  $P < .0001$ , was found between GF and IOP. The NP measure was also negatively correlated with IOP but with weaker association ( $R = -0.54$ ,  $P = .004$ ). The scatterplot for GF as a function of IOP and the linear regression line are shown in Fig 6A. Finally, both NP and GF were significantly negatively correlated with the CSF opening pressure, with  $R = -0.77$  ( $P = .0011$ ) and  $R = -0.67$  ( $P = .0089$ ), respectively. As expected, the maximal deformation measure had the largest association with the CSF opening pressure, with an  $R$  value of  $-0.86$  ( $P = .0001$ ). The scatterplot of MD with respect to the opening pressure is shown in Fig 6B.

## DISCUSSION

Flattening of the posterior sclera and protrusion of the optic nerve head are important MR imaging findings related to visual impairment in pathologies associated with increased ICP. Determining the presence and the degree of these globe distortions by visual inspection is challenging, subjective, and strongly influenced by the orientation of the MR images. Variability and limited consistency of subjective ratings are evident from the similar moderate  $\kappa$  values of interreader agreement between the experienced and the inexperienced readers and intrareader agreement of the experienced reader. The variability associated with subjective rating may partly explain reported differences in frequency of these findings in IIH and secondary IH.<sup>3,4</sup> Automated quantitation of the globe distortion may help to overcome the limitations associated with the subjective assessment and thereby improve diagnostic accuracy. The significant association between the subjective rating and the computer-derived GF measure supports the feasibility for a reliable automated quantitation of globe flatness.

The proposed automated method transforms the 3D globe geometry into a 2D distance map. The 2D computer-derived color-coded distance map provides a quantitative representation of the 3D morphology of the sclera in the posterior ocular hemisphere. Therefore, it has a distinctive advantage over the need for scrolling through individual MR images along different planes to gain a visual impression of the 3D globe deformation. Another advantage of the proposed analyses is the separate assessment of the contributions of globe flattening and nerve protrusion to the overall distortion of the globe. The reliability of the proposed computer-derived measures is supported by the statistical significance of differences in the globe distortion measures between the IIH and control cohorts, even with a relatively small number of subjects.

Whereas both the NP and the GF measures were significantly worse in the IIH cohort, the NP measure more strongly separates the patients with IIH from the healthy control subjects. Careful inspection of the distance maps of the overweight healthy cohort demonstrates some degree of globe flattening, but none had visible NP. This is also consistent with the fact that only the NP measure demonstrated a significant improvement after treatment in the

**Table 2: Pretreatment and posttreatment mean values of deformation measures in the IIH subcohort**

Measure	IIH Pre (n = 4)	IIH Post (n = 4)	P Value
NP	$0.91 \pm 0.032$	$0.94 \pm 0.017$	.036
GF	$0.90 \pm 0.021$	$0.92 \pm 0.023$	.09
MD	$0.88 \pm 0.024$	$0.91 \pm 0.024$	.011

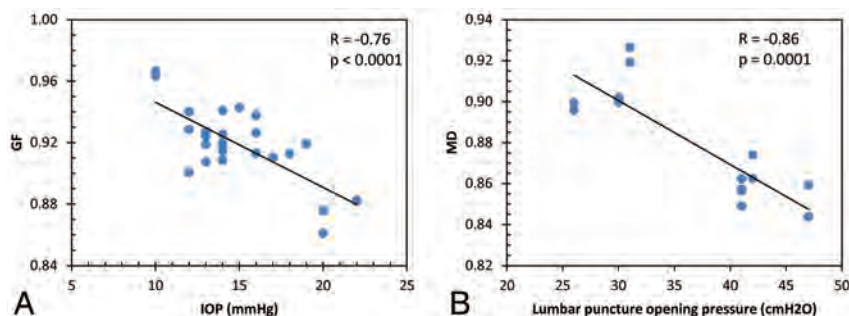


**FIG 6.** Scatterplots of the relationships between GF and intraocular pressure (A) and between MD and CSF opening pressure (B).

subcohort of patients with IIH who had a follow-up scan. The NP measure was also the one that was significantly associated with the clinical papilledema grading. These findings are consistent with recent optical coherence tomography studies demonstrating inward deflection of the peripapillary retinal pigment epithelium layer in papilledema.<sup>16,17</sup> On the basis of these observations and results, the extent of optic nerve protrusion appears to be the more clinically relevant marker for the risk of papilledema in IIH. Because larger protrusion implies larger mechanical stress around the nerve head region, it is likely that shear stress does play a role in the mechanism that leads to papilledema.<sup>9,16</sup> The MR measure of NP is a potential objective measure for papilledema severity compared with the subjective Frisen scale.<sup>12</sup>

Quantitative assessment of the 2 types of globe deformation in the patients with IIH and control subjects revealed that both GF and NP were significantly correlated with IOP, with the GF measure demonstrating the stronger association. The measured IOP values in all but 1 patient with IIH were <21 mm Hg, that is, the upper limit of normal IOP. Elevated IOP is not expected in IIH because it is not associated with impaired intraocular fluid circulation as it is in glaucoma.<sup>18</sup> Therefore, the stronger association between IOP and GF suggests that the flattening of the posterior wall by the increased ICP probably contributes to an increase in IOP but not to the extent that is caused by impaired absorption of the aqueous humor.

Another revealing finding is the significant correlation between the deformation measures and the CSF opening pressure. This relation is expected because the primary cause for the globe deformation is increased CSF pressure transmitted to the globe through the increased CSF volume within the subarachnoid space and optic nerve sheath.<sup>19</sup> This is consistent with the fact that MD, the combined deformation caused by NP and GF, demonstrated the strongest negative correlation with the CSF opening pressure, with an *R* value of  $-0.86$ .

The limitation of a small number of subjects in each cohort in the current study is somewhat lessened because both globes were assessed in each subject. Despite this, differences between patients with IIH and the healthy cohort of all 3 measures of globe deformations reached statistical significance. Furthermore, the improvement in the NP measure was statistically significant even with a subcohort size of 4 subjects. This demonstrates the reliability as well as the high sensitivity of the proposed quantitative measures of globe deformation. Furthermore, once validated in larger cohorts, the proposed analysis is suitable for clinical practice because of the relatively short scan time (<3 minutes) and computation time (~15 minutes).

## CONCLUSIONS

Assessment of ocular wall distortion on the basis of a 2D distance map provides a quantitative representation the posterior ocular geometry as well as clinically relevant measures of wall flattening and optic nerve protrusion. These measurements are likely to im-

prove diagnostic accuracy and sensitivity for detection of ocular changes before and after treatment in patients with IIH.

Disclosure: Noam Alperin—RELATED: Grant: NIH\*; Board Membership, Stock/Stock Options: Alperin Noninvasive Diagnostics (\*money paid to institution).

## REFERENCES

1. Brodsky MC, Vaphiades M. **Magnetic resonance imaging in pseudotumor cerebri.** *Ophthalmology* 1998;105:1686–93
2. Jinkins JR, Athale S, Xiong L, et al. **MR of optic papilla protrusion in patients with high intracranial pressure.** *AJNR Am J Neuroradiol* 1996;17:665–68
3. Agid R, Farb RI, Willinsky RA, et al. **Idiopathic intracranial hypertension: the validity of cross-sectional neuroimaging signs.** *Neuroradiology* 2006;48:521–27
4. Rohr AC, Riedel C, Fruehauf MC, et al. **MR imaging findings in patients with secondary intracranial hypertension.** *AJNR Am J Neuroradiol* 2011;32:1021–29
5. Mader TH, Gibson CR, Pass AF, et al. **Optic disc edema, globe flattening, choroidal folds, and hyperopic shifts observed in astronauts after long-duration space flight.** *Ophthalmology* 2011;118:2058–69
6. Kramer LA, Sargsyan AE, Hasan KM, et al. **Orbital and intracranial effects of microgravity: findings at 3-T MR imaging.** *Radiology* 2012;263:819–27
7. Hayreh SS. **Optic disc edema in raised intracranial pressure, V: pathogenesis.** *Arch Ophthalmol* 1977;95:1553–65
8. Tso MO, Hayreh SS. **Optic disc edema in raised intracranial pressure, IV: axoplasmic transport in experimental papilledema.** *Arch Ophthalmol* 1977;95:1458–62
9. Trobe JD. **Papilledema: the vexing issues.** *J Neuro-ophthal* 2011;31:175–86
10. Passi N, Degnan AJ, Levy LM. **MR imaging of papilledema and visual pathways: effects of increased intracranial pressure and pathophysiologic mechanisms.** *AJNR Am J Neuroradiol* 2013;34:919–24
11. Smith JL. **Whence pseudotumor cerebri?** *J Clin Neuro-ophthal* 1985;5:55–56
12. Frisen L. **Swelling of the optic nerve head: a staging scheme.** *J Neurol Neurosurg Psychiatry* 1982;45:13–18
13. Jenkinson M, Smith S. **A global optimisation method for robust affine registration of brain images.** *Med Image Analysis* 2001;5:143–56
14. Zhang Y, Brady M, Smith S. **Segmentation of brain MR images through a hidden Markov random field model and the expectation-maximization algorithm.** *IEEE Trans Med Imaging* 2001;20:45–57
15. Altman DG. *Practical Statistics for Medical Research.* London: Chapman & Hall/CRC; 1991:404–08
16. Kupersmith MJ, Sibony P, Mandel G, et al. **Optical coherence tomography of the swollen optic nerve head: deformation of the peripapillary retinal pigment epithelium layer in papilledema.** *Invest Ophthalmol Vis Sci* 2011;52:6558–64
17. Sibony P, Kupersmith MJ, Rohlf FJ. **Shape analysis of the peripapillary RPE layer in papilledema and ischemic optic neuropathy.** *Invest Ophthalmol Vis Sci* 2011;52:7987–95
18. Dielemans I, Vingerling JR, Algra D, et al. **Primary open-angle glaucoma, intraocular pressure, and systemic blood pressure in the general elderly population: the Rotterdam Study.** *Ophthalmology* 1995;102:54–60
19. Alperin N, Ranganathan S, Bagci AM, et al. **MRI evidence of impaired CSF homeostasis in obesity-associated idiopathic intracranial hypertension.** *AJNR Am J Neuroradiol* 2013;34:29–34

# Diffusion MRI Improves the Accuracy of Preoperative Diagnosis of Common Pediatric Cerebellar Tumors among Reviewers with Different Experience Levels

K. Koral, S. Zhang, L. Gargan, W. Moore, B. Garvey, M. Fiesta, M. Seymour, L. Yang, D. Scott, and N. Choudhury



## ABSTRACT

**BACKGROUND AND PURPOSE:** Although utility of diffusion MR imaging in the preoperative diagnosis of common pediatric cerebellar tumors is generally recognized, its added value has not been systematically studied previously. The purpose of this study was to evaluate the impact of diffusion MR imaging on the accuracy of preoperative diagnosis of common pediatric cerebellar tumors among reviewers with different experience levels.

**MATERIALS AND METHODS:** Review of the neuro-oncology data base yielded 96 patients whose preoperative brain MR imaging included both diffusion MR imaging ( $b = 1000 \text{ s/mm}^2$ ) and ADC maps. There were 38 pilocytic astrocytomas, 33 medulloblastomas, 17 ependymomas, and 8 atypical teratoid/rhabdoid tumors. Six reviewers (4 residents, 2 neuroradiologists) evaluated the examinations. Two sessions were conducted with each reviewer, without and with diffusion MR imaging data on 2 separate days. The impact of diffusion MR imaging on accuracy of diagnoses was assessed.

**RESULTS:** In choosing the correct diagnosis of the 4 alternatives, performances of 5 of the 6 reviewers improved significantly with inclusion of the diffusion MR imaging data, from 63%–77% ( $P = .0003$ – $.0233$ ). The performance of 1 reviewer also improved, but the difference did not attain statistical significance ( $P = .1944$ ). Inclusion of diffusion MR imaging data improved the likelihood of rendering a correct diagnosis (odds ratio = 3.16, 95% confidence interval = 2.07–4.00) over all tumor types. When embryonal tumors were regarded as a single group, the rate of correct diagnosis increased from 66%–83% with diffusion MR imaging data, and performances of all of the reviewers improved significantly ( $P = .0001$ – $.05$ ). The improvement in performances resulted from increased correct diagnoses of pilocytic astrocytomas, medulloblastomas, and atypical teratoid/rhabdoid tumors. There was no improvement in the correct diagnoses of ependymomas with inclusion of the diffusion MR imaging data.

**CONCLUSIONS:** Diffusion MR imaging improves accuracy of preoperative diagnosis of common pediatric cerebellar tumors significantly among reviewers with differing experience levels.

**ABBREVIATIONS:** AT/RT = atypical teratoid/rhabdoid tumor; PA = pilocytic astrocytoma; WHO = World Health Organization

The role of diffusion MR imaging in the preoperative diagnosis of pediatric brain tumors, and in particular of cerebellar tumors, has been studied previously.<sup>1–4</sup> The utility of diffusion MR imaging is generally attributed to the differences in the cellularity of common pediatric cerebellar tumors. Hypercellular tumors, such as medullo-

blastoma and atypical teratoid/rhabdoid tumor (AT/RT), usually display restricted diffusion because of the abundant barriers generated by the cell membranes and intracellular organelles, whereas paucicellular tumors such as pilocytic astrocytomas (PAs) are characterized by large extracellular spaces resulting in fewer obstacles to water diffusion. To our knowledge, however, the additional value of diffusion MR imaging to conventional MR imaging in the accurate preoperative diagnosis of common pediatric cerebellar tumors has not been reported previously. In this study, our hypothesis was inclusion of diffusion MR imaging data in the evaluation of common pediatric cerebellar tumors improves preoperative diagnostic accuracy of reviewers, irrespective of the level of experience.

## MATERIALS AND METHODS

This study was reviewed for issues of patient safety and confidentiality and was approved by the Institutional Review Board of the Uni-

Received January 29, 2013; accepted after revision February 26.

From the Departments of Radiology, University of Texas Southwestern Medical Center (K.K., W.M., B.G., M.F., M.S., L.Y., D.S.) and Children's Medical Center (K.K.), Dallas, Texas; Departments of Clinical Sciences (S.Z.) and Internal Medicine (N.C.), University of Texas Southwestern Medical Center Dallas, Texas; and Department of Neuro-Oncology (L.G.), Children's Medical Center, Dallas, Texas.

Please address correspondence to Korgun Koral, MD, Department of Radiology, University of Texas Southwestern Medical Center/Children's Medical Center, 1935 Medical District Dr, Dallas, TX 75235; e-mail: korgun.koral@utsouthwestern.edu

Indicates Evidence-Based Medicine Level 2

<http://dx.doi.org/10.3174/ajnr.A3596>

## Tumor types and patient demographics

Tumor	n	M:F	Mean age, y (min-max)
Medulloblastoma	33	23:10	6.49 (1.15–17.19)
Ependymoma <sup>a</sup>	17	14:3	4.20 (0.46–17.18)
PA	38	18:20	6.86 (1.44–18.73)
AT/RT	8	5:3	1.01 (0.25–2.29)
Total	96		

**Note:**—M:F indicates male:female.

<sup>a</sup> Four anaplastic (WHO grade 3) and 13 WHO grade 2 ependymomas.

versity of Texas Southwestern Medical Center and was compliant with the Health Insurance Portability and Accountability Act.

### Patient Population

Query of the neuro-oncology data base at Children's Medical Center from July 2003 through December 2011 revealed 168 patients with 1 of the 4 most common pediatric cerebellar tumors. There were 69 PAs, 67 medulloblastomas, 19 ependymomas, and 13 AT/RTs. Patients whose examinations did not include diffusion MR imaging data (both  $b = 1000$  s/mm<sup>2</sup> images and ADC maps) were excluded. Patients whose studies had suboptimal quality diffusion MR imaging data ( $n = 4$ ) caused by motion or artifacts generated by dental hardware were removed from the study list. The quality of the examinations was assessed by a pediatric neuroradiologist (K.K.) with 10 years of experience. The study population comprised 96 patients whose preoperative MR imaging examinations were performed at our institution and were available on PACS. All included patients underwent surgery, and tumor specimens were categorized according to the latest World Health Organization (WHO) Classification of Tumors of the Central Nervous System. The characteristics of the study population are given in Table 1.

### Imaging

The examinations were performed on 1.5T (2 Intera and 3 Achieva;  $n = 89$ ) and 3T (1 Achieva;  $n = 7$ ) scanners (Philips, Best, the Netherlands). All studies included sagittal and axial T1-weighted, axial and coronal T2-weighted, and axial FLAIR (for patients >15 months) and gadolinium-enhanced axial, coronal, and sagittal T1-weighted sequences. Additionally, since January 2008, a gadolinium-enhanced axial FLAIR sequence has been added to the imaging protocol in patients with brain tumors for evaluation of leptomeningeal dissemination. DWI was performed with the use of a spin-echo sequence, with  $b = 0$  and  $b = 1000$  s/mm<sup>2</sup>. ADC maps were generated with a monoexponential fit on a voxel-to-voxel basis for all imaging planes.

### Review of MR Imaging Examinations

Four radiology residents and 2 neuroradiologists were recruited. The radiology residents (W.M., B.G., M.F., M.S.) had completed 32 months of radiology training, including 12 weeks of pediatric radiology rotation, during which they were exposed to pediatric neuroradiology. All residents had been matched to neuroradiology fellowships to commence on the completion of their residencies. The review of the examinations took place, on average 5.75 months (2–8 months), after the completion of the last part of their pediatric radiology rotations. Although it is possible that the residents may have seen a minority of the study examinations during their rotations and at conferences, they had not participated

in the official read-outs for the examinations. The neuroradiologists were recruited from our institution's adult neuroradiology division; they were academic neuroradiologists practicing adult neuroradiology and were board-certified with Certificates of Added Qualification in neuroradiology. The neuroradiologists had 8 years (L.Y.) and 3 years (D.S.) of postfellowship experience. The more experienced neuroradiologist had completed her residency at our institution before the acquisition of the earliest examination in the study set. The other neuroradiologist was also a graduate of our residency program and, similar to the resident reviewers, may have seen some of the study examinations during his rotations and at conferences, but he was not one of the official readers in the radiology reports for any of the examinations. The reviewers were given relevant literature<sup>1,2,4-7</sup> on the imaging of pediatric cerebellar tumors and utility of diffusion MR imaging in discriminating common pediatric cerebellar tumors at least 2 days before their first session and maintained access to this material during the review sessions.

The examinations were presented to the reviewers by a fourth-year medical student (N.C.) who did not have access to the correct diagnoses. The studies were de-identified and randomly shown to the reviewers at clinical PACS workstations (iSite PACS Version 3.6.120.0, Philips). Twelve number sets (1–96) were generated (www.randomizer.org), and a separate number set was used at each session. Two sessions (1–13 days apart) were conducted with each reviewer. The session durations were recorded. No time constraints were imposed, and the reviewers were able to spend as much time as they wished during the sessions. When breaks were taken, their lengths were recorded and subtracted from the session durations. The reviewers were able to manipulate the studies similar to a clinical readout experience. At the first sessions, preoperative brain MR imaging studies without diffusion MR imaging data and at the second sessions preoperative brain MR imaging studies including the diffusion MR imaging data were evaluated. The reviewers were asked to render a single diagnosis. The correct diagnoses and their performances were not revealed to the reviewers after the completion of the sessions. Only the age and sex of the patients were disclosed on prompting.

### Statistical Analysis

The performance was evaluated on the basis of the correct diagnoses of the 4 possible choices (PA, medulloblastoma, ependymoma, and AT/RT) without and with diffusion MR imaging data. Performance was also evaluated when embryonal tumors (medulloblastoma and AT/RT) were grouped together without and with diffusion MR imaging data. We used mixed logistic models to evaluate the effect of diffusion MR imaging data. The indicators of diffusion MR imaging data and resident/neuroradiologist were included as fixed effects. These models also included random effects to account for the multilevel correlation among observations obtained from the same patient or the same reviewer. A value of  $P < .05$  was taken to represent statistical significance. All statistical analyses were performed with the use of SAS 9.3 (SAS Institute, Cary, North Carolina).

## RESULTS

In choosing the correct diagnosis of the 4 alternatives, the performances of 5 of 6 reviewers improved significantly with the addi-

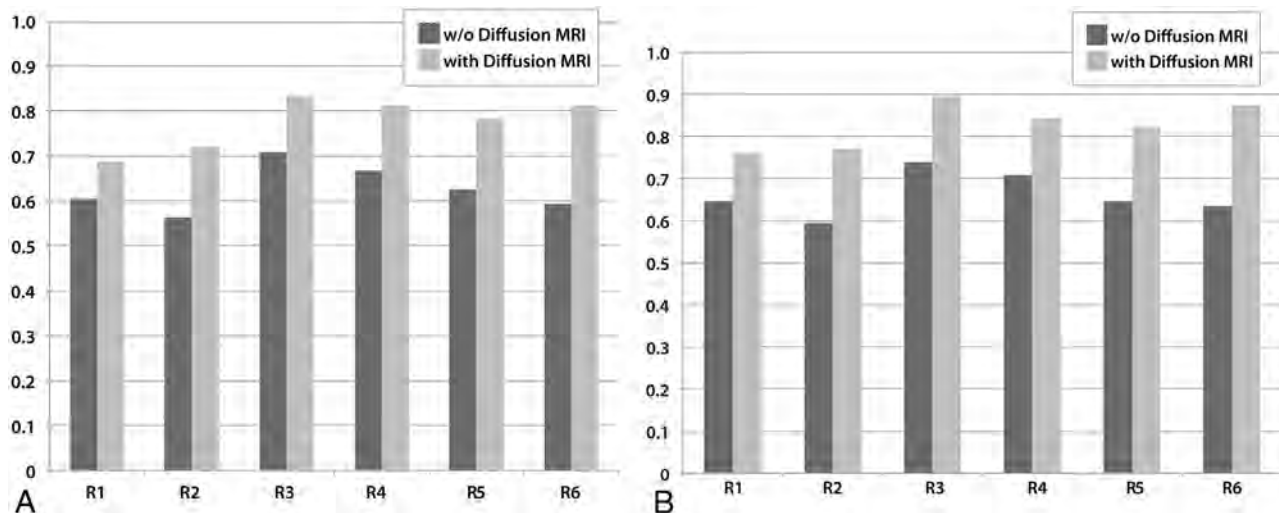


**FIG 1.** Graphs demonstrate the performances of the reviewers (R1–R4: residents, R5–R6: neuroradiologists) without (dark gray) and with (light gray) diffusion MR imaging data. *A*, When 4 choices are considered: PA, medulloblastoma, ependymoma, and AT/RT. *B*, When 3 choices are considered: embryonal tumors (medulloblastoma and AT/RT), ependymoma, and PA.

w/o Diffusion MRI with Diffusion MRI	Diagnosis				Total
	AT/RT	Ependymoma	Medulloblastoma	PA	
AT/RT	22 / 37	8 / 4	11 / 7	7 / 0	48 / 48
Ependymoma	10 / 5	81 / 81	6 / 7	5 / 9	102 / 102
Medulloblastoma	9 / 24	76 / 39	98 / 127	15 / 8	198 / 198
PA	6 / 0	31 / 23	31 / 4	160 / 201	228 / 228
Total	47 / 66	196 / 147	146 / 145	187 / 218	576 / 576

**A**

w/o Diffusion MRI with Diffusion MRI	Diagnosis			Total
	Ependymoma	Embryonal	PA	
Ependymoma	81 / 81	16 / 12	5 / 9	102 / 102
Embryonal	84 / 43	140 / 195	22 / 8	246 / 246
PA	31 / 23	37 / 4	160 / 201	228 / 228
Total	196 / 147	193 / 211	187 / 218	576 / 576

**B**

**FIG 2.** Impact of inclusion of diffusion MR imaging data to correct diagnoses. *A*, For 4 tumor categories. A total of 1,152 diagnoses (96 tumors × 6 reviewers × 2 sessions) were rendered. *B*, For embryonal tumors (medulloblastomas and AT/RTs combined), ependymomas, and PAs.

tion of the diffusion MR imaging data ( $P = .0003-.0233$ ). The performance of the remaining reviewer (a resident) also improved, but the difference did not attain statistical significance

the MR imaging diffusion data.

The mixed model suggested that there was no significant difference between the overall performances and performances with-

( $P = .1944$ ). The overall rate of correct diagnosis increased from 63%–77% with the addition of DWI data (Fig 1A).

When embryonal tumors (medulloblastoma and AT/RT) were regarded as a single group, the overall rate of correct diagnosis increased from 66%–83% with the inclusion of the diffusion MR imaging data. In this case, all of the reviewers showed statistically significant improvement with the addition of DWI data ( $P = .0001-.05$ ) (Fig 1B).

When 4 choices (PA, medulloblastoma, ependymoma, AT/RT) were considered, inclusion of the diffusion MR imaging data significantly improved the likelihood of rendering a correct diagnosis (odds ratio = 3.16, 95% confidence interval = 2.07–4.00) over all tumor types (Figs 2 and 3). By including the interaction between the diffusion MR imaging data and tumor categories into the model, we showed that there was no significant difference in the improvement effect of diffusion MR imaging data on the correct diagnosis of PAs, medulloblastomas, and AT/RTs. Of the 102 (17 ependymomas × 6 reviewers) possible correct ependymoma diagnoses, 81 correct diagnoses were provided both without and with diffusion data, indicating correct ependymoma diagnoses did not improve with the inclusion of

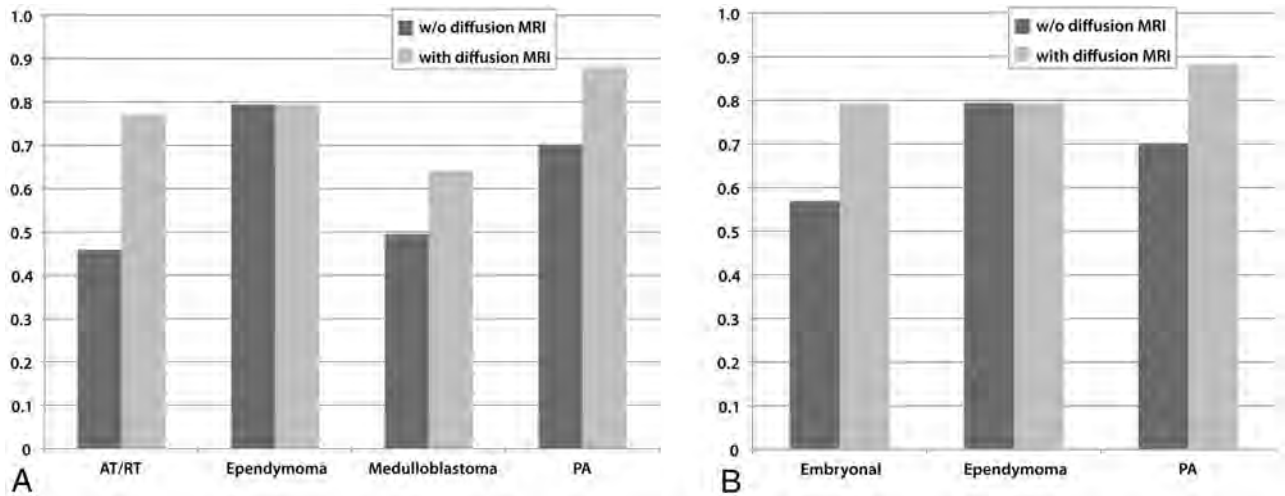


**FIG 3.** Graphs depict the percentages of correct diagnoses for tumor categories without (dark gray) and with (light gray) diffusion MR imaging data. *A*, When 4 choices are considered: PA, medulloblastoma, ependymoma, and AT/RT. *B*, When 3 choices are considered: Embryonal tumors (medulloblastoma and AT/RT), ependymoma, and PA.

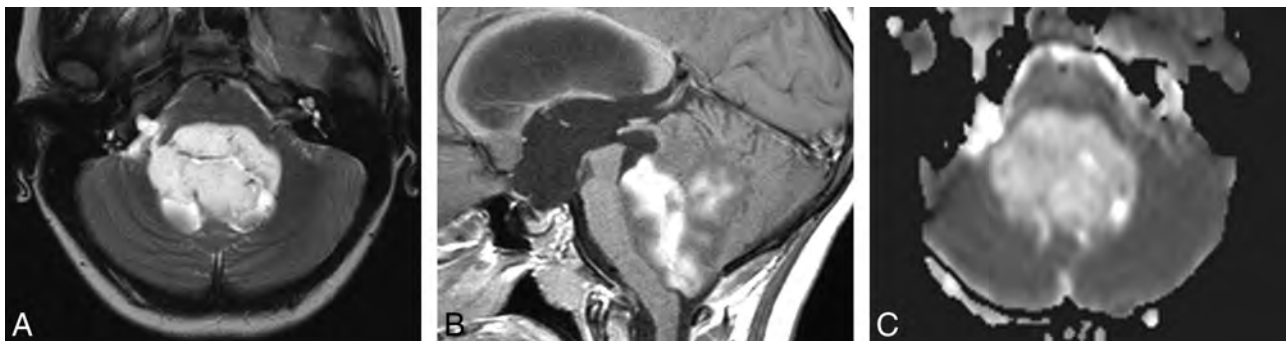


**FIG 4.** PA in a 10-year-old girl. Without diffusion MR imaging data, 5 reviewers were incorrect. Four selected ependymoma and 1 selected medulloblastoma. With diffusion MR imaging data, 5 reviewers were correct. One reviewer (a neuroradiologist) still chose ependymoma. *A*, Axial T2-weighted image displays a markedly hyperintense tumor. *B*, Sagittal gadolinium-enhanced T1-weighted image demonstrates intense and heterogeneous enhancement of the mass. *C*, ADC map shows facilitated diffusion within the mass compared with the uninvolved cerebellum.

out and with diffusion MR imaging data among the radiology residents and the neuroradiologists. The session durations were  $121.2 \pm 31.9$  minutes (min-max, 81–170) and  $120.8 \pm 40.7$  minutes (min-max, 80–170) for those without diffusion MR imaging data and with diffusion MR imaging data, respectively.

## DISCUSSION

Tumors of the posterior fossa comprise approximately 50% of intracranial tumors in children.<sup>8</sup> When brain stem tumors and choroid plexus papillomas are excluded, PAs, medulloblastomas, ependymomas, and AT/RTs make up approximately 93% of pediatric cerebellar tumors.<sup>1</sup> Therefore, when a new pediatric cerebellar tumor is encountered, it is very likely that the diagnosis will be 1 of these 4 tumors. Conventional MR imaging findings of common cerebellar tumors are well known.<sup>5,9–11</sup> PAs are characteristically well delineated, with markedly T2-weighted hyperintense solid components that may show intense enhancement with intravenous gadolinium administration. Cysts with enhancing mural nodules are associated with PAs. Ependymomas are known for their spread on the surfaces of the cerebellum and brain stem. Medulloblastomas and AT/RTs have similar conventional MR imaging findings: Both tumor categories are relatively hypoin-

tense on T2-weighted images. Medulloblastomas are more commonly midline tumors, and AT/RTs are seen in younger children (Figs 4–6). The performance of our reviewers is similar to what was reported in a study of 33 pediatric cerebellar tumors.<sup>12</sup> In this study, a pediatric neuroradiologist chose the correct diagnosis, without diffusion MR imaging data, 73% of the time among 3 groups: primitive neuroectodermal tumors, astrocytomas, and ependymomas/others.<sup>1</sup> <sup>1</sup>H-MR spectroscopy has also been used in the preoperative diagnosis of pediatric cerebellar tumors. In a study of 20 children with cerebellar tumors, reviewers blinded to the histopathologic diagnoses achieved high diagnostic accuracy—approximately 90%—with the use of <sup>1</sup>H-MR spectroscopy data.<sup>13</sup>

Diffusion MR imaging offers an important utility in the preoperative diagnosis of pediatric cerebellar tumors, primarily because of the vastly different cellularity and extracellular architecture of the common tumor types. For example, PAs are relatively paucicellular neoplasms with large extracellular spaces.<sup>14</sup> These features are likely to be responsible for the facilitated diffusion that PAs display.<sup>1,2,4,15</sup> Conversely, medulloblastomas and AT/RTs are hypercellular tumors with diminutive extracellular matrices, resulting in relatively decreased ADC val-

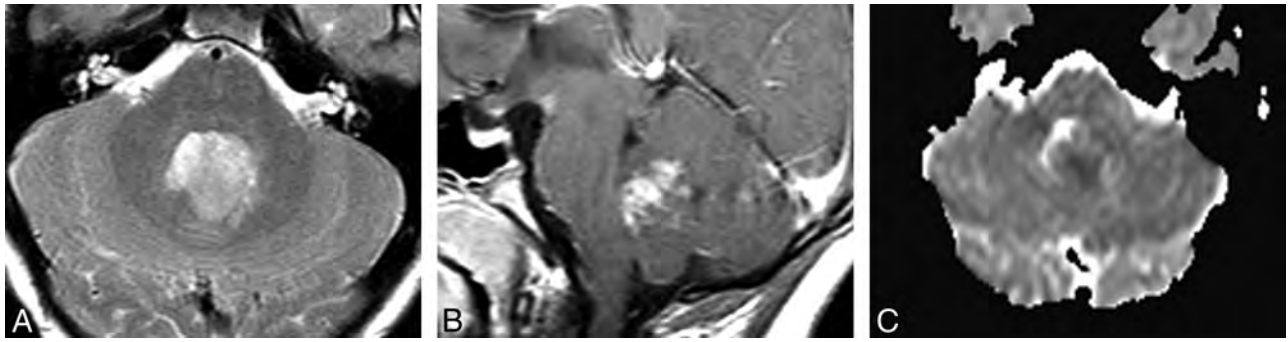


**FIG 5.** Medulloblastoma in a 12-year-old boy. Without diffusion MR imaging data, 4 reviewers (3 residents and 1 neuroradiologist who chose ependymoma) were incorrect. With diffusion MR imaging data, all reviewers were correct. A, Axial T2-weighted image shows that the tumor in the fourth ventricle is relatively hypointense. B, Sagittal gadolinium-enhanced T1-weighted image shows that the tumor enhances intensely and heterogeneously. C, ADC map shows that the tumor is slightly hypointense to isointense compared with the normal cerebellum.

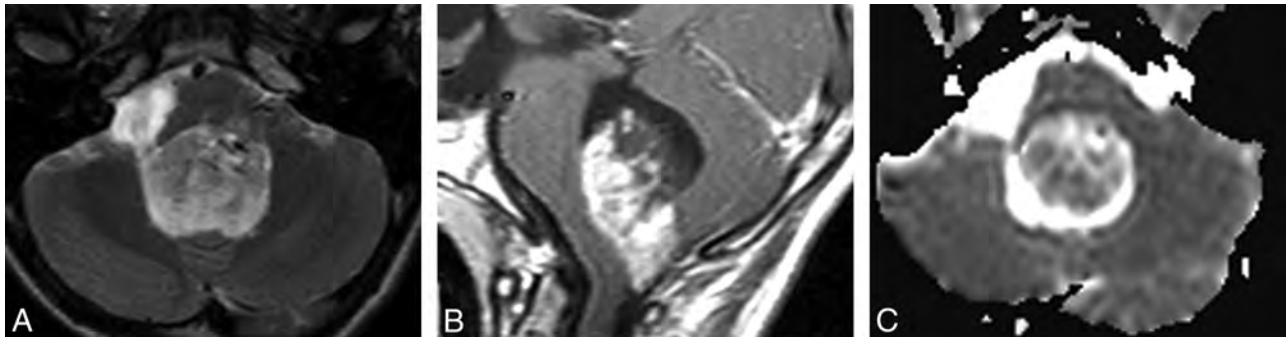


**FIG 6.** Ependymoma (WHO grade 2) in a 15-year-old boy. Without diffusion MR imaging, all reviewers were correct. With diffusion data, 3 reviewers (2 residents and 1 neuroradiologist) changed their diagnoses to medulloblastoma. A, Axial T2-weighted image demonstrates a hyperintense mass extending toward the right foramen of Luschka. B, Sagittal gadolinium-enhanced T1-weighted image shows that the tumor is heterogeneous, but intense with enhancement. C, ADC map shows that the mass is isointense to slightly hyperintense compared with normal cerebellum.

ues and hyperintensity on  $b = 1000 \text{ s/mm}^2$  or exponential diffusion images.<sup>15-17</sup>

Although the usefulness and limitations of diffusion MR imaging in the preoperative diagnosis of cerebellar tumors have been studied previously,<sup>1,2,4,17,18</sup> to our knowledge, there are no publications that evaluated the additional value of diffusion MR imaging in improving the accuracy of preoperative diagnosis in this context. Our results show that inclusion of diffusion MR imaging into the imaging protocol significantly improved the performance of all but 1 reviewer (a resident) in choosing the correct diagnosis of the 4 possible choices. This reviewer's performance improved as well, but the improvement did not reach statistical significance. We found that the percentage of correct ependymoma diagnosis did not change with the inclusion of the diffusion MR imaging data. The improvement in the performances of the reviewers with usage of the diffusion MR imaging data resulted from increased correct diagnoses of PAs, medulloblastomas, and AT/RTs. Difficulty in deciding whether ependymomas displayed restricted, facilitated, or normal (ie, isointense to normal brain on ADC maps) diffusion may have contributed to the lack of improvement in the evaluation of ependymomas with the diffusion MR imaging data.

It is justifiable to consider the embryonal tumors (medulloblastoma and AT/RT) of the posterior fossa as a single group, given their very similar imaging characteristics on conventional MR imaging and diffusion MR imaging. The main discriminators

between medulloblastomas and cerebellar AT/RTs are the age of the patient at presentation and, to a lesser extent, the location of the tumor. When choices were between embryonal tumors, ependymoma, and PA, there was statistically significant improvement in the performances of all the reviewers with inclusion of the diffusion MR imaging data. The improvement in performance was achieved without additional cost in time to arrive at a diagnosis.

The lack of statistically significant difference between the performances and improvements in the performances of the residents and neuroradiologists may be attributed to the relative ease with which to distinguish the characteristics of the common pediatric cerebellar tumors. The more recent exposure of the residents to pediatric neuroradiology at a tertiary referral center in which there is a busy neuro-oncology program may have contributed to their performances favorably. At our pediatric neuroradiology service, during read-outs with residents and at teaching sessions, the utility of diffusion MR imaging in the diagnosis of pediatric cerebellar tumors is discussed emphatically. The neuroradiologists, on the other hand, were exclusively practicing adult neuroradiology without routine exposure to pediatric neuroradiology.

One potential limitation of our study is the exclusion of posterior fossa tumors other than the 4 most common cerebellar tumors. The justification for the exclusion of brain stem tumors is the relative ease with which to distinguish them from the cerebel-

lar tumors; therefore brain stem tumors are not generally considered in the differential diagnosis of pediatric cerebellar tumors. The reason for the exclusion of the choroid plexus tumors was 2-fold: First, their imaging characteristics—intensely enhancing intraventricular masses with nodular surface features resembling a frond—allow for relatively easy discrimination of choroid plexus tumors from other tumors of the posterior fossa. Second, they are relatively infrequent compared with the 4 tumor categories included in this series. Gangliogliomas were also excluded as they rarely involve the cerebellum in children.<sup>1</sup> In a report of 10 gangliogliomas (including 2 patients under the age of 18 years), the minimum ADC values were provided.<sup>19</sup> These values appear to approximate values reported for PAs.<sup>1,2,4</sup> Although gangliogliomas of the cerebellum may be considered in the differential diagnosis of a pediatric cerebellar mass that shows facilitated diffusion, given their low incidence, in practice, they are rarely included.

Whether seeing the examinations for the second time improved the performance independent of the diffusion MR imaging data may be considered as a confounding factor and thus a limitation; however, because the correct diagnoses were not disclosed after either the first or the second session, the impact of this probably is minimal, if any. Additionally, recall is not considered a factor in the study design because the correct diagnoses and information on the reviewers' performances were not given after the first session.

It is also important to emphasize that the purpose of our study was not to demonstrate the utility of diffusion MR imaging in the preoperative diagnosis of common cerebellar tumors but to show the improvement, if any, provided by the inclusion of the diffusion MR imaging data into the imaging protocol among reviewers with different experience levels. Therefore, we believe that it was reasonable to limit the possible diagnoses offered to the reviewers to the most common pediatric cerebellar neoplasms for which usefulness of diffusion MR imaging was previously described.

## CONCLUSIONS

Our results show that inclusion of diffusion MR imaging data in the imaging protocol significantly improves the accuracy of preoperative diagnosis of common pediatric cerebellar tumors among reviewers with different experience levels. The improvement results from increased correct diagnoses of PAs, medulloblastomas, and AT/RTs. We found no impact of diffusion MR imaging on the correct diagnosis of ependymomas. The improvement in the performance of the reviewers was achieved with minimal additional penalty in imaging time (<1 minute) and without penalty in interpretation duration.

## REFERENCES

- Gimi B, Cederberg K, Derinkuyu B, et al. **Utility of apparent diffusion coefficient ratios in distinguishing common pediatric cerebellar tumors.** *Acad Radiol* 2012;19:794–800
- Jaremko JL, Jans LB, Coleman LT, et al. **Value and limitations of diffusion-weighted imaging in grading and diagnosis of pediatric posterior fossa tumors.** *AJNR Am J Neuroradiol* 2010;31:1613–16
- Kan P, Liu JK, Hedlund G, et al. **The role of diffusion-weighted magnetic resonance imaging in pediatric brain tumors.** *Childs Nerv Syst* 2006;22:1435–39
- Rumboldt Z, Camacho DL, Lake D, et al. **Apparent diffusion coefficients for differentiation of cerebellar tumors in children.** *AJNR Am J Neuroradiol* 2006;27:1362–69
- Koral K, Gargan L, Bowers DC, et al. **Imaging characteristics of atypical teratoid-rhabdoid tumor in children compared with medulloblastoma.** *AJR Am J Roentgenol* 2008;190:809–14
- Poretti A, Meoded A, Huisman TA. **Neuroimaging of pediatric posterior fossa tumors including review of the literature.** *J Magn Reson Imaging* 2012;35:32–47
- Raybaud C, Barkovich AJ. **Intracranial, orbital, and neck masses of childhood.** In: Barkovich AJ, Raybaud C, editors. *Pediatric Neuroimaging*. 5th ed. Philadelphia: Lippincott Williams & Wilkins; 2012:637–807
- Harwood-Nash DC. **Primary neoplasms of the central nervous system in children.** *Cancer* 1991;67:1223–28
- Koeller KK, Rushing EJ. **From the archives of the AFIP: pilocytic astrocytoma: radiologic-pathologic correlation.** *Radiographics* 2004;24:1693–708
- Smith AB, Smirmiotopoulos JG, Horkanyne-Szakaly I. **From the radiologic pathology archives: intraventricular neoplasms: radiologic-pathologic correlation.** *Radiographics* 2013;33:21–43
- Yuh EL, Barkovich AJ, Gupta N. **Imaging of ependymomas: MRI and CT.** *Childs Nerv Syst* 2009;25:1203–13
- Arle JE, Morriss C, Wang ZJ, et al. **Prediction of posterior fossa tumor type in children by means of magnetic resonance image properties, spectroscopy, and neural networks.** *J Neurosurg* 1997;86:755–61
- Harris LM, Davies N, Macpherson L, et al. **The use of short-echo-time <sup>1</sup>H MRS for childhood cerebellar tumours prior to histopathological diagnosis.** *Pediatr Radiol* 2007;37:1101–09
- Scheithauer BW, Hawkins C, Tihan T, et al. **Pilocytic astrocytoma.** In: Louis DN, Ohgaki H, Wiestler OD, et al, eds. *WHO Classification of Tumours of the Central Nervous System*. Lyon, France: International Agency for Research on Cancer; 2007:14–21
- Gauvain KM, McKinstry RC, Mukherjee P, et al. **Evaluating pediatric brain tumor cellularity with diffusion-tensor imaging.** *AJR Am J Roentgenol* 2001;177:449–54
- Yamashita Y, Kumabe T, Higano S, et al. **Minimum apparent diffusion coefficient is significantly correlated with cellularity in medulloblastomas.** *Neurol Res* 2009;31:940–46
- Rumboldt Z. **The Holy Grail and the quest for the gold standard.** *AJNR Am J Neuroradiol* 2010;31:1617–18
- Forbes JA, Reig AS, Smith JG, et al. **Findings on preoperative brain MRI predict histopathology in children with cerebellar neoplasms.** *Pediatr Neurosurg* 2011;47:51–59
- Kikuchi T, Kumabe T, Higano S, et al. **Minimum apparent diffusion coefficient for the differential diagnosis of ganglioglioma.** *Neurol Res* 2009;31:1102–07

# No Evidence for Impairment of Venous Hemodynamics in Children or Young Adults with Pediatric-Onset Multiple Sclerosis

S. Laughlin, C.K. Macgowan, J. Traubici, K. Chan, S. Khan, D.L. Arnold, R.A. Marrie, and B. Banwell



## ABSTRACT

**BACKGROUND AND PURPOSE:** Chronic cerebrospinal venous insufficiency is a postulated etiologic factor for multiple sclerosis, but the higher frequency with longer disease duration and progressive disability suggests that chronic cerebrospinal venous insufficiency is secondary to chronic disease. We evaluated the presence of chronic cerebrospinal venous insufficiency in pediatric-onset MS.

**MATERIALS AND METHODS:** Twenty-six pediatric patients with MS (18 years of age or younger), 26 age-matched healthy controls, and 13 young adults with pediatric-onset MS underwent sonography of the internal jugular, vertebral, and deep cerebral veins. Five venous hemodynamic criteria were assessed, with 2 criteria required for chronic cerebrospinal venous insufficiency. MR imaging studies, performed in the pediatric patients with MS and healthy control groups, included intracranial 2D time-of-flight MR venography and velocity-sensitive phase-contrast sequences. Contrast-enhanced brain MR images were obtained in pediatric patients with MS to further evaluate venous patency. We used paired *t* tests, Wilcoxon matched pairs, McNemar tests, and exact conditional logistic regression to estimate the association of chronic cerebrospinal venous insufficiency with MS.

**RESULTS:** Fifty participants (73.5%) had normal ultrasound findings, 15 (23.1%) met 1 venous hemodynamic criterion, and 2 pediatric patients with MS and 1 young adult with pediatric-onset MS met chronic cerebrospinal venous insufficiency criteria. Chronic cerebrospinal venous insufficiency was not associated with MS (odds ratio, 2.41; 95% CI, 0.19-infinity). Demographic and disease characteristics did not differ between the patients with MS meeting chronic cerebrospinal venous insufficiency criteria (*n* = 3) and those who did not (*n* = 36; all, *P* > .05). The mean (SD) MR imaging measures of intracerebral flow did not differ between the 2 pediatric patients with MS meeting chronic cerebrospinal venous insufficiency criteria ( $0.85 \pm 0.11$ ) and healthy controls ( $0.87 \pm 0.16$ , *P* = .50); no child demonstrated venous obstruction.

**CONCLUSIONS:** Chronic cerebrospinal venous insufficiency is rarely observed in children or young adults with pediatric-onset MS. Venous anatomy and flow rates indicate that venous outflow is intact in pediatric patients with MS. Our findings argue against chronic cerebrospinal venous insufficiency as a component of MS etiology.

**ABBREVIATIONS:** APOMS = young adults with pediatric-onset MS; CCSVI = chronic cerebrospinal venous insufficiency; EV = epidural vein; HC = healthy control; IJV = internal jugular vein; pedMS = pediatric patients with MS; RRMS = relapsing-remitting MS; VH = venous hemodynamic

Chronic cerebrospinal venous insufficiency (CCSVI), a sonography-defined pattern of cerebral venous drainage, has been reported in a variable proportion of adults with multiple sclerosis (reviewed in Awad et al<sup>1</sup> and Laupacis et al<sup>2</sup>). A combination of

findings of altered venous flow, venous stenoses with presumed secondary venous drainage patterns (termed “excision circles”), or reflux in extracranial draining veins led to the term CCSVI.<sup>3</sup> In the original report of CCSVI in adult patients with MS, sonographic studies of the internal jugular and vertebral veins and transcranial Doppler studies of deep cerebral venous structures showed  $\geq 1$  of 5 parameters that were absent in healthy subjects.<sup>4</sup>

Received December 16, 2012; accepted after revision January 29, 2013.

From the Departments of Diagnostic Imaging (S.L., J.T.), Medical Biophysics (C.K.M., K.C.), and Neuroscience and Mental Health (S.K., B.B.), The Hospital for Sick Children and Research Institute, University of Toronto, Ontario, Canada; McConnell Brain Imaging Center (D.L.A.), McGill University, Montreal, Quebec, Canada; Departments of Internal Medicine (Neurology) and Community Health Sciences (R.A.M.), University of Manitoba, Winnipeg, Manitoba, Canada; and Department of Neurology (B.B.), Children's Hospital of Philadelphia, Philadelphia, Pennsylvania.

Statistical analysis was performed by Ruth Ann Marrie. Drs Laughlin, Banwell, Arnold, Marrie, and Macgowan contributed to the study concept and design. Drs Laughlin, Banwell, and Macgowan and S. Khan, K. Chan, and J. Traubici were instrumental in the acquisition of data. Drs Marrie, Banwell, Laughlin, and Macgowan provided data analysis and interpretation. Drs Laughlin, Banwell,

Marrie, and Macgowan provided critical revision of the manuscript for important intellectual content. Dr Banwell was primarily responsible for study supervision and procurement of grant support.

This work was supported by grants from the Multiple Sclerosis Society of Canada.

Please address correspondence to Brenda Banwell, MD, Division Chief, Neurology, Professor of Pediatrics (Neurology), Children's Hospital of Philadelphia, 34th and Civic Center Blvd, Philadelphia, PA. 19104-4399; e-mail: banwellb@email.chop.edu

Indicates article with supplemental on-line table

<http://dx.doi.org/10.3174/ajnr.A3661>

These parameters included reflux in the internal jugular veins (IJVs) or vertebral veins in sitting or supine positions (in contrast to the anticipated venous flow toward the heart); spontaneous intravenous reflux ascending superiorly into at least 1 of the deep cerebral veins, including the internal cerebral veins, basal veins of Rosenthal, or vein of Galen; evidence of proximal IJV stenosis with B-mode echo color high-resolution Doppler sonography; lack of detectable venous flow on Doppler sonography in the IJVs or vertebral veins; and reversed postural control of the main cerebral venous outflow pathway. Transfemoral catheter venography was used in these studies to more fully delineate the venous anatomy.<sup>3</sup>

On the basis of these observations, it was postulated that impaired venous drainage, particularly when accompanied by reflux of flow, may lead to increased intracerebral venous pressure, which, in turn, may exacerbate transudation of inflammatory cells through the perivenous endothelial cells of the blood-brain barrier. If impaired cerebrospinal venous drainage is the fundamental pathologic underpinning of MS, then such impairment should be evident from the onset of disease. However, data showing a higher frequency of CCSVI in persons with MS who are older,<sup>5</sup> have secondary-progressive MS,<sup>5</sup> or have greater physical disability<sup>5,6</sup> suggest that CCSVI reflects chronic disease rather than being an etiologic factor as originally proposed.<sup>3</sup>

If CCSVI is an etiologic factor for MS, it should be evident even in the youngest patients with MS. Before exploring such an assertion, it is first important to establish whether pediatric-onset and adult-onset MS are comparable clinical disorders. The onset of MS during childhood or adolescence is associated with a relapsing-remitting MS (RRMS) clinical course in >95% of patients.<sup>7</sup> While clinical relapse features are similar in pediatric and adult patients with RRMS, the relapse rate appears higher in pediatric patients with MS,<sup>8</sup> and very young pediatric patients with MS may experience relapses associated with encephalopathy.<sup>9</sup> The 2010 revision of the McDonald diagnostic criteria for MS encompassed pediatric patients with MS<sup>10</sup> and has now been validated in pediatric patients with MS<sup>11</sup> with the caveat that very young children may have unique clinical and MR imaging features at the onset and a more typical adult-onset phenotype with time.<sup>12</sup> Overall, clinical, biologic, and neuroimaging data all support a shared biology between pediatric- and adult-onset MS.

Patients with pediatric-onset MS provide an opportunity to evaluate the prevalence of CCSVI in a young MS population without the potential confounders of disability or age-related comorbid health conditions. While the presence of CCSVI in a pediatric MS population would support an etiologic role for CCSVI, we hypothesized that CCSVI is not a component of MS etiology and, if present, is a consequence of long-standing disease and aging vessels. We thus evaluated the frequency of CCSVI in children with MS and a group of adult patients with MS who experienced MS onset during childhood and thus have prolonged disease duration but still young vasculature. We used the originally described<sup>4</sup> high-resolution echo color Doppler and transcranial color-coded Doppler sonography methods. A limitation of sonographic assessment of venous patency relates to artifactual narrowing induced by pressure on the vessel by the sonographic probe,<sup>13</sup> and we thus also evaluated venous anatomy by using

phase-contrast measurements in the upper neck and 2D TOF MR venography assessment of the dural venous sinuses. Finally, abnormalities of venous anatomy or compromised venous flow (stenosis) alone do not necessarily lead to global cerebrospinal venous insufficiency or to increased venous pressures. The cerebral and neck veins are part of a low-resistance system with considerable redundancy in terms of bilaterality and with respect to the capacity for the use of collateral vessels. Partial or complete obstruction of a single vessel may have little impact on total cerebral venous outflow. We thus also measured venous blood flow pulsatility as a surrogate for elevated venous pressure. Downstream constriction of venous flow tends to shift a greater proportion of the total pressure drop between the aorta and vena cava toward these constricted vessels. The vessels upstream of the constriction thereby experience higher pressures and greater cardiac pulsation. Using these 3 methods, we provide a comprehensive assessment of cerebral venous flow in pediatric MS.

## MATERIALS AND METHODS

Our primary study outcome was the frequency of CCSVI in pediatric patients with MS compared with age-matched healthy children based on sonography. We also aimed to correlate sonographic evidence of venous insufficiency in pediatric patients with MS and controls with MR venography and phase-contrast MR evaluation of venous outflow. A tertiary objective was to determine whether CCSVI was present in young adults with pediatric-onset MS and, if so, whether CCSVI was associated with disease duration.

**Participants.** To address our primary outcome, we consecutively enrolled 2 participant groups: 1) pediatric MS: children and adolescents, 18 years of age or younger, with relapsing-remitting MS<sup>14</sup> followed in the pediatric MS program at the Hospital for Sick Children between July 2010 and March 2012; and 2) healthy controls (HCs). All patients with RRMS registered in our MS program were notified by mail and in person during clinic visits. For each pediatric patient with MS (pedMS), an unrelated age-matched healthy control participant was recruited through local advertisement, none of whom had a first degree relative with MS. To address our tertiary study objective, we also enrolled young adults with pediatric-onset MS (APOMS) previously followed in the pediatric MS program. We did not enroll healthy adult controls, given that our goal was to explore whether features of CCSVI were present in young adults with pediatric-onset RRMS, not to compare the relative frequency of such features with those of healthy adults. Furthermore, a wealth of studies has already documented the frequency of sonographic features of CCSVI in healthy adult cohorts.

All participants were required to avoid caffeine-containing fluids on the day of testing. None of the participants were receiving stimulant medications or reported exposure to illicit drugs, had a history of head or neck injury, or had known cerebrovascular disease. All patients with MS were >30 days from most recent relapse or corticosteroid exposure. Demographic data, age at onset, disease duration, current medications, and Expanded Disability Status Scale scores were captured for all patients with MS on the day of the sonography.

All participants and their families provided informed consent, and the study was approved by the Research Ethics Board at the Hospital for Sick Children.

**Sonography.** Two experienced pediatric sonography technologists and 2 pediatric radiologists attended a 1-week Cerebral Venous Function and Anomaly Program at Buffalo Neuroimaging Analysis Center, The Jacobs Neurologic Institute, State University of New York, Buffalo (R. Zivadinov, MD, Program Director), which included instruction, demonstration, and hands-on training in cerebrospinal venous scanning by using similar sonographic methods previously outlined by Zamboni et al.<sup>3</sup>

Sonography technologists and pediatric radiologists were blinded to participant group. Participants were brought into the sonography suite and were positioned and draped by a study assistant before the ultrasonographer entered the room. All participants were requested to remain silent during the examination. After completing the sonography, the ultrasonographer left the room before the participant was permitted to move from the sonography table. All ultrasounds were observed by a study assistant to ensure compliance with blinding procedures. Because we did not match the APOMS group to controls, we cannot exclude the possibility that the sonography staff may have been unblinded to MS diagnosis in these older participants (all 23 years of age or younger).

Sonographic examinations were performed with participants positioned supine and at 90°(sitting) following 2 minutes of rest and normal breathing in each position by using an IU 22 sonography unit (Philips Medical Systems, Bothell, Washington). For studies of the neck, a high-frequency L9–3-MHz linear transducer or a C8–5-MHz small curved-array transducer was used to assess the internal jugular veins and vertebral veins bilaterally, applying minimal neck pressure. For the transcranial studies, a lower frequency probe was used (S5–1 transcranial sector probe) to assess either a basal vein of Rosenthal or internal cerebral vein. Sonographic data were scored by consensus according to the 5 venous hemodynamic (VH) criteria detailed by Zamboni et al.<sup>3</sup> CCSVI was considered present if 2 of the VH criteria were met (as detailed in the On-line Table).

**MR Imaging Studies.** As per our primary study objective, pedMS and HC groups were also offered noninvasive MR imaging assessment of the brain and intracranial venous anatomy, including 2D time-of-flight MR venography and phase-contrast MR imaging measures of venous flow interrogating overall cerebral blood circulation by using a standardized MR imaging protocol on the same 3T scanner (Magnetom TrioTim; Siemens, Erlangen, Germany), while contrast-enhanced MR imaging by using intravenous gadolinium was acquired in pedMS only (On-line Table). The TOF–MR venography contrast-enhanced MR imaging evaluated the patency of the jugular bulbs, dural venous sinuses, and internal cerebral veins.

**Phase-Contrast MR Imaging.** Axial-oblique phase-contrast MR imaging measures of venous flow data were acquired from the neck with the section oriented perpendicular to the dominant vessel orientations at the C2–C3 level. Participants were imaged supine during free breathing to maintain resting cardiovascular physiology. A segmented and cardiac-gated 2D phase-contrast

MR imaging sequence with through-plane velocity encoding was used (parameters listed in the On-line Table). Flow images were acquired at 2 velocity sensitivities, the first to measure right and left IJVs, internal carotid artery, and vertebral artery flows (maximum velocity without aliasing = 100 cm/s) and the second to measure slower right and left epidural vein (EV) flows (maximum velocity without aliasing = 30 cm/s). If aliasing was detected, the velocity sensitivity of the acquisition was reduced and the scan was repeated. The scan time for each series was approximately 2 minutes. To ensure that intraindividual flow values were stable, we acquired these sequences twice, within the first 10 minutes of imaging and just before completion of the MR imaging examination. The 2 flow values for each participant were compared for each of the 8 vessels.

For each vessel, total flow per minute (milliliter/min) was calculated by using the analysis package Segment (Version 1.8; Medviso, Lund, Sweden).<sup>15</sup> This validated software provided automatic detection of the vessel lumen throughout the cardiac cycle, based on an initial manual contour prescribed by the user, and enabled cinematic playback of the region of interest superimposed on the images to verify placement. Background phase correction was also applied on the basis of surrounding static tissue.<sup>16</sup> Region-of-interest assessment was performed independently by 2 investigators (K.C., C.K.M.). Data from a subset of subjects were analyzed twice by both investigators to test inter- and intraobserver reliability according to the intraclass correlation coefficient on a per-vessel basis.

If flow in a specific vessel could not be determined (vessel not visualized, aliasing of flow, artifacts) at both time points, the net flow rate for that participant was not calculated. To detect the potential redistribution of venous flow secondary to venous stenoses, we calculated the ratio of total measured venous flow to total measured arterial flow, (IJV + EV) / (Internal Carotid + Vertebral Artery). We hypothesized that this ratio would be lower in participants with venous insufficiency secondary to flow redistribution to alternative venous pathways.<sup>17,18</sup>

### **Statistical Analysis**

Continuous variables were summarized as mean (SD) or median (interquartile range) as appropriate. Categorical variables were described as frequency (percentage). Continuous variables were compared between the pedMS and HC groups by using a paired *t* test or Wilcoxon matched pairs test as appropriate. Categorical variables were compared by using the McNemar test. Exact conditional logistic regression was used to examine the association of CCSVI with pediatric MS among the pedMS and matched HCs; the number of affected individuals was too small to adjust for factors that were not matched. In the MS group, we evaluated sonographic findings as a function of time by comparing the disease duration between MS cases with and without CCSVI (as defined by the presence of 2 of the 5 VH criteria) by using a Wilcoxon test. Furthermore, we correlated disease duration with the total number of positive VH criteria by using a Spearman rank correlation. The mean and SD were calculated for the venous-to-arterial flow ratio for all pedMS and HCs, provided that values for all 8 vessels were recorded on at least 1 of the 2 phase-contrast–MR imaging time points. For paired comparisons, both

members of the matched pair were required to have results available for all 8 vessels. *P* values < .05 were considered significant. Analyses were performed by using SAS, Version 9.2 (SAS Institute, Cary, North Carolina).

## RESULTS

**Participants.** Table 1 details the demographic features of the 65 (26 pedMS, 26 HCs, and 13 APOMS) participants. Most patients with MS were receiving disease-modifying therapy; all were considered to have RRMS and all had normal ambulation.

**Sonography.** Sonographic study findings were completely normal, with no evidence for any of the 5 VH criteria in 47 of 65 participants (72.3%). Eighteen participants demonstrated 1 or 2 of the VH criteria (Table 2). VH criterion 3 was the most common finding, present in 14 of 65 participants (21.5%), while 6 participants met VH criterion 1 (9.2%) and 1 participant met VH criterion 5 (1.5%). None of the participants met VH criterion 2 or 4. The frequency of each criterion across the 3 participant groups is also detailed in Table 2. In an unmatched analysis of the pedMS and HC groups, the frequency of meeting any one criterion did not differ between groups (Fisher exact test; all, *P* > .05); findings were the same by using a matched analysis.

CCSVI criteria were met in 3 participants, 2 pedMS and 1 APOMS. All 3 participants met CCSVI criteria based on positive findings for criterion 1 and criterion 3. Using exact conditional logistic regression including the matched pedMS and HCs, we

found that the frequency of CCSVI did not differ between groups (odds ratio, 2.41; 95% CI, 0.19–infinity). Unconditional logistic regression adding the APOMS group produced similar findings (odds ratio, 2.60; 95% CI, 0.27–infinity). The 3 patients with MS meeting the criteria for CCSVI did not differ from the 36 who did not in terms of sex, average age of onset, disease duration, or Expanded Disability Status Scales score (data not shown).

**MR Venography.** On the TOF-MR venography (pedMS and HC) and postgadolinium sagittal T1 3D MPRAGE sequences (pedMS only), no MR imaging evidence of acute dural venous sinus thrombosis was noted. Some participants had dominant right or left transverse and/or sigmoid sinuses, while in others, these were codominant. Expected anatomic variants were also noted, including arachnoid granulations, accessory occipital sinuses, partial duplication of the superior sagittal sinus, and transosseous emissary veins. One patient with pediatric MS had a hypoplastic straight sinus, which had also been noted on previous clinical MR imaging and was stable. In addition to the MR venography, our protocol also included a sagittal postcontrast T1 3D MPRAGE sequence, which was reviewed carefully in all patients to confirm patency of the dural venous sinuses.

**Phase-Contrast Vascular Flow.** The mean venous-to-arterial flow ratio (l/min) did not differ between pedMS and HCs, being on average  $0.85 \pm 0.11$  in the pedMS population and  $0.87 \pm 0.16$  in HCs (*t* =  $-0.69$ , *P* = .50). The mean flow ratio in the 2 pedMS who met the CCSVI criteria was  $0.94 \pm 0.12$ , which did not differ from the ratio in the 39 pedMS and HCs who did not meet the CCSVI criteria ( $0.86 \pm 0.14$ , *P* = .49). Thus no difference in venous-to-arterial flow ratios was detected in subjects meeting CCSVI criteria.

Consistent identification of the internal jugular veins was possible by using not only vessel area and position but also flow direction (head-to-foot). Inter- and intraobserver agreement between flow measurements was excellent: The intraobserver intraclass correlation coefficient was >0.97, and the interobserver intraclass correlation coefficient

**Table 1: Demographic and clinical features of the 65 participants**

Feature	Healthy Pediatric Controls (n = 26)	Pediatric RRMS (n = 26)	APOMS RRMS (n = 13)
Female (No.)	18 (69.2%)	16 (61.5%)	8 (61.5%)
Age at enrollment (yr) (mean) (SD)	15.4 (3.6)	16.2 (2.5)	20.3 (2.9)
Range (yr)	(8.94–18.61)	(9.36–18.08)	(18.24–23.76)
Age at first attack (mean) (SD) (yr)	N/A	12.3 (3.9)	13.9 (3.6)
Disease duration (mean) (SD) (yr)	N/A	3.9 (4.4)	6.5 (3.7)
Range (yr)		(0.67–13.34)	(4.01–10.42)
EDSS (median, IQR)	N/A	1.5 (1.0, 2.5)	1.5 (1.0, 2.0)
Medications used (No.) (%)	N/A		
None		9 (34.7)	2 (15.4)
IFN		11 (42.3)	7 (53.9)
GA		4 (15.4)	2 (15.4)
Other		2 (7.7)	2 (15.4)

**Note:**—N/A indicates not applicable; EDSS, Expanded Disability Status Scale; IQR, interquartile range; IFN, interferon; GA, glatiramer acetate.

**Table 2: Ultrasound findings for adults and children with MS and HCs**

Group	Venous Hemodynamic Insufficiency Criteria					CCSVI
	1	2	3	4	5	
	Reflux in neck vessels	Reflux in deep cerebral veins	IJV stenosis, noncompliance and B-mode anomalies	Absence of Doppler flow	Negative IJV CSA	Minimum of 2 criteria
	IJV supine IJV 90°	ICV Basal vein of Rosenthal	CSA < 0.3 cm <sup>2</sup>	IJV VV		
	VV supine VV 90°					
PedMS (n = 26)	3 (11.5%)	0	7 (26.9%)	0	1 (3.8%)	2 (7.7%)
APOMS (n = 13)	2 (15.4%)	0	2 (15.4%)	0	0	1 (7.7%)
HCs (n = 26)	1 (3.8%)	0	5 (19.2%)	0	0	0

**Note:**—VV indicates vertebral vein; CSA, cross-sectional area; ICV, internal cerebral vein.

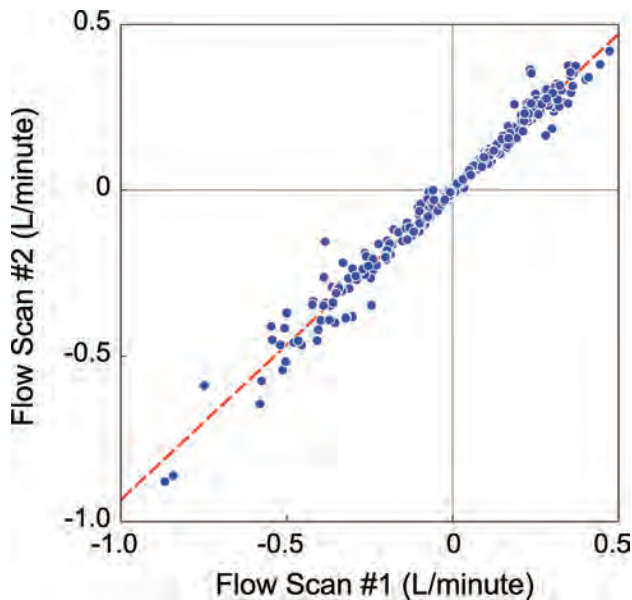


**FIG 1.** Reproducibility of vessel flow measurements on phase-contrast MR imaging between first and second measurements (across all vessels examined).

**Table 3: Average (SD) flow rates (L/min) in arteries and veins<sup>a</sup>**

Vessel	pedMS	HCs	P Value
ICA, right	0.26 (0.058)	0.26 (0.033)	.63
ICA, left	0.26 (0.058)	0.27 (0.038)	.92
IJV, right	-0.33 (0.18)	-0.33 (0.21)	.20
IJV, left	-0.19 (0.13)	-0.25 (0.15)	.19
VA, right	0.096 (0.05)	0.11 (0.033)	.14
VA, left	0.10 (0.037)	0.12 (0.045)	.30
EVs, right	-0.033 (0.029)	-0.054 (0.047)	.066
EVs, left	-0.037 (0.036)	-0.050 (0.030)	.056

**Note:**—VA indicates vertebral artery.

<sup>a</sup>Negative values represent flow in the superior-to-inferior direction.

was  $>0.93$ , indicating that inherent flow differences between subjects exceeded the variance of the measurement process itself. Arterial flows were obtained in all participants in at least 1 time point. In a small number of vessels, venous flows were not obtained at either time point as follows: 3 right IJVs, 1 left IJV, 1 left EVs, and 2 right EVs. These were the result of aliasing in 2 right IJVs and poor vessel visualization in the remaining cases.

Flows measured in individual vessels were highly reproducible between the start and end of the MR imaging examination (including all vessels,  $r = 0.94$ ; 95% CI, 0.92–0.95; Fig 1). However, absolute flows in a given vessel differed among individuals, particularly in the veins. For example, as shown in Table 3, the coefficients of variation in the right and left IJVs of HCs were 64% and 60%, respectively. This finding underscores the difficulty of attributing hemodynamic significance to individual venous flows at a particular location within the complex vascular network.

## DISCUSSION

In the original description of CCSVI, the 100% concordance with MS and its absence in healthy controls led to postulates that CCSVI might be congenital and etiologic in MS.<sup>4</sup> We demonstrate that CCSVI is not a key feature of pediatric MS, arguing against impaired venous drainage playing a role in the etiology of relaps-

ing-remitting MS. We also failed to demonstrate a relationship between CCSVI and prolonged disease duration in a group of young adult patients with pediatric-onset MS, suggesting that CCSVI is not an obligate feature of chronic MS, at least in patients without other comorbidities or aging vasculature. Finally, we demonstrated no difference in venous pulsatility in patients with MS compared with healthy controls, arguing against the concept of raised venous pressure in MS.

When comparing the sonographic features of the 26 pediatric patients with RRMS in our study with the 35 patients with RRMS originally described by Zamboni et al,<sup>3</sup> several contrasts are notable. More than 50% of the adult patients with RRMS met criterion 2, and  $>60\%$  met criterion 4, compared with none of our patients. Furthermore, 50%–77% of adult patients with RRMS met criterion 1 or 5, while only 4 children (7.7%) met either of these criteria, including 4 pedMS and 1 HC. However, criterion 3 was met by 26% of the adult patients with RRMS and 7 (26%) of our pediatric patients with RRMS. Here, the contrast between our work and that of Zamboni et al<sup>3</sup> relates to the frequency of criterion 3 detection in controls. We detected criterion 3 in 5 of 26 (19%) healthy children, no different from its detection in our pediatric RRMS group. Zamboni et al reported that only 1 of 235 controls met criterion 3. While criterion 3 emerged as the most common sonographic finding in our study, we could not detect any evidence of dural venous sinus thrombosis above the jugular bulbs by MR venography, nor did our phase-contrast venous flow studies suggest IJV flow impairment at the level of C2. Thus, we question whether the sonographic findings have physiologic relevance. With respect to the frequency of meeting the diagnostic requirements for CCSVI, only 2 of our pedMS (7.7%) met the criteria for CCSVI, in contrast to 100% of the adult patients with MS previously reported.<sup>4</sup>

Our study adds to the growing number of studies that have not replicated a high prevalence of CCSVI in RRMS.<sup>19–23</sup> In the largest venous sonography study to date, 56% of adult patients with MS met the criteria for CCSVI, compared with 42% of patients with other neurologic disorders and 22% of healthy adult controls.<sup>24</sup> In 2011, a meta-analysis supported a higher prevalence of sonographic features of CCSVI in MS compared with controls, but it highlighted numerous methodologic challenges, including a lack of blinding in some studies.<sup>2</sup> We used a stringent blinding procedure, which ensured that the sonography technicians and radiologists were unaware of disease status. Our sonographic findings are similar to those reported in an Italian pediatric MS cohort,<sup>25</sup> in which CCSVI was diagnosed (by consensus of 2 ultrasonographers) in 4 of 15 (26%) pedMS and 3 (18.8%) HCs. Pooling the data from both studies, which used similar sonographic techniques, yields a frequency of CCSVI of 17% (7 of 41) in pediatric patients with RRMS versus 7% (3 of 42) in age-matched healthy controls ( $P = .11$ ). Although the total number of pediatric patients with MS evaluated to date remains low, the number studied was sufficient to address our original power calculations, which were based on the 100% frequency of CCSVI in adult-onset MS initially reported.<sup>4</sup> As mentioned above, more recent analyses have indicated either no relationship or a much lower prevalence of CCSVI in some adult MS cohorts (summarized in Laupacis et

al<sup>2</sup>). As such, our sample size is not sufficiently large to exclude the possibility of a rare association of CCSVI in pediatric MS.

Our work adds to the work of Amato et al<sup>25</sup> by not only failing to find a relationship between CCSVI and pediatric MS but also providing evidence of normal venous pulsatility in children with MS. If raised venous pressure was an etiologic component of MS, even in the absence of visualized alteration in venous flow, then we would have expected to detect this in our pediatric patients with MS.

We hypothesized that if CCSVI were a feature of pediatric MS, then venous insufficiency should be identifiable by using quantitative methods. Zamboni et al<sup>3</sup> have proposed that CCSVI results in venous congestion and increased intracerebral venous pressure and ultimately in MS.<sup>26</sup> As expected, absolute arterial and venous flow rates varied among individuals owing to heart rate, body mass index, and blood pressure differences. The measured arterial inflow was highly comparable with measurable venous outflow (Table 3), and flow measures were highly reproducible within individuals (Fig 1). The venous-arterial flow ratios we measured are consistent with prior reports in adults (0.85).<sup>17</sup> Finally, venous-to-arterial flow ratios were similar in participants who did and did not meet CCSVI criteria; this finding suggests unimpaired venous outflow in the interrogated vessels of the subjects with CCSVI. This finding is consistent with the MR imaging observations that did not identify dural venous sinus thrombosis in either of the CCSVI-positive pedMS.

Some investigators have suggested that CCSVI is a consequence of chronic CNS illness, because of the higher frequency of CCSVI in patients with MS with longer disease duration and in those with more severe disability<sup>5</sup> and the low rate of CCSVI (18%) in adults with a clinically isolated syndrome.<sup>27-29</sup> In such patient populations, it is difficult to disentangle the effects of long disease duration, disability, increasing age of the cerebral vasculature, and comorbid health issues.<sup>30</sup> Therefore, we evaluated 13 young adults with pediatric-onset MS, a population with longer disease duration, little disability, no comorbidities, and young cerebral vasculature. Despite an average disease duration of 6.5 years, only 1 patient met the criteria for CCSVI and only 2 others had any abnormal VH parameters.

The plausibility of CCSVI as a component of MS pathobiology is further challenged by a recently published study using IJV ligation in a murine model.<sup>31</sup> Cerebral imaging and pathologic analyses were compared among mice undergoing ligation of the IJV, sham-operated animals, and mice induced to develop experimental allergic encephalomyelitis, an animal model of neuroinflammation similar to MS. The IJV-ligated mice developed collateral venous drainage but did not develop impaired blood-brain barriers or CNS inflammation, even with bilateral IJV ligation.

## CONCLUSIONS

We demonstrate that CCSVI is not a component of pediatric MS and thus is unlikely to be an etiologic component of MS. The controversy surrounding CCSVI was fueled by a powerful patient lobby for engagement, which extended to the pediatric MS population. Our study addressed our research aims and met the needs of our pediatric MS community. Many of the participants and their families commented that the ability to participate in a

search program evaluating a new theory for MS was empowering. Our ability to reassure our patients that CCSVI is not a key component of pediatric MS will help ensure that persons with pediatric-onset MS are not subjected to unwarranted procedures.

## ACKNOWLEDGMENTS

The authors thank A. Mohanta and J. Jarrin (senior sonography technologists); T. Rayner and R. Weiss (research MR imaging technologists); and R. Zivadinov, MD, and K. Marr for CCSVI training of sonography staff. We are indebted to the children and their families for their commitment to this study.

Disclosures: Suzanne Laughlin—RELATED: Grant: Multiple Sclerosis Society of Canada and the Canadian Multiple Sclerosis Foundation, UNRELATED: No disclosures. Christopher K. Macgowan—RELATED: Grant: Multiple Sclerosis Society of Canada and the Canadian Multiple Sclerosis Foundation, UNRELATED: Dr. Macgowan receives research funding from the Canadian Institutes of Health Research, the Ontario Research and Development Fund, and the Multiple Sclerosis Society of Canada. Jeffrey Traubici has no disclosures. Stephanie Khan—RELATED: Grant: Multiple Sclerosis Society of Canada and the Canadian Multiple Sclerosis Foundation, UNRELATED: No disclosures. Douglas L. Arnold—RELATED: Grant: Multiple Sclerosis Society of Canada and the Canadian Multiple Sclerosis Foundation, UNRELATED: Consultancy: Bayer Healthcare, Biogen Idec, EMD Serono, Genentech, Genzyme, Glaxo-SmithKline, NeuroRx Research, Novartis, Roche, Merck Serono, Teva, Employment: McGill University and NeuroRx Research, Grants/Grants Pending: CIHR, MSSC, Bayer Healthcare, Patents (planned, pending or issued): Arnold et al, US Patent No. 6,347,239, Comments: patent applies to a technology for MR spectroscopy (no relevance to current article), Stock/Stock Options: NeuroRx Research. Ruth Ann Marrie—RELATED: Grant: Multiple Sclerosis Society of Canada and the Canadian Multiple Sclerosis Foundation, UNRELATED: Ruth Ann Marrie receives research funding from the Canadian Institutes of Health Research, Public Health Agency of Canada, Manitoba Health Research Council, Health Sciences Centre Foundation, Multiple Sclerosis Society of Canada, Multiple Sclerosis Scientific Foundation, Rx & D Health Research Foundation and has conducted clinical trials funded by Bayer Inc and Sanofi-Aventis. Brenda Banwell—RELATED: Grant: Multiple Sclerosis Society of Canada and the Canadian Multiple Sclerosis Foundation, UNRELATED: Board Membership: Biogen-IDEc Advisory Board on fetal outcome from pregnancy, Comments: no financial reimbursement, Grants/Grants Pending: Multiple Sclerosis Society, Canadian Institutes of Health,\* Multiple Sclerosis Scientific Research Foundation,\* Dairy Farmers of Ontario,\* Payment for Lectures (including service on Speakers Bureaus): Serono, Biogen-Idec, Novartis.

## REFERENCES

1. Awad AM, Marder E, Milo R, et al. **Multiple sclerosis and chronic cerebrospinal venous insufficiency: a critical review.** *Ther Adv Neurol Disord* 2011;4:231–35
2. Laupacis A, Lillie E, Dueck A, et al. **Association between chronic cerebrospinal venous insufficiency and multiple sclerosis: a meta-analysis.** *CMAJ* 2011;183:E1203–12
3. Zamboni P, Galeotti R, Menegatti E, et al. **Chronic cerebrospinal venous insufficiency in patients with multiple sclerosis.** *J Neurol Neurosurg Psychiatry* 2009;80:392–99
4. Zamboni P, Menegatti E, Galeotti R, et al. **The value of cerebral Doppler venous haemodynamics in the assessment of multiple sclerosis.** *J Neurol Sci* 2009;282:21–27
5. Weinstock-Guttman B, Ramanathan M, Marr K, et al. **Clinical correlates of chronic cerebrospinal venous insufficiency in multiple sclerosis.** *BMC Neurol* 2012;12:26
6. Patti F, Nicoletti A, Leone C, et al. **Multiple sclerosis and CCSVI: a population-based case control study.** *PLoS One* 2012;7:e41227
7. Banwell B, Krupp L, Kennedy J, et al. **Clinical features and viral serologies in children with multiple sclerosis: a multinational observational study.** *Lancet Neurol* 2007;6:773–81
8. Gorman M, Healy B, Polgar-Turcsanyi M, et al. **Increased relapse rate in pediatric-onset compared with adult-onset multiple sclerosis.** *Arch Neurol* 2009;66:54–59
9. Mikaeloff Y, Caridade G, Husson B, et al. **Acute disseminated en-**

- cephalomyelitis cohort study: prognostic factors for relapse. *Eur J Paediatr Neurol* 2007;11:90–95
10. Polman CH, Reingold SC, Banwell B, et al. **Diagnostic criteria for multiple sclerosis: 2010 revisions to the McDonald criteria.** *Ann Neurol* 2011;69:292–302
  11. Sadaka Y, Verhey LH, Shroff MM, et al. **2010 McDonald criteria for diagnosing pediatric multiple sclerosis.** *Ann Neurol* 2012;72:211–23
  12. Chabas D, Castillo-Trivino T, Mowry EM, et al. **Vanishing MS T2-bright lesions before puberty: a distinct MRI phenotype?** *Neurology* 2008;71:1090–93
  13. Doepp F, Wurfel JT, Pfueller CF, et al. **Venous drainage in multiple sclerosis: a combined MRI and ultrasound study.** *Neurology* 2011;77:1745–51
  14. Polman CH, Reingold SC, Edan G, et al. **Diagnostic criteria for multiple sclerosis: 2005 revisions to the “McDonald Criteria.”** *Ann Neurol* 2005;58:840–46
  15. Heiberg E, Sjogren J, Ugander M, et al. **Design and validation of Segment—freely available software for cardiovascular image analysis.** *BMC Med Imaging* 2010;10:1
  16. Walker PG, Cranney GB, Scheidegger MB, et al. **Semiautomated method for noise reduction and background phase error correction in MR phase velocity data.** *J Magn Reson Imaging* 1993;3:521–30
  17. Stoquart-Elsankari S, Lehmann P, Villette A, et al. **A phase-contrast MRI study of physiologic cerebral venous flow.** *J Cereb Blood Flow Metab* 2009;29:1208–15
  18. Haacke EM, Feng W, Utriainen D, et al. **Patients with multiple sclerosis with structural venous abnormalities on MR imaging exhibit an abnormal flow distribution of the internal jugular veins.** *J Vasc Interv Radiol* 2012;23:60–68.e1–3
  19. Doepp F, Paul F, Valdueza JM, et al. **No cerebrocervical venous congestion in patients with multiple sclerosis.** *Ann Neurol* 2010;68:173–83
  20. Auriel E, Karni A, Bornstein NM, et al. **Extra-cranial venous flow in patients with multiple sclerosis.** *J Neurol Sci* 2011;309:102–04
  21. Baracchini C, Valdueza JM, Del Sette M, et al. **CCSVI and MS: a statement from the European Society of Neurosonology and Cerebral Hemodynamics.** *J Neurol* 2012;259:2585–89
  22. Sundström P, Wahlin A, Ambarki K, et al. **Venous and cerebrospinal fluid flow in multiple sclerosis: a case-control study.** *Ann Neurol* 2010;68:255–59
  23. Mayer CA, Pfeilschifter W, Lorenz MW, et al. **The perfect crime? CCSVI not leaving a trace in MS.** *J Neurol Neurosurg Psychiatry* 2011;82:436–40
  24. Zivadinov R, Marr K, Cutter G, et al. **Prevalence, sensitivity, and specificity of chronic cerebrospinal venous insufficiency in MS.** *Neurology* 2011;77:138–44
  25. Amato M, Saia V, Hakiki B, et al. **No association between chronic cerebrospinal venous insufficiency and pediatric-onset multiple sclerosis.** *Mult Scler* 2012;18:1791–96
  26. Singh AV, Zamboni P. **Anomalous venous blood flow and iron deposition in multiple sclerosis.** *J Cereb Blood Flow Metab* 2009;29:1867–78
  27. Baracchini C, Perini P, Calabrese M, et al. **No evidence of chronic cerebrospinal venous insufficiency at multiple sclerosis onset.** *Ann Neurol* 2011;69:90–99
  28. Blinkenberg M, Akeson P, Sillesen H, et al. **Chronic cerebrospinal venous insufficiency and venous stenoses in multiple sclerosis.** *Acta Neurol Scand* 2012;126:421–27
  29. Yamout B, Herlopian A, Issa Z, et al. **Extracranial venous stenosis is an unlikely cause of multiple sclerosis.** *Mult Scler* 2010;16:1341–48
  30. Dolic K, Weinstock-Guttman B, Marr K, et al. **Risk factors for chronic cerebrospinal venous insufficiency (CCSVI) in a large cohort of volunteers.** *PLoS One* 2011;6:e28062
  31. Atkinson W, Forghani R, Wojtkiewicz GR, et al. **Ligation of the jugular veins does not result in brain inflammation or demyelination in mice.** *PLoS One* 2012;7:e33671
  32. Zamboni P, Galeotti R, Menegatti E, et al. **A prospective open-label study of endovascular treatment of chronic cerebrospinal venous insufficiency.** *J Vasc Surg* 2009;50:1348–58.e1

# Prevalence of Subdural Collections in Children with Macrocrania

M.V. Greiner, T.J. Richards, M.M. Care, and J.L. Leach



## ABSTRACT

**BACKGROUND AND PURPOSE:** The relationship between enlarged subarachnoid spaces and subdural collections is poorly understood and creates challenges for clinicians investigating the etiology of subdural collections. The purpose of this study was to determine the prevalence of subdural collections on cross sectional imaging in children with macrocephaly correlating with subarachnoid space enlargement.

**MATERIALS AND METHODS:** The radiology information system of a large pediatric medical center was reviewed for “macrocrania” and “macrocephaly” on reports of cranial MRI/CT examinations in children <24 months of age, over a 24-month period. Head circumference was obtained from the clinical record. Studies were reviewed blindly for subdural collection presence and subarachnoid space size. Children with prior cranial surgery, parenchymal abnormalities, hydrocephalus, or conditions predisposing to parenchymal volume loss were excluded. Chart review was performed on those with subdural collections.

**RESULTS:** Imaging from 177 children with enlarged head circumference was reviewed. Nine were excluded, for a final cohort of 168 subjects (108 with enlarged subarachnoid space). Subdural collections were identified in 6 (3.6%), all with enlarged subarachnoid space (6/108, 5.6%). In 4, subdural collections were small, homogeneous, and nonhemorrhagic. In 2, the collections were complex (septations or hemorrhage). Two children were reported as victims of child abuse (both with complex collections). No definitive etiology was established in the other cases.

**CONCLUSIONS:** The prevalence of subdural collections in imaged children with macrocrania was 3.6%, all occurring in children with enlarged subarachnoid space. Our results suggest that enlarged subarachnoid space can be associated with some subdural collections in this cohort. Despite this, we believe that unexpected subdural collections in children should receive close clinical evaluation for underlying causes, including abusive head trauma.

**ABBREVIATIONS:** SS = subarachnoid spaces; BESS = benign enlargement of the subarachnoid spaces; SDH = subdural hemorrhage; SDC = subdural collections; HC = head circumference; AHT = abusive head trauma; CAT = child abuse team

Enlargement of the subarachnoid spaces (SS) is a common finding in children undergoing cranial imaging evaluation for various clinical conditions. In the setting of large or rapidly growing head circumference (HC), normal or mildly enlarged ventricles with enlargement of the SS, particularly over the frontal lobes, these children are usually diagnosed with “benign enlargement of the subarachnoid spaces” (BESS).<sup>1-5</sup> Children with BESS typically

have no neurologic or long-term developmental abnormalities with resolution of clinical and imaging findings within the first 2 years of life.<sup>6</sup>

Some investigators have suggested that children with macrocrania and enlargement of the SS may be at increased risk for subdural hemorrhage (SDH) after minimal or no trauma.<sup>7-15</sup> A clinical dilemma often arises when subdural collections (SDC) are identified in children with enlarged SS because the identification of SDC in an infant without an appropriate traumatic history raises the concern for abusive head trauma (AHT).<sup>3,12,16,17</sup>

The literature connecting enlarged SS and risk of SDC is based predominately on case reports or small case series. No current data are available on the prevalence of SDC in children with macrocrania and enlarged SS.<sup>8</sup> The lack of scientific evidence for the relationship between enlarged SS and SDC creates uncertainty for

Received October 31, 2012; accepted after revision February 27, 2013.

From the Department of Pediatrics (M.V.G.), Mayerson Center for Safe and Healthy Children, and Department of Radiology (T.R., M.C., J.L.L.), Cincinnati Children’s Hospital Medical Center, Cincinnati, Ohio.

Please address correspondence to Mary V. Greiner, MD, Cincinnati Children’s Hospital Medical Center, Department of Pediatrics, 3333 Burnet Ave, ML 3008, Cincinnati, OH 45229; e-mail mary.greiner@cchmc.org

Indicates article with supplemental on-line table.

<http://dx.doi.org/10.3174/ajnr.A3588>

**Table 1: Clinical presentation and follow-up in 6 children with enlarged subarachnoid spaces and subdural collections**

Patient	Age (weeks)/Sex	Presentation	Enlarged SS?	Clinical
1	24/M	Increased HC	Yes	CAT consult, normal Sk survey, characteristic RH. Reported as probable AHT
2	44/M	Increased HC	Yes	No CAT consult
3	35/F	Increased HC	Yes	No CAT consult
4	14/M	Increased HC, increased crying	Yes	CAT consult, normal Sk survey, no RH. Reported as probable AHT
5	33/M	Increased HC	Yes	No CAT consult, no treatment
6	31/M	Increased HC	Yes	No CAT consult, no treatment

**Note:**—RH indicates retinal hemorrhages; Sk survey, conventional radiographic skeletal survey; NS, neurosurgery.

clinicians in assessing for AHT. The purpose of this study was to determine the prevalence of SDC discovered on cross-sectional imaging in children with macrocrania during a defined time interval, correlating with SS enlargement.

## MATERIALS AND METHODS

This study was approved by the local institutional review board. The radiology information system of a large tertiary care academic pediatric medical center was reviewed for the period between January 1, 2008, through December 31, 2009, for the terms “macrocrania” and “macrocephaly” on reports of CT and MR imaging examinations of the head in children  $\leq 24$  months of age. Both CT and MR imaging were chosen to reflect clinical practice because these are both commonly ordered for concerns related to macrocrania. Children  $>24$  months of age were excluded because BESS is typically much less prevalent after this time.<sup>2</sup> Subjects with technically nondiagnostic examinations were excluded.

Only subjects with enlarged HC were included, defined as  $>95$ th percentile.<sup>18,19</sup> To limit secondary causes of SS enlargement and SDC development, subjects were first excluded if they had brain tumors, prior intracranial surgery, shunts, craniosynostosis, prior intracranial hemorrhage, prior meningitis/abscess, or parenchymal abnormalities on imaging. Patients with ventricular enlargement out of proportion to cerebral sulcal prominence suggesting the possibility of hydrocephalus were also excluded.

CT imaging was performed with the use of 5-mm contiguous axial images. MRI included sagittal and axial T1-weighted, dual-echo axial FSE PD/T2, axial gradient recalled-echo, and coronal FSE T2-weighted images (5.0-mm section thickness, 1.0-mm gap). Each examination was reviewed by a board-certified radiologist with added qualification in neuroradiology and 18 years’ experience interpreting neuroimaging (J.L.L.). Studies were reviewed in a blinded fashion for the presence and imaging characteristics of SDC and SS size (normal or enlarged). Differentiation of enlarged SS and SDC was made on the basis of standard imaging findings.<sup>3,16,20,21</sup> Results were compared with the clinical imaging report, and discrepancies were reviewed by another board-certified radiologist with added qualification in pediatric radiology and a pediatric neuroradiology fellowship (M.C.). Remaining discrepancies were resolved by consensus opinion. For included cases, all subsequent imaging studies were reviewed.

A secondary exclusion was performed to exclude causes of brain volume loss that could promote development of secondary SDC, including prior chemotherapy, brain irradiation, failure to thrive or malnutrition, chronic systemic illness, chronic corticosteroid therapy, significant prematurity (GA  $<28$  weeks), congenital anomalies, or brain atrophy pattern by imaging.<sup>22</sup> All cases

of identified SDC underwent a second chart review, to include dedicated retinal examination, skeletal survey, and child abuse team (CAT) reports.

Measurements of the SS were performed after qualitative assessment and after secondary exclusion. Measurements were made on axial CT images and axial T2-weighted MR images by use of a previously described technique.<sup>23</sup> The largest distance of the frontal SS perpendicular to the calvaria was measured by a single blinded reviewer (J.L.L.) by use of the electronic ruler in the PACS. Measurements were made from the inner table to the cortex surface, on images in which the ventricles were visible. The largest value for each case was recorded. If an SDC was present, the collection was not included in the measurement of the SS.

Statistical analysis was performed by use of Fisher exact test for categorical data and *t* test for continuous data, with  $P < .05$  deemed statistically significant.

## RESULTS

Two hundred seventy-nine CT/MR examinations fit initial study criteria. After initial exclusion, 242 cases (136 CT, 106 MR) formed the initial study group. Of these, 177 patients had an enlarged HC. Nine were excluded, for a final study group of 168 cases. Of the 168 cases, 108 had enlarged SS and 60 had normal SS. The final study group had an average age of 48.8 weeks (range, 9–101 weeks), with a predominance of boys (65%). The group with enlarged SS had a greater prevalence of boys (69%) compared with the normal SS group (52%) ( $P = .0298$ ) and was younger (median age,  $37.6 \pm 17.2$  weeks versus  $51.6 \pm 18.8$  weeks,  $P < .00001$ ).

Mean size of the frontal SS in children with qualitatively enlarged SS was  $7.0 \pm 2.0$  mm (range, 4.1–14.6 mm). Mean size of the frontal SS in children with qualitatively normal SS was smaller, at  $2.8 \pm 1.1$  mm (range, 1.1–5.6 mm) ( $P < .00001$ ).

Six SDC were identified, for an overall prevalence of 3.6%. All 6 SDC were identified in subjects with enlarged SS, giving a prevalence in this group of 5.6% (6/108). No SDC were identified in the 60 patients with normal SS. The prevalence difference between groups approaches statistical significance ( $P = .06$ ). The children with SDC were predominately boys (5:1), averaged 30.2 weeks of age, and were without reported recent accidental trauma (Table 1). Subjects with macrocrania and SDC were younger than those subjects without SDC (mean age, 30.2 weeks versus 40 weeks, respectively,  $P = .025$ ).

The SDC were identified initially on CT in 2 cases and on MRI in 4 (On-line Table). All SDC cases were referred because of macrocrania. Both CT cases had MRI within 9 days, which confirmed the CT findings. SDC were bilateral in 2 cases and unilateral in 4,

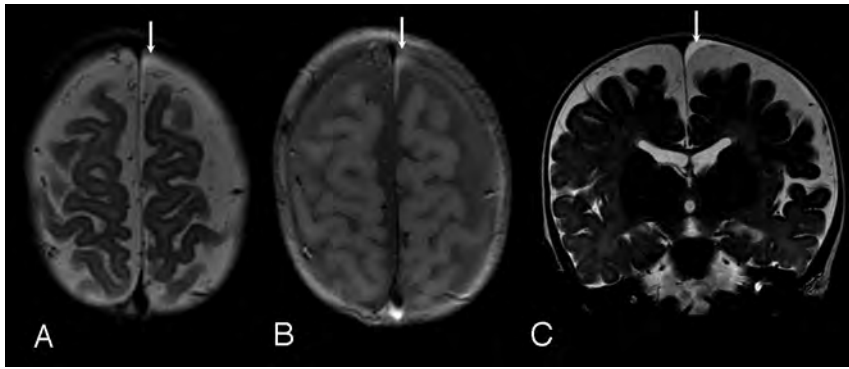


**FIG 1.** Case 3. *A*, Axial FSE T2-weighted image. *B*, Axial proton density-weighted image. *C*, Coronal FSE T2-weighted image; 8-month-old girl. Clinical indication for examination: macrocrania. Typical small homogeneous subdural collection, similar to those identified in cases 2, 5, and 6. Note diffuse prominence of subarachnoid spaces. Small left frontal vertex subdural collection is identified (arrows), slightly hyperintense to CSF on T2-weighted images (*A* and *C*), and moderately hyperintense to CSF on proton density images (*B*). The collection was isointense to CSF on T1-weighted images and showed no blooming on gradient-echo sequences. Follow-up CT 3 months later showed decrease in prominence of the subarachnoid space, normal ventricles, and no evidence of subdural collection.

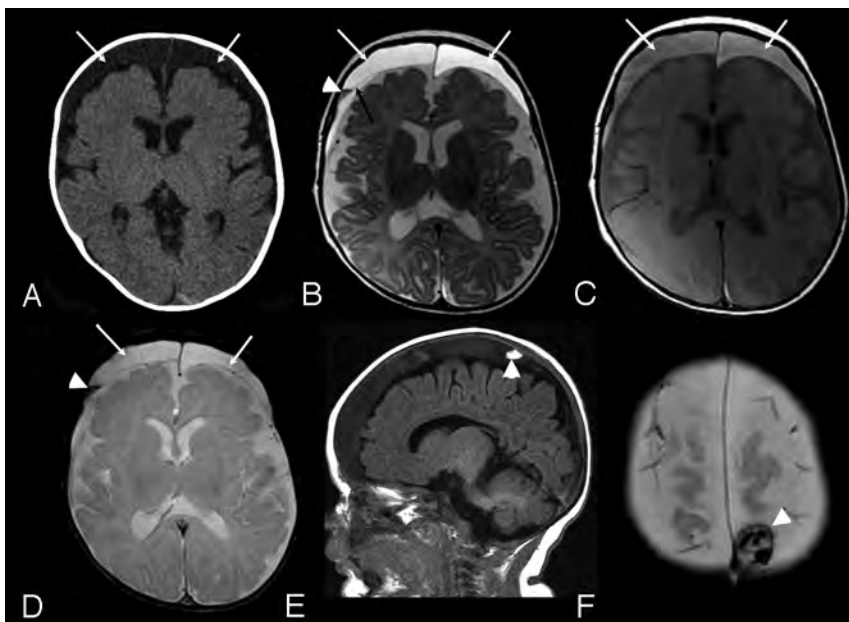


**FIG 2.** Case 4. *A*, Axial CT image. *B*, Axial FSE T2-weighted image. *C*, Axial proton density-weighted image. *D*, Axial gradient-recalled-echo image. *E*, Sagittal T1-weighted image. *F*, Axial gradient-echo image: 3-month-old boy with macrocrania. Initial CT examination (*A*) demonstrates moderate-sized bilateral subdural collections (arrows), slightly hyperattenuated relative to CSF. MRI examination was performed 14 hours later. Bilateral subdural collections are again identified (white arrows, *B*, *C*, and *D*) hyperintense to CSF on both T2 and proton density-weighted images (*B* and *C*). A thin septation is identified on the right (black arrow, *B*). A layering region of decreased T2 signal is seen on the right (arrowhead, *B*), which was hyperintense to CSF on T1-weighting (not shown) and blooms on the gradient-echo sequence (arrowhead, *D*) compatible with blood products. A localized area of increased signal on T1-weighted images in the right parietal vertex subdural collection was noted (arrowhead, *E*), which was hyperattenuated to brain on CT (not shown) and exhibited blooming on the gradient-echo sequence (arrowhead, *F*) consistent with additional blood products.

localized over the convexities, with a mean size of 5.4 mm (range, 1–9.6 mm). In 4 cases (cases 2, 3, 5, and 6), the SDC were homogeneous, unilateral, and small in size, with similar features on MRI (Fig 1). None of these subjects had recent (within 2 weeks) CT imaging for review. In 2 cases, the SDC were larger, bilateral, and complex in appearance. In case 4, there were heterogeneous

signal changes on MRI and increased attenuation on CT, which suggests recent hemorrhage with identified membranes within the collections (Fig 2). In case 1, there was heterogeneous internal signal with visible membranes and different signal intensity components. No CT or gradient-echo evidence of acute hemorrhage was identified.

A multidisciplinary CAT consultation was requested for 2 of 6 cases with SDC (cases 1 and 4). Both had normal initial and follow-up skeletal surveys, and both had dedicated retinal examinations. In case 1, there were retinal hemorrhages characteristic for abuse. Two additional children with SDC had dedicated retinal examinations for hyperopia and astigmatism, and no retinal hemorrhages were seen. None had unexplained bruising. One child (case 6) with small, homogeneous, unilateral right-sided SDC had a history of a left-sided parietal skull fracture 3 months before the index examination. A CAT consultation at that time resulted in clinical findings consistent with accidental trauma. On CT examination at the time of skull fracture, the SS were noted to be prominent; however, no intracranial hemorrhage or SDC were identified. Ultimately, 2 children were reported to Children's Services as probable abuse, including the case with the retinal hemorrhages and complex SDC (case 1) and the case with the signal changes suggesting recent hemorrhage (case 4). The remaining 4 cases not reviewed by the CAT were not reported to Children's Services.

Four subjects with SDC had prior cranial imaging varying from the same day as the index study to 6 months previously. In case 3 (index MRI examination demonstrated small vertex SDC), a head sonography was performed 4 weeks previously. The SDC were not described on the original sonography report but were visible on retrospective review. In case 5, head sonography was performed 6 and 2 months before the

index study and showed no evidence of SDC. In case 4, sonography was performed the same date as the index study, identifying bilateral SDC. In case 6, head CT was performed 4 months before the index MR imaging examination, with no evidence of SDC.

Follow-up imaging was performed in 5 cases from 3 weeks to 7 months after the index study. The SDC became smaller or re-

solved in each case with no intervention. In 1 case (case 4) 6 weeks after the index case showing bilateral SDC, a follow-up CT demonstrated smaller size, but with new increased attenuation within the right-sided collection. Repeat skeletal survey was negative. Clinical follow-up (range, 1–4 years) was available on 5 of 6 subjects. None of the children with SDC had a known bleeding disorder or genetic condition. None of the subjects required surgical drainage for treatment.

## DISCUSSION

Previous reports state that the most common cause of subdural hemorrhage in children is AHT.<sup>17,24</sup> The finding of unexplained SDC in a young child should initiate consideration of AHT; however, this must be closely correlated with the clinical context, other imaging, and laboratory findings. Bleeding diatheses, various genetic conditions (eg, glutaric aciduria type I), overshunting, and rapid decreases in brain volume have been associated with SDC in children after minimal or no trauma<sup>3,16,25</sup> and should be kept in mind when evaluating these patients.

Enlarged SS have been described in association with SDC in children by several authors and have been implicated as a predisposing cause.<sup>7,9-11,20,26-31</sup> Variable methodology, cohort makeup, clinical assessments for AHT, and imaging techniques in these studies make conclusions regarding SDC etiology difficult.

SDC in children can have a wide range of appearances, depending on etiology, imaging test used, and age of the collection.<sup>12,14,16</sup> “Subdural hematoma” has been used very loosely in the literature in this population and probably has described a wide range of SDC with different etiologies, including “subdural hygroma,”<sup>25</sup> “chronic subdural hematoma,”<sup>16</sup> “chronic subdural hematoma with rebleeding,”<sup>12</sup> and “hemato-hygroma.”<sup>14</sup> In clinical practice, it is often difficult to differentiate these, adding to the complexity in evaluating these children.<sup>12,25</sup> For this reason, we chose to use the nonetiologic term “subdural collections” in our study to describe these collections.

Five previous studies have described SDC in populations of children with enlarged SS with prevalence estimates between 8–23% in series with between 20–142 subjects. The largest of these studies described a mixed group of children with enlarged extra-axial spaces on head sonography.<sup>30</sup> They found 33 SDC in 142 subjects over a 4-year period. Twenty-five were anechoic (CSF-like) and 8 were echogenic or complex; 103 of these subjects had macrocrania, though the presence of macrocrania and enlarged spaces was not correlated with SDC visualization. Although children with prior major hemorrhage were excluded, children with prior meningitic effusions, white matter injury of prematurity, and “malformative syndromes” were included in their cohort, limiting conclusions. Few subjects had CT imaging, limiting detection of acute hemorrhage. Of the children with SDC, 4 cases were “battered children”; however, AHT evaluation details are limited. Azais and Echenne<sup>29</sup> describe 5 SDC in 41 children with “benign enlargement of the SS” identified primarily with sonography, 29 (72%) of whom had macrocrania. They excluded children with prematurity, intrauterine growth restriction, malnutrition, and neonatal distress. Three SDC were “unexpected” and not associated with any reported trauma. One was related to accidental trauma and 1 was related to probable AHT.

Hellbusch<sup>26</sup> described 9 SDC in 47 highly selected children referred for neurosurgical evaluation of enlarged extra-axial spaces. Traumatic cases (both accidental and AHT) were excluded, and no detailed description of imaging findings was reported.

Three recent studies specifically evaluated SDC in children with enlarged extra-axial spaces.<sup>10,11,32</sup> However, because the cases were identified on the basis of the presence of SDC, no inference as to the true prevalence of SDC in the overall group with enlarged extra-axial spaces is possible. Ghosh and Ghosh<sup>10</sup> described 9 patients (3 months to 2 years of age) with SDH and enlarged extra-axial spaces identified by searching for the ICD-9 diagnoses of “nontraumatic SDH” and “hydrocephalus” over a 10-year period. They excluded patients with true hydrocephalus, shunts, head injury, and cerebral atrophy. The identified collections were bilateral in 6 and exhibited a wide range of imaging appearances. All were evaluated for AHT, but only 1 subject was reported to children’s services. McNeely et al<sup>11</sup> described 7 children with SDC and enlarged SS identified in a nonspecified manner in a 6-year period. Children with known AHT and bleeding diatheses were excluded. Collections were bilateral in 3. One was involved in a major motor vehicle collision and 1 had a reported fall with skull fracture. The others were identified on imaging performed for macrocrania or lethargy, and no other etiology was identified. Vinchon et al<sup>32</sup> described 16 children with “spontaneous” SDH (no traumatic history, bleeding disorder, or AHT) identified from a prospective neurosurgical data base; 12 had enlarged SS, and 12 had macrocrania. They compared patients with spontaneous SDH with a group with AHT or accidental trauma and found that the children with spontaneous SDH were much more commonly macrocephalic (75% versus 20%).

Although the published associations between enlarged SS and SDC as well as data from our study suggest a link, documented spontaneous SDC in children with enlarged SS and prior imaging without SDC, are rare. We could find only 12 previously reported spontaneous, nontraumatic SDC in children with prior imaging documentation.<sup>7,20,26,31-33</sup> The best documented of these reports is from Amodio et al,<sup>20</sup> who described a 3.5-month-old, former 32-week preterm boy, with grade 1 germinal matrix hemorrhage presenting with macrocrania. Initial head ultrasound examination demonstrated enlarged extra-axial spaces but no SDC. With continuing HC increase, a 6-week follow-up head ultrasound examination was performed that demonstrated new bilateral SDC containing low-level echoes. A subsequent MRI demonstrated large bilateral SDC with layering hemorrhagic material, confirmed at surgical drainage. Evaluation for AHT (including skeletal survey and retinal examination) was negative. In evaluating the images in this report, marked diffuse subarachnoid space enlargement is noted, however, suggesting brain volume loss. In our study, 4 patients with SDC had previous imaging (ultrasound examination, 3; CT, 1). In 3 patients, SDC were not identified on prior imaging, though the size of the identified SDC probably would have been too small to visualize on the imaging test performed (ultrasound examination and CT). In 1 case, retrospective assessment of a prior head ultrasound examination documented small SDC, not mentioned on the clinical report.

Data from the current study and the limited literature do support that SDC may arise in children with enlarged SS, after mini-

mal or no trauma. The exact etiology is incompletely understood. However, some theories have been postulated.<sup>12,14</sup> Enlargement of the subarachnoid space may stretch and place increased strain on bridging veins, with resultant rupture and SDH formation.<sup>7,13,29</sup> This potential increased strain on bridging veins has been modeled mathematically<sup>13</sup> but is not universally accepted.<sup>34</sup> Membranes surrounding an aging subdural hematoma are highly vascularized and have been postulated to potentially allow re-bleeding either spontaneously or with minimal trauma.<sup>12,35,36</sup> A rent in the arachnoid could occur, allowing communication of the subdural and SS and subsequent subdural CSF collections to form.<sup>14</sup>

Although numbers are small and the clinical child abuse directed assessment was not performed on all patients, our report suggests small homogeneous SDC on cross-sectional imaging, without definite evidence of hemorrhage, may occur in the setting of BESS and may not indicate inflicted injury. In our study, 2 of the 6 children with SDC had findings suggesting child abuse. Both of these subjects had moderate-sized, bilateral, heterogeneous collections. The remaining 4 patients had radiographically similar SDC that were small, homogeneous, and localized over the convexities. Heterogeneous, more complex collections, particularly with clear evidence of hemorrhage by CT or MRI, could represent an important finding that suggests inflicted injury in the appropriate clinical scenario.

Only a few of the previous studies of SDC in children with enlarged SS report documentation of a dedicated evaluation of AHT.<sup>7,8,10,20</sup> In these studies, a total of 14 cases of SDC in the setting of enlarged SS have been described. All were investigated, but only 1 was thought to be related to AHT. Although imaging findings are incompletely described, 1 controversial case report describes a small “acute” SDH in a 4-month-old boy with macrocrania and enlarged extra-axial spaces who fell from a standing position to a carpeted floor.<sup>8</sup> CT images were not presented in the report; however, MR images document small mixed intensity SDC. Although these studies document SDC in children after minimal or no trauma, they are all limited to varying degrees by incomplete description of imaging findings, variability in clinical assessment of potential abuse, and selection bias.

Age and sex differences were noted between subgroups of patients in our study. A male predominance in both the overall group of patients with macrocrania and those with enlarged SS was noted, consistent with prior studies.<sup>2</sup> Subjects with macrocrania and enlarged SS were younger than those subjects with normal SS, a finding described in other studies of BESS.<sup>2</sup> Enlarged SS typically normalize by 2–3 years of age in BESS.<sup>2,22,37</sup> The patients with macrocrania and normal SS in our study may be at the later stages of this condition.

There are some limitations to this study. Although all subjects had enlarged HC and many (61%) had enlarged SS, how many of this group fulfilled the full clinical scenario of “benign enlargement of the subarachnoid spaces” is unknown. Given our extensive exclusionary process, most subjects with macrocrania and enlarged SS probably did fit the criteria for BESS. Evaluation of subarachnoid space size was subjective for categorization in our study but did rely on the assessments of at least 2 radiologists. Our subjective assessment was subsequently validated by a quantita-

tive analysis. Prior studies of normative subarachnoid space size in children are few; however, findings on cross-sectional imaging and ultrasound examination<sup>23,38</sup> correlate well with the results of our study. No sampling of the SDC was performed to assess the etiology of the collections. In 1 case, there was definite imaging evidence of hemorrhage. In the other cases, no hemorrhage could be documented and the collection contents remain unknown.

Those cases in which sonography provided the only evaluation were excluded, which potentially introduced selection bias. It is possible that those evaluated by cross-sectional imaging may be a different clinical group, with more concern regarding neurologic function, than those evaluated only by sonography. Although sonography can identify large SDC, its sensitivity for smaller collections is limited compared with CT/MRI. We chose not to include this group for the purposes of this study. MRI is the most sensitive test for SDC in this population,<sup>21</sup> and small SDC could have been missed in subjects who only had CT imaging. Of the identified SDC in our study, 2 were initially identified by CT, with subsequent confirmation by MRI. The remaining subjects were identified by MRI. A study using only MRI for evaluation would be expected to identify a larger number of SDC. Further prospective studies should consider the use of MRI for evaluation in this cohort. Not all children with SDC received a dedicated clinical assessment for child abuse, limiting the ability to draw definite conclusions on the basis of imaging appearance of the collections. The appearance of some of the collections on imaging (large, complex, and clearly hemorrhagic) probably introduced bias for investigation of potential AHT in these subjects. It is possible that some of the other children with SDC identified in this study were, in fact, victims of child abuse. On the basis of clinical and imaging follow-up available, we believe that this is unlikely.

## CONCLUSIONS

In summary, our CT and MR imaging study of children with macrocrania demonstrates a 5.6% prevalence of unexpected SDC in children with enlarged SS. No SDC were found in subjects with normal SS. This study, in addition to prior anecdotal and descriptive studies, supports that enlarged SS may predispose these children to small, nonovertly hemorrhagic SDC overlying the convexities, with little or no recognized trauma. Despite these findings, we strongly believe that every unexpected subdural collection in a young child requires close clinical evaluation for underlying causes including AHT. Future studies building on this detailed retrospective investigation are needed to further understand the clinical and pathophysiologic relationships in this scenario.

## ACKNOWLEDGMENT

We thank Stephen Boos, MD, for assistance with study design.

Disclosures: Mary V. Greiner—UNRELATED: Expert Testimony: I am a child abuse pediatrician, so I frequently testify as an expert in child abuse in court. I have not testified in any medical malpractice cases; Grants/Grants Pending: 2011: Primary Investigator: A Medical Home for Foster Care Children, The American Academy of Pediatrics Community Access To Child Health (CATCH) Planning Funds, Total awarded: \$12,000\*; Comments: None of these grants support my salary; Travel/Accommodations/Meeting Expenses Unrelated to Activities Listed: By my institution, Cincinnati Children's Hospital Medical Center, to attend meetings. James Leach—OTHER RELATIONSHIPS: CCHMC has a clinical cooperation agreement with

## REFERENCES

1. Ment LR, Duncan CC, Geehr R. **Benign enlargement of the subarachnoid spaces in the infant.** *J Neurosurg* 1981;54:504–08
2. Zahl SM, Egge A, Helseth E, et al. **Benign external hydrocephalus: a review, with emphasis on management.** *Neurosurg Rev* 2011;34:417–32
3. Raybaud AB, Barkovich AJ. **Hydrocephalus.** In: Barkovich AJ, ed. *Pediatric Neuroimaging*. 5th ed. Philadelphia: Lippincott Williams & Wilkins; 2012
4. Babcock DS, Han BK, Dine MS. **Sonographic findings in infants with macrocrania.** *AJR Am J Roentgenol* 1988;150:1359–65
5. Carolan PL, McLaurin RL, Towbin RB, et al. **Benign extra-axial collections of infancy.** *Pediatr Neurosci* 1985;12:140–44
6. Nickel RE, Gallenstein JS. **Developmental prognosis for infants with benign enlargement of the subarachnoid spaces.** *Dev Med Child Neurol* 1987;29:181–86
7. Ravid S, Maytal J. **External hydrocephalus: a probable cause for subdural hematoma in infancy.** *Pediatr Neurol* 2003;28:139–41
8. Piatt JH Jr. **A pitfall in the diagnosis of child abuse: external hydrocephalus, subdural hematoma, and retinal hemorrhages.** *Neurosurg Focus* 1999;7:e4
9. Kapila A, Trice J, Spies WG, et al. **Enlarged cerebrospinal fluid spaces in infants with subdural hematomas.** *Radiology* 1982;142:669–72
10. Ghosh PS, Ghosh D. **Subdural hematoma in infants without accidental or nonaccidental injury: benign external hydrocephalus, a risk factor.** *Clin Pediatr (Phila)* 2011;50:897–903
11. McNeely PD, Atkinson JD, Saigal G, et al. **Subdural hematomas in infants with benign enlargement of the subarachnoid spaces are not pathognomonic for child abuse.** *AJNR Am J Neuroradiol* 2006;27:1725–28
12. Swift DM, McBride L. **Chronic subdural hematoma in children.** *Neurosurg Clin N Am* 2000;11:439–46
13. Papasian NC, Frim DM. **A theoretical model of benign external hydrocephalus that predicts a predisposition towards extra-axial hemorrhage after minor head trauma.** *Pediatr Neurosci* 2000;33:188–93
14. Zouros A, Bhargava R, Hoskinson M, et al. **Further characterization of traumatic subdural collections of infancy: report of five cases.** *J Neurosurg* 2004;100:512–18
15. Gennarelli TA, Thibault LE. **Biomechanics of acute subdural hematoma.** *J Trauma* 1982;22:680–86
16. Kleinman PK. *Diagnostic Imaging of Child Abuse*. Baltimore: Williams & Wilkins; 1987
17. Tzioumi D, Oates RK. **Subdural hematomas in children under 2 years, accidental or inflicted? A 10-year experience.** *Child Abuse Negl* 1998;22:1105–12
18. Alvarez LA, Maytal J, Shinnar S. **Idiopathic external hydrocephalus: natural history and relationship to benign familial macrocephaly.** *Pediatrics* 1986;77:901–07
19. Hamill PV, Drizd TA, Johnson CL, et al. **Physical growth: National Center for Health Statistics percentiles.** *Am J Clin Nutr* 1979;32:607–29
20. Amodio J, Spektor V, Pramanik B, et al. **Spontaneous development of bilateral subdural hematomas in an infant with benign infantile hydrocephalus: color Doppler assessment of vessels traversing extra-axial spaces.** *Pediatr Radiol* 2005;35:1113–17
21. Aoki N. **Extracerebral fluid collections in infancy: role of magnetic resonance imaging in differentiation between subdural effusion and subarachnoid space enlargement.** *J Neurosurg* 1994;81:20–23
22. Maytal J, Alvarez LA, Elkin CM, et al. **External hydrocephalus: radiologic spectrum and differentiation from cerebral atrophy.** *AJR Am J Roentgenol* 1987;148:1223–30
23. Prassopoulos P, Cavouras D, Golfopoulos S, et al. **The size of the intra- and extraventricular cerebrospinal fluid compartments in children with idiopathic benign widening of the frontal subarachnoid space.** *Neuroradiology* 1995;37:418–21
24. Parent AD. **Pediatric chronic subdural hematoma: a retrospective comparative analysis.** *Pediatr Neurosurg* 1992;18:266–71
25. Lee KS. **The pathogenesis and clinical significance of traumatic subdural hygroma.** *Brain Inj* 1998;12:595–603
26. Hellbusch LC. **Benign extracerebral fluid collections in infancy: clinical presentation and long-term follow-up.** *J Neurosurg* 2007;107:119–25
27. Medina LS, Frawley K, Zurakowski D, et al. **Children with macrocrania: clinical and imaging predictors of disorders requiring surgery.** *AJNR Am J Neuroradiol* 2001;22:564–70
28. Nishimura K, Mori K, Sakamoto T, et al. **Management of subarachnoid fluid collection in infants based on a long-term follow-up study.** *Acta Neurochir (Wien)* 1996;138:179–84
29. Azais M, Echenne B. **[Idiopathic pericerebral swelling (external hydrocephalus) of infants].** *Ann Pediatr (Paris)* 1992;39:550–58
30. Veyrac C, Couture A, Baud C. **Pericerebral fluid collections and ultrasound.** *Pediatr Radiol* 1990;20:236–40
31. Laubscher B, Deonna T, Uske A, et al. **Primitive megalencephaly in children: natural history, medium term prognosis with special reference to external hydrocephalus.** *Eur J Pediatr* 1990;149:502–07
32. Vinchon M, Delestret I, DeFoort-Dhellemmes S, et al. **Subdural hematoma in infants: can it occur spontaneously? Data from a prospective series and critical review of the literature.** *Childs Nerv Syst* 2010;26:1195–205
33. Mori K, Sakamoto T, Nishimura K, et al. **Subarachnoid fluid collection in infants complicated by subdural hematoma.** *Childs Nerv Syst* 1993;9:282–84
34. Raul JS, Deck C, Willinger R, et al. **Finite-element models of the human head and their applications in forensic practice.** *Int J Legal Med* 2008;122:359–66
35. McLone DG. **Ultrastructure of the vasculature of central nervous system tumors of childhood.** *Childs Brain* 1980;6:242–54
36. Moskala M, Goscinski I, Kaluza J, et al. **Morphological aspects of the traumatic chronic subdural hematoma capsule: SEM studies.** *Microsc Microanalysis* 2007;13:211–19
37. Muenchberger H, Assaad N, Joy P, et al. **Idiopathic macrocephaly in the infant: long-term neurological and neuropsychological outcome.** *Childs Nerv Syst* 2006;22:1242–48
38. Libicher M, Troger J. **US measurement of the subarachnoid space in infants: normal values.** *Radiology* 1992;184:749–51

# White Matter Microstructural Abnormality in Children with Hydrocephalus Detected by Probabilistic Diffusion Tractography

A. Rajagopal, J.S. Shimony, R.C. McKinstry, M. Altaye, T. Maloney, F.T. Mangano, D.D. Limbrick, S.K. Holland, B.V. Jones, S. Simpson, D. Mercer, and W. Yuan



## ABSTRACT

**BACKGROUND AND PURPOSE:** Hydrocephalus is a severe pathologic condition in which WM damage is a major factor associated with poor outcomes. The goal of the study was to investigate tract-based WM connectivity and DTI measurements in children with hydrocephalus by using the probabilistic diffusion tractography method.

**MATERIALS AND METHODS:** Twelve children with hydrocephalus and 16 age-matched controls were included in the study. Probabilistic diffusion tractography was conducted to generate tract-based connectivity distribution and DTI measures for the genu of the corpus callosum and the connectivity index. Tract-based summary measurements, including the connectivity index and DTI measures (fractional anisotropy, mean diffusivity, axial diffusivity, and radial diffusivity), were calculated and compared between the 2 study groups.

**RESULTS:** Tract-based summary measurement showed a higher percentage of voxels with lower normalized connectivity index values in the WM tracts in children with hydrocephalus. In the genu of the corpus callosum, the left midsegment of the corticospinal tract, and the right midsegment of the corticospinal tract, the normalized connectivity index value in children with hydrocephalus was found to be significantly lower ( $P < .05$ , corrected). The tract-based DTI measures showed that the children with hydrocephalus had significantly higher mean diffusivity, axial diffusivity, and radial diffusivity in the genu of the corpus callosum, left midsegment of the corticospinal tract, and right midsegment of corticospinal tract and lower fractional anisotropy in the genu of the corpus callosum ( $P < .05$ , corrected).

**CONCLUSIONS:** The analysis of WM connectivity showed that the probabilistic diffusion tractography method is a sensitive tool to detect the decreased continuity in WM tracts that are under the direct influence of mechanical distortion and increased intracranial pressure in hydrocephalus. This voxel-based connectivity method can provide quantitative information complementary to the standard DTI summary measures.

**ABBREVIATIONS:** AD = axial diffusivity; CI = connectivity index; FA = fractional anisotropy; CC = corpus callosum; mCST = midsegment of corticospinal tract; MD = mean diffusivity; PDT = probabilistic diffusion tractography; RD = radial diffusivity

Pediatric hydrocephalus is a common medical condition characterized by an imbalance in CSF production and absorption, leading to elevated intracranial pressure and ventriculomegaly. Previous studies of hydrocephalus have consistently found functional deficits in a series of neuropsychological domains, including visuospatial, motor,<sup>1</sup> and nonverbal learning,<sup>2</sup> presumably resulting from white matter damage or degeneration.<sup>3</sup>

DTI is a noninvasive MR imaging technique that quantifies diffusion properties of in vivo brain structures, especially in the

white matter. Fractional anisotropy (FA) values allow us to infer WM integrity, or the lack thereof, for underlying pathologic changes in myelin sheaths, axonal membranes, and intercellular/extracellular spaces. Past DTI studies in hydrocephalus have identified structural damage in the corpus callosum and internal capsule on the basis of abnormal diffusion properties in these important WM structures.<sup>4,5</sup>

The severe deformation in the hydrocephalic brain presents a unique challenge for imaging data processing and analysis. Past DTI studies of pediatric hydrocephalus have been based on region-of-interest analysis.<sup>1,6</sup> Although region of interest–based analysis has helped demonstrate evidence of structural abnormalities in key WM regions, there are limitations inherent in this type

Received December 13, 2012; accepted after revision March 11, 2013.

From the Pediatric Neuroimaging Research Consortium (A.R., T.M., S.K.H., B.V.J., S.S., W.Y.), Department of Radiology, Division of Biostatistics and Epidemiology (M.A.), and Division of Pediatric Neurosurgery (F.T.M.), Cincinnati Children's Hospital Medical Center, Cincinnati, Ohio; University of Cincinnati College of Medicine (M.A., F.T.M., S.K.H., B.V.J., W.Y.), Cincinnati, Ohio; Mallinckrodt Institute of Radiology (J.S.S., R.C.M.) and Department of Neurological Surgery (D.D.L., D.M.), Washington University School of Medicine, St. Louis, Missouri.

This work was supported by a grant from NIH/NINDS (1R01 NS066932).

The data reported in this manuscript have not been published elsewhere.

Please address correspondence to Weihong Yuan, PhD, Pediatric Neuroimaging Research Consortium, Department of Radiology, Cincinnati Children's Hospital, 3333 Burnet Ave, Cincinnati, OH 45229; e-mail: Weihong.Yuan@cchmc.org

Indicates open access to non-subscribers at [www.ajnr.org](http://www.ajnr.org)

<http://dx.doi.org/10.3174/ajnr.A3737>

of analysis: The delineation of the region of interest is limited to 1 or a small number of sections, usually subjectively selected, that may or may not lead to a full representation of the WM structure of interest. There have been new developments in image registration methods that have shown initial success in their applications in brains with large ventricles and/or distortion<sup>7-9</sup>; however, they are not tailored for application in the pediatric hydrocephalic brains with severe distortion, especially in children at a very young age.

The aim of the present study was to explore the feasibility of applying probabilistic diffusion tractography (PDT) in children with hydrocephalus to quantify structural integrity in a series of WM fiber tracts, including the genu of the corpus callosum (CC), splenium of the CC, and midsegment of corticospinal tract (mCST). The connectivity index (CI) (a measure of WM connectivity between 2 brain regions) was calculated for each voxel as the sum of the number of streamlines that started from the seed region, passed through the voxel, and reached the target region. The deviation of the CI from the normal range may indicate compromised integrity in the myelin sheath and axons under pathologic conditions. We examined the tract-based CI values and DTI values and explored the complementary aspect of the CI and FA in differentiating the hydrocephalus group from controls.

## MATERIALS AND METHODS

### Subjects

Twelve children (age range, 0–38.5 months) who were diagnosed with hydrocephalus and referred for surgical treatment were included in the present study. An age-matched control group ( $n = 16$ ; age range, 0.6–37.5 months) was also included for comparison. All participants were recruited for a multicenter study from either the Cincinnati Children's Hospital Medical Center (7 patients with hydrocephalus, 15 controls) or St. Louis Children's Hospital (5 patients with hydrocephalus, 1 control). The inclusion/exclusion criteria have been described elsewhere.<sup>1</sup> Both local institutional review board committees approved the study protocol, and written informed consent was obtained from parents of the participants.

### DTI Data Acquisition

DTI data were acquired at both sites during the clinical scans by using a 1.5T MR imaging system (either Signa; GE Healthcare, Milwaukee, Wisconsin or Avanto; Siemens, Erlangen, Germany). The imaging protocol included a single-shot EPI diffusion-weighted spin-echo sequence (FOV = 240 × 240 mm; matrix = 96 × 96; resolution = 2.5 mm isotropic; TR/TE = 9400/93.2 ms; NEX = 2) and a 3D anatomic T1 sequence (FOV = 256 × 256 mm; matrix = 256 × 256; resolution = 1 mm isotropic). Diffusion-weighting was applied along 15 directions with a b-value of 1000 s/mm<sup>2</sup>, and 1 additional image was acquired with no diffusion-weighting (b-value = 0 s/mm<sup>2</sup>). Siemens gradient weightings were programmed to match the implementation on the GE Healthcare scanner. The compatibility of MR imaging data acquired from different scanners at 2 different research sites was established initially by using an MR phantom (BIRN: Biomedical Informatics Research Network; <http://www.nbirn.net>) and a human phantom and then maintained annually. The interscanner difference was minimal (<1.1%) on the basis of mean diffusivity (MD) values measured from the BIRN phantom. The relative interscanner difference based on the human phantom was <3.3%

and 3.5% for FA and MD, respectively. The details of the quality assurance procedure have been reported in previous work.<sup>1,10</sup>

### DTI Data Processing and Probabilistic Diffusion Tractography

Image processing and analysis were performed by using the fMRI of the Brain Software Library (FSL; <http://www.fmrib.ox.ac.uk/fsl>). DTI data were preprocessed with eddy current correction and minor head motion by using affine registration to a reference volume. The preprocessed images were then fit to a diffusion tensor model at each voxel. Summary measures, including FA, MD, axial diffusivity (AD), and radial diffusivity (RD), were calculated on the basis of standard methods.

At each voxel, the Bayesian Estimation of Diffusion Parameters Obtained by using Sampling Techniques (BEDPOSTX) function in FSL was used to build up the distributions on diffusion parameters on the basis of the Markov Chain Monte Carlo sampling.<sup>11</sup> The outputs of the BEDPOSTX were used to compute the PDT by using Probtrackx<sup>12</sup> in FSL. The seed and target masks used in the PDT for genu of the CC were created on sagittal sections as illustrated in Fig 1. The 2 masks for the left or right mCST were created on axial sections placed between 1 section below the body of the corpus callosum and the entry of the posterior limb of the internal capsule to the cerebral peduncle (Fig 2). All masks were delineated by 1 operator (W.Y.) and confirmed by 3 pediatric radiologists (R.C.M., J.S.S., and B.V.J.) and 2 pediatric neurosurgeons (F.T.M., D.D.L.).

CI was extracted for all the voxels from the PDT-derived WM tracts. The fiber tracking drew 5000 samples from each voxel in the seed mask. The CI value for any voxel in the brain is the sum of all the tracking samples that originated from the seed mask, passed through the voxel, and reached the target region. Only the voxels between the 2 masks were retained for analysis. A threshold of 100 was used for the connectivity index to avoid spurious results as the consequence of partial volume effect and image noise.<sup>13,14</sup> We also tested more stringent threshold levels at 150 and 200, and the findings remained the same. Therefore, only the data based on a threshold of 100 are reported in the present study.

### Data Analysis

The comparison between the children with hydrocephalus and the control group was made in 4 PDT-derived WM tracts (ie, the genu of the CC, splenium of the CC, left mCST, and right mCST). The fiber tracking was successful in all participants in the control group for all the WM tracts. It was also successful in the hydrocephalus group for the genu of the CC, left mCST, and right mCST (successful rates were 11/12, 12/12, 12/12 for the 3 tracts, respectively). However, fiber tracking was not successful in the splenium of the CC in 9/12 children with hydrocephalus. Therefore, the data for the splenium of the CC were not included in the eventual analysis. This outcome may be due to the expansion of ventricle volume that caused the stretching of the occipital horn of the ventricles, leading to a sharp bend in the splenium of the CC.

Histograms of the distribution of CI values within a tract showed that they did not follow normal distribution. To quantify the degree of skewness for the within-tract CI and DTI measures, we used the following index: Skewness =  $\mu_3/\delta^3$ , where  $\mu$  is the mean,  $\mu_3$  represents the third moment about the mean  $\mu$ , and  $\delta$  is

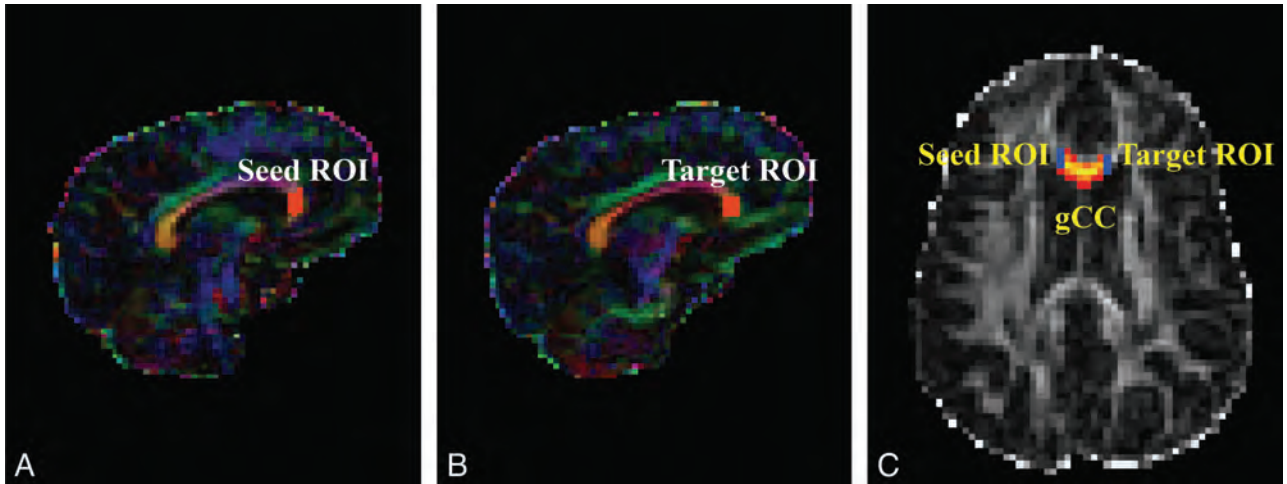


**FIG 1.** DTI maps demonstrating seed and target masks and resultant probabilistic fiber tracking of the genu of the CC in representative participants. A–C, hydrocephalus. A and B, Color-coded FA maps. C, FA map. The masks shown in orange in the sagittal maps can be seen as short blue lines on axial map.

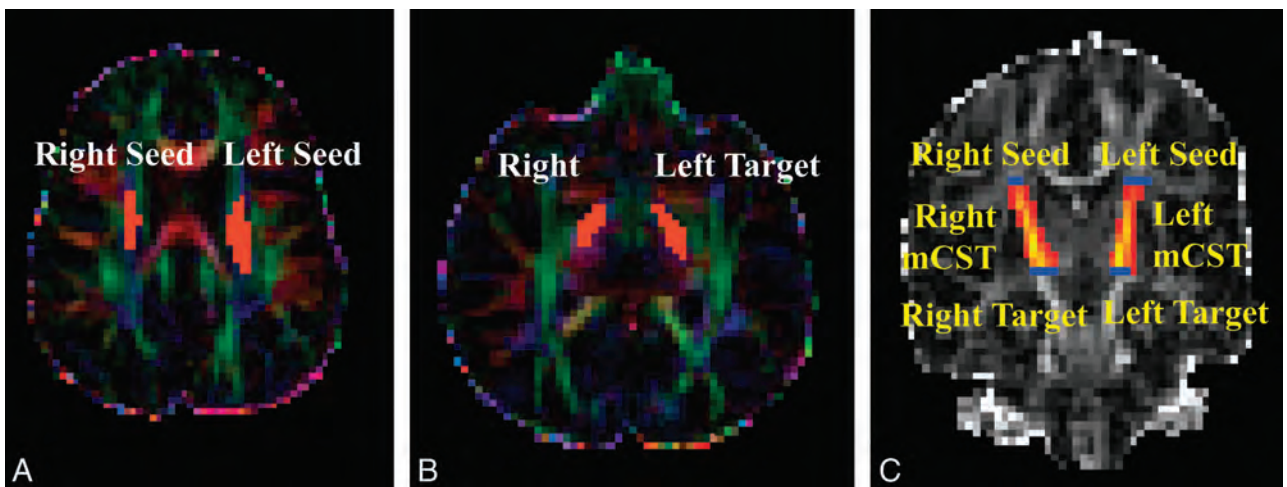


**FIG 2.** DTI maps demonstrating seed and target masks and resultant probabilistic fiber tracking of the left and right midsegments of the cortical spinal tracts in representative participants. A–C, Hydrocephalus. A and B, Color-coded FA maps. C, FA map. The masks shown in orange on the axial DTI maps can be seen as short blue lines on coronal FA map.

the SD. A skew to the left or right direction of a distribution was called a positive or negative skew, respectively. The skewness index was calculated for each tract in individual subjects first and then for group comparison.

Due to the age range of the study population and the expected developmental change in brain structures, it was not feasible to maintain the size and shape of the seed or target masks as constant across all subjects in the fiber tracking. Initial correlation analysis showed that in some cases the seed and target mask, as well as the tract volume, were significantly correlated with the median CI value from all the voxels within the tract. Thus, a new index, normalized CI (CI/tract volume, units of samples/voxel), was used in the study for group comparison. The tract volume (the number of voxels in the tract) is, in theory, affected by both seed and target mask size (as confirmed by our initial data). The drawing of these masks can also be affected by the brain tissue area, which is age-related, and are operator-dependent. Using the tract volume as the weighting factor in the index of normalized CI minimizes the above-mentioned factors.

### Statistical Analysis

The group difference of the skewness index was tested by using the Mann-Whitney *U* test. Multiple regression analysis was performed by using either the DTI measurement (FA, MD, AD, or RD) or the normalized CI as a dependent variable and group and age as independent variables. Multiple comparisons were corrected by using the false discovery rate method.<sup>15</sup>

## RESULTS

### Comparison of Within-Tract Skewness in Connectivity Index and FA Values

Skewness in CI for each tract is plotted in Fig 3. In all 3 tracts analyzed, CI values within a tract were found to skew to the left of the distribution with a long tail extended in the high CI direction (Fig 3 and Table 1). The CI within-tract skewness in any group/tract centered between 0.94 and 1.33, leading to a significant deviation from symmetric distribution in this index ( $P < .05$  for all groups). Therefore, the mean of the CI value is not considered a reflection of the CI values across all the voxels within a certain

tract. For subsequent analysis of CI measures, the 25th, 50th and 75th percentile values were selected. On the other hand, the skewness for within-tract FA was found to center close to zero; therefore, the mean value was an appropriate summary measure for further analysis and comparison.

No statistically significant group difference was found between the children with hydrocephalus and those in the control group in either CI skewness or FA skewness in any of the 3 tracts analyzed.

### Aggregated Normalized Connectivity Index Values in the Genu of the CC, Left mCST, and Right mCST

Figure 4 shows the percentile histograms of the aggregated normalized CI. In all 3 tracts, children with hydrocephalus were found to have a lower percentage of voxels with high normalized CI values. The percentage of the voxels with normalized CI values higher than 20 (an arbitrary value selected at approximately where the 2 distribution curves cross) in the genu of the CC (Fig 4A) was 30.5% for children with hydrocephalus and 56.3% for controls. Similar differences were also found in the left mCST (Fig 4B, 13.1% versus 27.0%) and right mCST (Fig 4C, 8% versus 27.1%).

In the mCST, the distribution curve for the hydrocephalus group skewed more toward the low end, with the tail ending at a value of 40, while the control still had 6.4% and 8.4% of the voxels

in the left mCST and right mCST, respectively, which are higher than 40 in normalized CI values (Fig 4E, -F).

### Tract-Based Summary Connectivity Measures (Normalized Connectivity Index Values)

As shown in Fig 5 and Table 2, the median within-tract normalized CI values in the patients with hydrocephalus were significantly lower than those in the control group ( $P < .05$ , corrected) in all 3 WM tracts examined. The difference was also significant ( $P < .05$ , corrected) or at trend level (right mCST in the first quartile of normalized CI) at both the first and the third quartiles of the within-tract normalized CI levels. Age was not found to be a significant predictor of normalized CI in any of the analyses.

### Tract-Based Summary DTI Measures (Mean FA, MD, AD, and RD Values)

As shown in Fig 6 and Table 3, on the basis of the multiple regression analysis, age was found to be a factor that affected all the DTI parameters examined in all 3 tracts at a statistically significant level ( $P < .05$ , corrected) or at least at trend level (AD in genu of the CC). After age was accounted for, significant group differences of tract-based DTI measurements were found in MD, AD, and RD in all 3 WM tracts and the group difference was significant in FA in the genu of the CC (all  $P < .05$ , corrected).

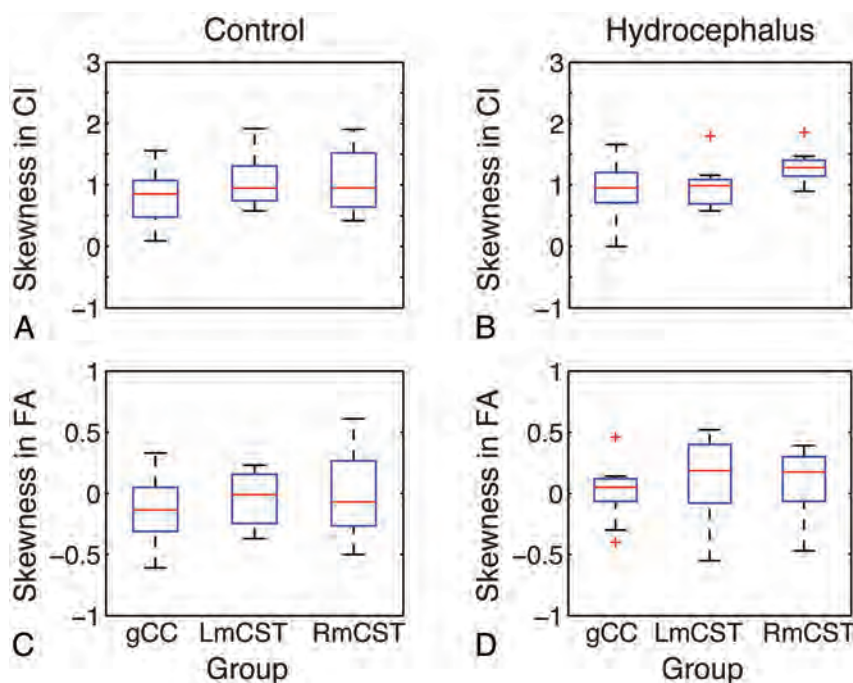


FIG 3. Boxplot showing the skewness index for connectivity index (A and B) and FA (C and D).

Table 1: Descriptive statistics of the within-tract connectivity index and FA skewness

Tracts	Group	CI			FA		
		Min	Median	Max	Min	Median	Max
gCC	Control (n = 16)	0.2	0.94	1.56	-0.61	-0.13	0.33
	Hydrocephalus (n = 11)	0.44	1.04	1.66	-0.4	0.1	0.46
Left mCST	Control (n = 16)	0.58	0.97	1.92	-0.37	0.00	0.23
	Hydrocephalus (n = 12)	0.58	1.05	1.80	-0.55	0.19	0.52
Right mCST	Control (n = 16)	0.42	1.10	1.91	-0.5	-0.01	0.61
	Hydrocephalus (n = 12)	0.9	1.33	1.86	-0.47	0.18	0.39

Note:—Min indicates minimum; Max, maximum; gCC, genu of the CC.

## DISCUSSION

Probabilistic tractography is a powerful fiber tracking method that calculates multiple pathways emanating from a seed region of interest and from each point along the reconstructed trajectories. It avoids the use of an FA threshold, thus allowing tracking to continue through brain regions where the level of uncertainty would cause a deterministic algorithm to fail.<sup>11,16-18</sup> In this study, we investigated tract-based WM connectivity and DTI measurements in children with hydrocephalus by using PDT. We tested and proved the working hypotheses: 1) The connectivity index derived from PDT is decreased in children with hydrocephalus; and 2) DTI measurements derived from PDT are abnormal in children with hydrocephalus, reflecting disruption in fiber continuity.

The most prominent functional deficits that are consistently reported in pediatric

patients with hydrocephalus are in such domains as motor, visuospatial, and other nonverbal intelligences.<sup>1-3</sup> These deficits have been associated with myelin sheath breakdown, axonal degeneration, or even loss of axons in the corpus callosum and periventricular white matter based on both human and animal neuropathologic studies.<sup>19</sup> In the present study, statistically significant differences in both the summary DTI measures and the connectivity measure were found in the comparison between children with hydrocephalus and those in the control group. We interpret this as evidence of WM changes as the result of neuropathology seen in hydrocephalus.

The connectivity index maps (Figs 1 and 2) are the connectivity distribution maps with the value at each voxel being the sum of the

sample streamlines passing through the voxel. In the present study, we defined a seed mask and a target mask for each subject on the basis of anatomic landmarks, to restrict the tractography in all the tracts examined to yield the specific tracts of interest. The connectivity measure is a quantification of the strength, or probability, of the connectivity for all those connections initiated from the seed voxels and reaching the target masks. Similar approaches based on PDT have been adopted by other studies to investigate the pathologic progression in amyotrophic lateral sclerosis,<sup>14</sup> to contrast the organization of prefrontal projection pathways in humans and macaque monkeys.<sup>20</sup>

In the present study, the histogram based on the aggregated normalized CI measures showed that children with hydrocephalus

had a lower percentage of voxels with higher connectivity and a higher percentage of voxels with low connectivity in all 3 tracts examined. The comparison of the within-tract summary connectivity measure between the 2 groups showed a consistent significant decrease in normalized CI values in children with hydrocephalus. As expected, examination of the connectivity index maps (Figs 1 and 2 as examples) showed that the voxels with high connectivity were located in the central portion of the tracts, while the voxels at the peripheral areas of a tract tended to have lower connectivity. We examined the summary connectivity measure (normalized CI) not only at the median but also at the lower and upper quartile values. The fact that the group contrast was significant at all 3 quartile levels indicates that this summary connectivity index, normalized CI, is sensitive to the pathology resulting from hydrocephalus throughout different portions of WM tracts in children with hydrocephalus.

Tract-based summary DTI measures showed a significant increase of MD, AD, and RD values, which was consistent in all

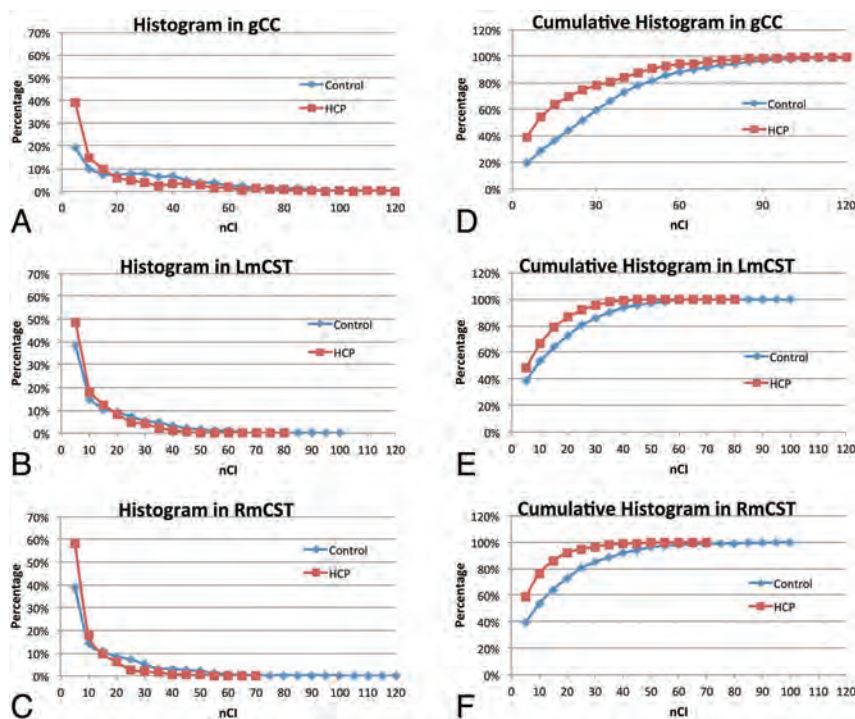


**FIG 4.** Percentile histograms of the normalized connectivity index (nCI) values for children with hydrocephalus and controls, respectively, in the genu of the CC (A) (30.5% and 56.3%), left mCST (B) (13.1% and 27.0%), and right mCST (C) (8% and 27.1%). The corresponding cumulative percentile histograms for the genu of the CC, left mCST, and right mCST are shown in D–F, respectively.

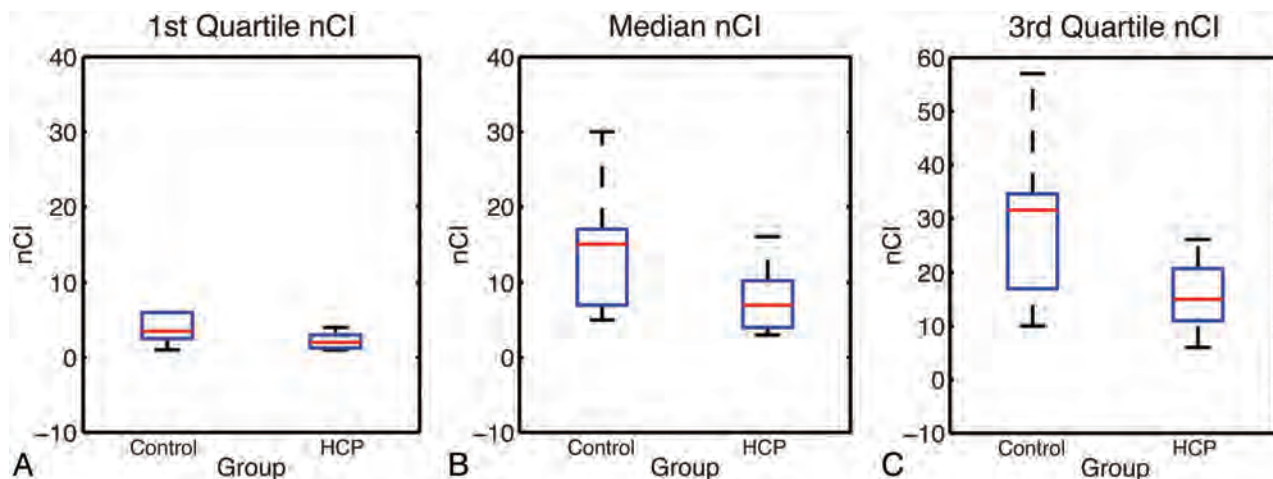


**FIG 5.** Boxplot showing the normalized CI for left mCST by using 3 different quartile levels of the normalized CI as a summary measurement. A, First quartile. B, Median. C, Third quartile.

**Table 2: Multiple regression analysis for each tract at 3 quartiles of normalized CI<sup>a</sup>**

	df	Dependent Variables	First Quartile			Median			Third Quartile		
			SE	T Value	P	SE	T Value	P	SE	T Value	P
gCC	24	Group	2.753	3.09	.015	6.452	3.26	.012	7.657	3.46	.018
		Age	0.118	-0.76	NS	0.277	-0.63	NS	0.329	-0.90	NS
Left mCST	25	Group	0.557	3.25	.015	2.334	3.03	.015	4.137	3.61	.023
		Age	0.024	-1.18	NS	0.103	-1.4	NS	0.182	-1.46	NS
Right mCST	25	Group	2.098	2.3	.059	4.997	2.92	.016	6.987	3.28	.019
		Age	0.092	-1.25	NS	0.2201	-1.13	NS	0.308	-1.21	NS

**Note:**—NS indicates not significant; SE, standard error; gCC, genu of the CC.

<sup>a</sup> All P values have been corrected for multiple comparisons using the false discovery rate method.

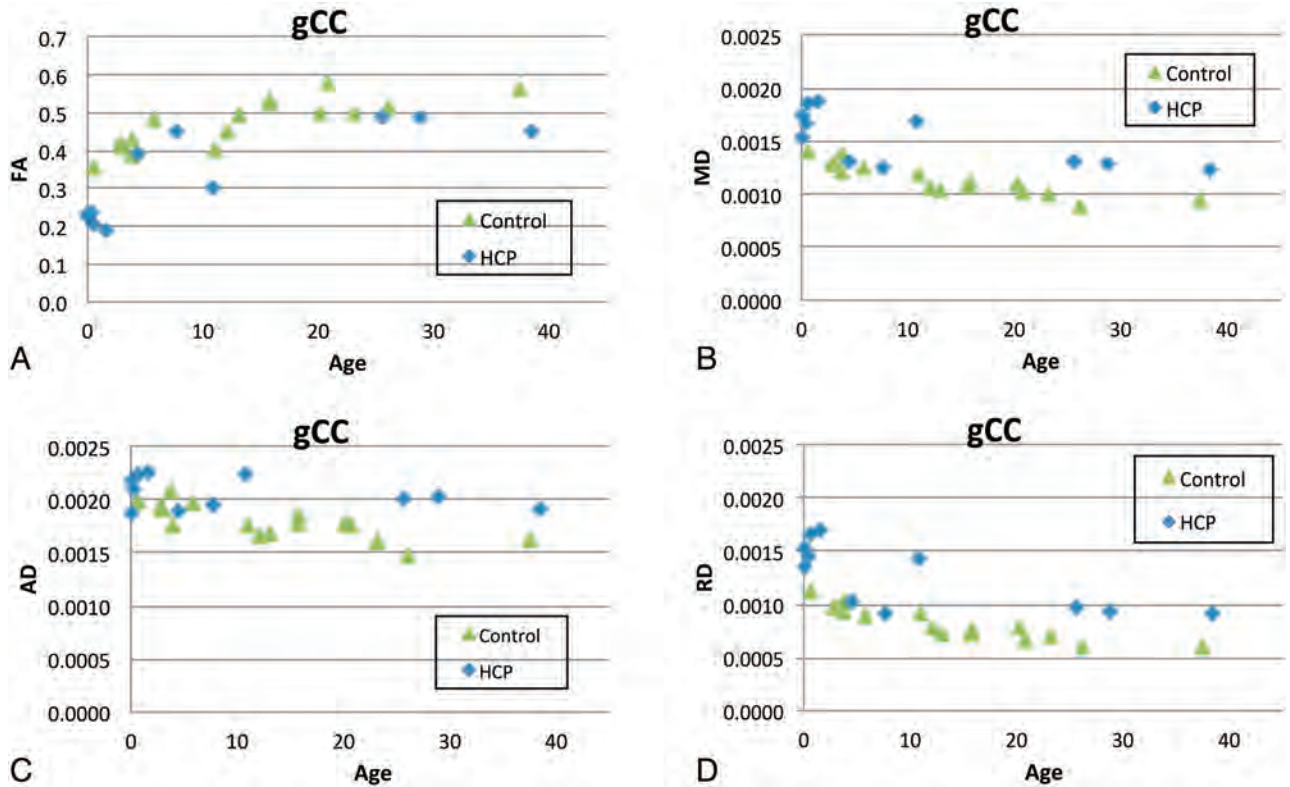


**FIG 6.** Comparison of DTI measures derived from PDT in the genu of the CC. A, FA, B, MD, C, AD, D, RD.

**Table 3: Multiple regression analysis for each tract and DTI variable<sup>a</sup>**

	df	Source	FA			MD			AD			RD		
			SE	T Value	P									
gCC	24	Group	0.022	5.36	.0024	0.000	-6.41	.0008	0.000	-4.57	.0005	0.000	-6.57	.0004
		Age	0.001	6.67	.0012	0.000	-4.62	.0006	0.000	-2.11	.0523	0.000	-5.33	.0003
Left mCST	25	Group	0.023	0.47	NS	0.000	-3.74	.0015	0.000	-4.25	.0005	0.000	-3.18	.0052
		Age	0.001	6.60	.0003	0.000	-4.62	.0003	0.000	-2.79	.1080	0.000	-5.25	.0002
Right mCST	25	Group	0.020	0.89	NS	0.000	-4.26	.0005	0.000	-3.46	.0028	0.000	-2.91	.0090
		Age	0.001	6.81	.0002	0.000	-5.26	.0002	0.000	-2.94	.0088	0.000	-5.19	.0002

**Note:**—NS indicates not significant; SE, standard error; gCC, genu of the CC.

<sup>a</sup> All P values have been corrected for multiple comparisons using the false discovery rate method.

tracts examined in children with hydrocephalus after accounting for age. FA in the genu of the CC was also found to be significantly lower in the children with hydrocephalus. These tract-based findings are consistent with previously reported region of interest-based results in terms of the patterns of abnormality,<sup>5</sup> and the differences in the patterns of DTI abnormalities between the genu of the CC and the mCST in the present study lend further credence to the concept of region-specific multifactorial variation in underlying white matter injury mechanisms in hydrocephalus.<sup>1,6</sup>

Although the group difference of FA in the left mCST and right mCST was not significant between the children with hydrocephalus and the controls (because some children with hydrocephalus had abnormally low FA while others had abnormally high FA values), the reduction in the connectivity measures in children with hydrocephalus remained statistically significant; this outcome emphasizes the importance of including both summary DTI measures and connectivity measures in future studies.

Differences in the normalized connectivity index between the children with hydrocephalus and those in the control group in the left and right mCSTs, illustrated in Fig 4D, -E, suggest that WM connectivity is subtly decreased in these long pathways in the patient group. This apparent reduction in the volume of WM with the highest connectivity might suggest an expectation or decreased sensorimotor function in children with hydrocephalus relative to the controls.

### Limitations

We note that the success of the PDT method may depend on the tract of interest, especially when it is performed in brains with large deformations, such as those in children with hydrocephalus. Even though the tracts were carefully examined to avoid extending into ventricle areas and different threshold levels were tested to ensure the consistency of the methodology, partial volume effect is difficult to quantify and cannot be excluded as a potential factor that may bias the results. The attempt to track the splenium of the CC was not successful in 9 of 12 children with hydrocephalus; this outcome can be attributed to the significant damage or even agenesis of the area. Our initial attempt to track the whole corticospinal tract was unsuccessful, likely due to the severe distortion of anatomic structures, which may have caused imaging and modeling errors, accumulated over a long pathway, to exceed even a very lenient threshold set in the PDT. This study may also suffer from the limited sample size and the lack of pathologic evidence to support the predictive value of the PDT-based measures. Nevertheless, the findings in the present study represent an initial success in the application of PDT in analyzing WM abnormalities in pediatric hydrocephalus. The success also points to possible applications of this approach in patients with other pathologies that distort white matter tracts, such as brain tumors or tuberous sclerosis. Future studies should include a larger sample size and both short- and long-term follow-up so that we can investigate the longitudinal progression during the developmental stages of childhood.

### CONCLUSIONS

It was demonstrated that the summary measures of connectivity and DTI based on the results of probabilistic diffusion tractography are sensitive to differences in WM microstructure in children with hydrocephalus compared with healthy controls. The PDT method may be a useful noninvasive tool to serve as an imaging biomarker for predicting behavioral and neuropsychological outcomes in this patient population with hydrocephalus or in assessing therapeutic efficacy in the treatment of hydrocephalus.

Disclosures: Akila Rajagopal—RELATED: Grant: NIH/NINDS 1R01NS066932.\* Joshua S. Shimony—RELATED: Grant: NIH.\* Comments: The study is part of an NIH grant. Robert C. McKinstry—RELATED: Grant: NIH.\* Comments: R01 NS066932 (W. Yuan, Principal Investigator; D.D. Limbrick, Washington University Principal Investigator) September 30, 2009 to September 30, 2014. Cincinnati Children's Hospital/NIH/NINDS, Longitudinal DTI Study in Children Treated for Congenital Hydrocephalus, UNRELATED: Employment: I appeared in the Siemens PET/MRI commercial and advertisement campaign. This support had nothing to do with this manuscript. Payment for Lectures (including service on Speakers Bureaus): Siemens paid an honoraria, travel, meals, and lodging so that I could give lectures reporting our experience with the PET/MRI. These lectures had nothing to do with the manuscript. Thomas Maloney—RELATED: Grant: NIH/NINDS 1R01 NS066932.\* Francesco T. Mangano—RELATED: Grant: NINDS/NIH.\* Scott K. Holland—RELATED: Support for Travel to Meetings for the Study or Other Purposes: NIH R01 grant.\* Comments: Annual research group meeting for this project was held in St. Louis. The grant covered the travel and lodging costs for me and others involved in the meeting, UNRELATED: Grants/Grants Pending: NIH.\* Sarah Simpson—RELATED: Grant: NIH, Comments:

The grant that supports this research pays my salary. Weihong Yuan—RELATED: Grant: NIH/NINDS 1R01 NS066932.\* \*Money paid to the institution.

### REFERENCES

1. Yuan W, McKinstry RC, Shimony JS, et al. **Diffusion tensor imaging properties and neurobehavioral outcomes in children with hydrocephalus.** *AJNR Am J Neuroradiol* 2013;34:439–45
2. Rourke BP. *Syndrome of Nonverbal Learning Disabilities.* New York: Guilford; 1995
3. Mataró M, Junque C, Poca MA, et al. **Neuropsychological findings in congenital and acquired childhood hydrocephalus.** *Neuropsychol Rev* 2001;11:169–78
4. Del Bigio MR, Wilson MJ, Enno T. **Chronic hydrocephalus in rats and humans: white matter loss and behavior changes.** *Ann Neurol* 2003;53:337–46
5. Yuan W, Mangano F, Air EL, et al. **Anisotropic diffusion properties in infants with hydrocephalus: a diffusion tensor imaging study.** *AJNR Am J Neuroradiol* 2009;30:1792–98
6. Assaf Y, Ben-Sira L, Constantini S, et al. **Diffusion tensor imaging in hydrocephalus: initial experience.** *AJNR Am J Neuroradiol* 2006;27:1717–24
7. Hattori TI, Aoki S, Yuasa T, et al. **White matter alteration in idiopathic normal pressure hydrocephalus: tract-based spatial statistics study.** *AJNR Am J Neuroradiol* 2012;33:97–103
8. Oishi KF, Jiang H, Li X, et al. **Atlas-based whole brain white matter analysis using large deformation diffeomorphic metric mapping: application to normal elderly and Alzheimer's disease participants.** *Neuroimage* 2009;46:486–99
9. Hattingen EJ, Melber J, Blasel S, et al. **Diffusion tensor imaging in patients with adult chronic idiopathic hydrocephalus.** *Neurosurgery* 2010;66:917–24
10. Yuan W, Holland SK., Shimony J, et al. **Quality assurance in multi-institution and multi-scanner MRI neuroimaging research.** In: *Proceedings of the International Paediatric Society London 2011: 6th Congress and Exhibition of the Joint Societies of Paediatric Radiology,* London, UK. May 27–31, 2011
11. Behrens TE, Berg HJ, Jbabdi S, et al. **Probabilistic diffusion tractography with multiple fiber orientations: what can we gain?** *Neuroimage* 2007;34:144–55
12. Behrens TE, Woolrich MW, Jenkinson M, et al. **Characterization and propagation of uncertainty in diffusion-weighted MR imaging.** *Magn Reson Med* 2003;50:1077–88
13. Guye M, Parker GJ, Symms M, et al. **Combined functional MRI and tractography to demonstrate connectivity of the human primary motor cortex in vivo.** *Neuroimage* 2003;19:1349–60
14. Ciccarelli O, Behrens TE, Altmann DR, et al. **Probabilistic diffusion tractography: a potential tool to assess the rate of disease progression in amyotrophic lateral sclerosis.** *Brain* 2006;129:1859–71
15. Benjamini Y, Hochberg Y. **Controlling the false discovery rate: a practical and powerful approach to multiple testing.** *J R Stat Soc* 1995;57:289–300
16. Parker GJ, Haroon HA, Wheeler-Kingshott CA. **A framework for a Streamline-Based Probabilistic Index of Connectivity (PICo) using a structural interpretation of MRI diffusion measurements.** *J Magn Reson Imaging* 2003;18:242–54
17. Tuch DS, Belliveau JW, Wedeen VJ. **A path integral approach to white matter tractography.** In: *Proceedings of the 16th Scientific Meeting and Exhibition of the International Society of Magnetic Resonance in Medicine,* Toronto, Ontario, Canada. May 3–9, 2000;8:791
18. Jones DK, Pierpaoli C. **Confidence mapping in diffusion tensor magnetic resonance imaging tractography using a bootstrap approach.** *Magn Reson Med* 2005;53:1143–49
19. Del Bigio MR. **Neuropathological changes caused by hydrocephalus.** *Acta Neuropathologica* 1993;85:573–85
20. Ramnani N, Behrens TE, Johansen-Berg H, et al. **The evolution of prefrontal inputs to the cortico-pontine system: diffusion imaging evidence from Macaque monkeys and humans.** *Cerebral Cortex* 2006;16:811–18

# Abnormal Functional Network Connectivity among Resting-State Networks in Children with Frontal Lobe Epilepsy

E. Widjaja, M. Zamyadi, C. Raybaud, O.C. Snead, and M.L. Smith



## ABSTRACT

**BACKGROUND AND PURPOSE:** Epilepsy is considered a disorder of neural networks. The aims of this study were to assess functional connectivity within resting-state networks and functional network connectivity across resting-state networks by use of resting-state fMRI in children with frontal lobe epilepsy and to relate changes in resting-state networks with neuropsychological function.

**MATERIALS AND METHODS:** Fifteen patients with frontal lobe epilepsy and normal MR imaging and 14 healthy control subjects were recruited. Spatial independent component analysis was used to identify the resting-state networks, including frontal, attention, default mode network, sensorimotor, visual, and auditory networks. The Z-maps of resting-state networks were compared between patients and control subjects. The relation between abnormal connectivity and neuropsychological function was assessed. Correlations from all pair-wise combinations of independent components were performed for each group and compared between groups.

**RESULTS:** The frontal network was the only network that showed reduced connectivity in patients relative to control subjects. The remaining 5 networks demonstrated both reduced and increased functional connectivity within resting-state networks in patients. There was a weak association between connectivity in frontal network and executive function ( $P = .029$ ) and a significant association between sensorimotor network and fine motor function ( $P = .004$ ). Control subjects had 79 pair-wise independent components that showed significant temporal coherence across all resting-state networks except for default mode network–auditory network. Patients had 66 pairs of independent components that showed significant temporal coherence across all resting-state networks. Group comparison showed reduced functional network connectivity between default mode network–attention, frontal-sensorimotor, and frontal-visual networks and increased functional network connectivity between frontal-attention, default mode network–sensorimotor, and frontal-visual networks in patients relative to control subjects.

**CONCLUSIONS:** We found abnormal functional connectivity within and across resting-state networks in children with frontal lobe epilepsy. Impairment in functional connectivity was associated with impaired neuropsychological function.

**ABBREVIATIONS:** FLE = frontal lobe epilepsy; IC = independent component; ICA = independent component analysis; DMN = default mode network; RSN = resting-state network; TLE = temporal lobe epilepsy; FNC = functional network connectivity; DKEFS = Delis-Kaplan Executive Function System

Functional connectivity as measured by the use of fMRI is defined as the temporal synchronization of low-frequency fluctuations arising from spontaneous neuronal activities in distant brain regions.<sup>1</sup> Resting-state networks (RSNs) refer to spatially segregated brain regions that exhibit spontaneous low-frequency fluctuations and may represent intrinsic brain functional connec-

tivity in discrete neuroanatomic systems.<sup>2</sup> A variety of RSNs has been identified including default mode network (DMN), attention, sensorimotor, visual, and auditory networks.<sup>3,4</sup> Independent component analysis (ICA) has been increasingly used to examine functional connectivity.<sup>5-7</sup> ICA is a method for recovering underlying signals from linear mixtures of these signals and draws on higher-order signal statistics to determine a set of “components” that are maximally independent of each other.<sup>8</sup> ICA has been found to be useful and able to capture the complex nature of fMRI time courses as well as to produce consistent spatial components.<sup>9</sup> Within a given component, the regions are strongly temporally coherent as the result of ICA assumption of linear mixing. In spatial ICA, the different components are spatially independent but can have temporal dependencies. This temporal dependency among ICA components has been defined as func-

Received January 4, 2013; accepted after revision March 26.

From Diagnostic Imaging (E.W., M.Z., C.R., O.C.S.) and Division of Neurology, Hospital for Sick Children (E.W.), Toronto, Ontario, Canada; and Department of Psychology (M.L.S.), University of Toronto, Toronto, Ontario, Canada.

This work was supported by a GE-AUR award and the Derek Harwood Nash chair.

Please address correspondence to Elysa Widjaja, MD, 555 University Ave, Toronto, Ontario M5G 1X8, Canada; e-mail: Elysa.Widjaja@sickkids.ca

Indicates article with supplemental on-line table.

<http://dx.doi.org/10.3174/ajnr.A3608>

tional network connectivity (FNC). FNC provides a means of assessing temporal connectivity among RSNs.

Epilepsy has been postulated to be a disorder of large neural networks on the basis of electroencephalography, PET, and SPECT studies.<sup>10</sup> Several studies have evaluated RSNs by the use of fMRI in adults with temporal lobe epilepsy (TLE), generalized tonic-clonic seizures, and absence epilepsy<sup>11-16</sup> and found impairment in many of the individual RSNs. There is currently limited information available on functional connectivity in children with epilepsy.<sup>17,18</sup> Frontal lobe epilepsy (FLE) is a common localization-related epilepsy in childhood.<sup>19</sup> The interictal discharges arising from a unilateral frontal lobe focus in FLE are more likely to spread to both hemispheres and form secondary bilateral synchrony, and children with FLE are also more likely to have secondarily generalized tonic-clonic seizures relative to TLE.<sup>20</sup> Our hypothesis is that in children with FLE, functional connectivity within RSNs including frontal, DMN, and attention networks are abnormal, related to spread of seizure activity, or caused by underlying abnormal brain development that predisposed to epilepsy. The aims of this study were to assess functional connectivity within RSNs and FNC across RSNs by use of resting-state fMRI in children with FLE and to relate changes in RSNs with neuropsychological function.

## MATERIALS AND METHODS

### Subjects

This prospective study had the approval of the research ethics board at the Hospital for Sick Children, and written informed consent was obtained from parents and assent from subjects. Children with FLE were recruited from the epilepsy surgery clinic. Healthy control subjects without neurologic or psychiatric disorders were recruited through community publications.

### MR Imaging and Data Preprocessing

MR imaging was performed on a 3T scanner (Achieva; Philips, Best, the Netherlands) with the use of an 8-channel phased-array head coil in all patients and control subjects. Resting-state fMRI was acquired with the eyes closed in all subjects, by use of the following parameters: TR = 2000 ms, TE = 30 ms, flip angle = 90°, FOV = 220 mm, matrix = 88 × 86 mm, section thickness = 5 mm, and 180 volumes, aligned to the anterior/posterior commissure line. Axial and coronal FLAIR, axial and coronal T2 and proton density, and volumetric T1 sequences were performed in patients. An additional volumetric T1 sequence was performed in control subjects.

A series of data preprocessing steps was carried out by use of Analysis of Functional NeuroImages (AFNI<sup>21</sup>; <http://afni.nimh.nih.gov/afni/>) and FMRIB Software Library (FSL<sup>22</sup>; <http://www.fmrib.ox.ac.uk/fsl/>) software packages. The preprocessing steps included removing the first 10 volumes of each fMRI run to allow for T1-equilibrium effects, and the remaining volumes of the fMRI dataset were rigidly registered to the first volume of the same run. Section-timing correction was then performed on the motion-corrected data. The anatomic T1 and fMRI datasets were skull-stripped by use of AFNI. The fMRI dataset was first aligned to T1 by affine transformation, and subsequently the T1 was affinely registered to Montreal Neurological Institute's MNI152

brain template. The 2 transformations were then concatenated and used to resample the fMRI image to the MNI atlas. The fMRI data were then spatially smoothed by use of a gaussian kernel of 8-mm full width at half maximum.

### Independent Component Analysis

To identify RSNs, spatial ICA was used to decompose the data of all individuals in both control and patient groups into 75 independent components (ICs). Each component is associated with a waveform that corresponds to the temporal profile of a specific pattern of coherent brain activity and a spatial map that expresses the intensity with which this connectivity is found across the voxels.<sup>23</sup> We used the Infomax algorithm implemented in the group ICA of fMRI Toolbox (GIFT<sup>24</sup>; <http://icatb.sourceforge.net/groupica.htm>, version v2.0e). A high model order ICA (75 components) was chosen because it has been shown that higher orders resulted in refined components corresponding to known anatomic and functional composition.<sup>25-28</sup>

All ICs were spatially correlated with the T-maps of the 27 RSNs reported by Allen et al<sup>28</sup> (available on-line at [http://mialab.mrn.org/data/hcp/RSN\\_HC\\_unthresholded\\_tmaps.nii](http://mialab.mrn.org/data/hcp/RSN_HC_unthresholded_tmaps.nii)). Briefly, they identified a subset of ICs as resting-state components by inspecting the spatial maps and average power spectra. The resting-state components were grouped according to their anatomic and functional properties and included auditory systems represented by a single component; sensorimotor, visual, and attention networks, each captured by 6 components; and frontal and DMN, each captured by 4 components. The components corresponding to each RSN were extracted from all subjects in both groups. Intensity values in each spatial map were converted to *z* scores to reflect the degree to which the time series of each voxel correlated with the time series of a specific component, scaled by the standard deviation of the error term. In other words, the *z* score is a measure of how many standard deviations the signal is from the background noise.<sup>29</sup>

A random-effect analysis was done on the *Z*-maps of all RSN components within each group by means of a 1-sample *t* test. Thresholds were set at  $P < .005$  (false discovery rate corrected). Next, a 2-sample *t* test was performed to compare the *Z*-maps of the RSNs between the patient and control groups. In this case, the threshold was set at  $P < .005$  (uncorrected), and a minimum cluster size of 30 voxels was used. The group comparison was masked to the voxels within the networks of either the control or patient groups.<sup>15,30</sup>

### Neuropsychological Assessment and Clinical Parameters

Neuropsychological assessment was conducted in patients and control subjects to assess executive function (Delis-Kaplan Executive Function System [DKEFS] color-word interference test inhibition, DKEFS category switch, DKEFS sorting test, DKEFS verbal fluency, and Connor CPT II omission test), attention (Trail-Making tests A and B), and fine motor function (grooved pegboard dominant and nondominant tests). The raw scores of the neuropsychological tests were converted to *z* scores. The mean cognitive domain *z* scores for executive function, attention, and fine motor function were computed. The *z* scores of the clusters that were significant after group comparison for the frontal net-

work were regressed on executive function, DMN and attention networks were regressed on attention, and the sensorimotor network was regressed on fine motor function in all subjects. A value of  $P < .01$  was considered statistically significant.

The  $z$  scores of the clusters that were significant after group comparison were regressed against age at seizure onset and duration of epilepsy. A value of  $P < .01$  was considered statistically significant.

### **Functional Network Connectivity**

The ICA algorithm assumes that the time courses of brain areas within the same component are synchronous.<sup>31</sup> Despite being spatially independent, significant temporal correlations can exist between the components. We studied such temporal relationships by examining the time series of the resting-state components of interest by use of the FNC toolbox (available on-line at <http://mialab.mrn.org/software/fnc/index.html>). The constrained maximal lagged correlation was calculated between component time courses as previously described by Jafri et al.<sup>32</sup>

To enable detection of subrepetition time, hemodynamic delay differences between subjects, the time courses from all the resting-state components for all subjects were first interpolated by use of a low-pass interpolation algorithm implemented in Matlab (MathWorks, Natick, Massachusetts, 2000). The maximal lagged correlation between pair-wise combinations of all ICs of interest was then calculated with the maximum possible lag between time courses set at  $\pm 3$  seconds. More specifically, the correlation between 2 IC time courses, A and B, was calculated by circularly shifting B around A from  $-3$  to  $+3$  seconds. The maximum absolute correlation value was saved for all pairs of IC time courses for all subjects. Average correlation and lag values were then calculated for all pairs of ICs for control and patient groups separately. Statistically significant correlations from all possible pair-wise combinations were extracted by use of the Student  $t$  test for both groups,<sup>32</sup> uncorrected for multiple comparisons because of the exploratory nature of the analysis.

## **RESULTS**

### **Subjects**

Fifteen patients with FLE, with a mean age of 13.9 years ( $SD = 2.7$ ), consisting of 8 female and 7 male subjects were recruited. The diagnosis of FLE was based on video electroencephalography, magnetoencephalography, and  $^{18}\text{F}$ -fluorodeoxyglucose PET scan. Eight patients had left FLE and 7 had right FLE. All patients had normal MR imaging at 3T. The mean age of seizure onset was 8.2 years ( $SD = 3.8$ ), mean duration of epilepsy was 5.5 years ( $SD = 3.1$ ), mean seizure frequency was 12.3 per week ( $SD = 15.7$ ), and mean number of antiepileptic medications was 2.3 ( $SD = 0.6$ ). Fourteen healthy control subjects were recruited, with a mean age of 14.7 years ( $SD = 2.7$ ), consisting of 7 female and 7 male subjects. There was no significant difference between the age of the patients and control subjects ( $P > .05$ ).

### **RSNs in Control Subjects and Patients**

There were no group differences between rotational ( $P = .6213$ ) and translational ( $P = .4731$ ) motion. We identified 25 ICs as resting-state components, which correlated with the T-maps of

RSNs reported by Allen et al<sup>28</sup> (correlation ranging from 0.4–0.77). The frontal network was captured by 3 components (ICs 28, 40, and 46), including the bilateral middle frontal gyri and bilateral inferior frontal gyri. Components 4, 36, 50, and 75 represent DMN with activation in the areas of bilateral anterior cingulate gyri, bilateral middle frontal gyri, bilateral precuneus, and bilateral posterior cingulate gyri. The activation of the attention network was captured in 5 ICs (33, 35, 48, 59, and 65) located at bilateral insula, bilateral precuneus, bilateral superior parietal lobule, bilateral middle frontal gyri, right inferior parietal lobule, and right superior temporal gyrus. Six components (ICs 8, 12, 14, 42, 43, and 60) were classified as sensorimotor network with activation patterns in bilateral precentral gyri, bilateral postcentral gyri, bilateral inferior parietal lobule, bilateral paracentral lobule, and bilateral midcingulate. The auditory network was represented by a single component (IC 62) with activation focused in bilateral superior temporal gyri. Finally, the visual network was captured by 6 ICs (20, 41, 47, 52, 56, and 63) situated in bilateral inferior temporal gyri, bilateral calcarine, bilateral lingual, bilateral fusiform gyri, and left cuneus. The spatial maps of the 6 RSNs are shown in Fig 1. The identified RSNs were similar to those described by previous studies that used high model order.<sup>25,26,28</sup>

### **Group Comparison of Functional Connectivity within RSN**

A summary of regions showing group differences in spatial maps is presented in Fig 2. The frontal network was the only network that showed only reduced connectivity. The remaining 5 networks demonstrated both reduced and also increased functional connectivity within the RSNs. Within the frontal network, there was reduced connectivity in the right superior frontal gyrus in patients with FLE relative to control subjects. The DMN showed reduced connectivity in the right anterior cingulate, left medial superior frontal, and right superior frontal gyri in patients with FLE and increased connectivity in the left inferior parietal lobule. Within the attention network, there was decreased connectivity in the right precuneus, right operculum, and right superior frontal gyrus and increased connectivity in the left inferior parietal, right inferior frontal, and right superior temporal gyri in patients with FLE. The sensorimotor network demonstrated reduced connectivity in the right and left precentral, left insula, right paracentral lobule, right and left midcingulate, and right supplementary motor cortex in patients with FLE relative to control subjects and a single cluster of increased connectivity in the right postcentral gyrus. The auditory network showed reduced connectivity in the right superior temporal gyrus and increased connectivity in the left superior temporal gyrus in patients relative to control subjects. Finally, the visual network had decreased connectivity in the right parahippocampal and right fusiform gyri and increased connectivity in the right calcarine and right lingual cortex in patients.

### **Relation Between RSNs and Neuropsychological Function and Clinical Seizure Parameters**

Patients performed worse than control subjects on executive function ( $P = .004$ ), attention ( $P = .011$ ), and fine motor function ( $P = .002$ ). There was a weak relation between reduced connectivity in the right superior frontal gyrus of frontal network and

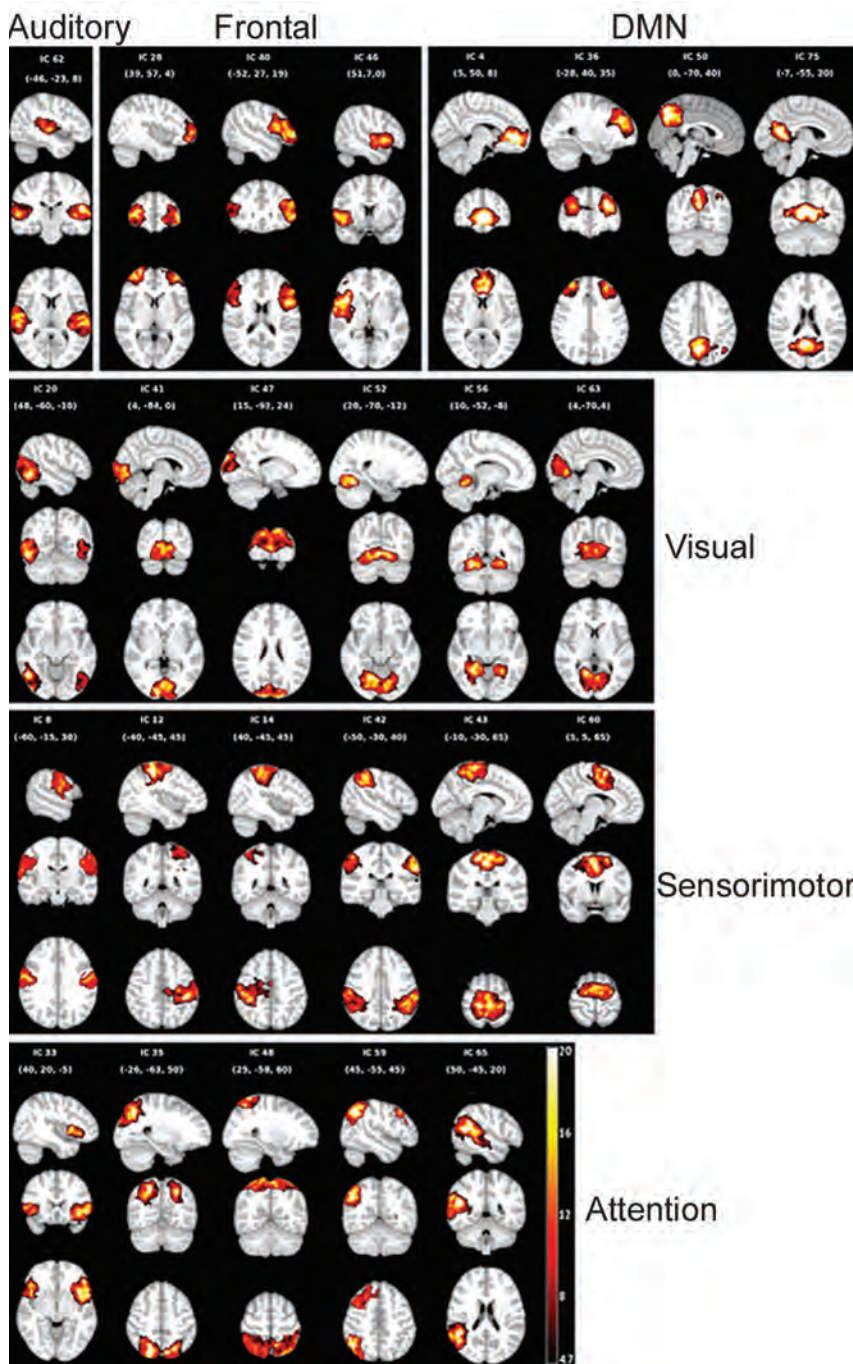


**FIG 1.** Spatial maps of the components identified as resting-state networks. Spatial maps are plotted as T-maps and overlaid on Montreal Neurological Institute 152 template. Top row (from left to right) shows the auditory, frontal, and default mode networks. Second, third, and fourth rows represent the visual, sensorimotor, and attention networks.

impaired executive function ( $t = 2.361, P = .029$ ). There was no significant association between regions of abnormal connectivity in DMN or attention networks with attention. Reduced connectivity in the right paracentral lobule of sensorimotor network was significantly associated with impaired fine motor function ( $t = 3.236, P = .004$ ).

Within the attention network, increased connectivity of right superior temporal gyrus was negatively associated with age at seizure onset ( $\beta = -0.226, t = -3.21, P = .009$ ). Within the auditory network, reduced connectivity of right superior temporal

gyrus was positively associated with age at seizure onset ( $\beta = 0.209, t = 3.291, P = .008$ ). There was no relation between significant clusters in attention and auditory networks and duration of epilepsy. There was no relation between z scores of significant clusters in the frontal, DMN, sensorimotor, and visual networks with age at seizure onset or duration of epilepsy.

### Functional Network Connectivity

Within the control group, there were 79 pair-wise ICs that showed significant temporal coherence, involving the following pairs of RSNs: frontal-attention, frontal-DMN, frontal-visual, frontal-sensorimotor, frontal-auditory, DMN-sensorimotor, DMN-attention, DMN-visual, attention-sensorimotor, attention-auditory, attention-visual, sensorimotor-visual, sensorimotor-auditory, and visual-auditory (On-line Table). The only pair of RSNs that did not demonstrate significant FNC in the control group was the DMN-auditory networks. Within the patient group, there were 66 pairs of ICs that showed significant temporal coherence across of all the 6 combinations of RSNs.

Group comparison of pair-wise ICs showed reduced FNC between DMN-attention (IC4-IC65), frontal-sensorimotor (IC46-IC12), and frontal-visual (IC46-IC52) and increased FNC between frontal-attention (IC40-IC65), DMN-somatosensory (IC50-IC60), and frontal-visual (IC40-IC63) (Fig 3) in patients relative to control subjects. There were no significant changes in FNC between frontal-DMN, frontal-auditory, DMN-visual, DMN-auditory, attention-sensorimotor, attention-visual, attention-auditory, sensorimotor-visual, sensorimotor-auditory, and visual-auditory.

### DISCUSSION

We found reduced functional connectivity in the frontal network and both reduced and increased connectivity in DMN, attention, sensorimotor, auditory, and visual RSNs in patients with FLE relative to control subjects. Reduced functional connectivity was thought to reflect dysfunction of the network, and increased functional connectivity has been interpreted as a compensatory mechanism or reorganization of the network.<sup>33</sup> Dysfunction of RSNs may be related to spread of seizures or may be caused by underlying abnormal brain development that predisposed to epilepsy. As shown in FNC analysis, these networks are functionally connected, and dysfunction in one network may lead to dysfunction in the other networks. We have also found

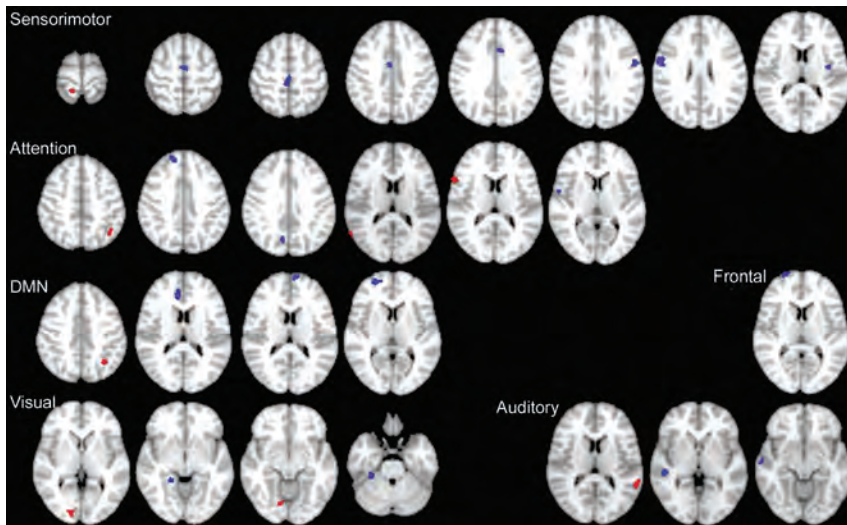


**FIG 2.** Regions showing group differences in spatial maps for the sensorimotor, attention, and default mode networks, and frontal, auditory, and visual networks.

fewer pair-wise ICs across the networks in patients relative to control subjects, and 6 of these pairs of ICs showed abnormal FNC.

Our findings of reduced and increased functional connectivity in the RSNs were similar to prior studies on adults with epilepsy. In patients with generalized tonic-clonic seizures, both decreased and increased functional connectivity in the DMN and dorsal attention networks have been identified.<sup>11</sup> In patients with left mesial TLE, there was a trend for decreased connectivity of the left anterior and posterior hippocampi link and a trend for increased connectivity of the right anterior and posterior hippocampi link.<sup>33</sup> In another study of adults with mesial TLE, 8 regions of reduced connectivity and 1 area of increased connectivity were found in the attention network.<sup>12</sup> More recently, Luo et al<sup>34</sup> found both reduced and increased functional connectivity in 16 patients with a variety of partial epilepsies.

Executive function,<sup>35,36</sup> attention,<sup>37,38</sup> and motor coordination<sup>39</sup> have previously been shown to be impaired in children with FLE. We have found an association between decreased connectivity in the RSNs and impaired neuropsychological function. There was a weak association between connectivity in the right superior frontal gyrus of the frontal network and executive function and a significant association between connectivity in the right paracentral lobule of sensorimotor network and fine motor function. Vaessen et al<sup>18</sup> also found that higher modularity scores on resting-state fMRI were associated with decreased cognitive performance, as measured by increased computerized visual searching task reaction time. These findings suggest that impaired functional networks may be part of the neural underpinning for neuropsychological impairment. The lack of significant association between connectivity in DMN and attention networks with attention in our study was not clear. Zhang et al<sup>12</sup> found a negative correlation between Trail-Making test (part B) scores and z scores in dorsal attention networks in adults with mesial TLE. Rocca et al<sup>40</sup> found significant correlations between left medial prefrontal and anterior cingulate DMN resting-state activity with the Paced

Auditory Serial Attention Test but not with the Trail-Making test. Failure to detect an association between resting-state DMN or attention networks and attention have numerous causes. We obtained the composite scores for 2 components of Trail-Making test (part A and B) for the purpose of data reduction. It is possible that impaired connectivity within the DMN or attention networks may have a greater association with a certain attention task, or the sample size in our study may be inadequate to detect the association.

We found a negative association between increased functional connectivity in the right superior temporal gyrus of the attention network with age at seizure onset and a positive association between reduced connectivity in right superior temporal gyrus of the auditory network with age at seizure onset. The data suggest that earlier age at seizure onset is associated with greater reduction in functional connectivity in some RSNs and greater compensatory increase in functional connectivity in other RSNs. However, it is not clear why some networks (attention and auditory networks) showed a significant association with age at seizure onset, whereas others did not (frontal, DMN, sensorimotor, and visual networks). It could be that the association is weaker with some networks, and a larger sample size is required to demonstrate the smaller association. In contrast, in the adult epilepsy literature, an association between functional connectivity has been reported with duration of epilepsy rather than age at seizure onset.<sup>11,15</sup> We have not found an association between functional connectivity and duration of epilepsy. It could be that the maturing brain in children is more vulnerable to disruption in functional connectivity, and this disruption occurs relatively early on in the disease. Alternatively, there is pre-existing disruption in functional connectivity related to subtle abnormal brain development not detected on structural MR imaging and hence the lack of association between functional connectivity and duration of epilepsy.

In our study, we found fewer FNCs in the FLE group than the control group, with 66 pair-wise ICs in patients relative to 79 pairwise ICs in control subjects. There was less FNC in patients, particularly those that involve the frontal network (frontal-attention, frontal-DMN, frontal-sensorimotor, frontal-auditory, and frontal-visual). Because the seizure focus is in the frontal lobe, spread of seizure activity may have led to fewer pair-wise IC correlations among those networks that were connected to the frontal network. Luo et al<sup>34</sup> also found decreased FNC in patients with TLE (15 pair-wise RSNs) and mixed partial epilepsy (10 pair-wise RSNs) relative to control subjects (19 pair-wise RSNs). We found more pair-wise ICs for the DMN-attention and DMN-auditory networks in patients relative to control subjects and fewer pair-wise ICs for the DMN-sensorimotor and DMN-visual networks. Jafri et al<sup>32</sup> found more pair-wise connectivity of the DMN with

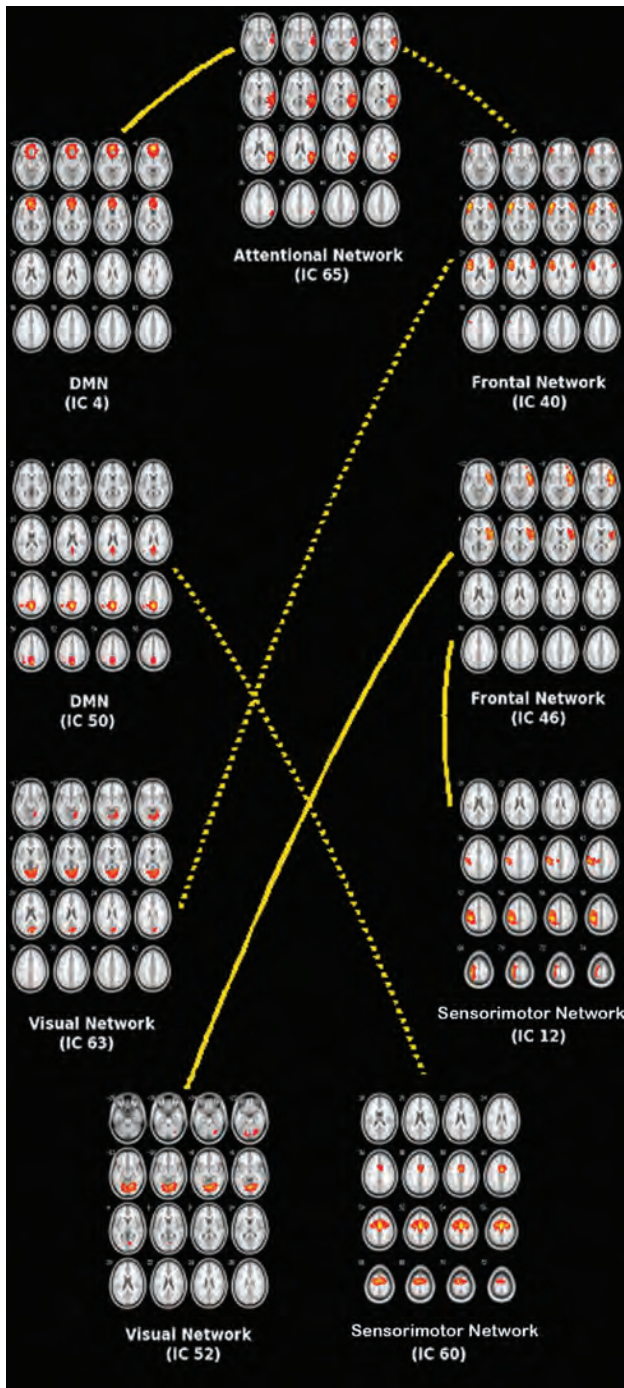


**FIG 3.** Functional network connectivity between resting-state networks. Group comparison of pair-wise independent components shows reduced FNC (solid line) between DMN-attention (IC4-IC65), frontal-sensorimotor (IC46-IC12), and frontal-visual (IC46-IC52) networks in patients and increased FNC (dotted line) between frontal-attention (IC40-IC65), DMN-sensorimotor (IC50-IC60), and frontal-visual (IC40-IC63) networks in patients relative to control subjects.

other networks in patients with schizophrenia, which was postulated to be due to greater dependency of brain regions in the DMN on the function of other neural circuits or vice versa during resting state. The greater number of pair-wise ICs for the DMN-attention and DMN-auditory networks in our study could be for the same reason. Vaessen et al<sup>18</sup> evaluated the resting-state con-

nectivity by use of graph theoretical metrics of whole-brain networks. They found that children with FLE have a decrease in long-range and an increase in interhemispheric connectivity, as well as higher modularity scores, suggesting the presence of more functionally isolated brain modules. The authors used a “global” approach to demonstrate a disruption of whole-brain networks. In contrast, we have used both a “local” approach of evaluating individual RSNs and a more “global” approach of assessing FNC. Despite differences in methodology, we arrived at the same conclusion that there is widespread disruption of brain networks in children with FLE.

Because of the small number of patients, we have not assessed differences in right and left FLE. Bettus et al<sup>33</sup> evaluated adults with mesial TLE and found that patients with left mesial TLE showed disruption of the left external capsule–anterior hippocampus link and a trend of decreased connectivity of the left anterior hippocampus–posterior hippocampus link. On the other hand, patients with right mesial TLE showed a trend of increased connectivity of the right anterior hippocampus–posterior hippocampus link.

## CONCLUSIONS

In summary, we found abnormal functional connectivity both within and across the RSNs in children with FLE, further supporting the concept that epilepsy is a disorder affecting neural networks. Impaired connectivity in the RSNs was associated with impaired neuropsychological function, which suggests that RSNs may be part of the neural underpinning of cognition. We have found not only reduced but also elevated functional connectivity within RSNs and also FNC across the RSNs, which suggests that brain plasticity may play a role in the reorganization of the neural networks.

Disclosures: Elysa Widjaja—RELATED: Grant: GE-AUR award and Derek Harwood Nash chair\*; UNRELATED: Grants/Grants Pending: Sickkids Foundation/CIHR Institute of Human Development, Child and Youth Health\* (\*money paid to institution).

## REFERENCES

1. Fox MD, Snyder AZ, Vincent JL, et al. **The human brain is intrinsically organized into dynamic, anticorrelated functional networks.** *Proc Natl Acad Sci U S A* 2005;102:9673–78
2. Fox MD, Raichle ME. **Spontaneous fluctuations in brain activity observed with functional magnetic resonance imaging.** *Nat Rev Neurosci* 2007;8:700–11
3. Fox MD, Corbetta M, Snyder AZ, et al. **Spontaneous neuronal activity distinguishes human dorsal and ventral attention systems.** *Proc Natl Acad Sci U S A* 2006;103:10046–51
4. Mantini D, Perrucci MG, Del Gratta C, et al. **Electrophysiological signatures of resting state networks in the human brain.** *Proc Natl Acad Sci U S A* 2007;104:13170–75
5. Calhoun VD, Adali T, Pearlson GD, et al. **Spatial and temporal independent component analysis of functional MRI data containing a pair of task-related waveforms.** *Hum Brain Mapp* 2001;13:43–53
6. Esposito F, Scarabino T, Hyvarinen A, et al. **Independent component analysis of fMRI group studies by self-organizing clustering.** *Neuroimage* 2005;25:193–205
7. McKeown MJ, Sejnowski TJ. **Independent component analysis of fMRI data: examining the assumptions.** *Hum Brain Mapp* 1998;6:368–72
8. Calhoun VD, Adali T. **Unmixing fMRI with independent component analysis.** *IEEE Eng Med Biol Mag* 2006;25:79–90

9. Turner GH, Twieg DB. **Study of temporal stationarity and spatial consistency of fMRI noise using independent component analysis.** *IEEE Trans Med Imaging* 2005;24:712–18
10. Spencer SS. **Neural networks in human epilepsy: evidence of and implications for treatment.** *Epilepsia* 2002;43:219–27
11. Wang Z, Lu G, Zhang Z, et al. **Altered resting state networks in epileptic patients with generalized tonic-clonic seizures.** *Brain Res* 2010;1374:134–41
12. Zhang Z, Lu G, Zhong Y, et al. **Impaired attention network in temporal lobe epilepsy: a resting fMRI study.** *Neurosci Lett* 2009;458:97–101
13. Luo C, Li Q, Lai Y, et al. **Altered functional connectivity in default mode network in absence epilepsy: a resting-state fMRI study.** *Hum Brain Mapp* 2011;32:438–49
14. Liao W, Zhang Z, Pan Z, et al. **Default mode network abnormalities in mesial temporal lobe epilepsy: a study combining fMRI and DTI.** *Hum Brain Mapp* 2010;32:883–95
15. Zhang Z, Lu G, Zhong Y, et al. **Impaired perceptual networks in temporal lobe epilepsy revealed by resting fMRI.** *J Neurol* 2009;256:1705–13
16. Waites AB, Briellmann RS, Saling MM, et al. **Functional connectivity networks are disrupted in left temporal lobe epilepsy.** *Ann Neurol* 2006;59:335–43
17. Mankinen K, Jalovaara P, Paakki JJ, et al. **Connectivity disruptions in resting-state functional brain networks in children with temporal lobe epilepsy.** *Epilepsy Res* 2012;100:168–78
18. Vaessen MJ, Braakman HM, Heerink JS, et al. **Abnormal modular organization of functional networks in cognitively impaired children with frontal lobe epilepsy.** *Cereb Cortex* 2013;23:1997–2006
19. Lawson JA, Cook MJ, Vogrin S, et al. **Clinical, EEG, and quantitative MRI differences in pediatric frontal and temporal lobe epilepsy.** *Neurology* 2002;58:723–29
20. Hu Y, Jiang L, Yang Z. **Video-EEG monitoring differences in children with frontal and temporal onset seizures.** *Int J Neurosci* 2012;122:92–101
21. Cox RW. **AFNI: software for analysis and visualization of functional magnetic resonance neuroimages.** *Comput Biomed Res* 1996;29:162–73
22. Smith SM, Jenkinson M, Woolrich MW, et al. **Advances in functional and structural MR image analysis and implementation as FSL.** *Neuroimage* 2004;23(Suppl 1):S208–19
23. Celone KA, Calhoun VD, Dickerson BC, et al. **Alterations in memory networks in mild cognitive impairment and Alzheimer's disease: an independent component analysis.** *J Neurosci* 2006;26:10222–31
24. Calhoun VD, Adali T, Pearlson GD, et al. **A method for making group inferences from functional MRI data using independent component analysis.** *Hum Brain Mapp* 2001;14:140–51
25. Kiviniemi V, Starck T, Remes J, et al. **Functional segmentation of the brain cortex using high model order group PICA.** *Hum Brain Mapp* 2009;30:3865–86
26. Abou-Elseoud A, Starck T, Remes J, et al. **The effect of model order selection in group PICA.** *Hum Brain Mapp* 2010;31:1207–16
27. Ystad M, Eichele T, Lundervold AJ, et al. **Subcortical functional connectivity and verbal episodic memory in healthy elderly: a resting state fMRI study.** *Neuroimage* 2010;52:379–88
28. Allen EA, Erhardt EB, Damaraju E, et al. **A baseline for the multivariate comparison of resting-state networks.** *Front Syst Neurosci* 2011;5:2
29. Greicius MD, Kiviniemi V, Tervonen O, et al. **Persistent default-mode network connectivity during light sedation.** *Hum Brain Mapp* 2008;29:839–47
30. Greicius MD, Flores BH, Menon V, et al. **Resting-state functional connectivity in major depression: abnormally increased contributions from subgenual cingulate cortex and thalamus.** *Biol Psychiatry* 2007;62:429–37
31. Calhoun VD, Kiehl KA, Liddle PF, et al. **Aberrant localization of synchronous hemodynamic activity in auditory cortex reliably characterizes schizophrenia.** *Biol Psychiatry* 2004;55:842–49
32. Jafri MJ, Pearlson GD, Stevens M, et al. **A method for functional network connectivity among spatially independent resting-state components in schizophrenia.** *Neuroimage* 2008;39:1666–81
33. Bettus G, Guedj E, Joyeux F, et al. **Decreased basal fMRI functional connectivity in epileptogenic networks and contralateral compensatory mechanisms.** *Hum Brain Mapp* 2009;30:1580–91
34. Luo C, Qiu C, Guo Z, et al. **Disrupted functional brain connectivity in partial epilepsy: a resting-state fMRI study.** *PLoS One* 2011;7:e28196
35. Riva D, Avanzini G, Franceschetti S, et al. **Unilateral frontal lobe epilepsy affects executive functions in children.** *Neurol Sci* 2005;26:263–70
36. Culhane-Shelburne K, Chapieski L, Hiscock M, et al. **Executive functions in children with frontal and temporal lobe epilepsy.** *J Int Neuropsychol Soc* 2002;8:623–32
37. Braakman HM, Vaessen MJ, Hofman PA, et al. **Cognitive and behavioral complications of frontal lobe epilepsy in children: a review of the literature.** *Epilepsia* 2011;52:849–56
38. Prevost J, Lortie A, Nguyen D, et al. **Nonlesional frontal lobe epilepsy (FLE) of childhood: clinical presentation, response to treatment and comorbidity.** *Epilepsia* 2006;47:2198–201
39. Hernandez MT, Sauerwein HC, Jambaque I, et al. **Deficits in executive functions and motor coordination in children with frontal lobe epilepsy.** *Neuropsychologia* 2002;40:384–400
40. Rocca MA, Valsasina P, Absinta M, et al. **Default-mode network dysfunction and cognitive impairment in progressive MS.** *Neurology* 2010;74:1252–59

# Surfer's Myelopathy: A Radiologic Study of 23 Cases

B.K. Nakamoto, A.M. Siu, K.A. Hashiba, B.T. Sinclair, B.J. Baker, M.S. Gerber, A.M. McMurtray, A.M. Pearce, and J.W. Pearce



## ABSTRACT

**BACKGROUND AND PURPOSE:** Surfing is an uncommon cause of an acute nontraumatic myelopathy. This study describes the MR imaging characteristics and clinical correlates in 23 subjects with surfer's myelopathy.

**MATERIALS AND METHODS:** This was a retrospective review of 23 cases of surfer's myelopathy from 2003–2012. Spinal cord MR imaging characteristics and neurologic examinations with the use of the American Spinal Injury Association scale were reviewed. Logistic regression was used to determine associations between MR imaging characteristics, American Spinal Injury Association scale, and clinical improvement.

**RESULTS:** All subjects (19 male, 4 female; mean age,  $26.3 \pm 7.4$  years) demonstrated "pencil-like," central T2-hyperintense signal abnormalities in the spinal cord extending from the midthoracic region to the conus with associated cord expansion and varying degrees of conus enlargement on spinal cord MR imaging within 24 hours of symptom onset. T1 signal was normal. Faint gadolinium enhancement was present in a minority. Although there was a strong correlation between initial American Spinal Injury Association score and clinical improvement ( $P = .0032$ ), MR imaging characteristics were not associated with American Spinal Injury Association score or clinical improvement.

**CONCLUSIONS:** Surfer's myelopathy should be considered in the radiographic differential diagnosis of a longitudinally extensive T2-hyperintense spinal cord lesion. MR imaging characteristics do not appear to be associated with severity on examination or clinical improvement.

**ABBREVIATIONS:** AP = anterior-posterior; ASIA = American Spinal Injury Association

First described in 2004 by Thompson et al,<sup>1</sup> surfer's myelopathy is a rare, nontraumatic spinal cord injury that usually occurs in novice surfers. A limited number of cases have been reported in the literature.<sup>1–10</sup> Most of the literature on surfer's myelopathy consists of single case reports.<sup>2–9</sup> Surfer's myelopathy affects novice surfers who have been lying prone on a surfboard with the lumbar spine hyperextended for prolonged periods of time. These individuals characteristically have a prodrome of back discomfort followed by an acute myelopathy with variable motor-sensory involvement and urinary incontinence.<sup>10</sup> Given the rarity and novelty of diagnosis, surfer's myelopathy may be underdiagnosed and under-reported. There are no treatments available that are

known to improve clinical outcomes. Recovery ranges from complete return of function to persistent paraplegia.

The etiology of surfer's myelopathy is unknown. Arterial insufficiency from hyperextension of the lumbar spine, venous hypertension associated with obstruction of the inferior vena cava by the liver while lying in a prone position, fibrocartilagenous embolism caused by retrograde embolism of the nucleus pulposus into the radicular spinal cord arteries, or avulsion of perforating arteries have all been proposed.<sup>10</sup>

Surfer's myelopathy is usually associated with a T2-hyperintense spinal cord lesion in the thoracic region, but the imaging findings of this disorder and their clinical correlates have not been carefully characterized.<sup>1,10</sup> This case series aims to describe the MR imaging characteristics in 23 individuals diagnosed with surfer's myelopathy and to determine if MR imaging characteristics are associated with severity on neurologic examination and clinical outcome.

## MATERIALS AND METHODS

### Identification of Patients

Subjects were identified by use of the investigators' data base of surfer's myelopathy cases treated or consulted on from 2003–2012 from 3 community hospitals in the state of Hawaii. Data collected from retrospective chart review included demographics,

Received January 30, 2013; accepted after revision March 14.

From the Department of Medicine (B.K.N.), University of Hawaii, Honolulu, Hawaii; Departments of Neurology (B.K.N., A.M.P., J.W.P.), Radiology (B.T.S., B.J.B.), and Neurosurgery (M.S.G.), Straub Clinic and Hospital, Honolulu, Hawaii; Hawaii Pacific Health Research Institute (A.M.S.), Honolulu, Hawaii; Summer Student Research Program (K.A.H.), Hawaii Pacific Health, Honolulu, Hawaii; and Department of Neurology (A.M.M.), Harbor-UCLA Medical Center, Torrance, California.

Please address correspondence to Beau Nakamoto, MD, Straub Clinic and Hospital, Department of Neurology, 888 South King St, Honolulu, HI 96813; e-mail: beau\_nakamoto@yahoo.com

Indicates article with supplemental on-line table

<http://dx.doi.org/10.3174/ajnr.A3599>

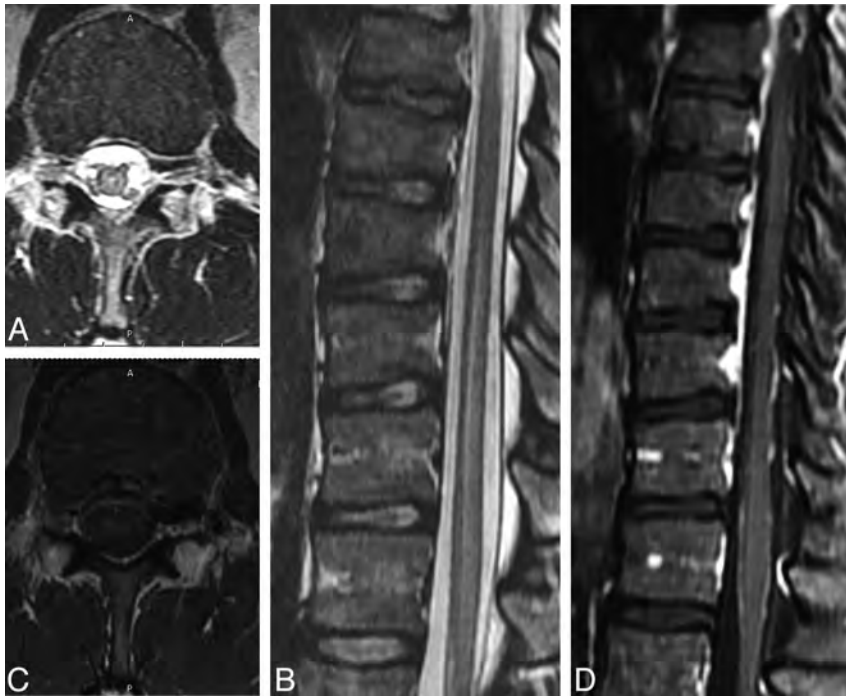


**FIG 1.** A and B, Axial and sagittal T2-weighted images demonstrate mild increased signal in the central aspect of the cord extending to the conus medullaris with cord enlargement. C, Axial T1-weighted image demonstrates normal signal intensity. D, Axial T1-weighted postgadolinium image with fat saturation demonstrates faint central cord enhancement.

presenting symptoms, medical/trauma history, American Spinal Injury Association (ASIA) score at admission and follow-up, presence or absence of urinary retention by postvoid residual, and treatment received.

#### **ASIA Score**

The ASIA scoring system is a widely used measurement of functional impairment from spinal cord injury.<sup>11</sup> The ASIA score is an ordinal scale labeled A–E and categorizes different severities of spinal cord dysfunction. “A” indicates complete spinal cord transection; no motor or sensory function is preserved in the sacral segments S4–S5. “B” describes preserved sensory but no motor function below the level of injury including the sacral segments S4–S5, “C” indicates preservation of motor function with more than half of the muscles being <3 on the Medical Research Council scale for testing muscle strength, and “D” is incomplete injury with at least half of the key muscles below the neurologic level being a muscle grade of  $\geq 3$ . “E” is normal motor and sensory function. ASIA scores were recorded at admission and follow-up after evaluation by the admitting neurologist or neurosurgeon.

#### **Radiologic Assessment**

MR imaging was performed at the treating hospital by use of conventional thoracic and lumbar imaging protocols that included sagittal T1-weighted (TR: 400/TE: 8/NEX: 1/section thickness, 3 mm at 4-mm intervals), T2-weighted (TR: 3400/TE: 84/NEX: 1.5/section thickness, 3 mm at 4-mm intervals), axial T1-weighted (TR: 617/TE: 11/NEX: 1/section thickness, 4 mm at 5-mm intervals), and T2-weighted fast spin-echo (TR: 4283/TE: 99/NEX: 2/section thickness, 4 mm at 5-mm intervals) sequences on a 1.5T GE Signa (Milwaukee, Wisconsin) or Phillips Achieva

(Andover, Massachusetts) scanner. Sagittal STIR sequence (TR: 3100/TE: 39/NEX: 1/section thickness, 3 mm at 4-mm intervals) was also used in 5 subjects. Intravenous gadopentetate dimeglumine (0.2 mL/kg) contrast was administered at the discretion of the radiologist at the time of initial evaluation. MR imaging characteristics were reviewed by 2 radiologists with a Certificate of Added Qualification in neuroradiology. Spinal cord MR imaging characteristics reviewed included T1-signal intensity, extent of continuous T2-signal abnormality on sagittal imaging, location of T2-signal abnormality on axial sections, number of involved vertebral body levels, continuous T2-signal abnormality length, degree of T2-signal abnormality, presence/absence of cord expansion, anterior-posterior (AP) conus diameter, and the presence of gadolinium enhancement when performed. Subtle T2-signal abnormalities in the spinal cord were defined as mild (Fig 1). Obvious T2-signal abnormalities were defined as moderate (Fig 2), and T2-signal abnormalities in the spinal cord that were the same as CSF intensity were defined as severe (Fig 3). T2 signal of the vertebral bodies was also assessed.

#### **Statistical Methods**

Statistical analysis was performed with the use of STATA/IC11.1 for Windows (StataCorp, College Station, Texas). Standard descriptive statistics were used to summarize clinical and MR imaging characteristics. Logistic regression was used to analyze the relationship between ASIA scores as the dependent variable and MR imaging characteristics (ie, number of vertebral body levels of involvement, continuous T2-signal abnormality length, degree of T2-signal abnormality, presence/absence of cord expansion, and AP diameter of conus) as the independent variables. ASIA score on admission and on follow-up were analyzed separately against MR imaging characteristics. Grouped ASIA scores (A and B, C–E) on admission and follow-up were created and analyzed against MR imaging characteristics. The degree of T2-signal abnormalities was recorded as an ordinal categorical variable (ie, mild, moderate, or severe). Fisher exact test was used for categorical variables when appropriate. Variables that were not normally distributed were analyzed by means of the nonparametric Kruskal-Wallis and Mann-Whitney tests. Logistic regression was used to analyze the relationship between clinical improvement as the dependent variable and MR imaging characteristics and treatment received as the independent variables. Clinical improvement was defined as an improvement of  $\geq 1$  ASIA grade from admission to follow-up. Spearman correlation was used with ordinal and nonparametric variables.

A determination of exemption from Institutional Review Board requirements and a waiver of Health Insurance Portability



**FIG 2.** A and B, Axial and sagittal T2-weighted images demonstrate moderate increased signal in the central aspect of the cord extending to the conus medullaris with cord enlargement. C and D, Axial and sagittal T1-weighted images demonstrate normal signal intensity.

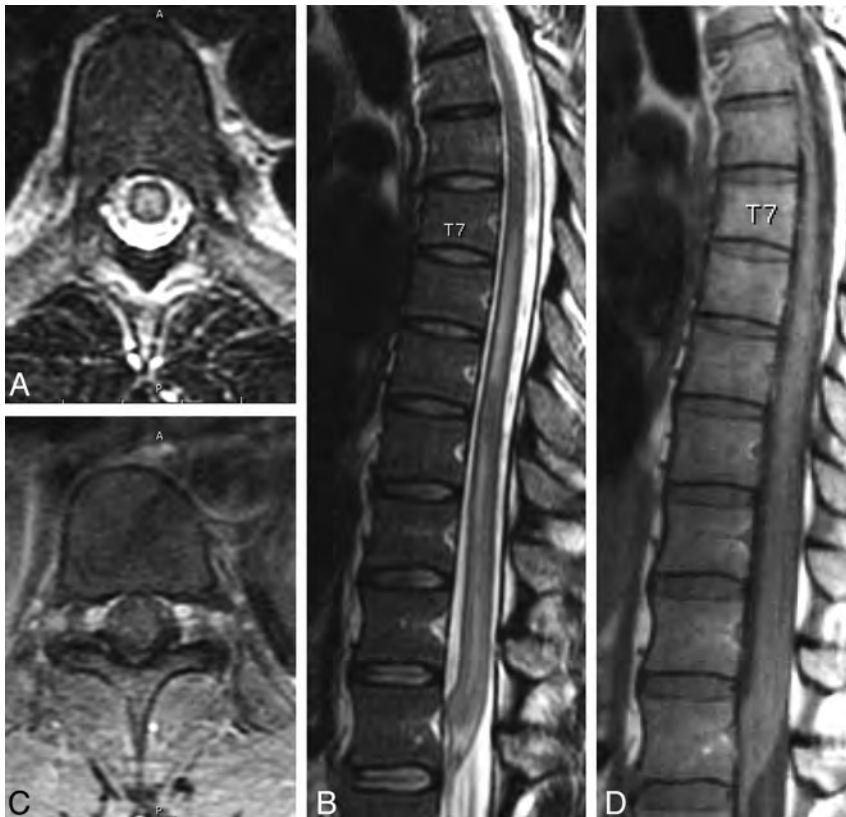


**FIG 3.** A and B, Axial and sagittal T2-weighted images demonstrate severe increased signal in the central aspect of the cord extending to the conus medullaris with cord enlargement. C and D, Axial and sagittal T1-weighted images demonstrate normal signal intensity.

and Accountability Act authorization were obtained for this retrospective chart review.

## RESULTS

### Clinical Characteristics

A total of 24 cases were identified. Twenty-three cases (19 male, 4 female; mean age,  $26.3 \pm 7.4$  years) had both clinical data and MR imaging data available for review. Race/ethnicity was equally distributed between Asian (11) and white (11), with 1 case reporting mixed race. All subjects were healthy individuals without a preceding systemic illness. Twenty-two subjects (22/23) presented with the acute low back pain associated with varying degrees of paraparesis while surfing. Fifteen subjects (15/23) presented with an ASIA score of C or better. On admission, 5 subjects had an ASIA score of A, 3 subjects had an ASIA score of B, 5 subjects had an ASIA score of C, 9 subjects had an ASIA score of D, and 1 subject presented with an ASIA score of E. Sixteen subjects had a sensory level ranging from T8–L3, whereas 6 subjects had a normal sensory examination. Sensory examination was not performed for 1 subject. Twenty-two subjects (22/23) had urinary retention on postvoid residual on admission. No subject reported a history of trauma. Seven subjects were treated with a full course of intravenous methylprednisolone on the basis of the Third National Acute Spinal Cord Injury Study protocol for acute spinal cord injury (ie, an intravenous bolus dose of methylprednisolone 30 mg/kg over 15 minutes, followed by a 45-minute pause, and then a 23-hour continuous intravenous infusion of 5.4 mg/kg per hour).<sup>12</sup>

Most patients included in this review were visitors to Hawaii and transferred to hospitals in their home location for additional follow-up and treatment. Follow-up data, therefore, were limited to outcome at discharge for many of the cases. Duration of follow-up ranged from 1 day to 8 years (median, 6 days; interquartile range, 3–14 days).

### MR Imaging Characteristics

All MR imaging studies were performed within 24 hours of symptom onset. Further details regarding time between symptom onset and time when the MR imaging was performed were unavailable. Follow-up MRI was not per-

formed. Refer to the On-line Table for individual patient MR imaging characteristics. All subjects had “pencil-like” longitudinally extensive hyperintense T2-weighted signal abnormalities extending from the midthoracic region to the conus with associated cord expansion and varying degrees of conus enlargement (mean,  $8.4 \pm 0.8$  mm; range, 7–10) on sagittal sequences, and these were located in the central cord on axial sequences. The cranial extent of continuous T2-signal abnormality ranged from T5–T10. The T2-signal abnormality extended down to the conus in all subjects. The number of vertebral body levels of involvement ranged from 3–7.5 levels (mean,  $5.1 \pm 1.4$ ). The mean length of T2-signal abnormality was  $13.8 \pm 3.1$  cm (range, 9–21). Degree of T2-signal hyperintensity ranged from mild (6/23, Fig 1), to moderate (7/23, Fig 2), to severe (10/23, Fig 3). The spinal cord was normal on T1-weighted sequences. No intramedullary hemorrhage was present. Gadolinium enhancement ranged from no gadolinium enhancement (7/11) to trace gadolinium enhancement (4/11). No other radiologic abnormalities were present. No subject had central canal stenosis, disk prolapse or herniation at the levels of T2-signal abnormalities, syrinx, fractures, dislocations, ligamentous injuries, hematomas, or perimedullary or intramedullary vascular dilations. T2-signal of the vertebral bodies was normal in all subjects. DWI sequences were not performed. No subject had evidence of inferior vena cava compromise.

#### **Association Between MR Imaging Characteristics and ASIA Score on Admission and Follow-Up**

The relationship between MR imaging characteristics (degree of T2-signal abnormality,  $P = .86$ ; number of vertebral body levels of involvement,  $P = .51$ ; length of continuous T2-signal abnormality,  $P = .25$ ; AP diameter of conus,  $P = .45$ ) and ASIA score on admission showed no associations when tested with the Fisher exact test. Similarly, there were no associations between MR imaging characteristics (degree of T2-signal abnormality,  $P = .42$ ; number of vertebral body levels of involvement,  $P = .28$ ; length of continuous T2-signal abnormality,  $P = .57$ ; AP diameter of conus,  $P = .99$ ) and ASIA follow-up score. There were no statistically significant associations between grouped ASIA scores on admission or follow-up and MR imaging characteristics.

#### **Association Between MR Imaging Characteristics and Clinical Improvement**

The median follow-up time was 6 days (interquartile range, 3–14 days). Approximately 65% of the cases showed no improvement in ASIA score from admission (13/20). Clinical improvement was not significantly associated with any MR imaging characteristics (degree of T2-signal abnormality,  $P = .20$ ; number of vertebral body levels of involvement,  $P = .96$ ; length of continuous T2-signal abnormality,  $P = .51$ ; AP diameter of conus,  $P = .79$ ) when tested with logistic regression. Follow-up time was not correlated with follow-up ASIA score ( $P = .67$ , Kruskal-Wallis) or grouped follow-up ASIA score ( $P = .23$ , Mann-Whitney).

#### **Association Between ASIA Score on Admission and Follow-Up**

There was a strong correlation between ASIA score on admission and clinical improvement ( $P = .0079$ , Spearman). All of the patients who presented with an ASIA score of A or B on admission showed no improvement at follow-up (7/20). Grouped ASIA scores on admission showed a strong association with clinical improvement ( $P = 0.22$ , Fisher exact). Follow-up time ( $P = .684$ , logistic regression) and treatment with intravenous methylprednisolone ( $P = .613$ , Fisher exact) were not significantly associated with improvement.

## **DISCUSSION**

### **Study Significance**

This is the largest case series to date detailing the radiologic characteristics of surfer’s myelopathy. Little attention has been given to MR imaging characteristics and their clinical correlates in previous case series of this rare disorder.<sup>10</sup>

### **Radiologic Characteristics of Surfer’s Myelopathy**

In our study, spinal cord MR imaging demonstrates a longitudinally extensive region of hyperintense T2-signal abnormality extending from the midthoracic region to the conus with associated cord expansion and variable degrees of fusiform enlargement of the conus on sagittal sequences. The hyperintense signal on T2-weighted sequences usually extends cranially to the midthoracic region, but the region of involvement can be as short as from the conus to T10 or as far cranially as T5. The T2 abnormality involves the central cord on axial sequences. Spinal cord signal is normal on T1-weighted sequences with either absent or trace regions of gadolinium enhancement. Our findings are consistent with previous descriptions of surfer’s myelopathy with the exception that others have also reported sparing of the conus in addition to enhancement of the ventral roots of the cauda equina.<sup>1,4,10</sup> Although T1-weighted noncontrast sequences are usually normal, patchy increased T1-weighted signal changes on initial presentation and repeat imaging 1 month later, presumably from petechial hemorrhage, have rarely been described.<sup>2,6</sup> The T1-weighted signal of the spinal cord was normal in all subjects in our study, and no subject had evidence of intramedullary hemorrhage. The trace gadolinium enhancement seen in the spinal cords of 4 subjects in our study and the rare case reports of petechial hemorrhage in other studies<sup>2,6</sup> are consistent with the slight inflammatory and hemorrhagic changes demonstrated on CSF analysis in individuals with surfer’s myelopathy in whom a lumbar puncture was performed.<sup>10</sup>

The evolution of the MR imaging findings associated with surfer’s myelopathy has not been well described because of the absence of consistent serial imaging and long-term follow-up in reported cases. Five published papers detailed the time between symptom onset and imaging, and conventional spinal cord MR imaging was abnormal within 2–12 hours.<sup>1,2,4,5,8</sup> One case reported by Kelly and Wright<sup>3</sup> was initially normal but was subsequently abnormal on repeat imaging within 24 hours of the initial MR imaging.<sup>3</sup> DWI with ADC mapping has inconsistently demonstrated restricted diffusion in cases of surfer’s myelopathy.<sup>10</sup>

In the acute setting, the abnormal T2-hyperintensity severity can increase and extend rostrally up to 4 vertebral body segments.<sup>1,2</sup> The abnormal T2-signal has been shown to resolve spontaneously in some studies and improve when subjects are treated with steroids in other studies.<sup>1,4,7</sup> Descriptions of chronic MR imaging changes in surfer's myelopathy have not been reported.

### **Radiologic Differential Diagnosis**

A characteristic history aids in narrowing the radiographic differential diagnosis to surfer's myelopathy. These individuals are young, inexperienced surfers who lay prone on a surfboard for a prolonged period and present with nontraumatic acute onset of back pain followed by symptoms of a myelopathy. Other radiographic considerations for a longitudinally extensive hyperintense spinal cord lesion on T2-weighted images associated with an acute intramedullary myelopathy have been reviewed elsewhere and include an idiopathic transverse myelitis, MS, longitudinally extensive transverse myelitis, venous hypertension associated with spinal dural arteriovenous fistula, and arterial infarct.<sup>13-16</sup> Idiopathic transverse myelitis, MS, and longitudinally extensive transverse myelitis are all acute inflammatory spinal cord syndromes that can be grouped under the umbrella term "transverse myelitis." Whereas there is a great deal of overlap in imaging appearances of these conditions, there are distinct imaging appearances that are helpful for differentiation. Idiopathic transverse myelitis, which is usually preceded by a viral illness or vaccination, has low signal intensity on T1-weighted images and high signal intensity on T2-weighted images. The spinal cord caliber can be normal or mildly enlarged, affecting the cervical and/or thoracic cord, and may have patchy or peripheral gadolinium enhancement. MS plaques but are peripherally located, typically involve the dorsolateral regions of the cord, and can also have brain involvement. Most MS spinal lesions are smaller than 2 vertebral body segments. In contrast, idiopathic transverse myelitis typically extends 3 to 4 vertebral segments in length, and longitudinally extensive transverse myelitis is a contiguous spinal cord lesion extending over  $\geq 3$  vertebral segments.<sup>13</sup> Neuromyelitis optica, or Devic syndrome, is one cause of longitudinally extensive myelitis that can also have an associated optic neuritis. Whereas all these conditions can be considered in the radiographic differential diagnosis, the characteristic contiguous, longitudinally extensive midthoracic to conus, central cord involvement, and historical correlate differentiate these entities from surfer's myelopathy.

The radiographic findings of surfer's myelopathy can be difficult to differentiate from venous hypertension and an arterial spinal cord infarct. Venous hypertension associated with a spinal dural arteriovenous fistula can be distinguished by the presence of dilated, tortuous perimedullary vessels seen as flow voids dorsally in the thecal sac and by the history of a chronic progressive myelopathy in contrast to the acute onset of symptoms after surfing in those with surfer's myelopathy. In our study, the radiologic characteristics on spinal cord MR imaging may be indistinguishable from an arterial thoracic spinal cord infarct.

### **Pathogenesis**

Although no definite histopathologic confirmation has been published in this population, surfer's myelopathy probably is the result of a vascular phenomenon involving dynamic compression, vasospasm, or thrombotic infarction of the artery of Adamkiewicz, which occurs as the result of hyperextension of the spinal cord while individuals are lying prone on a surfboard.<sup>10</sup> The MR imaging characteristics in our study support the hypothesis that surfer's myelopathy is the result of spinal cord infarction in the vascular distribution of the artery of Adamkiewicz. Unlike the cerebral vessels, the spinal arteries run along a mobile structure, making them prone to mechanical damage as may occur with prolonged hyperextension of the back during surfing. The thoracic spinal cord is at a greatest risk of ischemia as a result of poor collateral vascular supply in this region and is consistent with the variable levels of thoracic spinal cord involvement demonstrated in our study.<sup>17</sup> The variable levels of thoracic spinal cord involvement may be explained by the variable origins of the artery of Adamkiewicz, arising from T5–T8 in 15%, T9–T12 in 75%, and L1–L2 in 10% of the population.<sup>17</sup> The central cord involvement seen on MR imaging in all of our subjects may be explained by the small central vascular supply of the thoracic spinal cord, and, because the anterior and posterior spinal arteries run along the surface of the cord, the central cord is also a watershed region. A few studies have demonstrated increased diffusion restriction on DWI correlating with decreased signal on ADC mapping in surfer's myelopathy, supporting the hypothesis that the T2-signal abnormalities represent cytotoxic edema in the setting of an acute spinal cord infarction.<sup>8,10</sup> Conventional spinal angiograms were normal when performed in previously described cases.<sup>1,5,10</sup>

### **Clinical Correlates**

In our study, MR imaging characteristics were not associated with severity of the myelopathy as measured by the ASIA score and did not predict clinical improvement on follow-up. In a case series of 19 subjects, Chang et al<sup>10</sup> also reported that restricted diffusion on DWI with ADC mapping did not correlate with outcome. This analysis, however, was performed on subset of 10 patients in the case series who had DWI with ADC mapping, of whom 6 showed restriction. Our finding that ASIA score on admission predicts clinical improvement is consistent with those reported by Chang et al.<sup>10</sup> Treatment with high-dose intravenous methylprednisolone in 7 subjects in our study was not associated with clinical improvement, but this probably was a result of our small sample size.

### **Limitations**

Although our case series is the largest to date, our sample size may have been underpowered to detect a relationship between MR imaging characteristics, disease severity, and clinical improvement. Second, all subjects were not imaged with the same MR imaging protocol at standard times, which may have increased the variability of the abnormal T2-signal intensity, extent of involvement, and AP diameter of the conus on obtained images. DWI with ADC mapping was not obtained in our study, and the role of this sequence in the clinical evaluation of spinal

cord ischemia and surfer's myelopathy remains unclear. Third, lack of consistent long-term follow-up limits characterization of chronic radiographic characteristics of surfer's myelopathy. Finally, confirmatory histopathology to determine that surfer's myelopathy is a result of an arterial infarction was not feasible.

## CONCLUSIONS

In summary, surfer's myelopathy is a rare form of an acute myelopathy, which should be considered in the radiographic differential diagnosis of a longitudinally extensive T2-hyperintense spinal cord lesion in the context of a surfing history. Greater awareness of the characteristic history associated with this disorder is important to making the correct radiographic diagnosis. Severity of the radiographic characteristics of surfer's myelopathy is not associated with severity on initial examination or clinical improvement.

## ACKNOWLEDGMENTS

We thank our study participants and their families for their roles in this study.

Disclosures: Beau Nakamoto—RELATED: Grant: Research support from National Institutes of Health (grant U54MD007584)\* (\*money paid to institution).

## REFERENCES

1. Thompson TP, Pearce J, Chang G, et al. **Surfer's myelopathy.** *Spine* 2004;29:E353–56
2. Aviles-Hernandez I, Garcia-Zozaya I, DeVillasante JM. **Nontraumatic myelopathy associated with surfing.** *J Spinal Cord Med* 2007;30:288–93
3. Kelly M, Wright K. **A case of surfers' myelopathy.** *Am J Clin Med* 2010;7:74–75
4. Dhaliwal PP, Cenic A, Eesa M, et al. **An unusual case of myelopathy: surfer's myelopathy.** *Can J Neurol Sci* 2011;38:354–56
5. Chung HY, Sun SF, Wang JL, et al. **Non-traumatic anterior spinal cord infarction in a novice surfer: a case report.** *J Neurol Sci* 2011;302:118–20
6. Shuster A, Franchetto A. **Surfer's myelopathy: an unusual cause of acute spinal cord ischemia: a case report and review of the literature.** *Emerg Radiol* 2011;18:57–60
7. Karabegovic A, Strachan-Jackman S, Carr D. **Surfer's myelopathy: case report and review.** *Canadian Journal of Emergency Medicine* 2011;13:357–60
8. Lieske J, Cameron B, Drinkwine B, et al. **Surfer's myelopathy: demonstrated by diffusion-weighted magnetic resonance imaging: a case report and literature review.** *J Comput Assist Tomogr* 2011;35:492–94
9. Lin CY, Fu JH, Li SC, et al. **Surfer's myelopathy.** *QJM* 2012;105:373–74
10. Chang CW, Donovan DJ, Liem LK, et al. **Surfers' myelopathy: a case series of 19 novice surfers with nontraumatic myelopathy.** *Neurology* 2012;79:2171–76
11. **Reference Manual of the International Standards for Neurological Classification of Spinal Cord Injury.** Chicago: American Spinal Injury Association; 2003
12. Bracken MB, Shepard MJ, Holford TR, et al. **Administration of methylprednisolone for 24 or 48 hours or tirilazad mesylate for 48 hours in the treatment of acute spinal cord injury: results of the Third National Acute Spinal Cord Injury Randomized Controlled Trial: National Acute Spinal Cord Injury Study.** *JAMA* 1997;277:1597–604
13. Do-Dai DD, Brooks MK, Goldkamp A, et al. **Magnetic resonance imaging of intramedullary spinal cord lesions: a pictorial review.** *Curr Probl Diagn Radiol* 2010;39:160–85
14. Bou-Haidar P, Peduto AJ, Karunaratne N. **Differential diagnosis of T2 hyperintense spinal cord lesions: part B.** *J Med Imaging Radiat Oncol* 2009;53:152–59
15. Sheerin F, Collison K, Quaghebeur G. **Magnetic resonance imaging of acute intramedullary myelopathy: radiological differential diagnosis for the on-call radiologist.** *Clin Radiol* 2009;64:84–94
16. Kitley JL, Leite MI, George JS, et al. **The differential diagnosis of longitudinally extensive transverse myelitis.** *Mult Scler* 2012;18:271–85
17. Shamji MF, Maziak DE, Shamji FM, et al. **Circulation of the spinal cord: an important consideration for thoracic surgeons.** *Ann Thorac Surg* 2003;76:315–21

# Evaluation of the Intervertebral Disk Angle for the Assessment of Anterior Cervical Diskoligamentous Injury

L.M. Alhilali and S. Fakhran

## ABSTRACT

**BACKGROUND AND PURPOSE:** The anterior diskoligamentous complex is important for cervical spinal stability. Subjective widening of the disk space after trauma has been used to gauge disruption of the anterior diskoligamentous complex on CT scanning, but no quantitative CT measurements exist to evaluate injury. The purpose of our study was to evaluate if an increased intervertebral disk angle could serve as a more sensitive, reproducible indicator of disruption of the anterior diskoligamentous complex compared with subjective assessment.

**MATERIALS AND METHODS:** The intervertebral disk angle was retrospectively measured on CT scanning for 122 disk levels with disruption of the anterior diskoligamentous complex by MR imaging and 1095 disk levels with an intact anterior diskoligamentous complex by MR imaging. The intervertebral disk angle was measured between the anterior superior endplate and anterior inferior endplate, with angle apex at the midposterior disk. Area under the receiver operating characteristic curves for subjective disk widening and specific angle values were obtained. Intervertebral disk angle reproducibility was also evaluated.

**RESULTS:** Intervertebral disk angle measurements were “substantially reproducible.” No disk with an intact anterior diskoligamentous complex had an intervertebral disk angle greater than 18° or 2 standard deviations from the average intervertebral disk angle of the remaining disks. The area under the receiver operating characteristic curve for a criterion of subjective disk widening was 0.58. The area under the receiver operating characteristic curve for objective criteria, an intervertebral disk angle greater than 13 or above 1 standard deviation from normal values, was 0.85. The maximal area under the receiver operating characteristic curve was achieved if an intervertebral disk angle greater than 2 SD from the average angle of the other disks was used (0.86).

**CONCLUSIONS:** Subjective disk widening does not accurately detect disruption of the anterior diskoligamentous complex on CT scanning; an elevated intervertebral disk angle provides a more sensitive and objective measurement to help direct further imaging in trauma patients.

**ABBREVIATIONS:** ADL = anterior diskoligamentous complex; IDA = intervertebral disk angle; ALL = anterior longitudinal ligament; AUC = area under the receiver operating characteristic curve; ROC = receiver operating characteristic

Acute cervical diskoligamentous injury is difficult to detect with standard trauma screening protocols, with the incidence of occult cervical diskoligamentous injury, in patients with persistent midline tenderness and a negative result on cervical spine CT scan, estimated to be as high as 44%.<sup>1</sup> Timely diagnosis of these injuries is imperative, as the risk for neurologic sequelae is 10 times higher in patients with cervical injury missed on initial screening.<sup>2</sup> The anterior diskoligamentous complex (ADL), composed of the anterior longitudinal ligament (ALL) and the intervertebral disk, is a key component of anterior cervical spine sta-

bility. Catastrophic injury to the ADL may result in cervical instability and acute disability, whereas subcatastrophic injury may lead to chronic pathologic conditions including disk degeneration, facet osteoarthritis, and chronic instability.<sup>3</sup> Instability with ADL disruption may result in pain by compressing neural structures or muscle fatigue from increased reliance on the spinal musculature for stability.<sup>4</sup> ADL injuries heal poorly, and a missed ADL injury is thought to contribute to chronic neck pain.<sup>5</sup> Even in patients with other known cervical spine injuries, an unrecognized disk injury can be devastating, as potentially a higher number of columns may be injured. Identifying disruption of ligamentous integrity even in the setting of known fractures is critical, as knowledge of the extent of cervical column compromise is important in alerting clinicians to the potential for delayed instability.<sup>6</sup>

Although MR imaging is the standard method to analyze spinal soft tissue injuries, CT scan remains the first-line screening technique in cervical spine trauma, which relies heavily on verte-

Received December 18, 2012; accepted after revision February 25, 2013.

From the Department of Radiology, University of Pittsburgh School of Medicine, Pittsburgh, Pennsylvania.

Please address correspondence to Saeed Fakhran, University of Pittsburgh Medical Center, 200 Lothrop St, Presby South Tower, 8th Floor, 8 North, Pittsburgh, PA 15213; e-mail: Fakhrans@upmc.edu

<http://dx.doi.org/10.3174/ajnr.A3585>

bral body alignment to evaluate for ligamentous injury. Assessment of alignment is based on subjective evaluation of CT images because of a lack of clinically validated and reproducible criteria for alignment on CT scan. An overly sensitive assessment may lead to unnecessary MR imaging and its associated risk for transport in severely injured patients. Conversely, diminished sensitivity may result in missed injuries and the associated costs of both acute and delayed morbidity. Uniform measurements to detect ADL injury easily obtained on existing digitally based PACS systems could improve patient care by decreasing missed injuries and allowing for more judicious use of MR imaging.

The purpose of this study was to evaluate if an increased intervertebral disk angle (IDA) could serve as a more sensitive, reproducible indicator of ADL disruption compared with subjective assessment of disk space widening.

## MATERIALS AND METHODS

### Patient Selection and Image Acquisition

Our institutional review board approved this study with waiver of informed consent. All CT and MR examinations included were performed during the clinical care of patients, and results were retrospectively reviewed.

We searched our enterprise-wide electronic medical record, encompassing 20 academic and community hospitals, to identify patients with ADL disruption on MR imaging examinations. We searched for radiology reports of MR imaging examinations performed from July 1, 2007, to May 1, 2012, on a PACS-capable search system, by using the following individual keywords: *anterior longitudinal ligament*, *discoligamentous*, *ligament injury*, *ligament tear*, and *ligament disruption*. MR images were reviewed in consensus by 2 fellowship-trained neuroradiologists (L.M.A., S.F.), without taking into account the initial diagnostic interpretation, to confirm the findings of ADL disruption.

Multiple prior studies have demonstrated the usefulness and accuracy of MR imaging of ligamentous injury in the cervical spine.<sup>7-12</sup> For our study, the ADL was considered torn if a focal area of ALL/disk discontinuity could be identified on sagittal T2 or inversion recovery sequences. To further improve our specificity, we excluded patients if a focal point of ligament/disk discontinuity could not be definitively identified or if there was not agreement between the 2 neuroradiologists regarding the presence of ADL disruption. Prevertebral soft tissue swelling, ALL edema, or disk edema were not considered sufficient indicators of ADL disruption. Patients were also excluded if they did not have a comparison cervical spine CT examination performed within 7 days before the MR examination.

We identified control participants by searching the electronic medical record for cervical spine MR reports by using the keywords *cervicalgia*, *stenosis*, *pain*, and *disk disease*. Control participants were excluded if they had evidence of ADL disruption or edema on MR imaging, a history of trauma within the last 6 months, or no cervical spine CT examination performed within 1 month of the MR examination. Demographic data collected included age and sex. Clinical and imaging data collected included clinical history, initial CT findings/interpretation, reasons for MR imaging examination, level of ADL disruption, levels of disk degeneration, and final clinical management.

CT examinations were performed on 16- or 64-MDCT scanners (LightSpeed VCT; GE Healthcare, Milwaukee, Wisconsin). CT acquisitions were obtained from the infraorbital rim to the level of T1–T2 by use of the axial technique, 0.5 pitch, 1.2-mm collimation, 350 maximal mA, 120 kVp, and 18-cm FOV, in bone and standard algorithms, with 2.5-mm sagittal and coronal reconstructions. Patients were immobilized in a cervical collar during CT image acquisition.

MR imaging examinations were performed on 1.5T Optima 450W and 3T Discovery 750 systems (GE Healthcare) with neutral positioning by use of a standard spine coil. Sagittal sequences were obtained with 24-cm FOV and 256 × 192 matrix as follows: sagittal spin-echo T1-weighted (TR, 500 ms; TE, minimal; section thickness, 3 mm; NEX, 3), sagittal inversion recovery (TR, 9000–10000 ms; TE, 68 ms; section thickness, 3 mm; TI, 2200 ms), and sagittal gradient-echo (TR, 800 ms; TE, 25 ms; flip angle 20°; section thickness, 3 mm; NEX, 2). Additional axial 3D gradient-echo images (TR, 35 ms; TE, 13 ms; flip angle, 5°; section thickness, 2 mm; NEX, 1) were obtained with a 22-cm FOV and 256 × 192 matrix. Sagittal diffusion images (single-shot echo-planar; TR, 10,000 ms; TE, minimal; section thickness, 5 mm; matrix, 128 × 128) were also performed.

### IDA Measurements

For measurement of the IDA, 3 points are first identified: 1) the first point at the midpoint of the disk space at its most posterior margin, 2) a second point at the anterior aspect of the endplate of the upper vertebral body, and 3) a third point at the anterior aspect of the endplate of the lower vertebral body. A line is drawn between the first and second points and the first and third points. The IDA is defined as the angle formed between these 2 lines.

IDA was measured on midline sagittal CT images by use of the angle measurement tool on our PACS. If there were anterior osteophytes, the angle excluded the osteophytes (Fig 1A,-B). Vertebral body distraction, or relative parallel configuration of vertebral body endplates, did not affect angle measurement, as the angle apex is placed at the middle of the distracted disk at the posterior vertebral body (Fig 1C,-D). IDA was measured for all disk spaces from C2–3 to C7–T1 in both patients with ADL disruption and in control participants.

Reproducibility of the IDA was assessed by having 2 neuroradiologists independently measure the IDA for all disk spaces from C2–3 to C7–T1 in 17 randomly selected patients from both control and trauma groups (102 total disk spaces), with 10 of the tested disk spaces demonstrating ADL disruption on MR imaging. Radiologists were blinded to both each other's measurements and MR imaging findings. IDAs were then measured in all patients and control participants, in random order, at all levels from C2–3 to C7–T1 by 1 of the 2 neuroradiologists blinded to the clinical history and MR imaging findings.

Evaluation of subjective disk widening was performed with use of the prospective interpretation of the CT study by the initial interpreting radiologist. At our institution, cervical spine CT examinations are interpreted by fellowship-trained neuroradiologists and musculoskeletal radiologists. A true-positive finding of subjective disk widening was considered an initial interpretation

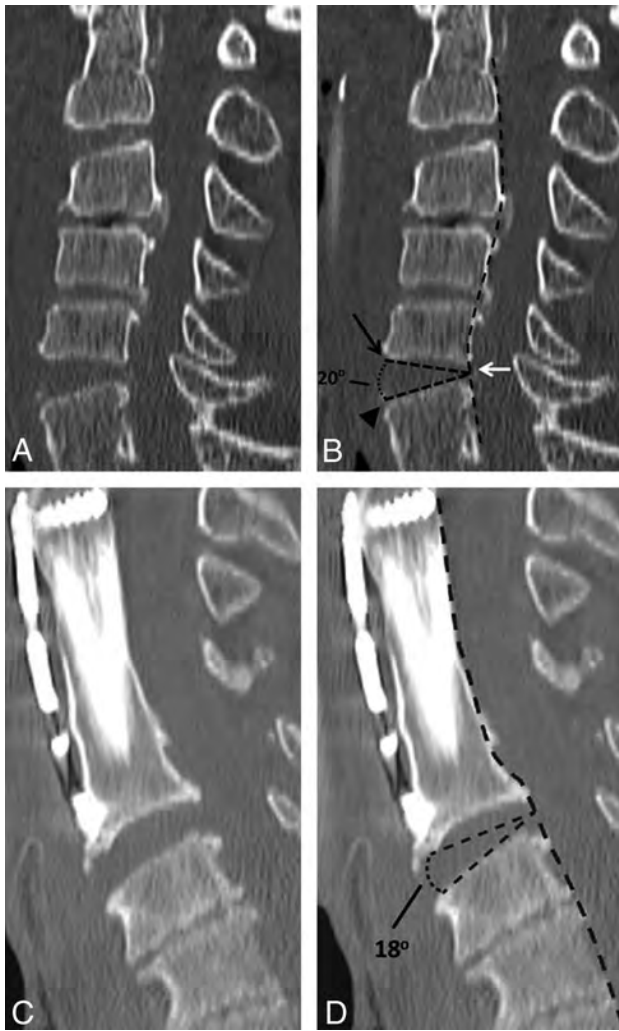


**FIG 1.** A, Sagittal CT reconstruction of the cervical spine in a 65-year-old man with blunt trauma demonstrating (B) measurement of the IDA in a level with ADL disruption, measured between the anterior superior endplate (black arrow) and anterior inferior endplate (arrowhead), with the apex of the angle at the midpoint of the posterior disk (white arrow) at the posterior vertebral body margin (broken black line). C, Sagittal CT reconstruction of the cervical spine in an 82-year-old man with a history of fall demonstrating measurement of an IDA in the presence of anterior osteophytes and vertebral body distraction, resulting in parallel endplates, at a level with ADL disruption. D, The IDA measurement excludes the osteophytes and is still measured at the midpoint of the distracted posterior disk.

of the CT scan, suggesting disk space widening at a level of injury seen on MR imaging.

#### Data Analysis

Confidence intervals for proportions used a continuity correction.<sup>13</sup> IDA reproducibility was assessed by the Lin concordance correlation coefficient,<sup>14</sup> interpreted according to McBride,<sup>15</sup> that is, poor agreement (< 0.90), moderate agreement (0.90 to < 0.95), substantial agreement (0.95–0.99), and almost perfect agreement (> 0.99). Sensitivity and specificity for subjective disk widening and IDA measurements were obtained, with confidence intervals obtained without a continuity correction.<sup>13</sup> Sensitivity and specificity for the various tests were compared with subjective assessment by use of the extended McNemar test with 2-tailed *P* values.<sup>16</sup> Positive predictive value and negative predictive value

**Table 1. Patient demographics**

	Trauma Patients	Control Patients	Total
No. of patients	103	104	207
No. of male patients (%)	77 (76)	73 (70)	150 (72)
Mean age, y (range)	56 (17–93)	52 (17–93)	54 (17–93)

of subjective assessment of disk widening, IDA measurements, and IDA variation were calculated. Receiver operating characteristic (ROC) curves were created for IDA measurements. Areas under the ROC curve (AUC) for subjective disk widening and specific angle values and angle variation were obtained<sup>17</sup> and were interpreted according to Hosmer and Lemeshow,<sup>18</sup> that is, no discrimination (AUC = 0.5), acceptable discrimination ( $0.7 \leq \text{AUC} \leq 0.8$ ), excellent discrimination ( $0.8 \leq \text{AUC} \leq 0.9$ ), and outstanding discrimination ( $\text{AUC} \geq 0.9$ ). Standard errors of the AUC values were calculated for each test.<sup>19</sup> *P* values comparing the diagnostic performance of subjective disk widening and specific angle values were obtained by paired analysis.<sup>20</sup> *P* values of < .05 were considered statistically significant.

## RESULTS

### Patient Selection and Image Acquisition

A total of 139 cervical spine MR imaging studies with ADL disruption were evaluated based on our search of the electronic medical record. A total of 172 MR imaging studies of control patients were reviewed. Demographic data are summarized in Table 1.

Among trauma patients, the most common history was either fall (41.7%; 95% CI, 32.2%–51.9%) or motor vehicle collision (33.0%; 95% CI, 24.3%–43.1%). Most of patients received an MR imaging examination for fractures on CT (62.1%; 95% CI, 52.0%–71.4%), whereas additional studies were obtained for persistent cervical pain (11.7%; 95% CI, 6.4%–19.8%) or continued neurologic deficit (12.6%; 95% CI, 7.2%–21.0%) in the absence of positive CT findings. MR imaging examinations in the remaining patients were obtained because of concern for ligamentous injury on the part of the radiologist interpreting the preceding CT study without evidence of bony fracture (11.7%; 95% CI, 6.4%–19.8%). Most patients required surgical stabilization for their injuries (53.4%, 95% CI, 43.3%–63.2%), whereas the remaining patients were either discharged from the hospital wearing a cervical collar (38.8%; 95% CI, 29.5%–49.0%) or died from either spinal or other injuries before treatment (5.8%; 95% CI, 2.4%–12.8%).

### Measurements of IDA

The Lin correlation coefficient ( $\rho_c$ ) for IDA measurements on test disk spaces, used to assess IDA reproducibility, was 0.9576 (95% CI, 0.9417–0.9692), indicating substantial agreement among observers. Concordance results are shown in Fig 2.

Among trauma patients, 122 levels of ADL disruption were identified. IDAs for the 122 disk levels with ADL disruption as well as the remaining 487 uninjured disk levels were measured. Nine disk levels were excluded because of solid bony fusion. Among control patients, the IDAs for 608 uninjured disk spaces were evaluated, with 16 levels excluded for solid bony fusion. This provided 122 IDA measurements at levels with ADL disruption and 1095 IDA measurements at uninjured levels (487 IDA measurements at uninjured levels in trauma patients and 608 IDA

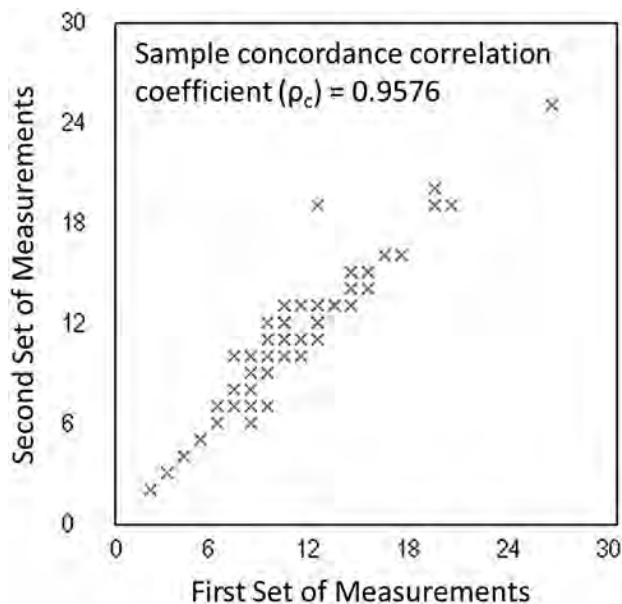


**FIG 2.** Concordance correlation coefficient plot measuring both precision and accuracy to determine how far the measured IDAs from the 2 different observers deviate from the line of perfect concordance (the line at 45° on a square scatterplot). The Lin coefficient increases in value as a function of the nearness of the data's reduced major axis to the line of perfect concordance (the accuracy of the data) and of the tightness of the data about its reduced major axis (the precision of the data).

**Table 2.** IDA measurements in 1095 uninjured disks

Disk Level	Average IDA	95% CI
C2–3	9.9	5.3–14.5
C3–4	9.4	3.8–15.1
C4–5	9.2	3.1–15.3
C5–6	8.6	2.2–14.9
C6–7	8.9	3.0–14.8
C7–T1	9.6	4.9–14.4

measurements at uninjured levels in nontrauma patients) for analysis. Average uninjured IDA values for each disk level were calculated (Table 2). The distribution of angles for uninjured and injured disks is shown in Fig 3.

Subjective disk widening had a low sensitivity (16.4%; 95% CI, 10.5%–24.3%) but a high specificity (99.4%; 95% CI, 98.0%–99.8%). The sensitivity increased with smaller IDA values as low as 13 (82.0%; 95% CI, 73.7%–88.1%) with a mild loss of specificity (89.1%, 95% CI, 87.1%–90.9%). When an angle of 12 was used, the sensitivity increased only marginally (85.2%; 95% CI, 77.4%–90.8%) with significant decrease in specificity (75.8%; 95% CI, 73.1%–78.2%). Maximal sensitivity was achieved by use of an IDA greater than 1 SD from normal values (86.1%; 95% CI, 78.3%–91.4%) or the average IDA of the remaining disks (86.1%; 95% CI, 74.7%–88.8%).

The highest diagnostic accuracy for a single IDA measurement was achieved with an IDA of 13 (0.884; 95% CI, 0.869–0.896). Using variation from normal values, we obtained the highest diagnostic accuracy by using an IDA greater than 1 SD from normal values (0.849; 95% CI, 0.834–0.859). The overall highest diagnostic accuracy was achieved by use of an IDA greater than 2 SDs from the remaining disks (0.972; 95% CI, 0.965–0.972). Diagnos-

tic performance for subjective disk widening, an IDA of 13, as well as IDA measurement variations are compared in Table 3.

ROC curves for progressively smaller IDA measurements (Fig 4A) as well as for IDA variation (Fig 4B, C) were obtained. The AUC for subjective widening of the disk was 0.58 (95% CI, 0.52–0.64), improving to 0.85 (95% CI, 0.81–0.90) if the criterion was an IDA of 13. Maximal AUC was achieved with an IDA greater than 2 SDs from the average IDA of the other disks (0.86; 95% CI, 0.82–0.90).

## DISCUSSION

CT scanning has excellent usefulness in the evaluation of the bony integrity of the cervical spine; however, diskoligamentous injury, particularly in the absence of listhesis, can be difficult to detect. Although flexion/extension radiography is useful in the gauging of potential cervical spine instability, it can be difficult to perform in the setting of cervical spine trauma and has been shown to have low usefulness in the evaluation of potential diskoligamentous injury.<sup>21–25</sup> Normative data have been published regarding the upper limits of acceptable prevertebral soft tissue thickness on CT scan,<sup>26</sup> and spinous process widening on plain film<sup>27</sup>; however, neither normative data regarding disk widening nor objective criteria for evaluation of potential ADL disruption have been published. Therefore, when evaluating the ADL on CT scan, radiologists are forced to rely on a subjective assessment of disk widening.

The purpose of our study was to evaluate the diagnostic performance of subjective disk space widening on CT scan for determination of ADL disruption and to evaluate if objective criteria based on the IDA can more accurately predict ADL disruption. Our results indicate that subjective disk space widening on CT scan is not adequate for evaluation of ADL disruption—achieving an AUC of only 0.58 (95% CI, 0.52–0.64) and a sensitivity of only 16.4% (95% CI, 10.5%–24.3%)—and that an elevated IDA provides a more objective, reproducible criterion to evaluate potential ADL disruption and guide further imaging.

Of all of the criteria evaluated for the detection of ADL disruption on CT scan, an IDA greater than 2 SDs from the average of the remaining disks offered the best diagnostic accuracy, 0.972 (95% CI, 0.965–0.972), and an AUC of 0.860 (95% CI, 0.817–0.903), with 72.1% sensitivity (95% CI, 63.2%–79.7%) and 100% specificity (95% CI, 99.6%–100%). However, we realize that a test requiring calculation of an SD is impractical for everyday use. Our results, however, also indicate that more practical tests relying on only a single angle measurement, easily performed on most PACS systems, can reliably predict ADL disruption.

Of 1095 total disks with an intact ADL evaluated (in both control patients and in those with ADL disruption at other levels), none had an IDA 18 or greater. We believe that an IDA of 18 or greater should always be considered abnormal and worthy of further evaluation with MR imaging. In our study, subjective assessment of disk widening on CT scan only detected ADL disruption when the IDA was 22 or greater; below this angle, subjective assessment failed to detect any of the abnormal levels. Considering an angle of 18 or greater as always being abnormal will improve detection of ADL disruption beyond subjective evaluation ( $P < .01$ ).

Although an angle of 18 was always abnormal in our study, as a criterion for ADL disruption, it still failed to detect a significant number of abnormal levels (sensitivity, 41.8%; 95% CI, 33.0%–51.1%). An angle of 13 or greater had a similar AUC to an IDA 2 SDs from the

average of the remaining disks (0.854; 95% CI, 0.832–0.876), with a sensitivity of 82.0% (95% CI, 73.7%–88.1%) and a specificity of 89.1% (95% CI, 87.1%–90.9%), with significantly greater ease of use. An IDA of 13 or greater may serve as a screening tool for ADL dis-

ruption, detecting significantly more injured levels than subjective widening alone ( $P < .01$ ), with knowledge that this will result in some false-positive results.

IDA measurements were less sensitive in patients with cervical kyphosis, because an injured disk compresses with flexion, possibly even more easily than a normal disk, and an injured disk may decompress through the disrupted anterior margin. However, in our study, injured disks with normal or decreased IDA in kyphosis usually demonstrated some degree of listhesis related to the ADL injury in combination with other ligamentous or bony injury. Therefore, although the IDA measurement alone did not detect these injured levels, in clinical practice, these abnormal levels may be detected by the overall constellation of findings. Therefore, our study underestimates the overall sensitivity provided by the IDA measurement in clinical practice, as the IDA should never be used in isolation from other imaging or clinical findings suggestive of injury.

In our study, approximately one-quarter of patients with ADL disruption underwent MR imaging because of clinical criteria of persistent pain or neurologic deficit. In consideration of the significant number of

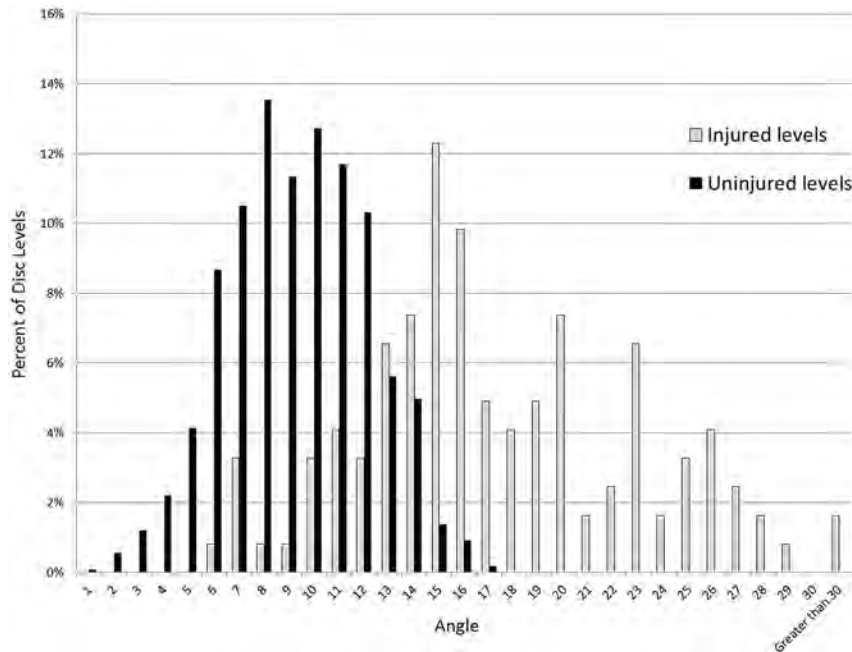


**FIG 3.** Distribution of disk angles among injured and uninjured disks, showing a Gaussian-like distribution of angles among uninjured disks, somewhat overlapping with angles in injured disks predominantly at 14° and below. Above an angle of 14°, there is minimal overlap.

**Table 3. Comparison of diagnostic performance among subjective disk angle measurements and IDA measurements**

	Subjective Disk Widening	IDA of 13	IDA > 2 SD from Other Levels	IDA > 1 SD from Normal Values
Sensitivity (%)	16.4	82.0	72.1	86.1
Specificity (%)	99.4	89.1	100	84.7
PPV (%)	87.0	45.7	100	38.6
NPV (%)	82.3	97.8	97.0	98.2
AUC	0.580	0.854	0.860	0.853
Interpretation	Poor discrimination	Excellent discrimination	Excellent discrimination	Excellent discrimination

**Note:**— NPV indicates negative predictive value; PPV, positive predictive value; SD, standard deviation.

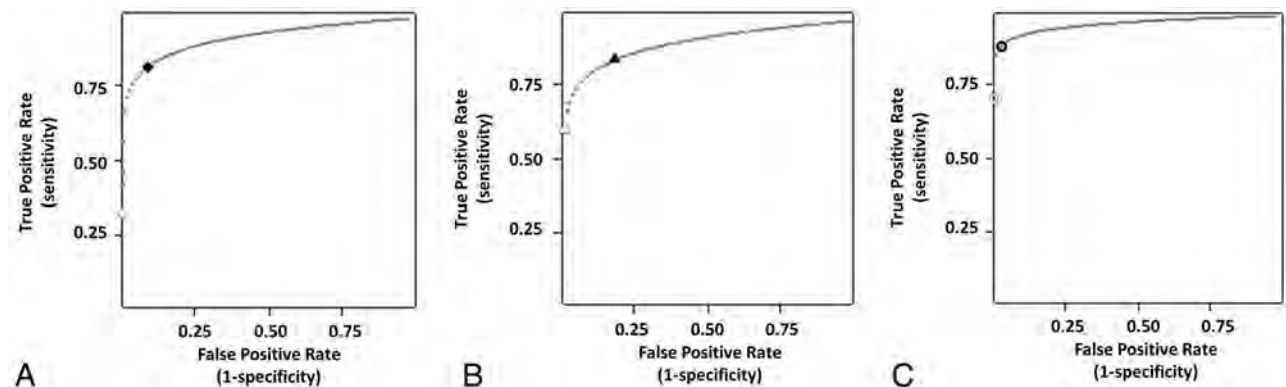


**FIG 4.** ROC curves for IDA measurements. A, ROC curve for progressively smaller IDAs, demonstrating marked increase in sensitivity with only minor loss in specificity as the angle is decreased from 20° (white diamond) to 13° (black diamond). B, ROC curve for deviation of the IDA from normal values, demonstrating an increase in sensitivity with only mild loss in specificity as the range is changed from 2 SDs from normal values (white triangle) to 1 SD (black triangle). C, ROC curve for deviation of IDA from the average IDA of the remaining disks also demonstrating an increase in sensitivity with only mild loss in specificity as the range is changed from 2 SDs from the average (white open circle) to 1 SD (black open circle).

trauma patients with possible cervical injury who are obtunded or are otherwise unable to cooperate with a full clinical examination, an objective, highly sensitive criterion for ADL disruption on CT scanning would be a vital tool to prevent missed injuries in obtunded patients unable to compensate for CT oversights by providing physical examination clues to their injury.

Furthermore, multiple studies have demonstrated that the force required to disrupt the ADL are similar to, if not greater than, the forces required to disrupt the posterior longitudinal ligament and ligamentum flavum.<sup>28,29</sup> These findings suggest that patients with ADL disruption have received a significant blunt force, and if the force is sufficient to disrupt the ADL, they are at higher risk for additional ligamentous injury, making an MR imaging examination of these injuries even more important.

There were limitations to our study. First, as our study was retrospective, some images were evaluated by the same reader who performed the initial diagnostic evaluation. To eliminate potential recall bias, readers were blinded to patient information, and no study was re-evaluated by the same reader within 4 months of the initial reading. Second, we used MR imaging as our reference standard to identify ADL injuries. Although intraoperative correlation would have been ideal, most patients in our study who underwent intraoperative stabilization did not undergo an anterior fusion procedure, rendering direct operative correlation impossible. However, as prior studies have shown the high diagnostic accuracy of MR imaging in the detection of ALL and disk injury,<sup>7-12</sup> we do not believe that this affects our overall conclusions. Furthermore, we attempted to imbue our reference standard with a high specificity by setting stringent imaging criteria for the diagnosis of ADL disruption and requiring concordance between 2 neuroradiologists. A further limitation of the IDA measurement was that although an elevated IDA is associated with ADL disruption, the reverse does not hold true; namely, a normal IDA does not exclude ADL disruption and should not be used to do so. Finally, although our data strongly indicate a useful role for the IDA in cervical spine trauma, further validation of this through a prospective trial would be ideal.

## CONCLUSIONS

In trauma patients, subjective disk widening on CT scan does not accurately detect ADL disruption. An elevated IDA provides a more sensitive, objective, and reproducible measurement to help direct further evaluation with MR imaging. We recommend that an IDA greater than 13 warrants an MR imaging examination to exclude ADL disruption, noting that an IDA greater than 18 is always associated with ADL disruption.

## REFERENCES

1. Ackland HM, Cameron PA, Varma DK, et al. **Cervical spine magnetic resonance imaging in alert, neurologically intact trauma patients with persistent midline tenderness and negative computed tomography results.** *Ann Emerg Med* 2011;58:521-30
2. Harrison JL, Ostlere SJ. **Diagnosing purely ligamentous injuries of the cervical spine in the unconscious trauma patient.** *Br J Radiol* 2004;77:276-78
3. Herkowitz HN, Rothman RH. **Subacute instability of the cervical spine.** *Spine* 1984;9:348-57
4. Kontinen YT, Grönblad M, Antti-Poika I, et al. **Neuroimmunohistochemical analysis of peridiscal nociceptive neural elements.** *Spine* 1990;15:383-86
5. Hampton D, Laros G, McCarron R, et al. **Healing potential of the annulus fibrosus.** *Spine* 1989;14:398-401
6. Cusick JF, Yoganandan N. **Biomechanics of the cervical spine 4: major injuries.** *Clin Biomech* 2002;17:1-20
7. Emery SE, Pathria MN, Wilber RG, et al. **Magnetic resonance imaging of posttraumatic spinal ligament injury.** *J Spinal Disord* 1989;2:229-33
8. Kliewer MA, Gray L, Paver J, et al. **Acute spinal ligament disruption: MR imaging with anatomic correlation.** *J Magn Reson Imaging* 1993;3:855-61
9. Mirvis SE, Geisler FH, Jelinek JJ, et al. **Acute cervical spine trauma: evaluation with 1.5-T MR imaging.** *Radiology* 1988;166:807-16
10. Flanders A, Schaefer D, Doan H, et al. **Acute cervical spine trauma: correlation of MR imaging findings with degree of neurological deficit.** *Radiology* 1990;177:25-33
11. Katzberg R, Benedetti P, Drake C, et al. **Acute cervical spine injuries: prospective MR imaging assessment at a level I trauma center.** *Radiology* 1999;213:203-12
12. Goradia D, Linnau KF, Cohen WA, et al. **Correlation of MR imaging findings with intraoperative findings after cervical spine trauma.** *AJNR Am J Neuroradiol* 2007;28:209-15
13. Newcombe, RG. **Two-sided confidence intervals for the single proportion: comparison of seven methods.** *Stat Med* 1998;17:857-72
14. Lin LI. **A concordance correlation coefficient to evaluate reproducibility.** *Biometrics* 1989;45:255-68
15. McBride GB. **A proposal for strength-of-agreement criteria for Lin's Concordance Correlation Coefficient.** *NIWA Client Report: HAM* 2005;2005-62
16. Hawass NE. **Comparing the sensitivities and specificities of two diagnostic procedures performed on the same group of patients.** *Br J Radiol* 199;70:360-66
17. Eng J. **ROC analysis: web-based calculator for ROC curves.** Baltimore: Johns Hopkins University [updated 2006 May 17]. Available at: <http://www.jrocf.it.org>. Accessed October 10, 2012
18. Hosmer DW, Lemeshow S. *Applied Logistic Regression*, 2nd ed. New York: Wiley; 2000:156-164
19. Hanley JA, McNeil BJ. **The meaning and use of the area under a receiver operating characteristic (ROC) curve.** *Radiology* 1982;143:29-36
20. Hanley JA, McNeil BJ. **A method of comparing the areas under receiver operating characteristic curves derived from the same cases.** *Radiology* 1983;148:839-43
21. Duane TM, Scarcella M, Cross J, et al. **Do flexion extension plain films facilitate treatment after trauma?** *Am Surg* 2010;76:1351-54
22. Duane TM, Cross J, Scarcella N, et al. **Flexion-extension cervical spine plain films compared with MRI in the diagnosis of ligamentous injury.** *Am Surg* 2010;76:595-98
23. Gale SC, Gracias VH, Reilly PM, et al. **The inefficiency of plain radiography to evaluation the cervical spine after blunt trauma.** *J Trauma* 2005;59:1121-25
24. Freedman I, van Gelderen D, Cooper DJ, et al. **Cervical spine assessment in the unconscious trauma patient: a major trauma service's experience with passive flexion-extension radiography.** *J Trauma* 2005;58:1183-88
25. Insko EK, Gracias VH, Gupta R, et al. **Utility of flexion and extension radiographs of the cervical spine in the acute evaluation of blunt trauma.** *J Trauma* 2002;53:426-29
26. Rojas C, Vermess D, Bertozzi JC, et al. **Normal thickness and appearance of the prevertebral soft tissues on multidetector CT.** *AJNR Am J Neuroradiol* 2009;30:136-41
27. Eubanks A, Hipp J, Lador R, et al. **Reference data for assessing widening between spinous processes in the cervical spine and the responsiveness of these measures to detecting abnormalities.** *Spine J* 2010;10:230-37
28. Bass CR, Lucas SR, Salzar RS, et al. **Failure properties of cervical spinal ligaments under fast strain rate deformations.** *Spine* 2007;32:E7-13
29. Stemper BD, Yoganandan N, Pintar FA, et al. **Anterior longitudinal ligament injuries in whiplash may lead to cervical instability.** *Med Eng Phys* 2006;28:515-24



# 2014 Combined Scientific Meeting

Imaging and Radiation in Personalised Medicine

4-7 September 2014 | Melbourne Convention and Exhibition Centre

[www.csm2014.com](http://www.csm2014.com)



**Submit your abstract for 2014 CSM!**

Visit our website to find out more:  
[www.csm2014.com/abstract-information](http://www.csm2014.com/abstract-information)  
Submission deadline: **26 March 2014**

2014 CSM is proudly brought to you by:



## Simplify the MOC Process

## CMEgateway.org



## Manage your CME Credits Online

### It's Easy and Free!

Log on to CME Gateway to:

- View or print reports of your CME credits from multiple societies from a single access point.
- Print an aggregated report or certificate from each participating organization.
- Link to SAMs and other tools to help with maintenance of certification.

### American Board of Radiology (ABR) participation!

By activating ABR in your organizational profile, your MOC-fulfilling CME and SAM credits can be transferred to your own personalized database on the ABR Web site.

### Sign Up Today!

go to [CMEgateway.org](http://CMEgateway.org)

#### Available to Members of Participating Societies

American Board of Radiology (ABR)	Radiological Society of North America (RSNA)
American College of Radiology (ACR)	Society of Interventional Radiology (SIR)
American Roentgen Ray Society (ARRS)	SNM
American Society of Neuroradiology (ASNR)	The Society for Pediatric Radiology (SPR)
Commission on Accreditation of Medical Physics Educational Programs, Inc. (CAMPEP)	

THE UNIVERSITY OF TEXAS

**MDAnderson  
Cancer Center**

Making Cancer History®

The Section of Neuroradiology/ Head and Neck Radiology, within the Department of Diagnostic Radiology, has an immediate opening for a full-time, clinical faculty appointment. The Department of Diagnostic Radiology provides comprehensive diagnostic imaging services to patients with tumors. The department is the largest of the five departments in the Division of Diagnostic Imaging and the largest department within the institution.

The candidate must have a medical degree, a board-certification by the American Board of Radiology, licensure by the Texas State Board of Medical Examiners, certification in either Basic Life Support (BLS) or Advanced Cardiac Life Support (ACLS), and have fellowship training in Neuroradiology, Head and Neck Radiology. Prior research experience and publications in Brain Tumor Imaging or Head and Neck Imaging is highly desirable, as well as a certificate of added qualification in Neuroradiology.

Serious applicants should send a letter of interest, CV and list of references to: [plhon@mdanderson.org](mailto:plhon@mdanderson.org)

MD Anderson is an equal opportunity employer and does not discriminate on the basis of race, color, national origin, gender, sexual orientation, age, religion, disability or veteran status except where such distinction is required by law. All positions at The University of Texas MD Anderson Cancer Center are security sensitive and subject to examination of criminal history record information. Smoke-free and drug-free facility.

**Assistant Professor  
Clinical Faculty Appointment  
Diagnostic Radiology**

Ashok J. Kumar, M.D.  
Professor and Chief of Neuroradiology/  
Head and Neck Radiology  
Patricia Hon  
Office Manager  
Department of Diagnostic Radiology,  
Unit 1459  
The University of Texas  
MD Anderson Cancer Center  
1400 Pressler Street  
Houston, TX 77030-4009

**UCSF**

University of California  
San Francisco

*advancing health worldwide™*

## NEURORADIOLOGISTS

The Department of Radiology and Biomedical Imaging is seeking two Neuroradiologists for academic track faculty positions. The candidates will be appointed at the level of Assistant, Associate or Full Professor in the Clinical X or In Residence series depending on qualifications.

Responsibilities include clinical service, teaching and research. The applicants should be interested in developing a research program in one or more of the following areas: brain tumor imaging, psychiatric imaging, molecular imaging, pediatric neuroimaging, comparative effectiveness research in neuroimaging, or cerebrovascular imaging.

The incumbents will be expected to supervise and teach residents, fellows and medical students in neuroradiology. Obligations will include work at UCSF Moffitt/Long Hospital, the VA Medical Center, UCSF/Mt. Zion, Mission Bay Hospital and/or SF General Hospital, which are affiliated hospitals that neuroradiology covers.

This position requires an M.D. degree, the ability to practice medicine in California, board eligibility or board certification in Radiology, expertise in neuroradiology and research methodologies, and completion of at least 1 year, and preferably 2 years, of fellowship training in neuroradiology. Applicants will be expected to be board certified (or eligible) and to obtain a certificate of added qualification in neuroradiology.

Please apply online with CV and cover letter at:  
<http://apptrkr.com/408181>

In the cover letter please include a brief description of prior teaching and research experience.

UCSF seeks candidates whose experience, teaching, research, or community service has prepared them to contribute to our commitment to diversity and excellence.

UCSF is an Equal Opportunity/Affirmative Action/equal Employer. The University undertakes affirmative action to assure equal employment opportunity for underutilized minorities and women, for persons with disabilities, and for covered veterans. All qualified applicants are encouraged to apply, including minorities and women.

## NEURORADIOLOGISTS AVAILABLE

Attract the best neuroradiologists  
with an ad on the  
American Society of Neuroradiology  
Web site.

This free service is located at:  
<http://classifieds.asnr.org/>

DOTAREM® (gadoterate meglumine) injection, for intravenous use  
Initial U.S. Approval: 2013

**BRIEF SUMMARY OF PRESCRIBING INFORMATION**  
**CONSULT PACKAGE INSERT FOR FULL PRESCRIBING INFORMATION**

**WARNING: NEPHROGENIC SYSTEMIC FIBROSIS (NSF)**

Gadolinium-based contrast agents (GBCAs) increase the risk for NSF among patients with impaired elimination of the drugs. Avoid use of GBCAs in these patients unless the diagnostic information is essential and not available with non-contrast MRI or other modalities. NSF may result in fatal or debilitating fibrosis affecting the skin, muscle and internal organs.

- The risk for NSF appears highest among patients with:
  - Chronic, severe kidney disease (GFR < 30 mL/min/1.73m<sup>2</sup>), or
  - Acute kidney injury.
- Screen patients for acute kidney injury and other conditions that may reduce renal function. For patients at risk for chronically reduced renal function (e.g. age > 60 years, hypertension, diabetes), estimate the glomerular filtration rate (GFR) through laboratory testing (5.1).
- For patients at highest risk for NSF, do not exceed the recommended DOTAREM dose and allow a sufficient period of time for elimination of the drug from the body prior to any re-administration [see *Warnings and Precautions (5.1)*].

**1 INDICATIONS AND USAGE**

DOTAREM is a gadolinium-based contrast agent indicated for intravenous use with magnetic resonance imaging (MRI) in brain (intracranial), spine and associated tissues in adult and pediatric patients (2 years of age and older) to detect and visualize areas with disruption of the blood brain barrier (BBB) and/or abnormal vascularity. (1)

**4 CONTRAINDICATIONS**

History of clinically important hypersensitivity reactions to DOTAREM. (4)

**5 WARNINGS AND PRECAUTIONS**

**5.1 Nephrogenic Systemic Fibrosis**

Gadolinium-based contrast agents (GBCAs) increase the risk for nephrogenic systemic fibrosis (NSF) among patients with impaired elimination of the drugs. Avoid use of GBCAs among these patients unless the diagnostic information is essential and not available with non-contrast MRI or other modalities. The GBCA-associated NSF risk appears highest for patients with chronic, severe kidney disease (GFR < 30 mL/min/1.73m<sup>2</sup>) as well as patients with acute kidney injury. The risk appears lower for patients with chronic, moderate kidney disease (GFR 30 - 59 mL/min/1.73m<sup>2</sup>) and little, if any, for patients with chronic, mild kidney disease (GFR 60 - 89 mL/min/1.73m<sup>2</sup>). NSF may result in fatal or debilitating fibrosis affecting the skin, muscle and internal organs. Report any diagnosis of NSF following DOTAREM administration to Guerbet LLC (1-877-729-6679) or FDA (1-800-FDA-1088 or www.fda.gov/medwatch).

Screen patients for acute kidney injury and other conditions that may reduce renal function. Features of acute kidney injury consist of rapid (over hours to days) and usually reversible decrease in kidney function, commonly in the setting of surgery, severe infection, injury or drug-induced kidney toxicity. Serum creatinine levels and estimated GFR may not reliably assess renal function in the setting of acute kidney injury. For patients at risk for chronically reduced renal function (e.g., age > 60 years, diabetes mellitus or chronic hypertension), estimate the GFR through laboratory testing.

Among the factors that may increase the risk for NSF are repeated or higher than recommended doses of a GBCA and the degree of renal impairment at the time of exposure. Record the specific GBCA and the dose administered to a patient. For patients at highest risk for NSF, do not exceed the recommended DOTAREM dose and allow a sufficient period of time for elimination of the drug prior to re-administration. For patients receiving hemodialysis, physicians may consider the prompt initiation of hemodialysis following the administration of a GBCA in order to enhance the contrast agent's elimination. The usefulness of hemodialysis in the prevention of NSF is unknown [see *Dosage and Administration (2)* and *Clinical Pharmacology (12)*].

**5.2 Hypersensitivity Reactions**

Anaphylactic and anaphylactoid reactions have been reported with DOTAREM, involving cardiovascular, respiratory, and/or cutaneous manifestations. Some patients experienced circulatory collapse and died. In most cases, initial symptoms occurred within minutes of DOTAREM administration and resolved with prompt emergency treatment [see *Adverse Reactions (6)*].

- Before DOTAREM administration, assess all patients for any history of a reaction to contrast media, bronchial asthma and/or allergic disorders. These patients may have an increased risk for a hypersensitivity reaction to DOTAREM.
- Administer DOTAREM only in situations where trained personnel and therapies are promptly available for the treatment of hypersensitivity reactions, including personnel trained in resuscitation.
- During and following DOTAREM administration, observe patients for signs and symptoms of hypersensitivity reactions.

**5.3 Acute Kidney Injury**

In patients with chronically reduced renal function, acute kidney injury requiring dialysis has occurred with the use of GBCAs. The risk of acute kidney injury may increase with increasing dose of the contrast agent; administer the lowest dose necessary for adequate imaging. Screen all patients for renal impairment by obtaining a history and/or laboratory tests. Consider follow-up renal function assessments for patients with a history of renal dysfunction.

**5.4 Extravasation and Injection Site Reactions**

Ensure catheter and venous patency before the injection of DOTAREM. Extravasation into tissues during DOTAREM administration may result in tissue injury [see *Nonclinical Toxicology (13.2)*].

**6 ADVERSE REACTIONS**

GBCAs have been associated with a risk for NSF [see *Warnings and Precautions (5.1)*]. NSF has not been reported in patients with a clear history of exposure to DOTAREM alone. For hypersensitivity reactions and acute kidney injury see *Warnings and Precautions (5.2)* and (5.3).

**6.1 Clinical Studies Experience**

Because clinical trials are conducted under widely varying conditions, adverse reaction rates observed in the clinical trials of a drug cannot be directly compared to rates in the clinical trials of another drug and may not reflect the rates observed in clinical practice.

The data described below reflect DOTAREM exposure in 2813 patients, representing 2672 adults and 141 pediatric patients. Overall, 55% of the patients were men. In clinical trials where ethnicity was recorded the ethnic distribution was 74% Caucasian, 12% Asian, 4% Black, and 10% others. The average age was 53 years (range from 0.1 to 97 years).

Overall, 3.9% of patients reported at least one adverse reaction, primarily occurring immediately or several days following DOTAREM administration. Most adverse reactions were mild or moderate in severity and transient in nature.

Table 1 lists adverse reactions that occurred in ≥ 0.2% patients who received DOTAREM.

**Table 1: Adverse Reactions in Clinical Trials**

Reaction	Rate (%) n = 2813
Nausea	0.6%
Headache	0.5%
Injection Site Pain	0.4%
Injection Site Coldness	0.2%
Burning Sensation	0.2%

Adverse reactions that occurred with a frequency < 0.2% in patients who received DOTAREM include: feeling cold, rash, somnolence, fatigue, dizziness, vomiting, pruritus, paresthesia, dysgeusia, pain in extremity, anxiety, hypertension, palpitations, oropharyngeal discomfort, serum creatinine increased and injection site reactions, including site inflammation, extravasation, pruritus, and warmth.

**Adverse Reactions in Pediatric Patients**

During clinical trials, 141 pediatric patients (7 aged < 24 months, 33 aged 2 - 5 years, 58 aged 6 - 11 years and 43 aged 12 - 17) received DOTAREM. Overall, 6 pediatric patients (4.3%) reported at least one adverse reaction following DOTAREM administration. The most frequently reported adverse reaction was headache (1.5%). Most adverse events were mild in severity and transient in nature, and all patients recovered without treatment.

**6.2 Postmarketing Experience**

The following additional adverse reactions have been identified during postmarketing use of DOTAREM. Because these reactions are reported voluntarily from a population of uncertain size, it is not always possible to reliably estimate their frequency or establish a causal relationship to drug exposure.

- bradycardia, tachycardia, arrhythmia
- hypersensitivity / anaphylactoid reactions including cardiac arrest, respiratory arrest, cyanosis, pharyngeal edema, laryngospasm, bronchospasm, angioedema, conjunctivitis, ocular hyperemia, eyelid edema, lacrimation increased, hyperhidrosis, urticaria

- coma, convulsion, syncope, presyncope, parosmia, tremor
- muscle contracture, muscle weakness
- diarrhea, salivary hypersecretion
- malaise, fever
- NSF, in patients whose reports were confounded by the receipt of other GBCAs or in situations where receipt of other GBCAs could not be ruled out. No unconfounded cases of NSF have been reported with DOTAREM.
- superficial phlebitis

**7 DRUG INTERACTIONS**

DOTAREM does not interfere with serum and plasma calcium measurements determined by colorimetric assays. Specific drug interaction studies with DOTAREM have not been conducted.

**8 USE IN SPECIFIC POPULATIONS**

**8.1 Pregnancy**

**Pregnancy Category C**

There are no adequate and well-controlled studies with DOTAREM conducted in pregnant women. Limited published human data on exposure to other GBCAs during pregnancy did not show adverse effects in exposed neonates. No effects on embryo fetal development were observed in rats or rabbits at doses up to 10 mmol/kg/day in rats or 3 mmol/kg/day in rabbits. The doses in rats and rabbits were respectively 16 and 10 times the recommended human dose based on body surface area. DOTAREM should be used during pregnancy only if the potential benefit justifies the potential risk to the fetus. While it is unknown if DOTAREM crosses the human placenta, other GBCAs do cross the placenta in humans and result in fetal exposure.

Reproductive and developmental toxicity studies were conducted with gadoterate meglumine in rats and rabbits. Gadoterate meglumine was administered intravenously in doses of 0, 2, 4 and 10 mmol/kg/day (or 3.2, 6.5 and 16.2 times the recommended human dose based on body surface area) to female rats for 14 days before mating throughout the mating period and until gestation day (GD) 17. Pregnant rabbits were intravenously administered gadoterate meglumine at the dose levels of 0, 1, 3 and 7 mmol/kg/day (or 3.3, 10 and 23 times the human doses based on body surface area) from GD6 to GD19. No effects on embryo fetal development were observed in rats or rabbits at doses up to 10 mmol/kg/day in rats or 3 mmol/kg/day in rabbits. Maternal toxicity was observed in rats at 10 mmol/kg/day (or 16 times the human dose based on body surface area) and in rabbits at 7 mmol/kg/day (23 times the human dose based on body surface area).

**8.3 Nursing Mothers**

It is not known whether DOTAREM is excreted in human milk. Limited case reports on use of GBCAs in nursing mothers indicate that 0.01 to 0.04% of the maternal gadolinium dose is excreted in human breast milk. Because many drugs are excreted in human milk, exercise caution when DOTAREM is administered to a nursing woman. Nonclinical data show that gadoterate meglumine is excreted into breast milk in very small amounts (< 0.1% of the dose intravenously administered) and absorption via the gastrointestinal tract is poor.

**8.4 Pediatric Use**

The safety and efficacy of DOTAREM at a single dose of 0.1 mmol/kg have been established in pediatric patients from 2 to 17 years of age. No dosage adjustment according to age is necessary in this population [See *Dosage and Administration (2)* and *Clinical Studies (14)*]. The safety and efficacy of DOTAREM have not been established in pediatric patients below 2 years of age. GFR does not reach adult levels until 1 year of age [see *Warnings and Precautions (5.1)*].

**8.5 Geriatric Use**

In clinical studies of DOTAREM, 900 patients were 65 years of age and over, and 312 patients were 75 years of age and over. No overall differences in safety or efficacy were observed between these subjects and younger subjects. In general, use of DOTAREM in elderly patients should be cautious, reflecting the greater frequency of impaired renal function and concomitant disease or other drug therapy. No age-related dosage adjustment is necessary.

**8.6 Renal Impairment**

No DOTAREM dosage adjustment is recommended for patients with renal impairment. Gadoterate meglumine can be removed from the body by hemodialysis [see *Warnings and Precautions (5.1)* and *Clinical Pharmacology (12.3)*].

**10 OVERDOSAGE**

DOTAREM administered to healthy volunteers and to patients at cumulative doses up to 0.3 mmol/kg was tolerated in a manner similar to lower doses. Adverse reactions to overdosage with DOTAREM have not been reported. Gadoterate meglumine can be removed from the body by hemodialysis [see *Clinical Pharmacology (12.3)*].

**13 NONCLINICAL TOXICOLOGY**

**13.1 Carcinogenesis, Mutagenesis, Impairment of Fertility**

Long-term animal studies have not been performed to evaluate the carcinogenic potential of gadoterate meglumine. Gadoterate meglumine did not demonstrate mutagenic potential in *in vitro* bacterial reverse mutation assays (Ames test) using *Salmonella typhimurium*, in an *in vitro* chromosome aberration assay in Chinese hamster ovary cells, in an *in vitro* gene mutation assay in Chinese hamster lung cells, nor in an *in vivo* mouse micronucleus assay.

No impairment of male or female fertility and reproductive performance was observed in rats after intravenous administration of gadoterate meglumine at the maximum tested dose of 10 mmol/kg/day (16 times the maximum human dose based on surface area), given during more than 9 weeks in males and more than 4 weeks in females. Sperm counts and sperm motility were not adversely affected by treatment with the drug.

**13.2 Animal Toxicology and/or Pharmacology**

Local intolerance reactions, including moderate irritation associated with infiltration of inflammatory cells were observed after perivenous injection in rabbits suggesting the possibility of local irritation if the contrast medium leaks around the veins in a clinical setting [see *Warnings and Precautions (5.4)*].

**17 PATIENT COUNSELING INFORMATION**

**17.1 Nephrogenic Systemic Fibrosis**

Instruct patients to inform their healthcare provider if they:

- have a history of kidney disease, or
  - have recently received a GBCA.
- GBCAs increase the risk for NSF among patients with impaired elimination of the drugs. To counsel patients at risk for NSF:
- Describe the clinical manifestations of NSF.
  - Describe procedures to screen for the detection of renal impairment.
- Instruct the patients to contact their physician if they develop signs or symptoms of NSF following DOTAREM administration, such as burning, itching, swelling, scaling, hardening and tightening of the skin; red or dark patches on the skin; stiffness in joints with trouble moving, bending or straightening the arms, hands, legs or feet; pain in the hip bones or ribs; or muscle weakness.

**17.2 Common Adverse Reactions**

Inform patients that they may experience:

- Reactions along the venous injection site, such as mild and transient burning or pain or feeling of warmth or coldness at the injection site.
- Side effects of headache, nausea, abnormal taste and feeling hot.

**17.3 General Precautions**

Instruct patients receiving DOTAREM to inform their physician if they:

- Are pregnant or breastfeeding.
- Have a history of allergic reaction to contrast media, bronchial asthma or allergy.
- Are taking any medications.

Rx Only



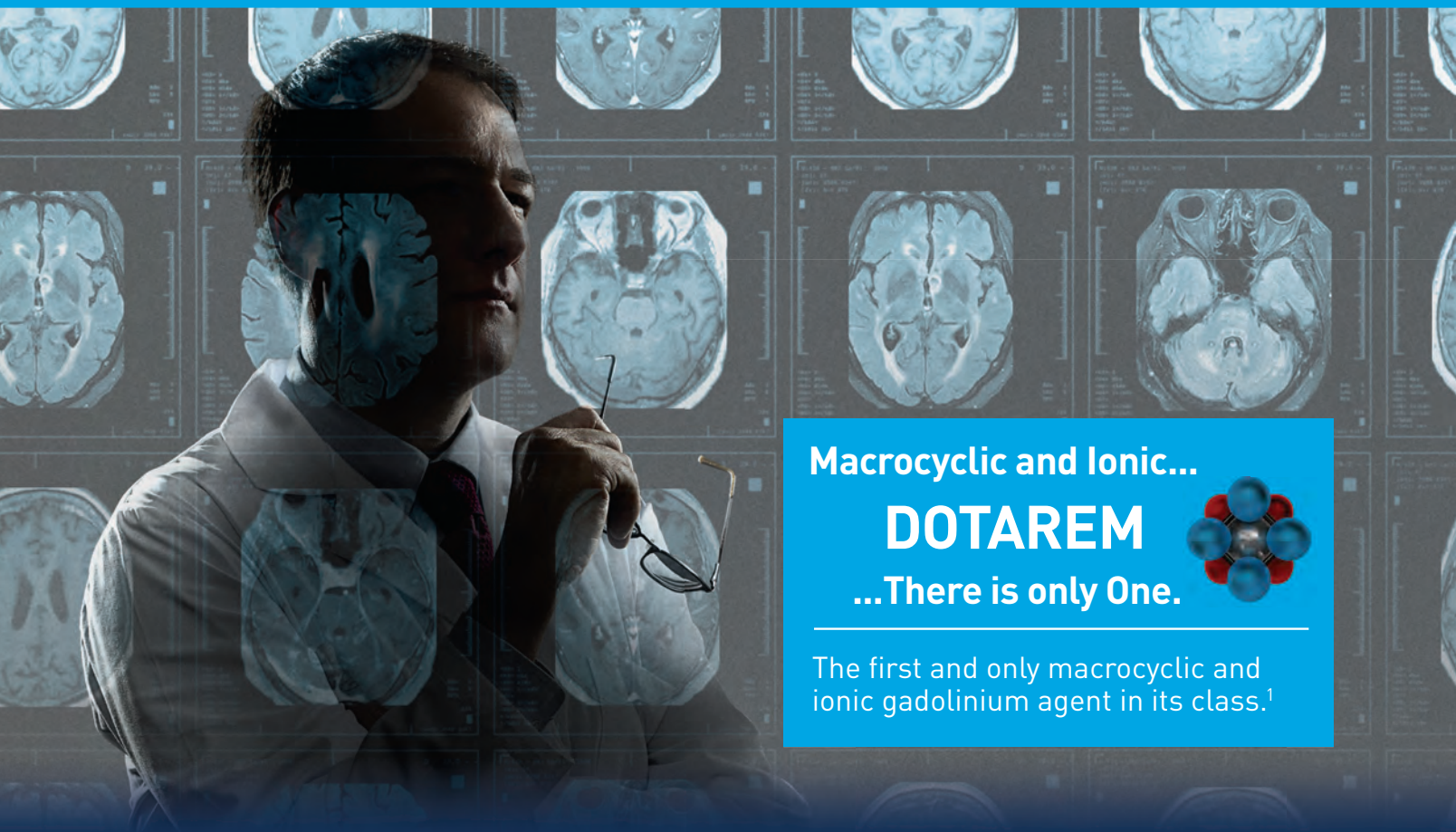
Pre-filled syringes manufactured by Catalent, Belgium for Guerbet  
Vials manufactured by Recipharm, France for Guerbet

GU06131043  
Revised 06/2013



# DOTAREM<sup>®</sup>

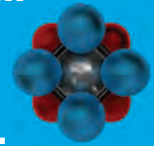
(gadoterate meglumine) Injection



Macrocyclic and Ionic...

## DOTAREM

...There is only One.



The first and only macrocyclic and ionic gadolinium agent in its class.<sup>1</sup>

Global clinical experience with over **37 million doses** administered outside the US.<sup>2</sup>

#### INDICATION<sup>1</sup>

DOTAREM is a gadolinium-based contrast agent indicated for intravenous use with magnetic resonance imaging (MRI) in brain (intracranial), spine and associated tissues in adult and pediatric patients (2 years of age and older) to detect and visualize areas with disruption of the blood brain barrier (BBB) and/or abnormal vascularity.

#### IMPORTANT SAFETY INFORMATION<sup>1</sup>

##### WARNING: NEPHROGENIC SYSTEMIC FIBROSIS (NSF)

Gadolinium-based contrast agents (GBCAs) increase the risk for NSF among patients with impaired elimination of the drugs. Avoid use of GBCAs in these patients unless the diagnostic information is essential and not available with non-contrast MRI or other modalities. NSF may result in fatal or debilitating fibrosis affecting the skin, muscle and internal organs.

- The risk for NSF appears highest among patients with:
  - Chronic, severe kidney disease (GFR < 30 mL/min/1.73m<sup>2</sup>), or
  - Acute kidney injury.
- Screen patients for acute kidney injury and other conditions that may reduce renal function. For patients at risk for chronically reduced renal function (e.g. age > 60 years, hypertension, diabetes), estimate the glomerular filtration rate (GFR) through laboratory testing (5.1).
- For patients at highest risk for NSF, do not exceed the recommended DOTAREM dose and allow a sufficient period of time for elimination of the drug from the body prior to any re-administration (5.1).

Contraindicated in patients with a history of clinically important hypersensitivity reactions to DOTAREM.

The possibility of serious or life-threatening anaphylactoid/anaphylactic reactions with cardiovascular, respiratory or cutaneous manifestations, ranging from mild to severe, including death, should be considered. Monitor patients closely for need of emergency cardiorespiratory support.

In patients with chronically reduced renal function, acute kidney injury requiring dialysis has occurred with the use of GBCAs. The risk of acute kidney injury may increase with increasing dose of the contrast agent; administer the lowest dose necessary for adequate imaging. Screen all patients for renal impairment by obtaining a history and/or laboratory tests. Consider follow-up renal function assessments for patients with a history of renal dysfunction.

The most common adverse reactions associated with DOTAREM in clinical studies were nausea, headache, injection site pain, injection site coldness, and burning sensation.

For more information about DOTAREM, including full Boxed WARNING, please see the Full Prescribing Information.

**Please see adjacent Brief Summary of Prescribing Information.**

DOTAREM is a registered trademark of Guerbet and is available by prescription only.

GU09131071

**References:** 1. Dotarem [package insert]. Bloomington, IN: Guerbet LLC; 2013. 2. Data on file, Guerbet LLC.